Springer Proceedings in Physics 178

Vinod Kumar Jain
Sunita Rattan
Abhishek Verma *Editors*

Recent Trends in Materials and Devices

Proceedings ICRTMD 2015

Springer

Springer Proceedings in Physics

Volume 178

The series Springer Proceedings in Physics, founded in 1984, is devoted to timely reports of state-of-the-art developments in physics and related sciences. Typically based on material presented at conferences, workshops and similar scientific meetings, volumes published in this series will constitute a comprehensive up-to-date source of reference on a field or subfield of relevance in contemporary physics. Proposals must include the following:

- name, place and date of the scientific meeting
- a link to the committees (local organization, international advisors etc.)
- scientific description of the meeting
- list of invited/plenary speakers
- an estimate of the planned proceedings book parameters (number of pages/articles, requested number of bulk copies, submission deadline).

More information about this series at http://www.springer.com/series/361

Vinod Kumar Jain · Sunita Rattan
Abhishek Verma
Editors

Recent Trends in Materials and Devices

Proceedings ICRTMD 2015

Springer

Editors
Vinod Kumar Jain
Amity Institute for Advanced Research and Studies
Amity University
Noida, Uttar Pradesh
India

Abhishek Verma
Amity Institute for Advanced Research and Studies
Amity University
Noida, Uttar Pradesh
India

Sunita Rattan
Amity Institute of Applied Sciences
Amity University
Noida, Uttar Pradesh
India

ISSN 0930-8989 ISSN 1867-4941 (electronic)
Springer Proceedings in Physics
ISBN 978-3-319-29095-9 ISBN 978-3-319-29096-6 (eBook)
DOI 10.1007/978-3-319-29096-6

Library of Congress Control Number: 2016950908

Printed on acid-free paper

This Springer imprint is published by Springer Nature
The registered company is Springer International Publishing AG
The registered company address is: Gewerbestrasse 11, 6330 Cham, Switzerland

Preface

The emerging development in the field of materials and devices are some of the most important factors in driving the growth of a nation's economy because of its potential contribution to manufacturing processes and innovative products. It is heartening to see that how during the past few years, the niches for research in the area of material science and technologies have multiplied exponentially and how the material scientists are contributing to global progress in the field.

The conference was organized with the aim to provide a common forum for eminent scientists, technologists, entrepreneurs, and scholars from various disciplines to present their work and discuss the latest advances and innovations in this exciting area of research. Materials science remains intrinsically interdisciplinary and the integration of different disciplines of sciences and outcome of R&D efforts from laboratory to practical devices was one of the focal themes of this conference wherein our faculty and students were exposed to the latest advancements in these fields. The conference provided an opportunity for the participants to interact and develop collaborative partnership.

The Book "*Recent Trends in Materials and Devices*" comprises of scientific contributions from different veins of semiconductors, composites, polymeric materials, devices, and the other related technologies. The contributions have been made by different researchers and eminent scientist from all over the world, who presented their papers in this International Conference on the Recent Trends in Materials and Devices, 2015. In view of the great efforts and initiative of the Government of India, especially the "Make in India" program, most of the NRI & PIO scientists, academicians, and technocrats are willing to help our country especially in research & development in the area of materials and devices leading to product development and production. The chapters include various latest and significant topics i.e. *Semiconductor Materials and Devices, Smart Materials, Polymeric Materials, Sensors, Photovoltaics and Energy Storage, Optoelectronics, Nanotechnology and Nanomaterials, MEMS and NEMS, and Emerging Technologies.*

Part I of the book gives the cutting-edge technologies in the field of *Nanotechnology and Nanomaterials*. It includes the latest findings of eminent

scientists discussing the thermal characterization of SWCNT and tungsten oxide-based nanomaterials; Carbon the future of nanomaterials; antireflection properties of nanoparticles assist black silicon for 3rd generation solar cells; dye removal using nanocellulose; thermos-physical properties of nanoparticle-enhanced phase change materials for thermal energy storage; silicone nanowire based transistors; surface engineering of colloidal quantum dots; graphene nanoballs; water splitting; nanocomposites; nanomaterial based sensors; and a lots more. The latest work in the field of *Optoelectronics* is compiled in Part II, such as structural and optical properties of single crystalline cerium-doped ZnO thin films; tailoring the band structures of GaSb and $InP_{1-x}Bi_x$ for LASERS, photodetectors, etc.; efficient metal clad optical waveguide polarizer. Part III includes the pioneering and front-line outcomes in the arena of *Photovoltaics and Energy Storage*, from the research work of various eminent scientists and young researchers. The contributions comprises of effect of silver nanoparticles as surface plasmonic layer to enhance efficiency of 3rd generation solar cells; graded index antireflection coating for efficient solar cells; dye-sensitized solar cells; photonic crystals as reflection and diffraction gratings for light trapping; synthesis of Cu_2ZnSnS_4 (CZTS); analysis of SnS nanolayer on ZnO nanowires; MWCNT for energy storage/conversion devices; etc. Part IV comprises the latest findings on *Sensors*, which includes the work such as Lossy Mode Resonance Sensor; Dual Dielectric p-MOSFET as Cumulative Gamma Dose Sensor. The contributions in the trust area of *Polymeric Materials* are discussed in Part V, which contains polymer nanocomposite films for energy storage applications; polymer separator for energy storage devices; efficient nanofiller embedded polymeric films; polypropylene/glass fiber composites for low cost orthotic aid. Part VI includes *Semiconductor Materials and Devices*, where the latest observations have been discussed on properties of nanocrystalline PbS films; Synthesis and properties of inorganic organic chloride-based perovskite; design, simulation, and analysis of 4×1 Mux at 90 nm CMOS. Further, in Part VII the cutting-edge researches from various eminent scientists and young scholars have been reported. It includes the clean energy harvesting using rare-earth magnet and ferro-fluid; findings on nonvolatile memory device applications; strengthen properties of cast Cu–Al alloys processed by cryorolling; twist grain boundary phases in liquid crystals; capping-ligand effect on colloidal CIGSe nanocrystals for thin film solar cell applications; and more findings. In the last, Part VIII includes the latest outcomes of various *Emerging Technologies*, such as novel design of fractal antenna; Nematic liquid crystal; and Carbon nanotube FET-based inverter. These contributory papers were full of new scientific knowledge, thought provoking ideas, skills, brain storming discussions, and exchange of ideas. Through this, every latest findings and researches will go ahead to our scientific world.

We are sure that all the latest results and findings reported here will be useful to the young researchers and scientists working in these areas.

These conference-related papers and the rich scientific-knowledge exchanged the result from the efforts of a large team of people who volunteered their time to serve the ICRTMD conference. We are indebted to all of them for their assistance and support. It is not possible to thank all of these individuals, but we would

like to thank, on behalf of the ICRTMD 2015, a number of people who made particularly significant contributions.

The editors wish to place on record our appreciation to Dr. Ashok K. Chauhan, Chief Patron—ICRTMD 2015 and Founder President, Amity University, Noida for his continuous guidance and encouragement to organize this important conference. Editors are also highly thankful to Dr. Balvinder Shukla, Vice Chancellor, Amity University, for her tremendous support, in making this conference a success event. Our sincere thanks and gratitude goes to Dr. Sangeeta Tiwari, Dr. R.S. Pandey, Dr. Prashant Shukla, and all the members of International Conference on the Recent Trends in Materials and Devices, 2015 (jointly organized by Amity Institute for Advanced Research and Studies (AIARS) and Amity Institute of Applied Sciences (AIAS), Amity University, Noida), for their support in organizing this conference.

Noida, India

Vinod Kumar Jain
Sunita Rattan
Abhishek Verma

Contents

Contributors

Abhinav Department of Electronic Science, Kurukshetra University, Kurukshetra, Haryana, India

Ishita Aggarwal Department of Electronics and Communication Engineering, Amity University, Noida, Uttar Pradesh, India

Shruti Agnihotri Centre for Physical Sciences, Central University of Punjab, Bathinda, India

M. Ahamed CSIR Network of Institutes for Solar Energy (NISE), CSIR-National Physical Laboratory, New Delhi, India; Amity Institute of Nanotechnology, Amity University, Noida, India

Arham Shareef Ahmed Department of Applied Physics, Aligarh Muslim University, Aligarh, India

Sidra Aijaz Department of Applied Physics, Amity Institute of Applied Sciences, Amity University, Noida, India

Firoz Alam Photovoltaic Laboratory, Centre for Energy Studies, Indian Institute of Technology Delhi, New Delhi, Delhi, India

Javid Ali Department of Physics, Jamia Millia Islamia, New Delhi, India

Ekta Arora Department of Electronics Science, Kurukshetra University, Kurukshetra, Haryana, India

Vijay K. Arora Department of Electrical Engineering and Physics, Wilkes University, Wilkes-Barre, USA

Anil Arya Centre for Physical Sciences, Central University of Punjab, Bathinda, India

Manisha Bajpai Soft Materials Research Laboratory, Centre of Material Sciences, Institute of Interdisciplinary Studies, University of Allahabad, Allahabad, India

Shankar Baliga General Monitors, Inc., MSA Company, Lake Forest, CA, USA

Jaspal P. Bange Department of Electronics, North Maharashtra University, Jalgaon, India

Bidyut Barman Amity Institute of Advance Research and Studies (Material & Devices), Amity University, Noida, Uttar Pradesh, India; Amity Institute of Renewable and Alternate Energy, Amity University, Noida, Uttar Pradesh, India

Rupesh Kumar Basniwal Amity Institute of Advanced Research and Studies (M&D), Amity University, Noida, Uttar Pradesh, India

S.S. Bawa Polymeric and Soft Material Section, CSIR (NPL), New Delhi, India

P.K. Bhatnagar Department of Electronic Science, University of Delhi South Campus, New Delhi, India

Chandni Bhatt Centre for Physical Sciences, Central University of Punjab, Bathinda, Punjab, India

Tejashree M. Bhave Department of Applied Physics, Defence Institute of Advanced Technology, Pune, India

Shalaka V. Bhole Department of Electronics Engineering and Technology, North Maharashtra University, Jalgaon, India

R. Brajpuriya Amity Institute of Nanotechnology, Amity University Haryana, Gurgaon, Haryana, India

F. Buonocore Surface Technology Laboratory Materials Technology Unit, Casaccia Research Centre, ENEA, Rome, Italy

Daniel Casimir Department of Physics and Astronomy, Howard University, Washington, DC, USA

Vishal Singh Chandel Department of Physics, Integral University, Lucknow, India

Neel Chatterjee Department of Electronics and Communication Engineering, Amity University, Noida, Uttar Pradesh, India

Ritu Chaudhary Department of Electronics Science, Kurukshetra University, Kurukshetra, Haryana, India

Shiv Chaudhary Amity Institute of Advance Research and Studies (Material & Devices), Amity University, Noida, Uttar Pradesh, India; Amity Institute of Renewable and Alternate Energy, Amity University, Noida, Uttar Pradesh, India

Vikas Chaudhary Department of Electronic Science, Kurukshetra University, Kurukshetra, India

Manisha Chaudhry Department of Physics, JSS Academy of Technical Education, Noida, India

Tapas K. Chaudhuri Dr. K. C. Patel Research and Development Centre, Charotar University of Science and Technology, Anand District, Gujarat, India

Parul Chawla CSIR Network of Institutes for Solar Energy (NISE), CSIR-National Physical Laboratory, New Delhi, India

Chetna Photovoltaics and Opto Electronics Lab, Department of Electronic Science, University of Delhi, South Campus, New Delhi, India

Kshitij Chopra Amity School of Engineering and Technology, Amity University, Noida, Uttar Pradesh, India

Ravi Kant Choubey Department of Applied Physics, Amity Institute of Applied Sciences, Amity University, Noida, India

Christina Craig REU in Physics Site, Department of Physics and Astronomy, Howard University, Washington, DC, USA; Department of Physics, University of Dallas, Irving, TX, USA

R. Dabrowski Institute of Chemistry, Military University of Technology, Warswa, Poland

Tushar Dhabal Das Department of ECE, National Institute of Technology, Yupia, Arunachal Pradesh, India

S.M. Dasharath Department of Metallurgical and Materials Engineering, Indian Institute of Technology Roorkee, Roorkee, Uttarakhand, India

Dipti Desai Department of Applied Physics, Defence Institute of Advanced Technology, Pune, India

Ranjana Devi Department of Electronic Science, Kurukshetra University, Kurukshetra, India

Ravindra Dhar Soft Materials Research Laboratory, Centre of Material Sciences, Institute of Interdisciplinary Studies, University of Allahabad, Allahabad, India

Sunanda Dhar Department of Electronic Science, University of Calcutta, Kolkata, India

Hrishikesh Dhasmana Amity Institute of Advanced Research and Studies, Amity University, Noida, Uttar Pradesh, India; Photovoltaic Laboratory, Centre for Energy Studies, Indian Institute of Technology, Delhi, India

T. Dikonimos Surface Technology Laboratory Materials Technology Unit, Casaccia Research Centre, ENEA, Rome, Italy

R.K. Diwan Directorate of Innovation and Technology, Amity University, Noida, Uttar Pradesh, India

Viresh Dutta Photovoltaic Laboratory, Centre for Energy Studies, Indian Institute of Technology Delhi, New Delhi, Delhi, India

Raul Garcia-Sanchez Department of Physics and Astronomy, Howard University, Washington, DC, USA

Khyati Gautam Department of Electronic Science, University of Delhi South Campus, New Delhi, India

Pinki Graak Department of Electronic Science, Kurukshetra University, Kurukshetra, India

Rakhi Grover Amity Institute of Renewable and Alternative Energy, Amity University, Noida, Uttar Pradesh, India; Amity Institute of Advanced Research and Studies (Materials and Devices), Amity University, Noida, Uttar Pradesh, India

Anita Gupta Amity Institute of Applied Sciences, AUUP, Noida, India

Nidhi Gupta Amity Institute of Advance Research and Studies (Material & Devices), Amity University, Noida, Uttar Pradesh, India; Amity Institute of Renewable and Alternative Energy, Amity University, Noida, Uttar Pradesh, India

Nikhil Deep Gupta Electronics and Communication Engineering, Malaviya National Institute of Technology, Jaipur, India

Vinay Gupta Department of Physics and Astrophysics, University of Delhi, New Delhi, India

Harsh Centre for Nanoscience and Nanotechnology, Jamia Millia Islamia, New Delhi, India

M. Husain Department of Physics, Jamia Millia Islamia, New Delhi, India; M.J. P. Rohilkhand University, Bareilly, Uttar Pradesh, India

Gurunath Jadhav Department of Applied Physics, Defence Institute of Advanced Technology, Pune, India

Amit Jain Department of Electronic Science, Rajdhani College, University of Delhi, New Delhi, India

Rohan Jain Electronics and Communication Engineering Department, Northern India Engineering College, New Delhi, India

Shefali Jain CSIR Network of Institutes for Solar Energy (NISE), CSIR-National Physical Laboratory, Delhi, India

Vinod Kumar Jain Amity Institute of Renewable and Alternate Energy, Amity University, Noida, Uttar Pradesh, India; Amity Institute for Advanced Research and Studies (Materials & Devices), Noida, Uttar Pradesh, India

Vijay Janyani Electronics and Communication Engineering, Malaviya National Institute of Technology, Jaipur, India

Himanshi Jauhari Amity Institute of Renewable and Alternative Energy, Amity University, Noida, Uttar Pradesh, India; Amity Institute of Advanced Research and Studies (Materials and Devices), Amity University, Noida, Uttar Pradesh, India

Naresh Jingar Defence Laboratory, Defence Research and Development Organisation (DRDO), Jodhpur, India

S.N. Kale Department of Applied Physics, Defence Institute of Advanced Technology, Pune, India

Sonal Kanwar Department of Chemistry, IIS University, Jaipur, India

Avinashi Kapoor Photovoltaics and Opto Electronics Lab, Department of Electronic Science, University of Delhi, New Delhi, India

Abhishek Kardam Amity Institute for Advanced Research and Studies (Materials & Devices), Amity University, Noida, Uttar Pradesh, India; Amity Institute of Renewable and Alternate Energy, Amity University, Noida, Uttar Pradesh, India

Chetan K. Kasar Department of Electronics, North Maharashtra University, Jalgaon, India

Parul Katyal Department of Electronic Science, Kurukshetra University, Kurukshetra, India

Davinder Kaur Department of Electronic Science, University of Delhi, New Delhi, India

Davinder Kaur Photovoltaics and Opto Electronics Lab, Department of Electronic Science, University of Delhi, New Delhi, India

Davinder Kaur Functional Nanomaterials Research Lab, Department of Physics and Centre of Nanotechnology, Indian Institute of Technology Roorkee, Roorkee, Uttarakhand, India

Harminder Kaur Department of Applied Sciences, PEC University of Technology, Chandigarh, India

Navneet Kaur Department of Electronic Science, Kurukshetra University, Kurukshetra, Haryana, India

Sunny Khan Department of Physics, Jamia Millia Islamia, New Delhi, India

Neeraj Khare Department of Physics, Indian Institute of Technology Delhi, New Delhi, India

Manjeet Kulhar Defence Laboratory, Defence Research and Development Organisation (DRDO), Jodhpur, India

Ajay Kumar Department of Electronic Science, Kurukshetra University, Kurukshetra, India

Amit Kumar Amity Institute for Advanced Research and Studies (Materials and Devices), Amity University, Noida, Uttar Pradesh, India; Amity Institute of Renewable and Alternative Energy, Amity University, Noida, Uttar Pradesh, India; Department of Electronic Science, Kurukshetra University, Kurukshetra, Haryana, India

Dheeraj Kumar Physics Department, Indian Institute of Technology Delhi, New Delhi, India

Dinesh Kumar Department of Electronics Science, Kurukshetra University, Kurukshetra, Haryana, India

Mintu Kumar Department of Electronic Science, Kurukshetra University, Kurukshetra, Haryana, India

Pramod Kumar Amity Institute of Advance Research and Studies (Material & Devices), Amity University, Noida, Uttar Pradesh, India; Amity Institute of Renewable and Alternative Energy, Amity University, Noida, Uttar Pradesh, India

Sacheen Kumar Department of Electronics Science, Kurukshetra University, Kurukshetra, Haryana, India

Sanjeev Kumar Department of Applied Sciences, PEC University of Technology, Chandigarh, India; Photovoltaics and Opto Electronics Lab, Department of Electronic Science, University of Delhi, New Delhi, India; Materials Science Group, Inter University Accelerator Centre, New Delhi, India

Sarvendra Kumar Amity Institute of Applied Sciences, Amity University, Noida, Uttar Pradesh, India

Vinod Kumar Department of Electronics Science, Kurukshetra University, Kurukshetra, Haryana, India

Vivek Kumar Amity Institute of Advance Research and Studies (Material & Devices), Amity University, Noida, Uttar Pradesh, India; Amity Institute of Renewable and Alternate Energy, Amity University, Noida, Uttar Pradesh, India

Monika Kumari Department of Electronic Science, Kurukshetra University, Kurukshetra, Haryana, India

Pallavi Kumari Department of Physics, Indian Institute of Technology Delhi, New Delhi, India

N. Lisi Surface Technology Laboratory Materials Technology Unit, Casaccia Research Centre, ENEA, Rome, Italy

Divya Madaan Photovoltaics and Opto Electronics Lab, Department of Electronic Science, University of Delhi, New Delhi, India

Madhubala Department of Chemistry, IIS University, Jaipur, India

Devinder Madhwal Amity Institute for Advanced Research and Studies (Materials & Devices), Amity University, Noida, Uttar Pradesh, India; Amity Institute of Renewable and Alternate Energy, Amity University, Noida, Uttar Pradesh, India

Ayesha Manocha Electronics and Communication Engineering Department, Northern India Engineering College, New Delhi, India

Rajiv Manohar Department of Physics, Lucknow University, Lucknow, India

Payal Mazumdar Amity Institute of Applied Science, Amity University, Noida, Uttar Pradesh, India

Mukesh Mishra Centre of Material Sciences, Institute of Interdisciplinary Studies, University of Allahabad, Allahabad, India

Prabhakar Misra Department of Physics and Astronomy, Howard University, Washington, DC, USA

Tanu Mittal Amity Institute of Applied Sciences, Amity University, Noida, Uttar Pradesh, India; National Physical Laboratory (CSIR), New Delhi, India

Jiya Ann Mohan Amity Institute of Advance Research and Studies (Material & Devices), Amity University, Noida, Uttar Pradesh, India; Amity Institute of Renewable and Alternate Energy, Amity University, Noida, Uttar Pradesh, India

Suhrit Mula Department of Metallurgical and Materials Engineering, Indian Institute of Technology Roorkee, Roorkee, Uttarakhand, India

Omita Nanda Amity Institute of Renewable and Alternative Energy, Amity University, Noida, Uttar Pradesh, India; Amity Institute of Advanced Research and Studies (Materials and Devices), Amity University, Noida, Uttar Pradesh, India

Chitkara Natasha Maharaja Agrasen College, University of Delhi, New Delhi, India

Sujata Pandey Department of Electronics and Communication Engineering, Amity University, Noida, Uttar Pradesh, India

R.S. Pandey Department of Applied Physics, Amity Institute of Applied Sciences, Amity University, Noida, India

Arun Pandya Defence Laboratory, Defence Research and Development Organisation (DRDO), Jodhpur, India

D.S. Patil Department of Electronics, North Maharashtra University, Jalgaon, India

Koteswara Rao Peta Department of Electronic Science, University of Delhi South Campus, New Delhi, India

Sonu Raghavan Directorate of Innovation and Technology, Amity University, Noida, Uttar Pradesh, India

Deepak Singh Rajawat Department of Chemistry, IIS University, Jaipur, India

Sangeeta Rattan Centre for Physical Sciences, Central University of Punjab, Bathinda, India

Sunita Rattan Amity Institute of Applied Sciences, Amity University, Noida, Uttar Pradesh, India

M. Sadiq Department of Physics, I.I.T. (BHU), Varanasi, India; Centre for Physical Sciences, Central University of Punjab, Bathinda, India

Sanjay Sahare Department of Applied Physics, Defence Institute of Advanced Technology, Pune, India

Dip Prakash Samajdar Department of Electronic Science, University of Calcutta, Kolkata, India

T.V.S.L. Satyavani Naval Science and Technological Laboratory, Visakhapatnam, India

Kanchan Saxena Amity Institute of Renewable and Alternative Energy, Amity University, Noida, Uttar Pradesh, India; Amity Institute of Advanced Research and Studies (Materials and Devices), Amity University, Noida, Uttar Pradesh, India

S. Shankara Narayanan Amity Institute for Advanced Research and Studies (Materials & Devices), Amity University, Noida, Uttar Pradesh, India; Amity Institute of Renewable and Alternate Energy, Amity University, Noida, Uttar Pradesh, India

A.L. Sharma Centre for Physical Sciences, Central University of Punjab, Bathinda, Punjab, India

Anmol Sharma Electronics and Communication Engineering Department, Northern India Engineering College, New Delhi, India

Anshul Kumar Sharma Department of Physics, Guru Nanak Dev University, Amritsar, Punjab, India

Parul Kumar Sharma Centre for Physical Sciences, Central University of Punjab, Bathinda, India

Rajiv Sharma Electronics and Communication Engineering Department, Northern India Engineering College, New Delhi, India

Richa Sharma Amity Institute of Applied Sciences, Amity University, Noida, Uttar Pradesh, India

Shailesh Narain Sharma Amity Institute of Applied Sciences, Amity University, Noida, Uttar Pradesh, India; National Physical Laboratory (CSIR), New Delhi, India; CSIR Network of Institutes for Solar Energy (NISE), CSIR-National Physical Laboratory, Delhi, India

Sugandha Sharma Department of Electronic Science, University of Delhi, New Delhi, India

Swati Sharma Department of Electronic Science, University of Delhi, South Campus, New Delhi, Delhi, India

V.K. Sharma Keshav Mahavidyalaya, University of Delhi, New Delhi, India

Virender Sharma Amity Institute of Renewable and Alternate Energy, Noida, Uttar Pradesh, India; Websol Energy System Limited, Falta, West Bengal, India; Indosolar Ltd., Greater Noida, Uttar Pradesh, India

Ruchi Shaw Amity Institute of Applied Sciences, Amity University, Noida, Uttar Pradesh, India

Shilpi Shital Photovoltaic Laboratory, Centre for Energy Studies, Indian Institute of Technology Delhi, New Delhi, Delhi, India

Poonam Shokeen Department of Electronic Science, University of Delhi, New Delhi, India

Prashant Shukla Amity Institute for Advanced Research and Studies (Materials & Devices), Amity University, Noida, Uttar Pradesh, India; Amity Institute of Renewable and Alternate Energy, Amity University, Noida, Uttar Pradesh, India

Akanksha Singh National Physical Laboratory, New Delhi, India

D.N. Singh Indosolar Ltd., Greater Noida, Uttar Pradesh, India

Fouran Singh Materials Science Group, Inter University Accelerator Centre, New Delhi, India

Gurwinder Pal Singh Department of Electronic Science, Kurukshetra University, Kurukshetra, Haryana, India

Inderpreet Singh Department of Electronics, SGTB Khalsa College, University of Delhi, New Delhi, India

Kirandeep Singh Functional Nanomaterials Research Lab, Department of Physics and Centre of Nanotechnology, Indian Institute of Technology Roorkee, Roorkee, Uttarakhand, India

Prateek Singh Electronics and Communication Engineering Department, Northern India Engineering College, New Delhi, India

Satyendra Pratap Singh Physics Department, AIAS, Amity University, Noida, India

Prachi Singhal Directorate of Innovation and Technology, Amity University, Noida, Uttar Pradesh, India

Ulhas S. Sonawane Department of Electronics, North Maharashtra University, Jalgaon, India

Sonia Department of Electronics Science, Kurukshetra University, Kurukshetra, Haryana, India

A. Srinivas Kumar Naval Science and Technological Laboratory, Visakhapatnam, India

M. Srinivas Naval Science and Technological Laboratory, Visakhapatnam, India

Ritu Srivastava National Physical Laboratory (Council of Scientific and Industrial Research), Physics for Energy Division, New Delhi, India

P.S.V. Subbarao Department of Physics, Andhra University, Visakhapatnam, India

Suman Department of Electronics Science, Kurukshetra University, Kurukshetra, Haryana, India

Surbhi Amity Institute of Applied Sciences, Amity University, Noida, Uttar Pradesh, India

Ram Swaroop Centre for Physical Sciences, Central University of Punjab, Bathinda, Punjab, India

Jayant Teotia Department of Physics, D.N. College, Meerut, Uttar Pradesh, India

Anjna Thakur Centre for Physical Sciences, Central University of Punjab, Bathinda, India

Priya Thakur Centre for Physical Sciences, Central University of Punjab, Bathinda, India

Sangeeta Tiwari Amity Institute of Applied Sciences, Amity University, Noida, Uttar Pradesh, India; National Physical Laboratory (CSIR), New Delhi, India

Malay Ranjan Tripathy Department of Electronics and Communication Engineering, Amity University, Noida, Uttar Pradesh, India

Dhaval Vankhade Dr. K. C. Patel Research and Development Centre, Charotar University of Science and Technology, Anand District, Gujarat, India

Abhishek Verma Amity Institute of Renewable and Alternate Energy, Noida, Uttar Pradesh, India; Amity Institute for Advanced Research and Studies (Materials & Devices), Noida, Uttar Pradesh, India

Daisy Verma Amity Institute of Renewable and Alternate Energy, Noida, Uttar Pradesh, India

Rohit Verma Department of Applied Physics, Amity Institute of Applied Sciences, Amity University, Noida, India

N. Vijayan CSIR Network of Institutes for Solar Energy (NISE), CSIR-National Physical Laboratory, New Delhi, India

Apurv Yadav Amity Institute of Advance Research and Studies (Material & Devices), Amity University, Noida, Uttar Pradesh, India; Amity Institute of Renewable and Alternate Energy, Amity University, Noida, Uttar Pradesh, India

Kamlesh Yadav Centre for Physical Sciences, Central University of Punjab, Bathinda, India

M.K. Yadav Department of Physics, D.N.College, Meerut, Uttar Pradesh, India

M. Zulfequar Department of Physics, Jamia Millia Islamia, New Delhi, India

Part I
Nanotechnology and Nanomaterials

Thermal Characterization of Single-Walled Carbon Nanotubes and Tungsten Oxide-Based Nanomaterials via Raman Spectroscopy

Prabhakar Misra, Daniel Casimir, Christina Craig, Raul Garcia-Sanchez and Shankar Baliga

Abstract The thermal characterization of single-walled carbon nanotubes (SWCNTs) and tungsten oxide (WO_3)-based nanomaterials through the use of Raman spectroscopy is the primary aim of this study, and is focused mainly on the applications of SWCNTs for energy storage and $WO_3$for toxic gas sensing, respectively. In the case of SWCNTs, the properties relevant to their performance obtained via resonant Raman spectroscopy were thermal expansion and thermal conductivity through the exploitation of the latter property's relationship to the thermal behavior of the Raman G^+-band of SWCNTs. In the case of the tungsten oxide-based nanomaterials, the responses of the various Raman signature peaks to different external stimuli, such as temperature variation, humidity changes, and toxic gas exposure, under controlled conditions were investigated.

1 Introduction

Resonance Raman spectroscopy has become one of the most common techniques in the characterization of single-walled carbon nanotubes (SWCNT) and other nanomaterials. It is possible to obtain rich detailed Raman spectra from samples with

P. Misra (✉) · D. Casimir · R. Garcia-Sanchez
Department of Physics and Astronomy, Howard University,
Washington, DC 20059, USA
e-mail: pmisra@howard.edu

C. Craig
REU in Physics Site, Department of Physics and Astronomy, Howard University,
Washington, DC 20059, USA

C. Craig
Department of Physics, University of Dallas, Irving, TX 75062, USA

S. Baliga
General Monitors, Inc., MSA Company,
26776 Simpatica Circle, Lake Forest, CA 92630, USA

V.K. Jain et al. (eds.), *Recent Trends in Materials and Devices*,
Springer Proceedings in Physics 178, DOI 10.1007/978-3-319-29096-6_1

little to no work in the way of sample preparation, in contrast to more expensive scanning probe methods, e.g. AFM and TEM. Understanding of the thermal expansion properties of carbon nanotubes provides potential insight into the process of storing thermal energy in these materials. Meanwhile, metal oxide gas sensors work by bringing about a change in conductivity in the sensor due to gas exposure caused by the chemisorption of oxygen. We have investigated these processes in which molecules are adsorbed into the metal oxide lattice structure with the goal of understanding how the Raman spectral features change as a result of varying conditions, especially temperature effects. The Raman spectroscopy data (Fig. 1) were recorded using a ThermoFisher DXR (532 and 780 nm) Smart Raman spectrometer and a Renishaw inVia Raman Microscope (514 nm).

2 SWCNT Experimental Details

This section first presents a novel robust and simple method of estimating the purity levels of bundled SWCNT samples based on Raman spectroscopy [1]. This method of carbon nanotube content estimation relies on the linear variation of the tangential mode G^+ Raman peak with temperature, where the sample heating is provided by increasing the laser power at the sample location.

By calibrating the Raman-based methods with purity estimates of high quality SWCNT samples via direct transmission electron microscopy (TEM) characterization, Terekhov et al.[1], were able to show that the slope of the G^+ band vs laser power density directly correlates with the amount of nanotube content present in one's sample. It was also noted in [1] that there were three different regions, each exhibiting a different slope in the G^+ frequency versus laser power density graphs (Fig. 2). The first region occurs for very low laser power levels, where the sample is not heated by the laser, resulting in an essentially flat level portion of the graph. In the second intermediate region, the slope value increases slightly, showing a noticeable departure of the G^+ peak from the graphite value of 1592 cm^{-1}; and finally in the third region at very high laser powers the nanotube sample is ablated at the laser spot and the shape of the G^+ band no longer changes [1]. The stretching out of the first region of the G^+ peak vs laser power plot occurs for SWCNT samples of higher purity, or stated another way, samples with more nanotube content present compared to other materials, such as amorphous carbon and metallic catalyst particles, have much longer initially flat first regions on plots of the G^+ peak frequency vs laser power. Also, since the thermal conductivity of the SWCNT sample is directly proportional to the slope of the G^+ band vs laser power density as shown in Eq. (1), we have yet another material property that is critical to the performance of SWCNT-based energy storage applications that can be characterized via Raman spectroscopy [2]. In Eq. (1), T is the sample

temperature, F_0 is the laser power density, κ is the effective thermal conductivity of the sample, and d is the laser beam diameter.

$$2(\Delta T)\kappa = \sqrt{\pi}d \times F_0 \quad (1)$$

3 WO_3 Experimental Details

In this section, we will discuss the Raman spectroscopy research on metal oxide gas sensors, mainly WO_3 variants, and how their Raman spectral features undergo changes based on increasing/decreasing temperatures, primarily focused on the 25–200 °C temperature range using 780 nm wavelength laser excitation. We have previously studied the behavior of temperature increases in the range 30–160 °C [3]. In this paper we discuss the effects of lowering the temperature, going from 190 to 30 °C, and the different effects the cycles have on the Raman spectral features of tungsten oxide.

We have focused our investigations strictly on the monoclinic form of WO_3 on a silicon substrate. The main features for monoclinic WO_3 are seen around ~807, ~716, and ~271 cm^{-1}, which correspond to the stretching of O–W–O bonds, stretching of W–O and the bending of O–W–O, respectively. Figure 1 illustrates the Raman spectral signature of WO_3 for 532 nm (top) and 780 nm (bottom) laser excitation wavelengths, respectively. Several other Raman peaks can be seen corresponding to other vibrations of W–O and O–W–O bonds. The peak around ~1550 cm^{-1} corresponds to OH–O and W–OH, which is a result of humidity effects on the sample. A complete listing of peak assignments as related to multiple WO_3 features can be found in our previously published study [3].

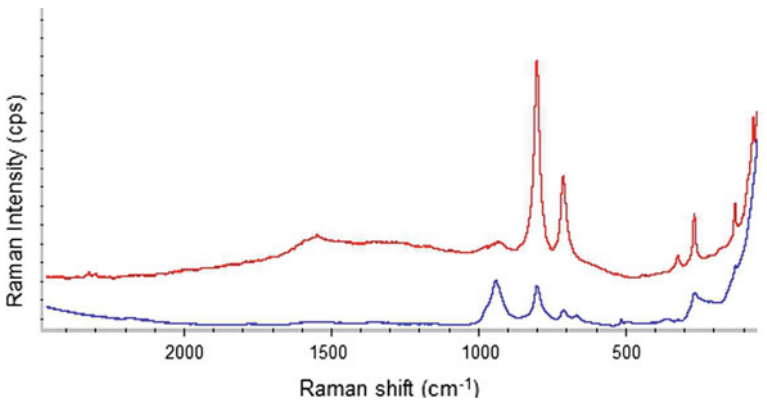

Fig. 1 Raman Spectrum of WO_3 at 30 °C using 532 nm wavelength (*top*) and 780 nm (*bottom*)

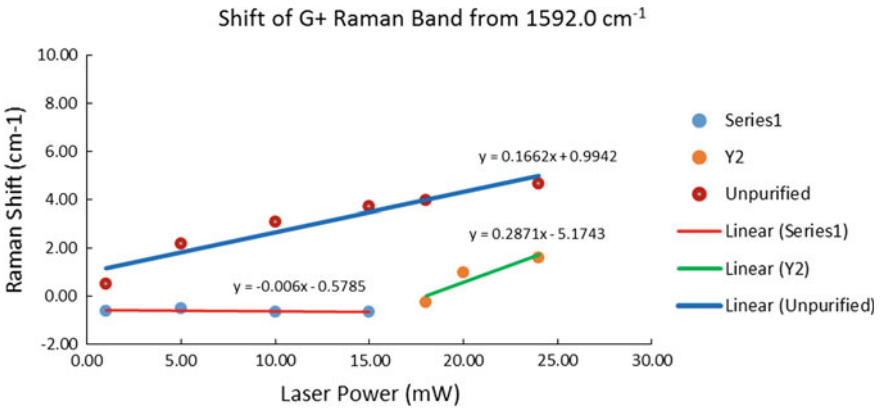

Fig. 2 Shift of the Raman G+ frequency from 1592.0 cm^{-1} for (*top*) unpurified Hipco SWCNT sample and (*bottom*) purified Hipco SWCNT sample versus laser power

4 Carbon Nanotube Results

Figure 2 shows the shift of the G^+ band frequency away from 1592.0 cm^{-1} versus laser power for purified and un-purified Hipco produced SWCNT samples. The lower plot of Fig. 2 is based on data from the purified sample, where the initially extended flat portion described by the red line shows the pronounced first region for highly purified SWCNTs, as discussed earlier in this section. The corresponding horizontal region for the unpurified sample is much closer to the vertical axis and is not noticeable on the upper blue plot. However, in the intermediate to high laser power range, the slope of the plot for the purified data is 0.287 cm^{-1}/mW, which is higher than the value of 0.162 cm^{-1} /mW for the unpurified sample. This discrepancy may be due to not excluding many of the other experimental factors influencing the laser heating rate of SWCNT samples discussed by [1], such as the laser spot size and shape, power instabilities, etc.

5 WO_3 Results

During our studies relating to increasing temperature [3], we found that the Raman spectra of a variety of nanomaterial samples, namely WO_3 on silicon, WO_3 nanopowder and WO_3 nanowires, exhibited changes as the temperature increased. We noted that certain features disappeared as temperature increased, potentially related to oscillations of the O–H feature around $\sim$1550 cm^{-1}, an effect caused by humidity. In addition, shifts occurred in the wavenumbers of these features and are illustrated in Fig. 3.

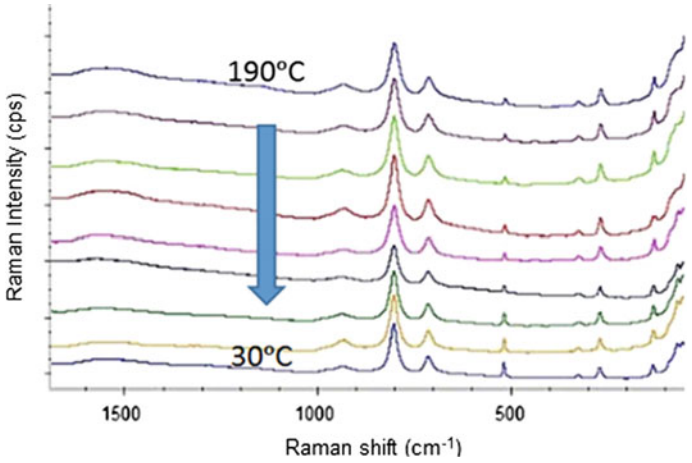

Fig. 3 The Raman spectra of WO_3 on Si with decreasing temperature from 190 °C (*top spectrum*) to 30 °C (*bottom spectrum*) at intervals of 20 °C

Figure 3 shows the case of lowering temperature (190–30 °C), and we find that just as the O–H vibrations become more pronounced with increasing temperature, reducing temperature decreases these O–H vibrations.

6 Conclusions

The present proceedings paper discusses how Raman spectroscopy, a powerful minimally invasive optical technique, can be an effective metrological technique for determining relevant properties of nanomaterials. Specifically, we have been able to qualitatively estimate the relative thermal conductivities between two SWCNT samples of differing purity levels, and shifts in the frequencies of the Raman peaks of Tungsten Oxide (WO_3) in response to thermal and other external stimuli. These results are an extension of previous work done by us [4], where we were able to quantify the thermal expansion of SWCNTs via Resonant Raman spectroscopy. In the current paper, the thermal conductivity-related measurements obtained by documenting the Raman spectral changes for SWCNTs as a function of laser power has ramifications for energy storage applications, while the Raman spectral changes of WO_3 with temperature and toxic gas exposure has implications for gas sensing applications.

Acknowledgments Christina Craig and Prabhakar Misra would like to gratefully acknowledge the financial support provided by the National Science Foundation (NSF PHY—1358727).

References

1. S.V. Terekhov et al., Appl. Phys. A **74**, 393–396 (2002)
2. S.V. Terekhov et al., in *AIP Conference Proceedings*, ed. by H. Kuzmany, J. Fink, M. Mehring, S. Roth. CP685, Molecular Nanostructures: XVII International Winterschool/European Conference on Electronic Properties of Novel Materials (2003), vol. 685, p 116
3. R. Garcia-Sanchez, T. Ahmido, D. Casimir, S. Baliga, P. Misra. J. Phys. Chem. A **117**, 13825–13831 (2013), Special Issue: Terry A. Miller Festschrift, doi:10.1021/jp408303p
4. P. Misra, D. Casimir, R. Garcia-Sanchez, S. Baliga, in *Conference Proceedings, TechConnect World Innovation Conference & Expo, Advanced Materials: TechConnect Briefs* (2015), pp. 55–58, ISBN: 978-1-4987-4727-1

Carbon: The Soul of Future Nanoelectronics

Vijay K. Arora

Abstract Quantum transport in carbon allotropes emerging from graphene/graphite nanolayers is described. Nonequilibrium Arora's distribution function (NEADF) includes the energy gained/lost in a mean free path (mfp) in the presence of an electric field. It is shown to organize the randomness in equilibrium to streamlined motion in extreme nonequilibrium leading to saturation of drift velocity and the current. A simple tanh form is obtained that is strictly valid for nondegenerate statistics, but is extended to degenerate statistics by defining a degeneracy temperature. Ballistic transport where device length is smaller than the scattering-limited mfp is shown to degrade the mobility. Resistance quantum is obtained in 1D configuration that is generalized to give contact resistance and channel resistance. Magnetotransport in graphene is discussed to demonstrate the utilization of magnetic field in characterization and performance evaluation.

1 Introduction

Graphene, a single layer of graphite with carbon atoms arranged in a honeycomb lattice is a perfect 2D conductor. As Fig. 1 shows, graphene can form a 0D nanostructure as a nanometer-size fullerene molecule, a 1D carbon nanotube (CNT) made of rolled-up sheets of graphene; a 1D graphene nanoribbon (GNR) cutouts from a graphene sheet with a narrow width of high aspect ratio; 3D with graphene layer stacked as in a graphite. The stacks of GNRs or 2D nanolayers can transform to multilayer graphene each with unique properties.

Each atom at the corner of honeybee hexagon is a carbon atom with electronic configuration that is similar to silicon as both come from Group 4 of the Periodic Table. Carbon ($_6C^{12}$) atom with 6 electrons has electronic configuration $1s^2 2s^2 2p^2$. It is a tetravalent material with four of its electrons in shell 2 and still able to

V.K. Arora (✉)
Department of Electrical Engineering and Physics, Wilkes University,
Wilkes-Barre PA 18766, USA
e-mail: vijay.arora@wilkes.edu

V.K. Jain et al. (eds.), *Recent Trends in Materials and Devices*,
Springer Proceedings in Physics 178, DOI 10.1007/978-3-319-29096-6_2

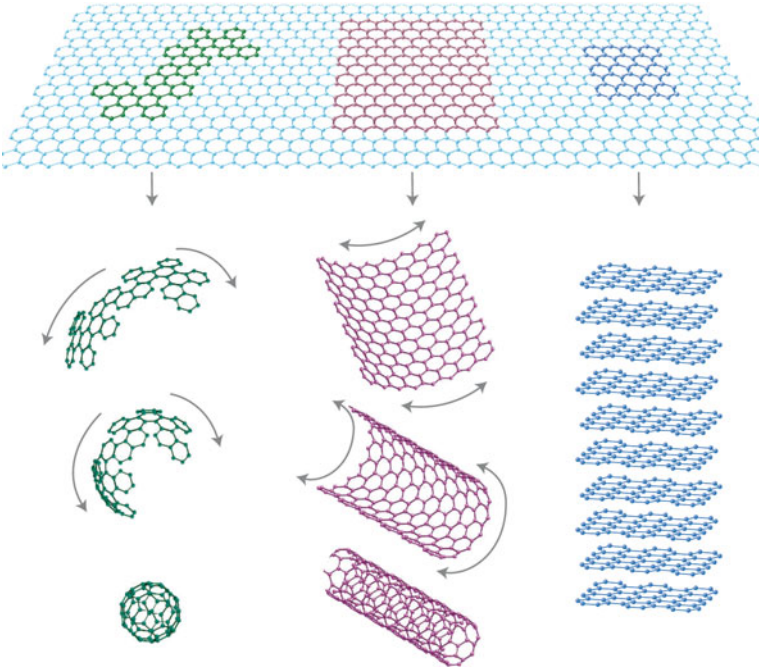

Fig. 1 Graphene sheet transforming to fullerene, carbon nanotube (CNT), graphene nanoribbon (GNR), and multilayer graphene each with unique properties. Copyright Macmillan Publishers Limited [4]

accommodate 4 more in 2p orbitals. However, carbon orbitals can hybridize because the s-orbital and p-orbitals of carbon's second electronic shell have very similar energies [1]. As a result, carbon can adapt to form chemical bonds with different geometries.

Graphene has many extraordinary electrical, mechanical, and thermal properties, such as high carrier mobility, ambipolar electrical field effect, tunable band gap, room temperature quantum Hall effect, high elasticity, and superior thermal conductivity. It is projected to be a material of scientific legend, comparable only to penicillin as a panacea. There is a modern adage: silicon comes from geology and carbon comes from biology. Cohesive band structure of graphene rolled into a CNT in a variety of chiral directions has recently been reported [2]. It is shown to exist in metallic and semiconducting states. Similarly GNR with narrow width are shown in three semiconducting modes with no metallic configuration [3]. All semiconducting states can be described with parabolic E-k relation with effective mass, while the effective mass for metallic state remains zero, as in graphene.

Quantum and ballistic transport offer a new outlook with the appearance of many outstanding properties of graphene and its allotropes [1]. Equilibrium carrier statistics with large number of stochastic carriers is the basis of any transport and is well established. However, nonequlibrium quantum transport based on the

Hamiltonian formulation is complex. One is easily lost in the computational maze of Monte Carlo experiments where myriad of parameters control the output. On the other hand, nonequilibrium Arora's distribution function (NEADF) [5] is distinctly simpler in its outlook with only the mean free path (mfp) as a parameter obtainable from low-field mobility that is always measured in any transport experiment. A new paradigm for characterization and performance evaluation of carbon allotropes is emerging from the application of NEADF to graphene and its allotropes. NEADF's unique feature is conversion of the stochastic carrier motion in equilibrium with no external influences into a streamlined one in a high-field-initiated extreme nonequilibrium for current to flow and get saturated. The mobility expressions are direct product of NEADF when limit to low-field domain is obtained. Similarly, the nondegenerate statistics is transformed to degenerate one by defining the degeneracy temperature to reveal higher energy in the degenerate state as the Fermi energy resides in one of the bands.

2 NEADF

NEADF is an outgrowth of the Fermi-Dirac distribution with the added energy lost/gained $q\vec{\mathscr{E}} \cdot \vec{\ell}_{o\infty} = q\mathscr{E}\ell_{o\infty}\cos\theta$ in and opposite to the electric field with $-1 \leq \cos\theta \leq +1$. The presence of cos θ favors those electrons drifting opposite to $\vec{\mathscr{E}}$ as shown in Fig. 2. The velocity at any collision is stochastic with average magnitude equal to intrinsic velocity v_i that is thermal velocity in nondegenerate (ND) domain and Fermi velocity in degenerate domain. This intrinsic velocity is the Fermi velocity $v_{Fo} = 10^5$ m/s at Dirac point. The saturation current is $I_{sat} = n_3 q v_{sat} A_c(3D)$, $I_{sat} = n_2 q v_{sat} W(2D)$, $I_{sat} = n_1 q v_{sat}(1D)$, where $v_{sat} = v_{id}$ for a given dimensionality d (3, 2, or 1). Saturation is further lowered by an onset of quantum emission. The mathematical form of NEADF is given by [6]

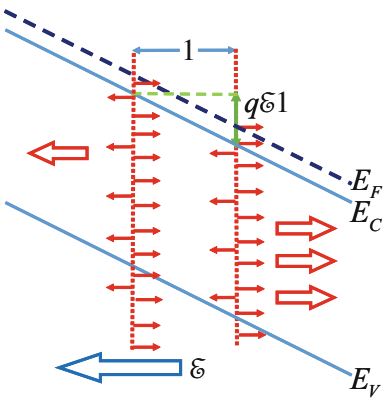

Fig. 2 Left-right asymmetry in the electric-field direction

$$f(E,\mathscr{E}) = \frac{1}{1+\mathrm{e}^{\frac{E-(E_F+q\vec{\mathscr{E}}\cdot\vec{\ell})}{k_BT}}} \tag{1}$$

The mfp ℓ, related to long-channel mfp $\ell_{o\infty}$, as modified by the quantum emission, is given by

$$\ell = \ell_{o\infty}\left(1-\mathrm{e}^{-\frac{\ell_Q}{\ell_{o\infty}}}\right) \tag{2}$$

with

$$\ell_Q = \hbar\omega_0(N_o+1)/q\mathscr{E} \tag{3}$$

$$N_o = 1/(e^{\Delta_Q}-1), \Delta_Q = \hbar\omega_o/k_BT \tag{4}$$

At any collision, the electron start from stochastic velocity directed at random. The component in and against electric field $\vec{\mathscr{E}}$ is affected. Those with intrinsic velocity directed in the +x direction (opposite to $\vec{\mathscr{E}}$) gain velocity $v_+ = v_i + q\mathscr{E}\tau_c$ and those directed towards –x direction decelerate with $v_- = -v_i + q\mathscr{E}\tau_c$, where $\tau_c \approx \ell_{o\infty}/v_i$ is the collision time. The average in a mfp results in net drift $v_D = q\mathscr{E}\tau_c/m* = \mu_{o\infty}\mathscr{E}$ proportional to $\mathscr{E}$ assuming equipartition ($n_+ = n_- = n/2$) of velocity until $v_- = 0$. As v_- turning point gets smaller than the mfp, anisotropy in the distribution sets in making $n_+ > n_-$. That is the initiation of unidirectional transport at the critical value $\mathscr{E}_c = v_i/\mu_{o\infty}$. The onset of quantum emission lowers the saturation velocity below v_i as $\ell_Q < \ell_{o\infty}$. In the extreme nonequilibrium $n_+ = n$ and $n_- = 0$ and carrier velocity vectors are unidirectional leading to saturation velocity and current.

3 Drift Response

Equilibrium 2D carrier concentration n_g in graphene is given by [5]

$$n_g = N_g\Im_1(\eta) \tag{5}$$

with

$$N_g = (2/\pi)(k_BT/\hbar v_F)^2 \tag{6}$$

$$\eta = (E_F - E_{Fo})/k_BT \tag{7}$$

$\Im_j(\eta)$ is the Fermi-Dirac integral (FDI) of order j [7, 8] with j = 1 for graphene. The linear carrier density of CNT is similarly described by

$$n_{CNT} = N_{CNT}\Im_{CNT}(\eta, e_g) \tag{8}$$

with $D_o = 4/\pi\hbar v_{Fo} = 1.93\,\mathrm{eV}^{-1}\mathrm{nm}^{-1}$, $e_g = E_g/k_BT$. $N_{CNT} = D_o k_B T$ is the effective density of states. $\Im_{CNT}(\eta, e_g)$ is the CNT integral that can be evaluated numerically [2]. Equilibrium carrier statistics for GNR is similarly obtainable [3].

The drift response v_D to an applied electric field in a graphene nanolayer is the average of $v_{Fo}\cos\theta$ using the NEADF and density of states, resulting in

$$v_D/v_{Fo} = \left(1/2\pi u_g\right)\int_0^{2\pi} \cos\theta\, d\theta \Im_1(H(\theta)) \tag{9}$$

The reduced Fermi energy η is now a function of electric field and is evaluated from the normalization condition

$$u_g = (1/2\pi)\int_0^{2\pi} d\theta \Im_1(H(\theta)), \quad u_g = n_g/N_g \tag{10}$$

Here $H(\theta) = \eta - \delta\cos\theta$ is the electrochemical Fermi energy that is directional. A simplified version of (9) is obtained by substitution of $\cos\theta = \pm 1/2$ in $H(\theta)$ as distribution is split into ± x-direction. $\theta = -\pi/2$ to $+\pi/2$ is for +x-direction and $\theta = +\pi/2$ to $+3\pi/2$ for –x-direction. $<\cos\theta> = \pm 1/d$ for an arbitrary dimensionality d = 3, 2, and 1 [9, 10]. With this substitution, the relative drift response of (9) is the same as difference of anisotropic carriers in an electric field as shown in Fig. 2. The drift response for 2D graphene is now obtained as

$$v_D = v_{Fo}\frac{\Im_1(\eta + \delta/2) - \Im_1(\eta - \delta/2)}{\Im_1(\eta + \delta/2) + \Im_1(\eta - \delta/2)} \tag{11}$$

where $n_{g\pm} = N_g\Im_1(\eta \pm \delta/2)$ is the carrier concentration with velocity vector component in the $\pm x$ direction with electric field in the $-x$ direction. The mobility expression follows naturally from (11) in the low-electric-field limit ($\delta \to 0$) and using $d\Im_j(\eta)/d\eta = \Im_{j-1}(\eta)$. The mobility expression is obtained as

$$\mu_{og} = \frac{q\ell v_{Fo}}{2k_BT}\frac{\Im_0(\eta_o)}{\Im_1(\eta_o)} \tag{12}$$

Here η_o is used in place of η to emphasize the fact that it is zero-field reduced Fermi energy. The mobility expression of (12) allows one to define ohmic degeneracy temperature T_{og} so mobility expression is re-written as

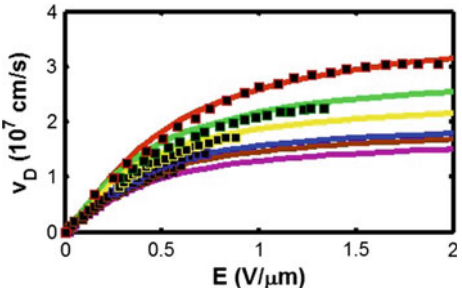

Fig. 3 Drift velocity v_D as a function of electric field $\mathscr{E}$ at room temperature T = 280 K for $n_g/10^{16}\mathrm{m}^{-2}$ = 1.6 (*top*), 2.8, 4.2, 6.4, 8.6, and 10.3 (*bottom*). The *solid line* represents v_D from theory (11). The *markers* are the experimental data of [12]

$$\mu_{og} = \frac{q\ell v_{Fo}}{2k_B T_{og}}, \quad T_{og} = T\frac{\Im_1(\eta_o)}{\Im_o(\eta_o)} \tag{13}$$

Figure 3 shows the graphene's drift response to high electric field with solid lines obtained from (11) with the mfp extracted from (12) for the experimental data on mobility. The comments on this drift response appear in [11].

The drift response in a CNT can be similarly evaluated. For a semiconducting CNT, it does involve CNT integral, but for a metallic CNT, the drift response is similar to that of (11) with $\Im_1(\eta)$ replaced with $\Im_o(\eta)$. The mobility for a metallic MCNT is given by

$$\mu_{oMCNT} = \frac{q\ell v_{Fo}}{k_B T_{oMCNT}}, \quad T_{oMCNT} = T\frac{\Im_{-1}(\eta_o)}{\Im_o(\eta_o)} \tag{14}$$

The current response I to the applied voltage is given by

$$I = I_{sat}\frac{\Im_o(\eta+\delta_o) - \Im_o(\eta-\delta_o)}{\Im_o(\eta+\delta_o) + \Im_o(\eta-\delta_o)} \tag{15}$$

A simplification of (15) is possible if CNT degeneracy temperature of (14) is utilized. The thermal voltage $V_t = k_B T/q$ is now replaceable with $V_F = E_F/q$ in extreme degeneracy. This will make the current response temperature independent. The current response of (15) is now simplified to

$$I = I_{sat}\tanh(V/V_c) \tag{16}$$

where $V_c = (V_F/\ell_{o\infty})L$. The sublinear nature of I-V curves of Fig. 4 obtained from (16) requires distinction between direct ($R = V/I$) and incremental resistance ($r = dV/dI$). In the ohmic domain ($I = V/R_o$), $r_o = R_o = 40\,\mathrm{k}\Omega$ due to constant I-V slope. However, in the sublinear regime beyond $V = V_c$, distinction between R and r is a must. R and r over the complete regime, as obtained from (16), are given by

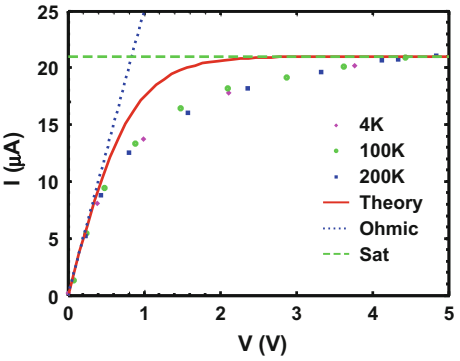

Fig. 4 The current response to the applied voltage in a metallic CNT

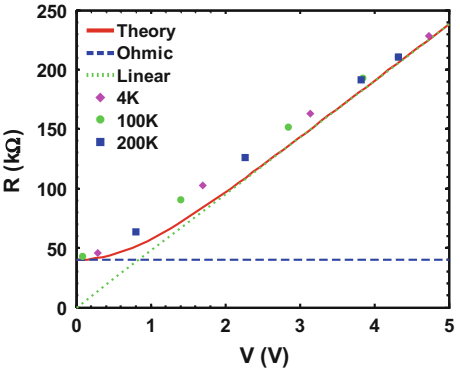

Fig. 5 The resistance as a function of applied voltage in an MCNT with ohmic resistance $R_o = 40\,\mathrm{k}\Omega$

$$R = R_o(V/V_c)/\tanh(V/V_c) \tag{16}$$

$$r = R_o \cosh^2(V/V_c) \tag{17}$$

Figure 5 shows direct resistance as a function of voltage. The resistance approaches its ohmic value in the limit of low value of the voltage ($V < V_c$), but rises linearly with voltage in the high-voltage limit ($V \gg V_c$). The experimental data in Figs. 4 and 5 is obtained from [13]. The direct resistance R as a function of voltage is shown in Fig. 5. As the figure shows, the resistance converges to constant R_o as $V \to 0$, but rises linearly with voltage consistent with (16) as $\tanh(V/V_c) \approx 1$ when $V \gg V_c$.

4 Ballistic Transmission

The absence of electron scattering in a conducting channel with length below the scattering-limited mfp is technically called ballistic transmission. The absence of scattering is conjectured to give higher mobility and hence the interest in ballistic

transmission. Contrary to this belief, the experiments show resistance rising and mobility degrading even in the ohmic domain where high-field effects are negligible [14–16].

In a 1D CNT, just like in a 1D nanowire [9, 17], the product of velocity and density of states (DOS) is constant [18]. In fact that is the general property of any 1D system. Differential DOS $(2g_K/hv(E))dE$ between E and $E+dE$ in a CNT is inversely proportional to velocity $v(E)$ [2], where $g_K = 2$ is K-K' degeneracy in hexagonal k-space. Only half the electrons, as shown in Fig. 6 are transmitted ballistically from left to right. Backward reflection at T = 0 K is blocked due to Pauli Exclusion Principle that forbids transmission in occupied destination states. With probability of occupation unity at low temperatures, the current I is obtained by integrating $qv(E)(4/hv(E))dE$ from E_{FR} to E_{FL} with $E_{FL} - E_{FR} = qV$. The current is then $I = (4q^2/h)V$, giving quantum resistance $R_Q = h/4q^2$. The same paradigm applies to graphene nanoribbons (GNRs) which are also 1 D in nature.

At extremely undersized dimensions L smaller than the scattering-limited long-channel mfp $\ell_{o\infty}$ ($L < \ell_{o\infty}$), Arora et al. [14, 16, 19, 20] show the probabilistic nature of the collisions that give a finite probability for scattering even in short channels leading to non-unity ballisticity [16] that takes into account ballistic injection from the contacts. The length-limited ballistic ohmic mobility μ_{oL} is given by [16]

$$\mu_{oLCNT} = \mu_{o\infty CNT}(1 - e^{-L/\ell_B}) \tag{18}$$

The ballistic mfp $\ell_B = \ell_{o\infty}(v_{inj}/v_{Fo})$ differs from the traditional low-field (o) long-channel (∞) mfp $\ell_{o\infty}$ by a factor (v_{inj}/v_{Fo}), where v_{inj} is the velocity of the injected carriers from the contacts. $\ell_B = \ell_{o\infty}$ as injection is limited to the Fermi velocity for a CNT. In the limit of $L \ll \ell_{o\infty}$, (18) coupled with (14) gives

$$\mu_{LCNT} \approx \frac{8qL}{n_{CNT}h} \tag{19}$$

The resistivity for a 1D metallic CNT is given by

$$\rho_{CNT} = \frac{1}{(n_{CNT}/2)q\mu_{LCNT}} = \frac{h}{4q^2}\frac{1}{L} \tag{20}$$

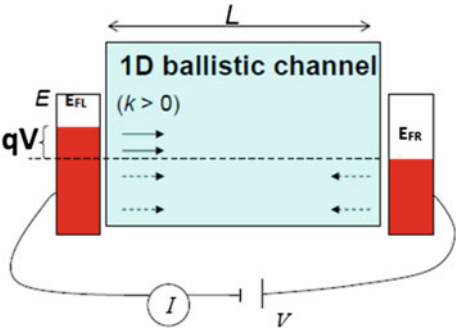

Fig. 6 A ballistic conductor of length L connected between two metallic reservoirs with shifted Fermi energy in the presence of an electric field $\mathscr{E} = V/L$ applied from right to left

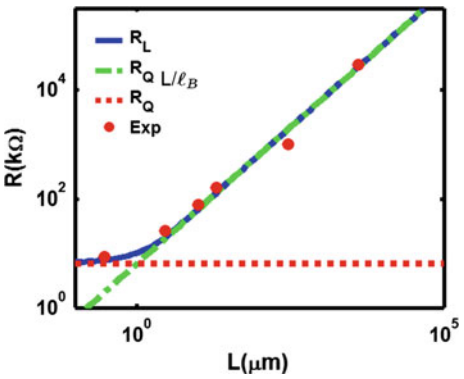

Fig. 7 The Resistance in a CNT as a function of channel length (*solid line*). The *dotted line* is applicable for long-channel behavior. The *flat line* is the ballistic quantum resistance

The quantum resistance R_Q now follows naturally from (20)

$$R_Q = \rho_{CNT} L = \frac{h}{4q^2} = 6.453\,\mathrm{k\Omega} \tag{21}$$

The length-limited resistance now follows the pattern

$$R/R_Q = 1/T_r = (L/\ell_B)/(1 - \mathrm{e}^{-\frac{L}{\ell_B}}) \tag{22}$$

where T_r is the transmission that is unity in the limit $L \to 0$. Figure 7 gives Resistance as a function of length, converging to R_Q as $L \to 0$ and a linear function of L as $L \gg \ell_B$. This type of scaling and electron mfp has been demonstrated by Purewal et al. [21] in a number of experiments on metallic and semiconducting nanotubes.

5 Magnetotransport

The appearance of quantum Hall effect in graphene is quite miraculous with the application of a magnetic field. Figure 10 is display of the doubly degenerate K-K′ band structure of graphene. However, this Dirac point may be lifted or depressed due to quantum effects, creating a bandgap as when a magnetic field B is applied normal to the graphene layer. The trajectory of an electron (or hole) is a circle in a magnetic field as is well known. The circumference of the trajectory must contain integral number of de Broglie waves, i.e., $2\pi R = n\lambda_D = n(2\pi/k)$ resulting in $k_n = n/R_n$. As shown in Fig. 9, the magnetic force $qv_{Fo}B = \hbar k v_{Fo}/R_n$. Quantized radius $R_n = (n\hbar/qB)^{1/2}$ is obtained when $k_n = n/R_n$ is utilized to eliminate k_n, which is the same expression as for a parabolic semiconductor. In fact, negative values of n can be attributed to hole transport. It is appropriate to take |n| in the expression for the radius (Fig. 8).

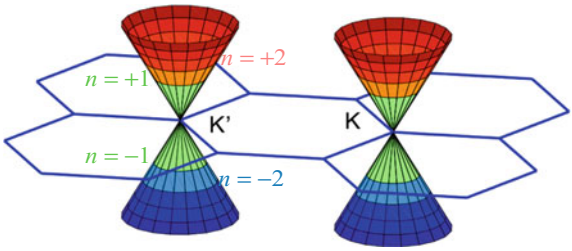

Fig. 8 2D graphene lattice with K–K′ Dirac cone displayed. The application of magnetic field introduces a bandgap

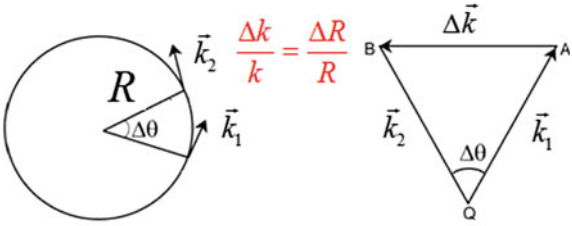

$$F = \frac{\Delta(\hbar k)}{\Delta t} = \frac{\hbar k}{R}\frac{\Delta R}{\Delta t} = \frac{v_{Fo}\hbar k}{R}$$

$$qv_{Fo}B = \frac{v_{Fo}\hbar k}{R} \Rightarrow k_n = \frac{qBR_n}{\hbar}$$

Fig. 9 Electron (hole) trajectory in a magnetic field B and associated centripetal force

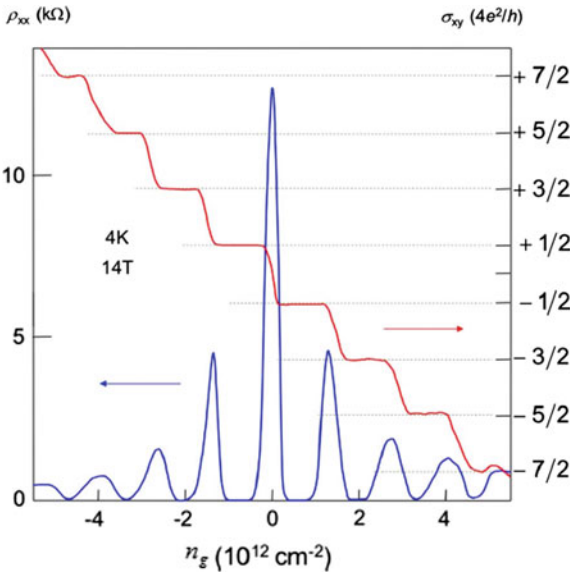

Fig. 10 Quantum Hall plateaus and vanishing resistivity in the localized domain [4, 22, 23]

The energy spectrum in a magnetic field now emerges as

$$E_n - E_{\pm o} = \pm\hbar v_{Fo} k_n = \pm\hbar v_{Fo} \frac{n}{R_n} = \pm v_{Fo}\sqrt{2nq\hbar B} \tag{23}$$

2D carrier density now splits into a number of quantum discs in k-space. The carrier concentration in each level is given by graphene statistics [1]

$$n_{gn} = N_g \Im_1(\eta) \approx (2/\pi)(k_B T/\hbar v_F)^2(\eta^2/2) \tag{24}$$

with $\eta = (E_F - E_{+o})/k_B T$. When electrons are localized in a quantum disc, the Fermi level resides there with $(E_F - E_{+o}) = v_{Fo}\sqrt{2nq\hbar B}$ for n > 1. K = 0 in the lowest state as no quantum states exist below this energy, therefore $n_{g1} = 1/2$ for a singular quantum state as DOS contains both k_+ and k_-. Collectively, when executed

$$n_{gn} = \frac{4qB}{h}\left(n - \frac{1}{2}\right) \quad n = 1, 2, 3, \ldots \tag{25}$$

The quantum energy reducing to half of that in a regular level is a direct result of Landau gauge in which the wavefunction is that of a harmonic oscillator. In parabolic semiconductors, it gives $1/2\hbar\omega_c$ due to potential energy of the oscillator, whereas the kinetic energy is quantized as $n\hbar\omega_c$ giving total energy $(n - 1/2)\hbar\omega_c$.

The components of resistivity ρ and conductivity σ are related by

$$\rho_{xx} = \frac{\sigma_{xx}}{\sigma_{xx}^2 + \sigma_{xy}^2} \quad \rho_{xy} = \frac{\sigma_{xy}}{\sigma_{xx}^2 + \sigma_{xy}^2} \tag{26}$$

where ρ_{xx} (σ_{xx}) is the longitudinal component and ρ_{xy} (σ_{xy}) is the Hall component. When the chemical potential (Fermi energy) is inside a region of localized states, the longitudinal conductivity vanishes $\sigma_{xx} = 0$ as electrons cannot freely move because all states are occupied. On the other hand, when the chemical potential is in a region of delocalized states, not in a quantized level, $\sigma_{xx} \neq 0$ and σ_{xy} varies continuously. In the localized domain

$$\rho_{xx} \approx 0 \tag{27}$$

$$\rho_{xy} \approx \frac{1}{\sigma_{xy}} = \frac{B}{qn_g} = \frac{h}{4q^2}\frac{1}{\left(n - \frac{1}{2}\right)} \quad n = 1, 2, 3\ldots \tag{28}$$

Figure 10 gives quantum plateaus as well as vanishing resistivity [4, 22, 23]. At the point where Hall plateau appears, the resistivity drops to zero.

6 Conclusions

The NEADF is unique for high-field applications as it seamlessly makes a transition from ohmic domain to nonohmic domain. The drive to reduce the size below the scattering-limited mfp to enhance transport behavior does not appear to be appropriate [7, 24–27]. That is perhaps the reason that observed experimental resistance of 40.0 kΩ as observed by Yao et al. [13] exceeds its ballistic value for 1-μm resistor. In fact, Greenberg and Del Alamo [24] have demonstrated that resistance surge in the parasitic regions degrades the performance of an InGaAs transistor. To sum it up, explorations of new physical phenomena on this length scale require the contributions from many different fields of science and engineering, including physics, chemistry, biology, materials science, and electrical engineering.

References

1. P.H.S. Wong, D. Akinwande, *Carbon Nanotube and Graphene Device Physics* (Cambridge University Press, Cambridge, 2011)
2. V.K. Arora, A. Bhattacharyya, Cohesive band structure of carbon nanotubes for applications in quantum transport. Nanoscale **5**, 10927–10935 (2013)
3. V.K. Arora, A. Bhattacharyya, Unified bandgap engineering of graphene nanoribbons. Physica status solidi (b). **251**(11) (2014)
4. A.K. Geim, K.S. Novoselov, The rise of graphene. Nat. Mater. **6**, 183–191 (2007)
5. V.K. Arora, M.L.P. Tan, C. Gupta, High-field transport in a graphene nanolayer. J. Appl. Phys. **112**, 114330 (2012)
6. V.K. Arora, *Nanoelectronics: Quantum Engineering of Low-Dimensional Nanoensembles* (CRC Press/Taylor and Francis Group, USA, 2015)
7. V.K. Arora, M.L.P. Tan, in *High-Field Transport in Graphene and Carbon Nanotubes, presented at the International Conference on Electron Devices and Solid State Circuits 2013 (EDSSC2013), IEEEXplore Digital Library*, Hong Kong Polytechnic University, 2013
8. V.K. Arora, *Nanoelectronics: Quantum Engineering of Low-Dimensional Nanoensemble* (Wilkes University, Wilkes-Barre, 2013)
9. V.K. Arora, D.C.Y. Chek, M.L.P. Tan, A.M. Hashim, Transition of equilibrium stochastic to unidirectional velocity vectors in a nanowire subjected to a towering electric field. J. Appl. Phys. **108**, 114314–114318 (2010)
10. V.K. Arora, *Quantum Nanoengineering* (Wilkes University, Wilkes-Barre, PA, 2012)
11. M.L.P. Tan, V.K. Arora, "Comment on "Theoretical analysis of high-field transport in graphene on a substrate". [J. Appl. Phys. 116, 034507 (2014)]," J. Appl. Phys. **116** (2014)
12. V.E. Dorgan, A. Behnam, H.J. Conley, K.I. Bolotin, E. Pop, High-field electrical and thermal transport in suspended graphene. Nano Lett. **13**, 4581–4586 (2013)
13. Z. Yao, C.L. Kane, C. Dekker, High-field electrical transport in single-wall carbon nanotubes. Phys. Rev. Lett. **84**, 2941–2944 (2000)
14. V.K. Arora, M.S.Z. Abidin, M.L.P. Tan, M.A. Riyadi, Temperature-dependent ballistic transport in a channel with length below the scattering-limited mean free path. J. Appl. Phys. **111**, 054301, 1 Mar 2012
15. V.K. Arora, M.S.Z. Abidin, S. Tembhurne, M.A. Riyadi, Concentration dependence of drift and magnetoresistance ballistic mobility in a scaled-down metal-oxide semiconductor field-effect transistor, Appl. Phys. Lett. **99**, 063106–063106–3 (2011)

16. M.A. Riyadi, V.K. Arora, The channel mobility degradation in a nanoscale MOSFET due to injection from the ballistic contacts. J. Appl. Phys. **109**, 056103 (2011)
17. P. Yang, R. Yan, M. Fardy, Semiconductor nanowire: What's next? Nano Lett. **10**, 1529–1536 (2010)
18. H.C. Chin, A. Bhattacharyya, V.K. Arora, Extraction of nanoelectronic parameters from quantum conductance in a carbon nanotube. Carbon **76**, 451–454 (2014)
19. V.K. Arora, *"Ballistic transport in nanoscale devices," presented at the MIXDES 2012: 19th International Conference MIXED Design of Integrated Circuits and Systems* (Wasaw, Poland, 2012)
20. V.K. Arora, M.S.Z. Abidin, M.L.P. Tan, M.A. Riyadi, Temperature-dependent ballistic transport in a channel with length below the scattering-limited mean free path. J. Appl. Phys. **111**, 1 Mar 2012
21. M.S. Purewal, B.H. Hong, A. Ravi, B. Chandra, J. Hone, P. Kim, Scaling of resistance and electron mean free path of single-walled carbon nanotubes. Phys. Rev. Lett. **98**, 186808, 4 May 2007
22. K.S. Novoselov, S.V. Morozov, T.M.G. Mohinddin, L.A. Ponomarenko, D.C. Elias, R. Yang, I.I. Barbolina, P. Blake, T.J. Booth, D. Jiang, J. Giesbers, E.W. Hill, A.K. Geim, Electronic properties of graphene. Physica Status Solidi B-Basic Solid State Phys. **244**, 4106–4111 (2007)
23. A.H. Castro Neto, F. Guinea, N.M.R. Peres, K.S. Novoselov, A.K. Geim, The electronic properties of graphene. Rev. Mod. Phys. **81**, 109–162 (2009)
24. D.R. Greenberg, J.A.d. Alamo, Velocity saturation in the extrinsic device: a fundamental limit in HFET's. IEEE Trans. Electron. Devices **41**, 1334–1339 (1994)
25. V.K. Arora, *"Quantum Transport in Nanowires and Nanographene," presented at the 28th International Conference on Microelectronics (MIEL2012)*, Nis, Serbia (2012)
26. T. Saxena, D.C.Y. Chek, M.L.P. Tan, V.K. Arora, Microcircuit modeling and simulation beyond Ohm's law. IEEE Trans. Educ. **54**, 34–40 (2011)
27. M.L.P. Tan, T. Saxena, V. Arora, Resistance blow-up effect in micro-circuit engineering. Solid-State Electron. **54**, 1617–1624 (2010)

Antireflection Properties of Multi-crystalline Black Silicon with Acid Textured Surfaces Using Two Step Metal Assisted Chemical Etching

Virender Sharma, Abhishek Verma, Vinod Kumar Jain and Daisy Verma

Abstract We have fabricated multicrystalline black silicon (B-Si) with two step texturing process, first using micro-scale conventional acid texturing and second using nano-textured (nT-Si) layer, directly on the micro textured surface. Instead of Lithography process, a two step silver assisted chemical etching process, is used to fabricate nano-texture surfaces in the aqueous solution of hydrogen peroxide (H_2O_2) and hydrofluoric acid (HF) at room temperature. The reflectivity has been investigated with the varying time of the nano-texturization. The surface morphology of nano-textured black Si was studied by SEM and the optical properties were studied by spectrophotometer. The average reflectivity has decreased to 4.3 % in wavelength range from 300 to 800 nm.

1 Introduction

Flat silicon wafer usually has reflectance greater than 40 % because of abrupt change in refractive index between silicon and air. In order to reduce surface reflectance generally antireflection coating of films such as silicon nitride is used to reduce reflection. The antireflection films work effectively only at a limited range and for special angles of incidence light. Further reflection is reduced using surface texturing. However even after acid texturing in mc-Si reflectivity is nearly 30 %. To further increase the antireflection property of mc-Si silicon, different texturing methods have been tried and investigated.

V. Sharma (✉) · A. Verma · V.K. Jain · D. Verma
Amity Institute of Renewable and Alternate Energy, 201303 Noida, Uttar Pradesh, India
e-mail: Virender@webelsolar.com

A. Verma · V.K. Jain
Amity Institute for Advanced Research and Studies (Materials & Devices), 201303 Noida, Uttar Pradesh, India

V. Sharma
Websol Energy System Limited, 743504 Falta, West Bengal, India

V.K. Jain et al. (eds.), *Recent Trends in Materials and Devices*,
Springer Proceedings in Physics 178, DOI 10.1007/978-3-319-29096-6_3

Nano structured surface is one of the most effective method to reduce reflection and is known as "black silicon" [1]. The first application of b-Si was the optimization of etching parameters in a reactive ion etching process (RIE) [2] but later on it became an interesting solar cell surface texture because of its low reflectance on a wide wavelength range and acceptance angle. Besides RIE, b-Si may also be fabricated using, laser texturing [3], metal assisted chemical etching [4] or plasma immersion ion implantation [5].

In this paper a relatively simple method of two step metal assisted chemical etching is used for producing a nanostructure on the multi-crystalline textured silicon surface. We have used electroless wet chemistry processes at room temperature. The reflectivity of black silicon formed for various texturization times has been studied and the surface morphology is also studied with the help of SEM.

2 Experimental Details

P-type multi-crystalline silicon wafer with dimension 156 mm × 156 mm and a thickness of 200 ± 20 µm with resistivity 1–3 Ω cm were micron-scale etched (≈3.7 µm each side) in RENE acid texturing tool. After this wafer were cut into 22 mm × 22 mm pieces for experimental use. The silicon pieces were sequentially cleaned with deionized (DI) water and dipped in piranha solution using sulfuric acid (H_2SO_4) and H_2O_2 in 3:1 (vol.) ratio for 10 min. The silicon samples were then rinsed thoroughly with DI water.

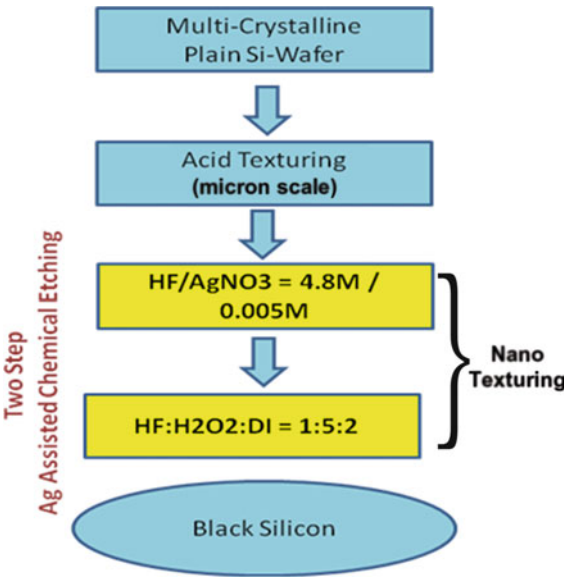

Fig. 1 Processing sequence for the preparation of black silicon

The nanotexturization was done using two step chemical etching as shown in Fig. 1. In step (i) a thin layer of Ag film was deposited over the textured silicon by immersing the samples in a mixture of 0.005 M $AgNO_3$ and 4.8 M HF at room temperature for different timings. This step deposited Ag nano-islands over the samples. Samples were rinsed in DI water thoroughly and dried in nitrogen. In step (ii) Ag deposited silicon samples were immersed in a mixture of HF:H_2O_2:DI water in the ratio 1:5:2 (vol.) solutions for different timings at room temperature. This step resulted in nanotexturization and silicon samples were turned into completely black. The residual Ag nanoparticals were removed completely by immersing in HNO_3 solution for 10 min at room temperature. Finally, the samples were rinsed in DI and dried in nitrogen and subjected to further investigations.

3 Results and Discussions

Morphologies and Cross sectional views of the samples were observed by scanning electron microscopy (SEM). Even with naked eye, it is possible to see the difference between them. The reflectance of all samples was tested at the wavelength from 300 to 800 nm at room temperature. The reflectance of all samples was measured using a purpose built integrating sphere attachment of a high accuracy spectrometer.

Figure 2 shows the reflectance of multicrystalline acid textured silicon wafer and the average reflectance measured is 25.9 %. Where as Table 1 shows the average reflectance chart for two step metal assisted chemical etching for 300–800 nm wavelength with different time steps. Figure 3 is the SEM images of multicrystalline acid textured and non-textured wafers after two step metal assisted chemical

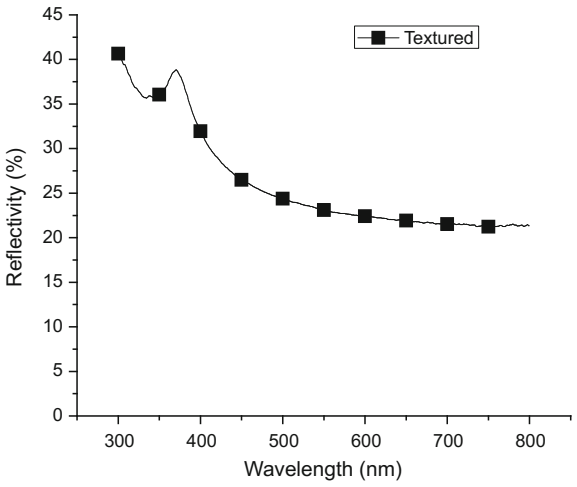

Fig. 2 The reflectance of the multicrystalline textured wafer

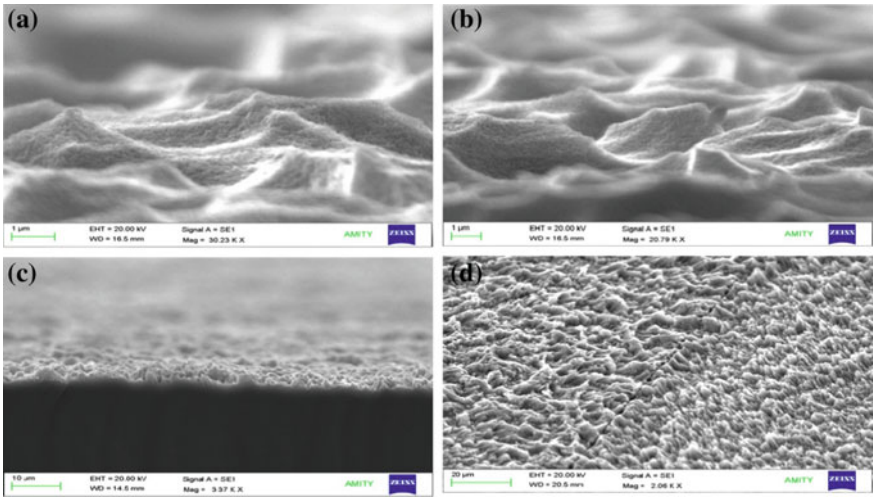

Fig. 3 SEM images of metal assisted chemical etching. Figure **a** and **b** are surface morphology on multi-crystalline textured wafer and figure **c** and **d** are the surface morphology on multi-crystalline without micron scale textured wafer

Table 1 Reflectance chart for two step metal assisted chemical etching for 300–800 nm wavelength range

Second Step ($HF:H_2O_2:DI$)					
	1 min	8.06	10.90	12.51	7.03
	1 min 30 sec	9.57	11.45	9.48	7.35
	2 min	8.89	7.40	6.95	4.64
	2 min 30 sec	7.61	8.93	9.24	4.54
	3 min	4.31	5.85	6.41	8.33
	4 min	9.95	5.54	5.39	6.37
	5 min	6.16	6.19	5.57	5.43
	10 min	6.12	5.70	6.18	6.40
	20 min	6.44	7.14	7.10	7.56
	TIME	30 sec	1 min	3 min	5 min
	First Step ($HF:AgNO_3$)				

RR < 6

6 < RR< 10

RR > 10

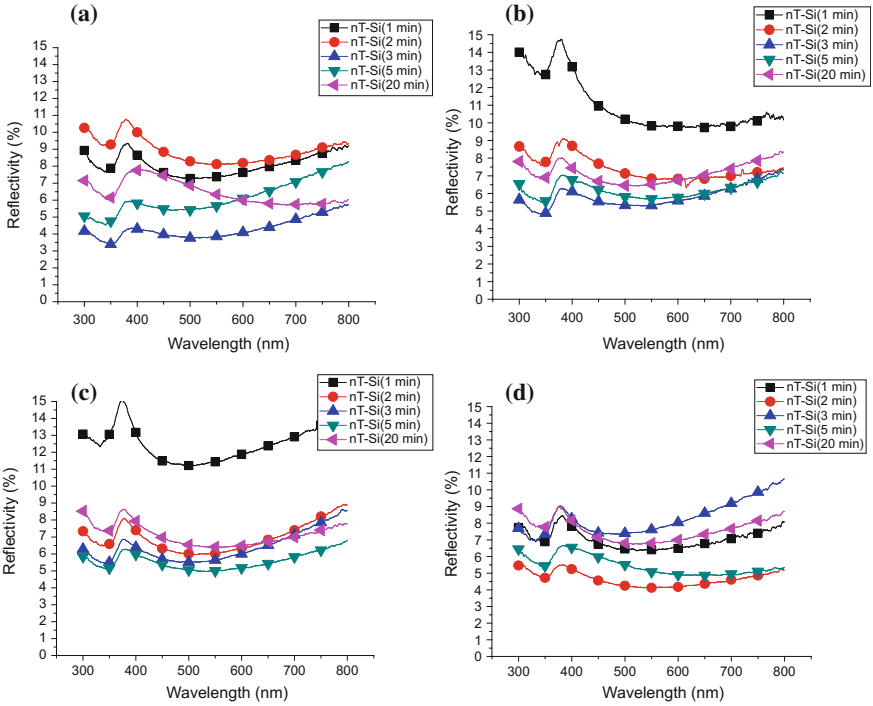

Fig. 4 The reflectance of the wafers textured by different conditions, First step etching (HF:$AgNO_3$) time for **a** 30 s. **b** 1 min, **c** 3 min, **d** 5 min, each graph has different timings of second step etching (HF:H_2O_2:DI)

etching. Figure 4 shows the reflectance of the wafers textured by different timings for first step etching (HF:$AgNO_3$) and second step etching (HF:H_2O_2:DI).

4 Conclusions

In this study we have fabricated multi-crystalline black silicon (B-Si) with two step texturing processes, first using micro-scale conventional acid texturing and second using nano-textured (nT-Si) layer, directly on the micro scale textured. A two step silver assisted chemical etching process is used to fabricate nano-textured surfaces in the aqueous solution of hydrogen peroxide (H_2O_2) and hydrofluoric acid (HF) instead of lithography process. The reflectivity has been studied with respect to the time of texturization. We have found that the average reflectivity has decreased to 4.3 % in wavelength range from 300 to 800 nm as compare to the nanotextured bare silicon where the reflectivity was $\sim$26 %. This striking property of the nano-textured black silicon may be utilized to enhance the performance (spectral response and the efficiency) of the silicon solar cell in the spectral range varying from 300 to 800 nm respectively.

References

1. M. Green, *High Efficiency Silicon Solar Cells* (Transactions on Technical Publications Ltd, Hardback, 1987)
2. H. Jansen, M. de Boer, R. Legtenberg, M. Elwenspoek, J. Micromech. Microeng. **5**, 115–120 (1995)
3. M. Halbwax, T. Sarnet, P.H. Delaporte, M. Sentis, H. Etienne, F. Torregrosa, V. Vervisch, I. Perichaud, S. Martinuzzi, Thin Solid Films **516**, 6791–6795 (2008)
4. S. Koynov, M.S. Brandt, M. Stutzmann, Phys. Stat. Solidi RRL. **1**, R53–R55 (2007)
5. Y. Xia, B. Liu, J. Liu, Z. Shen, C. Li, Sol. Energy **85**, 1574–1578 (2011)

Enhanced Removal of Cationic Dye Methylene Blue from Aqueous Solution Using Nanocellulose Prepared from Agricultural Waste Sugarcane Bagasse

Abhishek Kardam, Deepak Singh Rajawat, Sonal Kanwar and Madhubala

Abstract In the present communication nanocellulose was prepared from agricultural waste sugarcane bagasse and used for the removal of cationic dye methylene blue. Nanocellulose was prepared using bleaching treatment of agricultural waste followed by acid hydrolysis. SEM, TEM and TGA techniques were used to characterize prepared nanocellulose particles. Adsorption studies were optimized using simple batch experiments. Maximum sorption efficiency obtained for the removal of methylene blue using nanocellulose is 35 mg/g. The adsorption process fitted well for both Langmuir and freundlich isotherms. Regeneration studies signify that nanocellulose can be used successively up to 6 cycles of adsorption/desorption.

1 Introduction

Water is the most valuable element of our universe. A considerable saving of potable water can be achieved through reuse of wastewater that, in turn, requires the development of materials and methods, which are efficient, cost-effective, and reliable. Using better purification technologies can reduce problems of water

A. Kardam (✉)
Amity Institute for Advanced Research and Studies (Materials & Devices), Amity University, Noida 201303, Uttar Pradesh, India
e-mail: akardam@amity.edu

D.S. Rajawat · S. Kanwar · Madhubala
Department of Chemistry, IIS University, Jaipur, India

V.K. Jain et al. (eds.), *Recent Trends in Materials and Devices*, Springer Proceedings in Physics 178, DOI 10.1007/978-3-319-29096-6_4

shortages, health, energy, and climate change [1]. A wide range of environmental pollutants is involving in our day-to-day life. Among these pollutants, dyes are one of the priority pollutants. Dyes are used since a long ago. These include natural dyes [2]. The discovery of synthetic dyes overwhelmed the role of natural dyes in the society due to its low production cost, brighter colours, better resistance towards environmental factors and easy-to-apply factor. This has led to a higher consumption of synthetic dyes over natural dyes for most types of industrial applications [3]. Textile and dyeing industries are the major sources producing large volumes of wastewater containing dyes. Global concern about its toxic effects makes the removal of dyes essential.

Among several techniques for the decontamination of dye, adsorption is highly recommended technique. The advantages associated with adsorption are its treatment flexibility, reusability, environment friendliness and low cost [4]. A variety of adsorbent materials have been used for the removal of dyes from aqueous solution including plants, metals, polymers, biomaterials and nanomaterials [5–7]. Extensive studies have been undertaken in recent years with the aims of finding an alternative in the form of economic adsorbents for water treatment.

Among different materials available locally and abundantly, cellulose and cellulose-derived adsorbents can be a better option. Cellulose and cellulose-derived sorbents have been used previously. They presented significant adsorption efficiency for the removal of cationic pollutants. Incorporation of nanotechnology in adsorption, nanostructure adsorbents have exhibited much higher sorption efficiency. These are stable, economic, and more effective as compared with the already existing techniques. In the present piece of work nanocellulose was prepared by sugarcane bagasse, which was further used for the removal studies of cationic dye methylene blue.

2 Experimental Details

2.1 Chemical and Reagents

Sugarcane bagasse was obatained from the shops of local market Jaipur, India generated as a waste. A physical and chemical treatment was given to it before its application. The prepared nanocellulose was used as adsorbents for the sorption studies. Methylene blue was purchased from Merck. Sodium hydroxide, Hydrochloric acid, Nitric acid, Sulfuric acid was obtained from Merck. All the experiments were carried out at room temperature.

2.2 Preparation of Nanocellulose

The sugarcane bagasse was collected, washed with water, dried in oven and powered in grinder. Sugarcane bagasse was bleached with sodium hydroxide solution followed by washing and refluxed with $NaClO_2$. The generated cellulose was filtered, washed with distilled water and centrifuged at 3500 rpm at room temperature. The isolated cellulose will be subjected to alkaline hydrolysis followed by acid hydrolysis. The resulting suspension will be sonicated. The appearance of colloidal solution will be an indication for the preparation of nanocellulose.

2.3 Characterization

Morphological studies of the prepared materials were carried out using Scanning electron microscope, Transmission electron microscope and TGA techniques. The sample for SEM analysis was prepared by drop coat on a glass plate. Transmission electron microscope studies were carried out by drop coating the prepared suspension of nanocellulose on copper grid using Tecnai G2 20 (FEI) S-Twin. The grid was used for TEM analysis.

2.4 Sorption Studies

Sorption studies for the removal of dye Methylene blue was studied in batch experiments. 50 ml dye solution with desired concentration was prepared from stock solution. The pH of the solution was adjusted by adding HCl or NaOH in the dye solution. A fix amount of the prepared adsorbent (Nanocellulose) was mixed in the dye solution and stirred for a certain period of time. After stirring the solution was filtered and filtrate was used for concentration estimation and the residue was used for regeneration studies. Concentration of the dye after adsorption was evaluated by measuring absorption intensity using Shimadzu UV-1800 PC two beam spectrophotometer. All the experiments were performed at room temperature. Factors affecting sorption were analyzed within the range—Dye concentration, pH of dye solution, dosage of the Cellulose nanoparticles and contact time.

2.5 Regeneration Studies

Regeneration studies were conducted to regenerate the nanocellulose biomaterial using different desorption reagents (acid, base and neutral media). Dye-loaded

biomaterial obtained was transferred to Erlenmeyer flasks and shaken with 50 ml of each desorption reagents as a function of time (20, 40, 60, and 80 min) at room temperature. The suspensions were filtered using Whatman 42 filter paper and in the filtrate, estimation of dye concentration was carried out. Desorbed biomaterial was again subjected to sorption of dye followed by desorption at optimized contact time with optimized eluant concentration.

3 Results and Discussions

Scanning electron microscopic image of the prepared Nanocellulose is presented in Fig. 1. Spherical morphology of the prepared Nanocellulose particles is clearly visible from the SEM images. Transmission electron microscope results of the prepared Nanocellulose particles are presented in Fig. 2. The particles are spherical in 3D and size of the particles is less than 30 nm.

The thermogravimetric analysis curves for sugarcane bagasse and Nanocellulose are presented in Fig. 3a, b respectively. Graphs show the degradation pattern of the

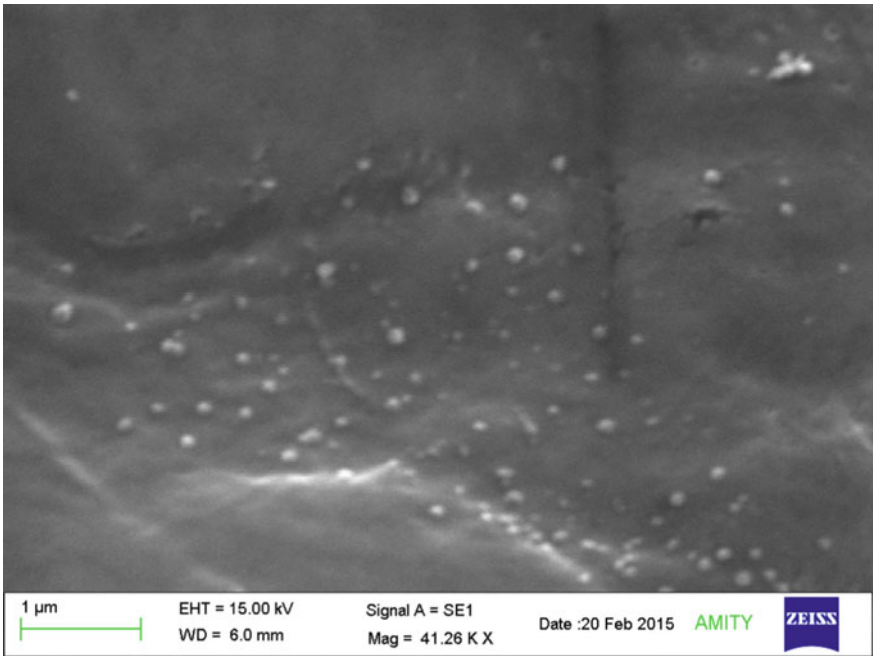

Fig. 1 Scanning electron microscope image of prepared nanocellulose

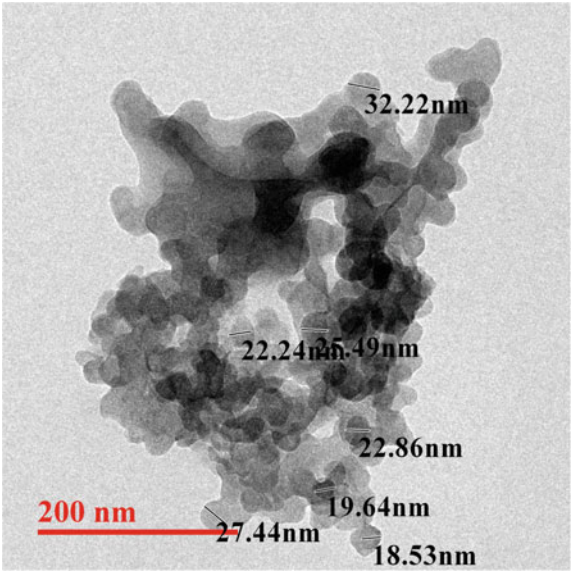

Fig. 2 Transmisson electron miscoscope image of nanocellulose particles

materials with increasing temperature. From the graphs it is clear that on converting sugarcane bagasse in nanocellulose the thermal stability of the biomass increased.

Figure 4 shows the variation of sorption efficiency of prepared material as a function of dosage of the material, pH of dye solution, contact time and dye concentration. Figure 4a represents the variation of sorption efficiency as a function of amount of Nanocellulose. A significant effect of amount of nanocellulose was observed on the removal effieciency for methylene blue.

Variation of sorption efficiency with pH of the dye solution is shown in the Fig. 4b. On increasing the pH sorption efficiency get increased regularly and attains a maximum value. Thereafter a decrease in the sorption efficiency was observed.

Effect of contact time and volume of dye solution is shown in Fig. 4c, d respectively. On increasing contact time increase in the sorption efficiency was observed due to the increase in the interaction between binding sites and dye molecules. After a sufficient contact time when all the available binding sites get occupied no further increase in the sorption efficiency was observed. Optimized conditions for the removal of Methylene blue are given in Table 1.

The sorption isotherm modeling is important in the design of biosorption systems. This indicates the capacity of the sorbent. Figure 5a, b shows the Langmuir and Freundlich adsorption isotherm for the removal of methylene blue. The linearity of Freundlich and Langmuir plots suggested the formation of homogenous monolayer of methylene blue on the outer surface of the biosorbent.

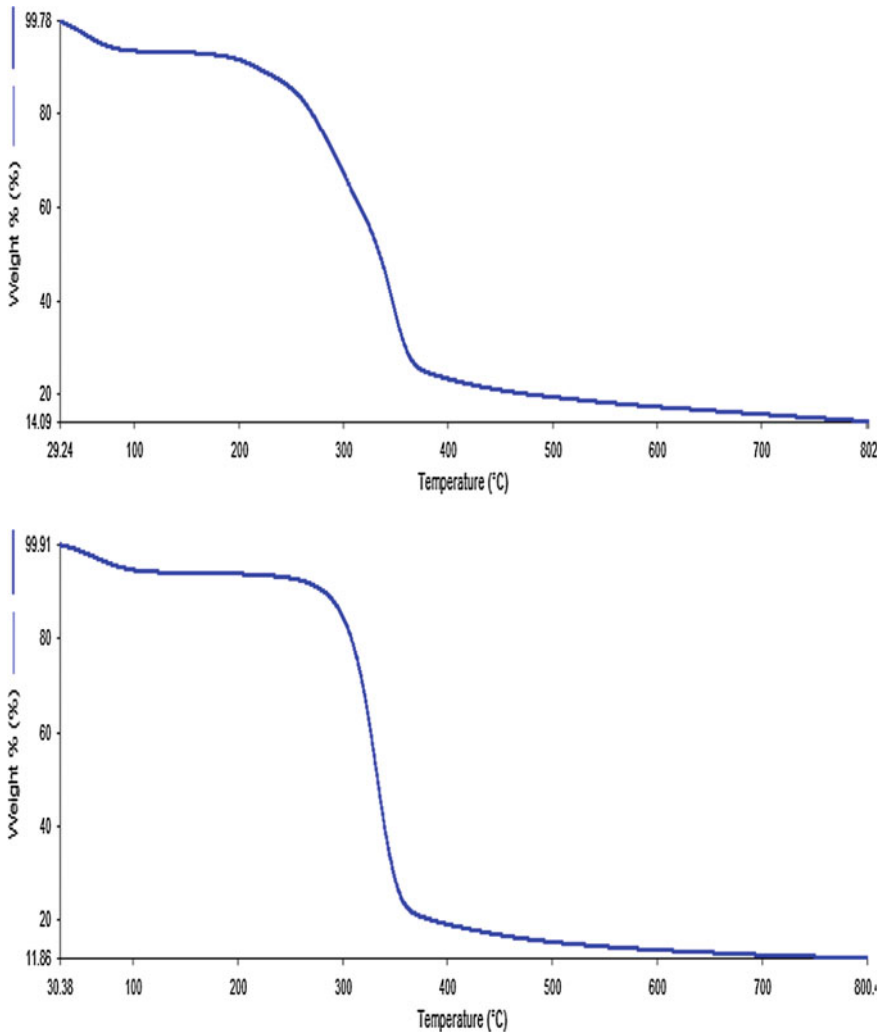

Fig. 3 Thermogravimetric analysis of sugarcane powder and nanocellulose

Maximum adsorption capacity of the prepared Nanocellulose particles is 35 mg/g. Regeneration studies signify that nanocellulose can be used successively up to 6 cycles of adsorption/desorption.

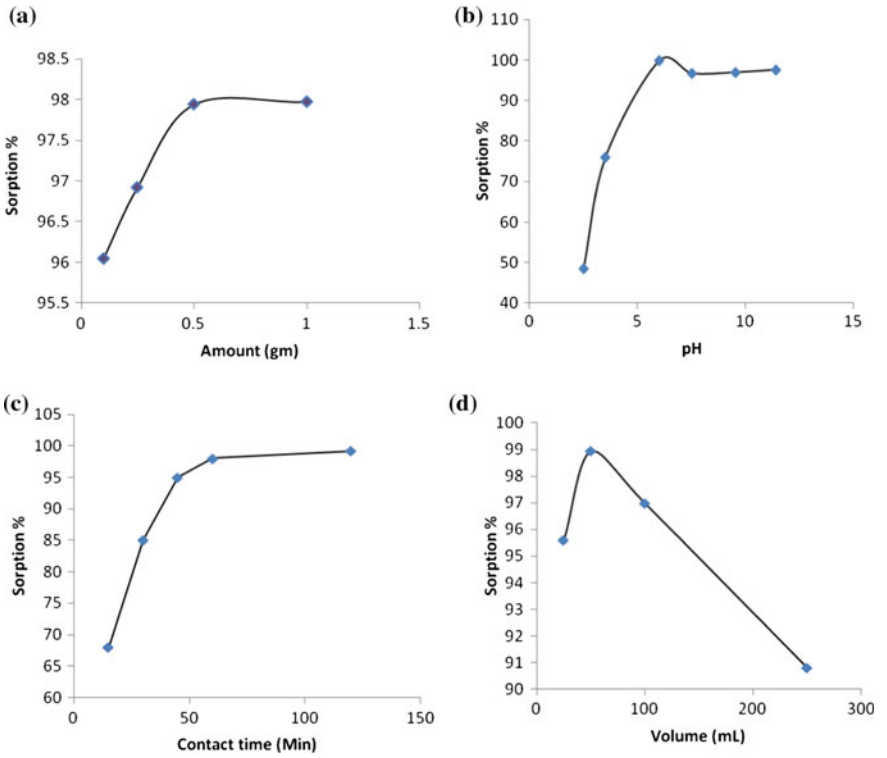

Fig. 4 Optimized conditions for the removal of methylene blue

Table 1 Optimized conditions for the removal of methylene from cellulose nanoparticles

Parameter	Value
Amount of Nanocellulose	0.5 g
pH of dye solution	9.2
Contact time	60 min
Volume of dye solution	50 mL

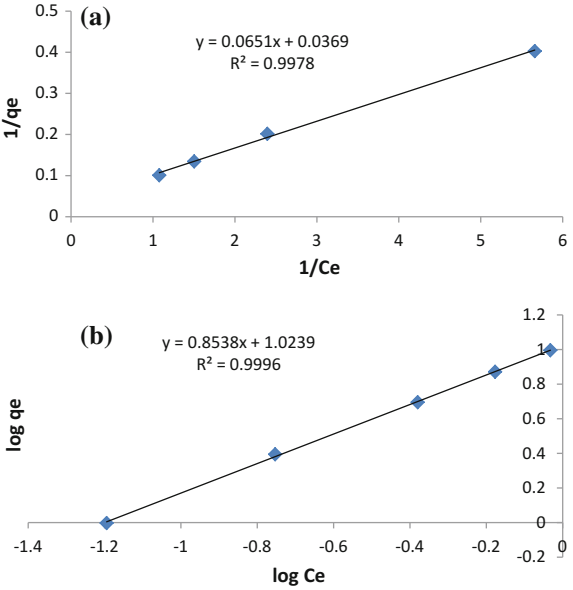

Fig. 5 **a** and **b** shows the Langmuir and Freundlich adsorption

4 Conclusions

Nanocellulose prepared from sugarcane bagasse have shown high adsorption capacity and potential for its reusability for removal of methylene blue dye from water bodies. Studies are recommended for structuring of filter candles at commercial level for removal of cationic dyes from water. Proposed method of dye removal is deemed to be a less expensive, domestic and environment-friendly green technology compare to other high tech methods.

References

1. J.C. Bowman, J.L. Zhou, J.W. Readman, Mar. Chem. **77**, 263–276 (2002)
2. S. De, S. Mondal, in *Micellar Enhanced Ultrafilteration: Fundamentals and Applications*. (CRC Press, Taylor and Francis)
3. F. Moussavi, M. Mahmoudi, J. Hazard. Mater. **168**, 806–812 (2009)
4. M.A. Kamboh, A.A. Bhatti, I.B. Solangi, S.T.H. Sherazi, S. Memon, Arab. J. Chem. **7**, 125–131 (2014)
5. A.A. El-zahhar, N.S. Awwad, E.E. El-Katori, J. Mol. Liq. **199**, 454–461 (2014)
6. F. Deniz, Sci. World J. (2013)
7. A. Rodríguez, G. Ovejero, J.L. Sotelo, M. Mestanza, J. García, J Environ Sci Health A Tox Hazard Subst Environ Eng. **45**(12), 1642–1653 (2010)

A Review on Thermophysical Properties of Nanoparticle-Enhanced Phase Change Materials for Thermal Energy Storage

Apurv Yadav, Bidyut Barman, Vivek Kumar, Abhishek Kardam, S. Shankara Narayanan, Abhishek Verma, Devinder Madhwal, Prashant Shukla and Vinod Kumar Jain

Abstract A review of current experimental studies on variations in thermophysical properties of phase change material (PCM) due to dispersion of highly-conductive nanoparticles, coined as nanoparticle-enhanced PCMs (NePCMs), is presented in this article. The NePCMs may be considered as a solution to improve latent heat thermal energy storage performance. Thermophysical properties such as thermal conductivity, latent heat, viscosity and super cooling of PCMs could be changed for different physical properties of dispersed nanoparticle such as size, shape, concentration and surface properties. The present review focuses on the studies that describe the effect of addition of nanoparticles on the thermophysical properties of PCM with the help of available explanations in the literature.

1 Introduction

In recent years, due to the problems of fast depletion of conventional energy sources and ever increasing demand of energy, the implementation of proper thermal energy storage (TES) is one of the most important issues in energy conversion systems. TES technologies have grabbed the attention of researchers for its exceptional behavior, storing energy for usage at a later period, which would lead to a reduction in the overall energy demand. Among the various TES methods, Latent Heat Thermal Energy Storage (LHTES) system using Phase Change Materials (PCMs) is the most widely and favorable method due to its advantages such as high heat

A. Yadav · B. Barman · V. Kumar · A. Kardam · S. Shankara Narayanan (✉)
A. Verma · D. Madhwal · P. Shukla · V.K. Jain
Amity Institute for Advanced Research and Studies (Materials & Devices),
Amity University, Noida, Uttar Pradesh 201303, India
e-mail: ssnarayanan@amity.edu; shankar334@gmail.com

A. Yadav · B. Barman · V. Kumar · A. Kardam · S. Shankara Narayanan
A. Verma · D. Madhwal · P. Shukla · V.K. Jain
Amity Institute of Renewable and Alternate Energy, Amity University,
Noida, Uttar Pradesh 201303, India

V.K. Jain et al. (eds.), *Recent Trends in Materials and Devices*,
Springer Proceedings in Physics 178, DOI 10.1007/978-3-319-29096-6_5

storage capacity, small unit size and isothermal behavior during charging and discharging. In spite of the great advantages offered by PCMs, poor heat transfer performance is the common obstacle for most LHTES systems due to the low thermal conductivity of the PCMs employed.

In order to enhance the heat transfer performance of PCM for thermal energy storage applications, various techniques have been investigated to improve the poor thermal conductivity of PCM. The different techniques to increase thermal conductivity in PCMs include enlarging the heat-exchange area by designing heat exchanger with finned configuration, insertion of a metal matrix into the PCMs, micro-encapsulation of the PCM and enhancing the thermal conductivity of stored material by developing new phase change composite using additives [1]. Dispersing highly conductive nanoparticles could be a solution to enhance the thermal conductivity of PCMs. By introducing nanoparticles in PCM, thermophysical properties such as thermal conductivity, latent heat, viscosity, super cooling, etc. of the base PCM could be changed intensively. This paper reviews the present state of the art of phase change materials for thermal energy storage applications and provides a deep insight into recent efforts to develop new PCMs showing enhanced performance and safety. An extensive literature review has been performed to demonstrate the effects on thermophysical properties of PCM on dispersion of different nano particles.

2 Classification of PCMs

Broadly, PCMs are classified into three types: organic, inorganic and eutectic (Fig. 1). Based on the melting/freezing temperature and latent heat of fusion, a large number of organic and inorganic materials can be treated as PCM.

Organic PCMs are subdivided into paraffins, which consists of straight n-alkanes chain (C_nH_{2n+2}) and fatty acids (Fig. 1), that are made up of straight chain hydrocarbons ($CH_3(CH_2)_{2n}COOH$). Organic materials possess the capability of congruent melting without phase separation. These compounds are available in a wide range of melting points. They have high heat of fusion, safe and compatible with conventional storage materials. But they have low thermal conductivity and low volumetric latent heat storage capacity. These problems can be overcome to an extent by dispersion of nanoparticles in the PCM.

Inorganic PCMs can be divided into hydrated salts and metallic. Metallic PCMs are costlier and have very high melting points, which is not suitable for many applications. Salt hydrates have high volumetric latent heat storage capacity, cheaper and easily available. They have relatively high thermal conductivity and high heat of fusion, but they melt incongruently. Moreover, super cooling is major problem in solid-liquid transition of salt hydrates. Dispersion of nanoparticles improves the thermal properties and the problem of super cooling is reduced. A eutectic is a composition of two or more components such as organic–organic, organic–inorganic, inorganic–inorganic and each of them change their phase

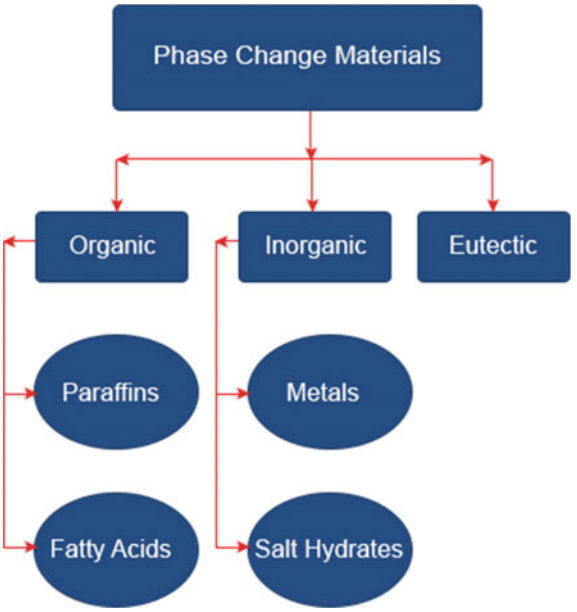

Fig. 1 Classification of PCMs

congruently and form a mixture of component crystal during crystallization. They have sharp melting points and slightly greater volumetric latent heat storage capacity than organic PCM. Eutectics generally melt and freeze congruently and leave no chances of separation of components. The different thermal, physical and chemical properties of PCM, which make them useful for different applications, are shown in Table 1.

Effective utilization of TES depends upon the selection of suitable PCM with appropriate phase change temperature and high latent heat of fusion. PCMs are subjected to approximately two hundred and fifty charging and discharging cycles per year. Therefore the possibilities of degradation in the thermal properties of PCM over time with respect to thermal cycles are to be thoroughly analyzed for designing a superior solar thermal energy storage system. A PCM is said to be reliable if the thermophysical properties are stable over large number of thermal cycles. It is essential to study the phase change temperature and latent heat of fusion for a

Table 1 Various thermal, physical and chemical properties of PCM

Thermal	Physical	Chemical
Suitable phase transition temperature High latent heat of transition Good heat transfer properties	Phase equilibrium is favourable High storage density Small volume changes	Prolonged chemical stability Compatibility with various materials of construction Non-toxic No fire hazard

minimum of one thousand accelerated thermal cycles to ensure the thermal reliability of a selected PCM [2]. A normal cycle in a latent heat solar TES system stands for one thermal charging and discharging process by the PCM in a day. If this thermal cycle is performed in controlled conditions at laboratory scale, it is said to be accelerated thermal cycle. Nikolic et al. [3] reported the 50 thermal cycles of methyl and cetyl of stearate and palmitate. The study reported that even after 18 months duration, thermal properties were stable and reliable for room temperature solar thermal applications. Sun et al. [4] reported the thermal reliability of Al–34 % Mg–6 % Zn alloy as a latent heat energy storage material with respect to 1000 thermal cycles. It is found that the melting temperature for the alloy varies in the range of 3.06–5.3 K, and the latent heat of fusion decreased to 10.98 % after 1000 thermal cycles.

3 Nanoparticle-Enhanced PCMs

In recent years, addition of nanoparticles to PCM has shown a tremendous promise in the field of thermal energy storage. Nanoparticles are used as additives to enhance the thermal properties of these PCM. When nanoparticles are added to the fluid, the resulting mixture is denoted by nanofluids, while by adding the nanoparticles to PCM, the resulting product is called nanoparticle-enhanced phase change materials (NePCMs), which has opened even new frontiers. Many research works have been carried out on NePCMs, which focused to investigate the thermophysical properties of PCMs with different nano particles. For example, Khodadadi et al. [5] published an article showing the suitability of nano particles in enhancing the thermal conductivity of PCMs for TES. Zeng et al. [6] prepared the Ag nanoparticles and added with 1-tetradecanol for improving the thermal conductivity and the result showed that as the concentration of Ag nanoparticles increased the thermal conductivity of the composite PCM also increased. Kalaiselvam et al. [7] reported that concentration of nanoparticles dispersed into PCMs should be optimal for better thermal and heat transfer characteristics of PCMs. Ho and Gao [8] studied the effective thermo physical properties, such as latent heat of fusion, density, dynamic viscosity and thermal conductivity of n-octadecane PCM embedded with alumina nanoparticles with various compositions.

Most of the research works in literature were conducted on the improvement of thermal properties of PCMs such as paraffins and fatty acids. Paraffin draws a great attraction to researchers for its desirable characteristics like, good heat storage density, melting or solidification compatibly with little or no sub cooling, low cost and non-reactivity with most common chemical reagents [9]. Fatty acids show the similar properties as paraffin. However, the main drawback of these PCM's is their low thermal conductivity. Dispersing high conductive nano particles could be a solution to enhance the thermal conductivity of these PCMs. Few published research works are presented in Table 2 related to investigation of he thermal properties of NePCMs using different kinds of nanoparticles.

Table 2 Summary of published experimental studies related to NePCMs

Organic PCM	Phase transition temperature (°C)	Latent heat (kJ/g)	Thermal conductivity [W/(mK)]	Dispersed nanomaterials	Thermal conductivity enhancement %	References
1-dodecanol	22	N/A	0.154	CNT	111	Zeng et al. [10]
n-octadecane	27	243.5	0.152	$MPSiO_2$	6	Motahar et al. [11]
Bio-based PCM	29.38	142.9	0.154	Exfoliated GNP	375	Jeong et al. [12]
1-tetradecanol	37	N/A	0.159	GNP	>200	Fan et al. [13]
n-eicosane	37	241	0.15	GNP	200	Fang et al. [14]
Lauric acid	44	178	0.147	GNP	230	Harish et al. [15]
Paraffin wax	45	190	0.48	Ag nanoparticles	0.66	Giriswamy et al. [16]
Paraffin wax	45	190	0.21	Al nanoparticles	N/A	Chaichan et al. [17]
Palmitic acid	59.48	200.3	0.318	MWCNT	30	Zeng et al. [18]
Palmitic acid	62	205	0.29	GNP	N/A	Mehrali et al. [19]
Palmitic acid	62.4	206.32	0.28	Nitrogen doped graphene	517	Mehrali et al. [20]
Palmitic acid	62.5	208	0.22	MWCNT	46	Wang et al. [21]
Stearic acid	64	200.2	0.26	Graphite nanoparticles	1200	Li et al. [22]
Stearic acid	64	203	0.17	MWCNT	10.5	Choi et al. [23]
Stearic acid	64	203	0.17	Graphene	18.2	Choi et al. [23]
Arachaic acid	76.4	223	0.178	Graphene	4300	Seki et al. [24]
Decane	N/A	N/A	0.132	Al_2O_3 nanoparticles	103	Schmidt et al. [25]

(continued)

Table 2 (continued)

Organic PCM	Phase transition temperature (°C)	Latent heat (kJ/g)	Thermal conductivity [W/(mK)]	Dispersed nanomaterials	Thermal conductivity enhancement %	References
Poly Alfa olefin	N/A	N/A	0.136	Al_2O_3 nanoparticles	106	Schmidt et al. [25]
Octadecanoic acid	N/A	N/A	0.184	Graphene aerogel	1332	Zhong et al. [26]

Inorganic PCMInorganic PCM	Phase transition temperature (°C)	Latent heat (kJ/g)	Thermal conductivity [W/(m/K)]	Dispersed nanomaterials	Thermal conductivity enhancement %	References
$CaCl_2 \cdot 6H_2O$	30.2	167	N/A	Cu Nanostructures	>50	Sreethawong et al. [27]
$CH_3COONa \cdot 3H_2O$	58	N/A	N/A	Aluminium nitride (AIN)	N/A	Hu et al. [28]
$Mg(NO_3)_2 \cdot 6H_2O$	129	N/A	1.138	Nanographite	95	Kardam et al. [29]
Aqueous KNO_3	334	N/A	N/A	SiO_2 nanoparticles	N/A	Chieruzzi et al. [30]
Aqueous KNO_3	334	N/A	N/A	Al_2O_3 nanoparticles	N/A	Chieruzzi et al. [30]
Aqueous $BaCl_2$	−8.16 °C	N/A	0.53 W/m K at −5 °C	TiO_2 nanoparticles	12.76	He et al. [31]
$CH_3COONa \cdot 3H_2O$	N/A	N/A	N/A	Ag nanoparticles	N/A	Ramirez et al. [32]

Eutectics PCM	Phase transition temperature (°C)	Latent heat (kJ/g)	Dispersed nanomaterials	Specific heat enhancement	References
Capric Acid + Lauric Acid + Palmitic Acid (59.7:30.1:10.02)	19.92	135.49	Expanded graphite	N/A	Huang et al. [33]
$NaNO_2 + NaNO_3 + KNO_3$ (40:7:53)	142	N/A	Al_2O_3 nanoparticles	19.90	Ho et al. [34]
$KNO_3 + NaNO_3$ (60:40)	220		Mica nanoparticles	13–15	Jung et al. [35]

(continued)

Table 2 (continued)

Eutectics PCM	Phase transition temperature (°C)	Latent heat (kJ/g)	Dispersed nanomaterials	Specific heat enhancement	References
KNO_3 + $NaNO_3$ (60:40)	220	110	SiO_2 nanoparticles	14.90	Chieruzzi et al. [36]
KNO_3 + $NaNO_3$ (60:40)	220	110	Al_2O_3 nanoparticles	19.90	Chieruzzi et al. [36]
KNO_3 + $NaNO_3$ (60:40)	220	110	TiO_2 nanoparticles	−6.00	Chieruzzi et al. [36]
KNO_3 + $NaNO_3$ (60:40)	220	110	SiO_2 + Al_2O_3 nanoparticles	57.70	Chieruzzi et al. [36]
KNO_3 + $NaNO_3$ (60:40)	220	110	MWCNT nanoparticles	N/A	Niu et al. [37]
KNO_3 + $NaNO_3$ (60:40)	220	110	CuO nanoparticles	10.48	Lasfargues et al. [38]
KNO_3 + $NaNO_3$ (60:40)	220	110	TiO_2 nanoparticles	4.95	Lasfargues et al. [38]
$BaCl_2$ + NaCl + $CaCl_2$ + LiCl (34:13:40:13)	378	N/A	SiO_2 nanoparticles	14.50	Shin et al. [39]
Li_2CO_3 + K_2CO_3 (60:40)	488	N/A	SiO_2 nanoparticles	25.00	Andreu-Cabedo et al. [40]
Li_2CO_3 + K_2CO_3 (60:40)	488	N/A	SiO_2 nanoparticles	26.00	Shin et al. [39]
Li_2CO_3 + K_2CO_3 (60:40)	488	N/A	CNT nanoparticles	42.00	Shin et al. [39]
Li_2CO_3 + K_2CO_3 (62:38)	490	N/A	CNT nanoparticles	N/A	Jo et al. [41]

4 Effects on Thermophysical Properties Due to Nano Particle Dispersion in PCMs

Effects on thermal conductivity: The rate of energy stored and released in a PCM are highly dependent on the thermal conductivity of the PCMs in both solid and liquid states. Simultaneously, different PCMs used in various TES systems have a great variation in operation temperature. In case of highly conductive nano particle dispersed into PCMs, the effect of thermal conductivity is an important factor to choose the appropriate PCM for that system. The performance of nanoparticle dispersed PCM in terms of thermal conductivity depends on mass concentration, surface and physical properties of nanoparticles that is dispersed.

Dispersing nanoparticles could enhance the conductivity of PCMs. The reason is as the size of nanoparticles decreases, the surface to volume ratio increases. This increases the heat transfer ability of nanoparticles. The different nanofillers which have been employed are metallic/oxide nanoparticles [6, 42], metallic nanowires [43, 44] and carbon nanomaterials. Various carbon nanomaterials include carbon nanofibers (CNFs) [45, 46], carbon nanotubes (CNTs) [47, 48], and the graphene/graphite nanoplatelets (GNPs) [49, 50]. These carbon nanomaterials have some exclusive physical properties that makes them a good candidate in the field of PCM based LHTS. For example, CNT and CNF have low weight and high thermal conductivity (1950–4000 W/mK), which has shown tremendous potential for heat transfer applications. The GNPs, owing to their unique two-dimensional planar structure, have been identified to even outperform the other wire-shaped carbon nanomaterials, i.e., CNFs and CNTs, in enhancing the thermal conductivity for engineered suspensions [51]. Recently, our group reported the heat transfer characteristics of two different kinds of NePCM composites: nanographite (NG)–PCM composites and multi-walled carbon nanotube (CNT)–PCM composites [29]. The prepared NPCM composites exhibited enhanced thermal conductivity and a faster heating rate than pristine PCMs. It was observed that upon solar illumination, both NG–PCM and CNT–PCM composites demonstrated an ultrafast heating rate (of the order of few seconds) and a higher heating temperature than the conventional heating based approach, which was attributed to the plasmonic heating effect of carbon nanomaterials, which instantly convert optical energy into heat at nanometer scale in addition to conventional thermal diffusion based slow heating. Out of the two carbon nanofillers used, CNTs were shown to have a better heat transfer performance than NGs to collect, convert and store the broad spectrum solar energy as thermal energy.

Effects on latent heat capacity: The size, shape, concentration and even the intermolecular attraction between the particle and PCM are the main factors which are attributed to a change in the latent heat behavior of NePCM composites. Shaikh et al. [52] investigated SWCNT (Single Wall Carbon Nano Tubes), MWCNT and CNF in paraffin wax. A maximum 13 % of latent heat was enhanced in PW/SWCNT composite corresponding to 1 % loading of SWCNT. The change in latent heat was discussed using an approximation for the intermolecular attraction

based on the Lennard-Jones potential. The concept was adopted from the work of Israelachvili [53] which deals with the change in enthalpy due to the CNT surface-PCM interaction. Wang et al. [48]. investigated the effects on latent heat capacity dispersing MWCNT in PW and concluded that, the latent heat capacity inconsistency increased with an increase in the mass fraction of MWCNT. With an increase in the mass fraction of MWCNT, the phase change temperature also decreased. Similar characteristic was also observer by Li et al. [22] while dispersing MWCNT in stearic acid as PCM. Decreasing latent heat capacity phenomena of PCM using MWCNT was also investigated by Wang et al. [47] and Zeng et al. [18]. In the experiment of Zeng et al. [18], it was found that the ΔH of composites would decrease radically comparing to that of PA as the MWCNT content is increased.

In NePCM, degradation of latent heat capacity was observed in dispersing metal and metal oxide nanoparticle such as Ag/Cu/Al and CuO/TiO_2 nanoparticle in different PCM. Wu et al. [54] dispersed Cu nanoparticle in paraffin and found a maximum reduction of 11.1 and 11.7 % in melting and freezing latent heat respectively. It was observed that increasing the volume fraction of Cu nanoparticle, the latent heat reduced. Parameshwaran et al. [55] investigated surface-functionalized crystalline silver nanoparticles dispersed Organic ester as PCM. In freezing and melting cycles, the reduction in latent heat capacity of SNOE PCMs varied from 1.78 to 7.88 % and 1.17 to 8.91 %, respectively for 0.1–5.0 wt% of AgNP mass loading. However, dissimilar characteristics of latent heat were observed by Yang et al. [56] while dispersing Si_3N_4 nano-particles in paraffin. They found increasing latent heat with 1 wt% of nano particles. Dissimilar characteristics in phase change temperature of PW was examined by Wang et al. [57] that indicated the phase change temperature both in solid and melting point shifted to a lower temperature due to the addition of Al_2O_3 into PW except the composite containing 1 % mass fraction of Al_2O_3 nano particle.

5 Conclusions

Dispersion of nanoparticles in PCM to improve the thermal properties of PCM is a subject of growing interest. A review on recent literature on thermophysical properties of NePCMs has been discussed. The data published in the literature on NePCM allow us to draw the conclusions that thermal conductivity of NePCM increases considerably with increase in the concentration of nanoparticle in PCM. The enhancements in thermal conductivity of NePCM make a remarkable reduction in the solidification and melting time of the composition. Different nanoparticle exhibits different enhancement in solidification of PCMs. From the NePCM literature it also seems, the latent heat capacity of PCM decreases with increasing nanoparticle concentration although it could increase in special cases. Different properties of nanoparticle affect the degradation of latent heat capacity in different ways. There should be an optimum level of nanoparticle concentration in which

thermal conductivity enhancement is maximum and latent heat capacity degradation is minimum. This optimum level of nanoparticle concentration in PCM has to be explored.

Acknowledgments The authors are grateful to Dr. Ashok K Chauhan, Founder President, Amity University, Noida, India for his continuous encouragement and support in carrying out the research work.

References

1. H. Mehling, L.F. Cabeza, Phase change materials and their basic properties. *Thermal energy storage for sustainable energy consumption*, (Springer Netherlands, 2007), pp. 257–277
2. M.K. Rathod, J. Banerjee, Renew. Sustain. Energy Rev. **18**, 246–258 (2013)
3. R. Nikolic, M. Marinovic-Cincovic, S. Gadzuric, I.J. Zsigrai, Sol. Energy Mater. Sol. Cells **79**(3), 285–292 (2003)
4. J.Q. Sun, R.Y. Zhang, Z.P. Liu, G.H. Lu, Energy Convers. Manag. **48**(2), 619–624 (2007)
5. L.W. Fan, J.M. Khodadadi, H. Babaei, Renew. Sustain. Energy Rev. **24**, 418–444 (2013)
6. J.L. Zeng, L.X. Sun, F. Xu, Z.C. Tan, Z.H. Zhang, J. Zhang, T. Zhang, J. Therm. Anal. Calorim. **87**(2), 371–375 (2007)
7. S. Kalaiselvam, R. Parameshwaran, S. Harikrishnan, Renew. Energy **39**(1), 375–387 (2012)
8. C.J. Ho, J.Y. Gao, Int. Commun. Heat Mass Transfer **36**(5), 467–470 (2009)
9. A. Abhat, Sol. Energy **30**(4), 313–332 (1983)
10. Y. Zeng, L.W. Fan, Y.Q. Xiao, Z.T. Yu, K.F. Cen, Int. J. Heat Mass Transf. **66**, 111–117 (2013)
11. S. Motahar, N. Nikkam, A.A. Alemrajabi, R. Khodabandeh, M.S. Toprak, M. Muhammed, Int. Commun. Heat Mass Transf. **59**, 68–74 (2014)
12. S. Jeong, O. Chung, S. Yu, S. Kim, S. Kim, Sol. Energy Mater. Sol. Cells **117**, 87–92 (2013)
13. L.W. Fan, Z.Q. Zhu, Y. Zeng, Q. Lu, Z.T. Yu, Int. J. Heat Mass Transf. **79**, 94–104 (2014)
14. X. Fang, L. Fan, Q. Ding, X. Wang, X. Yao, J. Hou, Z. Yu, G. Cheng, Y. Hu, K. Cen, Energy Fuels **27**, 4041–4047 (2013)
15. S. Harish, D. Orejon, Y. Takata, M. Kohno, Appl. Therm. Eng. **80**, 205–211 (2015)
16. B.G. Giriswamy, M. Eshwarmoorthy, M. Yellapa, N. Satyamurthy, Int. J. Mech. Eng. Res. **3**(1), 361–376 (2014)
17. M.T. Chaichan, H.A. Kazem, Int. J. Renew. Energy Res. **5**(1), 251–257 (2015)
18. J.L. Zeng, Z. Cao, D.W. Yang, F. Xu, L.X. Sun, X.F. Zhang, L. Zhang, J. Therm. Anal. Calorim. **95**, 507–512 (2009)
19. M. Mehrali, S.T. Latibari, M. Mehrali, T.M.I. Mahlia, H.S.C. Metselaar, M.S. Naghavi, E. Sadeghinezhad, A.R. Akhiani, Appl. Therm. Eng. **61**(2), 633–640 (2013)
20. M. Mehrali, S.T. Latibari, M. Mehrali, T.M.I. Mahlia, E. Sadeghinezhad, H.S.C. Metselaar, Appl. Energy **135**, 339–349 (2014)
21. J. Wang, H. Xie, Z. Xin, Y. Li, L. Chen, Sol. Energy **84**, 339–344 (2010)
22. T. Li, J.-H. Lee, R. Wang, Y.T. Kang, Int. J. Heat Mass Transf. **75**, 1–11 (2014)
23. D.H. Choi, J. Lee, H. Hong, Y.T. Kang, Int. J. Refrig. **42**, 112–120 (2014)
24. Y. Seki, S. Ince, M. Uzun, M.A. Ezan, L. Cetin, A. Turgut, A. Erek, C. R. Proceedings of the International Conference on Heat Transfer and Fluid Flow, Prague, Czech Republic, August 11–12, 2014, Paper No. 185
25. A.J. Schmidt, M. Chiesa, D.H. Torchinsky, J.A. Johnson, K.A. Nelson, G. Chen, J. Appl. Phys. **103**, 083529 (2008)
26. Y. Zhong, M. Zhou, F. Huang, T. Lin, D. Wan, Sol. Energy Mater. Sol. Cells **113**, 195–200 (2013)

27. T. Sreethawong, K.W. Shah, S.-Y. Zhang, E. Ye, S.H. Lim, U. Maheswaran, W.Y. Mao, M.-Y. Han, J. Mater. Chem. A **2**(10), 3417–3423 (2014)
28. P. Hu, D.-J. Lu, X.-Y. Fan, X. Zhou, Z.-S. Chan, Sol. Energy Mater. Sol. Cells **95**(9), 2645–2649 (2011)
29. A. Kardam, S.S. Narayanan, N. Bhardwaj, D. Madhwal, P. Shukla, A. Verma, V.K. Jain, RSC Adv. **5**, 56541–56548 (2015)
30. M. Chieruzzi, A. Miliozzi, T. Crescenzi, L. Torre, J.M. Kenny, Nanoscale Res. Lett. **10**, 273 (2015)
31. Q. He, S. Wang, M. Tong, Y. Liu, Energy Convers. Manag. **64**, 199–205 (2012)
32. B.M.L.G. Ramirez, C. Glorieux, E.S.M. Martinez, J.J.A.F. Cuautle, Appl. Therm. Eng. **62**, 838–844 (2014)
33. Z. Huang, X. Gao, T. Xu, Y. Fang, Z. Zhang, Appl. Energy **115**, 265–271 (2014)
34. M.X. Ho, C. Pan, Int. J. Heat Mass Transf. **70**, 174–184 (2014)
35. S. Jung, D. Banerjee, Dev Strateg Mater Comput Des II: Ceram Eng Sci Proc. **32**, 127–137 (2011)
36. M. Chieruzzi, G.F. Cerritelli, A. Miliozzi, J.M. Kenny, Nanoscale Res. Lett. **8**, 448 (2013)
37. D. Niu, Y. Lu, D. Wu, Bul. Chem. Commun. **46**(4), 873–881 (2014)
38. M. Lasfargues, Q. Geng, H. Cao, Y. Ding, Nanomaterials **5**, 1136–1146 (2015)
39. D. Shin, D. Banerjee, Int. J. Heat Mass Transf. **54**, 1064–1070 (2011)
40. P. Andreu-Cabedo, R. Mondragon, L. Hernandez, R. Martinez-Cuenca, L. Cabedo, J.E. Julia, Nanoscale Res. Lett. **9**, 582 (2014)
41. B. Jo, D. Banerjee, Acta Mater. **75**, 80–91 (2014)
42. S. Jesumathy, M. Udayakumar, S. Suresh, Heat Mass Transf. **48**, 965–978 (2012)
43. J.L. Zeng, Z. Cao, D.W. Yang, L.X. Sun, L. Zhang, J. Therm. Anal. Calorim. **101**, 385–389 (2010)
44. J.-L. Zeng, F.-R. Zhu, S.-B. Yu, L. Zhu, Z. Cao, L.-X. Sun, G.-R. Deng, W.-P. Yan, L. Zhang, Sol. Energy Mater. Sol. Cells **105**, 174–178 (2012)
45. A. Elgafy, K. Lafdi, Carbon **43**(15), 3067–3074 (2005)
46. Y. Cui, C. Liu, S. Hu, X. Yu, Sol. Energy Mater. Sol. Cells **95**(4), 1208–1212 (2011)
47. J. Wang, H. Xie, Z. Xin, J. Appl. Phys. **104**, 113537 (2008)
48. J. Wang, H. Xie, Z. Xin, Thermochim. Acta **488**(1), 39–42 (2009)
49. F. Yavari, H.R. Fard, K. Pashayi, M.A. Rafiee, A. Zamiri, Z. Yu, R. Ozisik, T. Borca-Tasciuc, N. Koratkar, J. Phys. Chem. C **115**(17), 8753–8758 (2011)
50. J. Xiang, L.T. Drzal, Sol. Energy Mater. Sol. Cells **95**(7), 1811–1818 (2011)
51. Z.-T. Yu, X. Fang, L.-W. Fan, X. Wang, Y.-Q. Xiao, Y. Zeng, X. Xu, Y.-C. Hu, K.-F. Cen, Carbon **53**, 277–285 (2013)
52. S. Shaikh, K. Lafdi, K. Hallinan, J. Appl. Phys. **103**, 094302–094306 (2008)
53. J.N. Israelachvili, *Intermolecular and Surface Forces*, 3rd edition (Academic press, Amsterdam, 2011)
54. S. Wu, D. Zhu, X. Zhang, J. Huang, Energy Fuels **24**(3), 1894–1898 (2010)
55. R. Parameshwaran, R. Jayavel, S. Kalaiselvam, J. Therm. Anal. Calorim. **114**, 845–858 (2013)
56. Y. Yang, J. Luo, G. Song, Y. Liu, G. Tang, Thermochim. Acta **597**, 101–106 (2014)
57. J. Wang, H. Xie, Y. Li, Z. Xin, J. Therm. Anal. Calorim. **102**(2), 709–713 (2010)

Multiphysics Analysis of Heat Transfer in Gate All Around (GAA) Silicon Nanowire Transistor: Material Perspective

Neel Chatterjee and Sujata Pandey

Abstract Gate all around silicon nanowire transistors have shown significant improvement at reduced gate lengths where conventional MOSFETs are terribly affected due to short channel effects and other issues. In this paper we analyze the stress and strain caused due to heat transfer in gate all around Silicon nanowire transistor. Important parameters like Von Mises stress, First Piola Kirchoff, Second Piola Kirchoff and Deviatoric stress tensor (Gauss point evaluation) have been analyzed using Multiphysics simulation software.

1 Introduction

Silicon Nanowire Transistor is one of the most efficient transistor designs devised till now. The gate all around the channel improves the channel current control. It also leads to more power efficiency due to lower leakage currents than the conventional designs.

A lot of emphasis has already been laid on analyzing Silicon GAA NWT [1–8] and were found to be good replacement for conventional MOSFET in CMOS designs. Later, III–V compound semiconductors such as GaAs, InAs, InSb, GaN [6] were also considered for these applications. GAA architecture allows superior control over the channel current. In junctionless nanowire transistor (JNT) there is no junction between source, channel, and drain. Thus, it is easy to fabricate it. Also, it's immunity to short channel effect is very high. Also doping concentration is same throughout the source, drain and channel. But, due to very high doping, its drive current gets limited and thus, it is having low mobility. To improve the mobility, compound semiconductor based GAA JNT is used. Also compound semiconductor based nanowires can be used for high frequency applications.

N. Chatterjee · S. Pandey (✉)
Department of Electronics and Communication Engineering, Amity University, Noida, Uttar Pradesh, India
e-mail: spandey@amity.edu

V.K. Jain et al. (eds.), *Recent Trends in Materials and Devices*,
Springer Proceedings in Physics 178, DOI 10.1007/978-3-319-29096-6_6

Due to smaller geometries and multiple layers the change in ambient temperature causes change in electrical properties of the device. Also stress and strain inside the device cause deterioration in the device characteristics at increased temperatures. Thermal stress analysis is important because these devices have to work at nominally high temperatures inside the electronic components. If the devices can't stand the stress created, it would lead to performance issues.

This paper addresses the stress analysis of the design due to the ambient temperature on GAA nanowire transistors. The paper mainly focuses on the mechanical properties of the semiconductor device. In this, Von Mises stress, First Piola Kirchoff, Second Piola Kirchoff and Deviatoric stress tensor (Gauss point evaluation) is analysed through Multiphysics simulation. Due to the movement of the carriers in the channel, the device temperature rises. But here, the analysis is mainly due to the ambient temperature of the device and not the internal stresses developed.

2 Device Design and Analysis

The radius of the nanowire is kept at 10 nm and channel length at 20 nm. The oxide layer of SiO_2 of 2 nm is deposited on the gate region. Figure 1 shows the structure of the nanowire and Table 1 shows the values of all parameters used.

Computational Method: The modules used in multiphysics simulation are the Semiconductor module and the Solid mechanics module. The semiconductor module solves the Poisson's equations using the appropriate boundary equation

$$\frac{1}{r}\frac{\partial}{\partial r}\left(r\frac{\partial}{\partial r}\varphi_i(r,z)\right)+\frac{\partial^2}{\partial z^2}\varphi_i(r,z)=-\frac{qN_D}{\varepsilon_j} \tag{1}$$

and the solid mechanics (heat transfer module) computes the various stresses where the ambient temperature is 343 K. The connective heat flux equation is given by

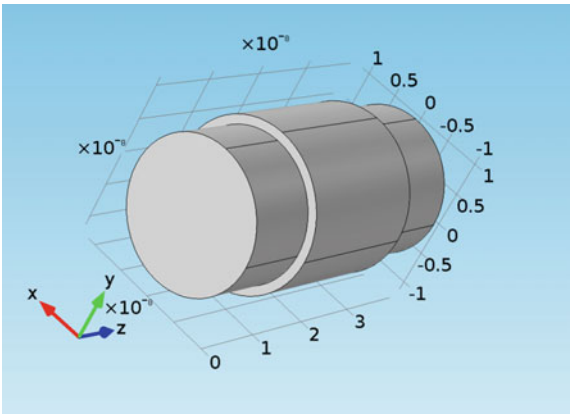

Fig. 1 Structure of the device simulated

Table 1 Parameters involved in simulation of the device

Parameters	Value
Radius of nanowire	10 nm
Channel length	20 nm
Source/drain length	10 nm
Oxide thickness	2 nm
Donor concentration	1E26 $1/m^3$
Acceptor concentration	1E23 $1/m^3$
Poisson's ratio	0.17
Heat transfer coefficient	60
Young's modulus	150 GPa

$$q_0 = h(T_{external} - T) \tag{2}$$

3 Results and Discussion

The semiconductor module along with the structural mechanics (thermal stress) is used to obtain the results. The reason for using thermal stress with the semiconductor module is pragmatic because the operating conditions of the device are such that they can be simulated for considering the thermal stresses. And also, the movement of the carrier in the device increases the temperature.

Figure 2 shows the temperature of the device in operating mode and Fig. 3 shows the isothermal contours.

It can be observed that the temperature is higher on the outside due to the ambient temperature of 343 K. The part which is exposed to the heat gets heated up the most. But one striking feature can be observed that due to cylindrical structure

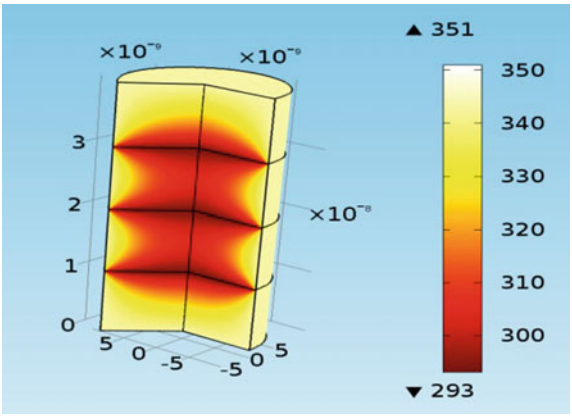

Fig. 2 Temperature distribution (3-D) of the device

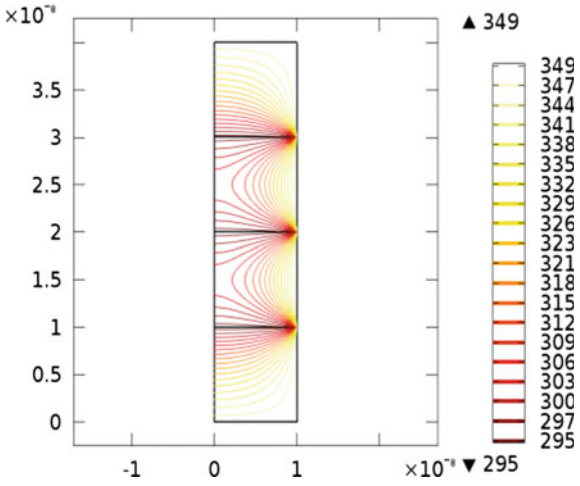

Fig. 3 Isothermal contours of the device

of the device, the internal part doesn't heat up much as the dielectric is all around the channel of the device. The source and the drain end are naturally at higher temperature because of the metal contacts at both the ends.

The isothermal contours gives the temperature distribution in a more subtle manner. As can be observed, the temperature variation is highest when we move from the gate towards the middle of the channel.

Von Mises stress is one of the major important stresses used in the engineering domain. It is considered to be a stress which if remains lower guarantees the stability of the device under the operating conditions. The Von Mises stress should be lower than the yield strength of the material. In the case of Silicon, the yield strength is 7000 MPa (Nm^2).

Figure 4a, b shows the Von Mises stress. Von Mises stress is one of the most important stresses used for material reliability. It can be clearly observed that the stress is very low and is concentrated at the drain and source sides of the transistor only. This implies that reliability can be maintained in the device.

There are some observations to be made here. At the drain side, it can be observed that the highest stress is at the centre of the device. It does exceed the yield strength of Si. But it doesn't practically cause any problems of the working of the device. That reason can be attributed to the fact that the Von Mises stress other than at the centre of source and drain side, is almost nil. Thus, the device remains immune to any stress. The reason for such high stress in the drain and source side is because of the high electron concentration at these ends. The voltage is applied at these ends and hence the stress caused is understandable.

Next we discuss about the true stress or Cauchy stress. The Cauchy stress tensors gives complete information about the current state of stress during the deformation, displacement etc. Mathematically, it is given by,

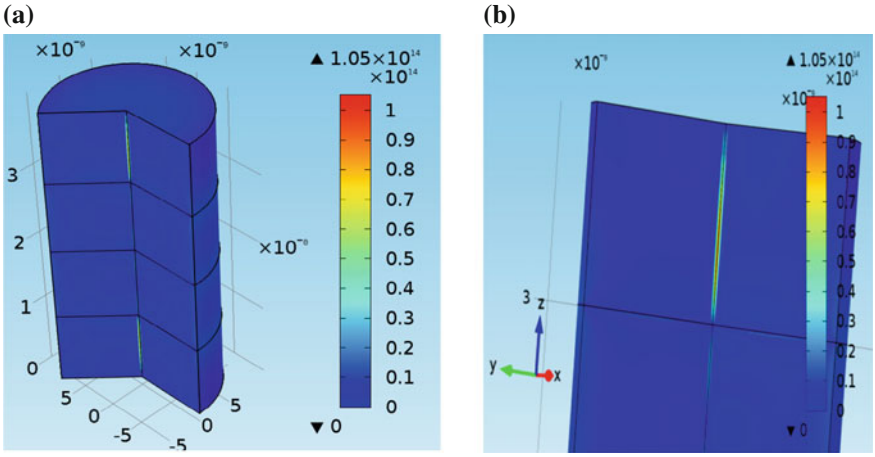

Fig. 4 **a** Von Mises stress. **b** Enlarged view of the drain side to view the Von Mises stress

$$T(n) = n \cdot \sigma \tag{3}$$

where σ is defined as below and n is the unit vector matrix. σ is the directional stress tensors.

$$\sigma = \begin{matrix} \sigma_{11} & \sigma_{12} & \sigma_{13} \\ \sigma_{21} & \sigma_{22} & \sigma_{23} \\ \sigma_{31} & \sigma_{32} & \sigma_{33} \end{matrix} \tag{4}$$

Now, the true stress is the most important property for deriving the stress-strain properties but it can't be computed directly because the deformation is in some different direction than the applied force and hence some other reference measure such as First and Second Piola Kirchoff stresses were developed. First is asymmetrical stress measure whereas the second is symmetrical. Also the second is always better if there is some non-linearity in the structure whose stress is being calculated such as bend in a pipe. The relationship between the true stress and first and second Piola-Kirchoff stresses are:

First Piola-Kirchoff stress,

$$P = J\sigma F^{-T}$$

Second Piola-Kirchoff stress,

$$S = JF^{-1}\sigma F^{-T}$$

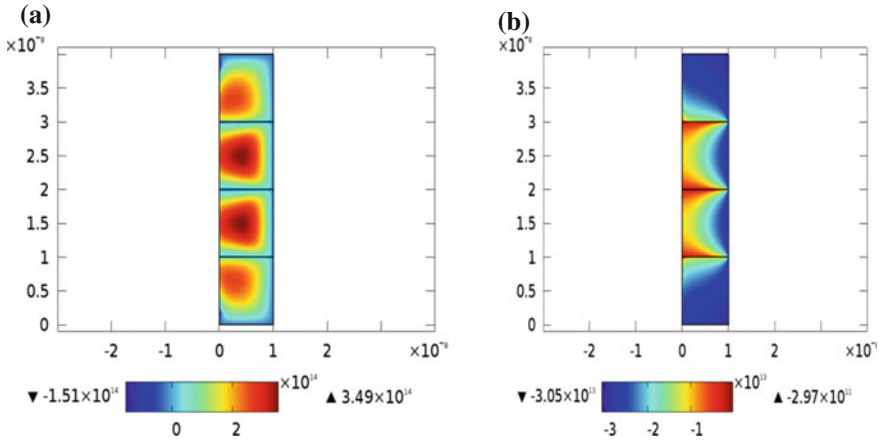

Fig. 5 **a** First Piola Kirchoff stress. **b** Second Piola Kirchoff stress

where σ is the 'real' or Cauchy stress, J is the jacobian of the deformation gradient which physically measures the change in volume caused by deformation and F is the deformation gradient.

Figure 5a, b show the First and Second Piola Kirchoff stresses. Both the stresses tend to point that the highest stress is developed in the channel where the electrons are flowing through the device for conduction. It is intuitive because the continuous flow of electrons generates heat due to the collision of a large number of electrons.

Now, these stresses show that the highest stress is at the channel side i.e., towards the central axis. This can be explained quite intuitively and physically. As positive gate voltage is applied, the electrons from the central axis and nearby regions migrate towards the gate. So at idle state, ideally most electrons reside near the central axis and repulse each other to cause tension. When negative voltage is applied to the gate, the electrons are forced towards the central axis from the gate. This causes even more stress at the centre.

Now it can be observed that the first Piola Kirchoff stress is not much indicative of the physical phenomenon that actually is taking place in the device whereas, second Piola-Kirchoff stress seems more intuitively correct due to its symmetrical nature and better adaptation to non-linearity of the structure.

4 Conclusion

It can be concluded that the device under consideration is quite stable and can be used as a paradigm for further device designs. The temperature distribution shows that the temperature has rose nearly by 8° when the device is under operation. The Von Mises Stress shows that the stress is below the failure point. The Piola Kirchoff

stresses shows the stress distribution of the whole device. This shows that the conventional MOSFET's can be replaced by the Silicon NWT as the device is reliable.

The stress analysis of the structure shows that the device is capable of handling ambient temperatures of about 343 K without much stress. The device is reliable and can be conveniently used for the CMOS processes to create full fledged electronics systems and sub-systems.

References

1. N. Clément, X.L. Han, G. Larrieu, Appl. Phys. Lett. **103**, 263504 (2013). doi:10.1063/1.4858955
2. J. Chen, T. Saraya, K. Miyaji, K. Shimizu, T. Hiramoto, Jpn. J. Appl. Phys. **48**, 1R (2009)
3. D.M. Kim, B. Kim, R.-H. Baek, *Nanowire Field Effect Transistors: Principles and Applications* (Springer, Berlin, 2013), pp. 63–87
4. S. Sasaki, K. Tateno, G. Zhang, H. Pigot, Y. Harada, S. Saito, A. Fujiwara, T. Sogawa, K. Muraki, Jpn. J. Appl. Phys. **54**, 4S (2015)
5. D.M. Kim, B. Kim, R.-H. Baek, Silicon nanowire field-effect transistor. *Nanowire Field Effect Transistors: Principles and Applications* (Springer, New York, 2014), pp. 63–87
6. M. Ohmori, P. Vitushinskiy, T. Kojima, H. Sakaki, Appl. Phys. Express. **6**(4), 045003 (2013)
7. Y. Cui et al., High performance silicon nanowire field effect transistors. Nano Lett. **3.2**, 149–152 (2003)
8. V. Schmidt et al., Realization of a silicon nanowire vertical surround-gate field-effect transistor. Small **2.1**, 85–88 (2006)

Surface Engineering of Colloidal Quantum Dots for Organic and Biocompatible Solution-Processable Materials

Shailesh Narain Sharma

Abstract In the present study, the objective of this work has been two-fold: (i) To render CdSe QDs water-soluble for its possible application in biosensors, ligand-exchange process has been initiated. Here, the surface engineering of CdSe QDs synthesized with different hydrophobic ligands (TOPO/TOP, Oleic acid/TOP) has been done using organic primary aliphatic amine (butyl amine); and (ii) For different applications of hybrid organic MEH-PPV-inorganic CdSe composites in organic electronic devices such as efficient electroluminescent (OLED) and photovoltaic (OPV) devices, a suitable non-ligand purification process has been attempted. Here, the studies of hybrid nanocomposites demonstrate the dominance of mainly energy transfer between host polymer (donors) and guest as-synthesized CdSe nanocrystals (acceptors) for OLED applications and an enhanced charge transfer upon purification of CdSe QDs in their corresponding polymer nanocomposites for OPV applications respectively. The ease of removal of the ligands (TOPO/OA) from the surface of CdSe QDs either through direct ligand-exchange through Butyl-amine or through non-ligand exchange through purification process dictates its role in biosensors and in conjunction with polymer (MEH-PPV) in OLED and OPV devices respectively.

1 Introduction

For an optimum performance of colloidal nanocrystal devices for a variety of applications such as photonic devices, solar cells and biological labelling, the determining factors are the nanocrystal surface and size [1, 2]. In this work, these two factors have been tuned via wet chemistry to tailor the material properties. Here, we have shown that through ligand-exchange process, the surface of the CdSe quantum dots (QDs) can be modified by replacing the longer-chain ligands of

S.N. Sharma (✉)
CSIR-National Physical Laboratory, CSIR Network of Institutes for Solar Energy (NISE), Dr. K.S. Krishnan Marg, New Delhi 110012, India
e-mail: shailesh@nplindia.org

V.K. Jain et al. (eds.), *Recent Trends in Materials and Devices*,
Springer Proceedings in Physics 178, DOI 10.1007/978-3-319-29096-6_7

conventional trioctyl phosphine oxide (TOPO) or oleic acid (OA) with shorter-chain ligand of butyl amine (BA). This imparts colloidal stability and water solubility to CdSe QDs for its potential applications in biosensors and biological imaging. It is conjectured that sizes of CdSe QDs and stereochemical compatibility of ligands (TOPO, oleicacid and butyl amine) greatly influences the photophysics and photochemistry of CdSe QDs.

For organic optoelectronic device applications, the surface engineering of CdSe QDS can be done by employing suitable purification (non-ligand) process. It has been observed that as-synthesized CdSe QDs which showed initially effective energy transfer after chemical treatment showed enhanced charge transfer mechanism thus making their corresponding nanocomposites useful for different applications in organic electronic devices such as efficient electroluminescent (QD-LED) and Hybrid solar cell (HSCs) devices respectively.

2 Experimental Details

The synthesis of CdSe nanoparticles were carried out by the chemical route using TOP/TOPO and TOP/oleic acid capping method to control the growth of the nanoparticles to desired sizes, and development of polymer composites whose details can be found elsewhere [2–4]. The materials used were of the purest quality available and used as received. For the preparation of polymer:CdSe nanocomposites, TOPO and OA surface ligands from CdSe QDs were removed by successive washing process in toluene and methanol mixture and the resultant nanocrystal precipitates were finally dispersed in MEH-PPV polymer matrix using chloroform solvent. The PL was measured using a home assembled system consisting of a two stage monochromator, a photomultiplier tube (PMT) with a lock-in amplifier for PL detection, and an Ar^+ ion laser operating at 488 nm and 5 mW (corresponding to 0.125 W cm^{-2}) power for excitation. Absorption spectra were recorded using Shimadzu 3101 spectrometer. FTIR spectra were measured using Perkin Elmer Spectrum BX spectrometer.

3 Results and Discussions

A change in the ratio of Cd:Se during the preparation conditions produced particles of different diameters [2, 3]. Using TOPO/TOP and oleic acid/TOP method, at Cd:Se ratio ($\sim$2:1) during the synthesis conditions, smaller-sized ($\sim$5–7 nm) CdSe nanoparticles with higher quantum yield (0.225, 0.182) were obtained. The crystallite sizes were measured by TEM and by the blue shift of the absorption edge with respect to bulk CdSe and the results commensurate well with each other.

The choice of butyl amine as a source of ligand-exchange comes from the fact that butylamine can dissolve in water by forming hydrogen bonds with water for its

possible applications in bio-processable materials. Moreover, butyl amine is a primary amine which can be adsorbed on CdSe with a high density without any steric-hindrance and thus can effectively passivate the surface defects behaving as a non-radiative recombination centre unlike other secondary and tertiary amines [2].

Figure 1A(a, b) shows that nearly all the emission from smaller-sized CdSe quantum dots corresponding to TOPO/OA is quenched at the concentration level of ~1.6 mM of butyl amine with higher rate of PL quenching being observed for CdSe nanocrystallites with TOPO-ligand ($\Delta PL/PL_i \sim 0.85$) as compared to the corresponding one with oleic acid-ligand ($\Delta PL/PL_i \sim 0.6$) respectively. At these concentration levels most of the CdSe particle surface is complexed with butyl amine. The fact that the emission maximum [λ_{max} ~510 and 550 nm for CdSe (TOPO) and CdSe(OA)] and spectral shape are independent of butyl amine concentration rules out formation of new surface states. From Fig. 1B(a, b), it is evident that butyl amine-capped smaller sized (~5 nm) CdSe QDs (TOPO) maintain its respective colour (yellowish-green) and uniformity both in butyl amine and water as solvent respectively. This demonstrates the successful ligand exchange from TOPO—to butyl amine respectively. However, ligand-exchange for oleic acid to butyl amine-capped CdSe QDs is partially successful in the sense that although it has rendered CdSe QDs water soluble but with appreciable change in uniformity with colour of emission being orange to brown with graded intensity [Fig. 1B (c, d)]. This can be understood on the basis of strong binding of OA to Cd as compared to TOPO ligand which discourages ligand exchange with BA.

From Fig. 2a, it is evident that TOPO has a long chain bulky-structure thus providing a steric hindrance to the passivation of CdSe nanocrystals and consequently, a weak binding to the CdSe surface. On the other hand, oleic acid ligand

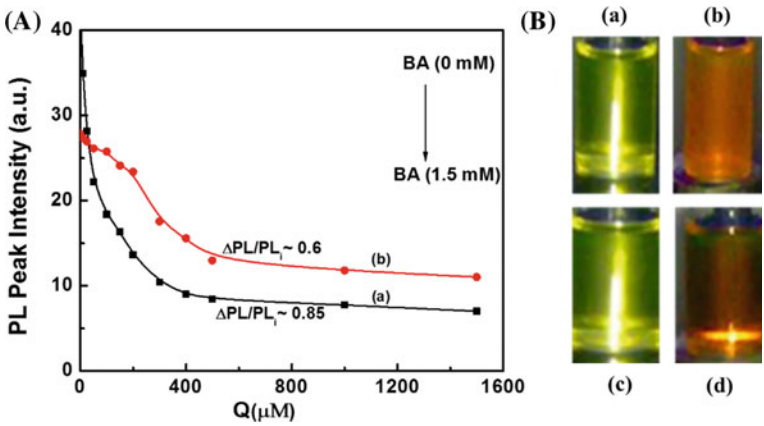

Fig. 1 **A** PL peak intensity of CdSe QDs as a function of butyl amine (BA) concentration; (*a*) Ligand: TOPO and (*b*) Ligand: Oleic acid; **B** Color photographs of luminescence under 365 nm UV-exposure from butyl amine-modified CdSe QDs, (*a* and *b*) Size ~5 nm, TOPO-Ligand, BA and BA + water solvent; (*c* and d) Size ~7 nm, OA-Ligand; BA and BA + water solvent

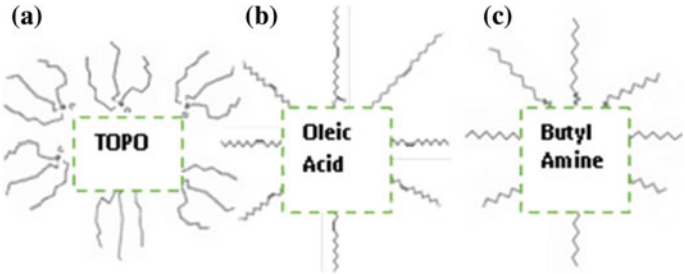

Fig. 2 Schematic view of different ligands **a** TOPO; **b** Oleic acid and **c** Butyl amine

has a simple straight hydrocarbon chain as shown in Fig. 2b; thus resulting in a perfect passivation for CdSe nanocrystallites and hence its strong binding to CdSe surface discourages ligand exchange by butyl amine. However, as evident from Fig. 2c, butyl amine possesses a simple, linear structure and can be adsorbed easily with high density on CdSe surface without any steric hindrance. Exchanging to shorter ligands such as butylamine from longer TOPO- and OA-ligands was found to produce an efficient passivation of surface states.

It is important to remove the insulating ligands (TOPO/OA) through an appropriate post-synthesis technique to facilitate better charge carrier exchange between conducting polymer and nanocrystals [4, 5] for application of hybrid organic (polymer):inorganic (CdSe) nanocomposites in organic (OLED/OPV) optoelectronic devices.

As discussed above, we have seen that the binding of TOPO-ligand to CdSe is the weakest as compared to oleic acid or oleylamine ligand. Thus, in a bid to remove the insulating ligand TOPO which acts as an interference for successful charge transfer between MEH-PPV and CdSe in hybrid nanocomposites, two-times washing of CdSe nanocrystals in toluene and methanol mixture has been done. The optimization of washing times was set to two on the basis of careful monitoring of no observation of any significant agglomeration of CdSe nanocrystallites upon desorption of TOPO-ligands as inferred from transmission electron microscopy studies. Without appropriate washing, there seems to be no interaction between CdSe nanoparticles with polymer as evident from TEM micrograph where phase separation between polymer and CdSe nanoparticles is quite evident. Although slight agglomeration of CdSe nanocrystallites cannot be avoided upon washing (Fig. 3a), however, beyond two-times washing, significant agglomeration of CdSe nanoparticles was observed (Fig. 3b) as the nanoparticles are rendered unpassivated which severely deteriorates their crystallinity and steric-stability and hence charge-accepting capabilities in their respective polymer nanocomposites.

Figure 4A(a, b) shows the FTIR spectra of MEH-PPV:CdSe composites before and after washing off the TOPO ligands. As evident from Fig. 4A(a, b), upon two-times washing, the removal of excess of TOP/TOPO species leads to the reduction in the area under the curve in 1180–1300 cm^{-1} wavenumber range (P = O stretching mode) and hence increment in PL quenching rate ($\sim$0.47) as

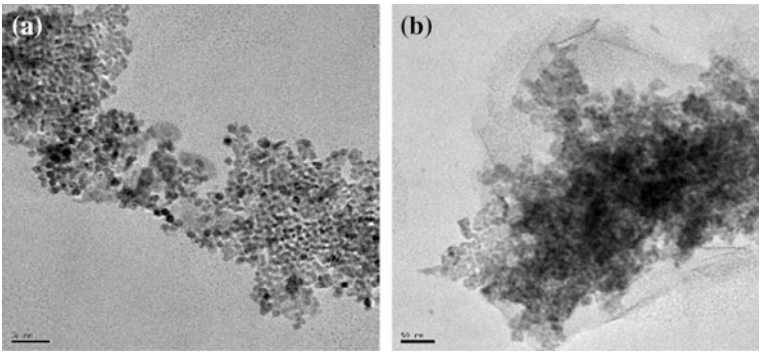

Fig. 3 TEM micrographs of MEH-PPV:CdSe nanocomposites; **a** 2-times purification and **b** 3 times purification

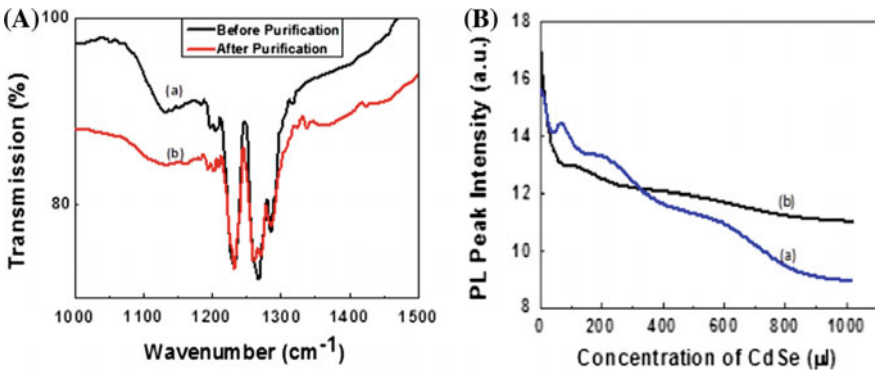

Fig. 4 **A** FTIR spectra of MEH-PPV:CdSe (TOPO) before (*a*) and after purification (*b*) and **B** PL peak intensity of MEH-PPV:CdSe composites as a function of CdSe concentration upon purification; (*a*) Ligand: TOPO and (*b*) Ligand: Oleic acid

compared to as-synthesized CdSe nanoparticles ($\sim$0.35) for MEH-PPV:CdSe nano composites [Fig. 4B(a, b)] respectively.

Figure 5a shows the pictorial model of CdSe QDs and MEH-PPV:CdSe (TOPO/OA) composites depicting ligand-exchange through butyl amine and non-ligand exchange through purification treatment respectively. Moreover, due to the inability of butyl amine and/or purification treatment to remove the OA-ligand from the surface of CdSe QDs effectively because of its strong coupling with Cd atoms renders energy transfer as the only viable mechanism of PL quenching of MEH-PPV polymer upon its interaction with CdSe (OA) QDs [6, 7] as evident from LHS of Fig. 5b. Similarly, as-synthesized CdSe (OA) QDs in conjunction with polymer MEH-PPV showed effective energy transfer due to presence of ligands (Fig. 5). The energy transfer mechanism is evident from the enhanced overlapping of absorbance spectra of CdSe (OA) with polymer (MEH-PPV) emission spectra

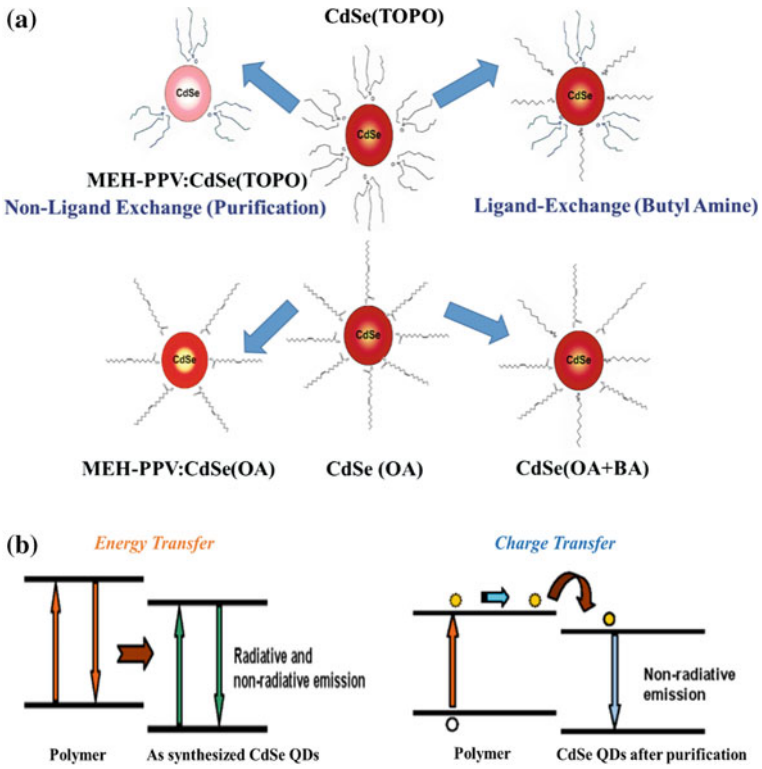

Fig. 5 **a** A pictorial model of CdSe QDs and MEH-PPV:CdSe composites depicting ligand- and non ligand-exchange processes upon butyl-amine and purification treatments respectively; **b** Schematic representation of energy transfer and charge transfer for MEH-PPV:CdSe composites for as-synthesized and after purification of CdSe (TOPO/OA) QDs

[8–10]. On the other hand, CdSe (TOPO) QDs upon repeated washing in a toluene and methanol mixture showed enhanced charge transfer mechanism as TOPO-ligand is easily removed from the surface of CdSe QDs leading to enhanced PL quenching of MEH-PPPV polymer as a consequence of enhanced interaction between the polymer and inorganic components and hence effective charge transfer observed in MEH-PPV:CdSe (TOPO) composites as shown in RHS of Fig. 5b. The faded orangish or pink colour denotes the desorption of TOPO-ligands while the CdSe with OA-ligands intact upon purification shows bright orange colour in their respective MEH-PPV:CdSe composites as shown in Fig. 5a. It is noteworthy to mention here that the observed processes of enhanced energy transfer and charge transfer in CdSe (OA) and CdSe (TOPO) based polymer nanocomposites would be very useful for light emitting applications (electroluminescent devices) and light-harvesting applications (photovoltaic devices) as depicted pictorially in Fig. 5 respectively.

4 Conclusions

In this work, surface engineering of CdSe QDs has been successfully demonstrated through ligand- and non-ligand-exchange processes without resorting to any harsh temperature or toxic treatment with pyridine for its effective utilization as biosensors and organic electronic devices respectively. The surface of the CdSe quantum dots (QDs) can be modified by replacing the longer-chain ligands of conventional trioctyl phosphine oxide (TOPO) or oleic acid (OA) with shorter-chain ligand of butyl amine. This imparts colloidal stability and water solubility to CdSe QDs for biosensing applications.

Without resorting to ligand-exchange process by using toxic, hazardous chemical like pyridine, interaction of polymer with CdSe-related materials takes place. Here, the post-synthesis treatment on CdSe nanoparticles for enhancing the electron transport in the interconnected nanocrystalline network of hybrid solar cells, chemical surface purification treatment for an optimized number of times has been performed. The ease of removal of ligands particularly TOPO upon purification renders polymer:CdSe composites useful in OPV applications whereas corresponding composites for as synthesized CdSe (TOPO/OA) QDs with ligands intact finds application in OLEDs respectively. The general strategies of post-synthesis treatment on CdSe nanoparticles through ligand exchange by butyl amine and or through purification process on the basis of dominance of energy/charge transfer mechanisms has been modelled pictorially.

References

1. W.U. Huynh, X. Peng, A.V. Alivisatos, Adv. Mater. **11**, 923 (1999)
2. S.N. Sharma, Z.S. Pillai, P.V. Kamat, J. Phys. Chem. B **107**, 10088 (2003)
3. U. Kumar, K. Kumari, S.N. Sharma, M. Kumar, V.D. Vankar, R. Kakkar, V. Kumar, Colloid Polym. Sci. **288**, 841 (2010)
4. H. Sharma, S.N. Sharma, G. Singh, S.M. Shivaprasad, Physica E. **31**, 180 (2006)
5. H. Sharma, S.N. Sharma, S. Singh, R. Kishore, G. Singh, S.M. Shivaprasad, Appl. Surf. Sci. **253**, 5325 (2007)
6. K. Kumari, U. Kumar, S.N. Sharma, S. Chand, R. Kakkar, V.D. Vankar, V. Kumar, J. Phys. Appl. Phys. **41**, 235409 (2008)
7. M. Kondon, J. Kim, N. Udawatte, D. Lee, J. Phys. Chem. C **112**, 6695 (2008)
8. A. Mehta, S.N. Sharma, P. Chawla, S. Chand, Colloid Polym. Sci. **292**, 301 (2014)
9. S.N. Sharma, T. Vats, N. Dhenadhayalan, P. Ramamurthy, A.K. Narula, Sol. Energy Mats. & Sol. Cells **100**, 6 (2012)
10. M. Anni, L. Mann, R. Cingolani, D. Valerini, A. Creti, M. Lomoscolo, Appl. Phys. Lett. **85**, 4169 (2004)

Optical and Structural Properties of Silica Nanoparticles Using Material Design Software: MedeA

Vikas Chaudhary, Parul Katyal, Ajay Kumar, Sacheen Kumar and Dinesh Kumar

Abstract MedeA is a computational software which is used for the simulation to design and analyse different kinds of materials. Due to attractive optical, electrical and thermal properties such as antiglare and antireflective coatings, thermal insulation, silica nanoparticles have a wide range of applications in the field of semiconductor industry and medical science. In the present work we simulate the XRD, Band structure, Optical spectra and Density of state for silica nanoparticles by using MedeA software.

1 Introduction

Silica nanoparticles have been widely researched interest in view of their excellent optical, electrical and thermal properties. Mesoporous silica nanoparticles (MSN) have been explored in materials research due to their unique properties, such as high surface areas, large pore volumes, tunable pore sizes with a narrow distribution and having high structure porosity [1, 2].

These nanoparticles can be extended to a wide range of application in various biotechnological, biomedical fields, bio sensing, electronic and thin film substrates and therapeutic world such as drug delivery system based on its properties like nontoxic, biocompatible, highly stable and porous in structure [1]. The mesoporous silica nanoparticles have a different role for above applications; the quality of these products is highly dependent on the size distribution of the particles. Silica (SiO_2) exist in both amorphous and crystalline form. Crystalline silica occurs in multiple forms such as α-quartz. Amorphous silica is divided into natural specimen such as silica glass and artificial products and also found in living organisms such as sponges, algae.

MedeA is a very powerful productivity tool for the simulation and analysis of materials. MedeA is designed for a range of materials issues related to application

V. Chaudhary · P. Katyal · A. Kumar · S. Kumar (✉) · D. Kumar
Department of Electronic Science, Kurukshetra University, Kurukshetra 136119, India
e-mail: sacheen3@gmail.com

V.K. Jain et al. (eds.), *Recent Trends in Materials and Devices*,
Springer Proceedings in Physics 178, DOI 10.1007/978-3-319-29096-6_8

areas such as electrical power generation, automotive applications, energy storage, alloy design, microelectronics, the chemical industry and petrochemicals. MedeA architecture consists of three levels, a graphical user interface, databases, and simulation programs. Communication between layers is through Job Servers and Task Servers. MedeA software comprises a number of modules, which are used according to the type of applications. MedeA implants modules in a fundamental framework with components that can be distributed over a network of computers i.e. large-scale supercomputers. This computational software helps to search and retrieve over 500,000 entries of materials data including crystal structure. Efficiently of this software explore the vast compositional space of materials with powerful computational capabilities. Build models of solids, surfaces, molecules, nanostructures, and interfaces between materials with a user-friendly interface. MedeA Compute mechanical, thermal, fluidic, catalytic, electrical, optical and magnetic properties of materials.

2 Experimental Details

From the tool box of MedeA Software, choose infomatica and to add the formula of SiO_2 go through search and add new criteria. With the help of (Pearson#1616500) edit the bonds of SiO_2 structure. VASP 5.3 provide access to state of the art first principle simulation method in a comprehensive and easy to use package. With the choice of band structure, optical spectra and Density of state from the VASP 5.3 tool box we simulate the result with the help of job server. For the XRD result of SiO_2 powder pattern is selected from the geometric analysis. These Figs. 1, 2 and 3 are the structure, edit bonds and build supercell SiO_2 by using MedeA software.

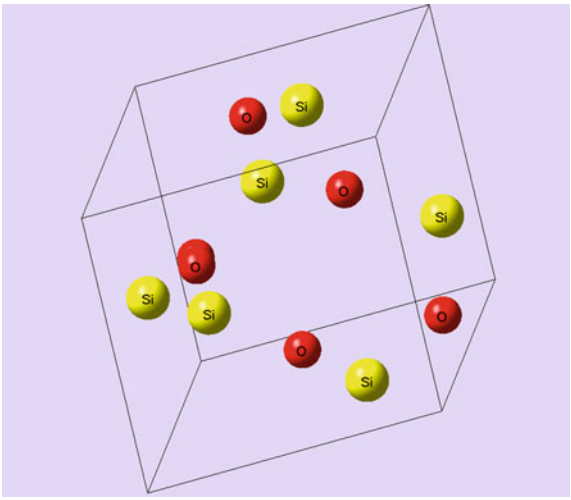

Fig. 1 Structure of SiO_2

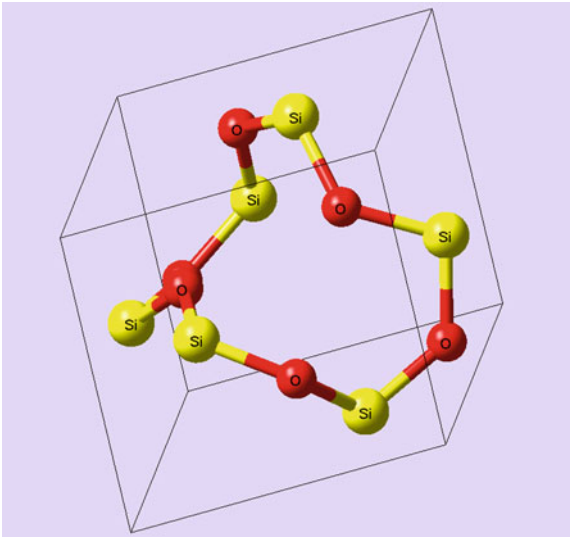

Fig. 2 Edit bond structure of SiO_2

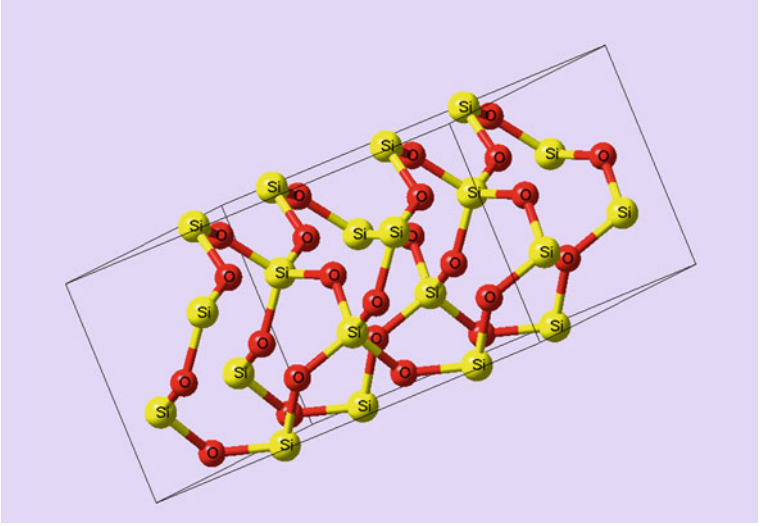

Fig. 3 Build supercell of SiO_2

3 Result and Discussion

3.1 X-Ray Diffraction Technique

X-ray diffraction (XRD) method is primarily used for phase identification of a crystalline material and provides information about unit cell dimensions, Interatomic distance and Bond angle. This technique was performed to conclude the structure and particle size of the silica nanoparticles [3]. X-ray powder diffraction (XRD) is a rapid technique primarily used for phase identification of a crystalline material and can provide information on unit cell dimensions. The particle size of SiO_2 nanoparticles are 262 nm by using X-ray diffraction technique (Fig. 4).

3.2 Band Structure

Band structure gives information about the electronic levels in (ideal) crystal structures. This is characterized by two basic parameters. First parameter is Bloch vector k and second is band index n. Bloch vector is an element of the reciprocal space (in units 1/length) and typically restricted to the first Brillouin zone. Some electrical, optical, and even some magnetic properties of crystals can be explained with the help of the band structure. Fermi energy play an important role in band structure. If the Fermi energy is located in a band gap, the material is insulating (or semiconducting) while it is metallic otherwise. Band gap of SiO_2 nanoparticles are 6.51 eV showing below in Fig. 5.

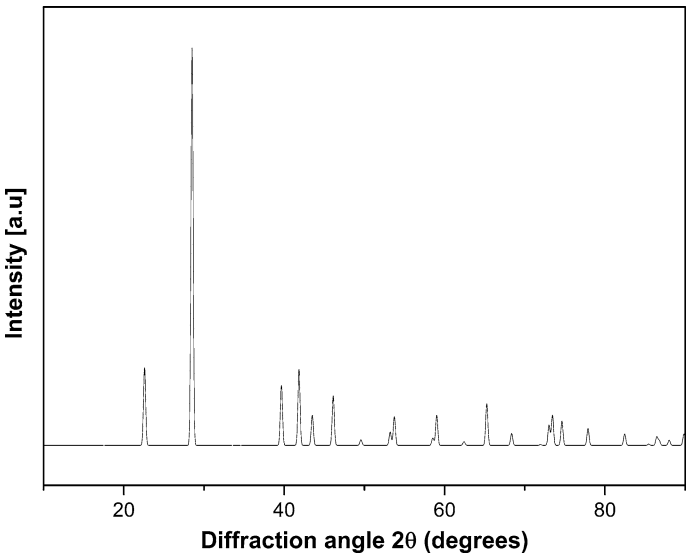

Fig. 4 XRD pattern of silica nanoparticles

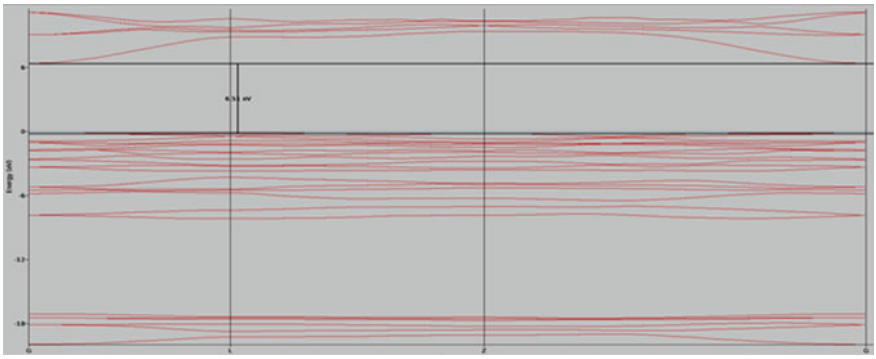

Fig. 5 Band structure of silica nanoparticles

3.3 Optical Spectra

This is result of quantum transitions between the energy level of atoms, molecules, liquid and solids. Optical spectra depend on state of substances. If at a particular temperature substance is state of thermodynamic equilibrium with radiation, then it emits continuous spectrum, whose energy distributed with respect to wavelength. If the substance is not in state of thermodynamic equilibrium with radiation, then optical spectra have various form. Optical spectra are used to find dielectric functions, refractive index, optical absorption index and conductivity as a function of frequency.

(A) **Dielectric Function**: Dielectric function is usually denoted by the Greek letter epsilon, ε, and involves of two parts called epsilon 1 and epsilon 2 written as ε1 and ε2, but often written simply as e1 and e2. Since the measures e1 and e2 vary with wavelength, frequency or photon energy. The type of material which describes the electrical and optical properties versus frequency, wavelength, or energy and also describes the polarization (electric polarizability) and absorption properties of the material. Dielectric function of SiO_2 lies from 0.73 to 6.5 eV (Fig. 6).

(B) **Refractive index**: In refractive index or index of refraction, n of an optical medium is a dimensionless number that describes how much light is bent, or refracted, when entering a material or we can say that how much light, or any other radiation, propagates through that medium. It is also defined as where c is the speed of light in vacuum and v is the phase velocity of light in the medium. Refractive index of SiO_2 is 1.47012 at 4 μm (Fig. 7).

(C) **Optical absorption index**: A measure of the attenuation caused by absorption of energy per unit of distance that occurs in an electromagnetic wave of given wavelength propagating in a material medium of given refractive index. Absorption index of SiO_2 is 10×10^{-6} cm^{-1} at 1 μm (Fig. 8).

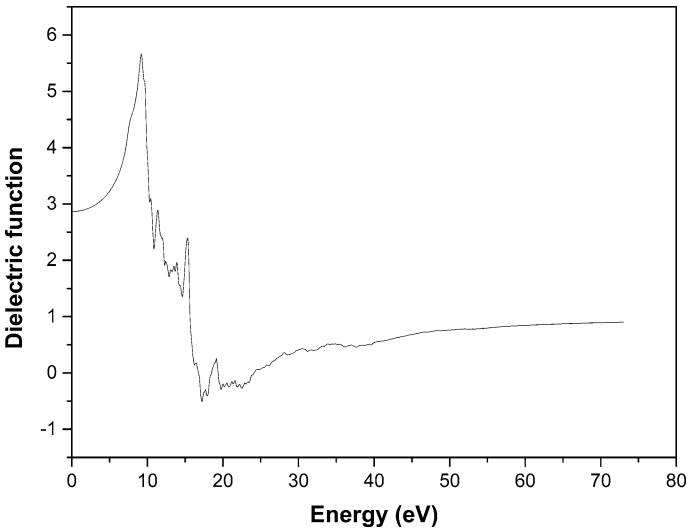

Fig. 6 Dielectric function

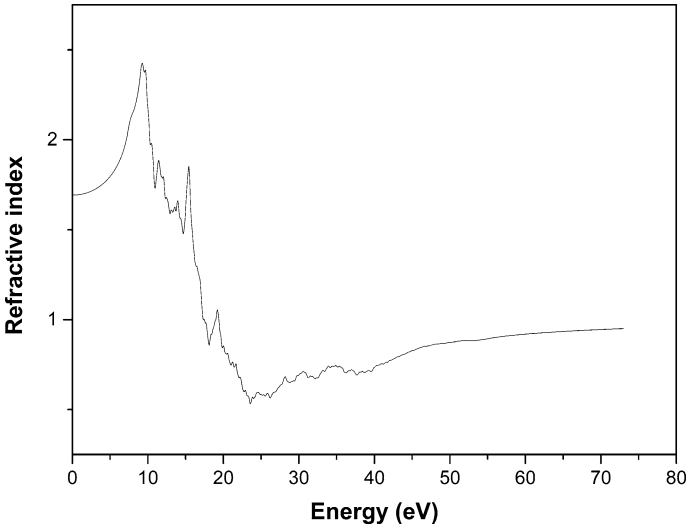

Fig. 7 Refractive index

(D) **Conductivity**: Conductivity (or specific conductance) of an electrolyte solution is a measure of its ability to conduct electricity. The SI unit of conductivity is Siemens per meter (S/m) which is used routinely in many industrial and environmental applications as a fast, inexpensive and reliable way of measuring the ionic content in a solution. Thermal Conductivity of SiO_2 is 1.38 Wm^{-1} K^{-1} (Fig. 9).

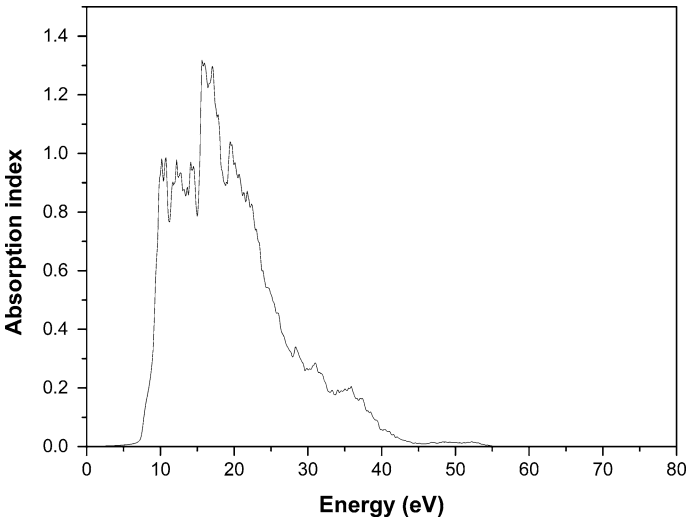

Fig. 8 Absorption index

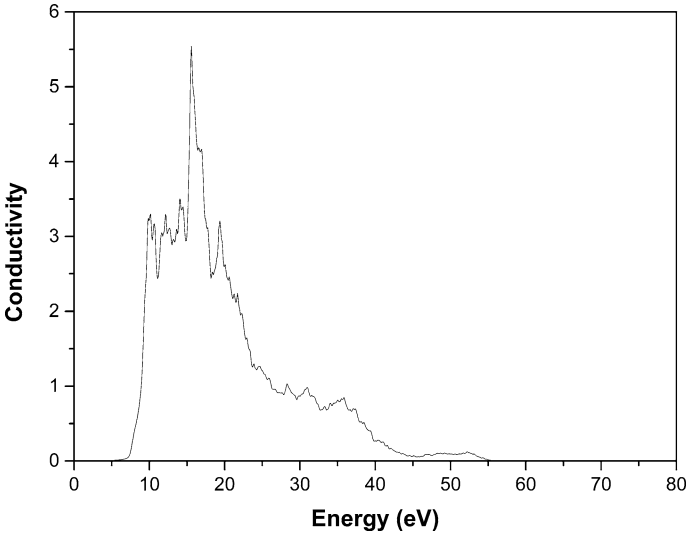

Fig. 9 Conductivity

3.4 Density of State

The density of states (DOS) of a system explain the number of states per interval of energy at each energy level that are available to be occupied. A high DOS at a specific energy level means that there are many states which are available for

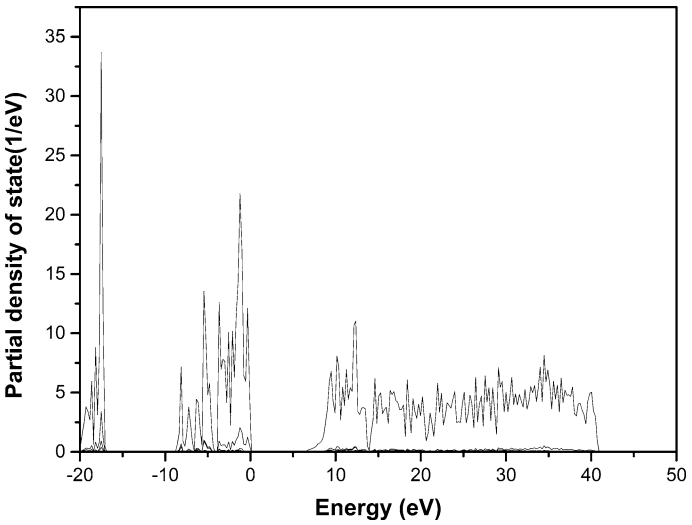

Fig. 10 Density of state

occupation. A DOS of zero means that no states can be occupied at that particular energy level. Local variations, mostly due to distortions of the original system, are called local density of states (LDOS) (Fig. 10).

4 Conclusion

By using computational software MedeA, we analyzed SiO_2 nanoparticle. Silica nanoparticles have a wide range of applications in the field of semiconductor industry and medical science because of it attractive optical, electrical and thermal properties. In the present work we simulate the XRD, Band structure, Optical spectra and Density of state for silica nanoparticles by using MedeA software. We have find band gap of SiO_2 nanoparticle nearly 6.51 eV and particle size of SiO_2 nanoparticles are 262 nm by using X-ray diffraction technique.

Acknowledgments Authors are thankful to DST-Nano mission for providing funding.

References

1. O.M. Sadek, S.M. Reda, R.K. Al-Bilali, Preparation and characterization of silica and clay-silica core-shell nanoparticles using sol-gel method. Adv. Nanopart. **2**, 165–175 (2013)
2. Y.H. Ju et al., Synthesis and characterization of ordered mesoporous anion-exchange inorganic/organic hybrid resins for radionuclide separation. Ind. Eng. Chem. Res. **39**(2), 550–553 (2000)
3. H.P. Klug, L.E. Alexander, *X-ray Diffraction Procedures* (Wiley, New York, 1954)

Stability Studies of Colloidal Indium Phosphide Quantum Dots: Humidity-Induced Photoluminescence Enhancement

Akanksha Singh and Shailesh Narain Sharma

Abstract InP quantum dots (QDs) and InP/ZnS core shell structures were synthesized using one pot hot injection technique. An increment in the PL intensity was seen after the growth of ZnS shell. A post synthesis HF treatment is given to the QDs in order to increase the PL intensity by removing surface defects. Humidity studies were done to observe the stability of InP QDs, treated InP and InP/ZnS QDs. An unusal increment in the PL intensity was observed for InP upon exposure to humidity. Within two weeks the PL intensity increased by 118 % without much change in the peak position. This can be attributed to the water molecules which get adsorbed on the surface of QDs and results in surface passivation. A similar trend was observed for treated InP QDs but in the second week, the PL increment was saturated and did not increase further. InP/ZnS showed a decrement in the PL intensity on exposure because it is robust to oxidation due to the formation of shell.

1 Introduction

In the recent years, Indium Phosphide QD has attracted significant attention of the researchers as it has varied applications such as LEDs [1], photovoltaic [2], bio-sensing and imaging [3]. InP belongs to III–V semiconductor QDs and hence offers various advantages as compared to II–VI semiconductor QDs. One of the greatest advantages is that it is Cd-free, so it can be used for biological applications. Secondly, it has large bohr radii, which gives a large window for the size variation of InP QDs [4]. The synthesis and stability of the III–V QDs has been a topic of discussion for researchers for a long while.

A. Singh · S.N. Sharma (✉)
National Physical Laboratory, Dr. K.S. Krishnan Marg, New Delhi, India
e-mail: shailesh@nplindia.org

A. Singh
e-mail: pakanksha5@gmail.com

V.K. Jain et al. (eds.), *Recent Trends in Materials and Devices*,
Springer Proceedings in Physics 178, DOI 10.1007/978-3-319-29096-6_9

In this work, we have synthesized InP QDs through one pot, hot injection technique. This approach takes less synthesis time and efforts as compared to previous approaches [5, 6]. The InP was coated with a wide-gap semiconductor ZnS shell which resulted in passivation of the QDs and enhanced PL intensity. A post synthesis HF treatment was done in order to increase the PL intensity by passivating the surface defects and the dangling bonds present on the surface. These surface defects acts as traps for the charge carriers and hence decreases the PL intensity of the QDs. Stability studies were performed on the QDs in order to study the defects and traps present on the surface of the QDs. Effect of humid atmosphere on QDs for all the three samples i.e. InP, InP/ZnS and treated InP QDs was observed. An increment in PL intensity was observed on exposure to humidity. The reason for increased PL intensity is explained in the later section.

2 Experimental Details

We have synthesized InP QDs by colloidal route method. One pot, hot injection technique was used which helps in controlling the size of the QDs by separating the nucleation and growth part. Novel precursors were used such as TOP for the synthesis. In situ coating of ZnS shell was done. TOP-S was injected at high temperature which reacted with the zinc present in the solution mixture formed the shell around the InP QDs. QDs were then dispersed in toluene and films were coated on glass slide. These films were exposed to humidity by keeping them with water in a closed atmosphere for two weeks. The films were removed and PL measurements were done. The films were kept back in the same atmosphere and the PL measurements were done after the end of the second week.

3 Results and Discussion

One of the important active components of the ambient atmosphere is water vapor, therefore understanding the effect of water molecules on the luminescent properties of InP QDs with different surface chemistry would be of great importance towards better understanding the role of nanocrystallite surfaces on the optical properties. Efforts have been made by various researchers toward intentionally enhancing the luminescence efficiency of CdSe, InP QDs by post-synthesis methods such as HF-dipping, exposure to humid ambient etc. Figure 1 shows the PL intensity profiles of InP QDs upon exposure to humid atmosphere.

As shown in Fig. 1, the rate of increment in PL intensity ($\Delta PL/PL_i$) is (72–73 %) for the first week and later rate of increase in PL intensity is relatively higher ($\Delta PL/PL_i \sim 118$ %). This unexpected PL enhancement is due to the passivation of

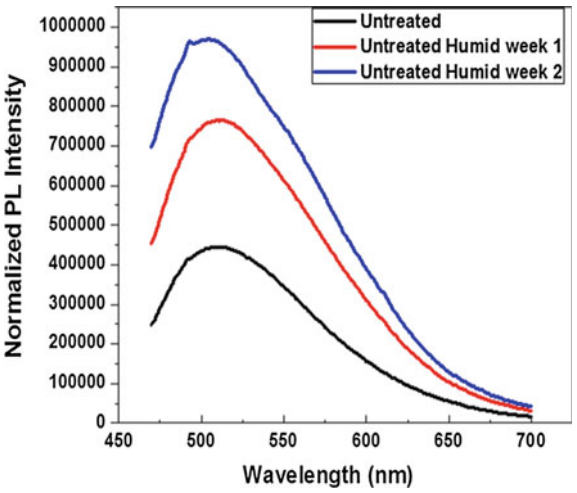

Fig. 1 PL spectra of InP QDs for initial week, after 1st week and after 2nd week

defects present on the surface of QDs. The water molecules get adsorbed on the surface and it removes the quenching centers or the traps, quite similar to those observed by Cordero et al. in the case of CdSe QDs [7]. These traps are actually non recombination center which decreases the PL efficiency of the QDs. Water molecules removes these traps and hence PL enhancement is seen on exposure to humidity. Similar increment in PL has been observed by the adsorption of oxygen molecules and passivation of surface states [8].

Post synthesis HF treatment is given to InP QDs which will remove the defects and dangling bonds present on the surface. Figure 2 shows the PL intensity profiles of InP QDs upon HF etching treatment corresponding to different interval of time. As evident from Fig. 2, the PL intensity decreases beyond an optimized exposure time of 15 min. Upon treatment, etching of undesirable configurations responsible

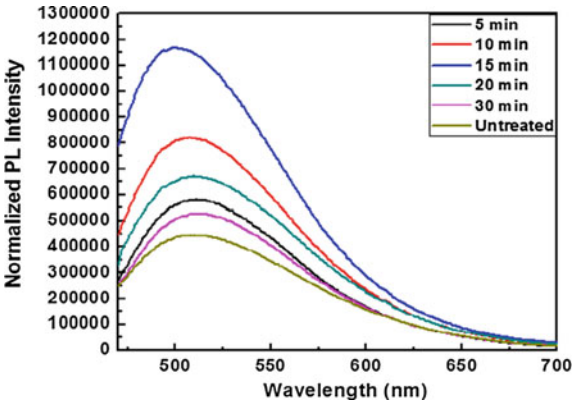

Fig. 2 Optimization of exposure time to HF treatment. The films were exposed to different intervals of time and the optimized time was observed

for non-radiative recombination centers leads to enhanced PL intensity of InP QDs. However, increased etching time could lead to excessive etching of the fragile InP nanocrystallite skeleton thus leading to decrease in PL intensity due to destruction of luminescent structures of InP QDs.

As shown in Fig. 3, the rate of increment in PL intensity (ΔPL/PLi) is comparable (72–73 %) for both untreated and treated InP QDs for first week and later rate of increase in PL intensity is (ΔPL/PLi ∼ 78 %) for treated InP QDs. Here, the saturation in PL intensity is observed for treated InP QDs which is not so in case of untreated InP QDs which sheds light on the compactness, stability and porous nature of InP QDs upon HF-treatment. Treated InP has lesser number of surface defects as compared to untreated InP. Therefore lesser number of water molecules got adsorbed in the second week and hence no further increment in PL was observed.

Whereas on the other hand, PL depreciation is observed for InP-ZnS (core-shell) nanocrystallites which can be seen clearly from Fig. 4. However, as expected the existence of ZnS shell for InP-ZnS core-shell nanocrystallites plays the role of a barrier by slowing down the interaction between water molecule and QDs [9]. The purpose of coating the shell was fulfilled as the QDs became robust to any kind of environmental effects.

Table 1 shows the systematic increase in the PL intensity of InP QDs and decrement in the case of InP/ZnS core shell nanocrystallites.

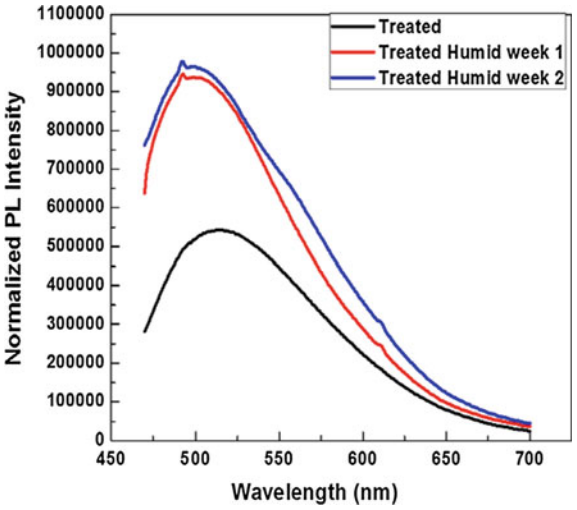

Fig. 3 PL spectra of treated InP for initial week, after 1st week and after 2nd week

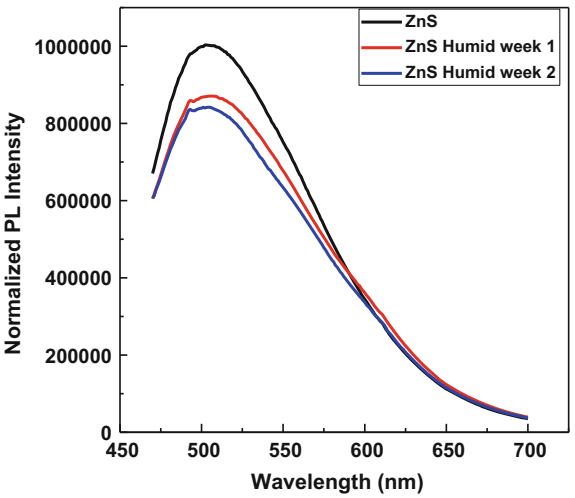

Fig. 4 PL spectra of InP/ZnS core shell nanocrystallites for initial week, after 1st week and after 2nd week

Table 1 Table showing the percentage increase and decrease of PL intensity in InP, treated InP and InP/ZnS respectively

System	After week 1	After week 2
InP	Increment of 72 %	Increment of 118 %
Treated InP	Increment of 73 %	Increment of 78 %
InP/ZnS	Decrement of 12.5 %	Decrement of 16 %

A simple model approach has been shown in Fig. 5 for all the above mentioned situations i.e. InP, treated InP, InP/ZnS QDs. Figure 5a shows that untreated InP has higher number of surface defects and hence more number of water molecules are adsorbed. This resulted in continuous increase of PL as a result of direct band to band recombination. The PL increased even after second week. Treated InP has less number of defects on the surface and less water molecules get adsorbed as compared to untreated InP as shown in Fig. 5b. This leads to the saturation of PL enhancement. Figure 5c shows the presence of shell does not allow water molecules to get adsorbed on the surface and PL intensity is decreased due to some defects aroused on exposure to humid atmosphere.

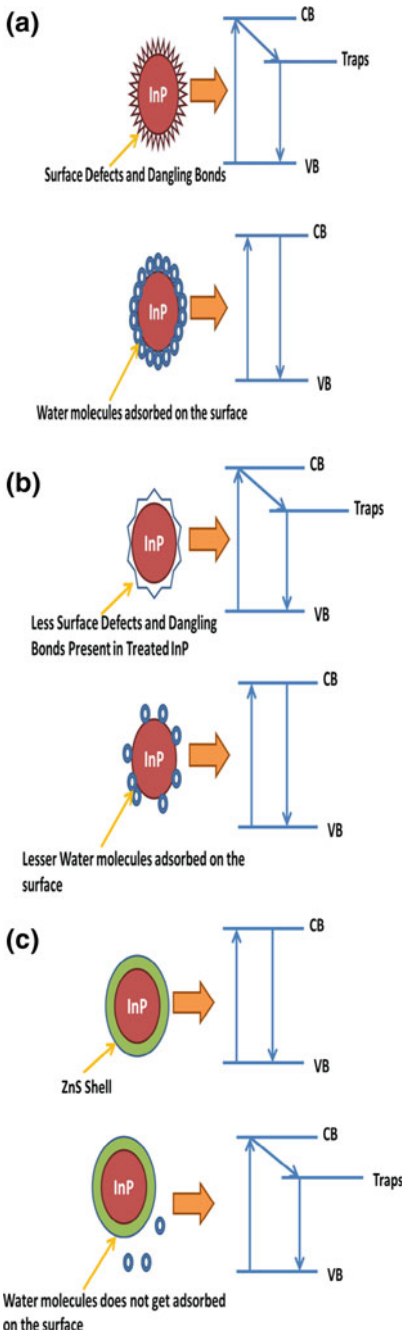

Fig. 5 Model depicting the effect of humidity and PL enhancement on adsorption of water molecules

4 Conclusions

Humid treatment is an effort towards enhancing the quantum yield in InP nanocrystallites by adsorbed water molecules on their surfaces. The results suggest that the adsorbed molecules can passivate the surface trap states and hence improve PL efficiency of InP QDs. Treated InP having lesser defects due to treatment adsorbs lesser water molecules. Hence PL enhancement saturates after second week. On the contrary, InP/ZnS core shell structure showed decrement in PL as an artifact of photo-oxidation mechanism as the shell coating made the QDs more robust to humidity.

References

1. J. Lim, M. Park, W.K. Bae, D. Lee, S. Lee, C. Lee, K. Char, ACS Nano **7**, 9019–9026 (2013)
2. J. Wallentin, N. Anttu, D. Asoli, M. Huffman, I. Åberg, M.H. Magnusson, G. Siefer, P. Fuss-Kailuweit, F. Dimroth, B. Witzigmann, Science **339**, 1057–1060 (2013)
3. K.-T. Yong, H. Ding, I. Roy, W.-C. Law, E.J. Bergey, A. Maitra, P.N. Prasad, ACS Nano **3**, 502–510 (2009)
4. P. Mushonga, M.O. Onani, A.M. Madiehe, M. Meyer, J. Nanomaterials **2012**, 12 (2012)
5. D. Battaglia, X. Peng, Nano Lett. **2**, 1027–1030 (2002)
6. C. Carrillo-Carrión, S. Cárdenas, B.M. Simonet, M. Valcárcel, Chem. Commun. 5214–5226 (2009)
7. S. Cordero, P. Carson, R. Estabrook, G. Strouse, S. Buratto, J. Phys. Chem. B **104**, 12137–12142 (2000)
8. N. Myung, Y. Bae, A.J. Bard, Nano Lett. **3**, 747–749 (2003)
9. B. Dabbousi, J. Rodriguez-Viejo, F.V. Mikulec, J. Heine, H. Mattoussi, R. Ober, K. Jensen, M. Bawendi, J. Phys. Chem. B **101**, 9463–9475 (1997)

Structural and Morphological Characterization of Transition Metal (Fe, Co) Doped SnO_2 Nanoparticles

Anita Gupta, Harminder Kaur and Sanjeev Kumar

Abstract Pure and transition metal (Fe, Co) doped SnO_2 nanoparticles have been successfully synthesized using sol-gel method having the general formula $Sn_{(1-x)}Co_xO_2$ with x = 0, 0.2 and $Sn_{(1-x)}Fe_xO_2$ with x = 0, 0.2, 0.5, 0.7, 1. The synthesis of tinoxide nanoparticles is followed by their characterization by various spectroscopic techniques. X-ray diffraction (XRD) studies depict the crystalline nature of SnO_2 nanoparticles. Peak broadness in the XRD patterns indicates the very small size of the nanoparticles. Size of sol-gel synthesized SnO_2 nanoparticles observed was lying in the range of 40–70 nm using scanning electron microscopy (SEM). Further Fourier transform infrared (FTIR) spectroscopy was used to confirm the presence of organic solvent in the sol-gel synthesized SnO_2 nanoparticles. These sol-gel synthesized SnO_2 nanoparticles can have their potential applications in the field of photo-catalysis and solar cells.

1 Introduction

The Nano-structure material is a single phase or multiphase polycrystalline solids. It exhibits significantly different properties, depending on the fabrication route [1, 2]. Sol gel method of synthesizing Nano materials is widespread among chemist and employed to prepare oxide materials. SnO_2 is n-type semiconductor when undoped. It has numerous such properties which results in countless applications. Crystalline and thin films of tin oxide are used in resistors, transparent antistatic coatings as well as

A. Gupta (✉)
Amity Institute of Applied Sciences, AUUP, Noida 201305, India
e-mail: agupta3@amity.edu

H. Kaur · S. Kumar
Department of Applied Sciences, PEC University of Technology, Chandigarh 160012, India
e-mail: hkaur@pec.ac.in

S. Kumar
e-mail: sanjeev@pec.ac.in

V.K. Jain et al. (eds.), *Recent Trends in Materials and Devices*,
Springer Proceedings in Physics 178, DOI 10.1007/978-3-319-29096-6_10

solid state gas sensors. It has significant catalytic properties also which lead to its use during oxidation of amino olefins [3]. Thin films of SnO_2 are used in transparent antistatic coating. Tin oxide is well known transparent compound, just because its specific electrical properties, this is used in solid state gas sensors. It is also used in electrochemical and catalytic applications. Because of its high catalytic properties it is also used in amino oxidation of olefins. Tin oxide has many industrial applications that is gas sensors of toxic materials and catalytic support [4, 5]. In the recent inventions it has been used as transparent electrodes for solar cells, anodes for lithium ion batteries, liquid crystal display and nanoultrafiltration membranes.

2 Experimental

2.1 Materials

$SnCl_4$ (98 %) and ethylene glycol were obtained from Loba Chem and Iron Nitrate nonahydrate (99 %) from Aldrich, used as precursor materials.

2.2 Methods

Samples of $Sn_{(1-x)}Fe_xO_2$ are prepared via the conventional sol gel method. The nominal compositions were x = 0, 0.1, 0.3, 0.5, 1.0. Then a 0.1 M% $SnCl_4$ and measured iron nitrate nonahydrate solution in ethylene glycol is prepared by dissolving appropriate amount of $SnCl_4{\cdot}5H_2O$ in ethylene glycol. Then the solution is kept at magnetic stirrer with vigorous stirring at temperature between 80 and 90 °C until colourless and transparent solution are obtained. The solution became viscous as the time passes. The solution is then heated to 120 °C and is kept at the same temperature to evaporate water and hydrochloride. When the solvent is completely removed, a dark brown gel is obtained. The gel is then aged for 30 mins and is stirred without heating for 15 h. Now for the preparation of pure Tin oxide, Tin tetrachloride is dissolved in ethylene glycol at 80 °C, colourless and transparent solution is formed. The solution is then heated at about 120 °C so that water and hydrochloride are removed. A dark brown gel is formed after the removal of solvent. Then thereafter the gel is aged for 20–30 mins and is then dried at 150 °C for 24 h. The drying process has been essentially completed within the first 8 h [6]. After the drying process is over, xerogel is heat treated at temperatures varied from 250 to 600 °C. The pure and iron doped nanosized tin oxide powder is obtained by heat treatment at 600 °C for up to 2 h [7]. Then the small amount of powder was taken and mixed with KBr and then pressed uniaxially in the pellet form. These pellets were used for FTIR spectroscopy studies. The layout of the reaction occurring in a basic sol gel process is shown in Fig. 1.

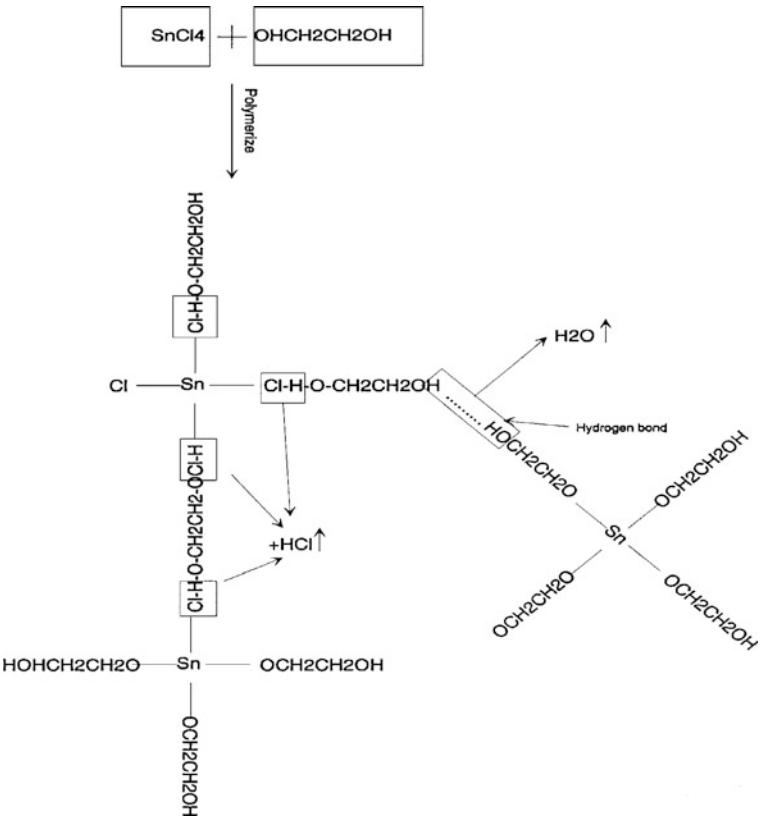

Fig. 1 Reaction occurring in sol gel process

3 Results and Discussion

FTIR is taken after the calcination at 600 °C for 4 h. Figure 2 shows the FTIR spectra of the pure SnO_2 nanoparticles whereas Fig. 3 shows vibrational spectra for the doped sample. A typical broad band nearer to 3400 cm^{-1} that is 3370 cm^{-1} indicates that a strong hydrogen bond have been formed between the hydroxyl groups from ethylene glycol. On continuing to the spectra, the formation of some O–Sn–O bridging bond has been confirmed by the small peak localized at 631.94 cm^{-1}. The Sn–O terminal mode was not observed in the sol due to the existence of excess of ethylene glycol in the samples. Satoshi et al. revealed that the presence of residual chloride ions that decreases the colloidal stability of sols when water is used as solvent. When the sol was washed with small amount of distilled water, the excess of residual ions (chloride and ammonium) were removed and

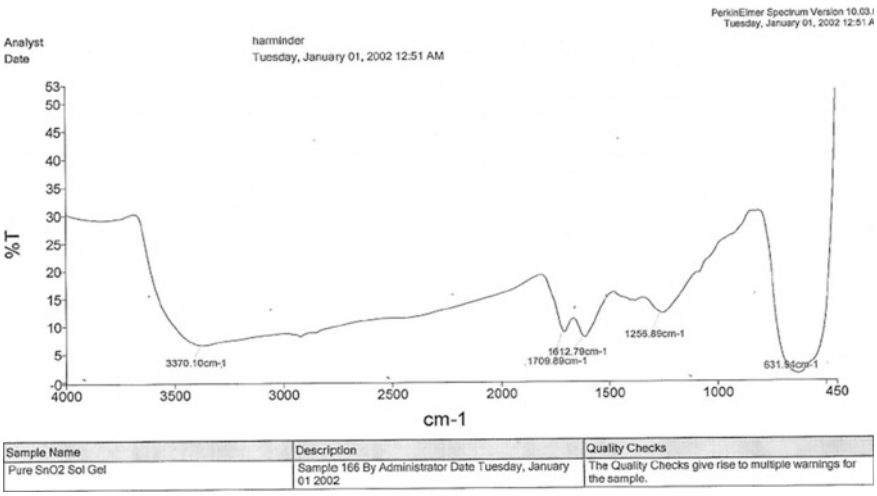

Fig. 2 FTIR spectra of pure SnO_2

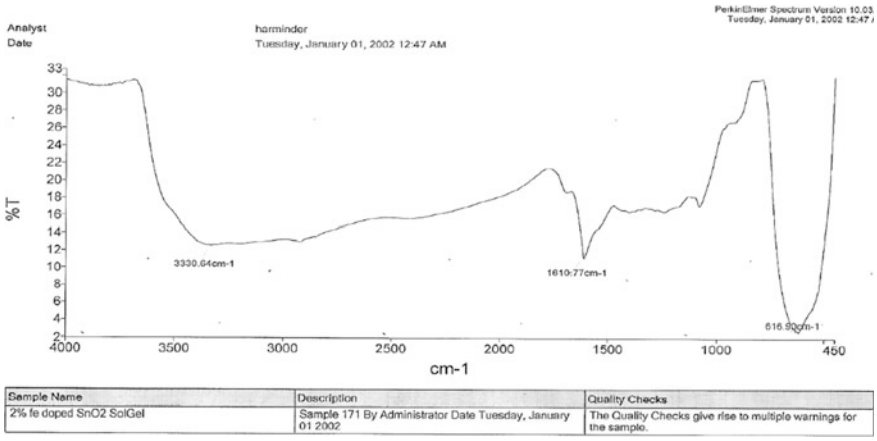

Fig. 3 FTIR spectra of $Sn_{0.98}Fe_{0.02}O_2$

finally they yielded a stable sol. It has been believed that the residual Cl^- ions might modify the physical and chemical characteristics of the solution and the interfacial properties of the colloidal particles in suspension may change that could result in the formation of aggregate. It was found that the sol solution was not at all susceptible to the Cl^- and was quite stable even when the concentration of tin ions reaches 1 M. One of the possible explanation is that tin ions present in the solution

are surrounded by –OCH2CH2O– group, and their molecular size is much bigger than that of hydroxyl group and, therefore, prevention of Cl^- ions from accessing to the tin ions. In addition to it, the large amount of protons are released by the reaction which will be adsorbed on the surface of the particles so that they become positively charged, as it also improve the stability of the sol solution through preventing particles from aggregation. Additionally, as the free ethylene glycol and HCl are liberated, the formation of O–Sn–O bonds also promotes the interconnectivity of the system.

During XRD, Fig. 4 shows the peaks corresponding to the crystalline rutile structure of SnO_2. The doping of iron in tin oxide did not affect the original tetragonal structural cell of SnO_2. While Fig. 5 shows the XRD peaks and indexing for doped sample.

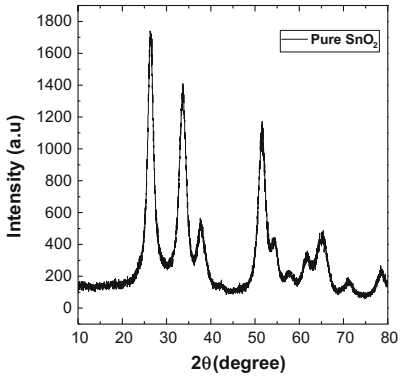

	A	B	C	D
1	Equation	y = y0 + (2*A/PI)*(w/(4*(x-xc)^2 + w^2))		
2	Adj. R-Square	0.99428		
3			Value	Standard Error
4	B	y0	136.04401	2.01333
5	B	xc	26.40568	0.00281
6	B	w	1.54913	0.00981
7	B	A	3895.57743	21.42057
8	B	H	1736.94256	

Fig. 4 The XRD pattern of pure SnO_2

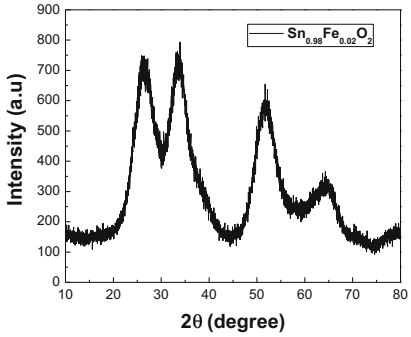

	A	B	C	D
1	Equation	y = y0 + (2*A/PI)*(w/(4*(x-xc)^2 + w^2))		
2	Adj. R-Square	0.97732		
3			Value	Standard Error
4	B	y0	80.51321	3.04226
5	B	xc	26.73152	0.01456
6	B	w	6.03054	0.0725
7	B	A	5977.63448	81.53473
8	B	H	711.54768	

Fig. 5 The XRD pattern of $Sn_{0.98}Fe_{0.02}O_2$

Using Debye Scherrer formula crystallite size of SnO_2 is found to be 5.5 nm and that of 2 % Fe doped SnO_2 is 1.41 nm.

From SEM analysis, Figs. 6 and 7; we came to know about the sizes of nanoparticles. The size of iron doped tin oxide nanoparticles was found to be 44.5 nm and that of pure tin oxide nanoparticles was found to be 46.7 nm. Also the EDAX analysis in Fig. 8 shows that the iron contents present in the doped tin oxide have 0.44 %.

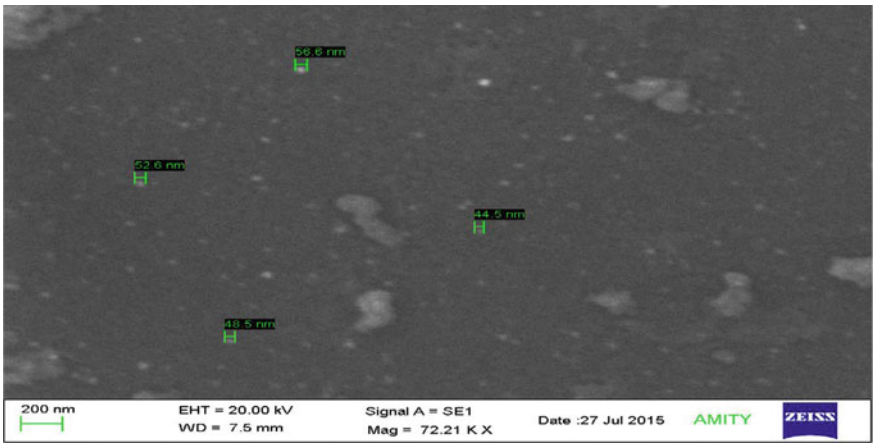

Fig. 6 SEM images of $Sn_{0.98}Fe_{0.02}O_2$

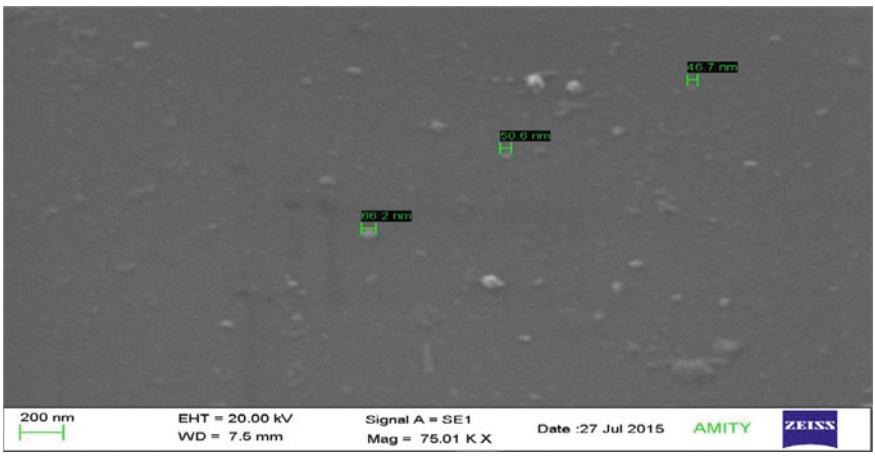

Fig. 7 SEM image of pure SnO_2

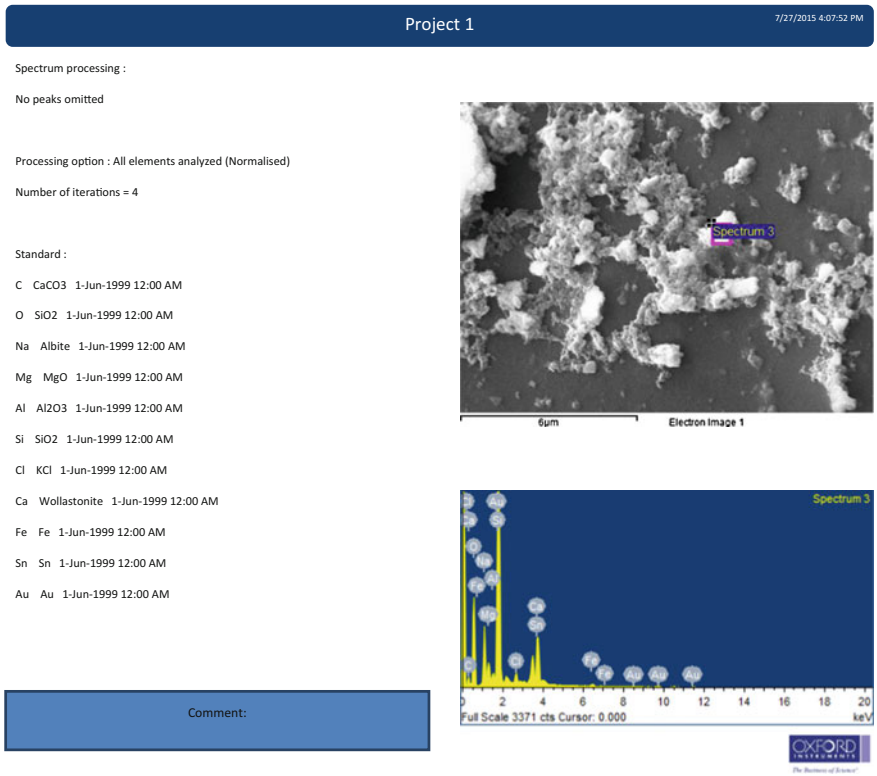

Fig. 8 EDAX analysis of doped sample

Element	Weight (%)	Atomic (%)
C K	10.26	17.78
O K	38.47	50.03
Na K	6.25	5.66
Mg K	1.68	1.44
Al K	0.48	0.37
Si K	27.08	20.06
Cl K	1.14	0.67
Ca K	4.26	2.21
Fe K	0.46	0.17
Sn L	8.05	1.41
Au M	1.86	0.20
Total	100.00	

4 Conclusions

In conclusion, Nanostructured powder of pure and doped SnO_2 have been successfully prepared using a sol-gel method. This method use tin tetrachloride and ethylene glycol as the main precursor. This method of preparation is simple to control and the solution was extremely stable even in the presence of high concentration of hydrochloride. In this process the ethylene glycol act as a complexing agent and forms polymeric network. XRD pattern clearly confirms the crystalline phase of the composition. The average crystallite size of pure and 2 % Fe^{3+} SnO_2 is found to be 5.5 and 1.41 nm. Low value of transmittance in FTIR confirms the presence of organic solvent in the powders. So the calcinations at 300 °C is not enough even though we have got the crystalline phase. With high calcinations temperature organic compounds can be removed. SEM analysis shows that the iron doped tin oxide nanoparticles were within the range of 100 nm.

References

1. C.A. Martinez-Huitle, E. Brillas, Decontamination of wastewaters containing synthetic organic dyes by electrochemical methods: a general review. Appl. Catal. B **87**(4–5), 105–145 (2009)
2. J.J. Beltran, Crystallographic and magnetic properties of Fe doped SnO_2 nanopowders obtained by a sol–gel method: J. Mat. Sci **45**(18), 5002–5011 (2010)
3. M. Dimitrov, T. Tsoncheva, S. Shao, R. Kohn, Novel preparation of nanosized mesoporous SnO_2 powders: physicochemical and catalytic properties. Appl. Catal. B **94**(1–2), 158–165 (2010)
4. N. Wang, J. X. Xu, L. H. Guan, Synthesis and enhanced photocatalytic activity of tin oxide nanoparticles coated on multi-walled carbon nanotube. Mater. Res. Bull. **46**(9), 1372–1376 (2011); Obtained by a sol-gel method. J. Mater. Sci. (2010)
5. T. Krishna Kumar, N. Rajesh, J.C. Kannan, S.G. Leonardi, G. Neri, Sensing behavior to ethanol of tin oxide nanoparticles. Sens. Actuators, B Chem, **194**, 96–104 (2014)
6. Z. He, Z. Zhu, J. Li, N. Wei, J. Zhou, Characterization and activity of mesoporous titanium dioxide beads with high surface areas and controllable pore sizes. J. Hazard. Mater. **190**(1–3) (2011)
7. Z. Zhu, J. Zhou, Z. He, Effects of heat treatment scheme on luminescence properties and photocatalytic activity of Mo_2O_3/TiO_2 nanowire prepared via solvo-thermal method. J. Nanoeng. Nanomanuf. **2**(1), 80–84 (2012)

Morphological, Optical and Thermal Properties of $(TiO_2)_x$ Embedded $(PVC/PE)_{1-x}$ (Where x = 0.0, 0.1, 0.2, 0.3, 0.4 and 0.5) Blend Nanocomposites

Anjna Thakur, Priya Thakur and Kamlesh Yadav

Abstract Present study deals with the dispersion of TiO_2 nanoparticles in PVC/PE blends. The prepared blend nanocomposites have been characterized using FESEM, FTIR, UV-Visible spectroscopy, TGA, and EDX to study the morphology, optical and thermal properties of prepared samples. FESEM confirms the dispersion of nanoparticles in polymer blend and formation of blend nanocomposites. Decrease in optical band gap has been observed by addition of TiO_2 content. Variation in melting point is studied by TGA. Thermal stability is enhanced with increasing TiO_2 content in polymer blend

1 Introduction

The development of composite materials was started in the beginning of 1940s and are being used in airplanes, helicopters, rockets because these are light in weight and mechanically strong. After the discovery of composites, material scientists tried to go beyond the microscale and to build materials atoms by atoms (nanoscale) in order to make the complex materials, which can function as device at microlevel. Thus, composites has generated a new way of thinking about the interface between the two phases. Because of mechanical properties of heterogeneous structure depend upon the quality of interface between the reinforcing material and host matrix. Thus, interfaces and surfaces become main concern of material science & technology. Surface science has thus opened a new field of research.

A. Thakur · P. Thakur · K. Yadav (✉)
Centre for Physical Sciences, Central University of Punjab, Bathinda 151001, India
e-mail: kamlesh.yadav001@gmail.com

A. Thakur
e-mail: anjna56@gmail.com

P. Thakur
e-mail: priyathakur1191@gmail.com

V.K. Jain et al. (eds.), *Recent Trends in Materials and Devices*,
Springer Proceedings in Physics 178, DOI 10.1007/978-3-319-29096-6_11

Composites are playing an important role in the field of polymers. In the polymer industry, composite materials has increased the emergence of new, light weighted polymer for a variety of applications in the market of plastic. Polymer blend technology has the property to form the materials with desired properties which are non-attainable with polymer. Thus, this area of research has gained the attention of researchers, since last few years. Such polymeric material offered new opportunity to scientists and engineers for designing new materials. Polymer blending gives a new range of materials with improved mechanical and thermal properties and enhanced fracture resistance and chemical resistance [1, 2]. In the present time, nanotechnology has opened the new door to use the polymer blend as host matrices for the incorporation of nano sized particles. These incorporated nanoparticles causes to change the polymer-polymer interface and different spatial arrangement can be obtained, depending on the interaction between them [3, 4]. Thus, nanocomposites possesses the improved property which are not possible to obtain by polymer combinations in blends.

A lot of work have been performed on the mechanical, thermal and optical properties of polymer blends. Glass transition temperature has been an important property of polymers to study due to abrupt changes in the mechanical and thermal properties at glass transition temperature. It is due to the reason that many polymer exist in the amorphous glassy state at these ambient temperature. There is a non-equilibrium state, where on heating, material changes towards the equilibrium liquid state [5]. The improved mechanical and rheological properties of poly vinyl chloride/Poly (ethyl methacrylate) (PVC/PEMA) blend nanocomposites on adding montmorillonite (MMT) by melt processing have been reported [6]. TiO_2 nanoparticles has been incorporated into PVC/ENR (epoxidized natural rubber) blend nanocomposites to study the morphology and mechanical properties of polymer blend nanocomposites [7]. Mathur et al. (2015) reported enhancement in thermal conductivity on adding CdS nanoparticles into polystyrene/poly vinyl chloride (PS/PVC) and polystyrene/poly methyl methacrylate (PS/PMMA) polymer blend nanocomposites [8]. Incorporating zinc oxide (ZnO) nanoparticles enhances the thermal, optical, structural and mechanical properties of PC/PMMA and PC/PS blend nanocomposites [9, 10]. Also, improvement in mechanical strength of poly vinyl alcohol/Poly (hydroxybutyrate-co-valerate) (PVA/PHBV), Poly (lactic acid)/ poly (ε-caprolactone) PLA/PCL, Poly (hydroxybutyrate-co-valerate)/poly (ε-caprolactone) (PHBV/PCL) and effect on morphology and thermal stability of PHBV/PCL blends and their nanocomposites on adding TiO_2 has been reported [11, 12].

Present work, therefore focuses on the results of adding TiO_2 nanoparticles into PVC/PE (polyethylene) host matrix to investigate the miscibility of polymer blends and their nanocomposites by FESEM, thermal stability by TGA and optical properties by FTIR and UV-visible spectroscopy.

2 Materials Used and Experimental Procedure

This chapter involves the summary of various materials used to prepare polymer blend nanocomposites and experimental procedure used to prepare the polymer blend nanocomposites. The characterization of prepared polymer blend nanocomposites using different characterizing tools have been discussed in this chapter. In the present work, PVC and PE have been used as basic polymeric materials. TiO_2 nanoparticles incorporated into polymer blend matrices were also purchased from Sigma Aldrich and further used without any purification.

2.1 Materials Used

PVC and PE were purchased from Sigma Aldrich with average molecular weight of 80,000 and 4000 by GPC. Nanoparticles of TiO_2 used with primary particle size 21 nm were also purchased from sigma Aldrich.

2.2 Preparation of Samples

To prepare PVC/PE/TiO_2 blend nanocomposites, PVC and PE (purchased from Sigma Aldrich) were mixed in an equal appropriate weight ratio (PVC-50 wt% and PE-50 wt%). Subsequently, TiO_2 nanoparticles (Sigma Aldrich) were added to this polymeric mixture with concentration x = 0.0, 0.1, 0.2, 0.3, 0.4, and 0.5. Resulting mixtures were then mixed and grinded for 50 min and pressed into pellets (circular, 1 mm × 1 mm) at a pressure of 8.5 MPa. Then, pellets were sintered at 200 °C for 2 h in air in order to make the connection between adjacent TiO_2 nanoparticles and polymer blend matrix. Low temperature was used in order to avoid reaction of polymer blends and TiO_2 nanoparticles.

2.3 Characterization Techniques

The prepared blend nanocomposites have been characterized using field emission scanning electron microscopy (FESEM), fourier transform infrared spectroscopy (FTIR), UV-Visible spectroscopy, thermal gravimetric analysis (TGA), and energy dispersive X-ray spectroscopy (EDS) to study the morphology, optical and thermal properties of prepared samples. The surface morphology of prepared PVC/PE/TiO_2 was investigated by FESEM (Card Ziess Merlin Compact), optical characterization was performed using FTIR (Bruker Tensor-27) in the range 400–4000 cm^{-1} and UV-Visible spectrophometer (UV-2450) in the range 200–800 nm. Thermal study

was performed using TGA (SHIMDZU-DTGG-60 H) in the temperature range from 30 to 580 °C at heating rate 10 °C/min. EDS analysis was done to confirm the presence of all the elements and compositions as per stoichiometric ratio in the polymer blend nanocomposites.

3 Results and Discussion

The effect of adding TiO_2 as nano filler on the morphology, optical and thermal properties of PVC/PE blend nanocomposites have been characterized from various characterizing tools and results obtained from FESEM, EDS, FTIR, UV-Visible spectrometer and TGA analysis have been discussed.

3.1 FESEM Analysis

FESEM is used to observe the dispersion of TiO_2 nanoparticles in immiscible PVC/PE blends. The FESEM image of pure PVC/PE (Fig. 1a) shows that the continuous network of polymers blends is formed. Figure 1b–f shows the FESEM images of $(PVC/PE)_{1-x}/(TiO_2)_x$ (x = 0.1, 0.2, 0.3, 0.4, and 0.5) blend nanocomposites. Figure 1 (c), shows some white dots, which may indicate dispersed nanoparticles in polymer blends. Further, Fig. 1e, f show well dispersion of TiO_2 nanoparticles in PVC/PE blends. It is observed that in all the polymer blend nanocomposites samples TiO_2 filler are dispersed. As the content of TiO_2 increases the surface becomes rough with some segregation of filler nanoparticles in the polymeric system. These results can be assign to the interaction between polymer blend and nanoparticles resulting the formation of polymer blend nanocomposites [13].

3.2 EDS Analysis

The EDS analysis confirms the presence of all the elements and compositions as per stoichiometric ratio within the experimental error in the polymer blend nanocomposites. The theoretical and experimental weight % of elements present in prepared samples is in agreement with experimental error and is listed in tabular form. Figure 2 represents the EDS plots of prepared PVC/PE/TiO_2 blend nanocomposites (Tables 1 and 2).

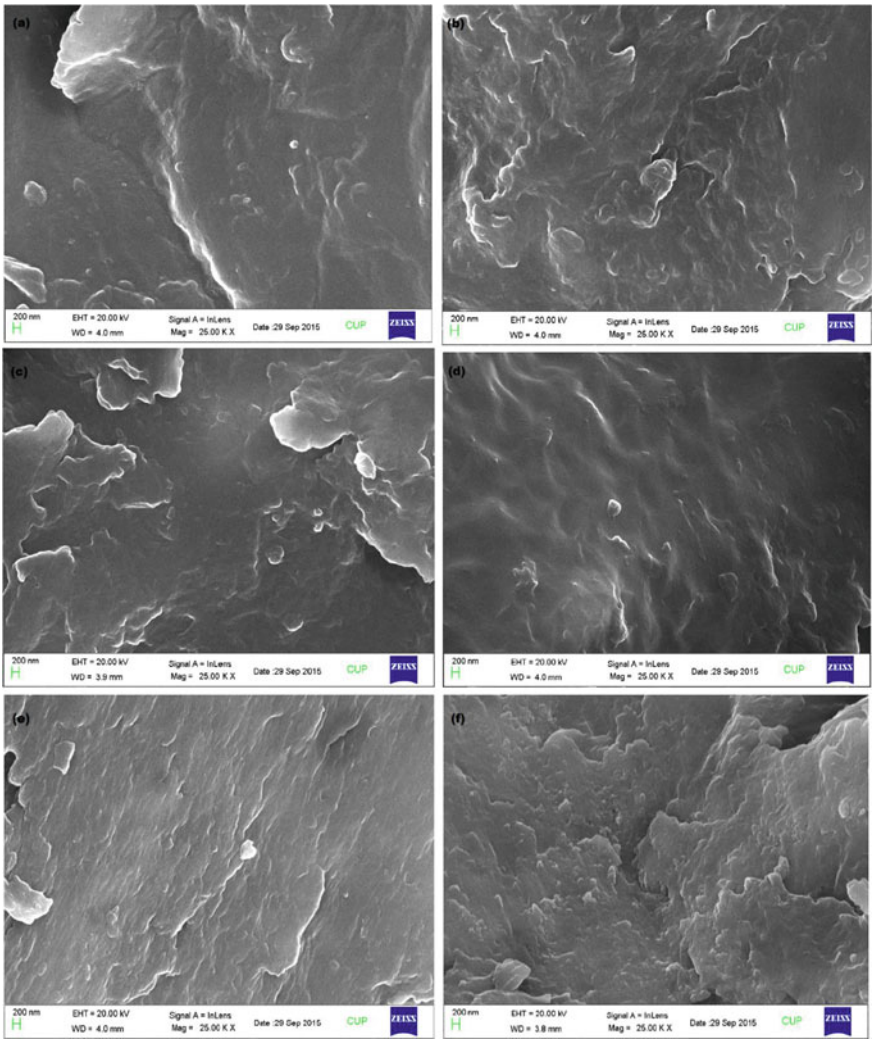

Fig. 1 FESEM images of $(PVC/PE)_{1-x}/(TiO_2)_x$ (x = 0, 0.1, 0.2, 0.3, 0.4, and 0.5) blend NC

3.3 FTIR Analysis

Figure 3 shows the FTIR spectra for $(PVC/PE)_{1-x}/(TiO_2)_x$ blend nanocomposites (where x = 0.0, 0.1, 0.2, 0.3, 0.4 and 0.5). Main characteristics absorbance band of pure PVC appears at 2919, 2843, 1710, 1463, 1091, 941, 643 cm^{-1} corresponds to stretching of C–H of CH–Cl bond, alkyl group, carbonyl group, deformation (wagging) of CH_2, stretching of C–C bond, rocking of CH_2, stretching of C–Cl respectively [14].

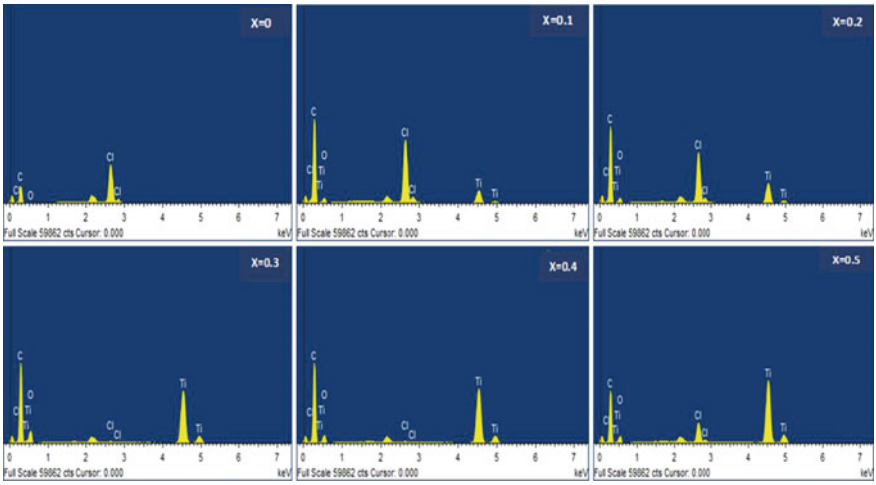

Fig. 2 EDS plots of $(PVC/PE)_{1-x}/TiO_2$ blend nanocomposites

These main peaks of pure PVC appear in FTIR spectrum of all the nanocomposite samples $(PVC/PE)_{1-x}/(TiO_2)_x$ blend for x = 0.1, 0.2, 0.3, 0.4, and 0.5. Further, absorbance bands of PE appear at 2854, 1463, 722 cm^{-1} which corresponds to stretching of C–H band and C–C bond respectively. Moreover, $(PVC/PE)_{1-x}/(TiO_2)_x$ blend NC shows the absorbance peak at 620 cm^{-1} corresponds to Ti–O–Ti bond. In addition to this, there is a small peak at 1595 cm^{-1} reveals the presence of TiO_2 nanoparticles in polymer blend indicating the interaction in polymer blend and TiO_2 nano filler [15]. Also, the band near the 645 cm^{-1} corresponds to Ti–O–Ti stretching vibrations. As there is no shift in the bands of polymer blend nanocomposite compared with the pure PVC/PE blend spectrum. Thus, there is no chemical bonding (almost negligible interaction) between the TiO_2 nanoparticles and pure PVC/PE blends [16].

3.4 UV-Visible Spectroscopic Analysis

UV-Visible absorption spectroscopy is widely being used technique to examine the optical properties of polymer blend nanocomposites. Measurement of the UV-Visible absorption spectra of material is the most direct method to investigate the band structure of the materials. In the absorption process an electron is excited from a lower to higher energy state by absorbing a photon of known energy. The changes in the transmitted radiation can decide the types of possible electron transitions. The absorption refers to band-to-band transition. Optical absorption spectra of prepared polymer blend nanocomposite is observed as a function of wavelength.

Table 1 Theoretical and experimental weight % of elements in PVC/PE/TiO_2 blend NC

Element symbol	wt% x = 0 Theo.	wt% x = 0 Exp.	wt% x = 0.1 Theo.	wt% x = 0.1 Exp.	wt% x = 0.2 Theo.	wt% x = 0.2 Exp.	wt% x = 0.3 Theo.	wt% x = 0.3 Exp.	wt% x = 0.4 Theo.	wt% x = 0.4 Exp.	wt% x = 0.5 Theo.	wt% x = 0.5 Exp.
C	57.83	81.68	53.14	79.69	64.71	76.43	49.91	53.26	29.62	55.98	32.82	53.23
O	0.00	0.61	3.88	6.42	7.78	7.81	15.36	22.98	19.75	17.80	20.12	14.75
Cl	32.16	17.71	31.13	9.83	14.01	8.74	10.15	1.20	20.06	1.17	10.37	4.34
Ti	0.00	0.00	5.00	4.08	11.51	7.04	22.51	22.55	29.02	24.06	34.99	27.68

Table 2 Theoretical and experimental atomic % of elements in PVC/PE/TiO_2 blend NC

Element symbol	at.% x = 0 Theo.	at.% x = 0 Exp.	at.% x = 0.1 Theo.	at.% x = 0.1 Exp.	at.% x = 0.2 Theo.	at.% x = 0.2 Exp.	at.% x = 0.3 Theo.	at.% x = 0.3 Exp.	at.% x = 0.4 Theo.	at.% x = 0.4 Exp.	at.% x = 0.5 Theo.	at.% x = 0.5 Exp.
C	89.05	92.67	75.11	89.68	69.56	87.84	42.85	69.63	50.00	73.72	42.10	73.21
O	0.00	0.52	4.15	5.42	8.69	6.74	21.42	22.56	25.00	17.60	31.57	15.22
Cl	10.91	6.81	11.95	3.75	14.39	3.40	25.00	1.09	12.50	1.07	10.52	2.02
Ti	0.00	0.00	2.08	1.15	4.37	2.02	10.01	6.72	12.50	7.614	15.78	9.55

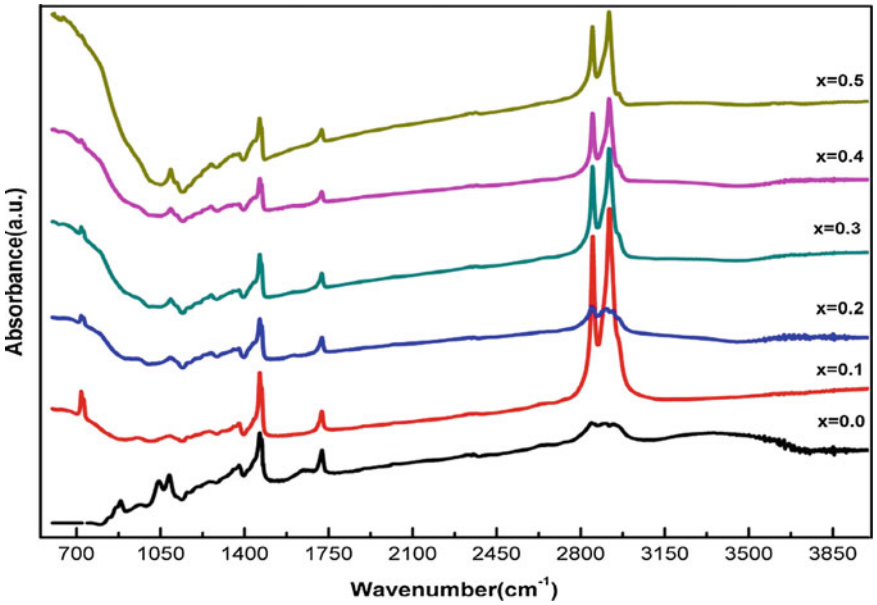

Fig. 3 FTIR spectra of $(PVC/PE)_{1-x}/(TiO_2)_x$ for x = 0.1, 0.2, 0.3, 0.4, and 0.5 blend nanocomposites

In UV-visible spectroscopic analysis, absorption intensity increases with increase in TiO_2 wt% in PVC/PE blend samples. The calculation of optical energy bandgap is done using Tau's plot by plotting the graph between $(\alpha h\nu)^{1/2}$ and $h\nu$, where α is absorption coefficient and ν is frequency of light used. The optical band gap has been calculated from the extrapolation of liner portion of the graph to the photon energy axis (Fig. 4).

Figure 5 shows the variation in optical energy band gap of polymer blends with varying concentration of TiO_2 nanoparticles. The energy band gap decreases with increasing the concentration of TiO_2 in the samples. It is due to the reason that wave functions of the electrons of host matrix bound to the TiO_2 nanoparticles start to overlap as the density of the TiO_2 nanoparticles increase in blend nanocomposites. This overlap forces the energies to form an energy band rather than a discreet level. This impurity band reduces the energy band of the polymer blend nanocomposites [17].

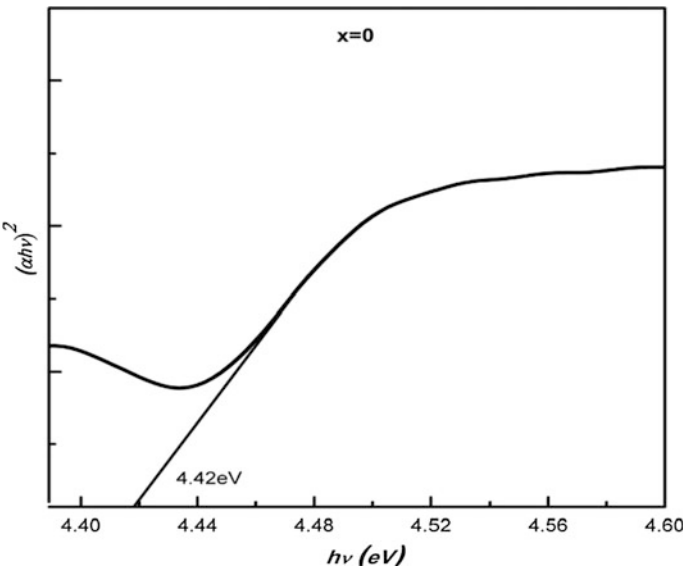

Fig. 4 Variation of $(\alpha h\nu)^{1/2}$ and hν for $(PVC/PE)_{1-x}/(TiO_2)_x$ for x = 0 blend nanocomposites

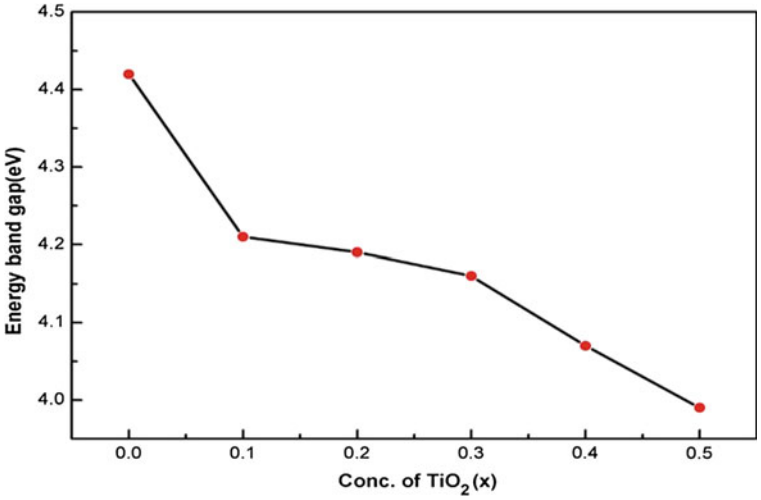

Fig. 5 Variation of energy band gap with the conc. of TiO_2 nanoparticles

3.5 TGA Analysis

TGA analysis is done to study the thermal stability of prepared polymer blend nanocomposites i.e. to observe the effect of TiO_2 nano filler on thermal stability of polymer blend. The introduction of 1 wt% TiO_2 nanoparticles has improved the thermal stability of PVC/PE blends.

Thermal stability of polymer blend nanocomposites is more as compared to PVC/PE blends polymer. It is due to closeness of nano fillers that leads to more hindrance of these nanofillers in escaping of thermally decomposed material. This results a longer path for degradation. It results an important role in enhancing the thermal stability [18].

However, increase in filler content has little effect on the thermal stability of polymer blends. This insignificant change in thermal stability is attributed to fact that with the increase in TiO_2 content, level of agglomeration increases. Thus, effective surface area and interaction with volatile degradation products, do not increases significantly in polymer blend nanocomposites [19].

The TGA studies of weight loss (%) of prepared samples as a function of temperature is shown in Fig. 6.

It is observed that the decomposition temperature of pure PVC/PE blend occurs at 270 °C. This value is less than the decomposition temperature for the polymer blend nanocomposites, which is at 310 °C. These results shows the enhancement in the thermal stability of prepared polymer blend nanocomposites (PVC/PE/TiO_2) as compared to pure polymer blends (PVC/PE).

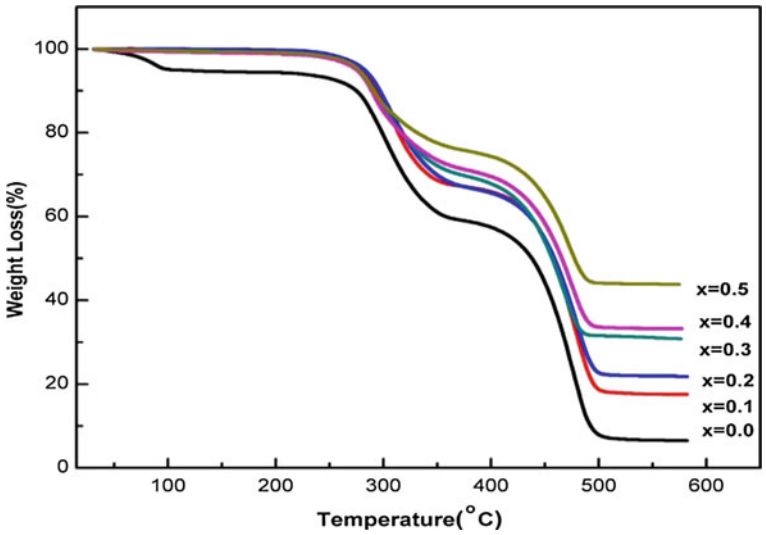

Fig. 6 TGA graph of $(PVC/PE)_{1-x}/(TiO_2)_x$ for x = 0.1, 0.2, 0.3, 0.4, and 0.5 blend nanocomposites

4 Conclusions

Morphological, optical and thermal properties of TiO_2 added PVC/PE polymer blends have been studied. FESEM analysis confirms the dispersion of TiO_2 nanoparticles into polymer matrix. The FTIR analysis manifested the conclusion that in the prepared samples there are strong interaction in polymer matrices and nano filler. The optical studies from UV-Visible absorption shows that polymer blend nanocomposite has more absorbance as compared to pure PVC/PE blend. Energy bandgap of blend nanocomposites have been calculated by using Tauc's relation. Lowest value of energy bandgap of PVC/PE/TiO_2 blend nanocomposite has been found for 50 wt% of TiO_2 nano filler. The calculated energy band gap decreases with increase in content of TiO_2 nano filler. Also, an improvement is observed in thermal stability of polymer PVC/PE/TiO_2 blend nanocomposites as compared to pure PVC/PE polymer blends. These results manifestate the conclusion that improvement in optical and thermal properties of polymer blends on adding TiO_2 nanoparticles. These blend nanocomposites can be used in plastic industry and various medical devices applications.

Acknowledgments Author (AT) is thankful to UGC for providing fellowship during M.Phil. One of the author (KY) is grateful to the Central University of Punjab for providing the Research Seed Money grant.

References

1. L.M. Robeson, Hanser Verlag **11** (2007)
2. D.R. Paul, C.B. Bucknall, *in Polymer Blends Volume 1: Formulation*, ed. by D. R. Paul and C. B. Bucknall, (Wiley, New York, 2000)
3. S.R. Suprakas, O. Masami, Prog. Poly. Sci. **28**, 1539 (2003)
4. B.A. Rozenberg, R. Tenne Prog. Poly. Sci. **33**, 40 (2008)
5. C. Zhang, R.D. Priestley, Soft Matter **9**, 7076 (2013)
6. A.V. Shikaleska, F.P. Pavlovska, I.O.P. Conf, Series: mater. Sci. & Engg. **40**, 012009 (2012)
7. N.A. Ramlee, C.T. Ratnam, S.A. Rahman, N.A. Samat, *IEEE Busi, Engg. & Indus. Appl. Colloquium* **10**, 533 (2013)
8. V. Mathur, D. Patidar, K. Sharma, Appl. Nanosci. **5**, 623 (2015)
9. S. Agarwal, V. Kulshrestha, V.K. Sarswat, Int. J. Sci. Tech. **2**, 1140 (2014)
10. S. Agarwal, V.K. Sarswat, Optical Mater **42**, 335 (2015)
11. J.P. Mofokeng, A.S. Luyt, Thermochimica Acta **613**, 41 (2015)
12. J.P. Mofokeng, A.S. Luyt, J Mater. Sci. **50**, 3812 (2015)
13. K.Y. Lee, L.A. Goettler, Poly. Eng. Sci. **44**, 1103 (2004)
14. S. Cho, W. Choi, J. Photochem. Photobiol. A. Chemistry **143**, 221 (2001)
15. A. Olad, S. Behboudi, A.A. Entezami, Chin. J. Poly. Sci. **31**, 481 (2013)
16. M. Hasan, A.N. Banerjee, M. Lee, Bull. Mater. Sci. **38**(2), 283 (2015)
17. J.G. Lu, S. Fujita, T. Kawaharamura, H. Nishinaka, Y. Kamada, T. Ohshim, B.H. Zhao, J. Appl. Phys. **101**, 83705 (2007)
18. N.G. Shimpi, J. Verma, S. Mishra, Polymer-Plastics Tech. Eng. **48**(10), 997 (2009)
19. A. Buzarovska, A. Grozdanov, M. Avella, G. Gentile, M. Errico, J Appl. Poly. Sci. **114**(5), 3118 (2009)

Effect of Annealing on Structural and Optical Properties of Graphene Nanoballs

Chetna, Sanjeev Kumar and A. Kapoor

Abstract Graphene nanoballs were produced via cost effective flame synthesis method, and influence of annealing temperature along with annealing time on configuration and quality of the samples were studied. The structural, morphologies, and optical properties of the so formed nanoballs were studied by means of X-ray Diffraction, Scanning Electron Microscopy, Raman Spectroscopy and Energy Dispersive Spectroscopy. The synthesis of graphene was confirmed by both X-ray diffraction and Raman spectroscopy. XRD studies showed the crystalline nature and phase purity of the graphene. Raman studies showed that sample annealed at higher temperature has more defects in comparison to un-annealed sample. Different optical and structural parameters were also performed to further analyze the nanoballs.

1 Introduction

Graphene, a two dimensional hexagonal lattice of carbon, has jumped to the forefront of the condensed matter research in the past few years as a high quality two dimensional electron system with intriguing scientific and practical applications. It has attracted great interest in recent years for its extraordinary mechanical, electrical, thermal and optical properties. Due to its unusual properties, Graphene holds a number of promising applications [1–3]. Now a days three dimensional (3D) graphene nanoballs is gaining considerable interest because of its potential applications in sensors, super-capacitors and catalytic electrodes [4]. There are various approaches used for graphene synthesis.

Chetna (✉) · S. Kumar · A. Kapoor
Photovoltaics and Opto Electronics Lab, Department of Electronic Science,
University of Delhi, South Campus, Benito Juarez Road, New Delhi 110021, India
e-mail: chetna2288@gmail.com

V.K. Jain et al. (eds.), *Recent Trends in Materials and Devices*,
Springer Proceedings in Physics 178, DOI 10.1007/978-3-319-29096-6_12

For synthesis of hollow graphene balls, recently a new method has been reported [5]. But all these methods are very complicated and consist of lots of processing steps. But in our work, we have gone for a well established traditional method. In this, we have synthesized graphene nanoballs by flame combustion of readily available refined mustard oil using cotton wick. Then the so formed samples were annealed at different temperatures and analyzed.

2 Experimental Details

Graphene Nanoballs Synthesis and Annealing. As a part of this experiment, we have successfully produced graphene nanoballs using a novel method. Readily available, refined mustard oil and cotton wick have been used as raw materials. To begin with, Acetone ($(CH_3)_2CO$) was sprayed on the cotton wick and then dried for few minutes. The dry wick was subsequently flamed in the clay lamp consisting of mustard oil. The clay lamp was in turn covered with a clay disk, in order to give a limited supply of air. The complete inflammation of the dried cotton wick resulted in the emission of carbon material, which got accumulated over the clay disk. This emitted material was in turn corralled and subsequently grounded with a pestle and mortar into a fine powdered sample using Acetone. Finally the sample was annealed in muffle furnace at 200 °C and 300 °C for an hour.

Structural and Optical Characterization. The structural characteristics of the sample were monitored by X-ray diffraction (XRD; Bruker D8 High Resolution Diffractometer) using CuKα1 (λ = 0.154 nm) radiation. For optical characterization, Raman spectra of the graphene powders were measured by using Avalon Raman Microscope with 532 nm diode laser excitation in the range of 0–3000 cm^{-1} . The morphology and structure of the sample were observed by a Scanning Electron Microscope.

3 Results and Discussion

X-ray diffraction (XRD) is a useful technique not only for the phase identification but also for the identification of the lattice structure [6]. X-ray diffraction (XRD) patterns are used for the analysis of recognition of Graphene. Figure 1 shows the XRD pattern of synthesized graphene balls in pristine form and at various temperatures. The presence of two very important diffraction peaks at 24.5° in {002} plane and 43.2° in {100} plane, confirmed the presence of hexagonal structure of graphene material. It is observed that as the temperature increases, the intensity of {100} diffraction line gradually weakened and sample becomes less crystalline. Several parameters were calculated to study X-ray diffraction and are tabulated in Table 1. It can be seen that dislocation density and strain increase while interplaner distance decrease with temperature.

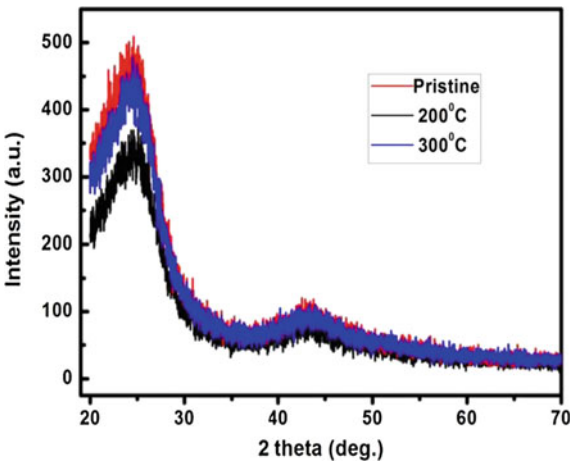

Fig. 1 X-ray diffraction pattern of pristine and annealed graphene nanoballs

Table 1 Significant parameters obtained from X-ray diffraction technique

Temperature (°C)	Average crystalline size (nm)	Dislocation density (nm^{-2})	Interplaner distance (A°)	Strain
Pristine	1.39	0.511	3.74	0.0258
200	1.35	0.543	3.63	0.0266
300	1.10	0.816	3.62	0.0326

Raman spectroscopy is a powerful nondestructive tool to characterize carbonaceous materials, particularly for distinguishing ordered and disordered crystal structures of carbon [7, 8]. Figure 2 shows the Raman spectra of produced graphene balls in pristine form and at various temperatures. The Raman spectrum of the pristine graphene nanoballs displays a strong G band at 1587 cm^{-1} which confirms the presence of carbon material in this sample of graphene and D band at 1347 cm^{-1} indicating the sp^2 hybridization of atoms of material. With the effect of annealing, the Raman spectrum of G band is broadened and shifted upward. At the same time, the intensity of the D band also increases substantially. This could be due to significant decrease of size of in-plane sp^2 domain and crystalline size.

Scanning Electron Microscopy has been extensively used as a rapid, non-invasive and effective manner for imaging the morphologies of graphene films especially at micro and nanoscales [9]. Figure 3 represents the scanning electron microscope images of spherical graphene nanoballs prepared by flame combustion method. Figure 3a shows graphene nanoballs in pristine form and Fig. 3b shows films annealed at 200 °C and Fig. 3c shows films annealed at 300 °C. It can be seen from Fig. 3a that aggregated particles were formed and as we gave the temperature,

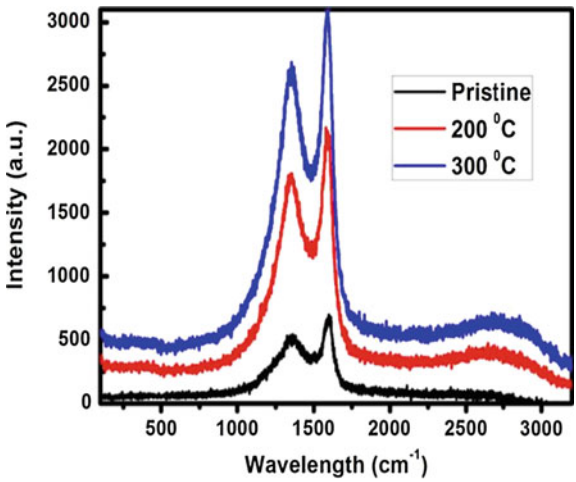

Fig. 2 Raman spectra of pristine and annealed graphene nanoballs

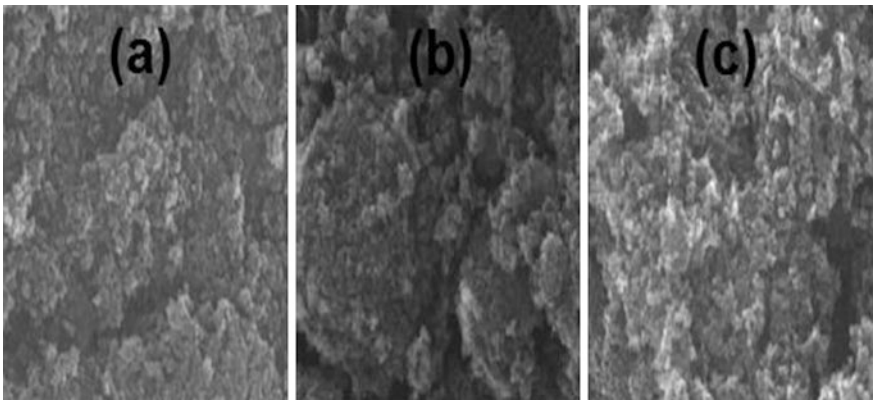

Fig. 3 SEM images of graphene nanoballs. **a** As-synthesised graphene nanoballs and **b** annealed graphene nanoballs at 200 °C and **c** annealed graphene nanoballs at 300 °C

the distribution of nanoparticles became homogenous (Fig. 3b) and also it is very clear that this homogeneity increases with rise in temperature (Fig. 3c).

Figure 4 shows the EDS analysis performed on graphene nanoballs. According to this figure, there is a large amount of carbon present in the sample with extremely small quantity of oxygen. Thus it can be concluded that there is no other metal catalyst present in the sample.

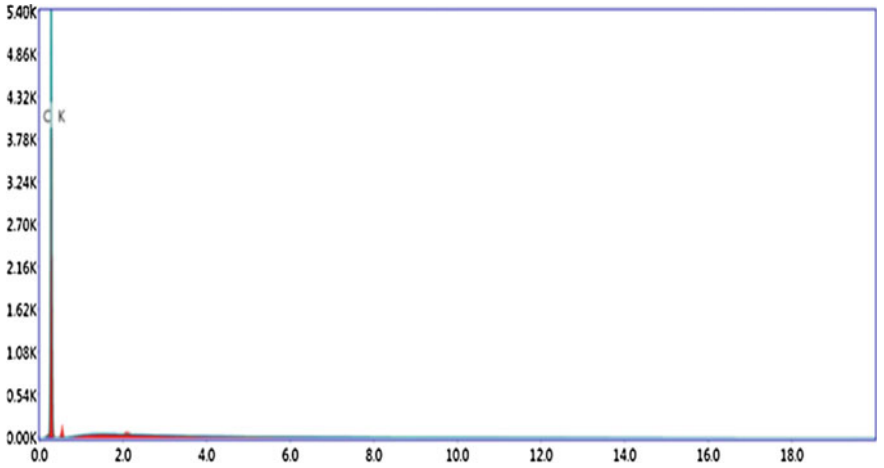

Fig. 4 EDS analysis of graphene nanoballs

4 Conclusions

We have successfully synthesized Graphene nanoballs and studied the effect of annealing at different temperatures (200 °C and 300 °C). XRD and Raman results were found in agreement with each other. The average crystalline size, dislocation density, interplaner distance and strain were calculated from the XRD data. The significant decrease of the crystalline size of graphene nanoballs is responsible for the shifting in Raman Spectrum. Our studies suggest that higher annealing temperature leads to less crystalline nature of the sample with more number of defects. Hence Crystallinity of nanoparticles reduces. Also, it can be seen from SEM that clusters of nanoparticles of uniform shape and size are obtained, and increase in temperature improves their distribution. EDS analysis confirms the absence of metal catalysts.

References

1. K. Geim, K.S. Novoselov, Nat. Mater. **6**, 183–191 (2007)
2. A.A. Balandin, Nat. Mater. **10**, 569–581 (2011)
3. K.S. Novoselov, A.K. Geim, S.V. Morozov, D. Jiang, Y. Zhang, S.V. Dubonos, I.V. Grigorieva, A.A. Firsov, Science **306**, 666–669 (2004)
4. S. Niyogi, E. Bekyarova, M.E. Itikis, J.L. McWilliams, M.A. Hammon, R.C. Haddon, J. Am. Chem. Soc. **128**, 7720 (2006)
5. S. Stankovich, R.D. Piner, X. Chen, N. Wu, S.T. Nguyen, R.S. Ruoff, J. Mater. Chem. **16**, 155 (2006)
6. B.D. Cullity, *Elements of X-ray diffraction*, 2nd edn. (Addission-Wesley Publishing Company, New York, 1978)
7. F. Tuinstra, J.L. Koenig, J. Chem. Phys. **53**, 1126 (1970)
8. A.C. Ferrari, J. Robertson, Phys. Rev. B **61**, 14095 (2000)
9. J. Xie, P.S. James, Agilent Technologies, 5991-0782 (2012)

Synthesis of $NaNbO_3$ Nanorods as a Photoanode Material for Photoelectrochemical Water Splitting

Dheeraj Kumar and Neeraj Khare

Abstract In the present work, $NaNbO_3$ nanorods have been synthesized by a hydrothermal method. XRD results confirm the single phase formation of $NaNbO_3$. TEM study reveals rod like structure of $NaNbO_3$. Photoelectrochemical measurements show enhanced current density under light irradiation which demonstrate the potentiality of $NaNbO_3$ nanostructures for water splitting applications.

1 Introduction

Since the discovery of the first water splitting system in 1972 by Fujishima and Honda, TiO_2 has become the most widely studied photocatalyst material for water splitting applications [1]. However, the major drawback using TiO_2 is the faster recombination rate of the photo-generated electron-hole pairs which limits its practical applications as a photoelectrode for hydrogen production. Thus, currently there is a lot of research interest focuses in the search of alternative materials to TiO_2 and many metal oxide semiconductor materials such as $BaTiO_3$, $SrTiO_3$, ZnO, Ta_2O_5 and CdS have been used as photoelectrodes [2–6].

In this paper, we have synthesized $NaNbO_3$ in the rod like structure and demonstrated its photoelectrochemical activity. The photoelectrochemical results confirm the potentiality of $NaNbO_3$ as a suitable photoanode material for photoelectrochemical water splitting applications.

D. Kumar (✉) · N. Khare
Physics Department, Indian Institute of Technology Delhi,
Hauz khas, New Delhi 110016, India
e-mail: dheeraj24kumar@gmail.com

V.K. Jain et al. (eds.), *Recent Trends in Materials and Devices*,
Springer Proceedings in Physics 178, DOI 10.1007/978-3-319-29096-6_13

2 Experimental Details

For the synthesis of $NaNbO_3$, 30 mM of Nb_2O_5 was dispersed in 80 mL of deionized water, followed by an addition of 3 M of NaOH solution. The resulting solution was allowed to stir at room temperature for 2 h. The mixture was then transferred to a 100 mL Teflon-lined stainless steel autoclave and was put into an oven at 150 °C for 48 h. After the heat treatment, the autoclave was allowed to cool at room temperature naturally. The resulting products were collected by centrifugation, washed several times with deionised water and finally dried at 70 °C for 4 h.

3 Results and Discussion

X-ray diffraction measurement was performed using a Rigaku, Ultima-IV diffractometer equipped with Ni filtered Cu Kα radiation (λ = 1.5418 Å) in the 2θ range of 20–70° at a scanning rate of 4°/min. Figure 1 shows XRD pattern of the $NaNbO_3$ nanorods. All the diffraction peaks correspond to single phase formation of the orthorhombic phase of $NaNbO_3$ (JCPDS card no. 895173). The crystallite size is calculated from the most intense peak using the Scherrer's Equation and is found to be 18 nm. Inset of Fig. 1 shows TEM picture of $NaNbO_3$ which clearly reveals nanorod like structure.

Figure 2 shows the linear sweep voltammograms of $NaNbO_3$ nanorods under dark and under light irradiation of intensity 100 mW/cm^2. The nanorods are found to exhibit current density of ∼11 mA/cm^2 at 1.8 V under light irradiation which is ∼2-fold higher as compared to its dark counterpart.

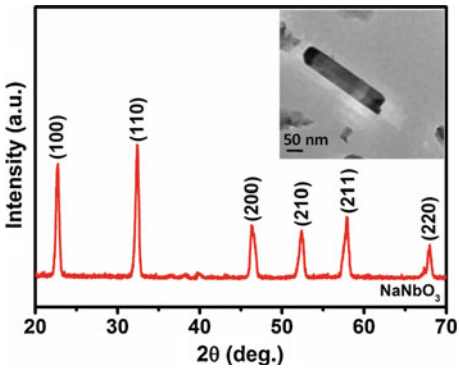

Fig. 1 X-ray diffraction pattern of $NaNbO_3$ nanostructure, Inset of figure shows TEM image of $NaNbO_3$

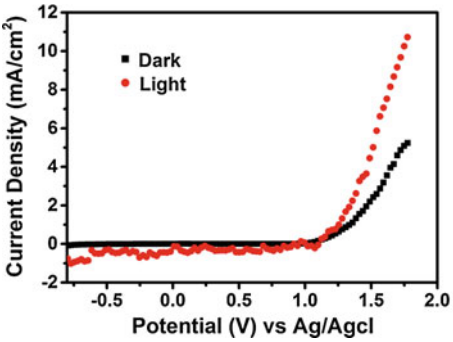

Fig. 2 Linear sweep voltammograms of $NaNbO_3$ nanorods in dark and light

4 Conclusions

In conclusion, $NaNbO_3$ nanorods have been synthesized by a simple hydrothermal method. XRD and TEM results confirm the formation of single phase with a rod like structure of the $NaNbO_3$. Photoelectrochemical measurements show enhanced photoresponse of $NaNbO_3$ nanorods.

References

1. A. Fujishima, K. Honda, Nature **238**, 37 (1972)
2. S. Upadhyay, J. Shrivastava, A. Solanki, S. Choudhary, V. Sharma, P. Kumar, N. Singh, V.R. Satsangi, R. Shrivastav, U.V. Waghmare, S. Dass, J. Phys. Chem. C **115**, 24373 (2011)
3. D. Sharma, S. Upadhyay, V.R. Satsangi, R. Shrivastav, U.V. Waghmare, S. Dass, J. Phys. Chem. C **118**, 25320 (2014)
4. J. Shi, M.B. Starr, H. Xiang, Y. Hara, M.A. Anderson, J.H. Seo, Z. Ma, X. Wang, NanoLett. **11**, 5587 (2011)
5. C. Li, T. Wang, Z. Luo, D. Zhang, J. Gong, Chem. Commun. **51**, 7290 (2015)
6. S. Singh, N. Khare, RSC Adv. (2015). doi:10.1039/C5RA14889H

Effect of Dopant Concentration on Structural and Optical Properties of Cu Doped SnO_2

Gurwinder Pal Singh, Navneet Kaur, Abhinav, Sacheen Kumar and Dinesh Kumar

Abstract Now a day, nanomaterial plays important role in every field due to their unique properties which are completely different from the bulk materials. Material Properties are dynamically changed with reduction in the crystallite size. Transparent conducting oxides (TCOs) are optically transparent to visible light, but electronically conductive. Owing to these properties, they have broad industrial applications such as optoelectronic devices and photovoltaics. Doped Tin Oxide is an oxygen deficient material which could be beneficial for transparent conducting oxide. The SnO_2 was doped with Cu as a dopant element at different concentration. Mede-A software for material design was used to obtain the theoretical data which is to be compared with the practical results. Co-precipitation method was used to prepare Cu-doped SnO_2. Studies on structural properties of undoped and doped SnO_2 were done by X-ray diffraction. The XRD results have shown that the size of the nanoparticles decreases down to 51 nm with increase in dopant concentration. Optical Properties were studied by UV-visible spectroscopy. Band gap was found to decreases down to 2.25 eV with increase of dopant content in samples.

1 Introduction

In the recent time nanoparticle plays important role in every field, due to their unique mechanical, chemical and electrical properties which are completely different from the bulk material. Semiconductor materials are widely used in electronic devices but in the field of optoelectronic these materials have some limitations. To overcome these limitations metal oxides are used. Transparent conducting oxides (TCOs) are electronically conductive and optically transparent to visible light. Due to these properties, they are extensively used in industrial applications such as optoelectronic devices and photovoltaics [1]. Transparent conductive oxide thin

G.P. Singh · N. Kaur · Abhinav · S. Kumar (✉) · D. Kumar
Department of Electronic Science, Kurukshetra University,
Kurukshetra, Haryana 136119, India
e-mail: sacheen3@gmail.com

V.K. Jain et al. (eds.), *Recent Trends in Materials and Devices*,
Springer Proceedings in Physics 178, DOI 10.1007/978-3-319-29096-6_14

film of ITO, SnO_2 and ZnO are widely used in the field of optoelectronic such as transparent electrode in touch panel, flat panel displays and OLED (Organic light emitting diode). Successful performance of these applications depends on a combination of good transparency and low resistivity of TCOs, mostly achieved by controlling chemical compositions of wide band-gap semiconducting materials with various doping agents [2]. Now a days ITO is most widely used material for TCO. SnO_2 is used in gas sensor, solar cell, display devices and other optoelectronic application. Indium is replaced by low cost and easily available material such as Cu. The electrical conductivity of SnO_2 is increased with introducing the foreign doping element [3]. SnO_2 has a rutile crystal structure in which Sn atoms are present at each corner and are surrounded by oxygen atoms. Doping can cause the impurity atoms to either replace Tin atoms or occupy the void space. The SnO_2 nanoparticle are prepared by using different method such as CVD, sol-gel, co-precipitation and thermal evaporation method [4]. Among the different methods for the doped and un-doped SnO_2 (multi-component TCO) production the co-precipitation method is the most useful method for mass production [5]. In the present work we have investigated the optical and structural properties of Cu doped SnO_2 and results are compared with the theoretical data obtained from the material design software Mede-A. For SnO_2 structural conformation and particle size calculation X-ray diffraction (XRD) is used. Doping of Cu in SnO_2 at different concentration is done to analyze the changes in band gap, conductivity and optical transmittance.

2 Experimental Details

Modelling

VASP 5.3 module of Mede-A was used to observe the structural and optical properties of undoped and doped SnO_2.

Figure 1 represent the designed model of undoped SnO_2 by material design software Mede-A in which there are 2 atoms of Sn are present and 4 atoms of oxygen are there and Fig. 2. Represent the designed model of Cu-doped SnO_2 using Mede-A in which 1 Cu atom is present, 15 Sn atoms and 32 atoms of oxygen are present.

Materials Used

The material used to synthesize Undoped and doped SnO_2 nanoparticles are Stannous Chloride Dihydrates ($SnCl_2.2H_2O$), Sodium Hydroxide (NaOH) and Cupric Chloride Dihydrate ($CuCl_2.2H_2O$). $SnCl_2.2H_2O$ was used as precursor to synthesized SnO_2 nanoparticles and NaOH was used as reducing agent. The $CuCl_2.2H_2O$ and $FeCl_3$ are the dopant materials. All the chemicals were used of Loba Chemie with high purity.

Synthesis Procedure

See Fig. 3.

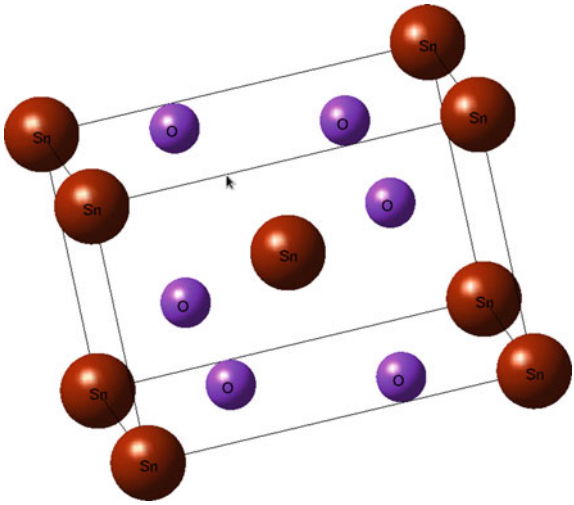

Fig. 1 Undoped SnO_2 model by Mede-A

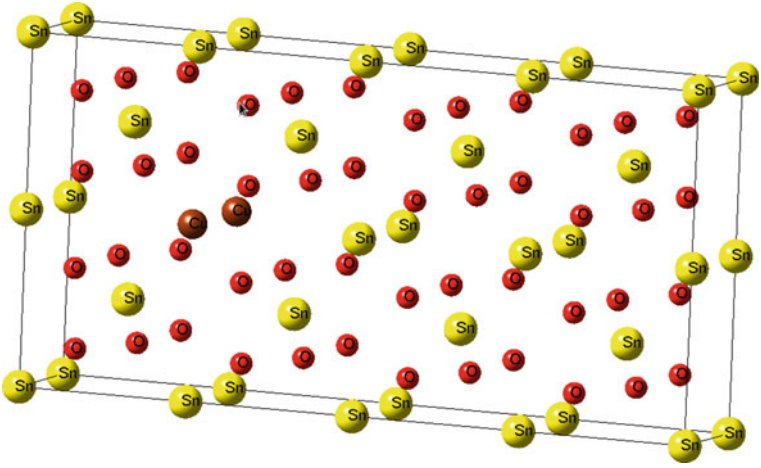

Fig. 2 Cu-doped SnO_2 model by Mede-A

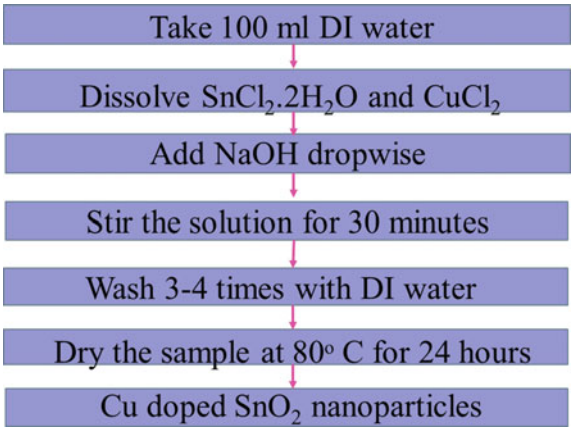

Fig. 3 Flowchart of synthesis procedure

3 Results and Discussion

Structural Properties

Structural properties are determined by the XRD pattern of all the prepared SnO_2 nanoparticles. XRD Results obtained from Mede-A are compared with the practical data of sample.

Scherrer formula is used to calculate the crystallite size using the following equation,

$$d = 0.91\lambda/\beta \cos \theta$$

where d is the crystallite size, λ is the wavelength of X-ray used, and θ is the Bragg angle of diffraction peaks. Figure 4 shows the XRD patterns of all the samples and Intense diffraction peaks of the SnO_2 were observed at 29.82°, 33.705°, 45.454° and 56.474° which were indexed to the (110), (101), (200) and (220) planes, respectively, up to 10 % of Cu doping. It is evident from XRD patterns that SnO_2 has rutile type structure with Sn at octahedral site and O at tetragonal site. The results show that as doping increases the crystalline size decreases.

Optical Properties

The reflection spectra in the UV-VIS range of SnO_2: Cu nanoparticles with 6 % Cu concentrations are presented in Fig. 5 The optical band gap (E_g) for Cu-doped SnO_2 nanoparticles can be determined by extrapolation from the absorption edge which is given by the following equation:

$$(\alpha h\nu)^2 = A\left(h\nu - E_g\right)$$

where A is a constant and hν is the photon energy. Cu doped SnO_2 powders showed optical band gap decrease from 3.17 down to 2.25 eV when the Cu concentration increased up to 10 %. This result was compared with the Mede-A results as shown in Fig. 6.

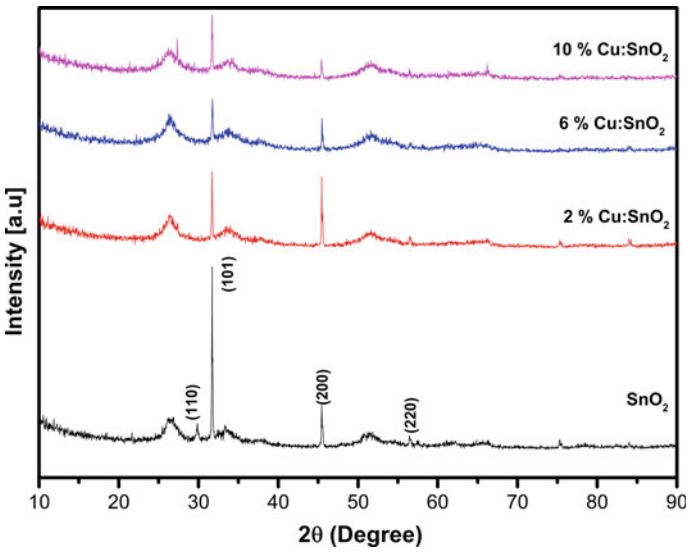

Fig. 4 XRD spectra of undoped SnO_2 and Cu-doped SnO_2

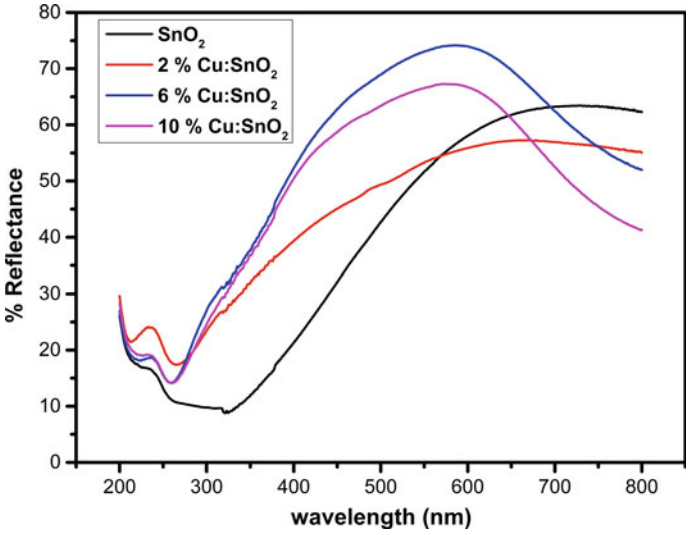

Fig. 5 UV-Vis spectra of undoped and Cu doped-SnO_2 nanoparticles

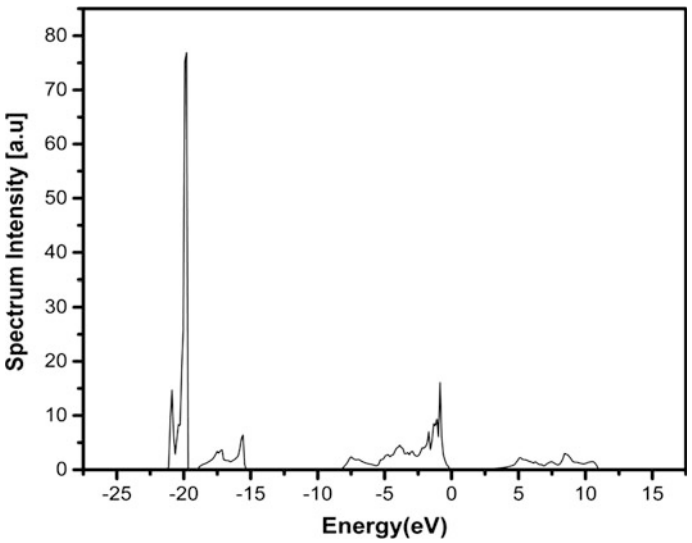

Fig. 6 Shows the calculated density of states of pure SnO_2 by material design software Mede-A

The density of states (DOS) of a system describes the number of states per interval of energy at each energy level that are available to be occupied. Unlike isolated systems, like atoms or molecules in gas phase, the density distributions are not discrete like a spectral density but continuous. A high DOS at a specific energy level means that there are many states available for occupation. A DOS of zero means that no states can be occupied at that energy level. In general, a DOS is an average over the space and time domains occupied by the system. The graph is plotted between the intensity and energy.

Table 1 shows the Bandgap and crystal size of the pure SnO_2 and Cu doped SnO_2. The Cu is doped in SnO_2 at different concentration. When the doping concentration of Cu is increased the crystal size is decrease from 90 to 51.46 nm. As well as with decreasing the crystal size the bandgap is also reduced from 3.17 to 2.25 eV. At lower doping concentration (2 %) of Cu there was an unexpected increment in the band gap from 3.17 to 4.49 eV. But when the doping concentration of Cu is increased from 2 to 6 and 10 % the band gap is decreased to 2.25 eV that is lower than pure SnO_2. It means with increasing the concentration of Cu in SnO_2 the conductivity is increased due to decreasing the Bandgap.

Table 1 Shows the crystal size and bandgap of pure SnO_2 and Cu doped SnO_2

Material	Bandgap (eV)	Crystallite size (nm)
Undoped SnO_2	3.17	90
SnO_2: Cu 2 %	4.49	75.83
SnO_2: Cu 6 %	2.34	66.49
SnO_2: Cu 10 %	2.25	51.46

4 Conclusions

In this study, Cu-doped SnO_2 nanoparticles were prepared by co-precipitation method. From UV-Vis spectroscopy it is found that the band gap of Cu doped SnO_2 shows a decrease from 3.17 to 2.25 eV with the Cu concentration increase up to 10 %. The XRD analysis revealed that the crystallites have the expected SnO_2 tetragonal phase and crystallite size reduces with Cu doping up to 10 mol% down to 51 nm.

References

1. A. Bouaine et al., Structural, optical, and magnetic properties of Co-doped SnO_2 powders synthesized by the co-precipitation technique. J. Phys. Chem. C **111**(7), 2924–2928 (2007)
2. S. Sohn, H.-M. Kim, Transparent conductive oxide (TCO) films for organic light emissive devices (OLEDs), organic light emitting diode—material, process and devices (2011)
3. J. Ni, Y. Xiong, Preparation and characterization of transparent conductive zinc doped tin oxide thin films prepared by radio-frequency magnetron sputtering. J. Wuhan Univ. Technol.-Mater Sci. Ed. **26**(3), 388–392 (2011)
4. H. Kim, R.C.Y. Auyeung, A. Piqué, Transparent conducting F-doped SnO_2 thin films grown by pulsed laser deposition. Thin Solid Films **516**(15), 5052–5056 (2008)
5. G.E. Patil et al., Preparation and characterization of SnO_2 nanoparticles by hydrothermal route. Int. Nano Lett. **2**(1), 1–5 (2012)

Synthesis of Graphene by Low Pressure Chemical Vapor Deposition (LPCVD) Method

Sunny Khan, Javid Ali, Harsh, M. Husain and M. Zulfequar

Abstract Graphene, the wonder material, is a one atom thick two dimensional crystal lattice having a honeycomb like structure. Its peculiar electrical, mechanical and optical properties have attracted the attention of the researchers like never before. Graphene film with two dimensional structure were successfully prepared via a physical method on Ni coated Si wafer using low pressure chemical vapor (LPCVD) method at temperature as low as 650 °C. For this growth acetylene was used as source gas and the hydrogen as the carrier gas in ratio of 1:20. The as-grown graphene was characterized using Scanning Electron Microscopy, Fourier transformation infra-red (FTIR) and Raman Spectroscopy. The SEM, FTIR and Raman spectroscopy confirmed the successful growth of multilayer graphene.

1 Introduction

Graphene is a one-atom thick two dimensional crystal lattice in which sp^2 hybridised C-atoms are arranged in the form of a honey-comb lattice [1–4]. It is often termed as the wonder material of 21st century, reason being it's outstanding physical, chemical, mechanical and electronic properties [1, 5]. Worth mentioning properties of graphene include large theoretical surface area (2600 $m^2\ g^{-1}$) [6], high value of Young's modulus (1060 GPa), excellent thermal conductivity (3000 $Wm^{-1}\ s^{-1}$) and fascinatingly high electron mobility (15,000 $cm^2\ v^{-1}\ s^{-1}$) at room temperature [7]. The single graphene layer is also called as semi-metal or zero band gap semi-conductors. A very high aspect ratio of graphene makes it ideal material for sensing applications. Thus graphene has great potential to be used as a

S. Khan · J. Ali · M. Husain · M. Zulfequar (✉)
Department of Physics, Jamia Millia Islamia, New Delhi, India
e-mail: mzulfe@rediffmail.com

Harsh
Centre for Nanoscience and Nanotechnology, Jamia Millia Islamia, New Delhi, India

M. Husain
M.J.P. Rohilkhand University, Bareilly, Uttar Pradesh, India

V.K. Jain et al. (eds.), *Recent Trends in Materials and Devices*,
Springer Proceedings in Physics 178, DOI 10.1007/978-3-319-29096-6_15

very effective engineering material like in ultrasensitive gas sensors [8], transparent electrodes in liquid crystal display devices [9], as electrodes in Li batteries [10] etc.

There are several techniques available to synthesize graphene which include chemical cleavage from graphite, epitaxial growth, chemical routes like Hummer's and Offemann method and chemical vapour deposition (CVD). The bulk production is possible through CVD method [11, 12]. The CVD by definition means deposition of thin films from a gaseous precursor on a heated substrate by means of thermal decomposition of the precursor on it. To assist the growth of graphene a thin layer of certain transition metal catalysts like Cu and Ni is deposited over the substrate. Here we have deposited Ni as a catalyst with the help of RF sputtering system. The acetylene has been used as source gas and Si as the substrate. The growth process involves the decomposition of source gas, dissolution of the carbon atoms into the Ni film and surface precipitation on cooling leading to formation of graphene layers [13, 14]. There are several types of CVD techniques for graphene growth like Atmospheric Pressure Chemical Vapor Deposition (APCVD), Low Pressure Chemical Vapor Deposition(LPCVD) and Plasma Enhanced Chemical Vapor Deposition (PECVD). In this work we have employed LPCVD method for graphene synthesis. The speciality of this method is that it operates at low pressure of order of few torr because of which the velocity of mass transport of the source gas gets reduced which makes the substrate more exposed to the gas leading to better and homogeneous deposition. The as grown sample was characterised by scanning electron microscopy (SEM), Raman spectroscopy and Fourier transform infrared spectroscopy (FTIR) which confirmed that the as grown sample was essentially the graphene.

2 Experimental Details

First of all, the Si substrate was ultra sonicated for 10 min in order to get rid of superficial impurities. We used Ni as the catalytic support for graphene growth. For this purpose 200 nm thin Ni film was deposited over the cleaned Si substrate with the help of RF sputtering system. The system used for Ni film deposition was Planar Magnetron RF Sputtering Unit (Model: 12" MSPT). After the deposition of catalyst over Si wafer, it was taken to the quartz tube which was evacuated to 10^{-3} Torr for LPCVD process. The system is connected with the precursor and carrier gas through MFCs. The Ni coated Si wafer was first heated to the required growth temperature i.e., 650 °C and annealed for 10 min. Afterwards, H_2 was flown, with 100 sccm flow rate, into the tube for 10 min in order to reduce the catalyst size and remove other impurities like oxygen. The subsequent 10 min, a mixture of C_2H_2 and H_2 was allowed into the tube. The flow rates of C_2H_2 and H_2 were kept at 15 and 300 sccm respectively. The growth was done at 650 °C for 10 min. The as grown sample has been characterised by scanning electron microscopy, Raman spectroscopy and fourier transform infrared spectroscopy and the growth of graphene is confirmed.

3 Results and Discussion

3.1 Scanning Electron Microscopy

The morphology of the as grown sample was studied by SEM (Model: Σigma by Carl Zeiss) employed with Gemini column (patented technology of Carl Zeiss) which enables inlens secondary electron detection. The SEM micrographs clearly show that there is a dense growth of graphene layers on the substrate. The layers are in ruffle like pattern as the graphene layers have a tendency of getting rolled up at the edges (Fig. 1).

3.2 Raman Spectroscopy

Raman spectroscopy was performed on the as grown sample to confirm the growth of graphene layers. The sample was irradiated with a wavelength of 488 nm. The Raman spectrum was recorded by employing a spectroscopic system consisting of a double monochromator (SPEX 1404), photomultiplier tube (9214B) as detector, an amplifier-discriminator assembly, notch filter and a photon counting arrangement.

Figure 2 shows the Raman spectrum of as synthesized graphene. The peak at 1320 cm^{-1} corresponds to D-band which tells about the level defects in the crystalline structure of graphene layers. The Stokes phonon energy shift caused by laser excitation creates two main peaks in the Raman spectrum. One is, G peak at 1580 cm^{-1} which is a primary in-plane vibrational mode and G′ peak at 2881 cm^{-1}, a second order overtone of a different in-plane vibration D (1320 cm^{-1}) [15]. From the comparison of G and G′ peak intensities we can speculate about the number of graphene layers. Since in our work the ratio between the G′ and G peak intensities is less then one, the as grown graphene is essentially multilayer graphene. The reduced intensity of G′ peak vis-à-vis G peak indicates the graphene so synthesized is multi-layered [16–18].

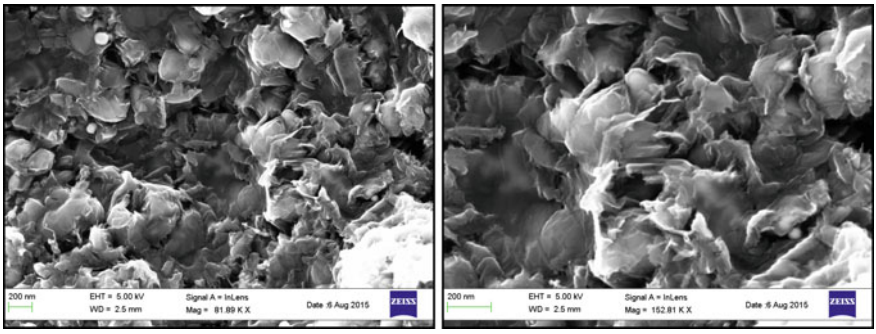

Fig. 1 SEM micrograph of the as grown sample

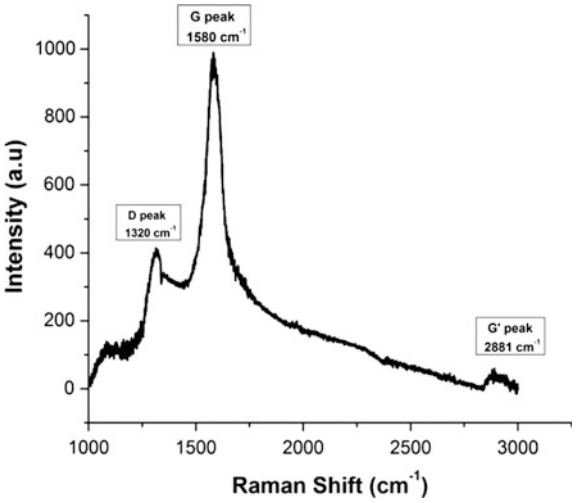

Fig. 2 Raman spectrum of the as grown sample

3.3 Fourier Transform Infrared Spectroscopy (FTIR)

We performed FTIR on the as grown sample to ascertain the nature of the sample. As it could be seen in the Fig. 3 there are two prominent stretching modes that we get at 1608 and 3188 cm^{-1}. Both these modes are indicative of aromaticity which forms the basic backbone of the graphene structure. Moreover, we don't observe any stretching due to the presence of any oxygen functionality which affirms us that there is no oxygen in between the graphene layers.

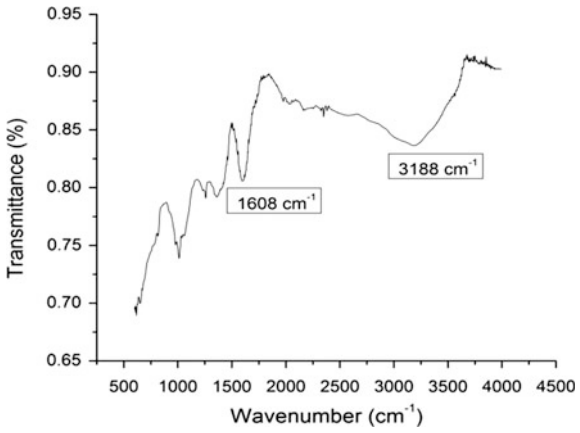

Fig. 3 FTIR spectrum showing aromatic character of the as grown sample

4 Conclusion

This paper presents a simple and effective method to deposit multi-layer graphene using Low Pressure Chemical Vapor Deposition system using acetylene as source gas and hydrogen as carrier. The Ni coated Si has been used as the substrate. The use of acetylene aided the growth of graphene at a lower temperature of 650 °C. The characterisations namely SEM, Raman spectroscopy and FTIR confirmed that the as grown samples were essentially multi layered graphene.

Acknowledgments One of the authors (Sunny Khan) is thankful to UGC for providing financial assistance in the form of SRF under Maulana Azad National Fellowship for Minority Students.

References

1. K.S. Novoselov, A.K. Geim, S.V. Morozov, D. Jiang, Y. Zhang, S.V. Dubonos, I.V. Grigorieva, A.A. Firsov, Science **306**, 666 (2004)
2. Y. Zhang, J.W. Tan, H.L. Stormer, P. Kim, Nature **438**, 201 (2005)
3. A.K. Geim, K.S. Novoselov, Nat. Mater. **6**, 183 (2007)
4. X. Li, X. Wang, L. Zhang, S. Lee, H. Dai, Science **319**, 1229 (2008)
5. A.K. Geim, K.S. Novoselov, Nat. Mater. **6**, 183–191 (2007)
6. H.K. Chae, D.Y. Siberio-Pérez, J. Kim, Nature **427**(6974), 523–527 (2004)
7. L.S. Schadler, S.C. Giannaris, P.M. Ajayan, Appl. Phys. Lett. **73**(26), 3842–3844 (1998)
8. F. Schedin, A.K. Geim, S.V. Morozov, E.W. Hill, P. Blake, M.I. Katsnelson, K.S. Novoselov, Nat. Mat. **6**, 662 (2007)
9. P. Blake, Nano Lett. **8**, 1704 (2008)
10. E. Yoo, J. Kim, E. Hosono, H. Zhou, T. Kudo, I. Honma, Nano Lett. **8**, 2277 (2008)
11. K.S. Kim, Y. Zhao, H. Jang et al., Nature **457**(7230), 706–710 (2009)
12. A. Reina, X.T. Jia, J. Ho et al., Nano Lett. **9**(1), 30–35 (2009)
13. Q.J. Yu, S. Lian, S. Siriponglert, H. Li, Y.P. Chen, S. Pei, Appl. Phys. Lett. **93**, 113103 (2008)
14. K.S. Kim, Y. Zhao, H. Jang, S.Y. Lee, J.M. Kim, K.S. Kim, J.H. Ahn, P. Kim, J.Y. Choi, B. H. Hong, Nature **457**, 706–710 (2009)
15. R. Saito, M. Hofmann, G. Dresselhaus, A. Jorio, M.S. Dresselhaus, Adv. Phys. **30**, 413–550 (2011)
16. A.C. Ferrari, J.C. Meyer, V. Scardaci, C. Casiraghi, M. Lazzeri, F. Mauri, S. Piscanec, D. Jiang, K.S. Novoselov, S. Roth, A.K. Geim, Phys. Rev. B **97**, 187401 (2006)
17. D. Graf, F. Molitor, K. Ensslin, C. Stampfer, A. Jungen, C. Hierold, L. Wirtz, Nano Lett. **7**, 238 (2007)
18. A. Gupta, G. Chen, P. Joshi, S. Tadigadapa, P.C. Eklund, Nano Lett. **6**, 2667 (2006)

Controlling the Morphology of ZnO Nanostructures During Growth Process

Khyati Gautam, Inderpreet Singh, P.K. Bhatnagar and Koteswara Rao Peta

Abstract In the present work, Zinc Oxide (ZnO) nanorods and nanotubes were fabricated in single synthesis step by hydrothermal method over ITO/glass. We have studied the growth mechanism behind the formation of ZnO nanotubes from nanorods. Finally, a control over the morphology of ZnO nanostructures during the growth process has been achieved. The as-synthesized nanorods and nanotubes were structurally characterized by field emission scanning electron microscopy (FESEM) and X-ray diffraction (XRD). Structural characterization confirms the formation of dense arrays of ZnO nanorods and nanotubes with a hexagonal crystal structure.

1 Introduction

Zinc Oxide (ZnO) with its unique properties such as wide band gap (3.37 eV) and high exciton binding energy (60 meV) has been drawing the attention of the researchers over the decades. It is amongst the few materials which offer a variety of nanostructures such as nanorods, nanotubes, nanorings etc. with potential application in solar cells [1], light emitting diodes [2] and sensors [3]. ZnO nanotubes are of particular interest because of their enhanced surface to volume ratio as compared to ZnO nanorods and nanowires, which makes them an excellent candidate for sensors and solar cell application.

ZnO nanostructure can be synthesized by a variety of methods such as catalyst assisted vapor-liquid-solid (VLS) [4], pulsed laser deposition (PLD) [5], chemical vapor deposition (CVD) [6] and hydrothermal method [7]. Owing to its simplicity, bio-compatibility and capability for large scale production, the hydrothermal

K. Gautam (✉) · P.K. Bhatnagar · K.R. Peta
Department of Electronic Science, University of Delhi South Campus, Benito Juarez Road, New Delhi 110021, India
e-mail: khyati34@gmail.com

I. Singh
Department of Electronics, SGTB Khalsa College, University of Delhi, New Delhi 110007, India

V.K. Jain et al. (eds.), *Recent Trends in Materials and Devices*,
Springer Proceedings in Physics 178, DOI 10.1007/978-3-319-29096-6_16

method has become popular among researchers in the last few decades. Growth parameters such as growth duration, temperature, concentration of precursors, pH, and chemical additives are found to affect the morphology of ZnO nanostructures grown by this technique [8, 9]. Some research groups have been focusing towards explaining the formation of ZnO nanotubes in view of variations of these parameters. Chae et al. [10] have reported that pH value of reaction solution greatly influences the morphology of the ZnO nanostructures. Tong et al. [11] have shown that with the decrease in precursor concentration with longer growth duration, tubular morphology of ZnO was obtained.

In the present work, we report the formation of ZnO nanotubes from nanorods by the facile hydrothermal method on ITO substrate. By merely allowing the reaction chamber to cool naturally to room temperature we were able to obtain well faceted hexagonal ZnO nanotubes. We propose the possible mechanism leading to the formation of these tubular morphology.

2 Experimental Details

All the chemicals, including zinc acetate dihydrate, zinc nitrate hexahydrate and hexamethylenetetramaine were commercially procured. For the synthesis of ZnO nanorods, first ZnO seeds were grown over the ITO/glass substrate by thermal decomposition of zinc acetate dehydrate at 350 °C. A solution of 0.005 M zinc acetate dihydrate in ethanol was prepared and homogenized by ultrasonication for $\sim$1 h. The solution was then drop cast on ITO substrate and annealed at 350 °C for 20 min in a muffle furnace. Two samples A and B covered with a layer of ZnO seeds were obtained following this procedure. ZnO nanorods were synthesized over these seed layer by using the Hydrothermal method. For this an equimolar precursor solution of 0.025 M zinc nitrate hexahydrate and hexamethylenetetramine in DI water was prepared by ultrasonication for $\sim$1 h. The seed layer coated substrates were finally immersed in the solution which was kept at 90 °C for 4 h in an oven. After that, sample A was taken out from the solution while the sample B was left in the solution for overnight to cool down naturally to room temperature. The samples were taken out and washed in DI water, followed by drying in air. Subsequently the samples were taken for structural characterization.

The as-grown ZnO nanostructures are structurally characterized by field emission scanning electron microscopy (FESEM) and X-ray diffraction (XRD).

3 Results and Discussion

Figure 1 shows the FESEM images of sample A and B. It can be clearly seen that ZnO nanorods are obtained in sample A which was taken out of the reaction chamber after 4 h (Fig. 1a). However, the gradual cooling of sample B in the

solution lead to formation of nanotubes, as observed in the FESEM images of sample B (Fig. 1b and c). The cross-sectional view of sample B (Fig. 1c) shows the formation of well faceted hexagonal crystal structure. In both the samples, high density of hexagonal nanorods and nanotubes are obtained over the substrate.

The orientations of the as-grown nanostructures are confirmed by XRD analysis. Figure 2 shows the typical XRD spectra of sample A and B. All the diffraction peaks obtained in the diffractogram, correspond to the hexagonal wurtzite structure of ZnO. The nanorods in sample A (Fig. 2a) exhibited no preferred orientation and are found to be randomly oriented along (100), (002) and (101) directions as also observed in the SEM micrographs. On the other hand, the XRD spectra of ZnO nanotubes in sample B (Fig. 2b) exhibit intense peaks along [100] and [101] directions. The diffraction peak corresponding to c-axis orientation, i.e. (002) is found to be absent in the XRD spectra of ZnO nanotubes.

Among the various planes of the hexagonal crystal structure of ZnO, (002) plane has maximum surface energy owing to its polar nature which further leads to its

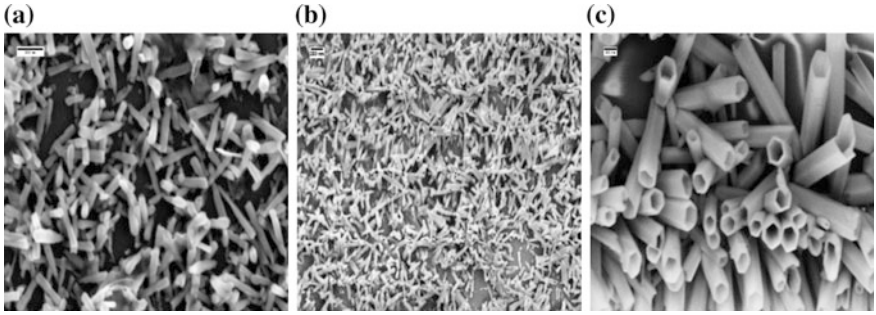

Fig. 1 FESEM images of **a** ZnO nanorods in sample A **b** ZnO nanotubes in sample B **c** cross sectional image of sample B

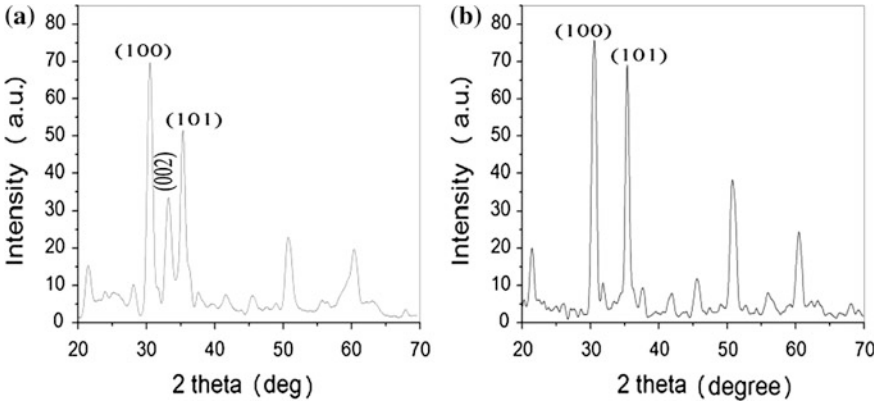

Fig. 2 XRD spectra of **a** sample A **b** sample B

instability [11]. The gradual decrease in the temperature during natural cooling of sample B in the reaction chamber, leads to the dissolution of high surface energy crystal face in order to have stable structure. The absence of the XRD peak corresponding to (002) plane in the XRD spectra of sample B is an evidence of the fact that these tubular structures are the result of dissolution of highly unstable (002) plane of ZnO nanorods which are formed at an earlier stage of the overall process. The depletion of zinc species in the solution with time also aids in this process [11]. The inner core appears to diffuse out from the nanorods over the time and thus hollow the inside of the nanorod. This process which is directed towards lowering of the surface energy of the overall structure, therefore, results in the formation of the tubular structures of ZnO.

4 Conclusions

We were able to successfully synthesize ZnO nanorods and nanotubes by the facile hydrothermal method on ZnO seeds/ITO/glass substrate. Structural characterization confirms the formation of hexagonal nanostructures with high density over the substrate. It was observed that the morphology of the nanostructures was critically affected by the natural cooling of the sample in the solution. This process, leads to the formation of tubular structures of ZnO from nanorods in order to minimize the overall surface energy of the final nanostructure.

Acknowledgments This work is supported by the University of Delhi under the grant Research and Development (2013–2016), and the authors Khyati Gautam and P.K. Bhatnagar wish to thank the University Grant Commission (UGC), India for supporting the junior research fellowship and BSR fellowship respectively.

References

1. A.B.F. Martinson et al., ZnO nanotube based dye-sensitized solar cells. Nano Lett. **7**(8), 2183–2187 (2007)
2. N.H. Alvi et al., Fabrication and comparative optical characterization of n-ZnO nanostructures (nanowalls, nanorods, nanoflowers and nanotubes)/p-GaN white-light-emitting diodes. Scripta Mater. **64**(8), 697–700 (2011)
3. C.S. Rout et al., Hydrogen and ethanol sensors based on ZnO nanorods, nanowires and nanotubes. Chem. Phys. Lett. **418**(4–6), 586–590 (2006)
4. N.H. Alvi et al., Influence of different growth environments on the luminescence properties of ZnO nanorods grown by the vapor–liquid–solid (VLS) method. Mater. Lett. **106**, 158–163 (2013)
5. A.L. Nikolaev et al., Preparation and investigation of ZnO nanorods array based resistive and SAW CO gas sensors, in *Advanced Materials*, ed. by S.-H. Chang, I.A. Parinov, V.Y. Topolov (Springer International Publishing, Berlin, 2014), pp. 27–36

6. S.S. Shariffudin et al., *Hybrid organic-inorganic light emitting diode using ZnO nanorods as electron transport layer,* in *IEEE Regional Symposium on Micro and Nanoelectronics 2013 (RSM)* (2013)
7. L. Vayssieres, Growth of arrayed nanorods and nanowires of ZnO from aqueous solutions. Adv. Mater. **15**(5), 464–466 (2003)
8. W. Zhong Lin, Zinc oxide nanostructures: growth, properties and applications. J. Phys.: Condens. Matter **16**(25), R829 (2004)
9. G. Amin et al., Influence of pH, precursor concentration, growth time, and temperature on the morphology of ZnO nanostructures grown by the hydrothermal method. J. Nanomater. **2011**, 9 (2011)
10. K.-W. Chae et al., Low-temperature solution growth of ZnO nanotube arrays. Beilstein J. Nanotechnol. **1**, 128–134 (2010)
11. Y. Tong et al., Growth of ZnO nanostructures with different morphologies by using hydrothermal technique. J. Phys. Chem. B **110**(41), 20263–20267 (2006)

Synthesis of Lithium Doped Cerium Oxide Nanoparticle by the Co-precipitation Method

Monika Kumari, Mintu Kumar, Amit Kumar, Sacheen Kumar and Dinesh Kumar

Abstract In our work we synthesized pure and doped cerium oxide nanoparticle with diameter range from 4 to 6 nm by the co-precipitation method. Cerium oxide widely used for the fuel cell application due to its high ion transport and large oxygen vacancies. These properties were enhanced by the doping of lithium (alkine metal). Properties of synthesized material characterized by XRD, FTIR and by the UV-absorption technique.

1 Introduction

From few decade cerium oxide has fetching great interest due to its large application in field of chemical-mechanical polishing, oxygen gas sensor, sunscreens for UV absorbent and most widely in solid oxide fuel cell as catalytic electrolyte because of its oxygen storage capacity and chemical reactivity [1]. It is known that nanoscale particles have been specific physical and chemical properties which are significantly different from those of bulk material. Cerium oxide has also showed exceptional properties at nanoscale. Cerium oxide has a cubic fluorite. Cerium oxide was used as electrolyte for the fuel cell application. SOFCs (solid oxide fuel cells) use the solid ceramic material as electrolyte. SOFCs consist of a cathode, anode and the electrolyte material, at one end oxygen is supplied which reduce oxygen ions, these ions form channel through the electrolyte under electrical load to the anode, react with the hydrogen and form water [2]. Electrolyte is the heart of the device. There are some requirement for the electrolyte materials these are high ion conductivity, minimum e-(electron) transportation, and thermodynamic stability, negligible interaction with electrode during the operation and the fabrication. SOFCs normally operate at high temperature but cerium oxide or ceria on the whole is more efficient. Ceria fuel cells operate at 600 °C where others operate at 800–

M. Kumari · M. Kumar · A. Kumar · S. Kumar (✉) · D. Kumar
Department of Electronic Science, Kurukshetra University,
Kurukshetra 136119, Haryana, India
e-mail: sacheen3@gmail.com

V.K. Jain et al. (eds.), *Recent Trends in Materials and Devices*,
Springer Proceedings in Physics 178, DOI 10.1007/978-3-319-29096-6_17

1000 °C [3]. At high temperature, fuel cell components fastly degrade where ceria work at low temperature is major advantage.

Cerium oxide has large oxygen vacancies that allow for greater reactivity and faster ion transport these properties make cerium oxide best material for SOFCs application [4]. With the different doping material enhanced the chemical reactivity and ion transport properties of cerium oxide. In our present work we used lithium as doping material. It increase the ion transport properties of cerium oxide which is very beneficial for fuel cell application. Various method are used to synthesize of doped or undoped cerium oxide e.g. sonochemical synthesis, thermal decomposition, sol-gel, mechanochemical, co-precipitation, combustion and spray pyrolysis [5–7]. In our work Cerium oxide nanoparticles are synthesize by co-precipitation method because of easy to do and low cost apparatus. Synthesized material has characterized by XRD, FTIR and by UV absorption spectroscopy.

2 Experimental

In our work we synthesis pure and doped CeO_2 by the co-precipitation method. In synthesis of lithium doped cerium oxide, cerium nitrate (Ce $(NO_3)_3 \cdot 6H_2O$), Sodium Hydroxide (NaOH) were used as starting material and lithium nitrate Li $(NO_3)_3$ used as doping material. $Ce(NO_3)_3.6H_2O$ (0.01 mol) add with $Li(NO_3)_2 \cdot 6H_2O$ (3, 6, 9 %) dissolved in of DI water and Sodium hydroxide (0.04 mol) dissolved in DI water. Ce $(NO_3)_3 \cdot H_2O$ solution was added drop wise into the solution of sodium hydroxide (NaOH). They are perfectly mixed by a magnetic stirrer apparatus on the 1000 r.p.m at room temperature for two hour. The resultant purple color precipitate was filtered. After then solution washed with DI water for 4–5 time and dried at 70–80 °C for 24 h. then the sample was crushed by the pestle mortar. During drying pure yellow colored doped CeO_2 was formed. Then the calcination was carried out at 300–400 °C for 4–6 h. During the calcination at high temperature crystalline yellow colored doped CeO_2 was formed.

3 Synthesis Procedure

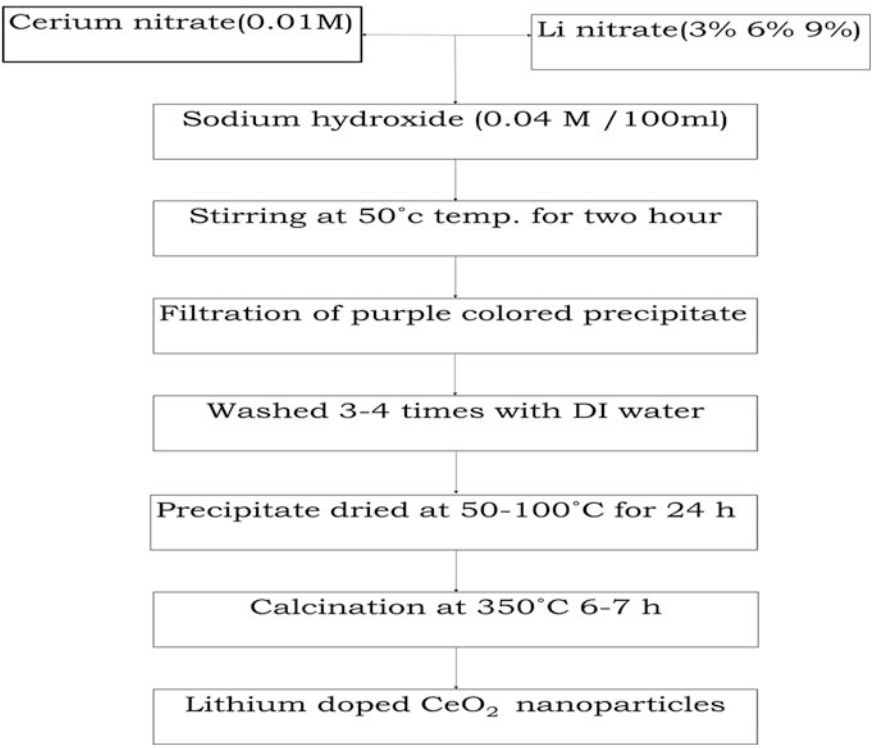

4 Characterization

4.1 X-ray Diffraction

Pure and doped cerium oxide nanoparticle were characterized with the XRD technique diffraction using panalytical Xpert Pro system using Cu as anode with Kα (λ = 1.545 Å). XRD technique was used to determine the crystallinity and particle size of the sample.

4.2 UV-Visible Spectroscopy

UV absorption technique was performed to calculate the optical properties of the nanoparticle. For UV absorption the instrument PERKIN UV-2450 System. Sample were analyzed in range from 200 to 800 nm.

4.3 FTIR Technique

FTIR characterization was performed with system Thermo scientific Nicolet IS10. Samples were analyzed with KBr method FTIR spectra of sample in wave number range from 500 to 4000 cm^{-1}.

5 Result and Discussion

In XRD graph showed the characterized peak are very close to fluorite structure of CeO_2 crystal. The sherror's formula $D = 0.9\lambda/\beta\cos\theta$ was used to calculate the particle size where lambda is wavelength of x-ray and β is (FWHM) full width half maxima. Size was little effected by the doping of Li showed in Fig. 1 pure CeO_2, 9,

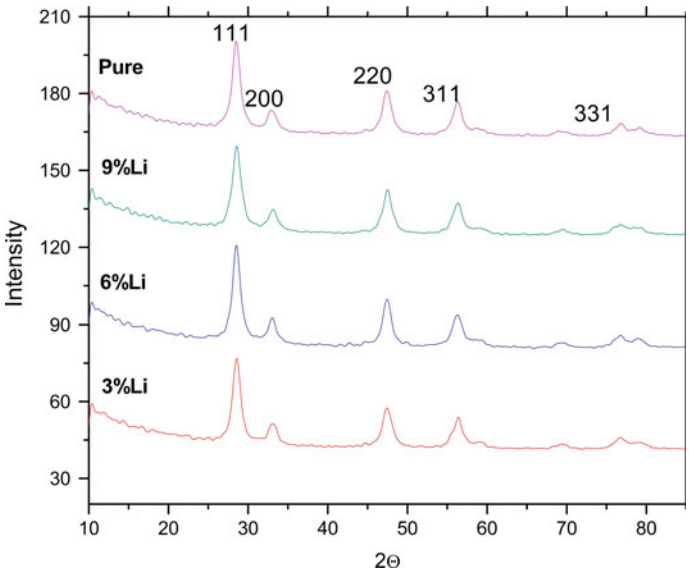

Fig. 1 XRD spectra of doped and undoped CeO_2

6, 3 % of Li peak correspond to the (111), (200), (220), (311) and (331) planes are located at 2θ = 28.5°, 32.8°, 47.2°, 56.3°, and 76.7° respectively.

6 UV-Visible Spectroscopy

Optical properties of pure and doped CeO_2 were determined by UV absorption technique. CeO_2 has strong absorption characteristics in the UV range. The absorption peak of undoped and doped 3, 6, 9 % with lithium showed in Fig. 2. The optical band gap was calculated based on the absorption spectrum of the nanoparticle by using equation.

$$E_{BG} = 1240/\lambda_{absorbEdge}$$

where λ is the absorption edge of the samples. The absorption edge for pure and 3, 6 and 9 % Li-doped cerium oxide nanoparticles are at ~370, 367, 372 and 376 nm, respectively. The corresponding band gap was calculated by UV absorption were found to be 3.08, 2.75, 2.83 and 2.90 eV respectively. Band gap of CeO_2 (3.08 eV) decreased up to (2.75 eV) with lithium. Doping with Li create oxygen vacancies due to formation of Ce^{3+} in CeO_2 increase the more energy state. Formation of large localized energy state that are closer to the conduction band and due to that band gap has decreased.

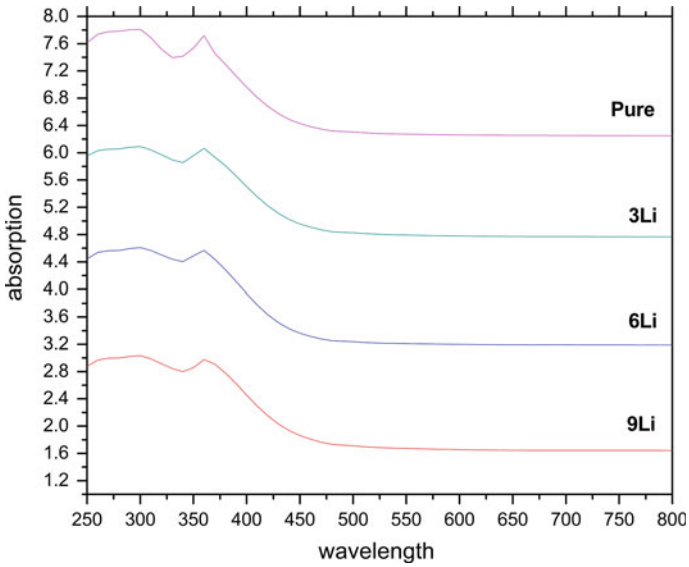

Fig. 2 UV-Vis spectra of pure and Li doped CeO_2

7 FTIR Technique

In the Fig. 3 shows the FTIR spectrum of pure CeO_2 and Li (3, 6, 9 %) doped nanoparticle. IR spectrum range of particle in wave number from 500 to 4000 cm^{-1}. Absorption peak are around the 1372 and the 1600 cm^{-1}. In addition the band due to the stretching frequency of Ce–O can be seen below 700 cm^{-1}. The band centered at 3400–3700 cm^{-1} corresponds to the –OH stretching vibration which is originate from physical absorbed H_2O or surface OH groups. The exhaustive band $\sim$1400 cm^{-1} represent N–O stretches due to presence of nitrate. Vibration mode $\sim$1000 cm^{-1} Li–O presence of lithium (Table 1).

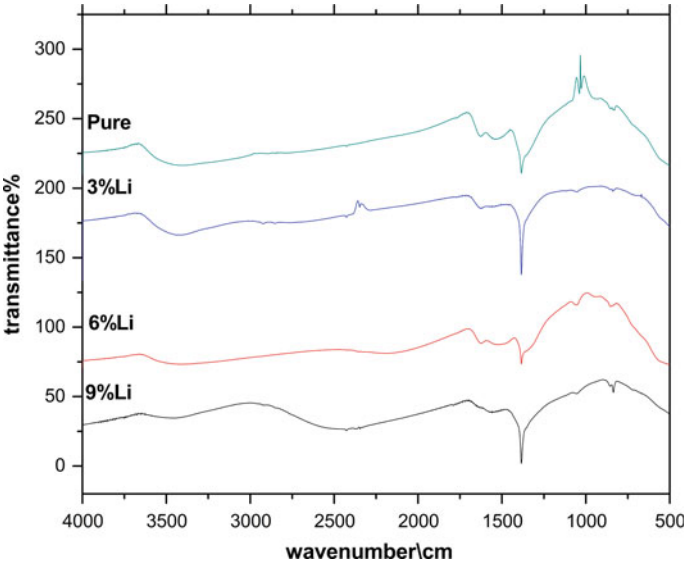

Fig. 3 FTIR spectrum of pure and doped CeO_2

Table 1 Comparison of structural and optical properties of pure and Li doped CeO_2

Sample	Pure CeO_2	3 % Mg doped CeO_2	6 % Mg doped CeO_2	9 % Mg doped CeO_2
Band gap (eV)	3.0817	2.7566	2.8304	2.9024
Crystallite Size (nm)	7.185	4.208	5.458	6.028

8 Conclusion

Doped cerium oxide nanoparticle with 4–7 nm in diameter were effectively synthesized by co-precipitation method. Size of nanoparticle reduces 4.20 nm from 7.18 nm study with XRD technique. Band gap of cerium oxide nanoparticle has reduced thereby increase in energy state of cerium. The structure of nanoparticle is fluorite-type structure in all the sample. Chances of formation of second phase was minimum. More oxygen vacancies create in cerium oxide with doping of lithium as study with UV absorption technique which increase the ion properties of cerium oxide.

Acknowledgments Authors are thankful to DST-Nanomission for providing funding.

References

1. C. Hu et al., Direct synthesis and structure characterization of ultrafine CeO_2 nanoparticles. Nanotechnology **17**(24), 5983 (2006)
2. Neelima Mahato, Alka Gupta, Kantesh Balani, Doped zirconia and ceria-based electrolytes for solid oxide fuel cells: a review. Nanomat. Energy **1**(1), 27–45 (2012)
3. A.E.C. Palmqvist et al., Total oxidation of methane over doped nanophase cerium oxides. Catal. Lett. **56**(1), 69–75 (1998)
4. J.J. Ketzial, A. Samson Nesaraj, Synthesis of CeO_2 nanoparticles by chemical precipitation and the effect of a sur-factant on the distribution of particle sizes. J. Ceram Process Res **12**(1), 74–79 (2011)
5. Q. Rui-Juan, et al., Sonochemical synthesis of single-crystalline $CeOHCO_3$ rods and their thermal conversion to CeO2 rods. Nanotechnology **16**(11), 2502 (2005)
6. W. Yarong, et al., Low-temperature synthesis of praseodymium-doped ceria nanopowders. J. Am. Ceram. Soc. **85**(12), 3105–3107 (2002)
7. A. Hartridge, A.K. Bhattacharya, Preparation and analysis of zirconia doped ceria nanocrystal dispersions. J. Phys. Chem. Solids **63**(3), 441–448 (2002)

Structural, Optical and Magnetic Properties of $Bi_{25}FeO_{40}$ Nanoparticles Synthesized by Hydrothermal Method

Pallavi Kumari and Neeraj Khare

Abstract $Bi_{25}FeO_{40}$ iron sillenite nanoparticles have been synthesized by hydrothermal method using KOH as mineraliser. Structural, optical and magnetic characterization of $Bi_{25}FeO_{40}$ nanoparticles have been carried out. XRD confirms the formation of $Bi_{25}FeO_{40}$ phase and the average crystallite size obtained as $\sim$25 nm. Magnetic characterization showed weak ferromagnetic behaviour at room temperature and optical characterization showed small optical band gap of $Bi_{25}FeO_{40}$ nanoparticles in the visible range of spectra.

1 Introduction

Sillenite materials have a general formula $Bi_{12}MO_{20\pm x}$ (M = Fe, Ni, Al, Pb), where M represents a tetravalent ions occupying tetrahedral sites in body centered cubic crystal structure that belongs to I23 space group. The sillenite materials show structural similarity to γ-Bi_2O_3. Due to piezoelectric, photoconductive, electrooptic, and photorefractive properties [1], sillenite materials have attracted lots of attention in the research field. $Bi_{25}FeO_{40}$ is a type of sillenite materials (iron sillenite) that has structural formula $Bi_{12}(Bi_{0.5}Fe_{0.5})O_{19.5}$ and cell parameter $\sim$1.018 nm [2]. Two different chemical formula $Bi_{25}FeO_{40}$ and $Bi_{25}FeO_{39}$ are given for iron sillenite in literature [3, 5]. In $Bi_{25}FeO_{40}$ structure, Bi^{3+} ions forms a cage of corner-connected BiO_5E-polyhedron, where E denotes inert $6s^2$ electron pair, by occupying octahedral sites, Bi^{5+} and Fe^{3+} ions occupy the tetrahedral sites within the cage [4, 5]. Some studies reported that oxygen vacancies accompany Bi^{3+} at tetrahedral sites [6, 7].

P. Kumari (✉) · N. Khare
Department of Physics, Indian Institute of Technology Delhi, New Delhi 110016, India
e-mail: pallavi02singh@gmail.com

N. Khare
e-mail: nkhare@physics.iitd.ac.in

V.K. Jain et al. (eds.), *Recent Trends in Materials and Devices*,
Springer Proceedings in Physics 178, DOI 10.1007/978-3-319-29096-6_18

$Bi_{25}FeO_{40}$ nanoparticles mainly come as by-product during synthesis of bismuth ferrite ($BiFeO_3$) nanoparticles and also it comes as an intermediate product for the synthesis of $BiFeO_3$ target crystallite during hydrothermal synthesis. The phase change can be controlled by adjusting mineraliser, temperature and duration of hydrothermal reaction. Magnetic properties of $Bi_{25}FeO_{40}$ have been investigated and paramagnetic behaviour was reported at room temperature [8].

In the present study, we report the synthesis of $Bi_{25}FeO_{40}$ nanoparticles by hydrothermal method and its structural, optical and magnetic properties.

2 Experimental

The $Bi_{25}FeO_{40}$ nanoparticles have been synthesized by hydrothermal method. Bismuth nitrate [$Bi(NO_3)_3$] and iron nitrate [$Fe(NO_3)_3$] in appropriate molar ratio were used as starting materials which were dissolved in diluted nitric acid (HNO_3) (10 %) and the mixture was put under stirring. The mineraliser potassium hydroxide (KOH) was slowly added to the resultant solution. Brown colored precipitate formed which was filtered, washed with deionised (DI) water to maintain neutral pH, and dried at 60 °C. Dried precipitate was dissolved in ethanol—water mixture and the solution was filled in Teflon—lined autoclave. The autoclave was put into oven at 120 °C for 16 h. It was then cooled to room temperature and washed with DI water for attaining neutral pH and dried at 80 °C. Resulted nanoparticles were characterized by RIGAKU Ultima IV X-ray diffractometer equipped with CuKα radiation (λ = 1.54 Å) to confirm the $Bi_{25}FeO_{40}$ phase, in addition scanning electron microscopy (SEM) has been done for structural characterization of the synthesized $Bi_{25}FeO_{40}$ nanoparticles. Optical characterization has been carried out using UV-Vis-NIR spectrometer in which barium sulfate ($BaSO_4$) powder was taken as reference and magnetic characterization has been carried out by alternating gradient magnetometer (AGM) at room temperature.

3 Results and Discussion

The X-ray diffraction (XRD) pattern of $Bi_{25}FeO_{40}$ nanoparticles is shown in Fig. 1 which confirms the formation of $Bi_{25}FeO_{40}$ phase. The diffraction peaks are obtained at 2θ = 27.68°, 30.32°, 32.90°, 35.28°, 37.55°, 39.56°, 41.68°, 43.66°, 45.47°, 49.02°, 52.50°, 54.16°, 55.68°, 57.01°, 61.74° and 63.02° which corresponds to (hkl) values (310), (222), (321), (400), (330), (420), (332), (422), (431), (521), (530), (600), (611), (620), (631) and (444) respectively (JCPDS data no.

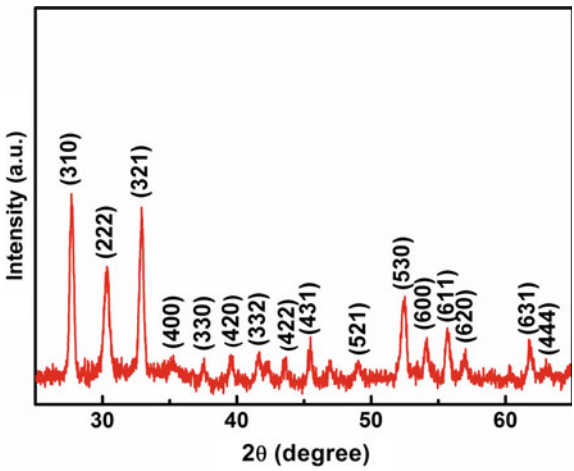

Fig. 1 XRD pattern of $Bi_{25}FeO_{40}$ nanoparticles synthesized by hydrothermal method

46-0416) of $Bi_{25}FeO_{40}$. The average crystallite size of $Bi_{25}FeO_{40}$ nanoparticles was determined by using Scherer's formula [9], which is given as

$$D = \frac{K\lambda}{\beta Cos\theta} \tag{1}$$

where K is Scherer's constant, β is the full width at half maximum (FWHM) of the XRD peak, θ is the Bragg's angle, λ is the wavelength of X-ray (1.54 Å), and "D" is the average crystallite size. The average crystallite size of $Bi_{25}FeO_{40}$ nanoparticles was obtained as ∼25 nm.

SEM image of $Bi_{25}FeO_{40}$ nanoparticles synthesized by hydrothermal method at 120 °C for 16 h is given in Fig. 2. Large number of $Bi_{25}FeO_{40}$ nanoparticles can be seen with varying size where some are small in size and some others are large in size. Large size may be due to the agglomeration of these $Bi_{25}FeO_{40}$ nanoparticles.

Magnetic characterization was done by M-H measurement using AGM. M-H plot of hydrothermal synthesized $Bi_{25}FeO_{40}$ nanoparticles is shown in Fig. 3, magnetisation at 10 kOe was obtained to be ∼8.80 emu g^{-1}. It was observed that synthesized $Bi_{25}FeO_{40}$ nanoparticles show weak ferromagnetic behaviour. The sample exhibit very small coercivity ∼50 Oe.

Optical properties of synthesized $Bi_{25}FeO_{40}$ nanoparticles were studied and diffuse reflectance spectra was taken by UV-Vis-NIR spectrometer. Figure 4a shows diffuse reflectance spectra of hydrothermal synthesized $Bi_{25}FeO_{40}$ nanoparticles. Analysis of the spectra was done by the Kubelka-Munk function [10]

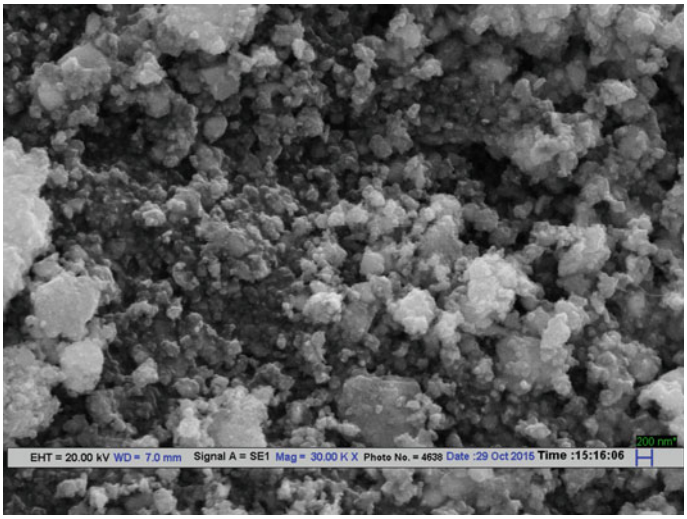

Fig. 2 SEM image of $Bi_{25}FeO_{40}$ nanoparticles synthesized by hydrothermal method

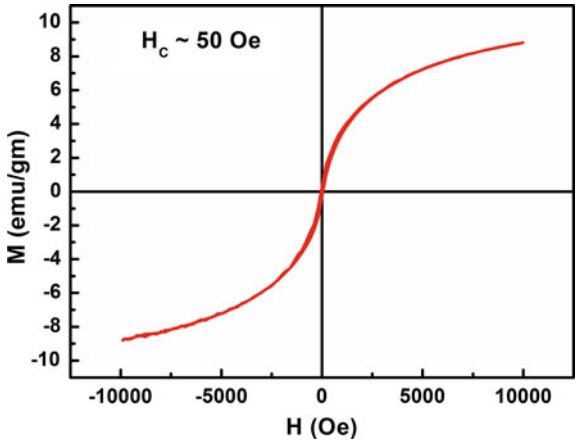

Fig. 3 M-H plot of hydrothermal synthesized $Bi_{25}FeO_{40}$ nanoparticles

$$F(R) = \frac{(1-R)^2}{2R} \tag{2}$$

where F(R) is the Kubelka-Munk function and R is the reflectance. The optical band gap was determined by $[F(R)\ h\nu]^2$ versus $h\nu$ plot (Fig. 4b) and direct band gap of $Bi_{25}FeO_{40}$ nanoparticles was obtained as $\sim$2.07 eV.

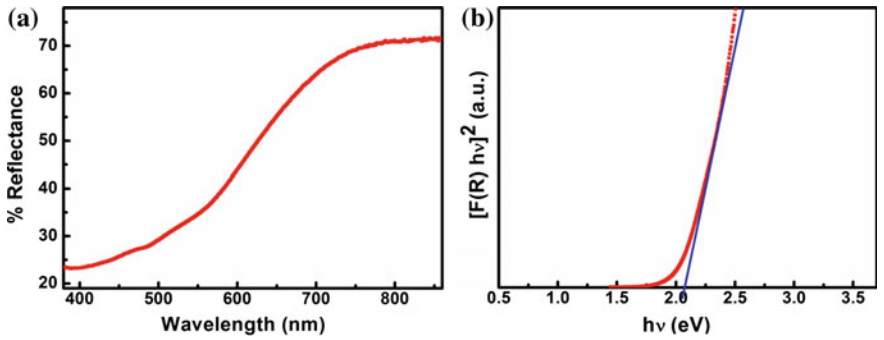

Fig. 4 **a** Diffuse reflectance spectra **b** $[F(R)\ h\nu]^2$ versus hν plot of hydrothermal synthesized $Bi_{25}FeO_{40}$ nanoparticles

4 Conclusions

$Bi_{25}FeO_{40}$ (iron sillenite) nanoparticles were synthesized by hydrothermal method using KOH as mineraliser. $Bi_{25}FeO_{40}$ nanoparticles were successfully obtained and the $Bi_{25}FeO_{40}$ phase confirmed by XRD pattern. $Bi_{25}FeO_{40}$ nanoparticles exhibit weak ferromagnetic behaviour and optical band gap of $\sim$2.07 eV. Small band gap of $Bi_{25}FeO_{40}$ nanoparticles makes them a suitable candidate for the photocatalytic and photovoltaic applications.

References

1. L. Zhang, X. Zhang, Y. Zou, Y. Xu, C. Pan, J. Hu, C. Hou, CrystEngComm **17**, 6527 (2015)
2. Y. Wu, H. Luo, X. Jiang, H. Wang, J. Geng, RSC Adv. **5**, 4905 (2015)
3. D.J. Arenas, T. Jegorel, C. Knab, L.V. Gasparov, C. Martin, D.M. Pajerowski, H. Kohno, M. W. Lufaso, Phys. Rev. B. **86**, 144116 (2012)
4. D.C. Craig, N.C. Stephenson, J. Solid State Chem. **15**, 1 (1975)
5. N. Rangavittal, T.N. Guru Row, C.N.R. Rao, Eur J Solid State Inorg Chem **31**, 409 (1994)
6. S.F. Radaev, L.A. Muradyan, V.I. Simonov, Acta Crystallogr. B **47**, 1 (1991)
7. S.F. Radaev, V.I. Simonov, Y.F. Kargin, V.M. Skorikov, Eur. J. Solid State Inorg. Chem. **29**, 383 (1992)
8. Y. Chen, Q. Wu, J. Zhao, J. Alloys Compd. **487**, 599 (2009)
9. M.Z. Ansari, N. Khare, J. Phys. D: Appl. Phys. **47**, 185101 (2014)
10. R. Köferstein, T. Buttlar, S.G. Ebbinghaus, J. Solid State Chem. **217**, 50 (2014)

Optical Properties of $(Fe_2O_3)_{1-x}/(Cr_2O_3)_x$ (Where x = 0.0, 0.1, 0.2, 0.3, 0.4 and 0.5) Nanocomposites

Priya Thakur, Anjna Thakur and Kamlesh Yadav

Abstract In this paper we report the preparation of $(Fe_2O_3)_{1-x}/(Cr_2O_3)_x$ (where x = 0.0, 0.1, 0.2, 0.3, 0.4 and 0.5) nanocomposites. The FESEM image of pure Fe_2O_3 sample shows that the uniform particle size distribution is observed. The average particle size of the Fe_2O_3 nanoparticles is 19 nm. The crystallite size increases from 20 to 28 nm with increasing the weight percentage of the Cr_2O_3 in the Fe_2O_3/Cr_2O_3 nanocomposite up to x = 0.5. The Fourier transform infrared spectroscopy (FTIR) spectra shows that the absorption peaks appear at 588 and 616 cm^{-1} which represent the Fe–O and Cr–O bond respectively. The values of band gap are found 2.1, 1.9, 1.8, 1.6, 1.4 and 1.2 eV for the x = 0.0, 0.1, 0.2, 0.3, 0.4 and 0.5 respectively by UV-Visible spectroscopy. Thus, the decrease in band gap and increase in refractive index with increasing concentration of Cr_2O_3 have been observed. These high refractive index materials can be used for making optical devices.

1 Historical Background and Introduction

Nanoscience" is the developing science of objects that are intermediate in size between the largest molecules and the smallest structures i.e. the science of objects with slightest dimensions range from a few nanometers to less than 100 nm. This range of sizes has in the past been associated with, micelles, colloids, polymer molecules, phase-separated regions in block copolymers, and comparable structures like very large molecules, or aggregates of many molecules, in the field of chemistry. Lately, structures such as silicon nanorods, buckytubes, and compound

P. Thakur · A. Thakur · K. Yadav (✉)
Centre for Physical Sciences, Central University of Punjab, Bathinda 151001, India
e-mail: kamlesh.yadav001@gmail.com

P. Thakur
e-mail: priyathakur1191@gmail.com

A. Thakur
e-mail: anjna56@gmail.com

V.K. Jain et al. (eds.), *Recent Trends in Materials and Devices*,
Springer Proceedings in Physics 178, DOI 10.1007/978-3-319-29096-6_19

semiconductor quantum dots enclose the mainly interesting classes of nanostructures. In physics and electrical engineering, nanoscience is often associated with quantum behaviour, and the behaviour of electrons and photons in nanoscale regime. Biology and biochemistry also have a profound interest in nanostructures as mechanism of the cell like loads of the most interesting structures in biology—from DNA and viruses to subcellular organelles and gap junctions which can be deliberated as nanostructures. Nanoscience has at present been with us for a decade. Nano sized particles having range lies below several 10 nm are of huge interest, due to the chemical and physical nature of the particles arising from the quantum confinement effect which are strangely different from those in bulk nature providing the great potential for use in applications in the electronic, chemical and mechanical industries, also in the related technologies using drug carriers, catalysts, sensors, pigments, also in magnetic and electronic materials [1]. Composites are a amalgamation of two materials in which one of the material is called the reinforcing phase, is in the form of fibers, sheets, or particles, and is surrounded in the other material called the matrix phase. Normally, reinforcing materials are strong with low densities on the other hand matrix is generally a ductile or tough material. If the composite is designed and synthesized correctly, it combines the strength of the reinforcement with the toughness of the matrix to attain a combination of pleasing properties not available in any single conservative material. Nanocomposites are a class of materials of more phases with nanoscale dimensions (0-D, 1-D and 2-D) are entrenched in a metal, ceramic, or polymer matrix. The properties of nanocomposites depends on a arrangement of variables, particularly the matrix material, which can reveal nanoscale dimensions, degree of dispersion, size, shape, and interactions between the matrix and the second phase [2]. Iron oxide (III) is a widely investigated material because of its magnetic, optical and catalytic properties. The iron oxide nanoparticle exhibits excellent transport properties [3]. Raj et al. [4] reported the nano sized and nanostructures of super-paramagnetic iron oxides have been investigated largely because of their wide-ranging applications in nano-fields such as ferrofluids, in biotechnology magneto caloric refrigeration reported by [5], and in vivo bio-medical field discussed by [6]. It has been broadly examined in various fields including catalysis reported by [7], environment protection discussed by [8], magnetic storage media explained by [9], clinical diagnosis [9], and cancer treatment studied by [6]. Nanomaterials may also be utilized in different technological demands, like refrigeration systems, medical imaging, drug targeting, other biological applications, and catalysis reported by [10]. By reducing the crystal dimension and enhancing the surface area of the materials of interest are an discretionary approach to get better the responses, because the reduction/oxidation reactions are mostly activated by the active surfaces area. Iron oxides and Cr_2O_3 are of great prominence in technological and industrial applications. The nanocomposites of iron oxide are used to investigate the humidity and gas sensing properties. Nanocomposite of Fe_2O_3 enhances the optical properties depends up on the type of filler. It is also reported that polymer magnetic nanocomposites scaling up the production to meet the larger quantity requirements

for EMI shield and other possible magnetic and RF applications by [11], Iron oxide aerogel nanocomposite are the fine candidate for applications in the field of magneto-optical sensors and magnetic devices discussed by [12], Ag/Fe_2O_3 nanocomposites to be possibly used in disinfection and biomedical applications also examined by [13]. It is also reported that increase of refractive index take place at low wavelength. The increase in refractive index with increase in doping concentrations is also well reported. But the optical properties of iron oxide nanocomposite with metal oxides are less studied. The optical properties of the nanocomposite are also very sensitively depending upon the preparation conditions. In this chapter, nanocomposite of $(Fe_2O_3)_{1-x}/(Cr_2O_3)_x$ (where x = 0.0, 0.1, 0.2, 0.3, 0.4 and 0.5) nanocomposites have been synthesized by the mixing of two pure form of nanoparticles of ferric oxide (Fe_2O_3) and chromium oxide (Cr_2O_3) by weight percent. The structural and optical properties of nanocomposite of $(Fe_2O_3)_{1-x}/(Cr_2O_3)_x$ are studied.

2 Experimental Methodology

Chemical Used

- Ferric Oxide (Fe_2O_3) having MW: 159.69 and particle size (TEM) <100 nm.
- Chromium oxide (Cr_2O_3) having MW: 151.99 and particle size (TEM) <100 nm.

The nanocomposite of $(Fe_2O_3)_{1-x}/(Cr_2O_3)_x$ (where x = 0.0, 0.1, 0.2, 0.3, 0.4 and 0.5) were prepared by mixing the Fe_2O_3 and Cr_2O_3 (Sigma Chemicals, particle size <100 nm) nanoparticle in proper ratio. The prepared samples were sintered at 400 °C for 2 h. The low temperature was selected to avoid the reaction between the Fe_2O_3 and Cr_2O_3 phases. The powder was ground for two hours and pellets were made with pellet press. Then, the as-prepared pellets were sintered at 400 °C for 2 h. At last, the grinding of each pellet was done for 2 h to attain the uniformity in sample.

3 Results and Discussion

FESEM Analysis Figure 1a–f shows the FESEM images $(Fe_2O_3)_{1-x}/(Cr_2O_3)_x$ nanocomposite where x = 0.0, 0.1, 0.2, 0.3, 0.4 and 0.5, and confirming that the particles obtained are in the nanometer range. We can see that the concentration of chromium oxide has influence on both the size and the morphology of iron oxide. It is found that the pure (Fe_2O_3) and nanocomposite are composed of uniformly distributed spherical and cylindrical particles. The micrograph shows the polycrystalline nature of nanoparticles with random distribution of grains with varying sizes. FESEM images also show that the Fe_2O_3 nanoparticles are covered with

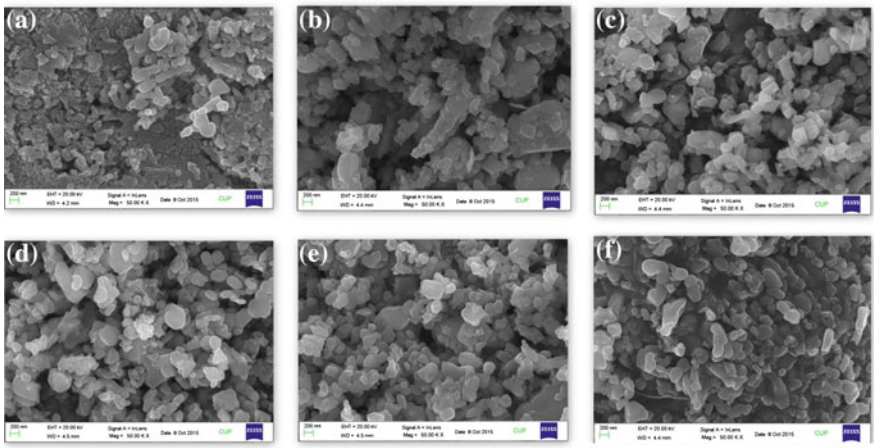

Fig. 1 Surface morphology (**a**–**f**) of $(Fe_2O_3)_{1-x}/(Cr_2O_3)_x$ nanocomposite where (x = 0.0, 0.1, 0.2, 0.3, 0.4 and 0.5)

Cr_2O_3 nanoparticles which indicate the strong interaction between the filler and matrix particles [14]. The particles size increases from 19 to 28 nm with the increase in the concentration of Cr_2O_3 form x = 0.1 to 0.5. In the sample having concentration is 0.5 (Fig. 1f) the occurrence of large agglomerates of particles displaying well-defined grain boundaries is observed [13].

EDS Analysis (EDS or EDX) is an systematic technique used for the elemental investigation or chemical characterization of a sample. It is one of the variants of X-ray fluorescence spectroscopy which relies on the examination of a sample through interactions between electromagnetic radiation and matter, analysing X-rays emitted by the matter in response to being hit with charged particles. Its characterization capabilities are due in large part to the fundamental principle that each element has a unique atomic structure allowing X-rays that are characteristic of an element's atomic structure to be recognized uniquely from one another. Energy dispersive spectroscopy (EDS) analysis shows that Fe, Cr and O elements were present in the nanocomposite in stoichiometric ratio within the experimental error. The calculated value of experimental and theoretical elemental composition is shown in Tables 1 and 2 respectively. It is clearly displayed that as grown synthesize materials contained only iron, oxygen and chromium elements, which presented in Fig. 2.

FTIR Analysis The infrared absorption spectra of the sample provide some important information about the structural changes. Figure 3 shows FTIR absorbance spectra (range 4000–500 cm^{-1}) of the sample at different concentrations. The absorption peaks appear at 588 and 616 cm^{-1} which represent the Fe–O and Cr–O bond respectively. In low frequency region Radial Breathing Modes the close view of FTIR spectra, a medium peak 540 cm^{-1} and this is indicative peak of Fe–O

Table 1 Experimental data of elemental composition $(Fe_2O_3)_{1-x}/(Cr_2O_3)_x$ nanocomposite where (x = 0.0, 0.1, 0.2, 0.3, 0.4 and 0.5)

Element	wt%	Atomic%	wt%	Atomic%	wt%	Atomic%	wt%	Atomic%	wt%	Atomic%	wt%	Atomic%
X	0.0	0.0	0.1	0.1	0.2	0.2	0.3	0.3	0.4	0.4	0.5	0.5
O K	29.81	59.71	37.10	67.18	41.50	70.97	39.74	69.19	39.52	69.07	39.92	69.05
Cr K	0.0	0.0	5.14	2.86	10.13	5.33	2.44	10.45	17.60	9.47	32.09	17.08
Fe K	70.19	40.29	57.76	29.96	48.37	23.70	39.82	19.86	42.88	21.47	27.09	13.87
Total	100	100	100	100	100	100	100	100	100	100	100	100

Table 2 Theoretical data of elemental composition $(Fe_2O_3)_{1-x}/(Cr_2O_3)_x$ nanocomposite where (x = 0.0, 0.1, 0.2, 0.3, 0.4 and 0.5)

Element	wt%	Atomic%	wt%	Atomic%	wt%	Atomic%	wt%	Atomic%	wt%	Atomic%	wt%	Atomic%
X	0.0	0.0	0.1	0.1	0.2	0.2	0.3	0.3	0.4	0.4	0.5	0.5
O K	30	60	30.1	60	30.3	60	30.57	60	30.76	60.01	30.99	60.01
Cr K	0.0	0.0	6.41	4	12.9	8	19.4	12	26.15	16	32.9	20
Fe K	70	40	63.39	36	56.7	32	49.9	28	43.07	24	36.12	20
Total	100	100	99.9	100	99.9	100	99.87	100	100.06	100.01	100.01	100.01

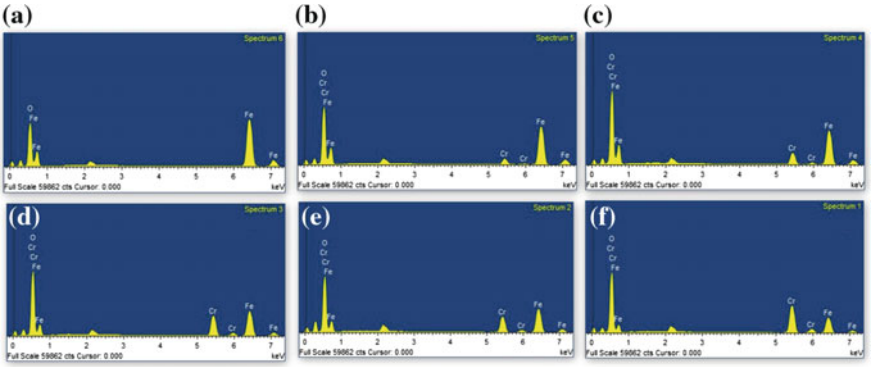

Fig. 2 EDS images (**a**–**f**) of $(Fe_2O_3)_{1-x}/(Cr_2O_3)_x$ nanocomposite where (x = 0.0, 0.1, 0.2, 0.3, 0.4 and 0.5)

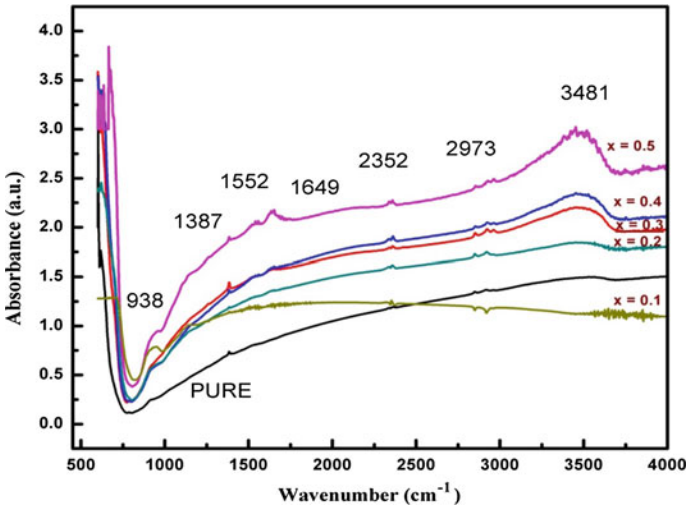

Fig. 3 FT-IR spectra of $(Fe_2O_3)_{1-x}/(Cr_2O_3)_x$ nanocomposite where (x = 0.0, 0.1, 0.2, 0.3, 0.4 and 0.5)

stretching vibration of iron oxide. More than this the peak observed at 620 and 690 cm^{-1} may be assigned to α-FeOOH and β-FeOOH phase, respectively. At low concentration of chromium oxide, no drastic change observed in the FTIR spectra, ranging 500–800 cm^{-1}, was observed. In addition, the peak observed at 1387 cm^{-1} can be ascribed to C–H bending vibration mode. The weak band centered around 1649 cm^{-1} is due to the bending mode of H–O–H absorbed at Fe_2O_3 structure. In addition the absorption bands near 3481 also refer to the O–H stretching mode and H–O–H bending mode respectively, indicating the presence of interstitial water in

the samples. The broadening of peaks with increasing the concentration of Cr_2O_3 is also observed. The broadening in the absorption line may be due to the combination of factors such as degeneracy of the vibration state, thermal broadening of lattice dispersion band and mechanical scattering from the powered samples. The broadening of peaks indicates the increase in the absorbance with the increase in the concentration of chromium oxide. The strong peak observed at 588 cm^{-1} which is the characteristic peak of α-Fe_2O_3. This result confirms that the thermal decomposition at 400 °C for 2 h decomposes α-FeOOH and β-FeOOH into final α-Fe_2O_3 [13].

Figure 2 shows the broadening in the characteristic bands at 938–1000, 588–616 and 1000–1387 cm^{-1}. The bands at 938–1000 cm^{-1} are assigned to Cr=O vibrations, 588–616 cm^{-1} are assigned to Cr–O vibrations and 1000–1387 cm^{-1} are relatively assigned to Cr–O–Cr vibrations [15].

UV-Visible

UV/visible absorption are a technique in which the outer electrons of atoms or molecules absorb radiant energy and undergo transitions to high energy levels. In this course of action, the spectrum obtained owing to optical absorption can be analysed to obtain the energy band gap of the semiconductor nonmaterials. In UV-visible spectroscopic analysis, absorption intensity increases with increase in Cr_2O_3 wt% in Fe_2O_3 samples. The optical band gap has been estimated using Tuac's equations [16]: $(\alpha h\nu)^n = A\,(h\nu - E_g)$, where $h\nu$ is the photon energy, α is the absorption coefficient, A is the constant relative to the material, n is both 2 for direct transition and 1/2 for indirect transition. Hence the optical band gap for absorption peak can be achieved by the extrapolating the linear portion of the $(\alpha h\nu)^n - h\nu$ curve to zero. For pure Fe_2O_3 the observed value of band gap $E_g = 2.1$ eV as shown in Fig. 4a [17].

Variation of Band gap with particle size and concentration of chromium oxide

The variation of band gap with concentration and particle size is shown in Fig. 4b. It is observed that band gap decreases with increase in particle size and concentration of Cr_2O_3 filler [18]. The band gap of the nanocomposite decreases when the particle size increases with increasing the concentration of Cr_2O_3. This case when increases the size, the absorbance decreases (Though, when using the doping (not reduce the surface area) with enhancement of the reflectance, that is why the band gap decreases pure material) also the band gap decreasing by shifting the absorbance to other region (like from UV to visible) which the doping by the N-type or p-type effects on the fermi level energy. This effect shows the reducing the band gap especially in powder form.

Refractive Index We have also calculated the refractive index of Fe_2O_3 nanoparticle and Fe_2O_3/Cr_2O_3 nanocomposite using Moss relation [19] i.e. $n^4 = (K/\text{Band gap})$ where, K is a constant with value of 108 eV. For Fe_2O_3

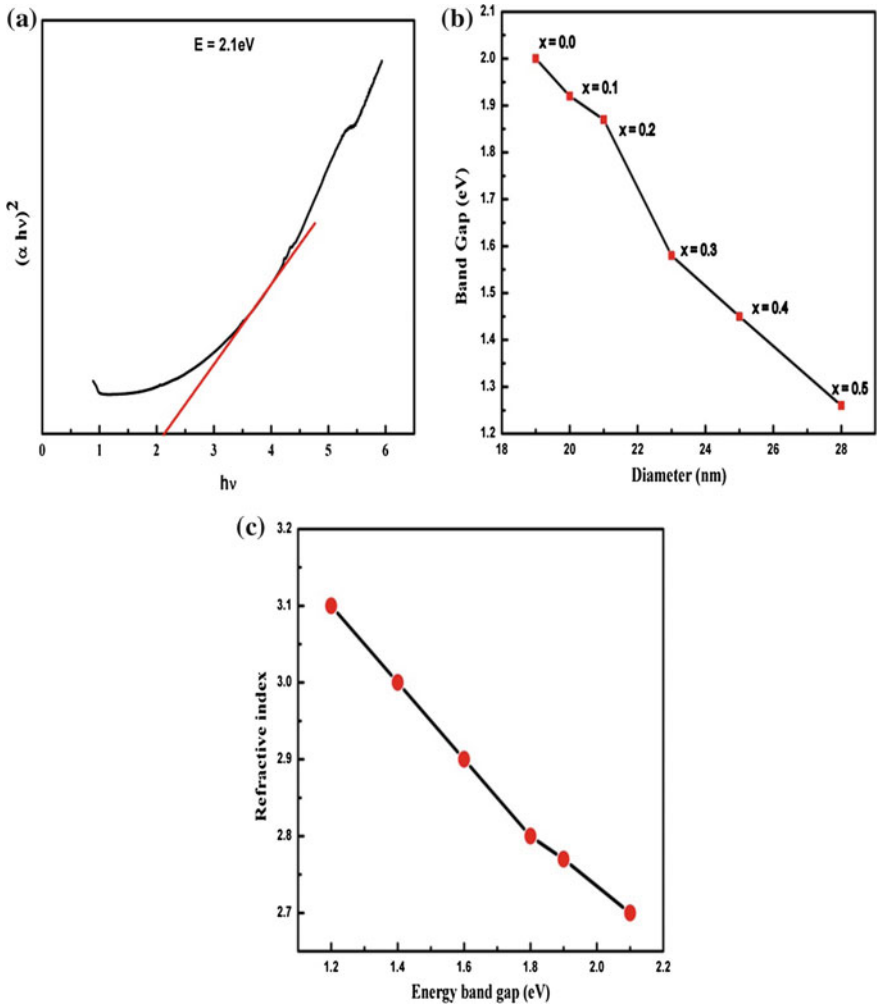

Fig. 4 **a–c** The curve of $(\alpha h\nu)^n$ against $h\nu$ for the calculation of direct band gap for pure Fe_2O_3 nanoparticles, variation of band gap with particle size and concentration of nanocomposite and Variation of Refractive index with band gap

nanoparticles the observed refractive index is 2.7 [20]. It is observed that the refractive index decreases with the increase in energy band gap as shown in Fig. 4c. The observed change in refractive index is due not only to the variation in inorganic materials but also due to the quantum size effect. In electron confinement phenomena a progressive increase in the band gap with a decrease in grain size is reported also by others.

Table 3 Calculated optical parameters of $(Fe_2O_3)_{1-x}/(Cr_2O_3)_x$ nanocomposite where (x = 0.0, 0.1, 0.2, 0.3, 0.4 and 0.5)

Sr. No.	Samples	Conc. (wt%)	Particle size (nm)	Band gap (eV)	Refractive index (n)
1	Fe_2O_3	0.0	19	2.1	2.7
2	$(Fe_2O_3)_{0.9}/(Cr_2O_3)_{0.1}$	0.1	20	1.9	2.75
3	$(Fe_2O_3)_{0.8}/(Cr_2O_3)_{0.2}$	0.2	21	1.8	2.8
4	$(Fe_2O_3)_{0.7}/(Cr_2O_3)_{0.3}$	0.3	23	1.6	2.9
5	$(Fe_2O_3)_{0.6}/(Cr_2O_3)_{0.4}$	0.4	25	1.4	3.0
6	$(Fe_2O_3)_{0.5}/(Cr_2O_3)_{0.5}$	0.5	28	1.2	3.1

4 Conclusion and Future Scope

We have used a appropriate method for the fabrication of $(Fe_2O_3)_{1-x}/(Cr_2O_3)_x$ nanocomposite where (x = 0.0, 0.1, 0.2, 0.3, 0.4 and 0.5) with average particle size is 19–28 nm. Nanocomposites are composed of uniformly distributed spherical and cylindrical particles having size increases as we increase the concentration of Cr_2O_3. The elemental composition of samples is confirmed by the EDS and also compares the theoretical and experimental data of as-prepared samples are equal within the experimental error. The strong peak observed at 588 and 616 cm^{-1} are the characteristic peaks of $(Fe_2O_3)/(Cr_2O_3)$ nanocomposite sample. The broadening of peaks in the samples indicates the increase in the absorbance with the increase in the concentration of chromium oxide. The observed value of bang gap for Fe_2O_3 is 2.1 eV using Tauc's relation, moreover small decrease in the band gap has been observed as we increase the concentration of Cr_2O_3. Beside this the refractive index of samples has also been calculated for pure Fe_2O_3 it is found to be 2.7. There are clear correlations between the particle size (nm), Band Gap (eV) and refractive index (n) as shown in Table 3, and the decrease in band gap and increase in refractive index with increasing concentration of Cr_2O_3 have been observed. These high refractive index materials can be used for making optical devices. From above results it is clear that prepared samples are good applicant in the field of magnetic devices and Magneto-optical sensors due to its low band gap and high refractive index.

Acknowledgments Author (PT) is thankful to UGC, New Delhi for providing fellowship during M.Phil. One of the authors (KY) is grateful UGC, New Delhi for providing the Start-up-Grant.

References

1. C. Huang, A. Notten, N. Rasters, J. Technol. Transf. **36**(2), 145–172 (2011)
2. L. Liu, Z. Qi, X. Zhu, J. Appl. Polym. Sci. **71**(7), 1133–1138 (1999)
3. M. Mohapatra, S. Anand, Int. J. Eng. Sci. Technol. **2**(8), 127–146 (2010)
4. K. Raj, B. Moskowitz, R. Casciari, Magn. Magn. Mater. **149**(1), 174–180 (1995)

5. R.D. McMichael, R.D. Shull, L.J. Swartzendruber, L.H. Bennett, R.E. Watson, J. Magn. Magn. Mater. **111**(2), 29–33 (1992)
6. M.M. Rahman, A. Jamal, S.B. Khan, M. Faisal, J. Nanopart. Res. **13**(9), 3789–3799 (2011)
7. A.S.C. Brown, J.S.J. Hargreaves, B. Rijniersce, Catal. Lett. **53**, 7–13 (1998)
8. J. Chen, L. Xu, W. Li, X. Gou, Adv. Mater. **17**(5), 582–586 (2005)
9. H. Zeng, J. Li, J.P. Liu, Z.L. Wang, S. Sun, Nature **420**(6914), 395–398 (2002)
10. V. Kesavan, P.S. Sivanand, S. Chandrasekaran, Y. Koltypin, A. Gedanken, Angew. Chem. Int. Ed. **38**(23), 3521–3523 (1999)
11. J.L. Wilson, P. Poddar, N.A. Frey, H. Srikanth, K. Mohomed, J.P. Harmon, S. Ktha, J. Wachsmuth, J. Appl. Phys. **95**(3), 1439–1443 (2004)
12. L. Casas, A. Roig, E. Rodriguez, E. Molins, J. Tejada, J. Sort, J. Non-Cryst. Solids **285**(1), 37–43 (2001)
13. R. Prucek, J. Tucek, M. Kilianova, A. Panacek, L. Kvitek, J. Filip, M. Kolar, K. Tomankova, R. Zboril, Biomaterials **32**(21), 4704–4713 (2011)
14. N. Adhlakha, K.L. Yadav, J. Mater. Sci. **49**, 4423–4438 (2014)
15. S.R. Ananda, N.M. Gowda, Mod. Res. Catal. **2**, 127–135 (2013)
16. X.Q. Zhang, S.W. Gong, Y. Zhang, T. Yang, C.Y. Wang, N. Gu, J. Mater. Chem. **20**(24), 5110–5116 (2010)
17. M. Shateriana, M. Enhessarib, D. Rabbanic, M. Asgharid, M. Salavati-Niasari, Appl. Surf. Sci. **318**, 213–217 (2014)
18. M.B. Sahana, C. Sudakar, G. Setzler, A. Dixit, J.S. Thakur, Appl. Phys. Lett. **93**, 231909–231911 (2008)
19. L. Hannachi, N. Bouarissa, Phys. B Condens. Matter **404**(20), 3650–3654 (2009)
20. M.N. Batin, V. Popescu, Optoelectronics and advanced materials-rapid communications **6**(7–8), 727–729 (2012)

Preparation and Characterization of Thin Film Prepared by Sodium Dodecyl Sulphate Stabilized Polythiophene

Ranjana Devi, Pinki Graak, Sacheen Kumar and Dinesh Kumar

Abstract The polythiophene (PT) polymer with short conjugated chain length has been derived with stabilization of Sodium Dodecyl Sulphate (SDS) surfactant under polymerization process with ferric chloride as oxidative agent. The average size of formed nanoparticles demonstrated with the help of AFM and found in range of 30–80 nm with r.m.s value of 2.42 nm. The various bending peaks have shown the formation of PT. The SDS-PT film has been deposited on to the silicon wafer and the thickness was determined to be 400 nm with Ellipsometer technique. The average energy bandgap was found 5.22 eV with absorption spectra of 360 nm observed under the UV-Visible spectroscopy supporting the formation of the Polythiophene nanoparticles.

1 Introduction

Polymers were being in scenario from last few decades due to exhibiting of their conducting behavior. In 1977 the discovery of intrinsically insulating organic polymer, polyacetylene was made highly conductive by exposing it to oxidizing or reducing agent. This procedure of oxidizing and reducing agent is referred to as doping process. This discovery led to development of various organic polymers which give conductive response in their oxidized and reduced form. A number of organic polymers are yielded with interesting properties by this effort. Polymers such as polythiophene, polypyrrole and polyparaphenyles are examples of such polymers [1].

In 1883 Victor Meyer had uncovered Thiophene as a contaminant in benzene. Thiophene is a colorless liquid at room temperature. It is conceded as aromatic, with the degree of aromaticity less than that of benzene. Polythiophene is made by polymerization [2]. Polythiophene is the one of bright class of conducting polymers for the technology use. This is aspect to their good environmental stability and their

R. Devi · P. Graak · S. Kumar (✉) · D. Kumar
Department of Electronic Science, Kurukshetra University, Kurukshetra 136119, India
e-mail: sacheen3@gmail.com

V.K. Jain et al. (eds.), *Recent Trends in Materials and Devices*,
Springer Proceedings in Physics 178, DOI 10.1007/978-3-319-29096-6_20

structural versatility [2]. Different preparative methods have been used to obtain the polymeric materials. They are categorized into three majored methods referred as metal catalyzed coupling reaction, oxidative polymerization and electrochemical method.

The Chemical oxidative anionic surfactant assisted polymerization method has been used to prepare the conductive polymer i.e. polythiophene. Polythiophene have combination of properties like low density, process ability and resilience against corrosion of plastic with metallic property. The applications of PT extending from antistatic coating to selectively modified electrodes and sensors. In order to use PT as sensing applications, thin film could be beneficial. Depending upon the starting monomer, different preparative methods have been used to obtain the polymeric material. They are classified into three major methods named as electrochemical chemical, metal catalyzed coupling reaction and oxidative polymerization method. The chemical oxidative polymerization method is more suitable than other two methods for preparation of bulk electrode material with controllable size. That is why PT thin films were prepared by spin coating method. Here PT is synthesized using anionic surfactant SDS (sodium Dodecyl sulphate) and $FeCl_3$ as a catalyzing agent. Organic compound sodium Dodecyl sulphate has formula CH_3 $(CH_2)_{11}SO_4Na$. It is an anionic surfactant used in many hygiene and cleaning products. The salt is of an organo sulphate contain 12 carbon tail attached to a sulphate group, giving the material amphiphilic properties required of a detergent. Derived from palm oils and inexpensive coconut, it is a common component of many domestic cleaning products. Iron chloride also called ferric chloride. This is a chemical compound with formula $FeCl_3$. $FeCl_3$ is used as oxidant. Further structural identification and morphological characterization was done by UV-visible spectroscopy, and Atomic Force Microscopy [3].

2 Experimental

2.1 Material Used

2,5-diidothiophene was purchased from Sigma-Aldrich. Sodium Dodecyl sulphate and Iron chloride were purchased from Fischer Chemicals. Purified water from Milipore system was used in all samples.

2.2 Synthesis of Polythiophene Nanoparticles

Various techniques could be used to produce polymer nanoparticles such as salting-out, solvent evaporation, micro-emulsion, mini-emulsion, dialysis,

supercritical fluid technology, surfactant assisted oxidative polymerization method, surfactant-free emulsion, and interfacial polymerization. The choice of method depends on a number of factors such as particle size distribution, particle size, area of applications etc.

2.2.1 Synthesis Process

Here PT nanoparticles are synthesized by anionic surfactant assisted oxidative polymerization method. The PT nanoparticles were prepared by adding 2, 5-Diidothiophene (0.00247 M) and surfactant SDS (0.0042 M) added in deionized water in a glass beaker and stirred for 30 min at 400–800 r.p.m (Figs. 1 and 2).

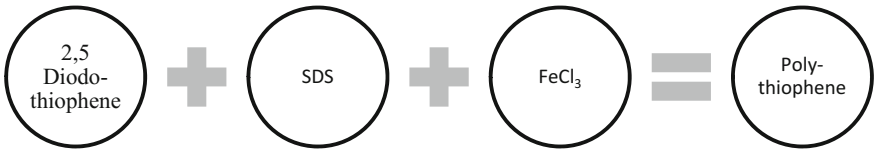

Fig. 1 Synthesis process

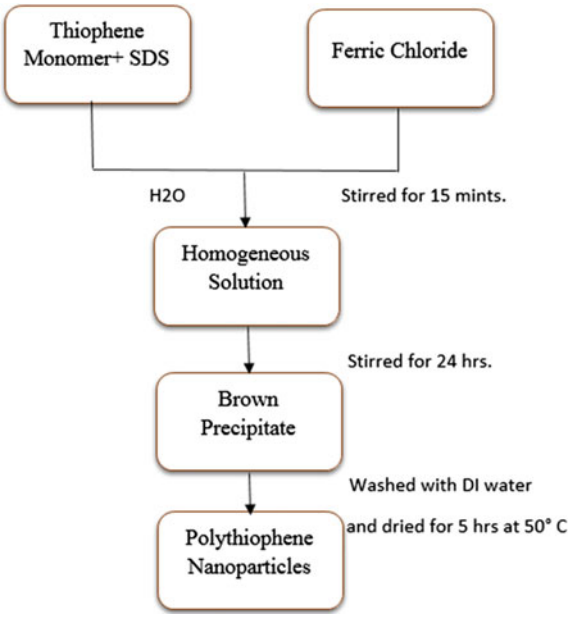

Fig. 2 Flow chart of synthesis method

2.3 Preparation of Thin Film by Spin Coating Method

The n-type silicon substrate was held on a chuck with the help of vacuum. Firstly silicon substrate was cleaned by of RCA cleaning. The silicon wafer cleaning was done in two steps. The first step was RCA 1 and the second one was RCA 2. In RCA 1 ammonium hydroxide and hydrogen peroxide with DI water was used. In RCA 2 HCL and hydrogen peroxide was used. Diluted HF dip was performed in the last. Then substrate put onto spin coater. Five to six drops of conducting polymer solution is put onto a substrate at a constant rate. Then the rotation of the spin coater is set to 3000 r.p.m. As the substrate rotate at the high speed, the PT solution spread over the substrate and a thin film formed. When first layer of PT formed, it dried with the help of a drier. After deposition of first layer, the second layer is coated with the same repeating procedure. Three coats of PT are given to the substrate. Here silicon and glass substrate are used for deposition thin film of PT. The silicon wafer has been chosen due to its semiconducting nature [3].

2.4 Characterization

The samples were diluted in methanol and coated on a silicon wafer for the various characterization techniques like UV visible spectroscopy, Ellipsometery and AFM. The thickness of the PT thin film measured by Ellipsometer technique. The surface roughness derived from the AFM. For UV-visible spectroscopy the instrument PERKIN UV [3] was used to determine the structural identifications and samples were analyzed at 360 nm. By computing the lambda max, shows the formation of the PT. The operating frequency of AFM lies in range from 146 to 236 kHz. Ellipsometery was used to determine the thickness of the deposited film on to the silicon. The model used for Ellipsometer was SE400adv (SENTECH).

3 Result and Discussion

UV-visible spectra were recorded to confirm PT formation. The observed λ_{max} for SDS coated PT 360 nm. In case of the obtained spectra, it shows blue shifts under the resolution range of 20 nm which sure the formation of short chain conjugates. The UV-Visible helped in order to get the absorption spectra from which the semiconducting behavior of the PT has been confirmed. The band gap of 5.3 eV has been obtained (Fig. 3).

From the literature refractive index and excitation coefficient values were taken as 1.64 and as 70×10^{-3} cm^{-1} for Ellipsometer observation [4]. The recorded thicknesses for the prepared PT nanoparticles suspension were found 400 nm. The

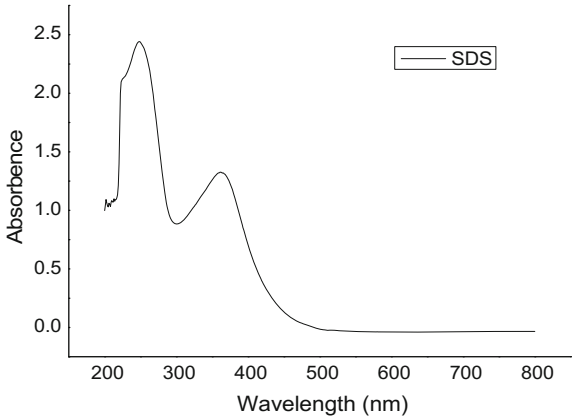

Fig. 3 UV visible spectra of SDS assisted PT

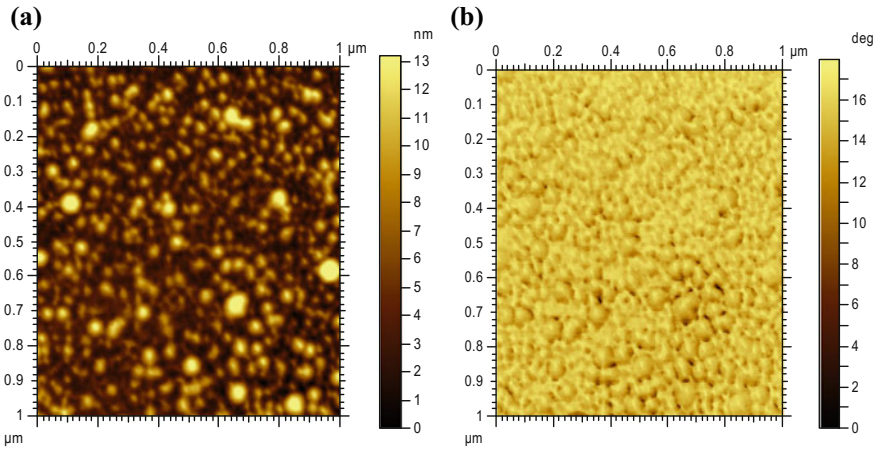

Fig. 4 **a** AFM topographical image of PT-SDS. **b** Phase diagram of topographical image

film of PT has been coated in order to find out the morphology and surface roughness. The obtained thin film on silicon wafer used for AFM.

In order to calculate the surface roughness or the surface morphology the Atomic Force Microscopy was used. In which a V shape probe is moved over the surface of the deposited thin film. There are three modes of AFM and here the intermittent mode has been used. It can be used for non-conducting and conducting surface so can be done either on glass or silicon wafer surface.

The surface roughness is found to be 2.42 nm from topographical image of AFM. Size of nanoparticles of SDS assisted PT were found in the range of 30–80 nm. The AFM analysis also predicts the morphological aspects which is simply predicts that it is of spherical in shape. The surface is found rough (Fig. 4).

4 Conclusion

The Thickness of the thin films was computed as 400 nm and the surface was found rough with r.m.s value of 2.42 nm. The particles size was observed in range of 30–80 nm with the AFM. The absorption spectra of the sample clearly indicated the formation of the PT and also indicated the semiconducting nature of the formed PT with energy band gap of 5.3 eV.

References

1. R. Hader, Towards the synthesis of segmented polythiophenes [microform]. M.Sc. Thesis, Simon Fraser University (1994)
2. M. Nasrollahzadeh, M. Jahanshahi, M. Salehi, M. Behzad, H. Nasrollahzadeh, Synthesis and characterization of nanostructured polythiophene in aqueous medium by soft-template method. J. Appl. Chem. **8**(27), 31–34 (2013)
3. P. Graak, R. Devi, D. Kumar, V. Singh, S. Kumar, Preparation and atomic force microscopy of CTAB stabilized polythiophene nanoparticles thin film. AIP Conf. Proc. **1728**, 020049 (2016)
4. K. Kaneto, K. Yoshino, Y. Inuishi, Electrical and optical properties of polythiophene prepared by electrochemical polymerization. Solid State Commun. **46**(5), 389–391 (1983)

Effect of Copper Doping on Physical Properties of Cadmium Oxide Thin Films

Gurunath Jadhav, Sanjay Sahare, Dipti Desai, Tejashree M. Bhave, S.N. Kale and Ravi Kant Choubey

Abstract Nanostructured materials have generated considerable interest owing to their physical and chemical properties that differ from those of their bulk counterparts. Cadmium oxide (CdO) is an important semiconducting material with varying band gap from 2.2 to 2.9 eV used for various applications. Due to its high electrical conductivity and optical transmittance in the visible region, this material is having potential application in photovoltaic devices as well. This study focuses on the preparation and characterization of CdO (undoped and 2 % Cu-doped) produced by facile sol–gel spin coating. Effect of Cu doping on the structural, optical and morphological properties of CdO have been studied.

1 Introduction

Electrical and optical properties are more significant in metal oxides like Cadmium oxide (CdO), Tin oxide (SnO_2), Indium oxide (In_2O_3), Titanium oxide (TiO_2) etc. which brings an attention in the optoelectronic industries [1]. Throughout the world, many of the researchers are working on intensively modified oxide materials, where most of the oxides act as Transparent Conducting Oxides (TCOs). In view of the fact that it's TCO, hence it has been used for large number of applications viz flat panel displays, optical communication, photo-transistors, solar cell, etc. [2]. This is also used in other type of applications like gas sensors, low-emissive windows,

G. Jadhav · S. Sahare · D. Desai · T.M. Bhave · S.N. Kale
Department of Applied Physics, Defence Institute of Advanced Technology, Pune 411025, India

R.K. Choubey (✉)
Department of Applied Physics, Amity Institute of Applied Sciences, Amity University, Sector-125, Noida 201 303, India
e-mail: ravikantchoubey@gmail.com

V.K. Jain et al. (eds.), *Recent Trends in Materials and Devices*,
Springer Proceedings in Physics 178, DOI 10.1007/978-3-319-29096-6_21

thin-film resistors, heat reflecting coatings on architectural windows, etc. Numerous methods have been used for preparing the CdO including sol gel, spray-pyrolysis, sputtering, chemical bath deposition [1–4] etc. Among all these techniques, sol gel method competes with the others due to its low costs and suitable properties. The physical properties of the CdO thin film can be tuned with doping of different ions like Aluminium, Indium, Yttrium, Titanium, Gallium etc. which enhances their electrical and optical properties. In general, Cu can be used as dopant easily in Cd, since it has less ionic radii that of Cd. Few studies have been done with this concept and could improved the physical properties of the CdO thin films.

In the present work, we have demonstrates an improvement in optical and electrical properties via Cu doping in CdO. Thin films were prepared with sol gel method followed by spin coating technique. Further, it would characterize with different techniques X-ray diffraction, UV-spectroscopy, Atomic force microscopy and Current-Voltage measurement.

2 Experimental Details

The CdO and Cu doped CdO thin films were grown on microscopic glass substrate i.e. cover slips (22 mm × 22 mm) using the spin-coating technique. Cadmium acetate dihydrate [$Cd(CH_3COO)_2{\cdot}2H_2O$], 2-Methoxyethanol, copper acetate anhydrous [$Cu(CH_3COO)_2$], Monoethanolamine have been used as a precursor material. Firstly, the CdO precursor solution was prepared by half mole of a cadmium acetate dihydrate Cd $(CH_3COO)_2{\cdot}2(H_2O)$ (98 %, Sigma Aldrich) was dissolved in 2-Methoxyethanol ($C_3H_8O_2$) at 1:10 ml, and stirred continuously at 60 °C for 10 min. Copper (II) acetate anhydrous $Cu(CH_3COO)_2$, was added slowly into the solution with constant magnetic stirring and heating. Thereafter, 0.5 ml of the Mono-Ethanolamine (C_2H_7NO; abridged MEA) as a stabilizer was added drop by drop till the homogeneous and clear solution obtained followed by continuous stirring and heating at 75 °C for 4 h. All procedure was done at the room temperature. The solution was then aged at ambient for one day till the gel was formed. The substrates thoroughly cleaned by chromic acid and subsequently washed 3–4 times with distilled water. The viscous homogenous solution was poured on the substrate to form thin film via Spin Coater (Apex NXG-P1). The parameters were kept constant for all the films. i.e. 800 rpm and 60 s for rotation and time respectively and dried at 130 °C for 10 min. Once it dried well, then kept for annealing at 400 °C for 1 h. The structural, optical and morphological studies of the films were carried out by the X-ray diffraction (XRD) technique using D8 Advance (Bruker systems), UV–visible–NIR spectrophotometer (SPECORD® 210 plus, Germany) and FE-SEM (Sigma-Carl Zeiss), respectively.

3 Results and Discussion

Figure 1 shows an XRD pattern of undoped CdO and Cu doped (2 %) CdO thin films. XRD peaks are reveals that both the films are polycrystalline in nature and the growth is preferential along (111) direction. This is also supported by literature where CdO films were synthesized by different techniques [1]. Another prominent peaks associated with (200), (220), (311) and (222) planes depicts cubic structure. The grain size is calculated by using Scherer's relation which is given by (1),

$$\text{Grain Size} = \frac{0.94\lambda}{\beta \operatorname{Cos} \theta} \tag{1}$$

where, λ is wavelength, β is full width at half maxima and θ is the Bragg angle. The average crystallite size calculated for undoped and Cu doped CdO films which is shown in Table 1.

The results demonstrate that, as increase the concentration of Cu doping, the grain size was decreased. The ionic radii of Cu and Cd are 0.73 and 0.95 Å, respectively. The ionic radii ratio of Cu:Cd is 0.77, this shows that Cu has the smaller radius than Cd. It might be easy to diffuse in the host CdO material. Therefore, the slight shifts in reflections from Cu doped CdO relative to the corresponding reflections from undoped CdO films were observed. The optical behavior is observed through UV-V is spectrophotometer is shown in Fig. 2a. It depicts the better optical response in terms of transmittance in both the cases, which gives more than 80 % in visible and NIR spectral regions.

An ability to absorbs light by the prepared thin films could be measured by the relation given by (2),

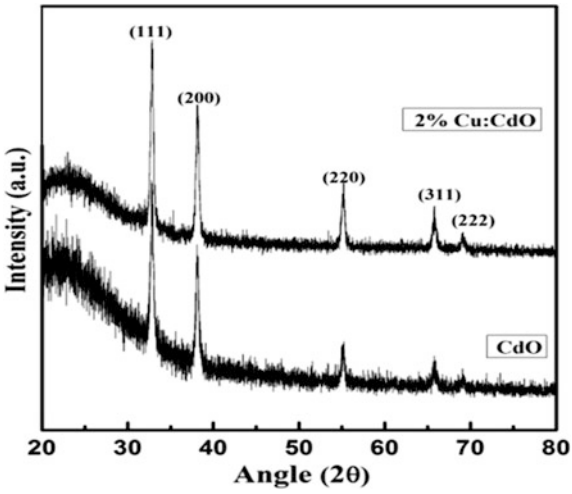

Fig. 1 X-rays pattern of pure and Cu doped CdO thin films

Table 1 Grain size and Band gap energy of CdO films

Sample names	Grain size (nm)	Band gap energy (eV)
CdO	21.47	2.95
Cu:CdO 2 %	20.84	2.8227

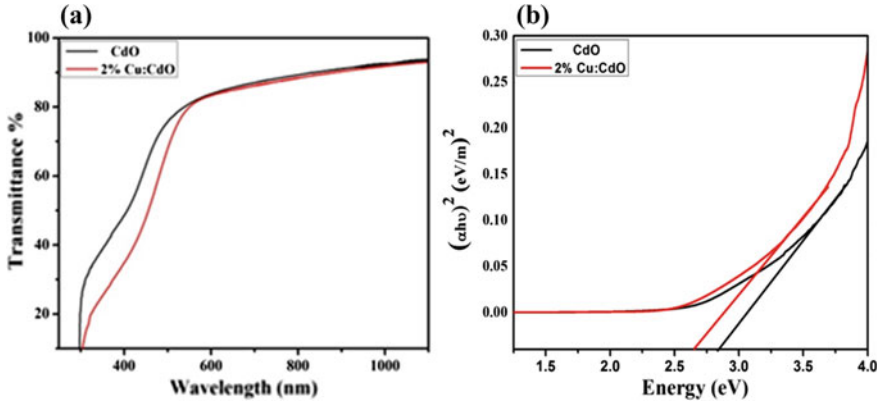

Fig. 2 **a** UV–Visible transmittance spectra of the pure and Cu doped CdO thin films. **b** Optical band gap of the pure and Cu doped CdO thin films

$$\alpha = \left(\frac{1}{d}\right) * \ln\left(\frac{1}{\mathrm{T}}\right) \tag{2}$$

where, α is Absorption coefficient, d is thickness of film and T is transmittance of film. Also, the optical band gap of the CdO films is estimated from the relation,

$$\alpha h\upsilon = (\alpha h\upsilon - Eg)^{1/2} \tag{3}$$

From the (3), the optical band gap values were obtained by extrapolating the plot towards $\alpha = 0$ in the graph of $(\alpha h\upsilon)^2$ versus $h\upsilon$ which is observed from Fig. 2b. The value of band energy of undoped CdO is found to be 2.95 eV, whereas it reduced to 2.8 eV after Cu doping. This might be due to the structural modification of CdO films. The structural modification of Cu:CdO thin films could be due to replacement of Cd interstitial or substitution by copper ions. This copper atom introduces some additional energy levels in CdO band gap close to valance band edge. This might results in consequent reduction of energy in transition energy. The electrical properties were observed with the help of two probe techniques. The resistivity of pure CdO was 198×10^{-4} Ω cm and it was decreases with Cu doping to 41.55×10^{-4} Ω cm. Hence, automatically the conductivity in Cu doped film gets improved. These results might be due to free charge carrier concentration increment

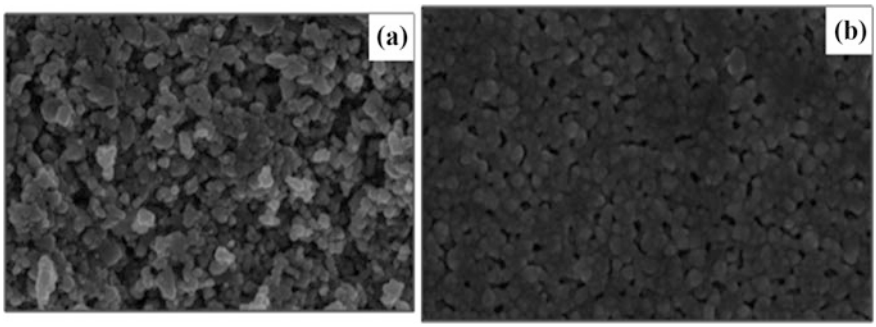

Fig. 3 SEM images of **a** Pure and **b** Cu doped CdO thin films

the films. The substitution of Cd atom by Cu atom may be responsible for it or Cu atom could occupy the lattice site in CdO crystal.

The morphological studies were done with SEM shown in Fig. 3a, b. These images recorded with magnification 100KX. This study revealed that films were uniform and spherical shaped in nature. From SEM study, we could determine the thickness of films and it was in $\sim$150 nm range.

4 Conclusion

Thin films were obtained with facile sol gel spin coating method. The n-type semiconductor CdO films with good structural, morphological, optical and electrical properties were synthesized. As synthesized and Cu doped CdO films are highly transparent and the optical band gap of film is slightly decreased after doping. It was observed that Cu doping improved electrical conductivity of the CdO films.

Acknowledgments The authors Ravi Kant Choubey and Dipti Desai are thankful to Department of Science and Technology, Science and Engineering Research Board, New Delhi for the financial support (Grant No. SR/FTP/PS-038/2012). The authors Ravi Kant Choubey and Gurunath Jadhav is also thankful to Defence Institute of Advanced Technology, Girinagar, Pune for the financial support (Grant No. DAIT/F/REG(G)/BS/Proj/2014/2).

References

1. M. Benhaliliba, C.E. Benouis, A.Tiburcio-Silver, F. Yakuphanoglu, A. Avila-Garcı´ad, A. Tavira, R.R. Trujillo, Z. Mouffak. J. Lumin. **132**, 2653–2658 (2012)
2. K.R. Murali, A. Kalaivanan, S. Perumal, N. Neelakanda Pillai. J. Alloys Compd. **503**, 350–353 (2010)
3. A.A. Dakhel, A.Y. Ali-Mohamed, J. Sol-Gel. Sci. Technol. **55**, 348–353 (2010)
4. A.A. Dakhel, Curr. Appl. Phys. **12**, 1–6 (2012)

Design of Fly Ash Based Core Shell Composites as Heat Reflective Coatings for Sustainable Buildings

Richa Sharma and Sangeeta Tiwari

Abstract Solar radiation consists of nearly 49 % near-infrared radiation (Thermal region, wavelength = 750–2500 nm). Heat reflective pigments increases the near infrared reflectance of exterior finishes and paints, there by dropping the surface temperatures of roofs and walls, which, in turn, reduces the cooling-energy demand of the building. However, the cost of developed pigments is prohibitive for wider acceptance of NIR reflective pigments. Fly ash is an industrial waste produced in large quantities by coal based power plants. It creates an environmental problem and therefore efforts are on for its safe disposal or to make value added products. In the present work, Flyash based core shell composite particles are prepared using flyash in the core and nano titanium dioxide as the shell. Coating of titanium dioxide over flyash improves its whiteness and renders high reflectivity which is useful for preparation of reflective coatings for building applications. The coatings possess good abrasion and chemical resistance due to flyash which is abrasive and has good chemical resistance. The composite particles were prepared by precipitation of nano titanium dioxide on flyash surface by two techniques: Insitu and Exsitu. The composite particles were characterized by X-ray diffraction, SEM and DRS (Diffused reflectance Spectroscopy) technique.

1 Introduction

The Sun's energy that reaches the earth's surface is divided into three main parts: UV accounts for about 5 % of the Sun's energy that reaches the earth's surface. Around 50 % of Sun's energy occurs in the visible region of electromagnetic spectrum and 45 % of total solar energy is in the non-visible infrared region. Heat is a direct consequence of infrared radiation incident on an object. Infrared radiations

R. Sharma · S. Tiwari (✉)
Amity Institute of Applied Sciences, Amity University, Sector-125, Noida, Uttar Pradesh, India
e-mail: stiwari2@amity.edu

V.K. Jain et al. (eds.), *Recent Trends in Materials and Devices*,
Springer Proceedings in Physics 178, DOI 10.1007/978-3-319-29096-6_22

range from 700–2500 nm wavelength. These radiations on absorption result in heating up of the surface.

With the growing concern for energy conservation, the concept of energy efficient buildings is fast growing. Cool coatings are an integral part of the energy efficient buildings and provide a cooler interior to any building structures they are applied on. The cooling effect of these coatings is due to the cool pigments incorporated in them which reflect the solar radiations in NIR region and thus help in reducing energy required to cool the interior of the buildings. The cool pigments in use are mostly based on rare earth oxides and some other oxides like titanium dioxide, Zinc oxide etc.

FA particles are inert and are known to have good extender properties [1] and thermal insulation characteristics [2] due to which it will prevent heat conduction to substrate. Low cost and easy availability of Fly ash as compared to other existing high cost near infrared reflective pigments will help in bringing down the cost.

IR reflective pigments are increasingly used for roof and building coatings because of their excellent weatherability. In the present work, we have modified the surface properties of Fly Ash by coating it with Titanium dioxide to improve its reflectivity so that it can be used in paints as a pigment to reflect near infrared rays and make the interior of the building cooler. It plays a crucial role in energy saving. Titania, because of its unique chemical, optical and electrical properties, is widely explored for a number of applications including photocatalysis [3], solar cells [4], pigment in paints [5] etc. Titania also shows ability to reflect NIR radiations [6, 7]. Nanoparticles of TiO_2 can be a potential materials for use as reflective pigment in cool coatings due to their high surface area, controlled morphology and high purity [8]. We have synthesized core-shell composite particles containing Fly ash in the core and Titanium dioxide as a shell by precipitation technique (insitu) and mix grinding process (exsitu) and used it to maximize reflectivity in the near infrared region. Core shell particles are highly functional materials with tailored properties, which are quite different than either of the core or of the shell material. They show modified and improved properties than their single component counterparts or nanoparticles of the same size. Their properties can be modified by changing either the constituting materials or core-to-shell ratio.

In the present case, they are prepared to reduce content of costly nano metal oxide thereby reducing the cost of NIR material. Titania-coated colloids are useful in reducing the cost of pigment and filler material, because a titania shell alone has nearly the scattering properties of titania, while the core is made up of a cheaper material i.e. Fly ash.

A simple and convenient method will be developed to prepare core-shell structures with Fly ash, an industrial waste by-product as a core and nano-titania in the shell. Titania is known to possess reflective property in NIR region but if used as such leads to high cost of coatings. Preparation of core-shell minimizes the use of titania as very small amount of titania precursor is required to precipitate

nano-titania on fly ash core. The challenge is to obtain a uniform and stable coating of titania on fly ash so as to produce maximum reflectivity in NIR region for which a method will be developed. The core-shells will offer additional benefits of self-cleaning due to photocatalysis and anti-microbial characteristics to the coatings in which they will be incorporated. The coatings so prepared will possess heat (NIR) reflectivity alongwith self-cleaning and anti-microbial properties and will find applications as multifunctional cool coatings for energy efficient buildings. The novelty of the proposed work lies in its new concept of using core shell material, flyash @titania, as extender pigment for cool coatings that offers properties of both core and shell in the final product. The approach would enable use of very little amount of precursor thereby largely reducing the amount of costly titania otherwise required to offer the same level of reflectivity as a pigment. The core of fly ash provides bulk to the material which has an advantage of being a cheaper material and functional advantages as good thermal and abrasion resistance property due to the presence of silica and alumina in its composition. Fly ash being an inert material, is also expected to provide good chemical and corrosion resistance to the coatings. Overall the core-shell material developed as a cool pigment will have multifunctional advantages and will find applications as interior and exterior as well as cool roof coatings.

2 Experimental Details

2.1 Materials

Flyash (NTPC Badarpur), Titanium isopropoxide, Sodium oleate, Ethanol, HCl, Distilled water.

2.2 Methods

2.2.1 Treatment of Fly Ash

Flyash particles were treated by froth floatation process to remove unburnt carbon and iron oxide particles were removed by using magnet.

2.2.2 Insitu Preparation

Flyash particles free of unburnt carbon and oxides of iron was used as core. Nano titanium dioxide was deposited insitu by sol gel route. For preparation, fly ash was taken in 70 % Ethanol, 1 % sodium oleate and 3–5 drops of conc. HCl. To this

mixture under vigorous stirring, was added Titanium isopropoxide. After addition, stirring was continued for 30 min. Distilled water was then added and the mixture was stirred for another 2 h in ambient conditions. Solvent was removed by evaporation at 50–60 °C for several hours until a dried powder was obtained. The composite particles were then heated in vacuum oven at 120 °C for 2 h.

2.2.3 Ex Situ Preparation

Commercially available Titanium dioxide was subjected to ball- milling in iso-propanol medium using tungstine carbide balls. Ball Milling was continued for 4 h at 200 rpm till nanosize was achieved which was confirmed by XRD analysis.

To prepare core shell by ex situ method, Treated Fly ash was mixed with 70 % ethanol solution and 1 % Sodium Oleate. The slurry was subjected to vigorous stirring for 1 h. Ball milled TiO_2 was added to this mixture and again stirred vigorously for 2 h. This was followed by ultrasonication for 2 h. Solvent was then removed by drying at 50–60 °C for several hours. The powder obtained was then heated in a vacuum oven at 120 °C for 2 h.

3 Results and Discussion

Tables 1 and 2 are showing elemental composition of untreated flyash and treated flyash respectively. It can be clearly seen that amount of carbon and iron is reduced after treatment of flyash.

The phases and composition of the samples were investigated by using XRD (Bruker, D-8 Advance) with CuK_α radiation ($\lambda = 1.54$ Å). Figure 1 shows the XRD pattern of untreated flyash and treated flyash. The peaks of silica and alumina remain the same but the peaks of hematite disappear after treatment of flyash. It confirms that the content of iron is reduced after treatment of flyash as hematite is the mineral form of iron oxide and it is disappearing after treatment of flyash.

Table 1 Elemental composition of untreated fly ash

Element	Element weight (%)	Atomic (%)
C	0.83	0.48
O	51.58	65.93
Mg	0.63	0.56
Si	23.93	17.36
Al	17.41	13.95
Fe	4.20	1.60
Ca	1.42	0.12
Total	100.00	100.00

Table 2 Elemental composition of treated fly ash

Element	Element weight (%)	Atomic (%)
C	0.11	0.24
O	56.84	66.97
Mg	0.57	0.56
Si	25.21	17.16
Al	15.30	10.17
Fe	0.14	0.15
Ca	1.83	0.37
Total	100.00	100.00

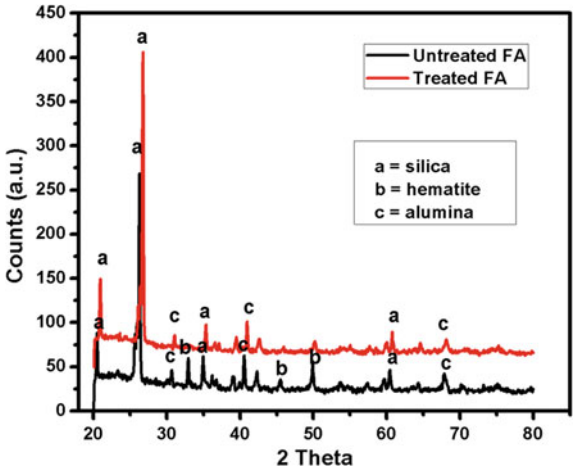

Fig. 1 XRD of untreated flyash and treated flyash

The morphology of the products was characterized by FESEM (Hitachi S-4800). Figure 2 shows the SEM images of treated flyash and FA-TiO_2 prepared by insitu (Fig. 2b) and exsitu (Fig. 2c) method respectively. Figure 2b shows homogeneous coating of TiO_2 on flyash. Figure 2c shows that extra flyash particles are not coated homogeneously by TiO_2 particles but extra TiO_2 is dispersed in the surroundings.

The near-infrared reflectance spectra of the samples were recorded with a UV-VIS-NIR spectrophotometer (Perkin-Elmer Lambda-950). Optical measurements were carried out in the range of 200–2500 nm. Figure 3 shows diffuse reflectance spectra of treated flyash and FA-TiO_2 prepared by insitu and exsitu method respectively. It can be clearly seen that the sample prepared by insitu method is showing highest reflectance.

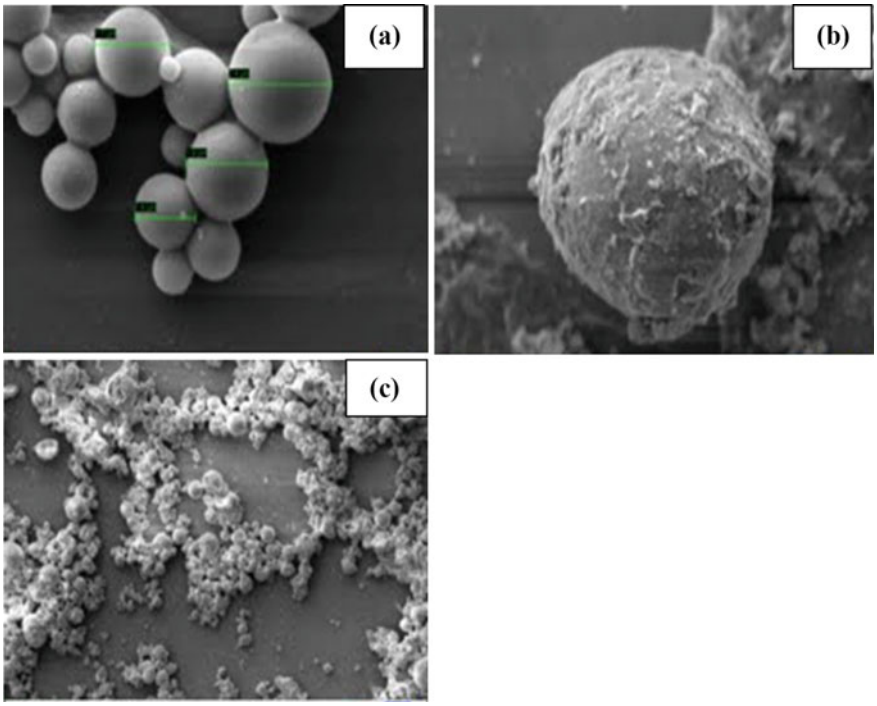

Fig. 2 SEM images of **a** treated flyash, **b** FA-TiO_2 (insitu method), **c** FA-TiO_2 (exsitu method)

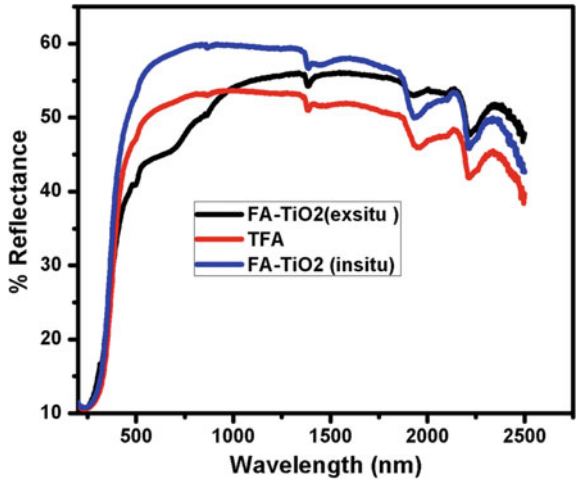

Fig. 3 DRS of FA-TiO_2 (exsitu), treated flyash (TFA) and FA-TiO_2 (insitu)

4 Conclusions

Carbon content is reduced in flyash after treatment which improves its whiteness. Also, peak of Hematite disappears after treatment of flyash as shown in XRD image. Homogeneous coating of TiO_2 shell on Flyash core is achieved in the core shell particles prepared by Insitu method as shown in SEM images. The novelty of the proposed work lies in its new concept of using core shell material, flyash @titania, as extender pigment for cool coatings that offers properties of both core and shell in the final product. The approach would enable use of very little amount of precursor thereby largely reducing the amount of costly titania otherwise required to offer the same level of reflectivity as a pigment. The core of fly ash provides bulk to the material which has an advantage of being a cheaper material and functional advantages as good thermal and abrasion resistance property due to the presence of silica and alumina in its composition. Fly ash being an inert material, is also expected to provide good chemical and corrosion resistance to the coatings. Overall the core-shell material developed as a cool pigment will have multifunctional advantages and will find applications as interior and exterior as well as cool roof coatings.

The prepared core shell composite particles can have diverse applications such as NIR reflectivity, Photocatalytic property and antibacterial property etc.

References

1. S. Zulu, D. Allopi, Influence of high content fly ash on concrete durability. Int. J. Eng. Innov. Tech. **3**, 150–155 (2014)
2. S. Tiwari, M. Saxena, Use of fly ash in high performance industrial coatings. Corros. Eng. Sci. Tech. **34**, 184–191 (1999)
3. G. Liu, L. Wang, H.G. Yang, H.M. Cheng, G. Qing (Max) Lu. J. Mat. Chem. **20**, 831–843 (2010)
4. Oomman K. Varghese, Maggie Paulose, Craig A. Grimes, Nat. Nanotechnol. **4**, 592–597 (2009)
5. B.B. Topuz, G.Gunduz, B. Mavis, U. Colak. Dyes Pigments. **90**, 123–128 (2011)
6. M. Baneshi, S. Maruyama, H. Nakai, A. Komiya, J. Quant. Spectrosc. Radiat. Transfer **110**, 192–204 (2009)
7. P. Jeevanandam, R.S. Mulukutla, M. Phillips, S. Chaudhuri, L.E. Erickson, K.J. Klabunde, J. Phy. Chem. C **111**, 1912–1918 (2007)
8. M. Santamouris, K. Pavlou, A. Seneca, K. Niachou, D. Kolokotsa, Energy Build. **39**, 859–866 (2007)

Synthesis and Characterization of Copper Doped Cobalt Oxide (Co_3O_4) by Co-precipitation Method

Ekta Arora, Ritu Chaudhary, Sacheen Kumar and Dinesh Kumar

Abstract Today nanomaterials play a key role in various fields such as electronics, aerospace, pharmaceutical sand biomedical because of their unique, physical, chemical and biological properties which are different from bulk materials. In this research work, we have reported a co-precipitation method used to synthesize the copper doped cobalt oxide nanoparticles. The characterization of nanoparticles were investigated by Fourier transform infrared spectroscopy (FTIR), X-ray diffraction (XRD) to determine the structural properties and particle size respectively. By XRD analysis, we confirm that Co_3O_4 nanoparticles are formed and mean grain size is decreased with increasing Cu doping (from 18 to 12 nm).

1 Introduction

In recent years, transition metal oxides have gained much more interest due to their desirable properties and applications in various fields [1]. Metal oxides can adopt a large variety of structural geometries with an electronic structure that may exhibit metallic, semiconductor, or insulator characteristics, enabling them with diverse chemical and physical properties. Therefore, metal oxides are the most important functional materials used for chemical and biological sensing and transduction. Moreover, their different and tunable physical properties have made themselves excellent applicants for electronic and optoelectronic applications. Nanostructured metal oxides have been actively studied due to both scientific interests and potential applications [2, 3]. Various pure and doped semiconducting oxides have been used as gas sensors. Nanomaterial has gained much more interest because of a much greater ratio of surface to bulk than bulk materials [4]. In addition, when the grain size decreases to nanometers, specifically when the dimension becomes less than twice the space-charge depth, a large section of atoms are present on the surface and

E. Arora · R. Chaudhary · S. Kumar (✉) · D. Kumar
Department of Electronics Science, Kurukshetra University,
Kurukshetra 136119, Haryana, India
e-mail: sacheen3@gmail.com

V.K. Jain et al. (eds.), *Recent Trends in Materials and Devices*,
Springer Proceedings in Physics 178, DOI 10.1007/978-3-319-29096-6_23

the surface properties become dominant. Hence, materials of conduction type come to be materials of surface conduction type. The sensing mechanism depends on the change in surface electrical conductivity due to a chemical reaction between target gases and the oxygen absorbed on the surface of Nano-sized metal oxides. Consequently, it is important to increase the rates of chemisorption and surface reaction [5–7].

Co_3O_4 is an important antiferromagnetic p-type semiconductor with excellent properties such as gas-sensing, catalytic and electrochemical properties, and has been studied widely for their applications in gas sensor, magnetic materials, catalyst, anode materials for rechargeable Lithium batteries, electro chromic devices, electrochemical systems and high-temperature solar selective absorbers [8, 9]. Co_3O_4 were found to have interesting magnetic, optical, field emission and electrochemical properties that are attractive in device applications, when reduced down to the nanometer scale. The difference in oxygen defect, oxygen holes and oxygen adsorbed in different state of cobalt in Co_3O_4 are thought to be the reason for high activity and selectivity of this metal oxide catalysts [10]. In recent years, tremendous efforts have been directed to the synthesis and investigation of properties of Co_3O_4 nanostructures. Therefore, in this field a variety of methods have been reported for preparing Co_3O_4 nanoparticles, including sol–gel, reduction/oxidation route, thermal decomposition, metal organic chemical vapor deposition (MOCVD), chemical spray pyrolysis, micro emulsion, solvo thermal, hard templating, hydrothermal, mechanochemical and chemical combustion [1]. All of the above physical and chemical methods need some specific instruments and harsh conditions. However we report a novel precipitation method that is more facile, easy, simple and effective to synthesis Co_3O_4 nanoparticles that have not been reported in the literatures.

2 Experimental Details

Materials used:

The materials used for synthesis of undoped and doped Co_3O_4 nanoparticles are cobalt nitrate $Co(NO_3)_2{\cdot}6H_2O$, cupric acetate, Potassium hydroxide (KOH) and Deionized water.

Synthesis Procedure:

I. Method for undoped cobalt nanoparticles: Cobalt nitrate $Co(NO_3)_2{\cdot}6H_2O$ was dissolved in 100 ml. deionized water. Then 100 ml. KOH aqueous solutions were added drop wise to the precursor solution. Pink precipitate appeared immediately which easily to oxidized by air and low heat or weak oxidizing agents to $Co(OH)_3$. The dark brown precipitate was separated and washed with deionized water and dried in an oven at 110 °C for 20 h. For the preparation of

cobalt oxide Co_3O_4, the dark brown cobaltic hydroxide was heated at 100 °C for 3–4 h.

Reaction Occur [1]:

$$\begin{aligned} Co(No_3)_2{\cdot}6H_2O + KOH &\rightarrow Co(OH)NO_3 + KNO_3 \\ Co(OH)NO_3 + KOH &\rightarrow Co(OH)_2 + KNO_3 \\ 4Co(OH)_2 + O_2 + H_2O &\rightarrow 4Co(OH)_3 \\ 6Co(OH)_3 &\rightarrow 2Co_3O_4(s) + 9\,H_2O(g) + 1/2O_2(g) \end{aligned}$$

Flow chart for synthesis process:

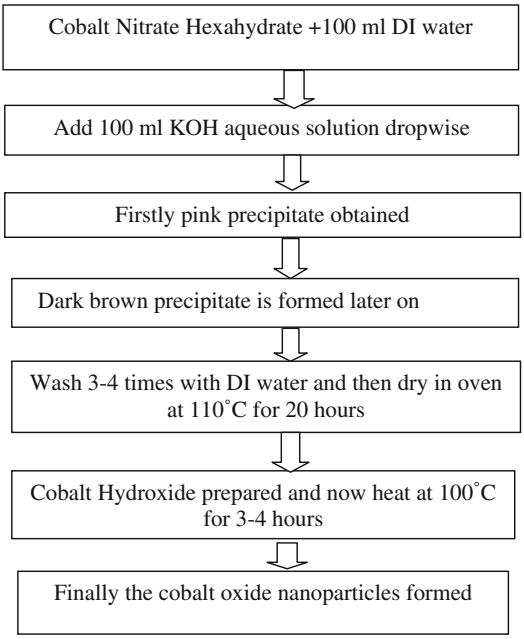

II. Method for copper doped cobalt nanoparticles: Cobalt nitrate $Co(NO_3)_2{\cdot}6H_2O$ was dissolved in 100 ml. deionized water and cupric acetate is dissolved in separate beaker. Now, mix both the solutions. Then 100 ml. KOH aqueous solutions were added drop wise to the precursor solution. Pink precipitate appeared immediately which easily to oxidize by air and low heat or weak oxidizing agents to $Co(OH)_2$. The dark black brown precipitate was separated and washed with deionized water and dried in an oven at 110 °C for 20 h. For the preparation of cobalt oxide Co_3O_4, the dark brown cobaltic hydroxide was heated at 100 °C for 3–4 h.

3 Characterization

3.1 X-ray Diffraction

Pure and Copper doped cobalt oxide nanoparticle were characterized with the XRD technique diffraction using panalytical Xpert Pro system using Cu as anode with Kα (λ = 1.545 Å). XRD technique was used to determine the crystallinity and particle size of the sample.

3.2 FTIR Technique

FTIR characterization was performed with system Thermo scientific Nicolet IS10. Samples were analyzed with KBr method. FTIR spectra of sample in wave number range from 500 to 4000 cm^{-1}.

4 Results and Discussion

4.1 X-ray Diffraction

To investigate the crystalline structure of Cu doped Co_3O_4 nanoparticles were analyzed with X-ray diffraction. Figure 1 showed the XRD pattern of the final products obtained using co precipitation method. XRD pattern shows the intact structure after copper doping. It was observed that crystalline size decreases as the content of Copper increases. The result was collected in 2Θ range of 10°–80°, with a step size 0.02° and scan step size 2°. Almost all of peaks intensities of (111), (220), (311), (222), (400), (422), (511), (440), (622), (533) can be perfectly indexed to a pure cubic phase (space Group: Fd3m) of Co_3O_4 (a = 8.0840A) reported in the literature (JCPDS 74-2120) [11].

The crystallite size of Co_3O_4 nanoparticles is calculated by Scherer formula. The crystallite size from Scherer formula is calculated by using the equation,

$$d = 0.91\lambda/\beta\cos\theta$$

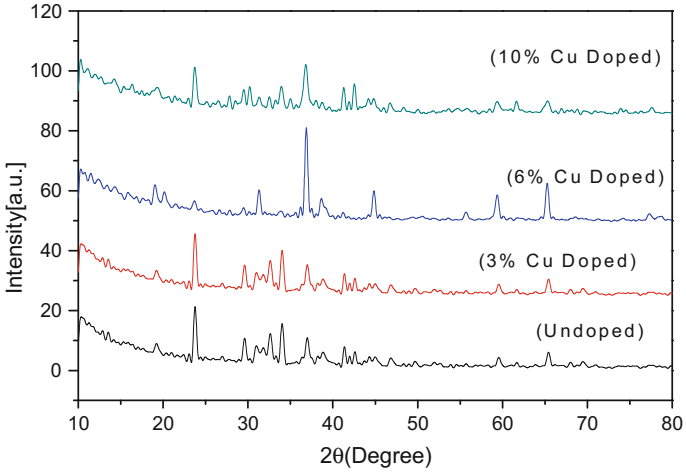

Fig. 1 XRD pattern of Cu doped cobalt oxide

Table 1 Results of X-ray diffraction pattern for Cu doped Co_2O_3

Sample	Mole ratio Cu/Co (%)	2θ	β	D (nm)
1	0	23.8015	0.7680	18.44
2	3	23.7538	0.7680	18.02
3	6	36.8528	1.1520	12.68
4	10	36.7537	1.1520	12.67

where d is the crystallite size, λ is the wavelength of X-ray used, β_{is} the full width half maximum (FWHM) of the metal oxide diffraction peaks and θ is the Bragg angle of diffraction peaks. The crystallite size of nanoparticles is varies from 12 to 18 nm. Hence, the crystallite size of the particles decreases with increase in the dopant concentration (Table 1).

4.2 FTIR

Figure 2 shows the FTIR spectra of copper–cobalt compound oxide nanoparticles. IR spectrum range of particle in wave number from 500 to 4000 cm^{-1}. The bands at 576 and 668 cm^{-1} are attributed to vibration of the Co–O bond due to Co_3O_4. The peaks at ~1400 and ~3500 cm^{-1} should be assigned to –OH stretching and bending modes of water respectively which absorbed by the sample [3].

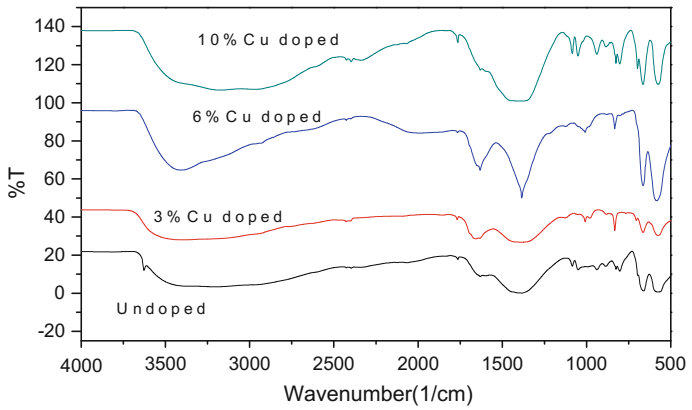

Fig. 2 FTIR spectra of Cu doped cobalt oxide

5 Conclusion

We have clearly demonstrated the importance of the preparation Co_3O_4 nanoparticles using precipitation method. It is concluded that the best method for preparation of Co_3O_4 nanoparticles is the co-precipitation method. We have found that the size of nanoparticles get decrease with increase in dopant concentration.

Acknowledgments Authors are thankful to DST-Nanomission for providing funding.

References

1. S.L. Sharifi et al., Characterization of cobalt oxide Co_3O_4 nanoparticles prepared by various methods: effect of calcination temperatures on size, dimension and catalytic decomposition of hydrogen peroxide. Int. J. Nanosci. Nanotechnol. **9**(1), 51–58 (2013)
2. R.E. Cavicchi, R.H. Silsbee, Coulomb suppression of tunneling rate from small metal particles. Phys. Rev. Lett. **52**(16), 1453 (1984)
3. P. Ball, L. Garwin, Science at the atomic scale. Nature **355**, 761–766 (1992)
4. Z.S. Mehrabadi et al., Synthesis and characterization of Cu doped cobalt oxide nanocrystals as methane gas sensors. Phys. Scr. **84**(1), 015801 (2011)
5. M.S. Niasari, A. Khansari, F. Davar, Synthesis and characterization of cobalt oxide nanoparticles by thermal treatment process. Inorg. Chim. Acta **362**(14), 4937–4942 (2009)
6. G. Zhang, M. Liu, Effect of particle size and dopant on properties of SnO_2-based gas sensors. Sens. Actuators B: Chem. **69**(1), 144–152 (2000)
7. O.K. Tan et al., Nano-structured oxide semiconductor materials for gas-sensing applications. Ceram. Int. **30**(7), 1127–1133 (2004)
8. O.K. Tan et al., Ethanol sensors based on nano-sized α-Fe_2O_3 with SnO_2, ZrO_2, TiO_2 solid solutions. Sens. Actuators B: Chem. **93**(1), 396–401 (2003)

9. M. Ando et al., Optical recognition of CO and H2 by use of gas-sensitiveAu–Co_3O_4 composite films. J. Mater. Chem. **7**(9), 1779–1783 (1997)
10. V.R. Shinde et al., Supercapacitive cobalt oxide (Co_3O_4) thin films by spray pyrolysis. Appl. Surf. Sci. **252**(20), 7487–7492 (2006)
11. H.S. Lee et al., An organometallic approach for microporous organic network (MON)–Co_3O_4 composites: enhanced stability as anode materials for lithium ion batteries. Chem. Commun. **48**(1), 94–96 (2012)
12. W.-Y. Li, L.-N. Xu , J. Chen, Co_3O_4 nanomaterials in lithium-ion batteries and gas sensors. Adv. Funct. Mater. **15**(5), 851–857 (2005)

Single Walled Carbon Nanotubes Persuaded Optimization of the Thermodynamic, Electrical and Electro-optical Characteristics of a Room Temperature Liquid Crystal Display Material "4-Pentyl-4′ cyanobiphenyl"

Rohit Verma, Mukesh Mishra, Ravindra Dhar and R. Dabrowski

Abstract Carbon nanotubes, extreme-aspect ratio cylinders with walls of sp^2 hybridized carbon atoms, have many interesting and highly anisotropic physical properties such as high electrical and thermal conductivity or mechanical rigidity along the tube axis. Nematics are orientationally ordered fluids whose average orientation direction can be manipulated on application of electric and magnetic fields. The self-organizing properties of nematics can be used to align the carbon nanotubes dispersed in them. In the present work, we have dispersed single walled carbon nanotubes (of 2 nm dia) in a room temperature nematic liquid crystal 4-pentyl-4′cyanobiphenyl and carried out many experimental studies.

1 Introduction

Dispersions of carbon nanotubes (CNTs) with liquid crystals have enticed much interest because they pave the way for creating new materials with added functionalities [1–7]. The added functionalities of these compound materials are achieved by combining the self-organisation of a liquid crystal with the characteristics of nanotubes, which exhibit a major difference in electric and thermal

R. Verma (✉)
Department of Applied Physics, Amity Institute of Applied Sciences,
Amity University, Noida, India
e-mail: rverma85@amity.edu

M. Mishra · R. Dhar
Centre of Material Sciences, Institute of Interdisciplinary Studies,
University of Allahabad, Allahabad 211002, India

R. Dabrowski
Institute of Chemistry, Military University of Technology, Warswa 00-908, Poland

V.K. Jain et al. (eds.), *Recent Trends in Materials and Devices*,
Springer Proceedings in Physics 178, DOI 10.1007/978-3-319-29096-6_24

conductivity between their long and short axis. M. Yakemseva and colleagues have studied the influence of CNTs on the physical properties, such as tilt angle, spontaneous polarisation, response time, viscosity, and the strength and frequency of its dielectric relaxation [1]. N. Puech et al. have shown that shortening nanotubes allows the formation of liquid crystals that can easily be oriented under the form of large macroscopic monodomains [2]. They have also shown that the orientational order parameter of single-wall nanotube liquid crystals measured by polarized Raman spectroscopy at the isotropic-nematic transition exceeds by far the value reported in previous experiments. In the present work, we have dispersed single walled CNTs (of 2 nm) in a room temperature nematic liquid crystal 4-pentyl-4′ cyanobiphenyl (5CB) and carried out many experimental studies.

2 Experimental Details

The LC sample was obtained from Prof. R. Dabrowski, Institute of Chemistry, Military University of Technology, Poland. For the dielectric measurements, INSTEC made homogeneous cells of thickness 5.0 μm having sheet resistance less than 25 Ω/Cm^2 have been used. Capacitance (C) and conductance (G) of the cell filled with material were determined in the frequency range 1 Hz–35 MHz using N4L's phase sensitive multi-meter (model PSM 1735) coupled with Impedance analysis interface (model IAI-1257). A measuring electric field of 0.5 V_{rms} has been applied across the sample. Acquired data of C and G in homogeneous alignment of the molecules were used to determine the frequency dependent relative dielectric permittivity (ε') and dielectric loss (ε''). Temperature of the sample for dielectric and optical texture studies has been controlled with the help of a hot stage of Instec (model HS-1) having accuracy of ±0.1 °C and a resolution limit ±0.003 °C. Temperature near the sample has been determined by measuring thermo emf of a copper-constantan thermocouple with the help of a six and half digit multi-meter with the accuracy of ±0.1 °C. Further details about the experimental techniques used for the dielectric measurements are given in our earlier publications [8–11].

3 Results and Discussion

From the thermodynamic studies, we find that the phase transition temperature of the SWCNT dispersed samples is decreased as compared to that of the pure sample.

The temperature dependence of the transverse and longitudinal components of the relative permittivities of the pure and SWCNT dispersed 5CB is shown in Fig. 1. In the temperature variation of permittivity plot a discontinuity is observed at the isotropic (I) to nematic (N) transition. From which we determine the transition temperature. The I-N transition temperature, as obtained from the dielectric studies, for the pure 5CB, 0.02 wt% and 0.05 wt% SWCNT dispersed samples are 35.1,

33.4 and 32.0 °C respectively. Therefore from the dielectric studies, it has been observed that the I-N transition temperature of the SWCNT dispersed samples is decreased. The values of the isotropic to nematic transition temperature (T_{IN}), longitudinal $(\varepsilon_{II}^{'})$ and transverse $(\varepsilon_{\perp}^{'})$ components of the relative permittivities and dielectric anisotropies ($\Delta\varepsilon^{'}$) for the pure, 0.02 and 0.05 wt% SWCNT dispersed samples are also shown in Table 1. From Fig. 1, we can see that both the longitudinal as well as the transverse components of the dielectric permittivity of the dispersed sample decrease as compared to those of the pure sample. From Fig. 1 and Table 1, we can also see that the dielectric anisotropy of the dispersed sample also decrease as compared to those of the pure sample.

Figure 2 shows the dark and bright states of the 0.05 wt% SWCNT and 0.02 wt% SWCNT in 5CB samples. The upper textures are recorded at 0 V applied AC electric field and lower textures are recorded respectively at 1.5 and 1.0 V for the 0.05 and 0.02 wt% dispersed 5CB samples.

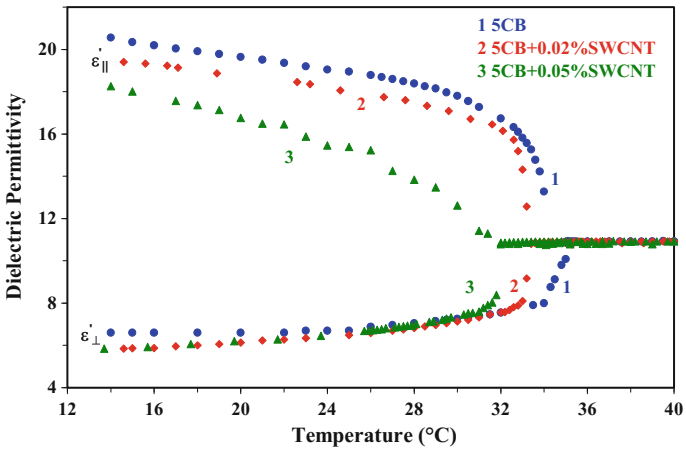

Fig. 1 Temperature variation of the transverse and longitudinal components of dielectric permittivity of the pure and single walled carbon nanotubes dispersed 5CB

Table 1 Values of the isotropic to nematic transition temperature (T_{IN}), longitudinal $(\varepsilon_{II}^{'})$ and transverse $(\varepsilon_{\perp}^{'})$ components of the relative permittivities and dielectric anisotropies ($\Delta\varepsilon^{'}$) for the pure, 0.02 and 0.05 wt% SWCNT dispersed samples

Sample	$T_{I\text{-}N}$	$\varepsilon_{II}^{'}$	$\varepsilon_{\perp}^{'}$	$\Delta\varepsilon^{'}$
Pure 5CB	35.1	20.6	6.6	14.0
5CB + 0.02 wt% SWCNT	33.4	19.4	5.9	13.5
5CB + 0.05 wt% SWCNT	32.0	18.6	5.9	12.7

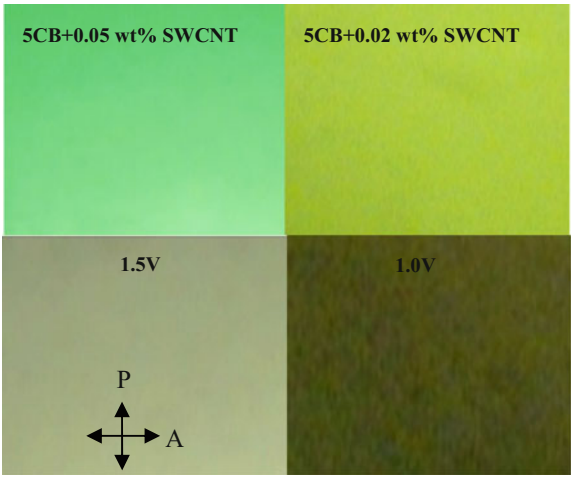

Fig. 2 Optical textures of the SWCNT dispersed samples obtained in the crossed polarizer condition

4 Conclusions

From the above results and discussion, we can conclude that both the components of the permittivity and hence the dielectric anisotropy of the dispersed sample is decreased as compared to those of the pure 5CB. The isotropic to nematic transition temperature of the dispersed sample is decreased as compared to that of pure 5CB. The threshold and switching voltages of the dispersed samples are decreased as compared to those of pure sample.

References

1. M. Yakemseva, I. Dierking, N. Kapernaum, N. Usoltseva, F. Giesselmann, Eur. Phys. J. E **37**, 7 (2014)
2. N. Puech, C. Blanc, E. Grelet, C.Z. Ledezma, M. Maugey, C. Zakri, E. Anglaret, P. Poulin, J. Phys. Chem. C **115**(8), 3272–3278 (2011)
3. J.P.F. Lagerwall, G. Scalia, J. Mater. Chem. **18**, 2890–2898 (2008)
4. C. Zakri, Ch. Blanc, E. Grelet, C. Zamora-Ledezma, N. Puech, E. Anglaret, Ph Poulin, Phil. Trans. A **371**, 20120499 (2013)
5. N. Ould-Moussa, Ch. Blanc, C. Zamora-Ledezma, O.D. Lavrentovich, I.I. Smalyukh, M.F. Islam, A.G. Yodh, M. Maugey, Ph Poulin, E. Anglaret, M. Nobili, Liq. Cryst. **40**, 1628 (2013)
6. N. Puech, M. Dennison, Ch. Blanc, P. van der Schoot, M. Dijkstra, R. van Roij, Ph Poulin, E. Grelet, Phys. Rev. Lett. **108**, 247801 (2012)
7. M. Laudon (ed.), *Nanotechnology 2008: Materials, Fabrication, Particles and Characterization*. Proceedings of the Nano Science and Technology Institute (CRC Press, Cambridge, MA, USA, 2008), p. 1

8. R. Verma, R. Dhar, R. Dabrowski, M. Tykarska, V.K. Wadhawan, M.C. Rath, S.K. Sarkar, J. Phys. D: App. Phys. **42**, 085503 (2009)
9. R. Verma, R. Dhar, R. Dabrowski, M. Tykarska, V.K. Wadhawan, M.C. Rath, S.K. Sarkar, Liq. Cryst. **36**, 1003 (2009)
10. R. Verma, R. Dabrowski, R. Dhar, Liq. Cryst. **42**, 1785 (2015)
11. R. Dhar, R. Verma, V.K. Wadhawan, M.C. Rath, S.K. Sarkar, M. Tykarska, R. Dabrowski, Appl. Phys. Lett. **92**:014108 (1–3) (2008)

Biogenic Silver Nanoparticles Synthesis Route Based on Microalgae

Rupesh Kumar Basniwal and Vinod Kumar Jain

Abstract Now a day's biogenic synthesis of metal nanoparticles have become need of time because of their affordability, biocompatibility, nontoxicity and their economical fabrication. The main driving force for the current research was the algal ability to withstand variable extremes of environmental conditions and several microorganisms like bacteria, virus and fungi for optimal synthesis of silver nanoparticles. Here, we present an economical and biocompatible way for the synthesis of silver nanoparticles (AgNPs) based on *Chlorella* species. In the present study, algal derived extract was more effective instead of using directly algae to synthesize the silver nanoparticles. The synthesized silver nanoparticles were characterized with the help of standard techniques like UV-visible spectroscopy and Dynamic light scattering. Algal derived AgNPs were in the range of nanoscale which supported the biogenic synthesis method for large scale production of the silver nanoparticles at industrial level. Biogenic synthesis pathway of silver nanoparticles helped us in reducing the greenhouse gases (GHG) and its biodegradability and photocatalytic nature makes them perfect entity for waste water treatment.

1 Introduction

Nanotechnology is a branch of science which dealt with synthesizing and processing of particles on nanoscale size (100 nm) for the particular applications. Advanced and unique physico-chemical properties of nanoparticles make them suitable, ideal and desirable for various human welfare purposes. Nanoparticles poses high surface to volume ratio compare to bulk material, which makes it superior over bulk material for electronic, optical, mechanical, magnetic and chemical properties [1–3]. Among all nanoparticles, metal nanoparticles have many attractions because of their tremendous applications like in water purification [4], in

R.K. Basniwal (✉) · V.K. Jain
Amity Institute of Advanced Research and Studies (M&D), Amity University, Noida, Uttar Pradesh, India
e-mail: rkbasniwal@amity.edu

V.K. Jain et al. (eds.), *Recent Trends in Materials and Devices*,
Springer Proceedings in Physics 178, DOI 10.1007/978-3-319-29096-6_25

textile industry, in bio imaging, in sensor and diagnosis, and their novel therapeutic uses in the biomedical fields. Recently silver nanoparticles, which have unique optical, electrical and chemical properties and their diverse applications like in medical field as bio labelling, antimicrobial, as fillers for infected dental cavities, as thin coating on medical devices to prevent bacterial biofilm formation and their applications for textile and water purification industries have also attracted much more attention of innovators and researchers [5–9]. These nanoparticles have been continuously used in mass spectrometry of peptides, colorimetric determination of histidine and ammonia and sensor for DNA sequences due to their fluorescence and surface plasmon resonance characteristics character [10]. Moreover it's toxicity for human system can also be controlled through their optimum size, structure and concentrations. One of the key aspects that control its suitability for the applications is the synthesis protocol. Several physical and chemical methods have been reported in the literature like reduction of silver salt solution, thermal decomposition of silver compound, sonication etc. for producing a palette of designed nanostructures [11–14]. Other methods like laser ablation [15], gamma irradiation [16], and electron irradiation [17] have been also reported in the literature for the synthesis of AgNPs. Mostly reported methods were costly, shows higher energy consumption and involvement of toxic and hazardous chemicals, which may pose potential environmental and biological risks. Despite their ease fabrication their reliability in creating complex morphology of Ag nanoparticles, toxicity and biocompatibility concerns have severely obstructed their application in critical domains, e.g., in medical healthcare field. Many investigators have proposed the use of microorganisms (bacteria, yeast, fungi, micro and macro algae) [18–20], enzymes [21], plant or plant extract [22–24] and flower extract [25] and for clean, green and workable route to overcome from the above mentioned problem. Biogenic synthesis of nanoparticles promises for better control over crystal growth due to their slower kinetics and the method almost reduce or eliminates the use of toxic and hazardous chemicals and decreases the cost of downstream processes, which paved the path for more economical route [26–28]. Despite their preliminary promise, controlling the dispersity and crystallinity as well as obtaining reliable morphology of the AgNPs in such microorganisms remain outstanding challenges [29, 30]. Moreover, our elementary understanding of silver nanoparticles synthesis from microorganism obstruct us to enter into applications of high value based market products. Advantage of algae for biosynthesis of silver nanoparticles over other microorganism is the capacity to function under variable extremes of temperature, pressure and pH. An alga *Chlamydomonas reinhardtii* [31] have been reported for intracellular and extra cellular AgNPs production. Microlage has been reported for intracellular production of gold, latinum, palladium, ruthenium, rhodium and iridium [32]. Cyanobacterial algae like *Calothrix, Anabaena* and *Leptolyngbya,* have been reported to synthesize intracellular Gold (Au), Silver (Ag), Palladium (Pd) and Platinum (Pt) nanoparticles [33]. In this manuscript, we have investigated the potential of a novel algal platform featuring *Chlorella* sp. in producing predictable, standardized Ag NPs. Advantages of this alga over other microorganism are high growth rate and easy to harvest with less cultivation time.

2 Experimental Methodology

Chemicals, Glass Wares and Instruments: All chemicals were of analytical grade and of Merck, Qualigens and Fisher Scientific companies unless otherwise stated, and used as received. These chemicals were procured from local vendor. Mostly glass wares like conical flask, measuring cylinders were of standard companies like Borosil and Rankem. The major instruments were UV-visible spectrophotometer (Shimadzu Co.), Dynamic light scattering (DLS) (Nanoplus Co.), Laminar air flow horizontal (Atlantis Co.), Micro centrifuge (EltekTC4815D Co.) used for the current research.

Culture and Growth Conditions: Algal culture of *Chlorella* sp. was procured from Indian Agricultural Research Institute (IARI), New Delhi, India in the form of agar slant. Batch cultures of *Chlorella* sp. were grown in BG-11 medium [34], which has the following composition (gL^{-1}): $NaNO_3$ (1.5), K_2HPO_4 (0.04), $MgSO_4{\cdot}7H_2O$ (0.075), $CaCl_2{\cdot}2H_2O$ (0.036), Citric acid (0.006), Ferric ammonium citrate (0.006), EDTA (0.001), Na_2CO_3 (0.02) and A5 micronutrients i.e. H_3BO_3 (2.86), $MnCl_2{\cdot}4H_2O$ (1.81), $ZnSO_4{\cdot}7H_2O$ (0.222), $CuSO_4{\cdot}5H2O$ (0.079), $Na_2MoO_4{\cdot}2H_2O$ (0.39) and trace metal mix i.e. Co $(NO_3)_2{\cdot}6H_2O$ (0.0494). The pH for this medium was maintained at 7.0. Subsequent sub-culturing was done on regular basis by using BG-11 culture medium under aseptic conditions. The resultant cultures was maintained at 28 ± 2 °C under continuous illumination with white cool fluorescent light and having 3–4 K Lux light intensity and maintained at 16 h/8 h alternate light and dark hours of cycles. Growth kinetic study of algae was done with the help of UV-visible spectroscopy by recording their optical density (OD) at 680 nm on different time interval.

Biogenic synthesis of silver nanoparticles: The algal culture i.e. *Chlorella* sp. in exponential phases were taken into 50 mL falcon centrifuge tubes and centrifuged at 4000 rpm for 10 min at 4 °C. The pellets were repeatedly washed with deionized water to remove the traces of media and then washed algal pellets were subjected of heat treatment at 100 °C for 5 min in 100 ml deionized water and further sonicated for 5 min and then cooled at room temperature. After cooling they were filtered through Whattman filter paper (No1). This was further used for biosynthesis of silver nanoparticles. Ag NP's biosynthesis was carried out in 250 ml beaker containing 90 ml of 1 mM $AgNO_3$ solution and 10 ml of aqueous algal cell extract. Further this mixture was left at room temperature for 24 h for colour development. The change in colour of solution is indication of generation of silver nanoparticles from reduction of silver nitrate. The stock solution of biogenic synthesized Ag NPs was stored at 4 °C for further reference. In this experiment three sets were prepared, in the first set, AgNPs were synthesized through algal extract, in the second set, AgNPs were synthesized directly through algal cells instead of their filtrate and in the third set i.e. control, without AgNPs.

Silver nanoparticles (AgNPs) characterization: The bio-reduction of $AgNO_3$ to AgNPs was monitored at different time intervals by using UV-Vis spectrophotometer of Shimadzu Company. The 300–800 nm wavelength range was used to

scan the samples for their optical properties. To remove undesired biological or non-biological moieties from freshly synthesized Ag NPs, were centrifuged at high speed i.e. 10,000 rpm for 15 min; further, the pellet was washed with sterile double-distilled water. Centrifugation and washing of AgNPs was carried out continuously until unless they free from all undesirable moieties. The dynamic light scattering (DLS) method was further used for particle size characterization of freshly prepared AgNPs. Before going to analyse the sample through DLS, centrifugation and multiple washing steps were carried out for freshly prepared AgNPs. After proper purification, the sample was put into the cuvette of DLS instruments and then analysed through the standard operating procedure as prescribed in the manual of the instrument.

3 Results and Discussion

Chlorella sp. Platform for Ag NP Synthesis: *Chlorella* sp., a species of the freshwater green algae belongs to genus of *Chlorella*, has provoked sporadic interest as a source of alternative renewable energy fuel i.e. biodiesel, which was produced from transesterification of algal cell extract. Conventionally, the alga was used for nutritional supplement and for the cleaning of environment i.e. absorption of CO_2 from the environment for the photosynthesis process and thus, it was helping in reducing the level of greenhouse gases (GHG). Recently, the patients of hypertension and ulcerative collitis were treated with the help of *Chlorella* cell extract [35]. As this alga has tremendous applications in divergent fields and their rapid growth, composition and inherent resistance mechanism gave idea us to extend their utility to create a robust platform for the synthesis of silver nanoparticle. To examine this hypothesis, the feasibility study was carried out by culturing this alga in a standard BG-11 medium. During the growth of algal culture, three growth phases were noticed i.e. lag phase (adaptation phase), log phase (exponential phase) and stationary phase (static growth phase). This growth study was carried out with the help of UV-Visible spectrophotometer by measuring their absorbance at 680 nm at different time interval. In Fig. 1, lag phase (1–14 days), log phase (15–26 days) and stationary phase (27–34 days) were observed based on their optical density measurement study. The mid-log phase (i.e. on the 21st day) was most suitable phase to harvest the culture for the synthesis of AgNPs due to its highest and optimum activities of the cell biomolecules at this stage. Maximum reduction of the silver nitrates for the generation of silver nanoparticles took place at this stage. In the next step of experiment, the cell extracts of *Chlorella* sp. were prepared from their mid-exponential phase and incubated with 1 mM $AgNO_3$ solution for the production of AgNPs. Silver nanoparticles were produced from this incubation by seizing Ag+ ions from $AgNO_3$ environment with the help of cellular enzymes and then transformed into their respective elemental form i.e. AgNPs. Gradual color change from colorless to yellow and finally brown was observed during the synthesis of AgNPs. Stable brown color showed no further change in

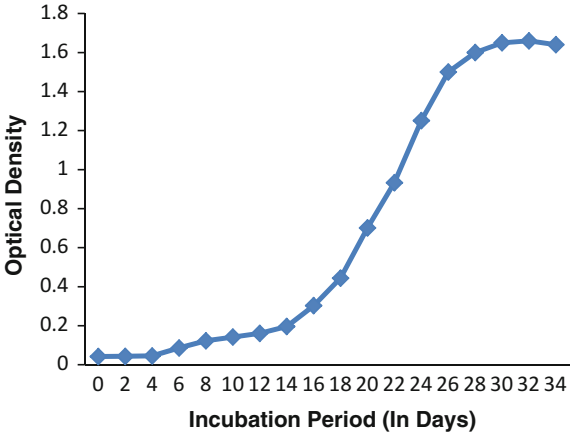

Fig. 1 Growth curve of *Chlorella* sp.

color due to completion of Ag NP synthesis process [36, 37]. The visual observations were confirmed through the UV-vis spectrophotometer absorption readings of the reaction solution.

Characterization of biologically synthesized AgNPs: Before moving for the steps of characterization, the algal derived AgNPs were subjected of purification to get-rid-of from undesired biomolecules [38]. Microbial biosynthesis has important aspect compare to conventional physicochemical fabrication methods, i.e. presence of high level of secreted enzymes and proteins that impart greater stability to the freshly synthesized nanoparticles (NPs) and also reduced the necessity of further downstream processing [39]. The sample analysis readings of algal derived Ag NPs through UV-Visible spectroscopy showed in the Fig. 2. Three samples were analyzed through UV-Vis spectrophotometer: first i.e. AgNPs derived directly from *Chlorella* sp., second i.e. AgNPs derived from cell extracts of *Chlorella* sp. and third i.e. control. In Fig. 2, a flat spectrum line graph was for control i.e. absence of

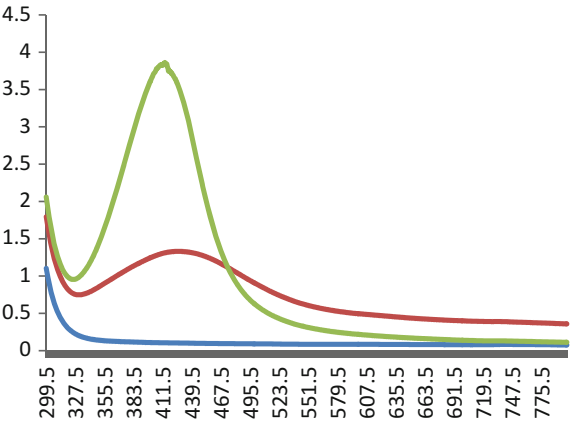

Fig. 2 UV-Vis spectroscopy of Ag-NPs

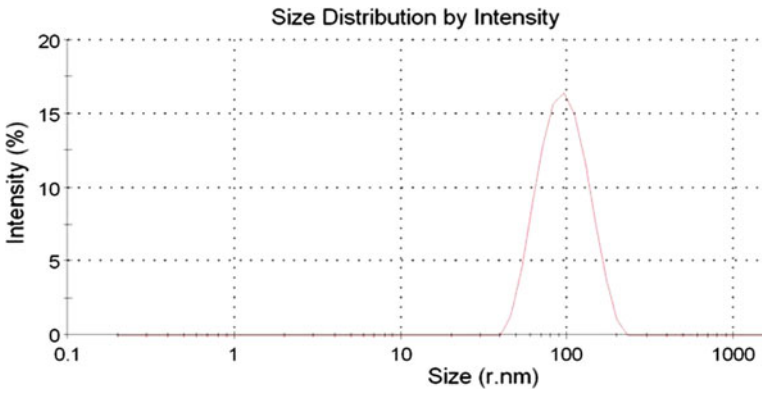

Fig. 3 Dynamic light scattering of Ag NPs

Ag NPs, middle spectrum line graph for synthesized Ag NPs directly from cells of *Chlorella* sp. and upper most spectrum line graph for freshly synthesized Ag NPs from the algal cells extract.

After analysis of these results, we found that effective Ag NPs synthesis were taken place in the cell extracts of *Chlorella* sp. and there absorbance peaks were in the range of 400–500 nm which were according to reported literature. Biologically synthesized AgNPs were further characterized through the dynamic light scattering (DLS) method. To analyse the particle size distribution of AgNPs, the samples were characterized through the well-known DLS technique. The results of the DLS data analysis as showed in Fig. 3, according to which mostly synthesized silver nanoparticles were in the range of 100 nm.

4 Conclusion and Future Scope

Recently, as the demand for clean and nontoxic methods for production of nanomaterial has been raised in few decades, the microbial biosynthesis route for nanoparticles synthesis has been emerged as an intriguing alternative method. Although microorganisms like bacteria and fungi have received considerable attention for the synthesis of nanoparticles of different morphologies, but here we presented a novel algal based platform for the synthesis of silver nanoparticles with appreciable control. The algae-based platform for the synthesis of silver nanoparticles has many advantages over the other microorganism like high growth rate and doesn't require any special organic supplement material for their growth; it requires just H_2O, CO_2 and sunlight for their optimum growth. This helps in reducing the cost of algal culture maintenance and ultimately it reduces the cost of AgNPs synthesis. Future research efforts will be focused on revealing the hitherto untapped pathways for the antimicrobial and photocatalytic mechanism of biologically

synthesized silver nanoparticles. Biologically synthesized AgNPs has a great potential to kill the wide range of diversified bacterial species and its potential as a photocatalytic for recalcitrant organic complexes will have great future impact on waste water treatment at economical level.

Acknowledgments Author (RK) want to express his gratitude to the Founder President of Amity University, Dr. Ashok K. Chauhan, for his continuous encouragement and guidance.

References

1. X. Yang, Q. Li, H. Wang, J. Huang, L. Lin, W. Wang, D. Sun, Y. Su, J.O. Berya, L. Hong, Y. Wang, N. He, L. Jia, J. Nanopart. Res. **12**, 1589–1598 (2010)
2. S. Sinha, I. Pan, P. Chanda, S.K. Sen, J. Appl. Bio. Sci. **19**, 1113–1130 (2009)
3. K.N. Thakkar, S.S. Mhatre, R.Y. Parikh, Nanotechnol. Biol. Med. **6**, 257–262 (2010)
4. R.R. Arvizo, S. Bhattacharyya, R.A. Kudgus, K. Giri, R. Bhattacharya, P. Mukherjee, Chem. Soc. Rev. **41**, 2943–2970 (2012)
5. B. Wiley, Y. Sun, Y. Xia, Chem. Res **40**, 1067–1076 (2007)
6. C.M. Niemeyer, Angew. Chem. Int. Ed. **40**, 4128–4158 (2001)
7. A.Y. Solov'ev, T.S. Potekhina, I.A. Chernova, Russ. J. Appl. Chem. **80**, 438–442 (2007)
8. H.J. Lee, S.H. Jeong, Text. Res. J. **75**, 551–556 (2005)
9. Buzea, C. et al., Biointerphases **2**, MR17–MR71 (2007)
10. K. Vijayaraghavan, S.P. Kamala, Nalini. Biotechnol. J. **5**, 1098–1110 (2010)
11. D. Chen, X Qiao, J. Chen Qiu, J. Mater. Sci. **44**, 1076–1081 (2009)
12. N. Shamim, V.K. Sharma, ACS Symp. Ser. (2013). doi:10.1021/bk-2013-1124
13. J. Xie, J.Y, Lee, D.I.C Wang, Y.P. Ting, ACS Nano, **1**, 429–439 (2007)
14. J. Xie, J.Y. Lee, D.I. Wang, Y.P. Ting, Small **3**, 668–672 (2007)
15. I. Lee, S.W. Han, K. Kim, J. Raman Spectros. **32**, 947–952 (2001)
16. D. Long, G. Wu, S. Chen, Radiat. Phys. Chem. **76**, 1126–1131 (2007)
17. K.A. Bogle, S.D. Dhole, V.N. Bhoraskar, Nanotechnology **17**, 3204–3208 (2006)
18. T. Klaus, R. Joerger, E. Olsson, C.G. Granqvist, Proc. Natl. Acad. Sci. U S A. **96**, 13611–13614 (1999)
19. R.R. Nayak, N. Pradhan, D. Behera, K.M. Pradhan, S. Mishra, L.B. Sukla, B.K. Mishra, J. Nanopart. Res. **13**, 3129–3137 (2011)
20. N. Pradhan, R.R. Nayak, A.K. Pradhan, L.B. Sukla, B.K. Mishra, Nanosci Nanotechnol Lett **3**, 1–7 (2011)
21. R.B. Willner, B. Willner. Adv Mater. **18,** 1109–1120 (2006)
22. R.G. Haverkamp, A.T. Marshall, J. Nanopart. Res. **11**, 1453–1463 (2009)
23. D. Vijayaraj, J. Anarkali, K. Rajathi and S. Sridhar. Int. J. Nanomat. Biostruct. **2**, 11–15 (2012)
24. S. Saha, M.M. Malik, M.S. Qureshi, Int. J. Nanomat. Biostruct. **2**, 1–4 (2012)
25. C. Nethradevi, P. Sivakumar, S. Renganathan, Int. J. Nanomat. Biostruct. **2**, 16–21 (2012)
26. P. Raveendran, J. Fu, S.L. Wallen, J. Am. Chem. Soc. **125**, 13940–13941 (2003)
27. K.N. Thakkar, S.S. Mhatre, R.Y. Parikh, Nanomedicine **6**, 257–262 (2010)
28. P. Premasudha, M. Venkataramana, M. Abirami, P. Vanathi, K. Krishna, R. Rajendran, Bull. Mater. Sci. **38**(4), 965–973 (2015)
29. N. Pantidos, L.E. Horsfall, J. Nanomed. Nanotechnol. **5**, 233 (2014)
30. T. Klaus, R. Joerger, E. Olsson, C.G. Granqvist, Proc. Natl. Acad. Sci. U S A. **96**, 13611–13614 (1999)
31. I. Barwal, P. Ranjan, S. Kateriya, S.C. Yadav, J. Nanobiotech **9**, 56 (2011)
32. T. Luangpipat, I.R. Beattie, Y. Chisti, R.G. Haverkamp. J Nanopart Res (2011)

33. R. Brayner, H. Barberousse, M. Hernadi, C. Djedjat, C. Yepremian, T. Coradin, J. Nanosci. Nanotechnol. **7**, 2696–2708 (2007)
34. R.Y. Stanier, R. Kunisawa, M. Mandel, G. Cohen-Bazire, Bacteriol. Rev. **35**, 171–205 (1971)
35. R.E. Merchant, C.A. Andre, Altern. Ther. Health Med. **7**, 79–91 (2001)
36. N. Jain, A. Bhargava, S. Majumdar, J.C. Tarafdar, J. Panwar, Nanoscale **3**, 635–641 (2011)
37. V. Patel, D. Berthold, P. Puranik, M. Gantar, Biotechnol. Rep. **5**, 112–119 (2015)
38. K. Murugan, B. Senthilkumar, D. Senbagam, S. Sohaibani, Int. J. Nanomed. **9**, 2431–2438 (2014)
39. A.E. Nel, L. Mädler, D. Velegol, T. Xia, E.M.V. Hoek, P. Somasundaran, F. Klaessig, V. Castranova, M. Thompson, Nat. Mater. **8**, 543–557 (2009)

Effect of Swift Heavy Ion Irradiation on the Structural and Optical Properties of CdO Thin Films

Sanjeev Kumar, Sugandha Sharma, Fouran Singh and A. Kapoor

Abstract In this study, effects of Ni^{7+} beam irradiation on structural and optical properties of cadmium oxide thin films deposited on indium tin oxide (ITO) coated glass substrates using sol-gel spin coating technique have been reported. Structural properties of irradiated films (fluence 3×10^{12} ions/cm^2) have been studied by glancing angle X-ray diffraction (GAXRD). The films exhibit cubic crystal structure and a high degree of crystallinity. UV-Visible absorption spectra reveal that Ni^{7+} beam irradiation causes an increase in blueshift of absorption edge for CdO pristine films, leading to enhancement in band gap energy as indicated by Tauc's plot studies.

1 Introduction

Transparent conducting oxide (TCO) thin films, such as indium oxide, tin oxide, zinc oxide, and cadmium oxide, have assumed great importance due to their high optical transmittance in the visible region, as well as superior electrical properties [1, 2]. These films find interesting applications in devices such as gas sensors, phototransistors, solar cells, transparent conducting electrodes and surface acoustic wave devices [3, 4]. In recent years, there has been a rising interest in the development of cadmium oxide based structures, which besides the merits of a good TCO also possesses an optimum band gap of 2.3 eV. For deposition of CdO thin films, we have used sol-gel technique based spin coating method. This method is a low cost atmospheric process easily adaptable to industrial use. The key to sol-gel method is in preparation of a stable solution for deposition of thin films. Irradiation

S. Kumar (✉) · S. Sharma · A. Kapoor
Department of Electronic Science, University of Delhi, South Campus, New Delhi 110021, India
e-mail: sanjeevkumarphy@gmail.com

S. Kumar · F. Singh
Materials Science Group, Inter University Accelerator Centre, Aruna Asaf Ali Marg, New Delhi 110067, India

V.K. Jain et al. (eds.), *Recent Trends in Materials and Devices*,
Springer Proceedings in Physics 178, DOI 10.1007/978-3-319-29096-6_26

of these films by an ion beam radiation induces damages which are material dependent and are expected to change the structural and optical properties of such metal oxide films. The main ingredient of metal oxide films is oxygen and it is highly vulnerable when exposed to ion beam radiation. Therefore, it will be of scientific and technological interest to investigate the effects of ion beam irradiation on CdO thin films.

The CdO thin films were irradiated by 100 meV Ni^{+7} ions using the 15UD Pelletron Accelerator facility at Inter University Accelerator Centre (IUAC), New Delhi. The Electronic energy loss (Se) and nuclear energy loss (Sn) was estimated from SRIM & TRIM simulations. The focused ion beam was scanned over an area of 1 cm^2 with a fluence of 3×10^{12} ions/cm^2 and the beam current was kept constant 1 pnA (particles nanoampere). In this study, modifications in structural and optical properties, expected mainly due to the electronic excitation induced by swift heavy ion (SHI) irradiation, were investigated.

2 Experimental Details

The precursor material used for sol preparation was cadmium acetate dihydrate, Cd $(CH_3COO)_2 \cdot 2H_2O$ (purity grade 99.99 %). 2-methoxyethanol and monoethanolamine (both procured from Merck chemicals, India) were used as the solvent and stabilizer, respectively. The cadmium precursor solution was prepared by dissolving cadmium acetate dehydrate in 2-methoxyethanol so as to achieve an optimum concentration of 0.2 mol/l. The solution was magnetically stirred for 120 min resulting in a transparent and clear precursor, which was further related for 48 h. An important advantage of this method is that it yields stable solutions, while requiring no heating or long mixing times during preparation of solutions.

The film was deposited on glass substrate previously cleaned using organic solvents and ultrasonic agitator. The substrate was degreased by agitating first in petroleum ether for 15 min, then in acetone for 10 min and finally in methanol for 10 min using an ultrasonic agitator. The substrate was washed thoroughly using deionized water. Finally, substrate was dried for 20 min in a clean and dust free oven maintained at 80 °C. The sol was coated on the surface of substrate, with the substrate holder of spin coating unit rotating at a fixed speed of about 3000 rpm for duration of 25 s. The coated films were first dried at 120 °C for 12 min and then fired in air for 25 min in a tubular furnace maintained at 500 °C. Preparation of sol and deposition of films was carried out under approximately identical laboratory conditions. The films obtained were smooth and homogeneous. Films of higher thicknesses were obtained by repeating the process of coating and drying [5].

3 Results and Discussion

The structural analysis of 100 meV Ni^{7+} ion irradiated films was carried out using XRD technique. Pristine GAXRD patterns (Fig. 1) reveal three prominent peaks [(111), (200) and (220)] corresponding to the cubic structure of CdO (JCPDS-097512). From Fig. 1, it is observed that intensity of diffraction peaks increases for the films irradiated at 3×10^{12} ions/cm^2 fluence, with respect to pristine films. The increase in peak intensity is an indicator of improvement in crystallinity of CdO thin films. The structural modifications induced by SHI irradiation can be explained by total energy deposited in electronic excitations or ionizations in the films by energetic ions. The imparted energy of the incoming ions in these films at higher fluence might result in overlapping of tracks to cause lattice disordering inside large grains. This is due to the excess of cadmium resulting from dissociation of CdO during evaporation. The absorption spectra of films irradiated 3×10^{12} ions/cm^2 and pristine films have been shown in Fig. 2 (Table 1).

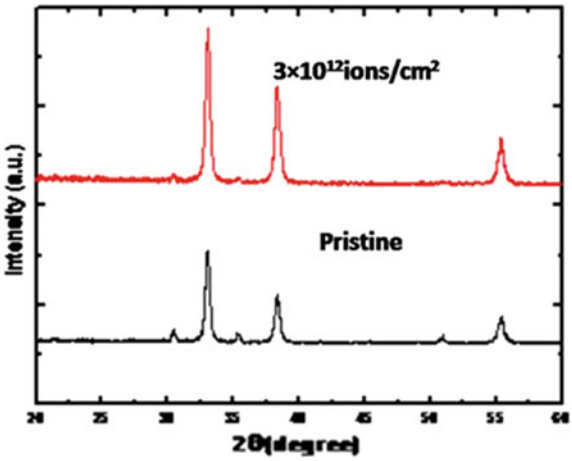

Fig. 1 GAXRD patterns of pristine and irradiated (fluence 3×10^{12} ions/cm^2) CdO films

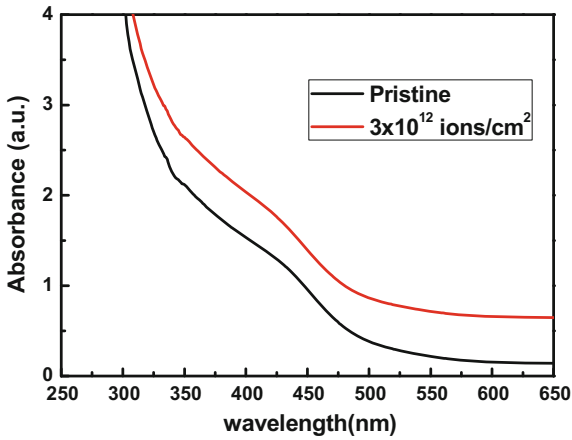

Fig. 2 Absorbance spectra of pristine and irradiated (fluence 3×10^{12} ions/cm^2) CdO films

Table 1 Significant parameters obtained from GAXRD analysis [6]

Irradiation (Ni ion/fluence ions/cm^2)	Average crystalline size (nm)	Dislocation density (nm^{-2})	Interplanar distance (Å)	Band gap (eV)
Pristine	14 ± 0.3	0.511	3.74	2.54 ± 0.01
3×10^{12}	17 ± 103	0.543	3.63	2.59 ± 0.01

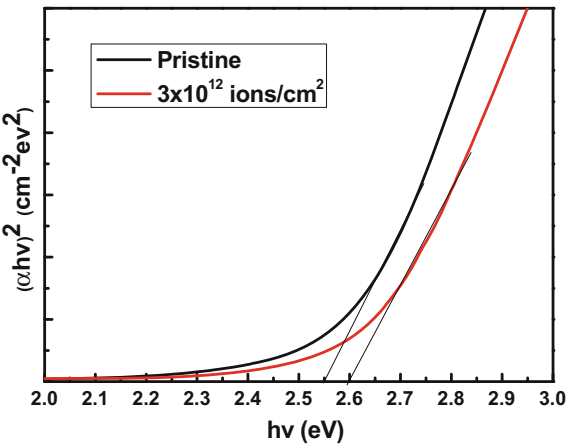

Fig. 3 Band gap of pristine and irradiated (fluence 3×10^{12} ions/cm^2) CdO films

The graphs suggest that there is no significant change in band edge after irradiation but absorption increases in the visible region. This implies that the basic crystal structure does not change. In other words, the lattice is not amorphized, since this structural transformation generally leads to a reduction in energy band gap of semiconductors. Absorption at low energy is ascribed to transitions between the intra-gap levels related to the defects such as oxygen vacancies, cadmium interstitial, etc. This is in good agreement with XRD results, since no shift in peak position is observed. We also noticed an increase in optical absorption in visible region in case of irradiated films, which may be due to creation of irradiation induced defects such as anti-site oxygen and oxygen vacancies in the film. Figure 3 demonstrates that the bandgap of ZnO shows a variation from 2.54 ± 0.01 to 2.59 ± 0.01 eV as a function of fluence. The possible reason for this incremental change in optical band gap can be traced to the change in the grain size of films [6].

4 Conclusions

We have investigated deposition of highly crystalline CdO thin films using sol-gel spin coating technique, which were irradiated with 100 meV Ni^{7+} ion beams in order to study the modification of structural, optical properties. XRD and UV–visible absorption studies show that growth of pristine films leads to the formation

of narrow-sized distribution of particles in the film. We observed that for irradiated films (ion fluence 3×10^{12} ions/cm^2), the formation of point defects and/or disorder is dominant over the grain growth. From XRD results, we conclude that the basic lattice structure of CdO does not change after 100 meV Ni^{7+} ion irradiation. An increase of 0.05 eV in band gap is observed for irradiated films with respect to pristine films. The observed modification in structural and optical properties is understood in terms of thermal spike model.

References

1. S.Y. Kim, K. Hong, J.L. Lee, K.H. Choi, K.H. Song, K.C. Ahn, Solid State Electron. **52**, 1 (2008)
2. Z.X. Yang, Y. Huang, G.N. Chen, Z.P. Guo, S.Y. Cheng, S.Z. Huang, Sens Actuators **140**, 549 (2009)
3. C.H. Kwon, H.K. Hong, D.H. Yun, K. Lee, S.T. Kim, Y.H. Roh et al., Sens. Actuators B **25**, 610 (1995)
4. R. Ferro, J.A. Rodriguez, O. Vigil, A. Morales-Acevado, G. Contreras-Puente, Phys Status **177**, 477 (2000)
5. F. Singh, S. Kumar, A. Kapoor, J. Appl. Phys. **112**, 073101 (2012)
6. S. Kumar, F. Singh, A. Kapoor, Optik **127**, 2055–2058 (2016)

Synthesis, Structural and Optical Properties of Transition Metal Doped ZnO Nanoparticles

Sidra Aijaz, Arham Shareef Ahmed, R.S. Pandey and Ravi Kant Choubey

Abstract Metal oxide Ni doped ZnO nanoparticles were synthesized through microwave method. Structural studies were carried out using XRD, and FTIR spectroscopy. XRD results clearly show the formation of all samples in single phase without any impurity and the average crystallite size has been observed to vary between 20.10 and 14.38 nm. Band at 380 cm^{-1} observed in FTIR spectrum is attributed to the Zn–O stretching confirms the formation of ZnO nanoparticles.

1 Introduction

This paper reports the modification induced in structural and optical properties of Ni doped ZnO nanostructure synthesized by microwave method. ZnO is gaining more interest because it is an abundant, inexpensive and non-toxic material as compared to others. ZnO is a II–VI semiconductor material with a wide band gap (3.37 eV) [1] and the large exciton binding energy (60 meV) at room temperature [2]. Zinc oxide nanoparticles are used in a variety of applications such as UV absorption, antibacterial treatment, catalyst, photo catalyst and additive in many industrial products. It is also used in the fabrication of solar cells, gas sensors, luminescent materials, transparent conductor, heat mirrors and coatings [2, 3].

S. Aijaz (✉) · R.S. Pandey · R.K. Choubey
Department of Applied Physics, Amity Institute of Applied Sciences, Amity University, Sector-125, Noida 201 303, India
e-mail: khanfaraz73@gmail.com

A.S. Ahmed
Department of Applied Physics, Aligarh Muslim University, Aligarh, India

V.K. Jain et al. (eds.), *Recent Trends in Materials and Devices*,
Springer Proceedings in Physics 178, DOI 10.1007/978-3-319-29096-6_27

2 Experimental Details

First, specific amount of Zinc acetate [Zn $(CH_3COO)_2 \cdot 2H2O$] and Zinc nitrate [Zn $(NO_3)_3 \cdot 9HO$] were dissolved in 200 ml of distilled water. The Ni molar contents in above samples were 0, 3, and 5 %. Required amount of Potassium hydroxide [KOH] (11 g) was added in above solution drop by drop. Then the solution was continuously mixed under microwave oven at 40 power for 20 min. The resulting suspension was continuously stirred for about 20 min a white coloured solution was founded. After that it was centrifuged at 4000 rpm and washed 3 times with water and 3 times with ethanol to eliminate organic pollutions. After washing, the nanoparticles were dehydrated at 80 °C for 24 h in an oven then grinded for uniformities of the powder. Finally, Ni doped ZnO nanoparticles were obtained.

3 Results and Discussion

3.1 X-ray Analysis

Figure 1 shows X-ray diffraction patterns of pure and Ni doped ZnO samples. All XRD patterns were analyzed using Powder X software which shows that all samples are in single phase with hexagonal structure and there are no anomalous peaks related to Ni metal Clusters or Ni oxides secondary phases.

3.2 Optical Properties

ZnO nanoparticles exhibit a fragile near band edge UV emission peak centered at 377.55 nm. The excitonic absorption point as arranged without and nickel doped samples become expansive as the concentration adds. It can be studied clearly from Fig. 2 which justifies that the absorbance decreases when the concentration of Ni adds from 0 to 5 %. In uniformity to determine the direct band gap we consumed the Tauc relation $\alpha\, h\nu = C\,(h\upsilon - Eg)^{\beta}$.

3.3 SEM Analysis

The image of pure SEM and Ni substituted SEM samples are presented in given Fig. 3.

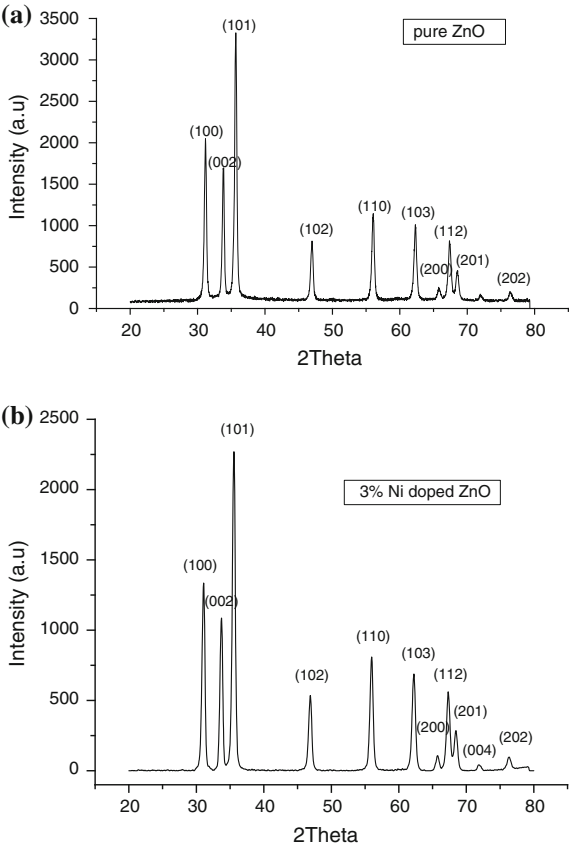

Fig. 1 **a** X-ray diffraction pattern of pure ZnO powder. **b** X-ray diffraction patterns of Ni doped ZnO powder

3.4 FT-IR Studies

In Fig. 4 FTIR spectra of pure and Ni doped ZnO nanoparticles are shown. The peak at 3400 cm^{-1} is the stretching vibration of the O-H bond. The absorption bands experimental in the ranges from 612 to 707 cm^{-1} are attached to the stretching forms of Zn-O (Liu et al.) in the tetrahedral and octahedral coordination correspondingly. The shift in values of vibration frequencies from 402 and 732 cm^{-1} is suggestive of incorporation of Ni in octahedral and tetrahedral sites obtainable in Wurtzite structure.

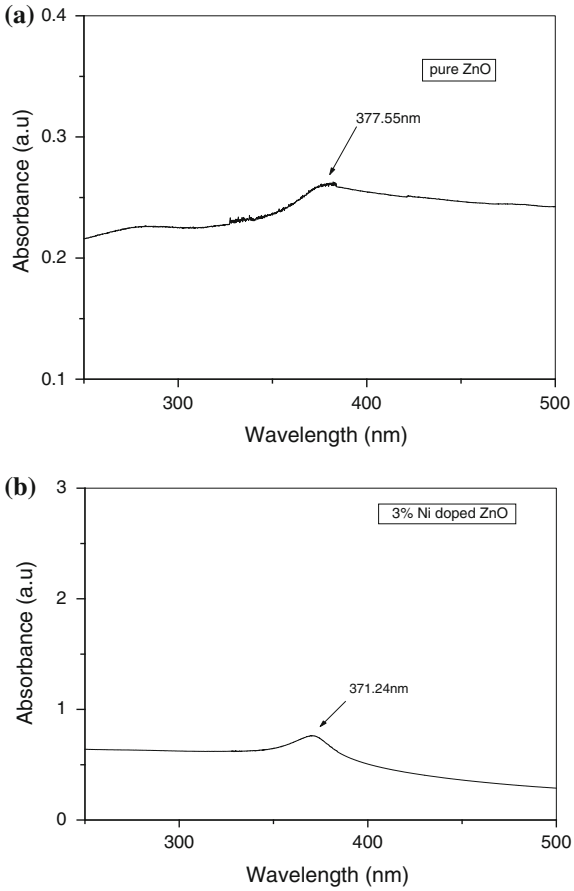

Fig. 2 **a** UV-Vis absorption spectra of pure ZnO. **b** UV-Vis absorption spectra of 3 % Ni doped ZnO

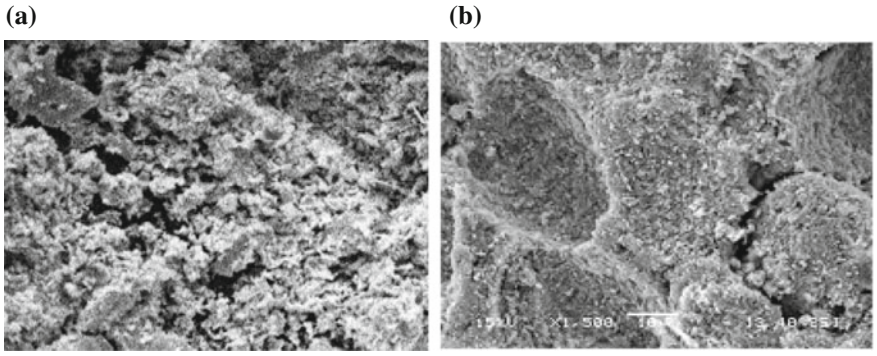

Fig. 3 **a** SEM image of Ni doped ZnO. **b** SEM of pure ZnO

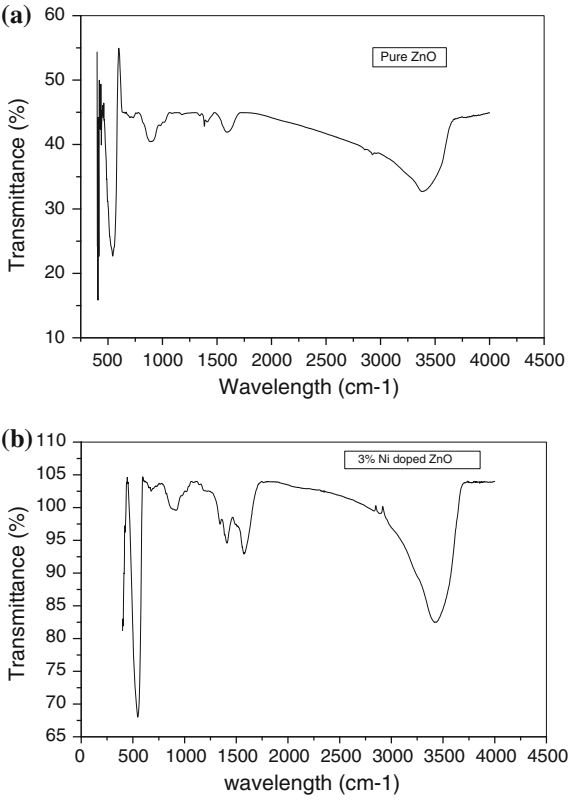

Fig. 4 **a** FTIR spectrum of Pure ZnO. **b** FTIR spectrum of 3 % Ni doped ZnO

4 Conclusions

In this work we have effectively synthesize (0, 3, and 5 %) Ni doped ZnO nanoparticles. Zinc Oxide was manufactured by microwave method a white colour ZnO precipitate was found. Categorization analysis was approved out consuming XRD, UV-Visible, FTIR and SEM. for phase identification and they presented quantity of impurities and structure depending on the peaks current in the structure; XRD pattern used. ZnO was instigating to be hexagonal in construction there is no variation in hexagonal construction. To find particle size of ZnO, XRD Scherer's formula is used ($0.9\ \lambda/(B\cos\theta)$). Crystal size and lattice constants were detected to decrease with increase concentration of Ni dopant. To find agglomeration, SEM was used for microstructure learning. Nanoparticles presented small quantity of agglomeration. We have successfully plot FTIR and the optical studies have been approved out using optical absorbance.

References

1. M.L. Fuller, A method of determining the axial ratio of a crystal from X-ray diffraction data: the axial ratio and lattice constants of zinc oxide. Science **70**, 196 (1929)
2. G.C. Yi, C. Wang, W. Park, ZnO nanorods: synthesis, characterization and applications. Semicond. Sci. Technol. **20**, 22–34 (2005)
3. Z.K. Tang, G.K.L. Wang, P. Yu, M. Kawasaki, A. Ohtomo, H. Koinuma, Y. Segawa, Room-temperature ultraviolet laser emission from self-assembled ZnO microcrystalline thin films. Appl. Phys. Lett. **72**, 3270 (1998)

Synthesis and Characterization of Cadmium Doped ZnO Nanoparticles

Suman, Sonia, Vinod Kumar, Sacheen Kumar and Dinesh Kumar

Abstract Cd doped ZnO ($Zn_{1-x}Cd_xO$, x = 0, 0.03, 0.06 and 0.09) were prepared via a chemical co-precipitation method using Zinc Acetate, Cadmium Acetate and Sodium Hydroxide at 50 °C. Hydrate nanoparticles were annealed in air at 300 °C for 3 h. Effect of doping is investigated with the help of X-ray Diffraction Technique, UV Visible spectroscopy, FTIR and RAMAN spectroscopy The result of X-ray Diffraction shows the change in nanoparticles size. The XRD measurement reveals that the prepared nanoparticles have different microstructure without changing a hexagonal wurtzite structure. We analyzed with the study of tauc plots that band gap decreases with the increment of doping concentration.

1 Introduction

Among the important metal oxides, zinc oxide (ZnO) has fascinated widespread interest because of its attractive properties such as direct wide band gap i.e., 3.2 eV and large exciton binding energy i.e., 80 eV high chemical stability and environment-friendly applications. [1] Due to these engrossed properties ZnO is highlighted in the field of optoelectronic devices. [2, 3]. The main focus for the application of ZnO materials is in optoelectronic devices, which means that it is important to modulate the band gap. Doping by different elements is an efficient way to tune the band gap of Zinc oxide [4].

Undoped ZnO is not stable at high temperature; this limitation can be minimizing with the help of doping elements. After doping conductivity of ZnO often increases. The effect of dopant element completely depends on its electro negativity and difference between ionic radius of zinc and the dopant material. With the help of doping elements Mg, Mn, Fe and Al band gap tuned in the range of 2.9–3.8 eV. Among all these doping elements, cadmium is a appropriate material for fine-tuning

Suman · Sonia · V. Kumar · S. Kumar (✉) · D. Kumar
Department of Electronics Science, Kurukshetra University,
Kurukshetra, Haryana 136119, India
e-mail: sacheen3@gmail.com

V.K. Jain et al. (eds.), *Recent Trends in Materials and Devices*,
Springer Proceedings in Physics 178, DOI 10.1007/978-3-319-29096-6_28

the band gap of ZnO and the properties of cadmium doped zinc oxide ($Zn_{1-x}Cd_xO$) have not yet been studied clearly, though it is one of the promising candidates in the field of optoelectronics and also for the fabrication of ZnO based devices [5].

CdO has very narrow bandgap of 2.3 eV but ZnO has a wide band gap of 3.2 eV so which possesses large exciton binding energy (60 meV) [6, 7].

ZnO has a wurtzite structure and Cd has the rock-salt structure, which is incompatible with each other. So heavy doping of Cd in ZnO is not stable. Here, in the present work we have investigated the optical and structural properties of lanthanum doped ZnO.

After experimental details of this research, photo catalytic property of zinc oxide in the terms of optical transmittance and band gap has been improved. The optical property investigates using transmission spectra in 200–900 nm wavelength range.

2 Experimental Details

Aqueous solution of 0.1 M of zinc acetate $(CH_3COO)_2Zn \cdot H_2O$ is dissolved in DI water by vigorous and continuous stirring. Then 3, 6 and 9 at.% cadmium acetate was added in the Zinc precursor solutions. About 0.3 M of NaOH is dissolved in DI water in another beaker which is then mixed in the above solutions. The final solution was stirred for 1 h and white precipitate are formed which are then washed 3–4 times with DI water and last washing with ethanol and nanoparticles are collected. At last, solution is dried in oven to form the oxide particles and to remove the impurity the process of annealing is done at 300 °C for 3 h.

3 Characterization Techniques

The structural and phase formations were identified by X-ray diffraction and done by using Panalytical Xpert Pro. Cu was used as anodic material with wavelength = 1.54 Å. The result was collected in 2θ range of 10–90°, with a step size 1°. The average crystalline size (d) has been calculated by using Scherer's relation:

$$d = 0.9\lambda/\beta \cos\theta \tag{1}$$

where, λ is wavelength of X Rays, β is (FWHM) Full width Half Maximum and θ is Bragg angle of diffraction peak.

For UV-Vis we used the Perkin Elmer Lambda 750 model by using integrated sphere detector. Quartz sample holder was used for holding the sample, in the range of UV-Vis wavelength 200–800 nm.

For FTIR we used the PerkinElmer FTIR model SPECTRUM 65 system. The dried sample (1–5 %) was mixed with KBr (95–99 %). Then we make the pellet of sample before performing the scan from wave number 4000–400 cm^{-1}.

4 Results and Discussion

4.1 Structural Properties

To investigate the crystalline structure of Cd doped ZnO nanoparticles were analyzed with X-ray diffraction. Figure 1 shows the XRD pattern of doped and pure ZnO nanoparticles which is prepared from co-precipitation method. XRD pattern shows the intact structure after cadmium doping.

It was observed that crystalline size decreases as the content of cadmium increases. The decrement in crystalline size is mainly due to the formation of Cd–O–Zn on the surface of Cd doped ZnO nanoparticles [8]. In 9 atm% concentration small peaks nearby 101 and 110 is shown which is due to secondary phase formation at higher concentration of cd doing. The highest intensity peak of plane 101 is getting narrow due to stress release at increase in doping concentration.

4.2 Optical Properties

Optical properties were investigated by UV visible spectroscopy.

Figure 2 shows the optical spectra of Undoped and doped ZnO with different cadmium concentration (3, 6, 9 %). Direct band gap is calculated by the formula:

$$(\alpha h\nu)^2 = A\left(h\nu - E_g\right) \tag{2}$$

Table 1 shows effect of concentration of cadmium on the band gap. Optical reflectance measurements showed a substantial shift of the band gap, which can be interpreted in terms of band gap modulation due to Cd doping. With the increase in Cd concentration, the band gap decreased from 3.26 to 3.17 eV (Table 2).

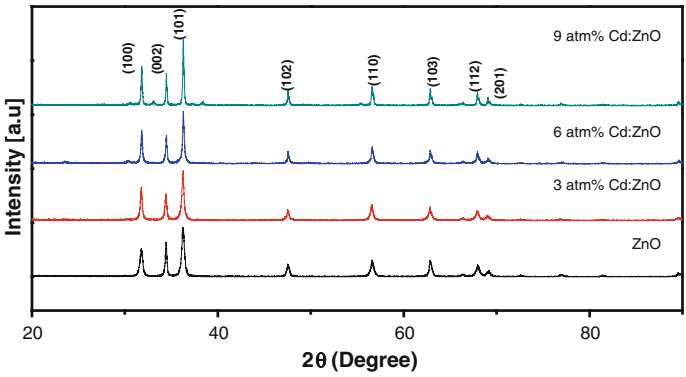

Fig. 1 XRD patterns of Cd-doped ZnO nanoparticles prepared by Co-precipitation method

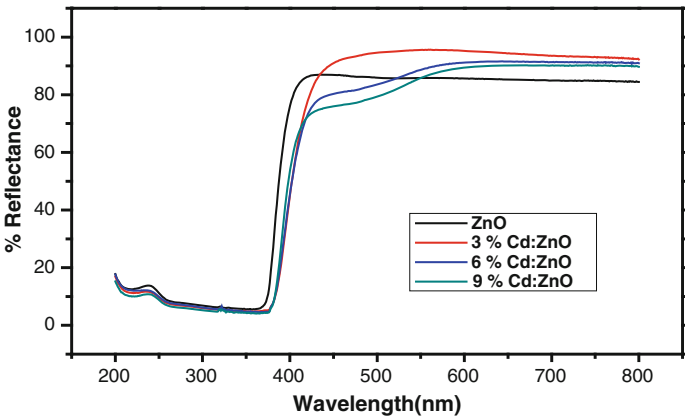

Fig. 2 UV Reflectance spectra of Cadmium doped and Undoped ZnO

Table 1 Comparison of crystalline size of pure and doped ZnO at different concentration

Sr. no.	Sample	Crystalline size
1	Pure ZnO	14.754
2	3 at.% Cd doped ZnO	8.9008
3	6 at.% Cd doped ZnO	9.6221
4	9 at.% Cd doped ZnO	3.3125

Table 2 Comparison of band gap of pure and doped ZnO at different concentration

Sr. no.	Sample	Band gap (eV)
1	Pure ZnO	3.26
2	3 at.% Cd Doped ZnO	3.22
3	6 at.% Cd Doped ZnO	3.20
4	9 at.% Cd Doped ZnO	3.17

4.3 Vibrational Analysis

FTIR spectra of the entire sample are shown in the Fig. 3. As shown in the Fig. 3 that there was a change in the position and size of IR peaks. The peaks showing that the pure ZnO and Cd doped ZnO have been incorporated in ZnO. The absorption peak at 1500 cm^{-1} for pure ZnO comes from bending vibration of Zn–O–Zn. We doped Cd with ZnO in different concentration. In case of Cd doped ZnO the absorption peaks are observed at 1403, 1409, 1421 cm^{-1} with respect to 3, 6 and 9 %, means when the doping concentration was increased the absorption peak shifted from 1403 to 1421 cm^{-1}. The spectra changes are recognised due to change in the size and shape of the ZnO particles. The peak around 1448 cm^{-1} is appeared due to symmetric and asymmetric stretching vibrations. In pure ZnO broaden peaks was observed at 3475 cm^{-1} which shows the stretching vibration for surface hydroxyl group.

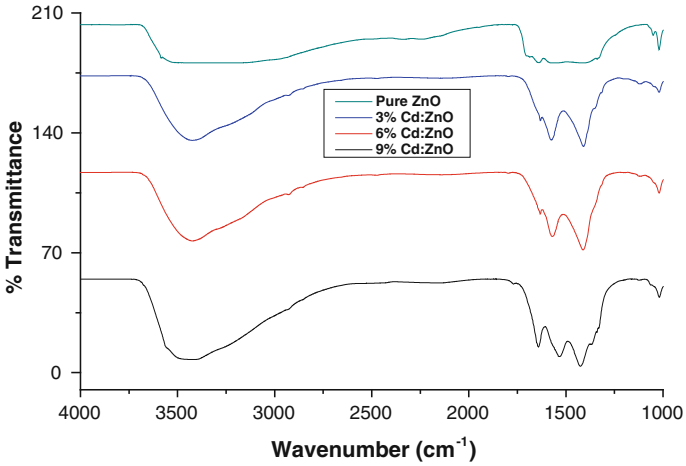

Fig. 3 FTIR of Undoped, doped and co doped ZnO

5 Conclusions

In this study, Cd-doped Zn nanoparticles were prepared by co-precipitation method. The XRD analysis revealed that crystalline size decreases from 14 to 3 nm and band gap tuned from 3.26 to 3.17 eV as Cd concentration increases. In UV Spectroscopy we evaluated that band gap decreases continuously with increasing cadmium concentration. Shifting of broaden peak was observed from 3438 to 3414 cm^{-1} with FTIR analysis i.e. there were clear changes in the positions, sizes and shapes of IR peaks indicating that doped (Cd) might have been incorporated in ZnO host. Raman spectroscopy results also concluded.

References

1. C. Cheng, R. Xin, Y. Leng, D. Yu, N. Wong, Inorg. Chem. **47**, 7868 (2008)
2. C.W. Sun, P. Xin, Z.W. Liu, Q.Y. Zhang, Appl. Phys. Lett. **88**, 221914 (2006)
3. Ü. Özgür, Y.I. Alivov, C. Liu, A. Teke, M. Reshchikov, S. Doğan, H. Morkoc, J. Appl. Phys. **98**(4), 041301 (2005)
4. F.P. Koffyberg, Phys. Rev. B: Solid State **13**, 4470 (1976)
5. F. Wang, Z.Z. Ye, D. Ma, L. Zhu, F. Zhuge, J. Cryst. Growth **283**, 373 (2005)
6. L.F. Dong, Z. Cui, Z.K. Zhang, Nanostruct. Mater. **8**, 815 (1997)
7. H. Cao, J.Y. Xu, D.Z. Zhang, S.H. Chang, S.T. Ho, E.W. Seeling, X. Liu, R.P.H. Chang, Phys. Rev. Lett. **84**, 5584 (2000)
8. S. Anandan, A. Vinu, K.S. Lovely, N. Gokulakrishnan, P. Srinivasu, T. Mori, V. Murugesan, V. Sivamurugan, K. Ariga, Photocatalytic activity of La-doped ZnO for the degradation of monocrotophos in aqueous suspension. J. Mol. Catal. A: Chem. **266**(1), 149–157 (2007)

Synthesis and Characterization of Yttrium Doped Zinc Sulphide Nanoparticles

Swati Sharma, Chitkara Natasha and Avinashi Kapoor

Abstract Pure zinc sulphide (ZnS) and Yttrium(Y) doped ZnS nanoparticles (5 and 10 wt%) have been synthesized via low cost chemical co-precipitation method. SEM, XRD and Photoluminescence spectroscopy have been employed to study structural and optical properties of the as prepared nanoparticles. Average crystallite size calculated from XRD is found to be 2–3 nm. Increase in Y doping concentration causes increase in crystallinity of the lattice and reduction in defects. Photoluminescence peak is observed at 361 nm which red shifts to 367 nm with incorporation of yttrium ions. PL intensity is quenched with increase in doping concentration.

1 Introduction

Study of nanomaterials is gaining popularity in the scientific community with each passing day due to their exciting applications. II–IV semiconductor nanomaterials have been extensively investigated for their unique properties and major applications in the field of optoelectronics, sensors, photovoltaic cells, biosensors, etc. [1, 2]. Among these, ZnS is one of the most important material as it is non toxic and has a wide band gap of $\sim$3.67 eV [3]. ZnS is a good host material for doping and optical properties of various ZnS doped nanocrystals have been reported by many groups [4]. Recently ZnS nanoparticles doped with transition and inner transition metals have received much attention as a particular class of luminescent materials. Doping and co-doping with Cu, Co, Mn, Cd, Pb, Ni, Eu and Sm have been reported in the literature for their unique photoluminescence properties [5].

S. Sharma (✉) · A. Kapoor
Department of Electronic Science, University of Delhi, South Campus, Benito Juarez Marg, New Delhi 110021, Delhi, India
e-mail: sharma.swati1507@gmail.com

C. Natasha
Maharaja Agrasen College, University of Delhi, New Delhi 110096, India

V.K. Jain et al. (eds.), *Recent Trends in Materials and Devices*,
Springer Proceedings in Physics 178, DOI 10.1007/978-3-319-29096-6_29

Recent studies on Yttrium (Y) doping in high band gap materials such as ZnO resulted in increased optical activity and photocatalytic efficiency [6]. Detailed study of Y doping on ZnS is not available in literature. Ranganaik Viswanath et al. have reported orange emission at 601 nm due to Y doping whereas Usha Raghvan et al. reported quenching of blue spectra due to Y doping [7, 8].

To further investigate Y doping in ZnS nanoparticles, in this work, pure and Y doped (5, 10 wt%) ZnS nanoparticles have been synthesized via low cost chemical co-precipitation method using Polyethylene Glycol (PEG) as a surfactant. Nanoparticles have been characterized using X-ray Diffraction (XRD), Scanning Electron Microscopy (SEM), UV-Visible and Photoluminescence spectroscopy.

2 Experimental Details

To synthesize of Yttrium doped ZnS, the following materials were used. Zinc acetate dihydrate ($Zn(CH_3\ COOH)_2 \cdot 2H_2O$),Yttrium nitrate hexahydrate ($Y(NO_3)_3 \cdot 6H_2O$, Polyethylene glycol (PEG) and sodium sulfide (Na_2S). The chemical reagents used were of analytical grade and used without further purification. Glassware used was cleaned using standard cleaning procedure. Ultrapure water was used for all dilution and sample preparation.

Undoped ZnS nanoparticles were synthesised using 0.5 M methanolic solution of zinc acetate dihydrate and 0.5 M solution of sodium sulphide (Na_2S) in water, which were separately obtained by ultrasonication. Na_2S solution was added to zinc acetate solution drop by drop with continuous stirring, till the mixture turned milky white. The precipitate was then vigorously stirred for 2–3 h and centrifuged at 5000 rpm for 10 min to obtain ZnS. The precipitate was then dried at 150 °C and grounded finely, to obtain ZnS nanoparticles.

Y doped nanoparticles were synthesized my mixing required amount of yttrium nitrate hexahydrate in zinc acetate solution to obtain Y concentration of 5 and 10 % by weight. Rest of the procedure was same as that of pure ZnS nanoparticles.

The structural properties of the nanoparticles were obtained using the Bruker D8 X-ray Diffractometer with CuKa radiation (k ¼1.5406 Å). Photoluminescence was studies using Shimadzu spectrofluorophotometer model RF-5301 PC. SEM was performed using JEOL JSM 6610LV.

3 Results and Discussion

3.1 Structural Properties

Figure 1 shows the XRD pattern of doped and pure ZnS nanoparticles exhibiting peaks at 2Θ values 28.46°, 48.14° and 56.64°. The peaks are identified to originate

from (111), (220), and (311) planes of cubic (zinc blend) structure of ZnS (JCPDS card No. 5-0566). Peaks are broadened indicating nanocrystalline nature of the synthesized particles. Size of the particles as calculated from Debye Scherrer's formula is found out to be 2–3 nm. No extra phases of Y^{3+} are observed due to low doping levels. The pattern remains same for all concentration of doped samples indicating that cubic structure is not tailored due to doping. Size of the nanoparticles is does not vary with increase in doping concentration. It is observed that crystallinity of the nanoparticles increases with increase in doping as depicted by the increase in intensity of the dominant phase [111] peak. Average grain size, strain, lattice constant and dislocation density of pure and doped nanoparticles are calculated and tabulated in Table 1 shown below. Strain and dislocation density are reduced as doping concentration is increased. This indicates that Y doping causes reduction in defects and ordering of the lattice. Lattice constant is not found to change with doping and is in good approximation of the reported values confirming the formation of cubic ZnS phase.

3.2 *Optical Studies*

Figure 2 shows the room temperature photoluminescence (PL) spectra of the as prepared nanoparticles with an excitation wavelength of 250 nm. Emissions in nano-structures are reported to originate from electrons in conduction band, exitonic states or trap states. In ZnS nanoparticles, blue emissions reported by many research groups are attributed to either emission from sulphur vacancies to valance band (421–445 nm) or donor acceptor emissions [9]. It is observed that pristine ZnS

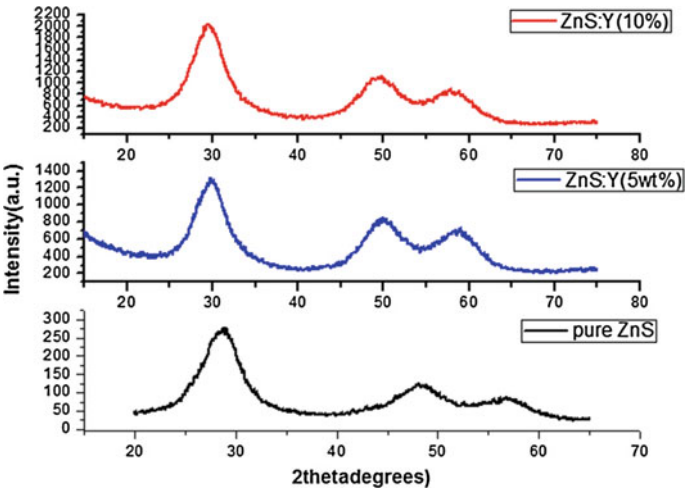

Fig. 1 XRD pattern of pure and Y doped ZnS nanoparticles

Table 1 Grain size, lattice constant, strain and dislocation density of ZnS nanoparticles with different Y concentrations

Doping conc.	Avg. grain size (nm)	Lattice constant (Å)	Strain ε	Dislocation density $\delta \times 10^{-19}(m-1)$
0 %	2.0542	5.406	0.07079	0.0956
0.5	2.0657	5.409	0.06921	0.0929
10 %	2.1015	5.407	0.06817	0.0900

nanoparticles exhibit peak at 361 nm which can be ascribed to exitonic emissions. With incorporation of dopant Yttrium ions, the PL spectrum shifts to 364 and 367 nm for doping concentrations of 5 and 10 wt% respectively. This can be attributed to introduction of new occupied electron states of the yttrium ions in the bandgap of ZnS nanoparticles which influences the energy level of the defect states. It is observed that as the doping concentration is increased, intensity of the PL spectrum is quenched. This demonstrates that energy absorbed by ZnS nanoparticles is transferred to interface states originated by yttrium ions which causes non-radiative emission. Ranganaik Vishwanath et al. reported orange emission at 601 nm which was stated to originate from emissions due 5d and 4f electrons of Y^{3+} ions [7]. No such peak is observed in our samples. It is possible that Yttrium ions exist in Y^{2+} form in our as prepared nanoparticles. Similar findings are reported for Eu ions doped ZnS nanoparticles by [10]. Owing to smaller size of the and high surface to volume ratio, nucleation of the dopant atoms near the surface of the nanoparticles is favorable [11]. The dopant centres situated near the surface rather than the interiors act as surface states for quenching luminescent centers. With further increase in doping concentration to 10 wt%, a broad peak at 450 nm is observed.

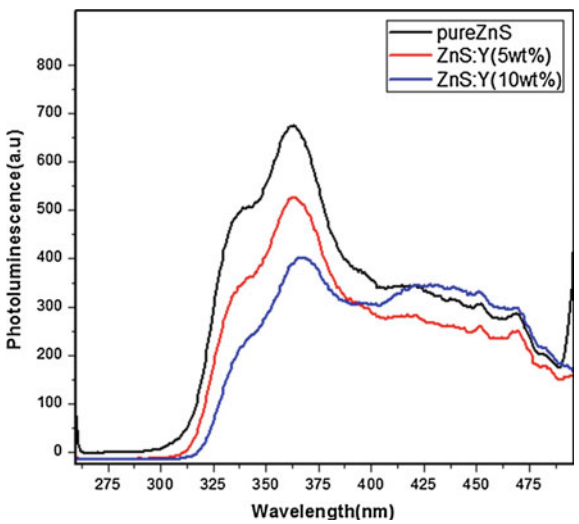

Fig. 2 Photoluminescence spectra of pure and Y doped ZnS nanoparticles

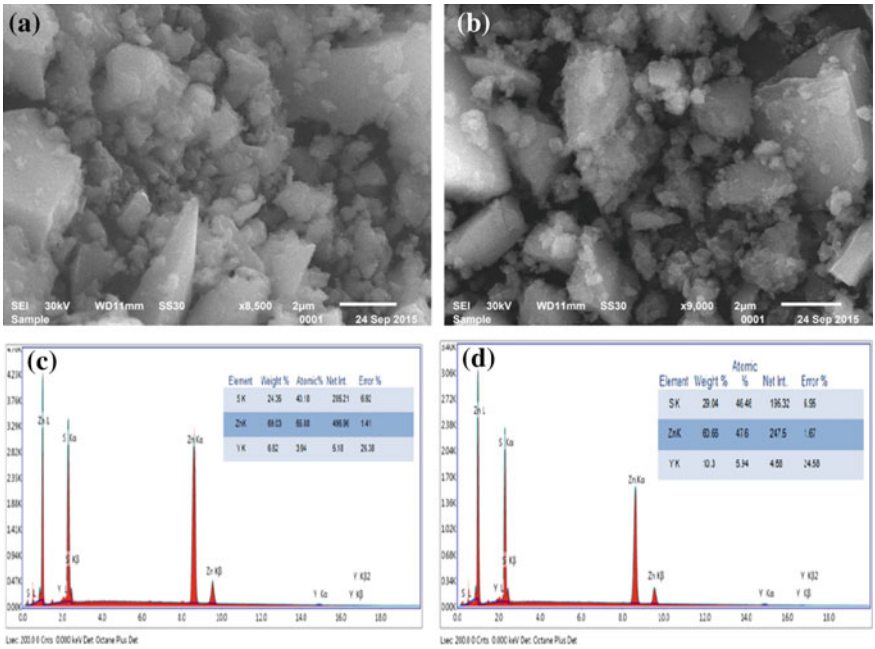

Fig. 3 SEM images (**a**, **b**) and EDAX images (**b**, **c**) of 5 and 10 wt% Y doping respectively

3.3 Morphological Studies

Figure 3a, b show SEM images of Y doped ZnS nanoparticles with doping concentrations 5 and 10 wt% respectively. Due to very small size of the nanoparticles, only clusters are observed in the scale of 2 µm. Figure 3(b) and (c) show EDAX results of the doped nanoparticles. EDAX studies confirm the relative doping percentage to be 3.94 and 5.34 % by wt. for samples prepared with doping concentration as 5 and 10 wt% respectively.

4 Conclusions

In conclusion, pure and Yttrium doped (5 and 10 wt%) ZnS nanoparticles have been successfully synthesized via low cost chemical precipitation technique using PEG as surfactant. Size of the nanoparticles is observed to be in the range of 2–3 nm. No extra phases or change in size is observed due to low level doping. Doping of Y ions causes increase in crystallinity of particles. Strain and dislocation density are also reduced with incorporation of dopant ions and further reduces with increase in doping concentration. Photoluminescence spectra indicates red shift in peak observed at 361 nm for pure ZnS nanoparticles to 364 and 367 nm with Y

doping concentration as 5 and 10 wt% respectively. Only emission due to ZnS nanoparticles is observed with no definite peak for Y^{3+} ions which can be attributed to Y ions being present in Y^{2+} state. The spectrum is quenched with increase in doping concentration.

References

1. K.N. Harish, H.S. Bhojya Naik, P.N. Prashanth Kumar, R. Viswanath, Catal. Sci. Technol. **2**, 1033–1039 (2012)
2. K.N. Harish, H.S. Bhojya Naik, P.N. Prashanth Kumar, R. Viswanath, B.K. Reddy, ACS Sustain. Chem. Eng. **1**(9), 1143–1153 (2013)
3. D. AmaranathaReddy, G. Murali, B. Poornaprakash, R.P. Vijayalakshmi, Solid State Commun. **152**(7), 596–602 (2012)
4. V. Ramasamy, K. Praba, G. Murugadoss, Spectrochim. Acta A **96**, 963–971 (2012)
5. T.T. Nguyen, X.A. Trinh, L.H. Nguyen, T.H. Pham, Adv. Nat. Sci. Nanosci. Nanotechnol. **2**, Article ID 035008 (2011)
6. J. Yang, R. Wang, L. Yang et al., J. Alloys Compd. **509**(8), 3606–363r12 (2011)
7. R. Viswanath, H.S.B. Naik, Y. Kumar et al., J. Nanotechnol. Article ID 924797 (2014)
8. U. Raghwan, Ph.D. thesis, University of Pune (2011)
9. S. Lee, D. Song, D. Kim et al., Mater. Lett. **58**(3–4), 342–346 (2004)
10. K. Ashwini, C. Pandurangappa, B.M. Nagabhushana, Phys. Scr. **85**(6), Article ID 065706 (2012)
11. W. Chen, J.Z. Zhang, A.G. Joly, J. Nanosci. Nanotechnol. **4**(8), 919–947 (2004)

Optimization of Microwave Synthesized Carbon Coated Nano $LiFePO_4$ Active Cathode Material Composition for Li-Ion Batteries

T.V.S.L. Satyavani, A. Srinivas Kumar, M. Srinivas and P.S.V. Subbarao

Abstract Lithium iron phosphate ($LiFePO_4$) is an attractive cathode material for lithium-ion batteries. Among various issues, the most important concern is its low intrinsic electronic conductivity and slow lithium-ion diffusion across the $LiFePO_4$/$FePO_4$ phase boundary during charge/discharge processes which limit the rate performance of this material. Different strategies are being employed to improve its electrochemical performance. The physical technique such as ball-milling of $LiFePO_4$ with carbon black followed by a unique synthesis route like microwave synthesis was used for formation of $LiFePO_4$ which yielded smaller particle size and more uniform size distribution. This carbon coated nano material is electrochemically characterized by fabricating half cells using CR2032 hardware. The preparation of cathodes is required to be optimized to get good electrochemical properties. The ratio of cathode active material, conductive additive acetylene black and binder PVdF to form slurry was optimized by fabricating several coin cells and testing them rigorously. Specific capacities and cycle life obtained for various compositions are reported. For optimized composition, different C-rate discharge characteristics are reported.

1 Introduction

Lithium Iron Phosphate ($LiFePO_4$) is known for its structural and chemical stability, high intercalation flat voltage profile, high theoretical discharge capacity, environmental benignity [1–3]. The constraints for its application are its poor electronic conductivity and low ionic diffusivity. The electrochemical performance, especially rate capability of $LiFePO_4$ is affected and can be enhanced by many

T.V.S.L.Satyavani (✉) · A. Srinivas Kumar · M. Srinivas
Naval Science and Technological Laboratory, Vigyan Nagar,
Visakhapatnam 530027, India
e-mail: tvslsatyavani@gmail.com

P.S.V. Subbarao
Department of Physics, Andhra University, Visakhapatnam 530003, India

V.K. Jain et al. (eds.), *Recent Trends in Materials and Devices*,
Springer Proceedings in Physics 178, DOI 10.1007/978-3-319-29096-6_30

factors like particle size, doping, carbon coating, synthesis route, conductive carbon loading and mixing procedure [1, 4–8]. Among different synthesis methods, microwave synthesis is the easiest and economical synthesis procedure for $LiFePO_4$ [9–16]. Microwave processed $LiFePO_4$ powders have smaller particle size, more uniform size distribution, smoother surface morphology and higher discharge capacity. The physical technique such as ball milling is used to grind the precursors along with conductive agent like carbon black for an optimized duration so that final product after synthesis is obtained with desired particle size. Electrical conductivity gets enhanced by reducing the particle size to nanolevel and providing carbon coating over each particle of $LiFePO_4$. The synthesized material is used to fabricate cathode. The other components of the formulation include PVdF binder, *N*-methyl-2-Pyrrolidone (NMP) solvent and carbon black conductive agent to improve the conductivity. The chemically stable organic binders hold all the individual particles in the mixture together to ensure a stable particle arrangement within the laminate. Higher concentrations of binder may improve the adhesion. Higher concentrations of conductive agent increase the conductivity. But they reduce the overall quantity of active material and deteriorate the performance of cells. The optimization of concentration of each component is required to produce high rate discharge capable cells. Electrodes are made of slurries of the above components. Mixing of viscous slurries, coating over aluminium foil and drying operations affect the final performance of the battery [17]. On the processing side, well mixed and homogeneous slurries are expected to increase cell durability and performance [18–20]. This mixing ensures homogeneous particle and current distribution throughout the laminates preventing localized heating which, if present can reduce safety characteristics, and increase cell impedance.

In the present work, the composition of active material, conductive agent and binder and the process of coating are optimized to obtain smooth coating, good adhesion, high specific capacity, more nos. of cycles and high C-rate discharge.

2 Experimental

In the present work, lithium carbonate, iron oxalate and ammonium dihydrogen phosphate which are commercially available (99.99 % purity, Sigma Aldrich) were taken as precursors of $LiFePO_4$ in stoichiometric ratio. A high energy centrifugal ball mill (Model SFM-3, 030756) was used (1200 rpm) to dry ground the mixture of precursors for optimized duration of 15 h finally to get $LiFePO_4$ as product of particle size 42 nm after synthesis [21]. The ball milled mixture of precursors was taken in quartz crucible with lid and placed in a domestic microwave oven and exposed to an optimized microwave power of 800 Watts for an optimized duration of 4 min [22]. Confirmation of purity of product in the form of single phase was also obtained using X-ray diffraction by PANalytical x'pert pro X-ray diffractometer to identify orthorhombic formation [22].

For preparation of cathode, the composition of active material, acetylene black and PVdF binder was optimized. The ratio of cathode active material, conductive additive acetylene black and binder PVdF to form slurry was optimized by fabricating several cathodes and coin cells, and testing them rigorously. Active material was taken in 75, 80, 85 and 90 % proportions in four different experiments. In all the experiments, quantity of conductive carbon was maintained constant at 5 %. Accordingly, percentage of PVdF was 20, 15, 10 and 5 %. In each experiment, active material (AM) and acetylene black (CC) were dry mixed thoroughly in a mortar with pestle, and PVdF solution in *N*-methyl pyrrolidone (NMP) was added as binder. This slurry was coated using automatic coating machine with doctor blade at a controlled speed of coating on an aluminum foil as current collector. Wet film thickness was 180 µm. Coating was kept for drying in the hot air oven at 80 °C for a time period of 15 h. Thickness of coating after drying was measured to be ~110 µm. Coating was calendared to 80 µm by hot rolled calendaring machine. Actual thickness of active material coating was 60 µm without Al foil (20 µm). Subsequently the cathodes were punched into 15 mm diameter discs. CR 2032 coin cell hardware was used and coin cells were assembled in an argon filled glove box (M-Braun UNIlab) by stacking a micro porous polyethylene separator and adding electrolyte of 1 M $LiPF_6$ in 1:1 EC/DMC. Lithium metal foil was used as anode (99.9 % purity, Sigma-Aldrich). After assembling the components, the half cell was crimped in the crimping machine. Open Circuit Voltage (OCV) of the coin cell was measured with a multimeter after crimping. The cathodes prepared from the slurries of compositions 75:5:20, 80:5:15, 85:5:10, 90:5:5 were used to fabricate coin cells. The cells were tested for their charge-discharge characteristics between 2.8 and 4.2 V at room temperature. Specific capacity was calculated for each composition. The rest time between charging and discharging was five minutes. The cells were also tested for their cycle life. The cells were discharged at different C-rates using 8-channel analyzer (MTI make).

3 Results and Discussion

Table 1 shows the specific capacities and maximum no. of cycles obtained for various compositions. As can be seen from the above Table, maximum capacity of 165 mAh g^{-1} is realized in 90:5:5 composition when discharged at C/10 rate. In the case of composition of 85:5:10, the same is 163 mAh g^{-1}. Similarly, about

Table 1 Specific capacity and cycles obtained for various compositions at C/10 rate

Ratio of AM, CC and PVdF	Specific capacity ($mAhg^{-1}$)	Max. No. of cycles
90:5:5	~165	~800
85:5:10	~163	~800
80:5:15	~162	>1200
75:5:20	60–100	150–200 (poor adhesion)

Fig. 1 Poor adhesion of 75:5:20 composition with substrate, getting peeled off from surface after drying

162 mAh g^{-1} capacity is realized for composition with 80 % LFP and 15 % binder. The capacity realized in the case of composition 75:5:20 is only 40 mAh g^{-1}. It is also seen that the adhesion of composition with the substrate is very poor and it is seen to peel off from the surface after drying as shown in Fig. 1.

Thus, as per the observations furnished in the above Table, it is concluded that 80:5:15 is the optimum composition to make slurry with cathode active material, conductive carbon and PVdF binder which has very good adhesion as shown in Fig. 2 and as it provided reasonably good specific capacity and high cycle life which are prerequisites to be used for secondary battery. It is also observed that the smoothness of coating, specific capacities, cycle life depends greatly on sources of precursors, their synthesis methods and particle sizes of components of slurry. Typical discharge characteristics of the coin cell when discharged at C/10, 1C, 5C, 10C, 15C and 20C yielding maximum specific capacities of 158, 120, 86, 62, 45, 10 mAh g^{-1} respectively are shown in Fig. 3.

Fig. 2 Dried coating of 80:5:15 composition and adhesion with substrate

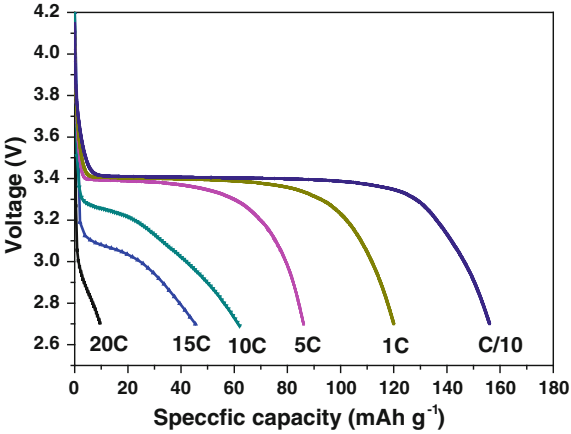

Fig. 3 C/10 to 20C rate discharges of microwave synthesized $LiFePO_4$/C half cell

4 Conclusion

Optimization of slurry to prepare cathode is carried out with different compositions. It is found that 80:5:15 composition yielded good quality coating and cells showed high specific capacity, more nos. of cycles and high C-rate discharge up to 20C.

Acknowledgments We wish to thank Sri C.D. Malleswar, Director, N.S.T.L. for his encouragement to carry out this work. We wish to acknowledge Sri M. Senthilkumar, Sri K. Sahoo and Sri V. Rajesh Kumar for their cooperation in carrying out this work.

References

1. A.K. Padhi, K.S. Nanjundaswamy, J.B. Goodenough, Phospho-olivines as positive-electrode materials for rechargeable lithium batteries. J. Electrochem. Soc. **144**(4), 1188–1194 (1997)
2. B.L. Ellis, K.T. Lee, L.F. Nazar, Positive Electrode Materials for Li-Ion and Li-Batteries. Chem. Matter. **22**(3), 691–714 (2010)
3. S.I. Nishimura, G. Kobayashi, K. Ohoyama, R. Kanno, M. Yashima, A. Yamada, Experimental visualization of lithium diffusion in LixFePO4. Nat. Mater. **7**(9), 707–711 (2008)
4. J.M. Tarascon, M. Armand, Issues and challenges facing rechargeable lithium batteries. Nature **414**, 359–369 (2001)
5. M.S. Whinttingham, Materials Challenges Facing Electrical Energy Storage. MRS Bull. **33**, 411–420 (2008)
6. T. Ohzuku, R.J. Brodd, An overview of positive-electrode materials for advanced lithium-ion batteries. J Power Sources **174**(2), 449–456 (2007)
7. D. Jugovic, D. Uskokovic, A review of recent developments in the synthesis procedures of lithium iron phosphate powders. J. Power Sources **190**(2), 538–544 (2009)
8. B. Scrosati, J. Garche, Lithium batteries: Status, prospects and future. J. Power Sources **195** (9), 2419–2430 (2010)

9. M. Higuchi, K. Katayama, Y. Azuma, M. Yukawa, M. Suhara, Synthesis of $LiFePO_4$ cathode material by microwave processing. J. Power Sources **119–121**, 258–261 (2003)
10. K.S. Park, J.T. Son, H.T. Chung, S.J. Kim, C.H. Kim, C.H. Lee, H.G. Kim, Synthesis of $LiFePO_4$ by co-precipitation and microwave heating. Electro Chem. Commun. **5**(10), 839–842 (2003)
11. L. Wang, Y. Huang, R. Jiang, D. Jia, Preparation and characterization of nano-sized $LiFePO_4$ by low heating solid-state coordination method and microwave heating. Electro chimica Acta **52**(24), 6778–6783 (2007)
12. S. Beninati, L. Damen, M. Mastragostino, MW-assisted synthesis of $LiFePO_4$ for high power applications. J. Power Sources **180**(2), 875–879 (2008)
13. A.V. Murugan, T. Muraliganth, A. Manthiram, Rapid Microwave- Solvothermal Synthesis of Phospho-olivine Nanorods and Their Coating with a Mixed Conducting Polymer for Lithium-Ion BatteriesElectro chemistry. Communications **10**(6), 903–906 (2008)
14. Y.V. Bykov, K.I. Rybakov, V.E. Semenov, High-temperature microwave processing of materials. J. Physics D: Applied Physics **34**, R55–R75 (2001)
15. W. Li, J. Ying, C. Wan, C. Jiang, J. Gao, C. Tang, Preparation and characterization of $LiFePO_4$ from $NH_4FePO_4{\cdot}H_2O$ under different microwave heating conditions. J. Solid State Electrochemistry **11**(6), 799–803 (2007)
16. Y. Zhang, H. Feng, X. Wu, L. Wang, A. Zhang, T. Xia, H. Dong, M. Liu, One - step microwave synthesis and characterization of carbon modified nano crystalline $LiFePO_4$. Electrochim. Acta **54**(11), 3206–3210 (2009)
17. D. Liu, L.-C. Chen, T.-J. Liu, T. Fan, E.-Y. Tsou, C. Tiu, An effective mixing for Lithium-ion battery slurries. Adv. Chem. Eng. Sci. **4**, 515–528 (2014)
18. S.E. Trask, Y. Li, J.J. Kubal, M. Bettge, B.J. Polzin, Y. Zhu, A.N. Jansen, D.P. Abraham, From coin cells to 400 mAh pouch cells: enhancing performance of high capacity lithium ion cells via modifications in electrode constitution and fabrication. J. Power Sour. **259**, 233–244 (2014)
19. S.J. Harris, P. Lu, Effects of Inhomogeneities – Nanoscale to mesoscale-on the durability of Li- ion batteries. J. Phys. Chem. C **117**, 6481–6492 (2013)
20. H.Y. Tran, G. Greco, C. Taubert, M. Wohlfahrt, Mehrens, W. Haselrieder, A. Kwade, Influence of electrode preparation on the electrochemical performance of $LiNi_{0.8}Co_{0.15}Al_{0.05}O_2$ composite Electrodes for lithium-ion batteries. J. Power Sources **210**, 276–285 (2012)
21. T.V.S.L. Satyavani, A.S. Kumar, M. Senthilkumar, P.S. Subbarao, Optimization of particle size to improve dc conductivity of microwave synthesized carbon coated nano $LiFePO_4$ for Li-ion based batteries for underwater applications, in *Accepted for International Workshop on Physics of Semiconductor Devices*, IWPSD (2015)
22. T.V.S.L. Satyavani, A.S. Kumar, P.S. Subbarao, Nano lithium iron phosphate cathode material for Li-ion based batteries for underwater applications. Phys. Semicond. Dev. 721–723 (2014) (Springer)

Unusual Photocatalytic Activity of Cr-Doped TiO_2 Nanoparticles

Tanu Mittal, Sangeeta Tiwari and Shailesh Narain Sharma

Abstract TiO_2 NPs synthesized via aqueous route shows better photocatalytic activity as compare to doped TiO_2 NPs. The presence of dopants inhibits the recombination of exciton. The photocatalytic activity of the nanomaterial have been reduced because of less adsorption sites are available for MB dye due to increase surface coverage of nanomaterial by increase in Cr loading and thus less degradation is shown by doped material. Undoped TiO_2 nanoparticles shows complete degradation of MB in 90 min, whereas doped TiO_2 takes 120 min for complete degradation. The results suggested as higher concentration of dopant material leads to reduction in photocatalytic efficiency.

1 Introduction

TiO_2 has been usually altered as suitable material for photocatalytic activity since it has demonstrated best performance compared to other oxide materials [1]. However, there are some limitations with TiO_2, like wide band gap, fast electron hole pair recombination, dispersion instability and reusability. A proper kind of metal ion doping could lead to overcome these limitations of TiO_2 nanomaterial for some extent [2, 3]. It has been demonstrated that doping inhibits charge recombination and improve photocatalytic activity of photocatalyst. A number of metals, such as Pt, Au, Pd, Rh and Ag, have been used as electron acceptors to separate the photo-induced hole/electron pair and excite interfacial charge-transfer processes [4].

TiO_2 doped with transition metal ion lead to reduce the band gap, it absorbs both in UV and visible range and thus shows high photocatalytic activity [5]. The doping

T. Mittal (✉) · S. Tiwari · S.N. Sharma
Amity Institute of Applied Sciences, Amity University, Noida, Uttar Pradesh, India
e-mail: Chemtanu9@gmail.com

T. Mittal · S. Tiwari · S.N. Sharma
National Physical Laboratory (CSIR), New Delhi, India

V.K. Jain et al. (eds.), *Recent Trends in Materials and Devices*,
Springer Proceedings in Physics 178, DOI 10.1007/978-3-319-29096-6_31

with higher than tetravalent cation valency could increase photocatalytic activity, whereas doping with trivalent or pentavalent metal ions does nor favors the photocatalytic activity also in UV visible region. Furthermore, the photo activity of quantum sized TiO_2 doped with metal ions transient absorption spectra d-electron configuration of the doped metal ions were found towards govern the photo electrochemical process in TiO_2 [6].

Photocatalytic performance of TiO_2 could be improved by doping with different metal ions for the degradation of various pollutants under visible light irradiations. The higher doping concentration of metal ions is a problem for photocatalytic activity. After doping new energy levels are formed in the band gap of TiO_2 by the distribution of metal ions in the matrix of TiO_2. An adequate doping of different metal ions in TiO_2 matrix could leads to less electron hole pair recombination during irradiations because the Schottky barriers are formed at the metal and TiO_2 interface. This cause decrease in recombination results enhanced photocatalytic activity. Metal ions are act as electron acceptor to the photogenerated electrons. Besides, the factors are responsible for the increase photocatalytic activity of metal doped TiO_2, there are another reasons that should be consider into account in the process of photocatalytic activity. As surface sites of nanomaterial can also be occupied by doped metal ions, the surface and optical properties and the (pzc) point of zero charge of TiO_2 possibly altered by doping and this depends upon the amount and type of doped metal ions [5, 7].

Consequently, the adsorption properties of TiO_2 could change by doping. Though, the photocatalytic activity of metal—doped TiO_2 possibly will provoked by doping metal concentration and efficiency of photocatalytic activity could enhanced at optimum metal ion concentration. Further than the optimum dopant concentration, there is decrease in photocatalytic degradation. It can be conclude that the dopant ion concentration below its optimum dosage level can act as electron-hole pairs separations centers, and therefore enhanced the photocatalytic efficiency, whereas the dopant metal ions with exceed dosage level to its optimum value, can act as electron-hole pair recombination centers which cause the decrease in photocatalytic activity.

Conventional doping incorporates hetero-ions into the bulk lattice. In the presence of the defects, few charge carriers are trapped to suppress band to band recombination. Our aim was to lowers the band gap of material confined it in nanodimensions and increased its absorption in visible light by doping with different metal ions, and hence photocatalytic efficiency of the TiO_2 nanomaterial via Cr doping. However, in our case, doped TiO_2 shows unusual photocatalytic activity as compared to as synthesized TiO_2 as enhanced photocatalytic activity was found to be in the undoped as compared to doped TiO_2 samples. Methylene blue MB is using as substrate for photocatalytic degradation of both doped and undoped TiO_2 nanomaterial.

2 Experimental Details

The TiO_2 Aq route/ethanol route based nanoparticles and Cr–TiO_2 nanomaterial were prepared by acid modified sol-gel method.

2.1 Aqueous Solution Hydrolysis Route

Prepare 0.1 M HCL solution (i.e. 2.08 ml of 37 % HCL in 250 ml of Distilled water at room temperature) and add drop wise solution of titanium isopropxide slowly to this solution with constant stirring overnight. A transparent colloidal suspension was formed. This Colloidal suspension of TiO_2 can be stabilized by adjusting the pH of the media (2–3) acidic conditions.

2.2 Cr-Doping

Chromium nitrate ($Cr(NO_3)3{\cdot}9H_2O$) were used as dopant starting material. A titanium isopropxide solution was used as the titanium source. Solution A was prepared by addition of chromium nitrate in 60 ml of deionized water and followed by addition of 5 ml glacial acid. Solution B was prepared by addition of 14 ml of titanium isopropxide in 40 ml ethanol. Then under vigorous stirring the solution of titanium was added to aqueous solution of chromium nitrate. Subsequently, the final solution was stirred for 3 h.

3 Results and Discussion

The absorption band edges were observed at 353 and 377 nm for TiO_2 aqueous and Cr doped TiO_2 nanoparticles respectively. The calculated bandgap was found in the range 3.5–3.3 eV for TiO_2 (Aq/Cr-doped) nanoparticles. An increase in bandgap values for both samples with respect to bulk (3.2 eV) gives the indication that particles are confined in nanodimensions. The band gap increases and the absorption edge shifted towards higher energy (blue shift) with decreasing particle size. Photodegradation ratio was increased with the high reduction and oxidation powers of electrons and holes. The surface area is depends upon the particle size of the nanomaterial, an increase in surface area results but decrease in particle size, this is favorable for the enhancement of photocatalytic reaction. These results are further confirmed by SEM micrographs.

SEM micrographs illustrates the spherical morphology of nanoparticles and distributed uniformly. TiO_2 Aq nanoparticles have spherical well controlled size

and less agglomeration as compare to Cr-doped nanoparticles having wider band gap than the corresponding bulk material (Figs. 1, 2).

TiO_2 Aq route based Nps shows better photocatalytic activity as compare to TiO_2 Cr-doped Nps. TiO_2 Aq degrade MB dye within 90 min, but Cr-doped TiO_2 takes 120 min for degradation of MB dye. Generally doping reduced the charge recombination and leads to better photocatalytic activity but in our case doped material shows less photocatalytic activity because there is less adsorption sites are available due to increased coverage of the nanomaterial by doping metal and hence sites expected to the available to the dye [6, 8, 9].

The reduction in particle size and the phase (anatase) of TiO_2 nanoparticles. Possibly resulted in high photocatalytic activity. The pH also effects the photocatalytic activity TiO_2 shows better photocatalytic degradation at high pH <6 and low activity in acidic medium for TiO_2 aq nanoparticles and Cr-doped nanoparticles respectively.

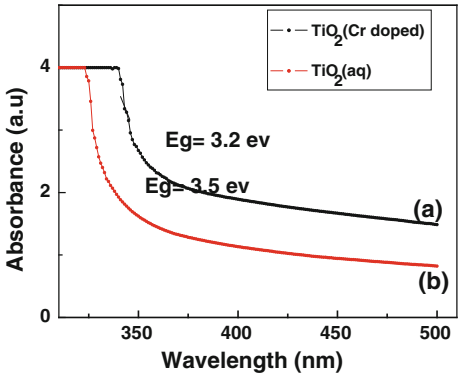

Fig. 1 UV-Vis absorption spectra of TiO_2 Aq (*a*) and Cr-doped nanoparticles (*b*)

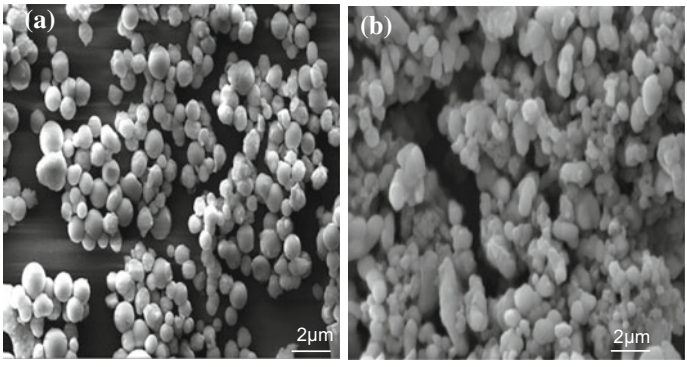

Fig. 2 SEM micrographs of TiO_2 Aq and Cr-doped TiO_2 respectively

In acidic media, to increase the degradation more electrons reacted to form oxidizing species. High photocatalytic activity depends upon the properties of the nanomaterial like size and dispersion stability of the nanomaterial. Less agglomeration or high dispersion stability leads to nanoparticles confined in Nano dimension which shows by blue shift In UV-Vis spectra [10, 11] (Figs. 3, 4).

We discuss the photocatalytic behavior of TiO_2 particles as a function of the degradation rate of MB, a model organic pollutant/dye, in the presence of UV irradiation. It is found that undoped TiO_2 leads to rapid discoloration of the dye as compared to the doped nanomaterial. Less surface adsorption sites are available for dye in Cr-doped material because increase coverage of nanomaterial by metal. As a consequences of this, decrease in penetration depth of light could also prevent the excitations of the TiO_2 semiconductor (Fig. 5).

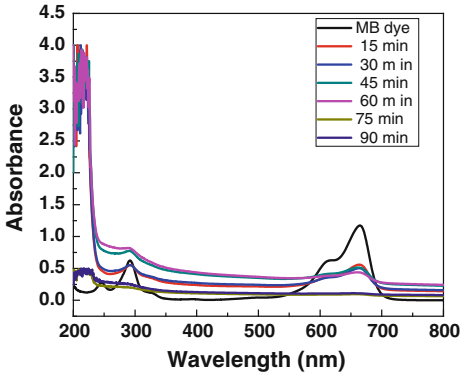

Fig. 3 Photocatalytic degradation of MB dye by TiO_2 aqueous route based nanoparticles

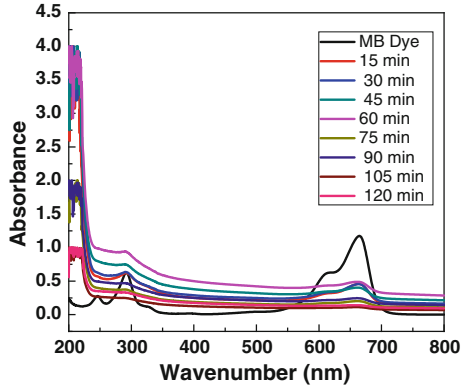

Fig. 4 Photocatalytic degradation of MB dye by Cr-doped nanoparticles

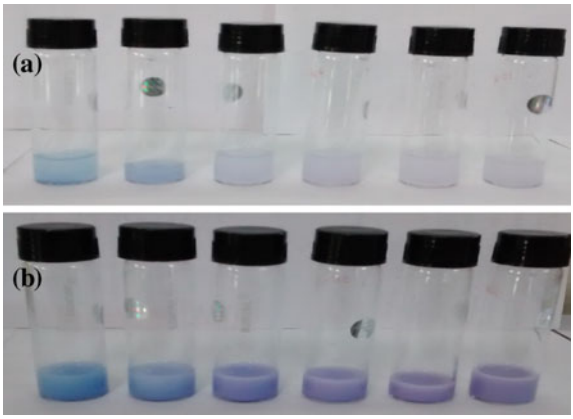

Fig. 5 MB dye discoloration during exposure to UV-irradiations in the presence of both doped (**b**) and undoped TiO_2 (**a**)

4 Conclusion

In conclusion, TiO_2 aqueous route based nanoparticles shows better photocatalytic activity as compare to doped TiO_2 nanoparticles. The increased incorporation of Cr^{3+} and Cr^{4+} ions in the TiO_2 matrix might screen the photocatalytic activity of doped TiO_2 as compared to undoped TiO_2. However, the detailed studies are underway.

References

1. M. Salmi, N. Tkachenko, R.-J. Lamminmäki, S. Karvinen, V. Vehmanen, H. Lemmetyinen, J. Photochem. Photobiol. A Chem. **175**(1), 8–14 (2005)
2. J. Liu, W. Wang, H. Yu, Z. Wu, J. Peng, Y. Cao, Sol. Energy Mater. Sol. Cells **92**, 1403 (2008)
3. H. Neugebauer, C. Brabec, J.C. Hummelen, N.S. Sariciftci, Sol. Energy Mater. Sol. Cell **61** (1), 35 (2000)
4. J.C.-S. Wu, C.-H. Chen, J. Photochem. Photobiol., A **163**(3), 509–515 (2004)
5. T. Asahi, A. Furube, H. Fukumura, M. Ichikawa, H. Masuhara, Rev. Sci. Instrum. **69**, 361 (1998)
6. P. Janoš, H. Buchtová, M. Rýznarová, Sorption of dyes from aqueous solutions onto fly ash. Water Res. **37**(20), 4938–4944 (2003)
7. A. Furube, T. Asahi, H. Masuhara, H. Yamashita, M. Anpo, Res. Chem. Intermed. **27**, 177 (2001)
8. H.K. Shon, S. Phuntsho, S. Vigneswaran, Effect of photocatalysis on the membrane hybrid system for wastewater treatment. Desalination **225**(1–3), 235–248 (2008)
9. B. Tryba, M. Piszcz, B. Grzmil, A. Pattek-Janczyk, A.W. Morawski, Photodecomposition of dyes on Fe-C-TiO_2 photocatalysts under UV radiation supported by photo-Fenton process. J Hazard. Mater. **162**(1), 111–119 (2009)
10. J. Choi, H. Park, M.R. Hoffmann, Effects of single metal-ion doping on the visible-light photoreactivity of TiO_2. J. Phys. Chem. C **114**, 783 (2010)
11. J.-M. Herrmann, Detrimental cationic doping of titania in photocatalysis: why chromium Cr^{3+}-doping is a catastrophe for photocatalysis, both under UV- and visible irradiations. New J. Chem. **36**, 883–890 (2012)

Part II
Optoelectronics

Structural and Optical Properties of Single Crystalline Cerium Doped ZnO Thin Films

Chetan K. Kasar, Ulhas S. Sonawane, Jaspal P. Bange and D.S. Patil

Abstract Ce doped ZnO thin films were prepared on a glass substrate by sol-gel spin coating technique. Effect of post annealing temperature from 250 to 450 °C on structural and optical properties of Ce doped ZnO thin films were studied. The influence of temperature on transparency, bandgap and crystallite size of Ce doped ZnO was observed. The nano thin films were characterized by X-ray Diffractometer and UV-Vis Spectrophotometer. Crystallinity of the deposited thin films was found to be improved with temperature. Increasing the post annealing temperature (250°–450 °C), increases the grain size of the samples gradually from 15.41 to 26.54 nm. In addition to the effect of post annealing temperature, the influence of average transmission, absorption, and band gap of the Ce doped ZnO thin films was investigated for optoelectronics applications.

1 Introduction

Zinc Oxide (ZnO) thin films are transparent semiconductor materials has exhibits unique Optical, Electrical, Structural and Photoluminances properties [1]. It has much attracting from last few decades for the fabrication of devices, due to their exclusive properties such as direct wide band gap (3.4 eV) and large exciton binding energy (60 meV). ZnO thin films having enormous applications: light emitting diodes (LEDs), gas sensor, flat panel, solar cell, display [2–4]. From last some year group III element and VI element was frequently doped into ZnO for better electrical and optical properties but now a day's ZnO thin films can be altered by doping rare earth (RE) element has much interested. RE doped ZnO thin films is a new research area to enhance the optical properties for optoelectronics application.

The many deposition techniques are available to prepared thin films such as RF magnetron sputtering molecular beam epitaxy (MBE), pulsed laser deposition

C.K. Kasar · U.S. Sonawane · J.P. Bange · D.S. Patil (✉)
Department of Electronics, North Maharashtra University, Jalgaon, India
e-mail: patildsp@rediffmail.com

V.K. Jain et al. (eds.), *Recent Trends in Materials and Devices*,
Springer Proceedings in Physics 178, DOI 10.1007/978-3-319-29096-6_32

(PLD) spray pyrolysis and sol-gel [5–7]. In this work RE doped ZnO thin films were prepared using sol-gel deposition techniques because of it's a number of advantages over than other techniques; simple route, easily prepared films with low cost, etc.

2 Experimental Details

Sol-gel Spin coating technique is used to prepared cerium doped ZnO thin films on to the glass substrate.

Zinc acetate dihydrate (Zn $(CH_3COO)_2 \cdot 2H_2O$) and cerium (III) nitrate hexahydrate were used for the starting precursor of zinc and cerium respectively. 2-Methoxyethanol was used as solvent. The transparent and clear solution was prepared by using the Zinc acetate dihydrate, cerium (III) nitrate hexahydrate powder in 25 ml 2-methoxyethanol simultaneously. 0.5 M solution were prepared by dissolving 2.7437 g of Zinc acetate dihydrate and the concentration of Cerium (III) nitrate hexahydrate kept constant at 5 at.% mixed in 25 ml 2-methoxyethanol. The mixture of solution was vigorously stirred on hot magnetic plate at 70 °C for half an hour and finally aged the solution for few hours at room temperature. Now 5 at.% Ce doped ZnO solution was used for deposit the films. Before depositing the films, glass substrates were cleaned with sequence by chromic acid, acetone and deionised water (DI) respectively. Obtained solution was deposited on to the microscopic glass substrate with homemade spin coater. Spin rate of the system was maintained at 2000 rpm for 30 s. The procedure was carried out repeatedly twelve times to achieve desired thickness. After each deposition, deposited films ware pre-heating at 250 °C for 5 min in open air and cooled at room temperature. Pre heat is necessary for removing organic content in the films. Finally, samples were post annealed at various temperatures from 250 to 450 °C for an hour in closed furnace. Effect of post annealing temperatures on the 5 at.% Ce doped ZnO thin films studied. The deposited samples were characterized for structural and optical properties. Bruker Advance—D8 X-ray diffraction (XRD) having Cu-Kα source operating at wavelength 1.54059 Å was used to characterize the structural properties of the films. The optical transmission measurements were performed using Shimadzu UV-2600 spectrophotometer.

3 Results and Discussion

3.1 Structural Properties (XRD)

The Structural and optical properties of cerium doped ZnO thin films post annealed at different temperature were investigated, the post annealing temperature of the films was varied from 250 to 450 °C into closed furnace for an hour. XRD

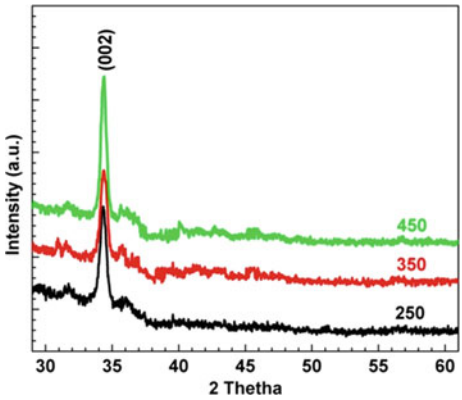

Fig. 1 XRD spectra of Ce doped ZnO thin films at different annealing temperature

spectrum of 5 at.% Cerium doped ZnO thin film post annealed at 250, 350, 450 °C respectively is shown in Fig. 1. These spectra reveals that the most intense peak observed at 34.42° is associated with the (002) orientation of hexagonal ZnO. The crystallite sizes of all the films post annealed at various temperatures have been calculated using Debey-Scherrer equation [8],

$$D = \frac{0.94 \times \lambda}{\beta \cos \theta}$$

where, D is grain size of crystal, λ (=1.54059 Å) is the wavelength of the X-ray source used, β is the broadening of full width at half maximum (FWHM) in radians and COSθ is the angle of diffraction peak. The grain sizes in the film were estimated as 15.41 nm for 250 °C, 17.63 nm for 350 °C, and 26.54 nm for 450 °C Ce doped ZnO thin films. The intensity of the diffraction peak (002) was increased with increasing the post annealing temperature. The full width at half maximum (FWHM) of the film is decreased from 0.0094 to 0.0054 however the grain size were increased from 15.41 to 26.54 nm for the (002) diffraction peak with increasing post annealing temperatures which shown in Fig. 2.

3.2 Optical Properties

Optical transmission spectrum was recorded using Shimadzu Spectrophotometer (UV-2600) in the range of 300–750 nm. Transmission spectrum of Ce doped ZnO thin films annealed at different post annealing temperatures are illustrated in Fig. 3. All the films exhibit more than 90 % transparency in visible region (400–700 nm)

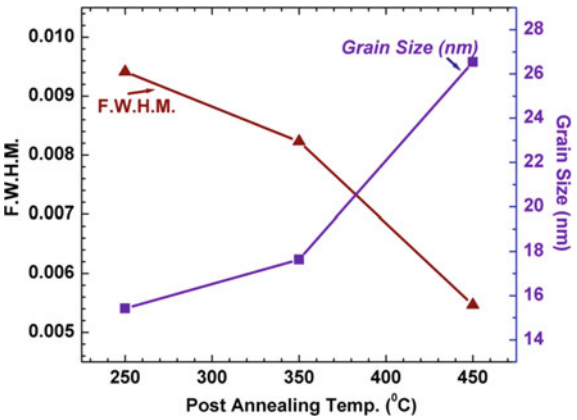

Fig. 2 Changes in F.W.H.M and grain size of Ce doped ZnO thin films with various post annealing temperature

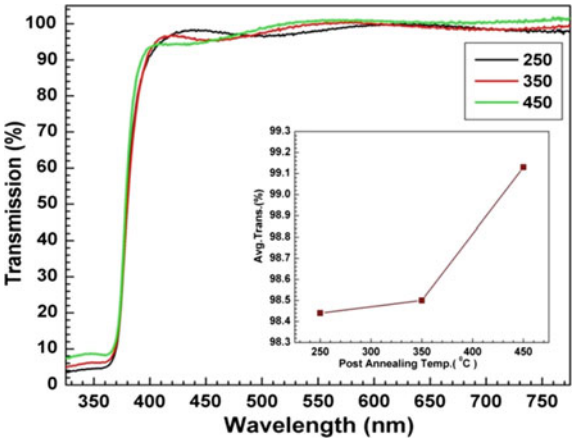

Fig. 3 Transmission spectrum of Ce doped ZnO thin films at different annealing temperature

and sharp absorption edge near ultraviolet region. Inset graph shows that average transparency slightly increased with increasing the annealed temperature.

ZnO is a direct band gap material. The optical band gap (Eg) of Ce doped ZnO thin films was determined using the absorption coefficient. The absorption coefficient was calculated from the following standard equation [9].

$$\alpha h\mu = A\,(h\mu - Eg)^{1/2}$$

Here, α is absorption coefficient, A is the constant and hν is the photon energy and Eg is the optical band gap. From the Fig. 4, extrapolation of the graph gave the optical band gap energy value of 3.240, 3.265, 3.278 eV for post annealing at 250, 350, 450 °C respectively.

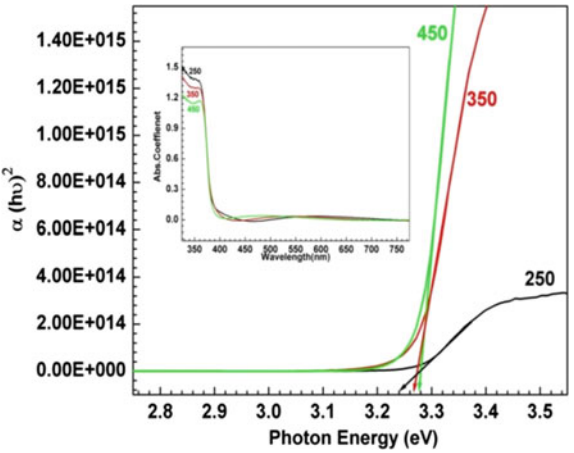

Fig. 4 Optical band gap of Ce doped ZnO thin films

4 Conclusions

The Ce doped ZnO films were synthesized using Sol-gel spin coating method on to a glass substrate and the effect of post annealing temperature on structural and optical properties of deposited thin films have been investigated. XRD spectra show the single crystalline nature of the films. Grain size of the films gradually increased with post annealing temperature. Optical properties confirmed more than 90 % transparency in all the films within the visible range (400–700 nm). We were able to tailor optical band gap from the 3.240 to 3.278 eV.

Acknowledgments Authors Chetan K. Kasar and Ulhas S. Sonawane would like to thank University Grant commission, New Delhi, India for providing financial assistance to carry out this work through UGC-BSR Research fellowship scheme.

References

1. V. Shelke, B.K. Sonawane, M.P. Bhole, D.S. Patil, J. Non-Cryst. Solids **355**, 840 (2009)
2. M. Zhu, H. Huang, J. Gong, C. Sun, J. Appl. Phys. **102**, 043106 (2007)
3. B.G. Lewis, D.C. Paine, MRS Bull. **25**, 22 (2000)
4. M.P. Bole, D.S. Patil, J. Phys. Chem. Solids **70**, 466 (2009)
5. K.-M. Lin, P. Tsai, Mater. Sci. Eng., B **139**, 81 (2007)
6. H.S. Kang, J.W. Kim, J.H. Kim, S.Y. Lee, J. Appl. Phys. **99**, 066113 (2006)
7. H. Tanaka, S. Fujita, S. Fujita, Fabrication of wide-band gap $Mg_xZn_{1-x}O$ quasi-ternary alloys by molecular-beam epitaxy. Appl. Phys. Lett. **86**, 192911 (2005)
8. M.F. Malek, M.H. Mamat, M.Z. Sahdan, M.M. Zahidi, Z. Khusaimi, M.R. Mahmood, Thin Solid Films **527**, 102 (2013)
9. S. Singh, P. Chakrabarti, Comparison of the structural and optical properties of ZnO thin films deposited by three different methods for optoelectronic applications. Superlattices Microstruct. **64**, 283–293 (2013)

Calculation of Valence Band Structure of $GaSb_{1-x}Bi_x$ Using Valence Band Anticrossing Model in the Dilute Bi Regime

Dip Prakash Samajdar, Tushar Dhabal Das and Sunanda Dhar

Abstract Valence Band anticrossing model is used to estimate the reduction in band gap and increase in spin-orbit splitting energy for $GaSb_{1-x}Bi_x$. Interaction of the heavy hole (HH), light hole (LH) and the SO bands of GaSb with the Bi related impurity level causes restructuring of the valence band structure of the III-V-bismide. While the HH/LH sub band moves in the upward direction, SO band moves in the downward direction to result in a significant increase in spin orbit splitting energy. The decrease in band gap and the increase in the splitting energy results in the formation of $\Delta_{SO} > E_{Bi}$ regime which suppress the loss mechanisms such as Auger recombination and Intervalence Band Absorption in GaSb based LASERS and photodetectors.

1 Introduction

III-V-Bi alloy systems have attracted the attention of the researchers worldwide in the last few years by virtue of their potential applications in near- and mid-infrared optoelectronic devices. A detailed review of this novel class of materials is presented in a recent Springer Series volume [1]. The incorporation of dilute concentrations of bismuth into the III-V binary semiconductors cause significant changes in the valence band structure of the Bi free host compounds by substantial reduction in band gap and increase in spin-orbit splitting energy [2]. These Bi induced changes occur due to a Bi related impurity level located in the vicinity of valence band maximum of the host semiconductors. GaSbBi appears to be a

D.P. Samajdar (✉) · S. Dhar
Department of Electronic Science, University of Calcutta,
92 A. P. C. Road, Kolkata 700009, India
e-mail: dipprakash010@gmail.com

T.D. Das
Department of ECE, National Institute of Technology,
Yupia 791112, Arunachal Pradesh, India

V.K. Jain et al. (eds.), *Recent Trends in Materials and Devices*,
Springer Proceedings in Physics 178, DOI 10.1007/978-3-319-29096-6_33

potential member of the III-V-Bi family, where the band gap tuning property may be effectively utilized for fabricating devices in the mid-infrared regions [1, 3, 4].

In this paper, we have calculated the valence band structure of $GaSb_{1-x}Bi_x$ using the 12 × 12 Hamiltonian proposed by Alberi et al. [5]. Interaction of the HH, LH and SO bands with the Bi related impurity levels causes the splitting of these bands into E_+ and E_- sub bands. The upward movement of the LH/HH band and the downward movement of the SO E_+ bands are respectively responsible for the band gap reduction and spin-orbit splitting energy in III-V-Bi alloys.

2 Mathematical Modelling

The incorporation of a small amount of bismuth into GaSb leads to the formation of localized defect states near the extended states of the host valence band matrix. The splitting of light hole (LH), heavy hole (HH) and spin-orbit split-off band (SO) into E_+ and E_- sub bands is caused by the Bi impurity states and the energy values corresponding to these six energy levels are obtained by solving a 12 × 12 Hamiltonian. The solution of this Hamiltonian yields six different eigen values corresponding to the six E_+ and E_- sub bands. The details of this Hamiltonian which consists of 6 p-like states of the host and 6 p-like states of the defect Bi [6] is described in details in [5].

At the Γ point where **k** = 0, the solution of the Hamiltonian yields four distinct values given by the following set of equations [7]:

$$E_{HH/LH\pm} = \frac{1}{2}\left(H + E_{Bi} \pm \sqrt{(H - E_{Bi})^2 + 4V^2}\right) \tag{1}$$

$$E_{SO\pm} = \frac{1}{2}\left(S + E_{Bi-so} \pm \sqrt{(S - E_{Bi-so})^2 + 4V^2}\right) \tag{2}$$

where $H = L = \Delta E_{VBO}x$, $S = \frac{1}{2}(L+H) - \Delta_0 - \Delta_{SBO}x$, $V = C_{Bi}\sqrt{x}$. E_{Bi} and $E_{Bi\text{-}so}$ represent the location of Bi impurity levels and its corresponding spin-orbit split-off level respectively. C_{Bi}, the coupling parameter, gives the magnitude of the strength of interaction between the Bi related impurity levels and the valence sub bands HH, LH and SO. ΔE_{VBO} and ΔE_{SBO} gives the valence band offset and spin-orbit split-off band offset between the endpoint compounds respectively. The downward movement of the conduction band minimum (CBM) as can be predicted by the Virtual crystal Approximation (VCA) is given as [8]:

$$E_g^{III-V-Bi} = E_g^{III-V} - \Delta E_{CBO}x \tag{3}$$

where ΔE_{CBO} is the conduction band offset between GaSb and GaBi. Hence the total band gap reduction in III-V-Bi due to the upward movement of HH/LH band and the downward movement of the CBM can be written as [8]:

$$E_g^{III-V-Bi} = E_g^{III-V} - \Delta E_{CBO} x - E_{HH/LH+} \tag{4}$$

Equation (1) can be rewritten as [8]:

$$V = \sqrt{(E_{HH/LH\pm} - E_{Bi})(E_{HH/LH\pm} - H)} \tag{5}$$

Since V is proportional to C_{Bi}, we can conclude from (5) that the coupling parameter C_{Bi} is dependent on: (i) the value of the energy level $E_{HH/LH+}$ (ii) location of the Bi related impurity level E_{Bi} (iii) valence band offset ΔE_{VBO} and its magnitude is not only dependent on the electronegativity and size difference between Bi and Sb atoms as pointed out in [9, 10]. The values of different parameters required for the band structure and band gap calculation of GaSbBi is given in [11].

3 Results and Discussion

Figure 1 shows the variation of the positions of the E_+ and E_- energy levels corresponding to the HH/LH and SO subbands with Bi concentration. HH/LH E_+ energy level moves upward at the rate of 12.4 meV/at.%Bi whereas the SO E_+ level is pushed upward by 19.2 meV/at.%Bi due to anti-crossing interactions. The E_- energy levels move in the downward direction indicating the repulsive nature between the E_+ and E_- energy levels.

Figure 2 depicts the variation of virtual Crystal Approximation (VCA) and VBAC calculated bandgap as a function of Bi mole fraction. The VCA calculated band gap decreases by about 27.4 meV/at.%Bi whereas the VBAC calculated band

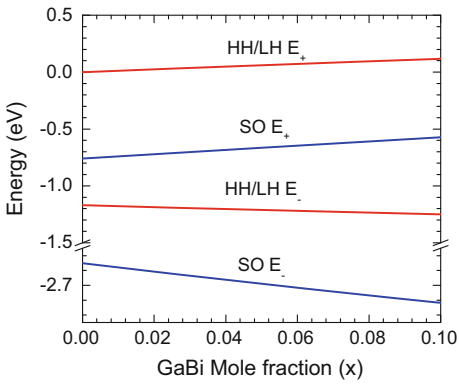

Fig. 1 Relative positions of the E_+ and E_- energy levels for the HH/LH and SO bands as a function of GaBi mole fraction

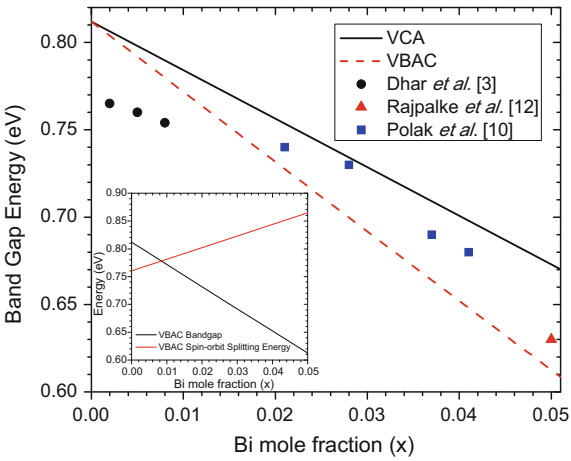

Fig. 2 Variation of VCA and VBAC calculated band gap as a function of Bi mole fraction. The decrease in band gap energy and the increase in spin-orbit splitting energy calculated by VBAC model is shown in the inset

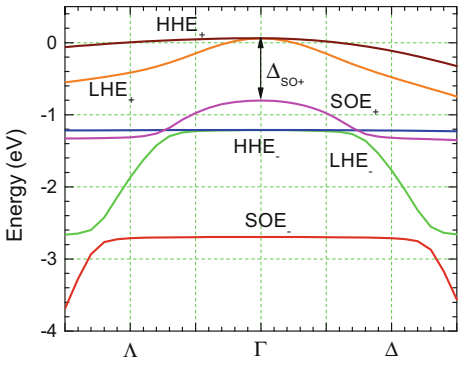

Fig. 3 Valence band structure of GaSbBi for a Bi concentration of 5 at.% in the crystal directions Δ <100> and Γ <111>

gap lowers by an amount 40.2 meV/at.%Bi. Clearly, the values of band gap reduction shows excellent agreement with the experimental data shown by using various symbols. GaSbBi behaves as a regular III-V alloy and so there is little difference between the VCA and VBAC calculated values in comparison to other III-V-Bismides such as GaAsBi, InAsBi and InPBi. The inset shows the intersection of the VBAC calculated band gap and spin-orbit splitting energy at a Bi concentration of 0.9 at.%. This results in the formation of $\Delta_{SO} > E_g$ regime which helps in suppressing the loss processes such as Auger recombination in optoelectronic devices.

Figure 3 shows the variation of E_+ and E_- energy levels corresponding to the HH, LH and SO bands for GaSbBi in the crystal directions Δ <100> and Λ <111> for a Bi concentration of 5 at.%. The value of SO E_+ energy level is obtained by subtracting a negative value of virtual crystal shift from the value of the SO related E_+ energy level obtained by solving the Hamiltonian proposed by Alberi et al. The

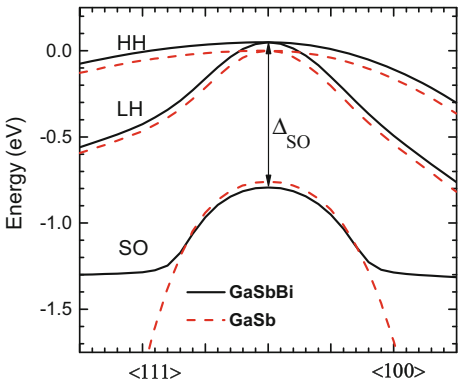

Fig. 4 Valence band structure of GaSbBi and its comparison with that of GaSb in the crystal directions <100> and <111>

value of spin-split off energy at a Bi concentration of 5 at.% comes out to be 0.862 which indicates an increase by about 0.102 eV from the value of 0.76 eV for GaSb.

Figure 4 depicts the valence band structure of GaSbBi with the LH, HH and SO sub bands in the <100> and <111> directions. The band structure of GaSb is also drawn to show the enhancement in spin-orbit splitting energy Δ_{SO} due to Bi incorporation and the upward movement of HH/LH bands. The downward movement of SO sub band is responsible for the increase in Δ_{SO}.

4 Conclusions

In conclusion, the reduction in band gap as well as the enhancement in spin-orbit splitting energy is well explained by the VBAC Model. The HH/LH band shifts upward by 12.4 meV/at.%Bi and the conduction band lowers by an amount 27.8 meV/at.% Bi which gives a total band gap reduction of 40.2 meV/at.%Bi. The spin orbit splitting energy increases by about 21 meV/at.%Bi. For a Bi concentration of 0.9 at.%, spin-orbit splitting energy for GaSbBi becomes greater than the direct band gap which causes the suppression of loss mechanisms in GaSbBi based optoelectronic devices.

References

1. H. Li, Z.M. Wang (eds.), *Bismuth-containing compounds (Springer series in Materials Science*, vol. 186 (Springer Science+Business Media, New York, 2013)
2. K. Alberi, O.D. Dubon, W. Walukiez, K.M. Yu, K. Bertulis, A. Kroktus, Appl. Phys. Lett. **91**, 051909 (2007)
3. S.K. Das, T.D. Das, S. Dhar, M. de la Mare, A. Krier, Infrared Phys. Technol. **55**, 156 (2012)
4. S.K. Das, T.D. Das, S. Dhar, Semicond. Sci. Technol. **29**, 015003 (2014)

5. K. Alberi, J. Wu, W. Walukiewicz, K.M. Yu, O.D. Dubon, S.P. Watkins, C.X. Wang, X. Liu, Y.J. Cho, J. Furdyna, Phys. Rev. B **75**, 045203 (2007)
6. R. People, S.K. Sputz, Phys. Rev. B **41**, 8431 (1990)
7. D.P. Samajdar, S. Dhar, The Sci. World. J. **2014**, 704830 (2014)
8. D.P. Samajdar, S. Dhar, Superlattices Microstruct. **89**, 112 (2016)
9. M. Usman, C.A. Broderick, A. Lindsay, E.P. O'Reilly, Phys. Rev. B **84**, 245202 (2011)
10. M.P. Polak et al., J. Phys. D Appl. Phys. **47**, 355107 (2014)
11. D.P. Samajdar, T.D. Das, S. Dhar, Mater. Sci. Semicond. Process. **40**, 539 (2015)
12. M.K. Rajpalke, W.M. Linhart, M. Birkett, K.M. Yu, J. Alaria, J. Kopaczek, R. Kudrawiec, T.S. Jones, M.J. Ashwin, T.D. Veal, J. Appl. Phys. **116**, 043511 (2014)

Effect of Bismuth Incorporation on the Growth Kinetics and Valence Band Structure for $InP_{1-x}Bi_x$ Grown Using Liquid Phase Epitaxy

Dip Prakash Samajdar, Tushar Dhabal Das and Sunanda Dhar

Abstract A mathematical model based on the one dimensional diffusive transport of bismuth atoms has been used to study the concentration profile of the bismuth atoms during the liquid phase epitaxial growth of InPBi. This model is used to determine the growth kinetics at equally spaced layers in the proximity of the grown epitaxial interface. Various growth parameters such as growth temperature, melt supercooling and the continuous cooling ramp applied during growth have been optimized to find out the suitable conditions of growth. The thickness of the epitaxial layers as a function time is also estimated. Valence Band anticrossing (VBAC) model is used to determine the reduction in band gap and increase in spin-orbit splitting energy for $InP_{1-x}Bi_x$. The valence band structure of InPBi is modified due to the interaction of the Bi related impurity levels with the light hole (LH), heavy hole (HH) and spin-orbit split-off (SO) sub bands. A 12×12 Hamiltonian is solved to find out the valence band structure of InPBi in the <100> direction.

1 Introduction

III-V-Bismides have become the source of attraction for the researchers worldwide due to two of its most important properties. Firstly the incorporation of bismuth into the III-V binary alloys facilitates the band gap tuning over a wide wavelength range for the fabrication of mid- and near-infrared optoelectronic devices. Secondly, there is an enhancement in the spin-orbit splitting energy of the bismides as compared to the host alloys which causes the suppression of different loss mechanisms in

D.P. Samajdar (✉) · S. Dhar
Department of Electronic Science, University of Calcutta,
92 A. P. C. Road, Kolkata 700009, India
e-mail: dipprakash010@gmail.com

T.D. Das
Department of ECE, National Institute of Technology,
Yupia 791112, Arunachal Pradesh, India

V.K. Jain et al. (eds.), *Recent Trends in Materials and Devices*,
Springer Proceedings in Physics 178, DOI 10.1007/978-3-319-29096-6_34

LASERs, LEDs and photodetectors [1]. The medium band gap semiconductor $InP_{1-x}Bi_x$ is another potential member of the III-V-bismide family for applications in InP based optoelectronic devices due to its broad emission spectrum which covers the telecommunication wavelengths, wavelength regime for gas sensing and super-luminescent infrared diode applications [2].

In this paper, we have used a one-dimensional diffusive transport model to study the concentration profile of Bi atoms in front of the epitaxial growth interface during the. A study of the growth parameters is done to optimize the growth conditions to ensure efficient transfer of Bi atoms to the solution. In the second part of the paper, the valence band structure of InPBi is analyzed to determine the reduction in bandgap and enhancement of spin-orbit splitting energy due to Bi incorporation using VBAC Model.

2 Mathematical Modelling

The one dimensional transport equation for the diffusion of Bi atoms relative to the moving interface as origin in case of liquid phase epitaxy [3] can be written as:

$$\frac{\partial C(x,t)}{\partial t} = D\frac{\partial^2 C(x,t)}{\partial x^2} \tag{1}$$

In the above equation, C(x,t) is the concentration of the solute species at a distance x from the grown epitaxial surface, D is the diffusion coefficient of bismuth atoms in the solution. Equation (1) can be solved by finite difference approximation to obtain the concentration in the *j*th segment which may be written as [4],

$$C_{j,n+1} = C_{j,n} + \frac{D\tau}{\varepsilon^2}\left(C_{j-1,n} - 2C_{j,n} + C_{j+1,n}\right) \tag{2}$$

Here τ denotes the time increment for the epitaxial layer growth, j is the segment number, ε gives the width of each segment and n is the number of time cycles. The factor $D\tau/\varepsilon^2$ is called modulus M. For a given value of D, we should choose values of τ and ε in such a way that $M \leq 1/3$ [5].

The final form of the equation that gives the concentration of Bi atoms in the In solution for the liquid phase epitaxial growth of InPBi is given by:

$$C_{Bi(In)} = 6.787 \times 10^{22} \exp\left[7.0816 - \frac{11827}{T}\right] \tag{3}$$

The incorporation of Bi atoms into the host III-V semiconductor alloy InP results in the formation of localized defect states near its valence band edge. These impurity states interact with the extended states of the host and causes the restructuring of the valence band by splitting the LH, HH and SO sub bands into a

series of E_+ and E_- energy bands. While the E_+ sub band maintains the extended nature of the host semiconductor lattice, the E_- sub band retain the localized character of the defect states [6]. The upward movement of the HH/LH E_+ energy band and the subsequent downward movement of the SO E_+ levels causes the reduction in band gap and increase in spin-orbit splitting energy in InPBi with respect to that of the host semiconductor InP.

The valence band structure of the III-V-Bismides can be best described by a 12 × 12 Hamiltonian proposed by [7]. The solution of the Hamiltonian yields six doubly degenerate eigen values corresponding to the three pairs of spin-degenerate sub bands denoted by $E_{LH\pm}$, $E_{HH\pm}$ and $E_{SO\pm}$ formed due to the interaction between the valence band (VB) and Bi impurity states. The valence band structure of InPBi in the <100> direction can be best described by the Hamiltonian given below:

$$H_v = \begin{pmatrix} H & \alpha & \beta & 0 & 0 & -i\sqrt{2}\beta & V(x) & 0 & 0 & 0 & 0 & 0 \\ 0 & L & 0 & \beta & \frac{iD}{\sqrt{2}} & 0 & 0 & V(x) & 0 & 0 & 0 & 0 \\ \beta^* & 0 & L & 0 & 0 & \frac{iD}{\sqrt{2}} & 0 & 0 & V(x) & 0 & 0 & 0 \\ 0 & \beta^* & 0 & H & -i\sqrt{2}\beta^* & 0 & 0 & 0 & 0 & V(x) & 0 & 0 \\ 0 & \frac{-iD}{\sqrt{2}} & 0 & i\sqrt{2}\beta & S & 0 & 0 & 0 & 0 & 0 & V(x) & 0 \\ i\sqrt{2}\beta^* & 0 & \frac{-iD}{\sqrt{2}} & 0 & 0 & S & 0 & 0 & 0 & 0 & 0 & V(x) \\ V(x) & 0 & 0 & 0 & 0 & 0 & E_{Bi} & 0 & 0 & 0 & 0 & 0 \\ 0 & V(x) & 0 & 0 & 0 & 0 & 0 & E_{Bi} & 0 & 0 & 0 & 0 \\ 0 & 0 & V(x) & 0 & 0 & 0 & 0 & 0 & E_{Bi} & 0 & 0 & 0 \\ 0 & 0 & 0 & V(x) & 0 & 0 & 0 & 0 & 0 & E_{Bi} & 0 & 0 \\ 0 & 0 & 0 & 0 & V(x) & 0 & 0 & 0 & 0 & 0 & E_{Bi-so} & 0 \\ 0 & 0 & 0 & 0 & 0 & V(x) & 0 & 0 & 0 & 0 & 0 & E_{Bi-so} \end{pmatrix}$$

At the Γ point, where **k** = 0, the off-diagonal elements of the 6 × 6 portion of H_V becomes zero. In this case, the above Hamiltonian reduces to a 4 × 4 reduced Hamiltonian H_R given below [8]:

$$H_R = \begin{bmatrix} H/L & 0 & V & 0 \\ 0 & S & 0 & V \\ V & 0 & E_{Bi} & 0 \\ 0 & V & 0 & E_{Bi-so} \end{bmatrix}$$

The above matrix is different from the matrix proposed by Usman et al. using the tight binding calculations [9] which predicts the downward movement of the spin orbit split off band due to conventional alloying effect. However in this model, the E_{SO+} energy level moves upward due to VBAC interaction which is taken care of by the terms S and $E_{Bi\text{-}so}$. The solution of H_R gives four distinct eigen values representing the HH/LH and SO $E_\pm$ bands.

3 Results and Discussion

Figures 1 and 2 show the concentration profiles of bismuth atoms during the growth of InPBi from In melt for the cooling rates of 0.3 and 3 K/min and supercoolings of 4, 8, 12 and 16 K below the equilibrium liquidus temperature of 933 K. From these data, we can observe that for higher cooling rates, we get highly non linear profile of Bi concentration near the interface. This is due to the fact that the growth rate becomes high and the Bi atoms are depleted rapidly near the interface for higher cooling rates.

Moreover the bismuth atoms get lesser time to reach the growth region by slow diffusion. For lower cooling rate of 0.3 K/min, Bi concentration decreases slowly at the interface and is almost linear even for higher supercooling of 16 K. Hence, a melt cooling rate near this value and supercooling up to 16 K seems to be the ideal choice for the growth of InPBi from In melt.

Figure 3 shows the variation of E_+ and E_- energy levels corresponding to the HH, LH and SO bands for InPBi as a function of InBi mole fraction. The upward movement of the HH/LH and SO E_+ energy level is responsible for the reduction in band gap and enhancement in spin-orbit splitting energy for InPBi. There is repulsive interaction between the E_- and E_- energy levels which pushes the E_- levels in the downward direction. HH/LH E_+ level moves upward by an amount 31.9 meV/at.%Bi and the SO E_+ energy level increases by about 21.7 meV.

Figure 4 shows the restructuring of the valence band structure of $InP_{0.96}Bi_{0.04}$ determined near Γ point in the crystal directions (Δ and Λ) using 12×12 Hamiltonian discussed above. The band diagram also shows the splitting of the HH, LH and SO subbands into their corresponding E_+ and E_- bands. The parameters required for the calculation of the band structure is given in [10].

Berding et al. [11] in 1988 predicted theoretically that among the three In containing bismides InPBi, InSbBi and InAsBi, the growth of InPBi is the most difficult but once grown, it forms the most stable alloy for mid-infrared optoelectronic applications. Two recent reports on the growth and characterization of InPBi

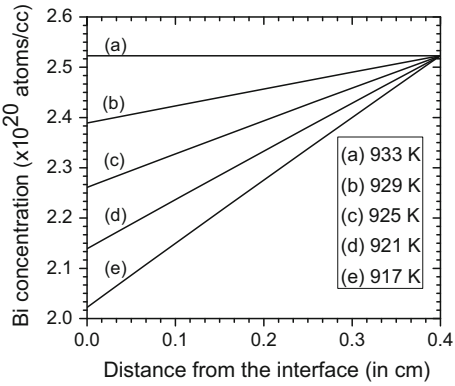

Fig. 1 Simulated concentration profiles of Bismuth in InPBi solution under different supercoolings below equilibrium temperature of 933 K and for a constant cooling rate of 0.3 K/min

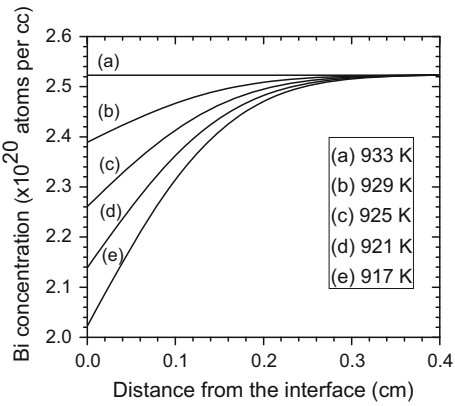

Fig. 2 Simulated concentration profiles of bismuth in InPBi solution under different supercoolings below equilibrium temperature of 933 K and for a constant cooling rate of 3 K/min

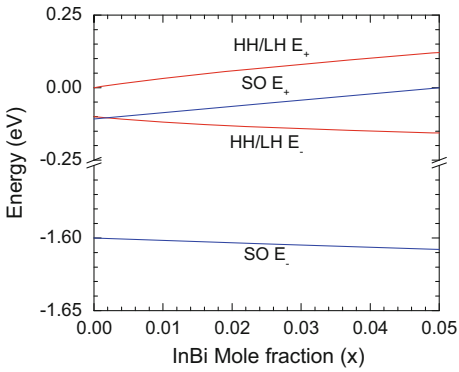

Fig. 3 Relative positions of the E_+ and E_- energy levels for the HH/LH and SO bands as a function of InBi mole fraction

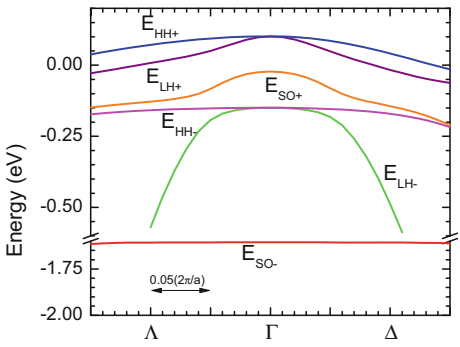

Fig. 4 Band dispersion in $InP_{0.96}Bi_{0.04}$ and InP showing the splitting of LH, HH and SO bands into E_+ and E_- energy levels in the Δ and Λ directions calculated using k•p method

by gas source molecular beam epitaxy (GSMBE) indicated band gap reduction values of 56 meV [2] and 46 meV [12] per percent of Bi content. A higher value of 53 meV/%Bi was obtained in $InP_{1-x}Bi_x$ grown by liquid phase epitaxy (LPE) [13]. Kopaczek et al. [14], on the other hand, reported a higher value of band gap

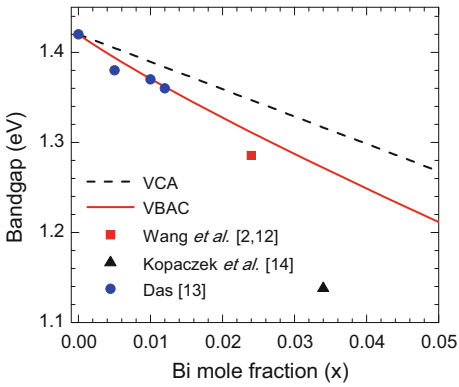

Fig. 5 Calculated band gap of InPBi as a function of Bi mole fraction using VCA and VBAC models

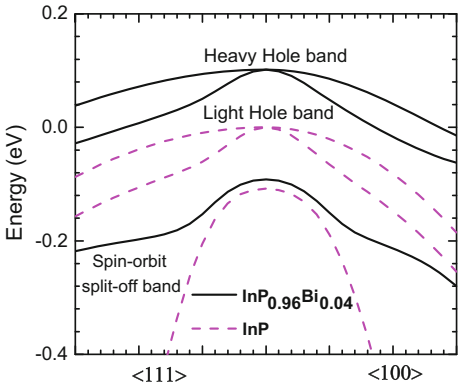

Fig. 6 Valence band structure showing the HH, LH and SO bands in the <100> and <111> directions for $InP_{0.096}Bi_{0.04}$

reduction of about 83 meV/Bi% in materials with $x \leq 3.4$. Figure 5 shows the comparison of these experimentally obtained values with the theoretically calculated band gap values for InPBi using Virtual Crystal Approximation (VCA) and VBAC Models. The comparison yields excellent results and is used to obtain a suitable value of the coupling parameter C_{Bi}.

Figure 6 shows the valence band structure of InPBi and InP showing the LH, HH and SO bands. There is an upward movement of LH, HH and SO bands for InPBi with respect to that of InP. For a Bi concentration of 4 at.%, HH/LH bands move upward by about 101.6 meV whereas the SO band moves upward by 16.3 meV indicating an increase of spin orbit splitting energy by 85.3 meV or 21 meV/at.%Bi [15].

4 Conclusions

In conclusion, the growth kinetics involved in the diffusion of bismuth atoms during the LPE growth of InPBi is discussed. The reduction in energy band gap and enhancement of spin-orbit splitting energy is explained using VBAC Model. The VBAC and VCA calculated values of band gap of InPBi are compared with the experimental results to yield excellent agreement. The HH/LH E_+ energy level moves upward by about by an amount 32 meV/at.% Bi and the SO E_+ energy level increases by about 21 meV/at.% Bi.

References

1. H. Li, Z.M. Wang (eds.), *Bismuth-containing compounds (Springer series in Materials Science)*, vol. 186 (Springer Science+Business Media, New York, 2013)
2. S. Wang, K. Wang, Y. Gu, W. Pan, X. Wu, L. Zhang, Y. Li, Q. Gong, in *ICTON'14: International Conference on Transparent Optical Networks*, (Graz Austria, C 5.4). doi: 10.1109/ICTON.2014.6876587
3. I. Crossley, M.B. Small, J. Cryst. Growth **11**, 157 (1971)
4. K. Jeganathan, S. Saravanan, K. Baskar, Mater. Chem. Phys. **49**, 141 (1997)
5. H.S. Carslaw, J.C. Jaeger, *Conduction of heat in solids* (Oxford University Press, Oxford, 1959), p. 468
6. K. Alberi, O.D. Dubon, W. Walukiez, K.M. Yu, K. Bertulis, A. Kroktus, Appl. Phys. Lett. **91**, 051909 (2007)
7. K. Alberi, J. Wu, W. Walukiewicz, K.M. Yu, O.D. Dubon, S.P. Watkins, C.X. Wang, X. Liu, Y.J. Cho, J. Furdyna, Phys. Rev. B **75**, 045203 (2007)
8. D.P. Samajdar, S. Dhar, The Sci. World. J. **2014**, 704830 (2014)
9. M. Usman, C.A. Broderick, A. Lindsay, E.P. O'Reilly, Phys. Rev. B **84**, 245202 (2011)
10. D.P. Samajdar, T.D. Das, S. Dhar, Comp. Mater. Sci. **111**, 497 (2016)
11. M.A. Berding, A. Sher, A.B. Chen, W.E. Miller, J. Appl. Phys. **63**, 107 (1988)
12. K. Wang, Y. Gu, H.F. Zhou, L.Y. Zhang, C.Z. Kang, M.J. Wu, W.W. Pan, P.F. Lu, Q. Gong, S.M. Wang, Sci. Rep. **4**, 5449 (2014). doi:10.1038/srep05449
13. T.D. Das, J. Appl. Phys. **115**, 173107 (2014)
14. J. Kopaczek, R. Kudrawiec, M.P. Polak, P. Scharoch, M. Birkett, T.D. Veal, K. Wang, Y. Gu, Q. Gong, S. Wang, App. Phys. Lett. **105**, 222104 (2014)
15. D.P. Samajdar, S. Dhar, Superlattices Microstruct. **89**, 112 (2016)

Design and Analysis of Efficient Metal Clad Optical Waveguide Polarizer

Divya Madaan, Davinder Kaur, V.K. Sharma and A. Kapoor

Abstract A multilayer metal clad optical waveguide polarizer is designed. Its attenuation characteristics are analyzed. The polarizer consists of polystyrene-glass waveguide cladded with silver metal with MgF_2 as a buffer inserted between them. And a superstrate layer of MgF_2 cover the metal layer. Here, metal film is kept thin to enhance the TM absorption by the lossy surface plasmon polariton by the resonant coupling of the guided mode. The structure was optimized for various values of buffer thickness and it was found that at particular buffer thickness TM losses are maximum, making it an efficient TE polarizer, allowing it to pass.

1 Introduction

Multilayer metal clad waveguides with a low index buffer layer can be designed as a highly efficient polarizer if various layer thicknesses are properly optimized. The polarizer is based on resonant coupling of guided modes to surface plasmon mode which are supported by metal layer. Metal clad optical waveguides are suitable for electro-optic, magneto optic devices and mode filters [1]. We investigate the Polystyrene-Glass TE Pass polarizer. Polarizing components are essential to ensure stability and enhance the performance of coherent optical communication devices. Several methods have been reported in the literature to produce a TE pass polarizer. Some use the birefringent polymer overlayers on the waveguide while other use the electro-optic effect in polymer layers to split the TE and TM modes [1–3]. Integrated optical waveguides polarizers have been proposed using semiconductor clad waveguide structures [4]. A structure is suggested with a buffer layer with high value of refractive index is inserted between the guiding layer and the metal clad [5]. Coupling occurs from a normal guided mode to a lossy surface plasmon mode

D. Madaan (✉) · D. Kaur · A. Kapoor
Department of Electronic Science, University of Delhi, New Delhi, India
e-mail: divyaphd14@gmail.com

V.K. Sharma
Keshav Mahavidyalaya, University of Delhi, New Delhi, India

V.K. Jain et al. (eds.), *Recent Trends in Materials and Devices*,
Springer Proceedings in Physics 178, DOI 10.1007/978-3-319-29096-6_35

at a particular critical value of the buffer layer thickness, which is analyzed as a resonant absorption peak. Function of the buffer layer (lower index) inserted between waveguide and the metal is to reduce the insertion losses. For designing such type of multilayer polarizers, the absorption peak is the most important.

2 Results and Discussion

First of all a simple structure is considered with metal layer in between two MgF_2 layers, where graph of real (Fig. 1) and imaginary (Fig. 2) part of Neff was drawn with respect to metal thickness. From Fig. 1, it is observed that as the metal thickness decreases, the losses keep on increasing, but at metal thickness 0.013 μm, it can be observed from Fig. 1 that the Neff of symmetric insulator-metal-insulator guide is 1.55 which matches the Neff value of waveguide with metal cladding. That's why we take a certain value in between. We are getting two modes, but we are considering only Mode 1 because only this mode interacts with the guided mode (short-range mode). From Fig. 2 it can be seen that as the metal thickness decreases, the losses of one mode goes on increasing while that of the other mode decreases. The mode whose losses increase is called the short-range mode while the other is long-range mode. Here, we are interested in the short-range mode. Now the whole multilayer structure is considered (Fig. 3) having the substrate as Glass, Polystyrene as waveguide, then a buffer layer, a metal cladding and a superstrate layer. The structure is analyzed at a wavelength of 1.55 μm. However when the optimized insulator-metal-insulator guide is placed on the dielectric waveguide, its Neff is modified. For index matching of the guided modes of the insulator-metal-insulator and the dielectric waveguide, the buffer thickness is varied. At certain buffer thickness (here 0.2 μm) the attenuation of TM mode becomes maximum. Higher buffer thickness can also reduce the loss of TM mode, thus increasing the extinction ratio (ratio of TM to TE losses). Figures 4 and 5 shows the variation of Neff (Real)

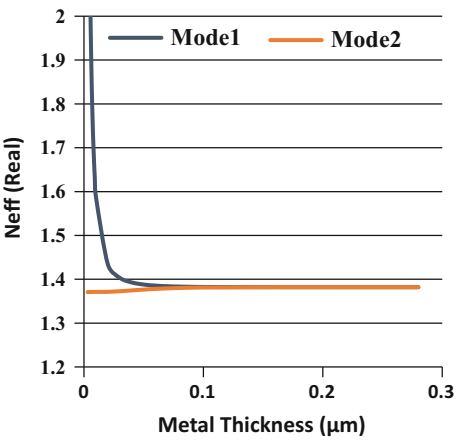

Fig. 1 Variation of Neff (real) with metal thickness for insulator-metal-insulator structure

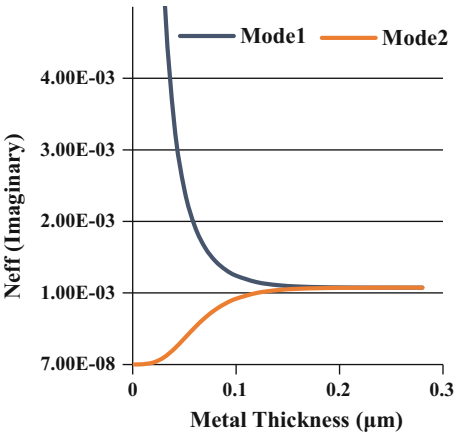

Fig. 2 Variation of Neff (imaginary) with metal thickness for insulator-metal-insulator structure

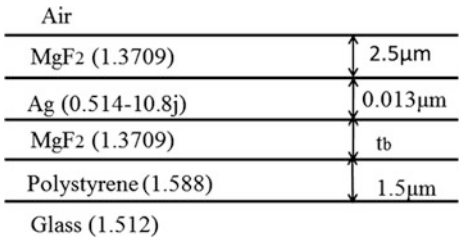

Fig. 3 Multilayer structure of TE pass polarizer

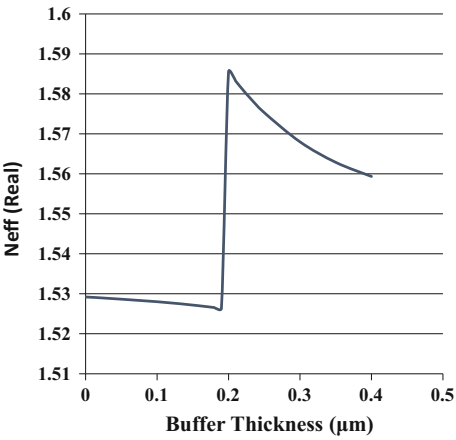

Fig. 4 Variation of Neff (real) with buffer thickness of polarizer structure

and LOSS (in dB/cm) with respect to buffer thickness respectively. From Fig. 4, it can be seen that at the critical buffer thickness (at 0.2 µm) there is an abrupt change in the effective index. It is this thickness at which the resonance occurs, when the

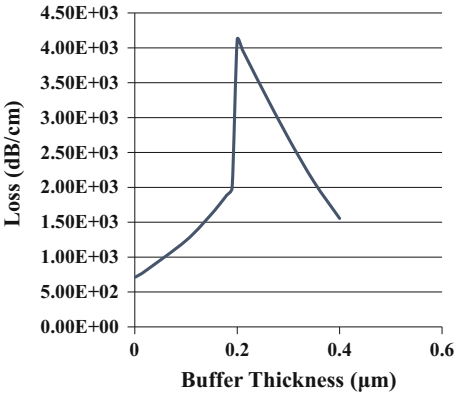

Fig. 5 LOSS (in dB/cm) variations of TM mode of polarizer with varying buffer thickness

lossy modes of metal and TM guided wave interact and get absorbed by the metal, allowing only TE to pass through the guiding layer, making it a TE pass polarizer. From Fig. 5, it can be seen that at a certain value of buffer thickness, the TM losses are maximum having the value 4.12×10^3 dB/cm.

3 Conclusions

In conclusion, at buffer thickness 0.2 μm we are getting the value of TM losses as 4.12×10^3 dB/cm. Such high value of TM losses makes it an efficient polarizer as by increased losses, the coupling between guided mode and lossy mode increases and at a certain value the resonance occurs and absorption peak is obtained for TM mode. However, TE losses at this buffer thickness are very low (0.02 dB/cm).

References

1. V.K. Sharma, A. Kumar, A. Kapoor, Opt. Commun. **284**, 1815 (2011)
2. A. Morand, C.S. Perez, P. Bench, S. Tedjini, IEEE Photonics Technol. Lett. **10**, 1599 (1998)
3. M.C. Oh, S.S. Lee, S.Y. Shin, W.Y. Hwang, J.J. Kim, Electron. Lett. **32**, 324 (1996)
4. R.F. Carson, T.E. Batchman, Appl. Opt. **29**, 2769 (1990)
5. D. Kumar, V.K. Sharma, K.N. Tripathi, J. Opt. **12**, 015003 (2010)

Effect of Substrate on Surface Plasmon Resonance of PLD Grown Silver Nanoparticles

Poonam Shokeen, Amit Jain, Avinashi Kapoor and Vinay Gupta

Abstract Present work discusses the importance of substrate for desired plasmonic responses. Silver nanoparticles are deposited on silica and zinc oxide substrate by pulsed laser deposition system. SEM, EDAX, XRD and UV-visible spectroscopy are used to study the effect of substrate on surface plasmon resonance of silver nanoparticles. A shift in resonance wavelength is observed for two substrates with a visible change in the intensity of the surface plasmons. Nanoparticles deposited on silica substrate show sharp SPR in comparison to nanoparticles deposited on zinc oxide. Nanoparticles deposited on ZnO cover a wide absorption spectrum in comparison to nanoparticles deposited on silica substrate. This generic study can be very helpful for design considerations of various plasmonic structures for photovoltaic applications.

1 Introduction

Increasing energy needs have brought the focus of the researchers towards the renewable resources of energy. Sun is the ultimate source of energy and harvesting the solar energy to meet the future needs is not only an environmental friendly but a practical solution to this problem. However, the high cost of conventional solar cells is hindering their popularity. Half of their costs are owing to the substrate material themselves. Silicon is among the most popular substrate material in

P. Shokeen (✉) · A. Kapoor
Department of Electronic Science, University of Delhi, South Campus,
Benito Juarez Road, New Delhi 110021, India
e-mail: poonamshokeen7@gmail.com

A. Jain
Department of Electronic Science, Rajdhani College, University of Delhi,
Mahatma Gandhi Marg, Raja Garden, New Delhi 110015, India

V. Gupta
Department of Physics and Astrophysics, University of Delhi,
North Campus, New Delhi 110007, India

V.K. Jain et al. (eds.), *Recent Trends in Materials and Devices*,
Springer Proceedings in Physics 178, DOI 10.1007/978-3-319-29096-6_36

commercial solar cells. Different groups across the world are working on different methods to reduce the cost per Watt. A thin film solar cell is among the most popular option among the lot. Their ease of installation options and cost effectiveness are one of the few reasons for their popularity. Gallium selenide, Cadmium Telluride, copper indium gallium selenide and amorphous silicon solar cells are among the popular thin film solar cells [1–4]. But efficiencies of all these thin film solar cells are very low in comparison to conventional silicon solar cells. Therefore, new geometrical models are required to enhance their optical absorption and to enhance minority carrier diffusion lengths.

Use of plasmonic nanostructures is among the popular light trapping technique in thin film solar cells [5]. It finds applications in various other optoelectronic systems as well like photodiodes, sensors, metamaterials, etc. [6, 7]. Conduction band electrons of novel metals oscillate at a resonant wavelength when exposed to electromagnetic radiations. The surface plasmon resonance (SPR) of metal nanoparticles shows strong optical and near field scattering around the particle [7]. It results in the enhanced scattering of the incident light and as a result, the optical path length is increased and chances of absorption of incident photon increase. Metal nanoparticles when placed on the dielectric medium, trap the incident light in the underlying substrate [6, 8]. SPR is dependent on the optical properties of the underlying substrate. The strength of interaction of the incident flux and the transmitted flux is highly influenced by the dielectric function of the surrounding media. Therefore, understanding the importance of appropriate substrate material is a prime requirement.

Zinc oxide and silicon dioxide are among the most popular transparent oxides used in solar cells. The dielectric constants of the two oxides are quite favorable for the excitation of surface plasmons and field propagation into the underlying absorber layers. However, the behavior of surface plasmons is dependent on the surrounding medium [7]. So, the choice of the appropriate hosting material is necessary for effective coupling of excited modes into the underlying substrate.

In this work, we study the optical properties of silver nanoparticles on silica and zinc oxide substrate. Uniform layer of Silver nanoparticles is deposited by pulsed laser deposition system. Various structural and electrical properties of samples are performed to study the involved phenomenon.

2 Experimental Details

Glass slides were used as the substrate and were cleaned with a soapy solution, followed by an ultrasonic bath for 15 min in a solution of H_2O_2, propanol and DI water (1:1:1). KrF pulsed laser deposition system operating at 248 nm was used for the fabrication of silver nanoparticles. 99.9 % pure silver target was ablated at 5 Hz with an energy of 200 mJ. The substrate was heated at 373 K to obtain uniform distribution of nanoparticles. For sample 1, deposition was carried out on a glass substrate directly. For sample 2, the zinc oxide precursor was spin coated at 2500 rpm for 30 s on the glass substrate. The film was dried at 473 K for 10 min.

This process was repeated 5 times to obtain 100 nm thick layer. The ZnO thin film was obtained after annealing it at 773 K for 2 h. Silver nanoparticles were deposited by PLD at a substrate temperature of 373 K. Samples so prepared were characterized using UV-visible spectroscopy, X-ray diffraction and scanning electron microscopy and Energy dispersive X-ray spectroscopy.

3 Results and Discussion

Figure 1 shows the SEM images of the samples. Regular sized uniform distribution of silver nanoparticles is obtained in both of the depositions. Silver nanoparticles deposited on the zinc oxide layer are relatively bigger in size in comparison to ones deposited on silica substrate. Inset of Fig. 1 shows the EDAX of the samples. The peaks observed at 0.26, 0.97, 3.0, 3.2 and 3.4 keV correspond to the binding energies of Ag M, Zn L, Ag Lα, Ag Lβ and Ag Lβ2 respectively. The peaks at 0.62 and 1.74 keV correspond to the binding energy of O K and Si K present in glass substrate, respectively. The rest of the peaks belong to sodium, calcium and magnesium existing in glass substrate. Silver content is almost same in two samples. It indicates the non-reactivity of the silver with underlying substrate. In inset of Fig. 1b, an increase in the content of oxygen is due to the presence of bounded oxygen of zinc oxide.

Figure 2 shows the XRD analysis of silver nanoparticles on ZnO and glass substrate. In Fig. 2a, Silver peaks are observed at 38.2° and 44.4° corresponding to (111) and (200) planes (PDF No. 893722). In Fig. 2b, 31.7°, 34.4°, 36.2°, 47.4°, 56.5° and 62.7° correspond to (100), (002), (101), (102), (103) and (220) plane of ZnO (PDF No. 891357) and, 38.2°, 44.4° and 64.4° correspond to (111), (200) and (220) plane of silver (PDF No. 893722). XRD shows the absence of any oxide formation of silver nanoparticles.

Figure 3 shows the UV-visible spectrum of the deposited samples. The prominent surface plasmon resonance of silver nanoparticles is observed due to uniform distribution of silver nanoparticles. ZnO shows an absorbance peak at 360 nm. SPR

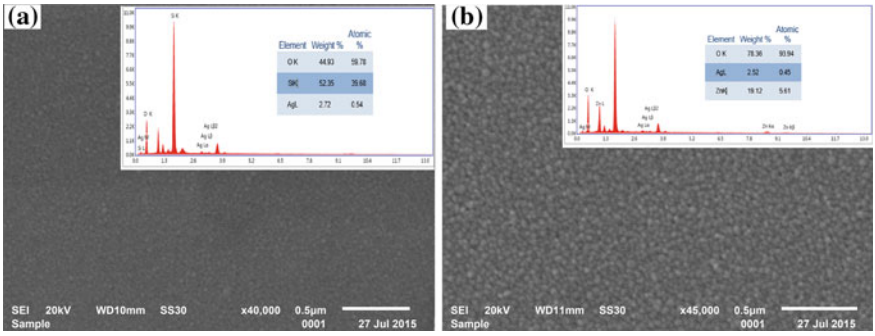

Fig. 1 SEM images of silver nanoparticles deposited on **a** glass substrate **b** ZnO substrate

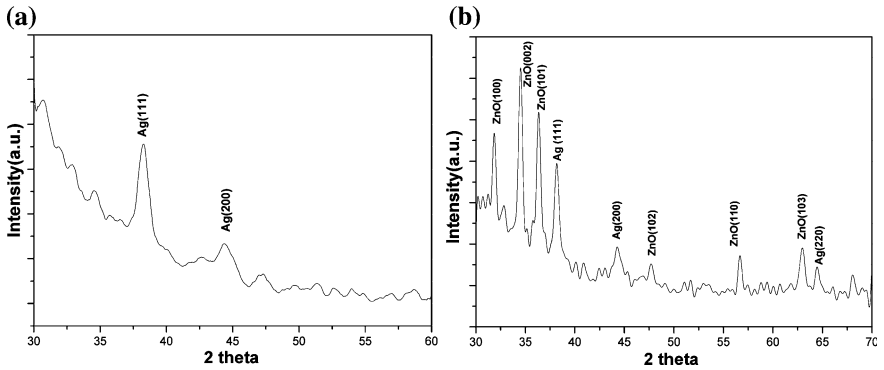

Fig. 2 XRD analysis of the silver nanoparticles deposited on **a** Silica and **b** ZnO substrate

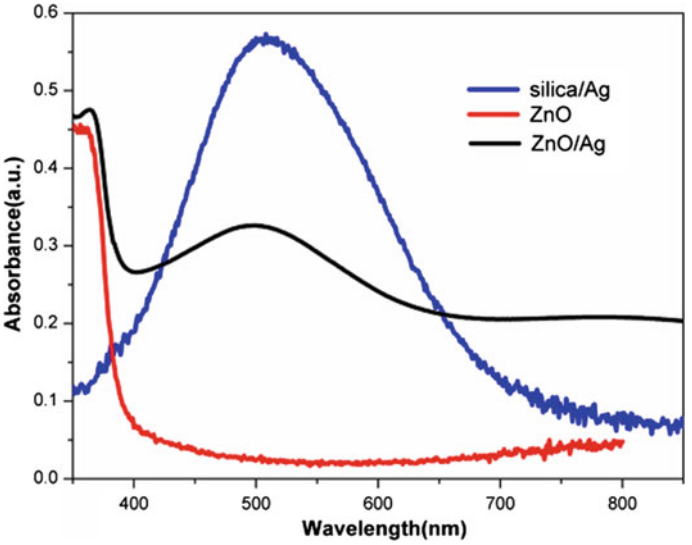

Fig. 3 UV-visible spectra of the pristine ZnO, silver nanoparticles on silica and silver nanoparticles on ZnO

peaks are obtained at 510 and 500 nm for silica and ZnO substrate respectively. SPR peak is slightly blue shifted for the ZnO substrate. It occurs mainly due to the relatively high dielectric constant of the ZnO. However, intense SPR is observed for the silica substrate. The difference in strength of interaction of incident electromagnetic waves with the underlying substrate is a function of the dielectric constant of the underlying oxide. However, the overall absorbance region is improved for silver nanoparticles deposited on the ZnO sample than silica sample. It is due to the fact that ZnO/Ag is able to retain the individual absorbance regions of silver and

ZnO, and final absorbance contains the regions covered by them simultaneously. Hence, the choice of appropriate transparent oxides with suitable dielectric constants can further improve the device performance still performing their desired function.

4 Conclusions

In this work, the silver nanoparticles are deposited on silica and zinc oxide substrate. As a result of the difference in the dielectric constants of the two substrates, intensity and wavelength variation are observed in surface plasmon resonance of the nanostructures. With the increase in dielectric constant of the underlying layer, resonance peak shifts to lower wavelengths and peak sharpness is also reduced. However, absorbance region is increased for silver nanoparticles deposited on the ZnO substrate as it covers the absorption region of silver and ZnO simultaneously. Hence, the choice of underlying substrate material plays a crucial role in the resonance behavior of plasmonic nanostructures and should be taken into consideration while working with various devices. Absorption over a wide spectrum can be obtained by engineering appropriate materials.

Acknowledgments Authors are thankful to University Grants Commission (University of Delhi —Sch./Non-NET/139/Ext-146/2015-16/333) and Department of Science and Technology (R&D grand-RC/2014/6820) for the financial support to carry out this work.

References

1. M. Singh, J. Jiu, T. Sugahara, K. Suganuma, Appl. Mater. Interfaces **6**, 16297–16303 (2014)
2. P. Liska, K.R. Thampi, M. Grätzel, D. Brémaud, D. Rudmann, H.M. Upadhyaya, A.N. Tiwari, Appl. Phys. Lett. **88**, 203103 (2006)
3. X. Wu, Sol. Energy **77**, 803–814 (2004)
4. H.R. Stuart, D.G. Hall, Appl. Phys. Lett. **73**, 3815 (1998)
5. H.A. Atwater, A. Polman, Nat. Matter. **9**, 205–213 (2010)
6. P. Shokeen, Y.P. Singh, A. Jain, A. Kapoor, J. Nanophotonics **9**, 093066 (2015)
7. S. Zhang, D.A. Genov, Y. Wang, M. Liu, X. Zhang, Phys. Rev. Lett. **101**, 047401 (2008)
8. P. Shokeen, A. Jain, A. Kapoor, V. Gupta, Plasmonics **11**, 669–675 (2016)

Part III
Photovoltaics and Energy Storage

Study of Growth of Silver Nanoparticles as Plasmonic Layer on pc-Si Wafer to Enhance the Efficiency of Solar Cells

Bidyut Barman, Apurv Yadav, Shiv Chaudhary, Vivek Kumar, Abhishek Verma and Vinod Kumar Jain

Abstract Localized Surface Plasmon Resonance (LSPR) phenomena are of great interest in the field of thin film solar cells due to its light trapping capabilities using metallic nanoparticles. In this research work, we have investigated the surface plasmonic effect on textured poly crystalline silicon (Tpc-Si) substrate with Ag Nanoparticles. The maximum reflection reduction of $\sim$13 % with average nanoparticles size $\sim$35 nm for 250 °C and 20 min annealing temperature and duration respectively, has been observed in the wavelength range 300–800 nm. As a consequence reflection reduction in the solar cell which in turn increase in absorption of light especially in the higher wavelength region which can increase the efficiency of poly crystalline solar cells.

B. Barman (✉) · A. Yadav · S. Chaudhary · V. Kumar · A. Verma · V.K. Jain
Amity Institute of Advance Research and Studies (Material & Devices), Amity University, Noida, Uttar Pradesh, India
e-mail: bidyut_b15@yahoo.co.in

A. Yadav
e-mail: apurb0210@gmail.com

S. Chaudhary
e-mail: snazy.07@gmail.com

V. Kumar
e-mail: vkumar19@amity.edu

A. Verma
e-mail: averma5@amity.edu

V.K. Jain
e-mail: vkjain@amity.edu

B. Barman · A. Yadav · S. Chaudhary · V. Kumar · A. Verma · V.K. Jain
Amity Institute of Renewable and Alternate Energy, Amity University, Noida, Uttar Pradesh, India

V.K. Jain et al. (eds.), *Recent Trends in Materials and Devices*,
Springer Proceedings in Physics 178, DOI 10.1007/978-3-319-29096-6_37

1 Introduction

Conventional wafer based Silicon (Si) solar cells have thickness in the range of 180–300 μm, where the major proportion of cost is associated with the high price of silicon material used and its processing [1, 2]. In order to reduce production and material cost, thin-film PV cells have gained popularity among research and commercial applications, alike which slashes down the cell thickness maximum in the range of 1–2 μm [1]. Further, it can be deposited on cheap module-sized substrates such as glass, plastic or stainless steel which can help achieve significant reduction in the cost of solar cell production [1].

However, light absorption for thin film PV especially in the near-band gap region is ineffective and its efficiency suffers as compared to standard solar cells due to its leaner geometry [2]. Typical surface texturing techniques used in wafer-based solar cells, including etching and sculpting are not possible in thin film cells due to its lean geometric thickness, which is in the range of 10 μm. Also, texturing of the substrate as an alternative was found to increase recombination losses because of excess surface area [3].

Light trapping mechanism in the form of surface Plasmon resonance using metallic nanoparticles can be devised in thin film solar cells to generate more electron-hole pair by increasing its light absorption from scattered light and consequently, its efficiency [2].

This research work focuses mainly on the growth and changes in surface morphology of silver nanoparticles to study surface plasmonic effect using thin-film deposition on textured poly crystalline silicon (Tpc-Si) substrate by sputtering for different thickness followed by rapid thermal annealing (RTA) technique with varying temperature and duration. The surface Plasmon resonance of a particle is affected by the size, shape and the dielectric medium [4]. Here we discusses the effects of size and shape which can be tuned using RTA depending on the solar cell application.

2 Experimental Methodology

The growth of plasmonic Ag NPs on T-pcsi substrate were performed by using RF (13.56 MHz) Sputtering (Model: HHV—12″ MSPT) followed by RTA (Model: MTI—EQ-OTF-1200X-4-RTP-HV). Silver is the metal of choice because of its low absorption losses compared to other metals [5]. Before deposition the poly Silicon substrate were cleaned sequentially in ultrasonic bath in acetone, isopropyl alcohol and deionized water for 15 min each. A silver thin film from its target of 99.999 % purity was deposited on thoroughly cleaned poly-Si p-type textured wafer using RF Sputtering, at the working power of 75 W for 10 s, in order to achieve the desired uniform coating. The working base pressure of the chamber was kept at

2.8×10^{-5} mbar. During deposition the growth pressure of the chamber was maintained at 6×10^{-2} mbar, with Argon gas flow rate of 2 kg/cm^2 into the chamber. In the present research the post deposition rapid annealing process was performed on as-prepared samples to achieve Ag NPs of various sizes and concentration at three different optimized temperatures of 200, 250, and 300 °C using rapid thermal annealing (RTA) process. The heating rate of RTA was set at 100 °C/s, whereas, natural cooling was adopted for reducing the substrate temperature back to ambient conditions (30 °C). The surface morphology along with the size of the Ag NPs were characterized using a Scanning Electron Microscope (Model: Zeiss—EVO-18) operated at 2.5 kV. Average sizes of the particles were calculated using the image processing program, ImageJ v1.45 software [6].

Further, the optical analyses (reflection) of the samples were performed using by Shimadzu ISR-2600Plus Integration Sphere. Figure 1 illustrate the protocol followed to achieve desired results.

3 Results and Discussion

In the present research work, silver thin-film deposited using RF Sputtering on Tpc-Si substrate followed by rapid thermal annealing, leads to formation of Ag NPs at specific annealing temperature and duration. It has been observed that the as prepared Ag NPs are poly-disperse in size and exhibits indistinct spacing between them due to the statistic formation process [6]. The RTA makes use of the distinct thermal properties of the host (as ploy Si) and the deposited metallic film (as silver), and thermal expansion coefficient of both materials, which plays a vital role in the formation of Ag NPs. Therefore, as a result of surface tension, thin-film gets break down into NPs. Due to the variation in size and shape of these particles are dependent on the heat treatment of the thin film, one can easily tune the desired plasmonic NP's size and hence the plasmonic frequency. The plasmonic behaviour can be varied by tuning the size, shape and material of the nanoparticles [4]. Additionally, the plasmonic behaviour exhibited by the nanoparticles is also

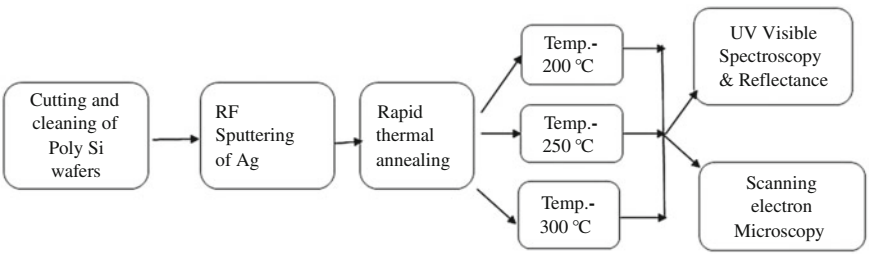

Fig. 1 Flowchart of particular sample preparation and characterization

dependent on the dielectric medium around the particle as a slight shift in dielectric surroundings can lead to a notable change in the resonant energy [7].

The SEM images of Ag NPs deposited on Poly-Si surface for different annealing duration of 5, 10, 15, 20 and 30 min at an optimal annealing temperature 250 °C is shown in Fig. 2. The SEM images in Fig. 2a–e shows the variation in surface morphology and size for different annealing durations.

With different annealing durations from 5 to 30 min, Ag NPs average size can be tune from 35.77 to 59.39 nm. At 250 °C for 5 min annealing duration the average sized of Ag NPs is 59.39 nm with a high density (Fig. 2a). An increase of annealing durations to 10 and 15 min led to change in NPs sizes with reduced surface coverage, this is due to the high atomic diffusion at higher temperatures which leads to aggregation and formation of larger particles because the surface tension of particles gets minimized. On increasing annealing (RTA) time duration up to 20 min the formation of NPs which were more distinctly spaced and spherical in appearance as shown in Fig. 2d.

On the other hand, it has been observed that further increase in the RTA duration to 30 min or more, at typical conditions, as shown in Fig. 2e, shows signs of coalescence between particles, where the adjacent NPs start merging with each other forming irregular shapes. The similar results have also been observed in the typical samples, grown at RTP annealing temperature of 200 and 300 °C. However, above 300 °C, the formation of plasmonic nanoparticles exhibit very high coalescence and non-spherical shape. Therefore, by optimally increasing the annealing temperature and time, these NPs can easily be controlled for a desired size and consequently, a desired plasmonic resonance peak [4]. Figure 3 shows the Time

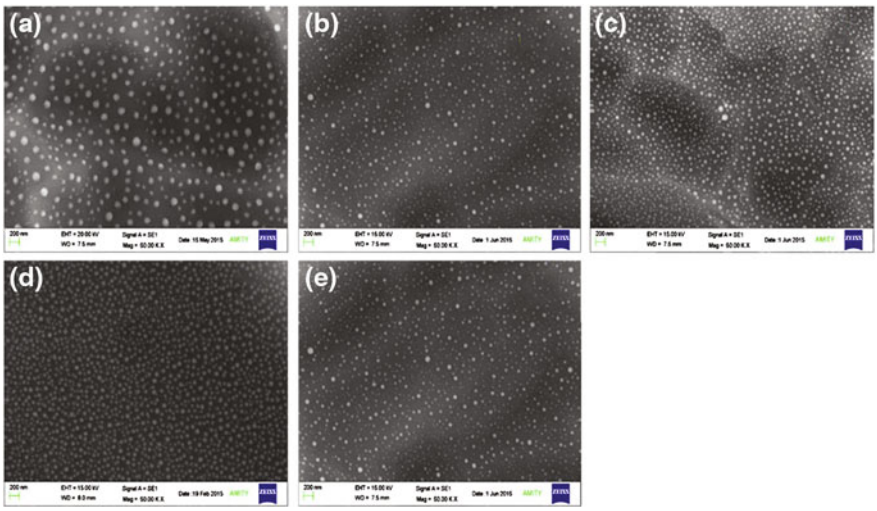

Fig. 2 SEM images showing RTA effect on Ag island film at constant 250 °C for different time durations (**a**) 5 min, (**b**) 10 min, (**c**) 15 min, (**d**) 20 min and (**e**) 30 min

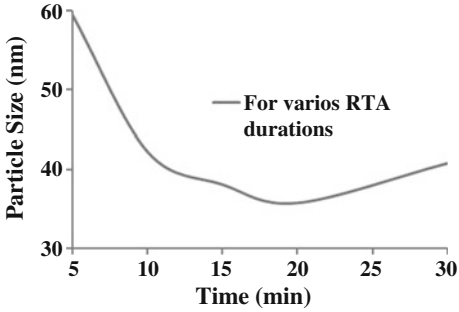

Fig. 3 Change in average particle size with annealing duration for Tpc-Si wafers

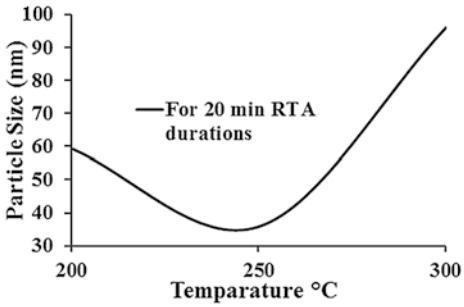

Fig. 4 Change in average particle size annealing temperature at constant annealing duration for Tpc-Si wafers

versus particles size graph for 250 °C for different annealing duration. Figure 4 shows change in average particles size with different annealing temperature for an optimal RTA duration of 20 minutes.

Figure 5 represents the total reflectance spectra of without and with the Ag NPs deposited on T-Si substrates for 5, 10, 15, 20 and 30 min followed by annealing at 250 °C, and the inset of Fig. 5 shows the percentage of reflectance reduction from the textured-Si substrate due to Ag NPs compared to bare T–Si average reflectance of 23 %. The reduced reflectance is relatively higher towards the higher wavelength region (600–800 nm) up to 20 min sample having the NPs sizes of 35.77 nm compared to the lower wavelength region. For 5 min deposition time, the reduction in reflectance is 11.52 % in the wavelength range from 300 to 800 nm. The maximum reflectance reduction of 66.84 % is observed for 20 min sample, which is reduced to 50.23 % for 30 min sample. Figure 6 shows the time vs reflectance graphs for 250 °C annealing temperature for various annealing durations and Fig. 7 illustrate the change in reflectance with different temperature at optimized annealing duration. From the figures we can observed that for an annealing temperature and duration of 250 °C and 20 min respectively it shows minimum reflectance value with an average reflectance of around 13 % compared to raw Poly silicon with an average reflectance of 23 %. It is attributed due to the fact that at 250 °C and 20 min annealing durations the nanoparticles formed were more distinctly spaced

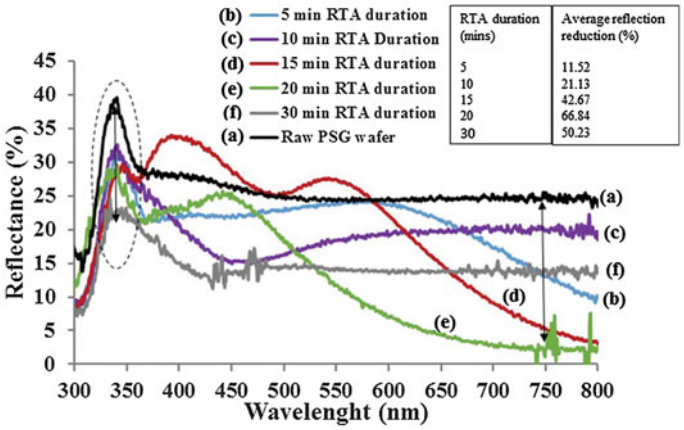

Fig. 5 Reflectance graph and its comparative analysis—for surface plasmonic layer fabricated on poly-crystalline Si solar cells

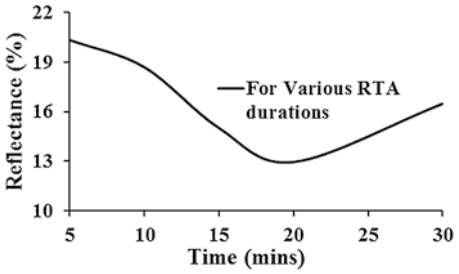

Fig. 6 Change in average reflectance with annealing duration, at 250 °C for Tpc-Si wafer

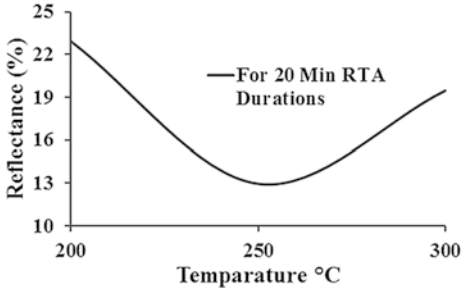

Fig. 7 Change in average reflectance with annealing temperature, at constant annealing duration of 20 min, for Tpc-Si wafer

and spherical in appearance [6, 8]. So we observed a significant reduction in reflectance value of the incident light. Therefore, by properly optimizing the RTP annealing temperature and duration, the reflectance can easily be reduced even below 13 %. This reduction in reflectance, as a consequence will definitely increase the absorption in thin film pc-Si solar cell, which in turn increase the efficiency of Tpc-Si solar cell by significant amount.

4 Conclusion

We have observed and analysed the growth and changes in surface morphology of silver nanoparticles to study surface plasmonic effect on Tpc-Si substrate by sputtering for different thickness followed by rapid thermal annealing (RTA) technique with varying temperature and duration. Here we observed reduce reflections form Tpc-Si substrate with Ag nanoparticles with maximum reflection reduction of around 13 % for 250 °C with an annealing duration of 20 min with average nanoparticles size 35.77 nm in the wavelength range 300–800 nm. Hence there is a significant reflection reduction of incoming light from the front surface of a solar cell which in turn will increase charge collection and as a consequence the short circuit current of solar cell increases and so there is increase in efficiency of thin film solar cell.

Acknowledgments Authors are thankful to Department of Science and Technology (DST), Govt. of India, India for financially supporting this research work. Authors also wish to thank to Dr. D. N. Singh, CTO, IndoSolar Pvt. Ltd. for his valuable time and support. Authors also wish to acknowledge Dr. Ashok K. Chauhan, Founder President, Amity University, Noida for his continuous encouragement and kind support to carry out present research.

References

1. K.R. Catchpole, A. Polman, Opt. Express **16**(26), 21793–21800 (2008)
2. H.A. Atwater, A. Polman, Nat. Mater. **9**, 205–213 (2010)
3. J. Samarth, V. DePauw, V.D. Miljkovic, A. Dmitriev, C. Trompoukis, I. Gordon, P. Van Dorpe, O. El Daif, Progress, in *Photovoltaics: Research and Applications*, 1–18 (2013)
4. S. Chakravarty, L. Arunagiri, S. Chaudhary, A. Verma, V.K. Jain, Phys. Semicond. Devices **17**, 305–308 (2013)
5. N. Adamovic, U. Schmid, e & i Elektrotechnik und informationstechnik **12**, 342–347 (2011)
6. S.K. Sardana, V.S.N. Chava, E. Thouti, N. Chander, S. Kumar, S.R. Reddy, V.K. Komarala, Appl. Phys. Lett. **104**(073903), 1–5 (2014)
7. P. Cheng, D. Li, D. Yang, Optoelectron. Adv. Mater.-Rapid Commun. **5**(3), 4455–4458 (2011)
8. K. R. Catchpole, A. Poleman, Design principles for particle plasmon enhanced solar cells. Appl. Phys. Lett. **93**(19), 191113 (2008)

Growth of Graded Si_xN_y ARC Films to Enhance the Efficiency of Multi-crystalline Silicon Solar Cells and Applicable in High Volume Production

Virender Sharma, Abhishek Verma, Daisy Verma, Vinod Kumar Jain and D.N. Singh

Abstract Optimized silicon nitride (SiN) film, which acts as an Anti-Reflection Coating (ARC), surface and bulk passivating layer is the key to enhance the efficiency in silicon solar cells particularly in multicrystalline silicon solar cells. In this work, SiN films with graded and non-graded profiles with different refractive indices have been prepared. The efficiency of a multi-crystalline silicon solar cell has been measured and followed by a module making process to evaluate the cell-to-module conversion power loss (CTMPL). It has been found that an optimized graded SiN film can reduce the surface reflection in ultraviolet (UV) and visible wavelength region significantly and hence enhances the efficiency compared to single step (non-graded) recipe. To develop more insight of the experimental work, simulation was carried out using PC1D solar cell simulator and it has been observed that refractive index (n) of 2.04 is the optimum value of refractive index in single step recipe as it enhances efficiency on cell level measurement among all different single step SiN recipes. Whereas, refractive index of 2.14 is the optimum value of refractive index in graded step recipe as it produces much higher efficiency on cell level measurement among all SiN recipes and even better than single step recipe. In this research work, it has been found that graded step refractive index recipe has reduced the reflectance of SiN films, enhanced spectral response and efficiency of the solar cells and higher refractive index of SiN film corresponds to reduced CTMPL values of the modules.

V. Sharma (✉) · A. Verma · D. Verma · V.K. Jain
Amity Institute of Renewable and Alternate Energy, Noida 201303, Uttar Pradesh, India
e-mail: virender.sharma15@gmail.com

A. Verma · V.K. Jain
Amity Institute for Advanced Research and Studies (Materials & Devices), Noida 201303, Uttar Pradesh, India

V. Sharma · D.N. Singh
Indosolar Ltd., Greater Noida 201305, Uttar Pradesh, India

V.K. Jain et al. (eds.), *Recent Trends in Materials and Devices*,
Springer Proceedings in Physics 178, DOI 10.1007/978-3-319-29096-6_38

1 Introduction

The optical losses of solar cells are due to reflection of incident light at metallic contacts, reflection at the front surface of the silicon and weakly absorbed wavelengths of light of energy lower than the bandgap of silicon. The reflection of photons from the front surface of a photovoltaic cell is one of the main reasons of lowering the efficiency of conversion of light to electricity. Because of abrupt change of refractive index on the interface between silicon and air, the reflectance from the surface of the silicon can be as high as 33 % [1]. To reduce surface reflectance and to enhance light absorption are very important aspects to improve the conversion efficiency of silicon solar cell. Various methods have been followed to reduce the reflection losses by texturing the front surface or by depositing an antireflection coating (ARC) on the top of the solar cells. Sometimes both the techniques have been used first textures the front surface of the solar cell and then deposit the ARC of silicon nitride to further to reduce the reflection losses [2, 3]. This ARC also helps in passivating the top surface of the solar cells. Coatings of other materials such as TiO_2, Ta_2O_5, ZnS and ZnO have also been used to have an antireflection coating on solar cells [4, 5], but SiN is most widely used ARC coating due to its high capability of passivation of the grain boundaries and defects in multi-crystalline solar cells. These processes have been followed in general in large volume production of silicon solar cells in industries. SiN film is deposited from the mixture of silane (SiH_4) and ammonia (NH_3) gas in a plasma chamber by PECVD. Refractive index is tuned by the NH_3/SiH_4 gas flow ratio. Higher ratio of NH_3/SiH_4 gives lower refractive index of SiN film due to less hydrogen incorporation [6]. Improvement of solar cell efficiency is obtained by reducing reflection losses of the light from the front surface of the solar cell, optimization of light absorption and the usage of charge carriers generated in the material [7–9]. Unlike many other optoelectronic devices, solar cells operate at a broad range of wavelengths, from 300 to 1200 nm, which means they need a broadband ARC. During the last decade the SiN film deposited by PECVD method have been extensively studied in order to understand the mechanism of passivation as well as ARC coatings and to find the fundamental requirements of these layers [8–16]. In an industry multi-crystalline silicon solar cells were fabricated by a single layer of SiN anti-reflection coating with an average thickness of $\sim$84 nm and average refractive index of $\sim$2.04 [3]. As discussed later, these layers do not minimise reflectance over a large range of wavelengths, although they reduce reflection drastically compared to a bare silicon surface. In this work, we have tried to optimize the SiN ARC coatings with different techniques for higher efficiency and compatible in the large volume production in industry. New type of graded refractive index SiN films were deposited on multi-crystalline silicon cells and optimized theoretically and experimentally, to obtain the minimum reflection in our lab. The lab optimised parameters of the graded refractive index SiN of ARC were also tested in the industry on the large scale production. Optimisation has been done by measuring the power output and

spectral measurements. It is found that graded refractive index recipe has reduced the reflectivity and enhanced the efficiency of the solar cells.

2 Theory

2.1 Texturization of Front Surface

In the case of texturization, silicon microstructures are formed on the silicon surface. These structures are able to redirect reflected light rays with the appropriate angle, impinging again the silicon surface. A schematic view of the underlying geometrical considerations is shown in Fig. 1, which represents a two dimensional simplification of the profile of a pyramid textured surface. The light incident normally to the textured silicon wafers falls upon the grooves at a point A. About 65 % of this light is transmitted into the silicon and the rest is reflected back. In the case of textured surface as shown in Fig. 1 the light incident on the one face of the textured surface and the reflected light is now angle downs to the neighbouring groove, instead of away from the silicon surface as would be case of planar cell. The reflected light is re-incident at the silicon surface for a second chance of transmission into the silicon at point B. The probability with which light will receive such double-bounce incidence or still higher orders of multiple incidences depends upon the facet tilt angles of the geometrical textures with respect to the surface of the wafer. In this way the light is more efficiently trapped into the silicon and reduce the reflection of light without the use of an anti-reflection coating. The angle and the height of the structures will influence the number of bounces on the front surface. The angle of the pyramid walls to the wafer surface α is 54.7º for the case of random pyramids produced by anisotropic alkaline etching, as determined by the angle of {100} and {111} Si planes. It has been calculated by other authors that 30 % of normally incident light impinges three times the front silicon surface textured with random upright pyramids. The minimum value of facet angles of 30° and 54° are required for double and triple bounce of the incident light. If the silicon solar cell encapsulated under the glass then it is possible to totally internal reflection of light arriving at glass-air interface at angle greater than the critical angle of glass (42°), then the light will again re-directed towards the silicon. This light will re-incident on the surface of the silicon that also reduce the reflection loss.

2.2 Antireflection Coating (ARC)

Another way of reducing the reflection is by applying the antireflection coating (ARC) on the front surface of the silicon solar cell. The single layer antireflection coatings are applied directly on the silicon solar cells. A set of optimized and well

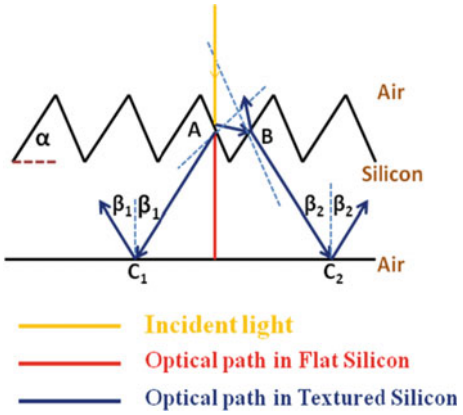

Fig. 1 Schematic arrangement of the optical path of incident light in silicon depending on the angle of incidence

designed anti-reflection coating on the front surface is an effective way to improve the optical absorption of the solar cell.

Figure 2 shows the basic principles of the anti-reflection film. When the reflection of light on second interface returns to the first interface, and if the phase difference between the two lights is 180°, the former will offset the latter to some extent. The thickness and refractive index of the single layer ARC is determined by the following conditions.

(a) The Phase Condition: For the destructive interference of the reflected light beams from the AR coated silicon surface, the optical path length (n_1.d) in the layer has to be equal to odd multiple of half of the light wavelength. This quarter–wave condition gives the thickness of the ARC:

$$d = \frac{\lambda}{4\,\mu} \tag{1}$$

where, λ is the wavelength of incident light at which destructive interference occurs and μ is the refractive index of the ARC.

(b) The amplitude condition: For complete destructive interference, the amplitudes of reflected light from the ARC–air and substrate–ARC interfaces have to be equal. The reflection from a coated surface is given by Fresnel's equation

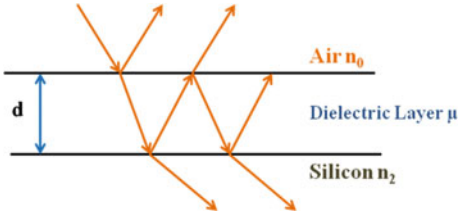

Fig. 2 Principles of antireflection coating

$$R_{\min} = \left(\frac{\mu^2 - n_0 n_2}{\mu^2 + n_0 n_2}\right)^2 \tag{2}$$

where, n_2 and n_0 are the refractive indexes of the silicon substrate and air respectively. For minimum value of R_{min} the numerator of the above equation is equal to zero. This condition gives the following relation

$$\mu = \sqrt{n_0 . n_2} \tag{3}$$

The refractive index of air is 1, then

$$\mu = \sqrt{n_2} \tag{4}$$

When the surface is coated with a film of refractive index (μ) that varies continuously from n_2 to unity and thickness larger than the reference wavelength, zero reflectance is obtained for the reference wavelength. The optimization of ARC's for silicon solar cells are usually done for a maximum current output in the terrestrial solar spectrum (AM1.5G). Due to this minimum reflectance is optimized at wavelength around 600 nm and hence the ARC's of finished cells look like blue colour. A vast literature [8–16] is available on the single step refractive index SiN layer to use as an ARC layer in order to reduce the reflection losses in silicon solar cells. But less information and data are available on another method to use the graded step refractive index SiN layer instead of single step refractive index SiN layer. Graded SiN film means multi-layers of nano-dimension Si_3N_4, in which high refractive index at silicon and Si_3N_4 interface and slowly decreasing refractive index as we go to surface as shown in Fig. 3 without enhancing manufacturing cost and reducing through output.

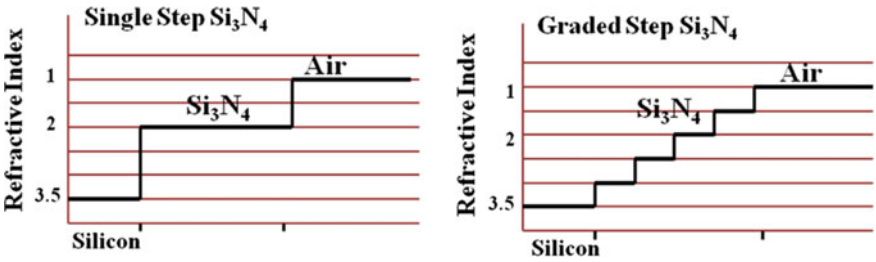

Fig. 3 Assumed refractive index profiles for single step and graded step recipe

3 Experimental Details

3.1 Description of PECVD System

The SiNA® (silicon-nitride deposition) system features an inline process with a continuous coating system, particularly developed to deposit silicon nitride (SiN) from silane/ammonia plasma onto silicon wafers [17]. The silicon-nitride coating process has to meet two requirements of silicon wafer based solar cells like formation of an anti-reflective layer and surface and bulk passivation. Both these features increase the efficiency of power generation.

Figure 4 shows the schematic arrangement of the PECVD system. Inside the process module of SiNA®, the silane and ammonia gases react according to the following chemical equation:

$$3\ SiH_4 + 4\ NH_3 \rightarrow Si_3N_4 + 12\ H_2$$

The PECVD system used for ARC layer of SiN films on silicon wafers is shown in Fig. 5. During this process, we have tried to minimise the dielectric mismatch between air and ARC by keeping higher refractive index of ARC at silicon and Si_3N_4 interface and followed by decreasing gradually to outside surface, as illustrated in Fig. 3. The gases NH_3/SiH_4 are distributed in process chambers with microwave sources and their distribution is given in Table 1. In this experiment, single step recipe is the base line recipe over which graded recipe has been performed with varying refractive indices in order to achieve higher efficiency of solar

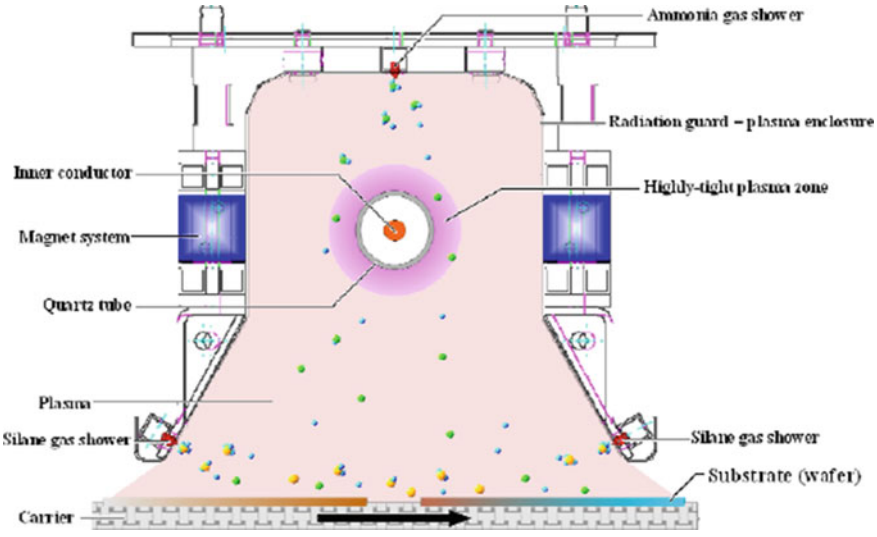

Fig. 4 Principal mode of function of remote plasma deposition process

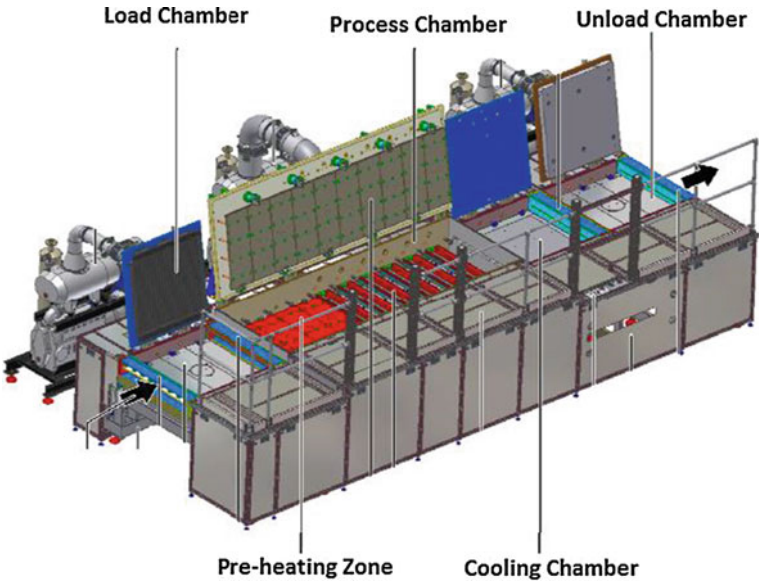

Fig. 5 Roth & Rau SiNA PECVD with chambers open

Table 1 NH_3/SiN_4 gas flow along the length of process chamber

PECVD recipe	Gas flow ratio (NH_3/SiH_4)			
	Microwave source (1–4)	Microwave source (5–8)	Microwave source (9–12)	Microwave source (13–14)
Graded with average refractive index = 2.24	1.41	2.20	3.00	4.00
Graded with average refractive index = 2.14	1.93	3.00	4.00	4.62
Graded with average refractive index = 2.04	2.82	3.89	4.74	5.38
Single step with average refractive index = 2.04	3.6	3.6	3.6	3.6

cells and lower cell-to-module conversion power loss (CTMPL) values. The refractive index and the thickness of the silicon nitride coated silicon wafers (both single step and graded recipe based SiN films) were measured with an ellipsometer having He–Ne laser of wavelength 632.8 nm.

Table 2 Typical process steps for multi-crystalline silicon solar cell manufacturing in industries is given by

Step	Description
1	Texturing
2	Phosphorous doping
3	Diffusion
4	Phosphosilicate glass removal and edge isolation
5	ARC Si_xN_y:H deposition
6	Screen printing front and back contacts
7	Co-firing contacts in IR belt furnace

3.2 Description of the Fabrication Steps of Silicon Solar Cells in Industry Scale

After the lab scale experiments of the growth of the SiN ARC layer process was shifted to the commercial scale of the fabrication of silicon solar cells. Silicon solar cells are fabricated in the industry using the textured wafers and also with SiN films as an antireflection coatings. The typical industrial process steps adopted during this research for manufacturing the mc-Si solar cell is discussed in Table 2. To study and analyse the effect of graded ARC in comparison of non-graded one, few observations have been taken, whose details are as follows:

1. Multi-crystalline silicon solar cells were prepared, and characterized for electrical parameters such as, short circuit current (I_{sc}), open circuit voltage (V_{oc}), Fill Factor (FF) and efficiency etc.; using solar cell simulator and analysed using Parkin Elmer (Lamda 1050) spectroscopy.
   (a) Single step recipe with an average silicon nitride refractive index 2.04, standard base line.
   (b) Graded recipes with different gas flow profiles with average silicon nitride refractive index of 2.04, 2.14 and 2.24.
2. Multi-crystalline silicon solar modules were manufactured with above mentioned all categories and compared for CTMPL, keeping the making process and the material similar of all modules.

For experimental analysis, we have taken standard multicrystalline silicon wafer of area 156 × 156 mm^2. During the process of fabrication of solar cells, we have appropriately tailored the PECVD deposition profile to make graded/multi-layer SiN_x ARC. Details of as prepared ARC coated films are listed in Table 4. After fabrication of silicon solar cells, solar modules were manufactured with different profile of SiN ARC films and characterized for CTMPL values. Flat (Albrino-S) glass and brucker ribbon of 1.5 × 0.8 mm^2 area were used in making modules. The modules that were used in this experiment were made with 60 cells (each solar cell has are of 156 × 156 mm^2) of multicrystalline silicon solar cells having 17.00 % efficiency. All electrical parameters were studied using solar cell tester: Cetis

PV-XF2-M, fully electronic xenon flasher AM1.5 class AAA to solar cell simulation, whose results are summarized in Table 5.

3.3 Simulation Conditions

A typical screen-printed solar cell with back contact of aluminium (Al) metal (back surface field) was used in the device simulation. Baseline screen printed solar cell parameters used for PC1D solar simulator software modelling are listed in Table 3.

Using PC1D, multi-crystalline silicon solar cells were simulated for electrical parameters such as efficiency, reflectivity and spectral density. Following simulation profile of ARC has been considered and summarized in Table 4.

Table 3 List of solar cell parameters used in PC1D to quantify the impact of silicon nitride antireflection coating on cell efficiency because of optical loss

Parameters	
Cell area	243.36 cm^2
Texture depth	3 μm
Cell thickness	200 μm
Cell material	Silicon
Sheet resistance	80 Ω/sq
Junction depth	0.29 μm
Wafer resistivity	0.9 Ω-cm
Bulk lifetime	9 μs
FSRV	7000 cm/s
BSRV	450 cm/s

Table 4 Different simulated silicon nitride profiles

Recipe		Average refractive index	Total thickness (nm)
Single step 2.04		2.04	84
Single step 2.14		2.14	84
Single step 2.24		2.24	84
Graded RI 2.04	Outer layer	2.00	40
	Mid layer	2.05	30
	Inner layer	2.15	14
Graded RI 2.14	Outer layer	1.96	20
	Mid layer	2.04	30
	Inner layer	2.34	34
Graded RI 2.24	Outer layer	1.98	20
	Mid layer	2.24	30
	Inner layer	2.35	34

The total thickness of all the ARC on solar cells is 84 nm

(a) Single layer of SiN ARC film with thickness of 84 nm and refractive index is of 2.04, 2.14 and 2.24 respectively.
(b) Graded SiN ARC film with weighted average varying refractive index of 2.04, 2.14 and 2.24 respectively.

4 Results and Discussion

4.1 Experimental Results

Figure 6 shows the plots of reflectance spectra which has been carried out on these samples. It has been found that optimized graded recipe is more beneficial to non-graded recipe because it reduces the surface reflectance of the front surface of solar cells, as indicated in Table 5. The plots of reflectance which has been carried

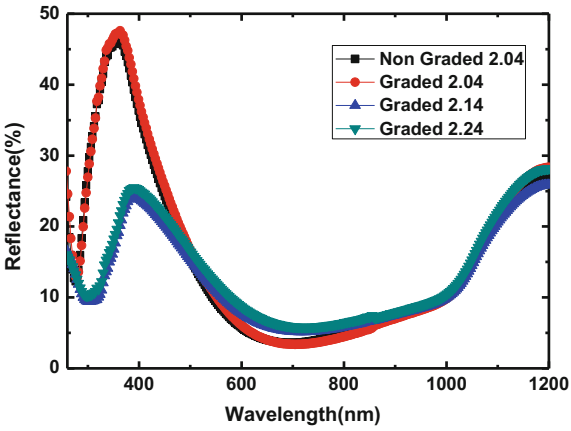

Fig. 6 Measured reflectance profile for SiNA PECVD coated wafers

Table 5 Experimental results summarized for different PECVD recipes

Recipe name	Single layer SiN_x	Graded or multi-layer SiN_x		
Refractive index	**2.04**	**2.04**	**2.14**	**2.24**
Avg. reflectivity (%) (300–1200 nm)	15.63	16.05	12.67	13.58
Efficiency (%)	**16.73 %**	**16.70 %**	**16.96 %**	**16.81 %**
Short circuit current Isc (A)	8.471	8.472	8.550	8.438
Voc (V)	0.6180	0.6175	0.6204	0.6213
FF (%)	77.76	77.69	77.80	78.05
CTMPL	3.37	3.47	3.37	2.67
No. of cells	6432	2078	6624	6871

Bold denotes different refractive index of silcon nitride and its calculated efficiencies

out on these samples, are shown in Fig. 6. It has been found that optimized graded recipe is more beneficial to non-graded recipe because it reduces the surface reflectance of the front surface of solar cells, as indicated in Table 5.

The definition of CTMPL can be given by:

$$CTMPL = \frac{(Epected\ Module\ wattage - Actual\ wattage)}{Expected\ Module\ watage} * 100\,\%$$

CTMPL has also been evaluated using sun simulator (AAA Class) for solar modules. It is very well clear from Table 5, that CTMPL keeps on decreasing with increase in refractive index. However, with further increase in refractive index the short circuit current starts decreasing, which in turn reduces the overall efficiency of solar cells. This may be possible due to the increase in the reflection of the front surface of silicon solar cells. Therefore, it has been observed from experimental results that by optimizing the graded reflective index of ARC films, we may be able to achieve improved spectral response and as well as improved efficiency along with reduced CTMPL values for crystalline silicon solar cells in comparison to conventional non-graded ARC films. In present case, we have achieved a significant enhancement in the efficiency of silicon solar cell from 16.73 to 16.93 % (average).

4.2 Simulation Results

In order to get more understanding and insights of experimental results, simulation has also been done, simulated results were also been analysed using PC1D solar cell simulator. From the simulation results it has been observed that non-graded recipe with increasing refractive index contributes to the reduction of average reflectance, in UV range, but increase in reflectance, in visible range, therefore, an average reflectance from 300 to 1200 nm range is found to be increased with increase in refractive index (as shown in Fig. 7e) and so the average cell efficiency is decreased with increasing refractive index in non-graded recipe profile. In graded recipe, a proper optimization leads to higher cell efficiency compared to non-graded recipe. In support to experimental observations, the simulated results have shown that increase in refractive index of ARC with graded recipe till particular value decreases its overall average reflectivity (as shown in Fig. 7f) and as an consequence, it enhances the spectral response and so the cell efficiency for particular solar cells.

However, as depicted in experimental observations, simulation analysis also confirms the decrease in average reflectance by further increase in average refractive index, using graded recipe, which in turn reduces the cell efficiency of Si solar cells. The maximum spectral response and the cell efficiency for graded refractive index ARC has been achieved at refractive index of 2.14. The initial condition used for simulating the practical conditions are discussed in Table 3 and whole analysis

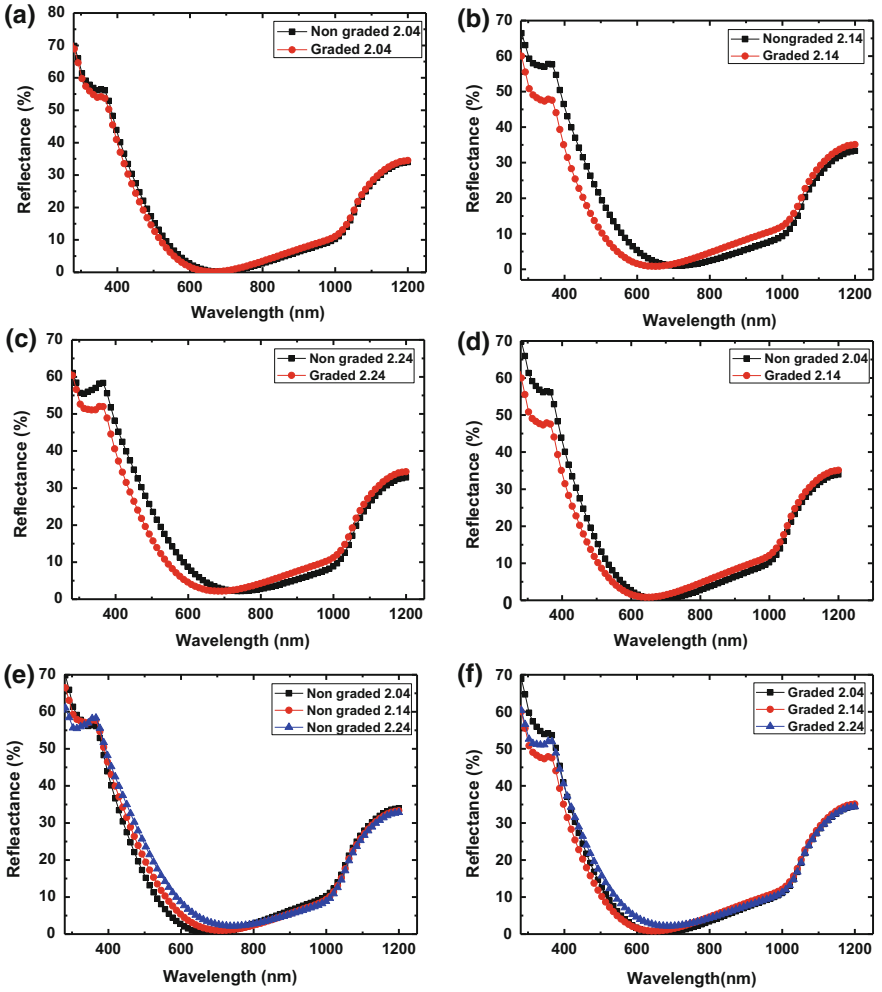

Fig. 7 PC1D simulated reflectance profile for different PECVD recipe. **a** Graded versus non-graded with 2.04 refractive index. **b** Graded versus non-graded with 2.14 refractive index. **c** Graded versus non-graded with 2.24 refractive index. **d** Graded with refractive index 2.14 versus non-graded with 2.04 refractive index. **e** Non-graded with refractive index 2.04, 2.14 and 2.24. **f** Graded with refractive index 2.04, 2.14 and 2.24

is summarized in Table 4 along with self explanation graphs of reflectance and spectral response, in Figs. 6 and 7, respectively. Figure 6 shows the decrease in reflectance by opting graded refractive indices (n) recipes of 2.04, 2.14 and 2.24, respectively. Figure 8 shows slight enhancement in spectral response, in support of increase in efficiency of solar cell using graded n recipes. It shows that the comparison of results of non-graded 2.04 (standard used in companies) and 2.14 with graded n sample, which has been observed as the best optimized n (Table 6).

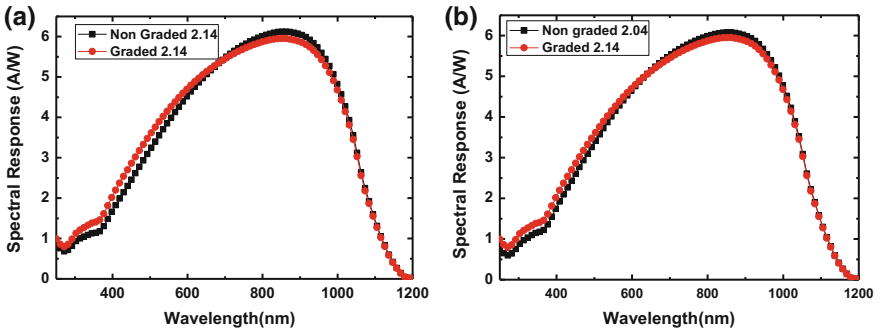

Fig. 8 Spectral response for different PECVD recipe. **a** Graded versus non-graded with 2.14 refractive index. **b** Graded with refractive index 2.14 versus standard baseline of 2.04 refractive index

Table 6 PC1D numeric simulation for different PECVD recipe

Recipe name	Single layer SiN_x			Graded or multi layer SiN_x		
Refractive index (n)	**2.04**	**2.14**	**2.24**	**2.04**	**2.14**	**2.24**
Avg reflectivity (%) (300–1200 nm)	17.56	18.29	19.27	17.12	16.36	17.78
Efficiency (%)	**16.71 %**	**16.49 %**	**16.21 %**	**16.80 %**	**16.86 %**	**16.54 %**
Short circuit current I_{sc} (A)	8.457	8.339	8.18	8.505	8.533	8.367
V_{oc} (V)	0.6176	0.6173	0.6168	0.6178	0.6179	0.6175
P_{max} (W)	4.067	4.014	3.946	4.089	4.103	4.026

Bold denotes different refractive index of silcon nitride and its calculated efficiencies

5 Conclusions

The performances of various SiN ARC films, using single step and graded recipes along with different refractive indices were studied experimentally as well as theoretically. In conventional single step/non-graded silicon nitride ARC, film efficiency decreases with increasing refractive index and refractive index of 2.04 is optimum value for single step silicon nitride ARC, whereas, in graded silicon nitride ARC, it has been observed that maximum efficiency may be achieved with average refractive index of 2.14, which may attribute to the fact that reflectance losses are reduced further and enhance spectral response, at typical conditions. The experimental observations were successfully supported by PC1D simulations. Therefore, it has been observed and analysed by optimizing the Si_3N_4 anti-reflection coating, we could reduce the surface reflection in range of 300–1200 nm from 15.63 % (non-graded n 2.04) to 12.67 % (graded n 2.14) and enhance the cell efficiency of multicrystalline silicon solar cells from 16.71 % (non-graded n 2.04) to 16.86 % (graded n 2.14), without compromising with

CTMPL. We have found that graded step refractive index recipe has reduced the reflectance of ARC SiN films, enhanced spectral response and efficiency of the solar cells and therefore reduced the CTMPL values of the modules.

Acknowledgements The author would like to thank Mr. H.R. Gupta, MD Indosolar Ltd. for giving opportunity to work on this project. We would also like to thank Dr. Vamsi, CES IITD, for allowing their lab facility. Authors also wish to acknowledge Dr. Ashok K. Chauhan, Founder President, Amity University, Noida for his continuous encouragement and kind support. We are thankful to DST, GOI, for their support.

References

1. L.L. Ma, Y.C. Zhou, N. Jiang et al., Wide-band black silicon based on porous silicon. Appl. Phys. Lett. **88**, 171907 (2006)
2. M. Lipinski, P. Panek, S. Kluska, P. Zieba, A. Szyszka, B. Paszkewicz, Defect passivation of multicrystalline silicon solar cells by silicon nitride coatings. Mater. Sci. **24**(4), 1009–1016 (2006)
3. M. Lipnski, P. Zieba, S. Joans, S. Kluska, M. Sokolowski, H. Czternastik, Optimization of SiN_x:H layer for multicrystalline silicon solarcells. Optoelectron. Rev. **12**, 41–44 (2004)
4. L.C. Chung, T.C. Jen, TiO_2-Ta_2O_5 composite thin films deposited by radio frequency ion beam sputtering. Appl. Opt. **45**, 36 (2006)
5. K. Stefan, *Solar Electric Power Generation* (Springer, Berlin, 1996), pp. 144–145
6. H. Mackel, R. Ludemann, Detailed study of the composition of hydrogenated SiN_x layer of high quality silicon surface passivation. J. Appl. Phys. **92**, 5 (2002)
7. M.H. Kang, K. Ryu, A. Upadhyaya, Ajeet Rohatgi, Optimization of SiN AR coating for si solar cells and modules through quantitative assessment of optical and efficiency loss mechanism. Prog. Photovolt: Res. Appl. **19**, 983–990 (2011)
8. P. Wurfel, *Physics of Solar Cells* (Wiley-VCH Verlag GmbH & KGaA, Weinheim, 2005)
9. M. Green, High Efficiency Silicon Solar Cells. Hardback, Transactions on Technical Publications Ltd (1987)
10. H.F.W. Dekkers, S. De Wolf, G. Agostinelli, F. Duerinckx, G. Beaucarne, Requirements of PECVD SiN_x:H layers for bulk passivation of mc-Si. Sol. Energy Mater. Sol. Cells **90**, 3244–3250 (2006)
11. I.G. Romijn, W.J. Soppe, H.C. Rieffe, A.R. Burgers, A.W. Weeber, in *Proceedings of the 20th European Photovoltaic Solar Energy Conference and Exhibition*, Barcelona, Spain, 2005, pp. 1352–1355
12. I.G. Romijn, H.C. Rieffe, A.W. Weeber, W.J. Soppe, Passivating Mc-Si solar cells using SiN_x:H: how to tune to maximum efficiencies, in *Proceedings of the 15th International Photovoltaic Science and Engineering Conference (PVSEC-15)*, Shanghai, China, 2005, pp. 303–304
13. M. Blech, A. Laades, C. Ronning, B. Schroter, C. Borschel, D. Rzesanke, A. Lawerenz, Detailed study of PECVD silicon nitride and correlation of various characterization techniques, in *Proceedings of the 24th European Photovoltaic Solar Energy Conference and Exhibition*, Hamburg, Germany, 2009, pp. 507–511
14. A.W. Weber, H.C. Rieffe, W.C. Sinke, W.J. Soppe, Structural and passivating properties of SiN_x:H deposited using different precursor gases, in *Proceedings of the 19th European Photovoltaic Solar Energy Conference and Exhibition*, Paris, France, 2004, pp. 1005–1008
15. A.W. Weeber, H.C. Rieffe, I.G. Romijn, W.C. Sinke, W.J. Soppe, The fundamental properties of SiN_x:H determine its passivating qualities, in *Proceedings 31th IEEE Photovoltaic Specialists Conference*, Florida, USA, 2005, pp. 1043–1046

16. A.J.M. van Ervan, R.C.M. Bosch, A.W. Weeber, M.D. Bijker, Effects of different firing profiles on layer characteristics and passivation. Properties of industrial ETP deposited silicon nitride films, in *Proceedings of the 19th European Photovoltaic Solar Energy Conference and Exhibition*, Paris, France, 2004, pp. 927–930
17. J.D. Moschner, J. Henze, J. Schmidt, R. Hezel, High-quality surface passivation of silicon solar cells in an industrial-type inline plasma silicon nitride deposition system. Prog. Photovoltaics Res. Appl. **12**, 21–31 (2004)

Theoretical Analysis of Surface Plasmonic Ag Nanoparticles Embedded in C-, Pc-, a-Si Thin-Film Solar Cell, Using Mie Scattering

Jiya Ann Mohan, Bidyut Barman, Abhishek Verma and Vinod Kumar Jain

Abstract Current research shows that, Light trapping mechanism using metallic Nanoparticles has shown a promising way to increase light absorption in thin film solar cells to a significant level. In this present work, we have investigated the effect of C-scattering and Q-scattering of light shown by silver nanoparticles embedded in different substrates using Mie scattering theory. We have observed, Silver nanoparticles embedded in monocrystalline silicon substrates showed better C scattering compared to all other substrates. Here we report a red shift of Surface plasmonic resonance of scattering as the particle size increases. Also the plasmonic behavior depends on the type of substrate used.

1 Introduction

Presently, thin-film solar cells are primarily considered as a cost-effective and main alternative to conventional wafer-based silicon solar cells. The thin film solar cell have very less thickness of around few microns (1–2 μm), due to which it considerably reduced the amount of semiconductor material required to a significant level. Hence, it lessens the production costs of silicon based solar cells [1].

J.A. Mohan · B. Barman (✉) · A. Verma · V.K. Jain
Amity Institute of Advance Research and Studies (Material & Devices),
Amity University, Noida, Uttar Pradesh, India
e-mail: bidyut_b15@yahoo.co.in

J.A. Mohan
e-mail: jiya_ann@yahoo.com

A. Verma
e-mail: averma5@amity.edu

V.K. Jain
e-mail: vkjain@amity.edu

J.A. Mohan · B. Barman · A. Verma · V.K. Jain
Amity Institute of Renewable and Alternate Energy, Amity University,
Noida, Uttar Pradesh, India

V.K. Jain et al. (eds.), *Recent Trends in Materials and Devices*,
Springer Proceedings in Physics 178, DOI 10.1007/978-3-319-29096-6_39

But, thin film has associated with some limitations due to their low light absorption capacity, it requires highly efficient light trapping mechanisms to enrich their performance as compared to the wafer-based solar cells. Typical surface texturing method used in wafer-based cells for light trapping [2, 3] including etching and sculpting cannot be applied in case of thin film cells due to its lean geometric thickness and recombination losses because of their submicron surface texturing which inevitably enhances the surface area. Light scattering phenomenon using surface plasmonic mechanism is a very promising way for light trapping in thin film solar cells.

1.1 Role of Plasmon's in Improving Efficiency of Solar cell

The Plasmonic solar cells convert the light energy (light photons) into electricity using plasmons. It is done in two ways.

- Metal nanoparticles are used on the top surface of the absorber layer so they can couple and trap freely propagating plane waves from the sun. These trapped light waves will be scattered and folded to increase the optical path [4].
- Surface plasmons are consistent oscillations of conduction electrons at metal/dielectric interface. By supporting these surface plasmons with metallic nanostructures using a corrugated metallic film on the back surface of absorber, we can increase the light absorption and improve efficiency of the solar cell [5].

Localized Surface Plasmonic Resonance (LSPR) is the collective oscillation of electrons at the metal/dielectric medium stimulated by the incident light. The oscillation charges can be confined to the surface of nanoparticleof mostly less than 200 nm diameter (Fig. 1).

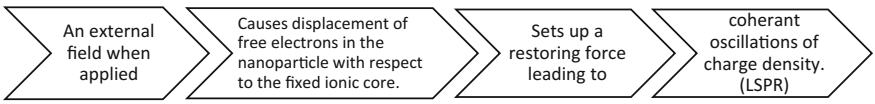

After getting excited, the localized surface plasmons decay in either of the two ways:

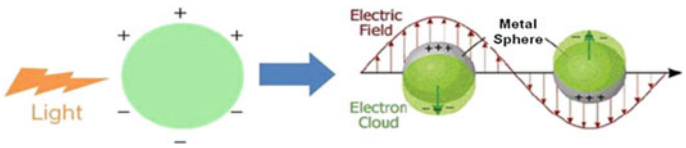

Fig. 1 Localised surface plasmon resonance

- Radiative decay which results in ***scattering***.
- Non radiative decay due to energetic relaxation (because of e-h pair formation) which results in ***absorption*** of light photons [6].

The ***Resonance Condition*** is when the light photon frequency matches the natural frequency of surface electrons. This allows direct absorption of light without any thick additional layers. Thereby an increase in the photocurrent will lead to the enhancement of solar cell efficiency [7] (Fig. 2).

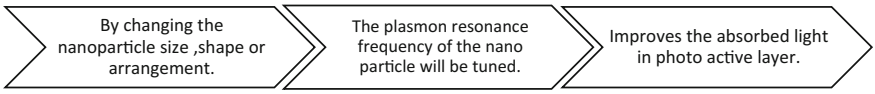

To maximize light scattering and coupling efficiency, the following factors should be considered—[8]

1. Nanoparticle size (smaller particles have larger coupling efficiency)
2. Geometry
3. Material (third generation solar cell uses Gallium Indium Phosphide, Gallium Indium Arsenide or Germanium)
4. Local dielectric environment.

In the present research work, we study the effect of surface plasmonic silver nanoparticles (AgNPs) embedded in the different substrates to enhance the solar cell efficiency using MIE scattering software to have better insight understanding of surface plasmonic nanoparticles in different types of silicon solar cells. Here, we study the C-scattering and Q-scattering of light shown by AgNPs embedded in

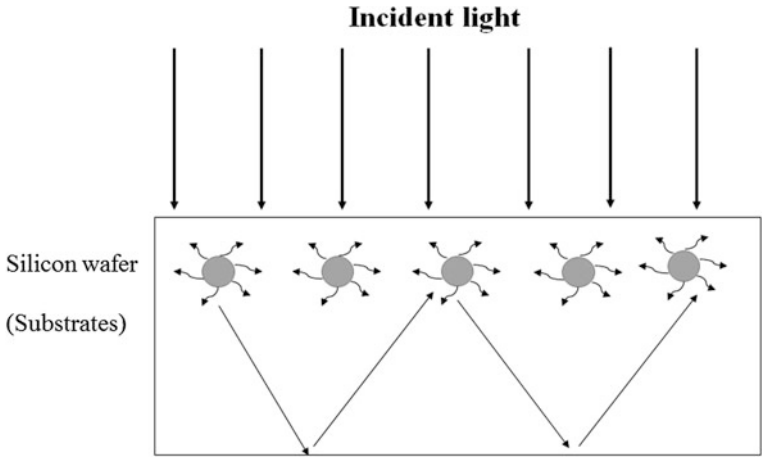

Fig. 2 Silicon substrate

different substrates like monocrystalline solar cell (cSi), polycrystalline solar cell (pSi) and amorphous solar cell (aSi).

2 Experimental Methodology

In this research work, we have analyzed MIE scattering effect of AgNPs using MIEPLOTV4305 software on different substrates such as monocrystalline solar cell (cSi), polycrystalline solar cell (pSi) and amorphous solar cell (aSi) with nanoparticle size varies from 20 to 200 nm for an optimal standard deviation of 10 %.

2.1 MIE Scattering

Electromagnetic scattering by a homogenous, isotropic sphere is called MIE Scattering. The Mie solution to Maxwell's equation describes scattering of electromagnetic radiation by a sphere. It is named after Gustav Mie (1868–1957) although he was not the first to formulate this electromagnetic scattering problem. Before him Alfred Clebsch (1833–72) and Ludvig Lorentz (1829–91) contributed to this problem. All the wavelengths of white light can be scattered equally in all directions with the help of the large particles in the atmosphere. When the above process occurs in all directions equally, MIE Scattering is said to happen. Due to this reason clouds appear white.

2.2 MIE PLOT

This is the software/program used throughout this project for scattering of light from a sphere using MIE theory.

The light scattering analysis was performed using different parameters in MIE PLOT software such as

- Intensity scale (logarithmic/linear)
- Horizontal scale (logarithmic/linear)
- Wavelength scale 200–1200 nm (minimum, maximum, 1000 no of steps)
- Drop size (diameter in μm, monodisperse/disperse).

The effect of particle size in Csca and Qsca of light were studied and compared their variation in peak wavelengths (Csca vs. wavelength) and (Qsca vs. wavelength), where Csca is coefficient of scattering and Qsca is efficiency of scattering. The following table illustrates the different values for wavelength of light and refractive index of the respective substrates used for the light scattering analysis (Table 1) [9–11].

Table 1 Different wavelengths and refractive index considered in present simulation at different substrates

For monocrystalline silicon (cSi)		For polycrystalline silicon (pSi)		For amorphous silicon (aSi)	
Wave length (μm)	Refractive index (R.I)	Wave length (μm)	Refractive index (R.I)	Wave length (μm)	Refractive index (R.I)
0.245	3.4404	0.24	1.6403	0.245	1.80595
0.456	3.423	0.46	4.737	0.434	5.1685
0.824	3.418	0.65	3.94028	0.654	4.4517
0.1025	3.4176	0.84	3.7156	0.84	4.0454

3 Results and Discussion

Here, the comparative study was performed for the analysis of Csca and Qsca of light using AgNPs of different size range such as 20, 60, 100, 160 and 200 nm for 10 % standard deviation which shows significantly better results which are also comparable to our previous experimental work [12]. The analysis of C-scattering for different substrates (cSi, pSi and aSi solar cells) at varying wavelengths is shown in Figs. 3, 4 and 5. For Fig. 3 we observed that cSi of particle size 20 nm shows minimum Csca in the wavelength range of 520–550 nm. As the particles size increases the Csca value also increases. The cSi substrate with a particle size of 200 nm gives maximum C-scattering (∼1.57E−13) in the wavelength range of 550–600 nm. So there seen a red shift of resonance wavelength as the particles size increase from 20 to 200 nm. For pSi and aSi (Figs. 4 and 5), all samples show a similar behaviour like cSi. For pSi substrate Csca efficiency is maximum for 200 nm (1.45E−13) particle in wavelength range of 500–600 nm. In Fig. 5 also we find c-scattering efficiency of all samples starts rising at wavelength 519 nm to max at 567 nm and falling at 597 nm and takes a steady pace with a maximum scattering value ∼1.27E−13.

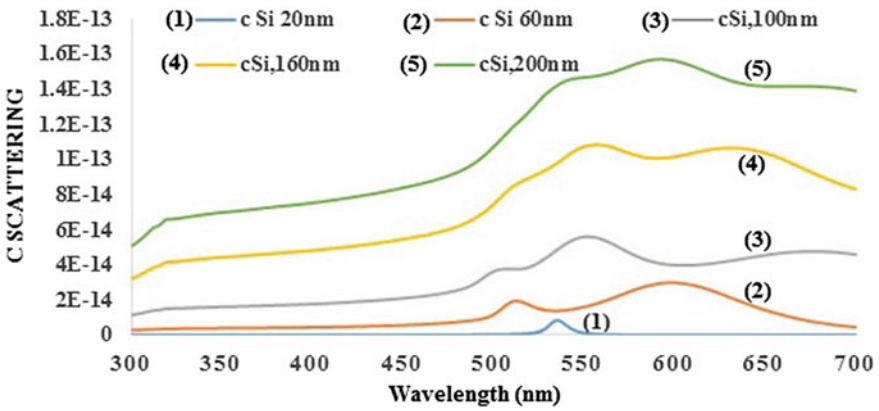

Fig. 3 Csca of AgNPs in cSi substrate

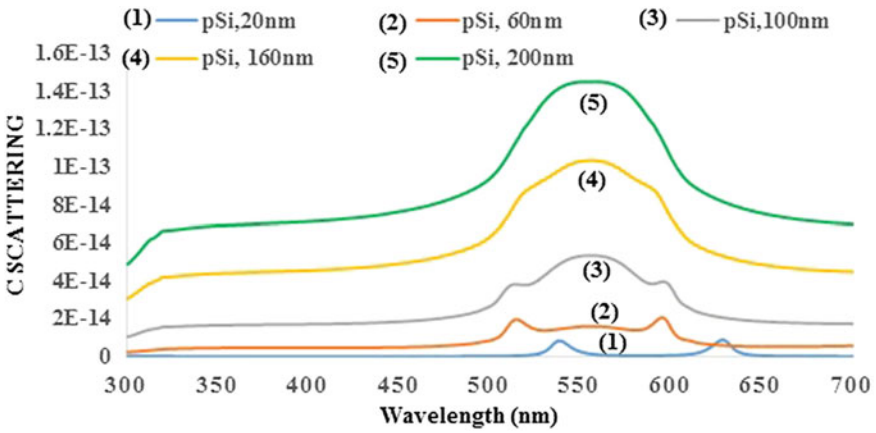

Fig. 4 Csca of AgNPs in pSi substrate

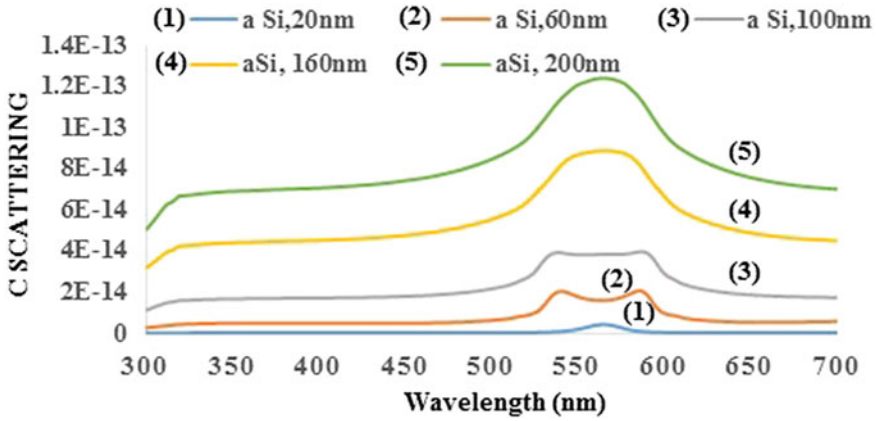

Fig. 5 Csca Of AgNPs I aSi substrate

Therefore, from the comparative study, we observed that Silver nanoparticles with cSi medium showed better light scattering compared to all other samples. Because of the high performance and efficiency of crystalline Si thin film solar cells, they are expected to be a better solution in the future thin-film solar cell market. Also from the above results, we can conclude that surface plasmonic resonance (SPR) frequency would be easily tuned by varying and optimizing the particles size of AgNPs.

Further in Fig. 6 the comparative analysis have been done to explains the variation of Q-scattering for different substrates, with varied nanoparticle sizes at different wavelengths. The results concluded that, AgNPs with smaller nanoparticle size shows maximum efficiency of scattering (Qsca) and it is maximum for cSi substrate with scattering value of 27.4 at 553 nm. Similaly we analysed it for aSi,

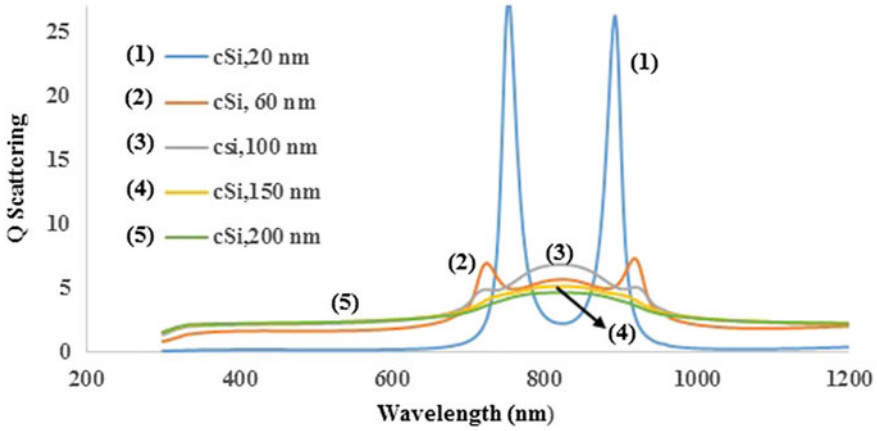

Fig. 6 Qsca of AgNPs in cSi substrate

particle size of 20 nm gives maximum Q-scattering efficiency at a wavelength around 850 nm. Therefore, there is a red shift of the resonance peak of Surface plasmonic AgNPs for aSi substrate as compared to cSi substrate for same AgNPs size of 20 nm. Again for pSi, 20 nm particle size gives the max Q scattering efficiency at around 750 nm wavelength. So from the above results, we can conclude that the value of Csca and Qsca depends on the size of AgNPs as well as the types of substrate used. Also, Mie scattering results, exhibits multipole oscillations which tend to decrease the scattering efficiency of the nanoparticles.

4 Conclusion

From the above analysis we have concluded that C scattering and Q scattering value depends on the nanoparticle size. It rapidly reduces to zero at higher wavelengths (>650 nm) when the particle size is less than 100 nm. Crystalline Silicon substrate found to give maximum C scattering and Q scattering compared to others. Therefore, it has potential application for future prospective. Also the results interpreted that SPR frequency can be tuned efficiently by varying the particles size and the type of substrate used.

Acknowledgments Authors are thankful to Department of Science and Technology (DST), Govt. of India, India for financially supporting this research work. Authors also wish to thank to Dr. D. N. Singh, CTO, IndoSolar Pvt. Ltd. for his valuable time and support. Authors also wish to acknowledge Dr. Ashok K. Chauhan, Founder President, Amity University, Noida for his continuous encouragement and kind support to carry out present research.

References

1. M.A. Green, *Third Generation Photovoltaics* (Springer, New York, 2006)
2. Y.A. Akimov, W.S. Koh, K. Ostirikov, Opt. Expr. **17**, 10195–10205 (2009)
3. J. Muller, B. Rech, J. Spriger, M. Vanecek, Sol. Energy **77**, 917–930 (2004)
4. SAYEED, in *Effect of Different Parameters in Enhancing the Efficiency of Plasmonic Thin Film Solar Cells*, IJAMS (2013)
5. Akimov, in *Enhancement of Optical Absorption in Thin-Film Solar Cells Through the Excitation Of Higher-Order Nanoparticle Plasmon Modes*, OSA (2009)
6. A. Centeno, in *Application of Localized Surface Plasmon resonance to Solar Energy harvesting*
7. J. Kim, in *Surface Plasmon Resonance for Photoluminescence and Solar Cell applications*, Electron. Mat. Lett. 351–364 (2012)
8. K.R. Catchpole, A. Polman, Plasmonic solar cells. Opt. Expr. **16**, 21793–21800 (2008)
9. A.D. Rakic, A.B. Djurisic, J.M. Elazar, M.L. Majewski, Appl. Opt. **37**, 5238–5271 (1998)
10. E. Palik, *Handbook of optical constants of solids*, vol. I (Academic Press, Orlando, 1985), pp. 577–580
11. M.J. Waber, *Handbook of Optical Materials*, vol. 19 (CRC press, 2002)
12. S. Chakravarty, L. Arunagiri, S. Chaudhary, A. Verma, V.K. Jain, *Physics of Semiconductor* (Springer, 2013), vol. 17, pp. 305–308

Effect of Blocking Layer on the Performance of Dye Sensitized Solar Cells

Himanshi Jauhari, Rakhi Grover, Omita Nanda and Kanchan Saxena

Abstract Dye Sensitized solar cells (DSSC) are a significant stepping stone in the field of photovoltaics. In DSSCs, a blocking layer is generally used in between the conducting electrode and the porous titanium dioxide layer. A compact blocking layer covers the rough surface of anode and reduces the probability of short-circuits between the electrolyte and the photoanode. However, a thick blocking layer can also act as a resistance. Therefore, efficient cells require a careful optimization of its thickness. In the present work, a compact blocking layer has been optimized for DSSCs based on a quasi solid state electrolyte and Eosin B as the sensitizer material. The porous semiconductor oxide layer and the optimized compact blocking layer have been characterized by scanning electron microscopy. In addition, the functionality of the blocking layer in DSSC is verified by solar cell characterizations. A significant enhancement has been obtained in DSSCs with blocking layer as compared to the reference cell.

H. Jauhari · R. Grover · O. Nanda · K. Saxena (✉)
Amity Institute of Renewable and Alternative Energy,
Amity University, Sector 125, Noida 201303, Uttar Pradesh, India
e-mail: ksaxena@amity.edu

H. Jauhari
e-mail: himanshi.jauhari@gmail.com

R. Grover
e-mail: rgrover1@amity.edu

O. Nanda
e-mail: onanda@amity.edu

H. Jauhari · R. Grover · O. Nanda · K. Saxena
Amity Institute of Advanced Research and Studies (Materials and Devices), Amity University, Sector 125, Noida 201303, Uttar Pradesh, India

V.K. Jain et al. (eds.), *Recent Trends in Materials and Devices*,
Springer Proceedings in Physics 178, DOI 10.1007/978-3-319-29096-6_40

1 Introduction

Dye sensitized solar cells (DSSCs) are one of the major emerging technologies as an alternative renewable energy source. They have become one of the most promising next generation photovoltaic devices due to their potential for low cost and significant efficiency performance [1, 2].

The basic functionality of a typical DSSC results from the interactions among its two electrodes, semiconductor oxide nanoparticles based layer coated with a light sensitive dye and a redox electrolyte. The electrolyte in between the dye and the counter electrode helps in the regeneration of dye molecules. The movement of electrons in the conduction band of semiconductor oxide is compensated by the diffusion of cations in the electrolyte matrix. Therefore, the generation of electrical power does not result in any permanent chemical transformation of the cell components.

However, the practical application of these cells requires a careful optimization of cell parameters to enhance efficiency and lifetime. One of these important parameter is charge carrier recombination inside the cell structure [3] which acts as a significant channel of charge carrier loss and hence efficiency loss. In general, recombination losses inside DSSCs can be reduced by the application of a blocking layer between conducting anode and the porous TiO_2 layer [4–6]. Furthermore, the best efficiencies of DSSCs have been reported with liquid electrolyte. However, due to the limitations of liquid electrolytes e.g. temperature sensitivity, corroding nature of iodine to platinum and majorly the leakage problem associated with it, the research and studies are being primarily focused on quasi-solid state and gel type electrolytes [7–9]. The efficiency in quasi state electrolyte based DSSCs is reported up to 9.61 % [10] with a large possibility of performance enhancement by optimizing the device architecture. In the present work, quasi solid state electrolyte based DSSCs have been fabricated. Titanium (IV) tetraisopropoxide (TTIP) has been optimized as a blocking layer in DSSCs based on Eosin B as the sensitizer.

2 Experimental Methodology

TiO_2 nanopowder and TTIP were purchased from Sigma Aldrich and were as such without further purification. Optically transparent Fluorine doped tin oxide coated films (7 Ω sq^{-1}), dye Eosin B, polyethylene glycol (PEG), iodine (I_2), succinonitrile (SCN) and acetonitrile (ACN) were also purchased from Sigma Aldrich. Potassium iodide (KI) and acetic acid (ACN) were purchased from Excel R and Merck respectively.The morphology of porous TiO_2 film and compact layer of TiO_2 was examined using scanning electron microscopy (Carl Zeiss). DSSCs have been fabricated using Eosin B as the sensitizer material with and without blocking layer (TTIP). A composition of PEG, KI, I_2, TiO_2 and SCN prepared in ACN was used as gel electrolyte. The photovoltaic properties of the DSSCs were measured using Keithley 2400 source meter under different light intensities.

3 Results and Discussion

The morphology of the TiO_2 porous layer and blocking layer is an important parameter to be studied for their application inside DSSCs. This was performed by the SEM image analysis. Figure 1a, b show the SEM image of porous semiconductor oxide layer and the blocking layer on FTO coated glass.

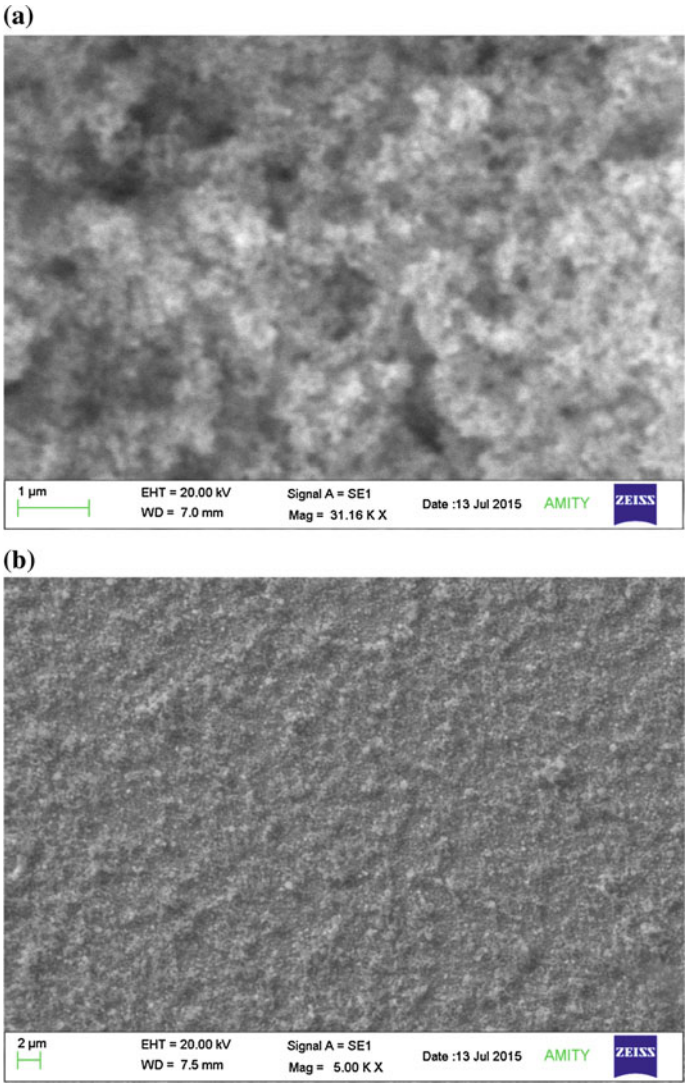

Fig. 1 SEM image of **a** TiO_2 layer and **b** blocking layer grown on FTO coated glass plates

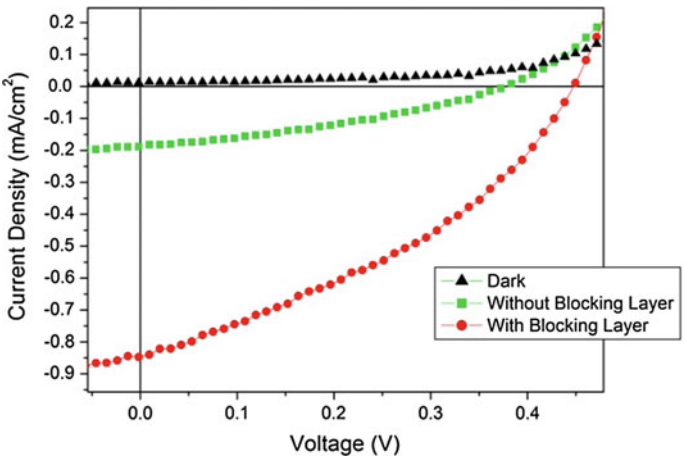

Fig. 2 J–V curves of devices fabricated with and without blocking layer

The difference in morphology of the two films can be easily seen in the SEM images. Figure 1a shows the SEM image of porous TiO_2 layer. It is evident from the figure that the film is highly porous so that the dye molecules can easily get adsorbed on the TiO_2 molecules. Figure 1b shows the SEM image of blocking layer prepared using TTIP. It is observed that the film is uniform, without any cracks or porosity, thereby reducing the chances of recombination of electrons and holes occurring between the FTO and the electrolyte. It was further verified by the analysis of current-voltage measurements. Figure 2 shows the current–voltage characteristics of the devices with and without blocking layer with dark current as reference. The value of short circuit current density (Jsc) increases rapidly, stating that more electrons flow through the circuit, thus reducing the recombination probability. The cells fabricated showed consistent photovoltaic properties even after 24 h of storage under ambient conditions.

The cells with blocking layers resulted in approximately one order of enhancement in short circuit current density under illumination intensity of 120 mW/cm^2.

4 Conclusion

In conclusion, DSSCs based on quasi solid state electrolyte and Eosin B as sensitizer have been fabricated. The effect of blocking layer inside these cells has been studied in detail. The insertion of thin and compact blocking layer between transparent conducting electrode and porous semiconducting oxide has been found to increase the efficiency of these cells significantly.

Acknowledgments The authors are thankful to Dr. Ashok K. Chauhan, Founder President and Dr. V.K. Jain, Distinguished Scientist and Professor, Amity University, Noida, India for their continuous encouragements and Mr. Pramod Kumar for providing technical help.

References

1. B. O'Regan, M. Grätzel, Nature **353**, 737–740 (1991)
2. M. Grätzel, Acc. Chem. Res. **42**, 1788–1798 (2009)
3. L. Kavan, N. Tetreault, T. Moehl, M. Gratzel. J. Phys. Chem. C. **118**, 16408–1641 (2014)
4. A. Burke, S. Ito, H. Snaaith, U. Bach, J. Kwiatkowski, M. Gratzel, Nano Lett. **8**, 977–981 (2008)
5. A.K. Chandiran, M.K. Nazeeruddin, M. Gratzel, Adv. Funct. Mater. **24**, 1615–1623 (2014)
6. L. Li, S. Chen, Y. Zhao, N.G. Rudawski, K.J. Ziegler. ACS Appl. Mat. Interfaces. **6**, 20978–20984 (2014)
7. J.N. de Freitas, A.F. Nogueira, M.A. De Paoli, J. Mater. Chem. **19**, 5279–5294 (2009)
8. S. Bai, C. Bu, Q Tai, L Liang, Y Liu, S You, Z Yu, S Guo, X Zhao, ACS Appl. Mat. Interfaces. **5**, 3356–3361 (2013)
9. M.B. Achari, V. Elumalai, N. Vlachopoulos, M. Safdari, J. Gao, J.M. Gardner, L. Kloo, Phys. Chem. Chem. Phys. **15**, 17419–17425 (2013)
10. L. Tao, Z. Huo, Y. Ding, Y. Li, S. Dai, L. Wang, J. Zhu, X. Pan, B. Zhang, J. Yao, M.K. Nazeeruddin, M. Grätzel, J. Mater. Chem. A **3**, 2344–2352 (2015)

ZnO Layer onto Si Surface by Continuous Spray Pyrolysis Reactor for Solar Cell Efficiency Enhancement

Hrishikesh Dhasmana and V. Dutta

Abstract The present investigation reports improvement of electrical parameters such as short circuit current and so efficiency of Si solar cell device by the deposition of ZnO layers onto Si surface via continuous spray pyrolysis reactor even under low temperature deposition conditions. In order to achieve this improvement, the ZnO layers are optimized directly on Si solar cell using kapton tape. This masking tape is helping to improve adhesion of ZnO layer along with changed surface morphology which is confirmed with respective SEM images. The report also suggests seed layer dominance in the resultant ZnO growth which is confirmed by changing precursor solution from Zinc acetate to Titanium tetraisopropoxide. The report is supported by XRD, SEM, reflectance and I-V measurements. The study suggest, if ZnO layers are suitably designed by this reactor on Si surface, the improvement in optical coupling can be achieved in cost effective manner for existing industrial Si solar cell fabrication line.

1 Introduction

The global scientific community is concerned over increase in greenhouse gases and catastrophic climate change due to the use of fossil fuel for electricity generation. So in recent years efforts towards alternative technologies have received greater attention. Among the technologies that may help to address these concerns is solar photovoltaic (PV), which utilizes solar energy for conversion directly to electrical energy. The current direct cost of solar PV power is still much greater than the dominated coal based electrical generation. So reducing solar electricity

H. Dhasmana (✉)
Amity Institute of Advanced Research and Studies, Amity University,
Noida 201313, Uttar Pradesh, India
e-mail: hrishikeshd07@gmail.com

H. Dhasmana · V. Dutta
Photovoltaic Laboratory, Centre for Energy Studies,
Indian Institute of Technology, Delhi 110016, India

V.K. Jain et al. (eds.), *Recent Trends in Materials and Devices*,
Springer Proceedings in Physics 178, DOI 10.1007/978-3-319-29096-6_41

cost is a focus of research in this area by either reducing the process cost of the device fabrication or increasing the efficiency of the device or both, so that the cost in mass scale production can be reduced further. Despite the significant development over the past decades, the high cost of silicon solar cells (though rapidly declining) is seen as a limiting factor for the implementation of solar electricity generation on large scale. Increasing absorption capacity for the incident light and improving radiation to electricity conversion, thereby increasing the efficiency, could be a helpful methodology [1]. Thus, development of material engineering is going to create new photovoltaic materials and systems that could reduce the cost of solar cell in the future because of easy fabrication technologies involved [2, 3].

Zinc Oxide (ZnO) nanostructure layers on silicon (Si) substrate have received increased interest due to the advantages [4–6], viz. a good transparency in visible region, suitable refractive index (nearly 2) for antireflection coating (ARC), ability to form textured coating via anisotropic growth, can act as surface passivation layer etc.; which can be utilized in crystalline Si solar cell technology. ZnO as solar cell window can be an option for existing silicon solar cell fabrication line. The preparing condition like growth temperature, ambient environment depend on oxygen vacancies. The growth temperature rise enhances open circuit voltage and short circuit current due to better crystallinity attained by ZnO thin film. Higher growth temperature increases grain size and therefore scattering from grain boundaries weakens and mobility of charge carrier increases, which ultimately lead to better Photovoltaic (PV) effect [7]. Lee et al. [8] reported ZnO Nanorod structure on silicon surface, which may trap light efficiently and reduce optical loss due to porous structure. Further they have suggested that the nanostructure may be improved by controlling thickness of the layer, refractive index and tip tapering of nanorod arrays, which may help in reducing process cost for Si solar cell by removing texturization process with additional light trapping advantages. The existing reduced light reflectance by Si surface up to 42.7 % has enhanced Si solar cell efficiency by 112.4 % [9] for multicrystalline Si solar cell. The ZnO nanowhisker array on single crystalline Si solar cell has increased 3 % of existing Si solar cell efficiency by reduced light reflectance [10]. The reduced light reflectance by Si surface up to $\sim$55 % due to ZnO layer in 300–1200 nm region has been achieved by CoSP reactor, which may motivate researcher to work on improving Si solar cell efficiency via increase of photocurrent in simple, fast and cost effective manner [11].

The ZnO growths along with Au Nanoparticels (NPs) are already explored and it is observed that the ZnO growth, alignment, surface area coverage and surface reflectance depends on Au NPs size [12]. In these coatings, ZnO nanorods need to be suitably designed on top of Si surface which can reduce light reflectance along with good electrical characteristics. The ZnO nanorods growth in anisotropically etched Si surface suggests that the growth supported by Zn solution seed layer in Continuous Spray Pyrolysis (CoSP) reactor is site specific [13]. The measured data clearly reveals that suitable etch pits depth and growth time are helping in the growth of nanorods for enhanced light trapping property and Si surface area coverage. Thus surface roughness helps in ZnO nanorod growth and so can improve light trapping property of thin film. The light

coupling, homogenous growth and surface coverage is noticeably improved by Electric field assisted CoSP reactor [14].

The detail study of ZnO layer by CoSP reactor directly on Si solar cell is yet to be explored. This investigation presents study of ZnO layer directly on crystalline Si solar cell by CoSP reactor and reports improvement in device efficiency due to improved optical coupling of ZnO with Si surface.

2 Experimental Section

This CoSP reactor consists of three furnace zones i.e. evaporation, spray and deposition zone. After solvent evaporation of spray droplets at 550 °C, spray pyrolysis occurs in second zone at high temperature 850 °C and self assembly of spray pyrolysed NPs takes place in third zone at 550 °C (Fig. 1). Spray pyrolysis is a simple and low-cost technique for the preparation of semiconductor thin films and can be applied for large area production, high quality adherent films of uniform thickness. Perednis et al. reviewed thin film deposition by spray pyrolysis [15].

All the substrates chosen are single side polished boron doped (100) p-type Si wafers, with resistivity 1–10 Ω-cm. These substrates are polished Si wafers with thickness around 380 µm. All Si surface are treated with Zn solution seed layer which is prepared by dissolving 0.1 M Zinc chloride in 20 ml methanol. The Si surfaces are immersed in this solution for 5 min and then dried in air at 120 °C for 2 min. To prepare precursor solution, 0.1 M Zinc acetate (ZA) (Sigma–Aldrich 98 % pure) is dissolved in 100 ml distilled water and kept for stirring until it changes to a transparent solution. The solution flow rate and gas pressure in this reactor are kept constant at 2 ml/min and 2.2 kg f/cm^2 for 2 min deposition time with oxygen as carrier gas. The deposition is also carried out with Titanium tetraisopropoxide (TTIP) from Sigma Aldrich as precursors and ethanol as solvent.

In order to explore ZnO layer on Si solar cell, the attempts have been made to deposit ZnO layers directly on Si solar cell. For this, first optimization of CoSP reactor for low temperature deposition conditions at 350, 550 and 350 °C has been

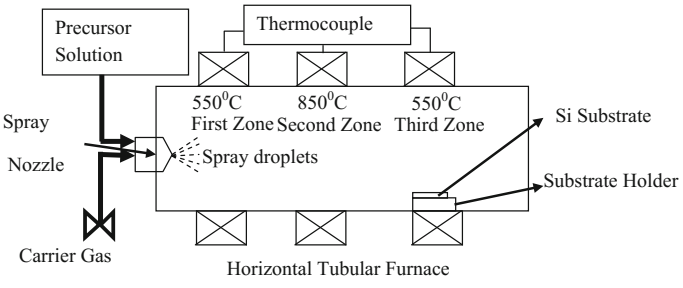

Fig. 1 Schematic diagram of CoSP reactor

made to protect existing metallic contact of Si solar cell. The ZnO layers are then deposited on low efficiency Si cell with and without masking conditions. The metallic contacts of Si cell are masked with kapton tape.

The crystal structure and surface morphology of ZnO nanostructures over (100) Si surface were investigated by Philips XPERT PRO (PW3040) X-Ray Diffractometer (XRD) and ZEISS EVO-50 model Scanning electron microscope (SEM). This SEM was also used to measure EDX spectrum for various ZnO thin films. Optical reflectance spectra in the wavelength region 300-1200 nm were obtained using Perkin-Elmer Lambda-1050 UV–VIS-NIR spectrophotome-ter. The device performance of Si solar cell was evaluated by J–*V* curve, measured by a

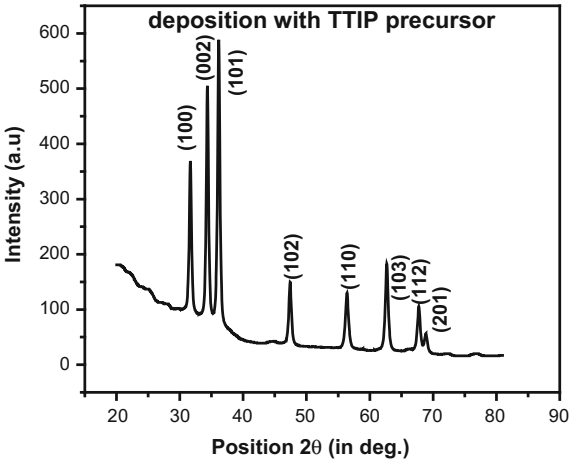

Fig. 2 XRD spectrum of ZnO with TTIP precursor

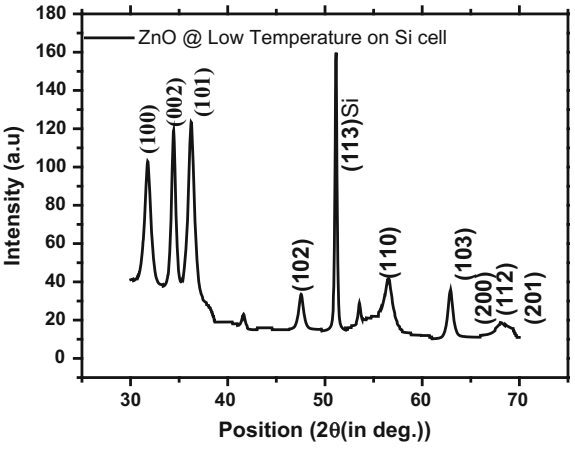

Fig. 3 XRD spectrum of ZnO on Si cell at low temperature

Keithley 2440 5A source meter under the illumination at 100mWcm^{-1} using Oriel Sol 3A simulator from Newport corporation.

3 Results and Discussion

3.1 XRD Study

The ZnO deposition with TTIP precursor clearly confirms that ZnO growth as seed layer dominant (Fig. 2). The ZnO layer deposition with mask onto Si solar cell under low temperature profile show poor crystalline film(Fig. 3).

3.2 SEM Study

ZnO deposition for 2 min by CoSP is carried out on bare Si solar cell under low temperature condition. The surface morphology of ZnO on bare Si solar cell is shown in Fig. 4a, depicting ZnO powder on textured Si cell surface with poor adhesion. When the metallic contact are masked in low temperature condition, surface morphology improved in the form of ZnO flakes as shown in Fig. 4b.

3.3 Reflectance Study

The reflectance behavior of ZnO layer on masked Si solar cell under low temperature deposition condition confirms a 39 % decrease of existing reflectance due to ZnO deposition in the measured wavelength region 300–1200 nm shown in Fig. 5.

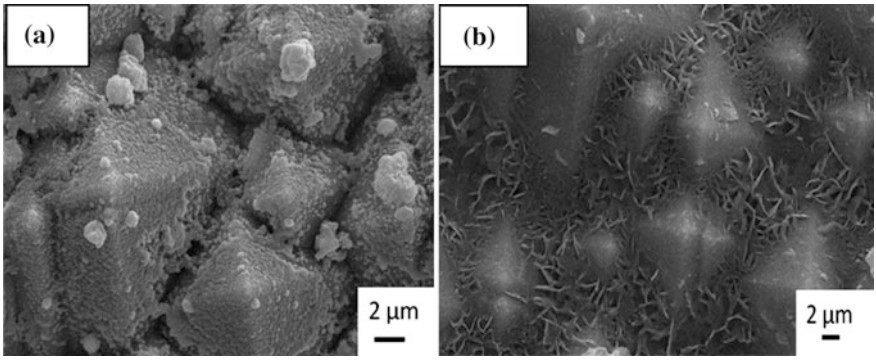

Fig. 4 SEM image of ZnO on bare and masked Si solar cell

3.4 I-V Measurment

The efficiency improvement of nearly 4.3 % of existing cell (B) efficiency is observed in Si solar cell after ZnO layer deposition (A) even under low temperature profile (Fig. 6).

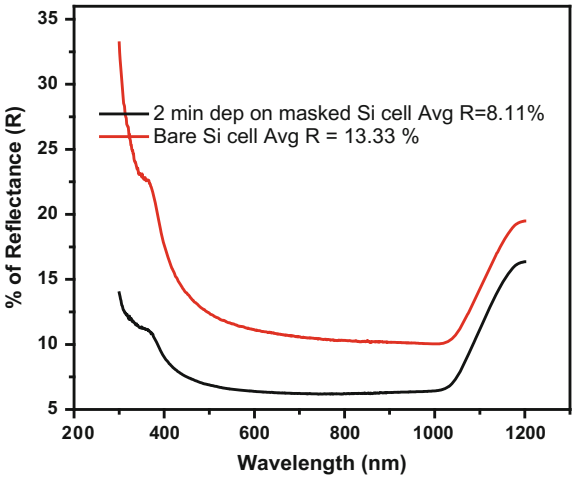

Fig. 5 Reflectance spectra of ZnO on bare and masked Si cell

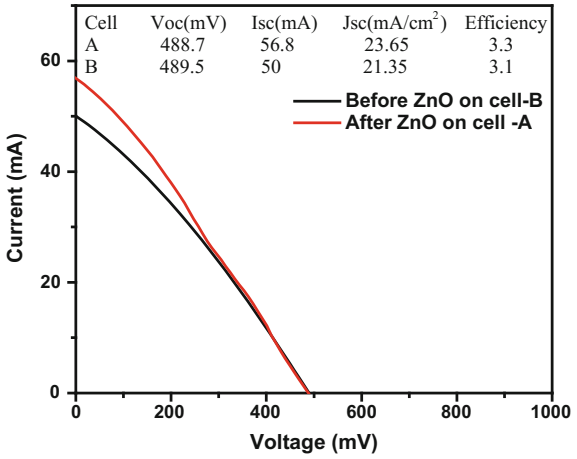

Fig. 6 I-V measurement of ZnO on bare, masked Si solar cell

4 Conclusions

To improve the device performance by increasing photocurrent via increased absorption of incident light, ZnO layers on Si surface for Si solar cell are explored in this present investigation. The XRD study reveals that lower temperature ZnO deposition is decreasing crystalline behavior of thin film. The change of ZA precursor into TTIP precursor shows dominant behavior of seed layer in the resultant ZnO thin film. SEM study reveals that masking of Si solar cell metallic contacts are required to enhance adhesions of ZnO layer with Si cell surface which is able to improve electrical characteristic such as short circuit current of the device in I-V measurement. Keeping in view of additional advantages of this CoSP reactor for Si cell fabrication line, this study suggest that if ZnO layer are suitably designed with proper metallic contacts, further improvement in device efficiency is possible via increase of photocurrent in simple and cost effective manner.

References

1. C. Escolano, J. Pérez, L. Bax, in *Roadmap Report on Thin films & coatings, Nanoroadmap project working paper* (2005)
2. E.S. Aydill, Nanotechnol Law Bus **4**, 275–319 (2007)
3. R. Singha, V. Rangarib, S. Sanagalpallia, V. Jayaramana, S. Mahendraa, V. Singha, Sol. Ener. Mater. Sol. cells **82**, 315–330 (2004)
4. S. Al-Heniti, R.I. Badran, A.A. Al-Ghamedi, F.A. Al-Agel, Adv. Sci. Lett. **4**, 1–5 (2011)
5. S.W. Lee, H.D. Cho, G. Panin, T.W. Kang, Appl. Phys. Lett. **98**, 093110 (2011)
6. J.Y. Chen, K.W. Sun, Sol. Energy Mater. Sol. Cells **94**, 930 (2010)
7. P. Anurag, O. Demircioglu, E. Firat, R. Turan, H.E. Unalan, J. Am. Ceram. Soc. **96**, 1253–1257 (2013)
8. Y.J. Lee, D.S. Ruby, D.W. Peters, B.B. McKenzie, J.W.P. Hsu, Nanoletters **8**, 1501 (2008)
9. Y.T. Cheng, J.J. Ho, S.Y. Tsai, Z.Z. Ye, W. Lee, D.S. Hwang, S.H. Chang, C.C. Chang, K.L. Wang, Sol. Energy **85**, 87–94 (2011)
10. Y. Xuegong, W. Dong, D. Li, G. Li, Y. Deren, Nanoscale Res. Lett. **7**, 306 (2012)
11. H. Dhasmana, C. Dwivedi, V. Dutta. Energy Procedia. **33,** 179–185 (2013)
12. H. Dhasmana, V. Dutta. J. Opto. Adv. Mater. **16** (11–12, 1344–1350) (2014)
13. H. Dhasmana, V. Dutta, J Mater Sci: Mater Electron. **26**, 583–589 (2015)
14. H. Dhasmana, V. Dutta, J Mater Sci: Mater Electron. **25**(3), 1244–1240 (2014)
15. D. Perednis, L.J. Gauckler, J. Electroceram. **14**, 103–111 (2005)

Effect of Plasmonic Enhancement of Light Absorption on the Efficiency of Polymer Solar Cell

Manisha Bajpai, Ritu Srivastava and Ravindra Dhar

Abstract We demonstrate the effect of insertion of Au nano clusters nano clusters (NCs) with various thickness on the power conversion efficiency (PCE) in bulk heterojunction polymer solar cells polymer solar cellbased on blended poly (3-hexylthiophene):[6, 6]-phenyl-C61-butyric acid methyl ester (P3HT:PCBM) (Li et al., Nat Photo 6:205, [1]). The Au NCs were vacuum deposited on pre cleaned indium-tin-oxide (ITO) substrates prior to deposition of poly (3,4-ethylene dioxythiophene:poly (styrene sulfonate) (PEDOT:PSS) buffer layer. It has been found that both short-circuit current density and PCE increase after incorporating Au NCs between ITO/PEDOT:PSS interface. The PCE enhancement is attributed to the localized surface plasmonic excitation of Au NPs (Tada et al., Nat Mat 10:450, [2]). The method employed has great potential in future practical applications.

1 Introduction

Photovoltaic devices based on organic semiconductors (OPVs) currently have developed one of the most fascinating substitutes for silicon solar cellsdue to simple processing and less cost [1]. Conjugated polymers have competed as growing substituent, due to their higher absorption in the visible region with suitable solar spectrum with small film thickness. Bulk heterojunction (BHJ) configuration with a donor and acceptor ensures a better absorption/charge collection due to the intermixing between the two components. Researchers have significantly progressed towards the higher efficiency of OPVs and up to date the maximum power conversion efficiency (PCE) over 8 % has been achieved in this field [2, 3].

M. Bajpai (✉) · R. Dhar
Soft Materials Research Laboratory, Centre of Material Sciences, Institute of Interdisciplinary Studies, University of Allahabad, Allahabad, India
e-mail: bajpaim@mail.nplindia.org; mansa83@gmail.com

R. Srivastava
National Physical Laboratory (Council of Scientific and Industrial Research), Physics for Energy Division, Dr. K.S. Krishnan Marg, New Delhi 110012, India

V.K. Jain et al. (eds.), *Recent Trends in Materials and Devices*,
Springer Proceedings in Physics 178, DOI 10.1007/978-3-319-29096-6_42

Higher external quantum efficiencies of the polymer in OPVs have been realized by the absorption of incident light. Hence, the photon absorption in a thin photoactive layer has been enhanced OPVs for higher PCE. Various strategies for light trapping i.e. using an optical spacer to spatially reallocate the light intensity and the incorporation of periodic nanostructures onto the active layer to increase the optical path length [4–8] etc. have been developed to enhance the light absorption.

Recently, the based on localized surface plasmon resonance localized surface plasmon resonance (LSPR) effect, we have approached for the enhancement characteristics of OPVs.

2 Experimental

The precleaned substrates with acetone, trichloroethylene and isopropanol were subsequently annealed at 150 °C in the vacuum oven for 20 min different thicknesses of Au NCs were deposited onto the precleaned ITO substrates. Over the Au deposited ITO substrates, PEDOT:PSS (Sigma Aldrich, USA) were spin casted. The substrates were further baked at 120 °C for 15 min in the vacuum oven. The P3HT:PCBM polymer blend (chlorobenzene solvent) were then spin coated and annealed at 120 °C for 15 min under inert atmosphere in glove box. Finally, metal (Al) electrodes were deposited with thickness 150 nm in the deposition unit through shadow mask. The current density-voltage (*J-V*) characteristics of the OPV devices were recorded using Keithley 2420 Source Meter unit.

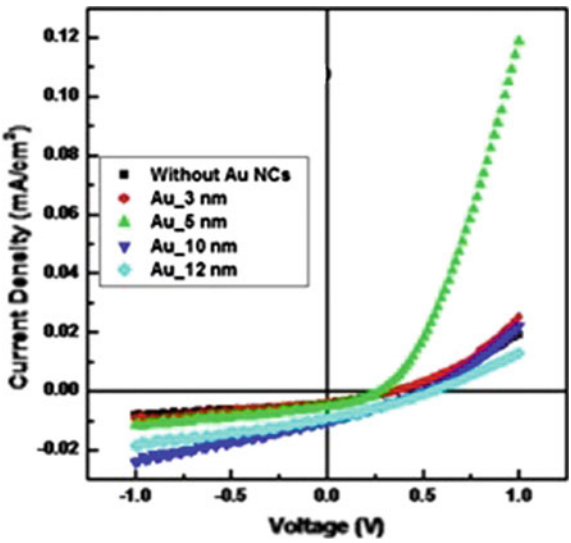

Fig. 1 J-V characteristics of OPV devices with and without Au NCs

Table 1 Extracted parameters of the devices

Device	Voc (V)	J_{Sc} (mA/cm^2)	Fill factor (%)	Efficiency (%)
Without Au	0.33	3.86×10^{-2}	33	0.29
Au_3 nm	0.35	3.47×10^{-2}	28	0.31
Au_5 nm	0.247	5.17×10^{-2}	40	0.52
Au_10 nm	0.358	1.02×10^{-2}	28	1.16
Au_12 nm	0.523	1.02×10^{-2}	29	1.48

3 Results and Discussion

The J-V characteristics of OPV devices in the configuration ITO/with or without Au (NCs)/PEDOT:PSS/P3HT:PCBM/Al is shown in Fig. 1. The parameters extracted from Fig. 1 are summarized in Table 1. The OPV device without gold NCs has the power conversion efficiency (PCE) 29 % with fill factor (FF) 33, an open-circuit voltage (Voc) 0.33 and short-circuits current density (Jsc) 3.86×10^{-2} mA/cm^2. By incorporating with Au NCs, the best cell exhibits dramatically enhance the performance. The current density versus voltage characteristics and device parameters are tabulated in Table 1.

4 Conclusions

From above discussion we have concluded that the plasmonic enhanced OPVs in presence of Au NCs over the PEDOT:PSS layer. Au NCs into OPV architecture have accomplished to introduce the plasmonic effect and thereby the electrical properties.

References

1. G. Li, R. Zhu, Y. Yang, Nat. Photo. **6**, 205 (2010)
2. A. Tada, Y. Gang, Q. Wei, K. Hashimoto, K. Tajima, Nat. Mat. **10**, 450 (2011)
3. G. Yu, J. Gao, J.C. Hummelen, F. Wudl, A.J. Heeger, Science **270**, 1789 (1995)
4. N.S. Saraciftci, L. Smilowitz, A.J. Heeger, F. Wudl, Science **258**, 1474 (1992)
5. P. Peumans, S. Uchida, S.R. Forrest, Nature **425**, 158 (2003)
6. G. Qiang, F.S. Tong Lee, Q Q Zhuo,J. J. Zhu, J.X. Tang, Z. Q. Xu,P.P. Cheng, Y.Q. Li, X.H. Sun, J. Mater. Chem. **22**, 15614 (2012)
7. F. Yang, M. Shtein, S.R. Forrest, Nature Mater. **4**, 37 (2005)
8. Q. Liu, Y. Cui, D. Gardner, X. Li, S. He, I.I. Smalyukh, Nano Lett. **10**, 1347 (2010)

Efficiency Enhancement in Thin Film GaAs Solar Cell Using Photonic Crystals as Reflection and Diffraction Gratings for Light Trapping

Nikhil Deep Gupta and Vijay Janyani

Abstract In the paper, GaAs based thin film solar-cells, combining 2D-Photonic Crystals (PhC) as diffraction-grating with either metallic or Distribute Bragg Reflector (DBR) as specular reflectors and also as single back-reflector for light trapping, have been optimized and compared. The results have shown that PhC diffraction-gratings with DBR as specular reflector outperforms others.

1 Introduction

One of the most important techniques for solar cell thin film technology is the enhancement of light trapping in the absorber layer. The light trapping in solar cells are usually been achieved through the back mirror, which could reflect back photons of high wavelength by scattering them as much as they could at large oblique angles. Typically, simple metallic layer at the back of the absorbing layer served the purpose of reflections, but due to its inherited disadvantages and limitations [1], researchers are looking at alternates which could improve the performance of thin film solar cells.

During the past few years, interest in PhC for light trapping in solar cells has been studied, and the results have shown its promising advantages [2, 3] but these structures are mainly aims for silicon and germanium materials based solar cells. Our group has been working for the design and simulation of III–V compound semiconductors, especially GaAs, as these compounds have several advantages, and also most suitable for solar energy conversion [4], yet the use of the material for terrestrial solar cell applications is still restricted. These factors motivated us to look at several possible PhC based design structures which may help to take the device

N.D. Gupta (✉) · V. Janyani
Electronics and Communication Engineering,
Malaviya National Institute of Technology, Jaipur, India
e-mail: nikhildeep.gupta@gmail.com

V. Janyani
e-mail: vjanyani.ece@mnit.ac.in

V.K. Jain et al. (eds.), *Recent Trends in Materials and Devices*,
Springer Proceedings in Physics 178, DOI 10.1007/978-3-319-29096-6_43

made up of GaAs material near to its maximum efficiency and make it viable for terrestrial applications. In the paper, we have proposed, 2D PhC to be used as a diffraction grating, having plane of periodicity perpendicular to the incident light, designed basically for non-specular reflections, having an added advantage that it could reflect light from any angle or medium within its bandgap. We have designed three different structures using PhC for light trapping mechanism and then optimized and compared them.

2 Design of the Structure

The most part of the design of the proposed structures are basically taken from our earlier work [4], which includes

1. Anti-reflection coating (ARC) at the top.
2. Thin heavily doped front window layer of p type AlGaAs, used to reduce surface recombinations.
3. Active layers of GaAs forming p-n junction, including thin heavily doped p-type emitter layer followed by relatively thick n-type base, having total thickness of 1 μm.
4. Thin heavily doped back window layer of n-type AlGaAs.
5. Back light trapping structures, which consists of either one of the three back light trapping structure:
   (a) 2D PhC having hexagonal lattice for both specular and non-specular reflections, where plane of periodicity is parallel to the direction of light propagation.
   (b) 2D PhC having hexagonal lattice diffraction layer, having plane of periodicity perpendicular to the direction of light propagation.
   (c) 2D PhC having hexagonal lattice diffraction layer between window layer and DBR.

Layers are mentioned in the same order as they are shown in Fig. 1. For light trapping mechanism, the PhC layers are included at the back of the window layer of n-AlGaAs. The advantage of PhC here is to introduce diffraction, where the photon momentum (k) can be scattered away from the specular direction thus helps in keeping the light within the absorption layer with $\left(k^{||} = k_i^{||} + G\right)$ [3], where G is a reciprocal lattice vector. 2D PhC structure consists of hexagonal lattice of GaAs rods in the SiO_2 background, so chosen as the dielectric contrast of the two materials needs to be high enough for sufficient diffraction. The motive of the study is to show the effectiveness of the 2D PhC as a diffraction grating in thin film solar and systematically optimize its parameters cell to maximize absorption. The specular reflections are provided through either metallic BR or through DBR.

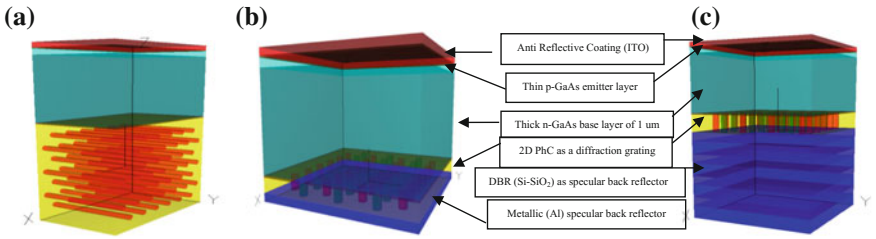

Fig. 1 Schematic structure for thin film GaAs solar cell having **a** 2D PhC as Back reflector for both specular and non specular reflections, **b** 2D PhC as diffraction grating with metallic specular reflector, **c** 2D PhC as diffraction grating with Distributed Bragg Reflector for specular reflections. PhC consists of GaAs rods in SiO_2 background. Other parameters as in [1] (Thickness of the layers is not to scale)

Aluminum (Al) is used as a metallic specular BR whereas DBR consists of alternating layers of Si and SiO_2, used in order to get desired bandgap for reflections.

The simulations have been done using the Plane Wave Expansion (PWE) and FDTD method. Periodic Boundary Condition (PBC) are considered in x and y directions, whereas Perfectly Matched Layer (PML) conditions are used in the vertical (z) directions. Plane wave is used as an incident spectrum. The frequency dependent semiconductor material parameters considered are taken from [5, 6].

3 Results and Discussion

We have optimized the PhC structure for its period (a), radius (r) and grating depth (d). The period of the structure is found out to be 650 nm, r/a is found out to be 0.35 and the grating depth for optimum structure is found out to be 100 nm. For the structure having metallic BR, the optimized thickness of the Al BR is found out to be 80 nm, which is in well contention considering 750 nm as a Bragg's central wavelength. The optimized thickness for the Si layer thickness in DBR is found out as 50 nm and for SiO_2 layer it is 115 nm, and the combination gives us the band gap from 600 to 850 nm.

After the design of the structure, we have computed and analyzed the optical absorption, reflectance and transmission performance of the three structures, considering absorption only in the active layer. The results shown in Fig. 2 clearly indicate the performance enhancement while using 2D PhC as a diffraction grating in comparison to using it as a single back reflector, which is basically due to the improvement in non-specular performance of the structure. Among the two PhC based diffraction grating structure, the structure having DBR has little edge over the metallic BR.

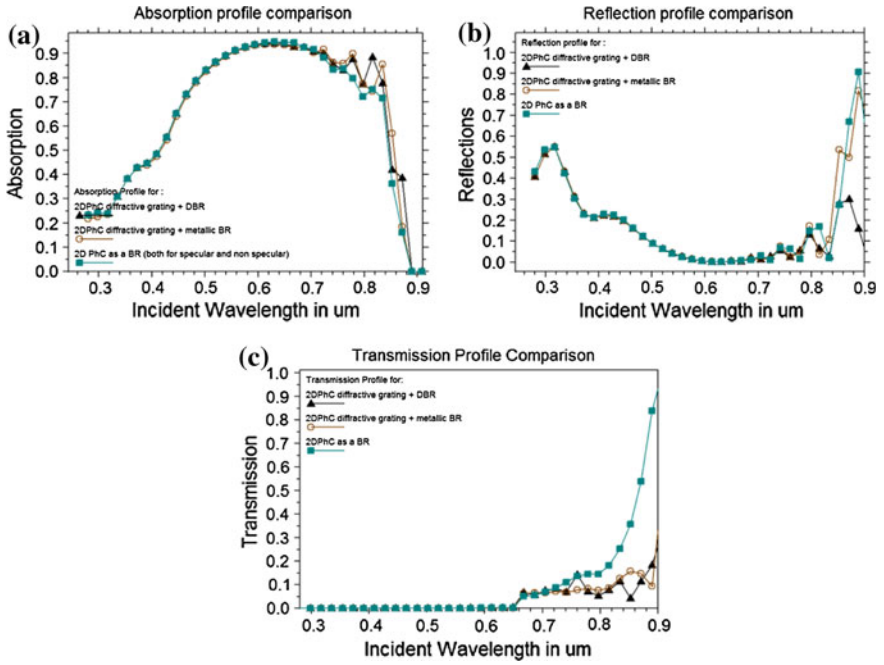

Fig. 2 **a** Absorption, **b** Reflection and **c** Transmission profile for the proposed structures

4 Conclusion

In the paper, we have presented the optical performance analysis of the PhC based various light trapping mechanism for the GaAs based thin film solar cell considering only 1 μm thick absorbing layer. The results have shown that the PhC light trapping mechanism using 2D PhC as a diffraction grating performs better than the 2D PhC design used for both type of reflection mechanism. Also, between the two designs using PhC as diffraction mechanism using metallic BR and DBR for specular reflection, design with DBR has little edge over the metallic BR design as far as optical performance is considered. Also, the due to dielectric nature of DBR, the structure having DBR would perform better than the metallic specular reflector, as metallic reflector has its inherited disadvantages. Although there are challenges in the fabrication of the design, but still this area is very promising with a lot of potential, which could ultimately lead to the efficiency enhancement of thin film solar cells.

References

1. J. Nelson, *The Physics of Solar Cell* (Imperial College Press, United Kingdom, 2008), pp. 253–288
2. N.D. Gupta, V. Janyani, in *Study and Possible Modifications of Various Designs for Photonic Crystals Based Thin Film Solar Cells*. Paper presented at IONS-Asia 6, IIT, Kharagpur, 2014
3. D. Zhou, R. Biswas, J. Appl. Phys. **103**, 093102 (2008)
4. N.D. Gupta, V. Janyani, in *Design and Simulation of Light Trapping in Thin Film GaAs Solar Cell using Photonic Crystals as back reflector*. Paper presented at 12th International Conference on Fiber Optics and Photonics, OSA Technical Digest (online), IIT Kharagpur India, 2014
5. J. Piprek, *Semiconductor Optoelectronic Devices* (Academic Press, London, United Kingdom, 2003)
6. O. Madelung, *Semiconductors—Basic Data*, 2nd edn. (Springer-Verlag, Berlin, Germany, 1996)

Annealing Free, High Quality CVD Graphene Growth and Transfer

R. Brajpuriya, T. Dikonimos, F. Buonocore and N. Lisi

Abstract Among the different graphene synthesis methods, chemical vapor deposition of graphene on low cost copper foil shows great promise for large scale applications. Here we report on the growth and transfer of uniform and continuous large-sized thin-films composed of single- and few-layered graphene. The foils were grown by chemical vapor deposition (CVD) on polycrystalline copper (Cu) foils at low pressure using ethanol and were transferred onto the destination substrates using a cyclododecane supporting layer. Structural and optical characterizations indicate that the graphene films are composed of single or few layers depending on the growth conditions and exhibit low defect density. The graphene films can be transferred to arbitrary substrates with the help of a green transfer method based on an organic molecule, cyclododecane.

1 Introduction

Today graphene, with other 2D materials, is considered as an encouraging material that could be the foundation for future generations of low-power, faster, smaller and economic electronic devices [1, 2]. The route toward the commercial exploitation of graphene's unique properties hinges entirely on the development of adequate graphene growth and integration technologies, which is still a great challenge. The key to solving this challenge requires us to develop synthesis and transfer methods to employ in the fabrication and transfer of single layer graphene films with an optimal degree of control. In this paper, therefore, our aim is to obtain improved and

R. Brajpuriya (✉)
Amity Institute of Nanotechnology, Amity University Haryana, Manesar, Gurgaon 122413, Haryana, India
e-mail: ranjeetbjp@yahoo.co.in

T. Dikonimos · F. Buonocore · N. Lisi
Surface Technology Laboratory Materials Technology Unit, Casaccia Research Centre, ENEA, Rome 00123, Italy

V.K. Jain et al. (eds.), *Recent Trends in Materials and Devices*,
Springer Proceedings in Physics 178, DOI 10.1007/978-3-319-29096-6_44

sustainable growth method of high-quality graphene and a green method which permits the transfer of continuous and crackles films onto arbitrary substrates.

2 Experimental Details

Sample Growth: Continuous graphene films were grown on 25 μm thick Cu foils using low-pressure CVD technique and ethanol diluted in Argon as carbon precursor [3]. Before synthesis, the as-received Cu foils of a few cm^2 were pre-cleaned by ultra-sonication in acetone and ethanol. The boat supporting the Cu foils was inserted into a hot zone, and the samples were annealed in Ar/H_2:20/20 sccm for 20 min at 1000 °C. Afterwards, the gaseous carbon source, ethanol (C_2H_5OH) diluted in Ar (0.5 % in 20 sccm of Ar) was introduced in the tube with 100 sccm of H_2 for 30 min to perform the graphene growth. Finally, the samples were rapidly cooled under Ar down to ambient temperature before being removed from the chamber.

Sample Transfer: After the growth the graphene film must be removed from the metal substrate and transferred onto the appropriate substrate for characterizations and use. Conventional wet etching chemical transfer methods involve the use of protective supporting layers for graphene, such as PMMA, during the metal etching. Such layers need further processing steps for their complete removal, typically solvents and heat treatments, which are not always compatible with many desirable polymeric substrates [4]. Thus, for the necessary development and possible commercialization of high-performance electronic devices based upon graphene improved graphene transfer processes free from contaminations are desirable. Such methods should at the same time inhibit the formation of cracks and holes during transfer but it is desirable that it could also be non-toxic, fast and green.

At the ENEA laboratories, a new procedure has been developed [5] based on cyclododecane (CDD) as support material and a protective layer. In this work, the films were transferred onto a Si/SiO_2 (300 nm) substrate by using CDD. Due to ability to sublimate completely at ambient conditions, Graphene transfer using CDD is a fast and green method and does not result in the presence of contamination from resist residues. The graphene transfer process is shown schematically in Fig. 1.

The first step consists of the removal of graphene from the back surface of the Cu foil, by oxygen plasma treatment (30–90 s, 100 W RF power). Then a thin layer of cyclododecane (20 wt% up to saturation) diluted in ethyl ether or cyclohexane, was spin-coated onto graphene over the front side of the Cu foil at (1500 rpm for 60 s). The Cu substrate was then etched in a 50 g/l aqueous solution of Ammonium Per-sulphate (PSA). The graphene/CDD film floating on the solution was then thoroughly rinsed with DI water to remove any process residues. It has been reported [6] that when graphene film is transferred from water to the target substrate, the stack might not make a full contact with the surface and that the unattached region tends to break and form the cracks. Therefore, it is expected that the hydrophilicity of the surface of the substrate onto which the CDD/graphene stack will be transferred will have a crucial impact on the formation of the folds. A hydrophilic surface will spread

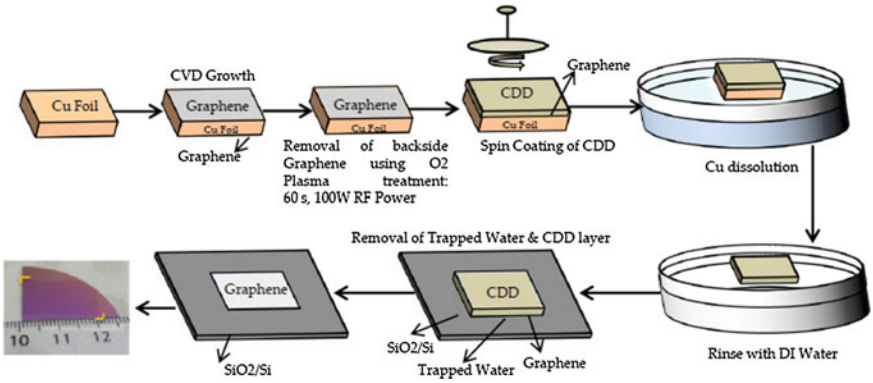

Fig. 1 Improved wet chemical process

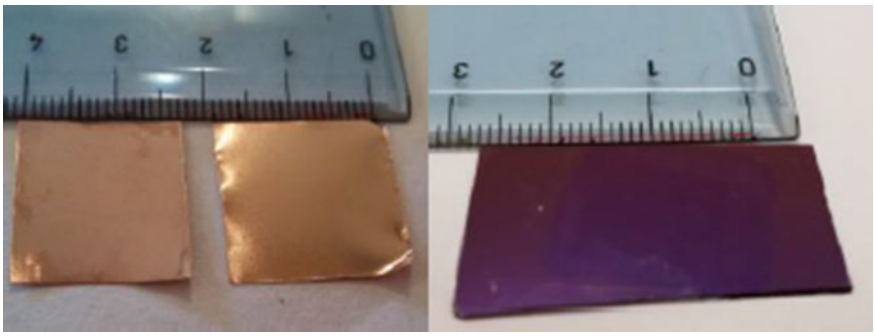

Fig. 2 Photographs of as-received Cu foil (*left*), and graphene film grown on Cu substrate (*Centre*). On the *right* the Graphene films transferred onto a SiO_2/Si substrate

the water more evenly during transfer and improve the smoothness of the CDD/graphene stack contact with the target.

In the present approach, we have transferred floating stack onto oxygen plasma treated hydrophilic SiO_2 (300 nm)/Si target substrate. In the last step, cyclododecane/graphene/SiO_2 (300 nm) is heated in air at 70 °C for the final removal of cyclododecane and interfacial water trapped underneath graphene. Since CDD melts at 62.5 °C, during this final step it should release the surface tensions improving the transfer. Figure 2 shows the appearance of graphene film after growth and transfer process.

Characterization methods: The morphology and microstructure of both as grown and transferred graphene films are investigated using a field emission scanning electron microscope (SEM) and X-ray photoelectron spectroscopy (XPS) measurements.

3 Results and Discussion

The cleanliness of the as-grown graphene film deposited on Cu foil was checked by XPS, as displayed in Fig. 3. It is very clear from the figure that only peaks corresponding to Carbon and Cu were present and all other peaks were absent, indicating that the deposited film does not contain any impurity or contaminants. The graphene film after its transfer onto the Si/SiO_2 (300 nm) substrate was examined using SEM, as displayed in the Fig. 4. The film is continuous and shows wrinkles and folds on its surface, which appear during cooling after the chemical vapor deposition (CVD) synthesis due to the difference in the thermal expansion coefficient of Cu and graphene [3]. It is also possible to observe the presence of regions with different numbers of layers since; different areas of the image appear with a different brightness.

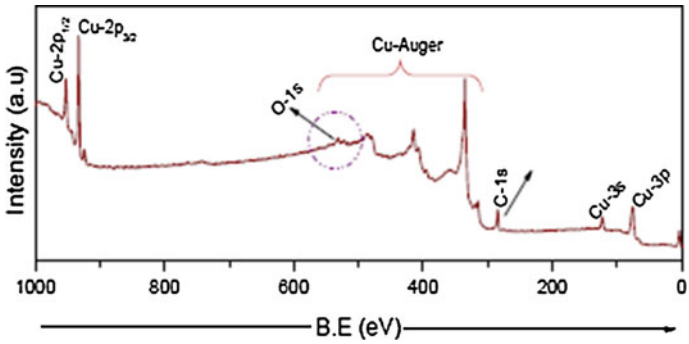

Fig. 3 Survey scans of graphene film grown on Cu foil

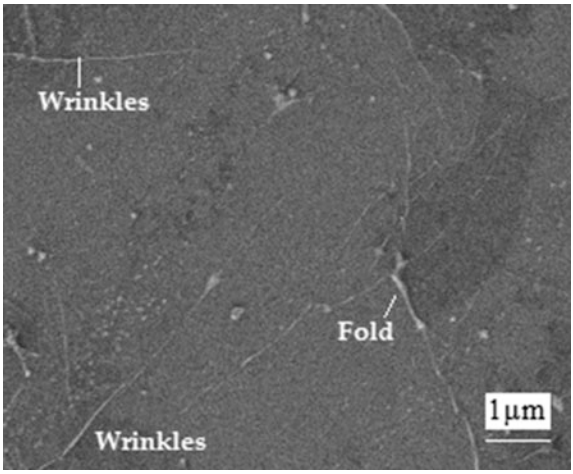

Fig. 4 SEM image of transferred graphene film

Fig. 5 Optical micrograph of transferred few layer graphene

The optical micrograph of the sample after transfer (Fig. 5) also show a film which is continuous and uniform; there are no holes or cracks, also it is evident the presence of secondary nucleation stripes, due to the copper lamination. These results imply that with this approach clean, crackless transfer of graphene is possible in a process requiring a very small amount of solvents, namely the few drops utilised during spin coating.

Further measurements are under way to demonstrate that no other impurities were added to graphene during the whole process and confirming effectiveness and cleanness of the transfer protocols.

4 Conclusions

In summary, authors have developed a method for the growth of large-area, continuous and uniform graphene films with ethanol as carbon precursor, and a green transfer method based on an organic molecule, cyclododecane, which grants high fidelity transfer onto arbitrary surfaces, including substrates which are sensitive to heat and to solvents. By combining an effective metal cleaning process, we have developed and demonstrated a transfer process that can improve both device yield and performance uniformity.

Acknowledgments The author (R. B) would like to acknowledge ENEA for providing the International Research Fellowship.

References

1. K.S. Novoselov et al., Science **306**, 666 (2004)
2. N. Tombros, Nature **448**, 571 (2007)
3. G. Faggio et al., J. Phy. Chem. C **117**, 21569 (2013)
4. X. Li et al., Science **324**, 1312 (2009)
5. A. Capasso et al., Appl. Phys. Lett. **105**, 113101 (2014)
6. X. Liang et al., ACS Nano **5**, 9144 (2011)

Compositional Optimization of Photovoltaic Grade Cu_2ZnSnS_4 (CZTS) Films Synthesized by Colloidal Route

Shefali Jain and Shailesh Narain Sharma

Abstract In recent years, kesterite structured $Cu_2ZnSn(S, Se)_4$ materials have attracted significant interest as second generation solar cell material. However, the capability of reproducibly synthesizing these nanocrystal (NC) inks with accurately controlled and specific compositions is very crucial for making efficient solar cell devices. In this work rod shaped CZTS nanoparticles are synthesized by cost effective and rapid hot injection technique using TOPO-TOP as capping ligand for various Zn/Sn precursor ratios. Since, for good solar cell device material (here, CZTS nanocrystals) higher zinc concentration are required so here, we varies zinc concentration and we find that mere increase in zinc amount in precursors for the synthesis of CZTS nanocrystals may not be necessarily advantageous for solar cell application. It should be optimized with respect to tin (Sn), phosphorus (P) and copper (Cu) for best PV properties and we find that incorporation of zinc into CZTS is higher in case where zinc amount is less in precursors. Different aspects of these nanorods are analyzed by EDAX, contact angle, transmission electron microscopy (TEM) and photoluminescence spectroscopy respectively.

1 Introduction

Colloidal semiconductor nanocrystals have great potential in future photovoltaic devices due to their novel size- and shape-dependent properties. Relatively low-cost of colloidal synthesis methods for nano inks ensure the commercial competitiveness of the fabricated devices, for these photovoltaic devices [1–5]. In recent years, thin films, based on chalcopyrites have shown a new way to approach Photovoltaic application. Chalcopyrites includes I_2-II-IV-VI_4 compounds such as copper indium

S. Jain · S.N. Sharma (✉)
CSIR Network of Institutes for Solar Energy (NISE),
CSIR-National Physical Laboratory, Delhi, India
e-mail: shailesh@nplindia.org

S. Jain
e-mail: jshefali85@yahoo.com

V.K. Jain et al. (eds.), *Recent Trends in Materials and Devices*,
Springer Proceedings in Physics 178, DOI 10.1007/978-3-319-29096-6_45

gallium selenide (CIGS), copper zinc tin selenide (CZTSe), sulfur-selenium alloy CZTSSe and pure sulphur based compound copper zinc tin sulphide (CZTS) [2, 3]. Among these, CZTS based compounds are more promising candidate as compared to CIGS based compounds. Cu_2ZnSnS_4 (CZTS) with a band gap of (1.2–1.6 eV) is a prominent low cost absorber layer as it utilizes abundant zinc and tin (rare-earth free metals) by replacing depleting indium (due to its usage in telecommunications) in CIGS, non-toxic and inexpensive material [4, 5]. However, significant research and development remains to be carried out in order to improve the efficiency of devices based on these materials which are currently 12.6 % for the related sulfur–selenium compound, $Cu_2ZnSn(S, Se)_4$ [6].

Guo et al. were first to publish report for synthesis of CZTS NCs for photovoltaic (PV) applications in 2009 [7]. Thereafter many synthesis reports were published, but only few explain the compositional effects on the quality of CZTS as absorber material in solar cell [8, 9]. The composition of the absorber layer strongly effect device performance and is very imperative issue to be studied [10].

However, it is really very difficult to obtain the pure phase CZTS since slight changes in the input precursor amount leads to the change in composition that can significantly alter the favorability of forming CZTS itself, different defects and defect complexes, which can significantly impact the device quality [11].

CZTS based nanocrystals are order destructive compounds i.e. they have non-stoichiometric compositions, which is a significant characteristics for the higher efficiency solar cell devices. Compositions for these compounds are typically reported in the cationic ratios of Cu/(Zn + Sn) and Zn/Sn, with ranges of 0.7–0.9 and 1.1–1.3, respectively [12–15]. These values are often used to describe a film as Cu-poor, Zn-rich, which is requirement for higher efficiency of solar cell device [16].

Here, in the present work, we have systematically studied the effect of Zn/Sn precursor ratio for pure sulphur based CZTS compounds and found that increased amount of zinc in precursors leads to zinc-poor CZTS nanocrystals with large amount of defects. Thus, optimization of Zn/Sn ratio in precursors is required during synthesis for good solar cell device application. Different analysis like shape and size, porosity, defects level and corresponding band structure are done by various characterization tools like EDAX, contact angle, transmission electron microscopy (TEM) and photoluminescence spectroscopy respectively. A Photoluminescence spectrum in our work does not illustrates band to band transition demonstrating the quantum confinement effect. It just expresses the defects level in various optical ranges of as synthesized CZTS nanocrystals, which is a unique study in itself. This effect can be explained by large size nanorods (200–300 nm) with one dimensional i.e. weaker quantum confinement effect as compared to that present in case of quantum dots where very stronger three dimensional confinement effects are present.

2 Experiment Detail

Here, we have successfully fabricated CZTS by colloidal route method. Figure 1 described elsewhere with some modifications [17]. In our experiment, indium is replaced by Zn:Sn in varying ratios 4, 2 and 1 respectively. Also, the reaction is kept at constant synthesis temperature for 15 min.

In first step, pure sulphur powder is dissolved in tri-n-octylphosphine (TOP) by constant heating at 60–70 °C which results into reddish brown colour TOP-S complex.

After the first step, all the precursors Copper (II) chloride ($CuCl_2$), Zinc chloride ($ZnCl_2$) and Stannous chloride ($SnCl_4$) were dissolved in TOPO with continues heating up to ∼300 °C. Precursors were taken such that Zn/Sn > 1 and Cu/(Zn + Sn) < 1, which is condition for good photovoltaic device [16]. All reagents were of analytical grade from Sigma Aldrich. The mixture was under constant stirring in inert gas atmosphere. A colour change from straw yellow to deep yellow to orange and then finally to coffee brown was observed.

Now, the reddish brown TOP-S solution prepared in first step was injected into a mixture of TOPO and precursor at ∼275 °C under an inert gas atmosphere. This changes the solution colour to black from coffee brown. After injection, reaction temperature reduces by 30–40 °C indicating that the reaction is of endothermic type. Now reaction temperature was again increased to the injection temperature and is kept constant for 15 min for different Zn/Sn precursor ratios. Obtained

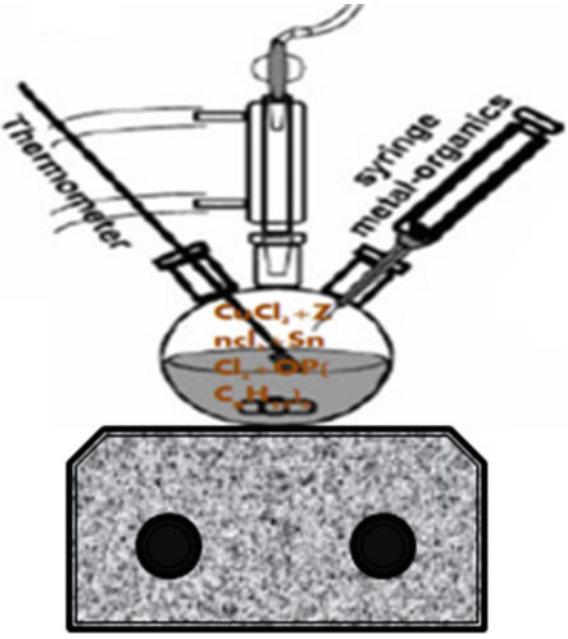

Fig. 1 Colloidal route synthesis set-up with a constant stirring in Ar-atmosphere at ∼300°C

nanocrystals are then washed with methanol and toluene to remove extra ligands and other impurities. Nanoparticles thus observed are analyzed for different properties like shape and size, porosity, defects levels and corresponding band structure.

3 Results and Discussion

EDAX measurements were taken for as synthesized CZTS nanoparticles with Zn/Sn ratios equal to 4 and 1 respectively. Zn/Sn, Zn/P, Zn/(Cu + Sn) and Zn/S output ratios were tabulated in Table 1 for two different input Zn/Sn (precursor ratios). It was shown in table that, zinc concentration is more w.r.t. Sn, P, Cu and S respectively in case where precursor Zn/Sn ratio (input) is less. This is due to the probability of formation of ZnS is higher in case of higher Zn/Sn ratio in precursors. ZnS formation might occur during nucleation time before the growth of CZTS nanoparticles as there no signature of ZnS is found in analysis of XRD and Raman spectroscopy. It may be due to the high reactivity of zinc compared to Cu and Sn with sulphur, which results into low Zinc concentration in final CZTS compound as revealed in Table 1. It can also be infer by Table 1 that Zn rich property given by Zn/Sn ratio and Cu-poor property given by Cu/(Zn + Sn) ratio [16] is also enhanced when input Zn/Sn ratio is equal to 1 which is necessary for good device efficiency.

The contact angle measurements for different CZTS nanocrystals are shown in Fig. 2. It is an angle between a solid surface of a porous material and liquid drop

Table 1 Various parameters obtained from EDAX measurements

(Input) Zn/Sn ratio	(Output) Zn/Sn	(Output) Cu/(Zn + Sn)	(Output) Zn/p	(Output) Zn/S
4	0.095	2.04	1.47	0.051
1	0.269	1.25	2.86	0.024

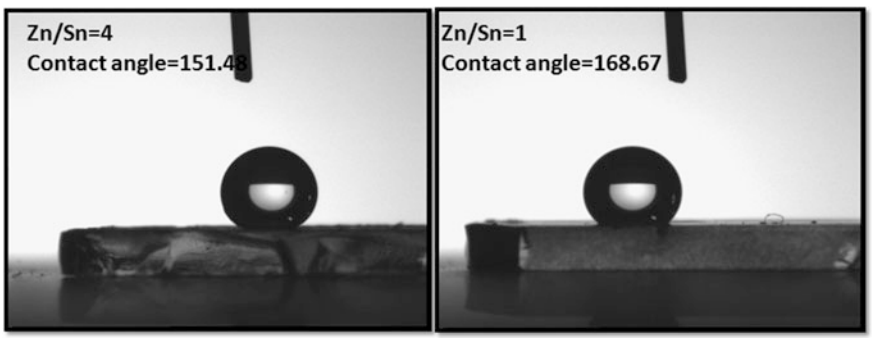

Fig. 2 Contact angle images for Zn/Sn = 4 and Zn/Sn = 1 respectively

when both materials come in contact together and is common method to measure hydrophobicity of material. The higher contact angle i.e. more than 90° indicates more hydrophobic nature of solid material [18].

We found contact angle of approximately 151° and 169° in case of Zn/Sn ratio 4 and 1 respectively. It shows relatively high hydrophobic and low porous nature of CZTS nanorods in case where input Zn/Sn precursor ratio is low (i.e. equal to one) as compared to high input Zn/Sn precursor ratio. Low porosity indicates smoothened surface and fewer defects in material which is also evident in TEM results and PL spectra analysis. This again leads to the fact that simply increased amount of zinc concentration in precursors may not leads to good and required properties for solar cell device material.

Figure 3 shows the TEM images for both the samples having input Zn/Sn precursor ratio equal to 4 and 1 respectively. Particle size analysis of these particles indicates higher monodispersity in case where input Zn/Sn precursor ratio is low. It also reveals that there is no shape change occurs due to the change in concentration of precursors. However, prominent change in size is observed. Decrease in particle size is observed with decrease in Zn/Sn ratio. Although, agglomeration is main drawback in case of colloidal route synthesis, we found fairly less agglomeration in case where input Zn/Sn precursor ratio is less i.e. the case where zinc incorporation in nanocrystals is high as compared to the case where input Zn/Sn precursor ratio is high. Less agglomeration represents less porosity and higher material quality required by photovoltaic material as previously analyzed by contact angle measurements.

The room temperature PL spectra of both the CZTS nanorods with input precursor ratio 4 and 1 is measured with the excitation wavelength of 350 nm. The PL spectra show a broad emission spectrum around 400–600 nm (not shown here). In our PL spectra we didn't observe any band to band transition at ~800 nm as in quantum confined CZTS particles [19]. This may be due to weaker one dimension confinement as CZTS nanoparticles synthesized are rod shaped. The absence of

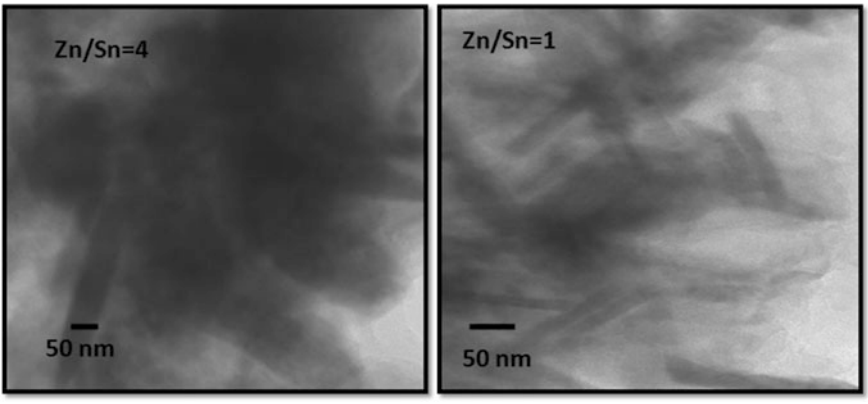

Fig. 3 TEM images for Zn/Sn = 4 and Zn/Sn = 1 respectively

transitions from band to band in PL spectra may also be attributed to the fact that defect type recombination are dominant in this material due to the large number of possible intrinsic defects as CZTS are order defect compounds.

Figure 4 shows the PL intensity versus input precursors Zn/Sn ratio curve in the wavelength range of 420–430 and 460–480 nm which lies in the purple and blue band of visible spectra. The PL peak in range 420–430 nm has been known due to the recombination between the sulfur-vacancy-related donor and the valance band [20, 21]. The blue emission peak in range 460–480 nm being observed [21] also arises due to native point defects i.e., due to recombination from zinc vacancy to the valance band [9]. It can be seen from Fig. 3 that CZTS nanoparticles with low Zn/Sn precursor ratio shows very less numbers of defect level compared to other nanoparticles with high Zn/Sn precursor ratio. Less number of defects leads to low porosity i.e. high quality material for solar cell device, as already confirmed by contact angle and TEM observations. Lower number of traps also implies less number of recombination sites which is necessary requirement for solar cell so that there are more number of free charge carriers.

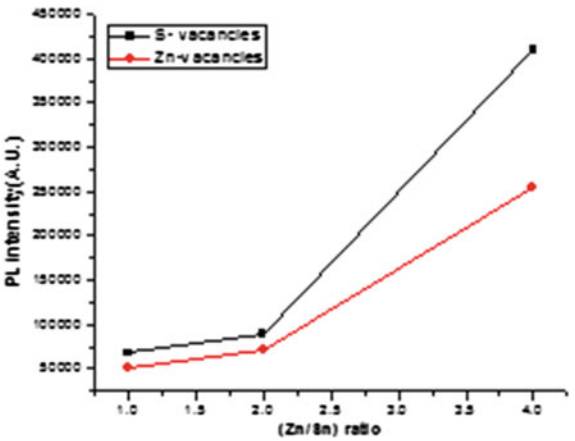

Fig. 4 PL intensity versus precursor Zn/Sn concentration ratios

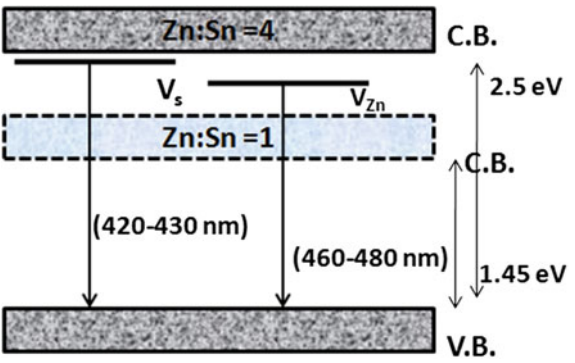

Fig. 5 Energy level diagram

Based on the PL results observed, the schematic energy-level diagram of CZTS nanorods in both cases is depicted and is shown in Fig. 5. Optimum range of band gap in case of CZTS nanoparticles lies in the range of 1.2–1.6 eV [4, 5]. However, in our case large band gap of ~2.7 eV is observed by absorption spectra (not shown here) in case CZTS nanorods corresponding to higher Zn/Sn ratio 4. This expansion of band may be due the defect/trap levels above the conduction band minima. As observed in Fig. 4 showing trap level intensity, it was confirmed that number of traps are very large in case of CZTS nanorods with high Zn/Sn precursor ratio thus large band expansion is observed in this case. However in other CZTS nanoparticles with Zn/Sn equal to one in precursor shows no significant change in band gap due to less number of traps. Thus we can say that CZTS nanorods with less input Zn/Sn precursor ratio i.e. the case where large amount of incorporation of zinc element as observed by EDAX is better as compared to CZTS nanorods of high input precursor ratio.

4 Conclusions

In this paper we studied the effect of change in zinc concentration in precursors during synthesis. EDAX analysis revealed that we get zinc rich CZTS nanorods in case of low Zn/Sn precursor ratio. The TEM studies have shown that smaller size CZTS nanorods can be prepared by decreasing Zn/Sn ratio in precursors during synthesis. Contact angle study shows increase in hydrophobicity and decrease amount of porosity with decrease in precursors Zn/Sn ratio (equal to one). PL Results shows that no band to band transition is observed due to weaker one dimensional confinement effect. Large number of defects and traps are observed which directly affects the band gap of material. These defects can be decreased by decreasing the input Zn/Sn precursor ratio during synthesis of CZTS nanocrystals.

In conclusion, we can say although high concentration of zinc is required but zinc amount present in output i.e. synthesized CZTS is important and should be optimized with respect to, tin (Sn), copper (Cu) and sulphur (S) for other properties. As zinc incorporation occurs differently during synthesis of CZTS of good electrical characteristics.

References

1. F.J. Fan, L. Wu, S.H. Yu, Energy Environ. Sci. **7**, 190 (2014)
2. K. Kihwan, H. Park, G.M. Hanket, W.K. Kim, W.N. Shafarman. Prog. Photovoltaics: Res. Appl. **23**(6), 76 (2015)
3. S.M. Bhosale, M.P. Suryawanshi, J.H.Kim, A.V. Moholkar. Ceram. Int. **41**(7), 8299 (2015)
4. C.K. Miskin, W.C. Yang, C.J. Hages, N.J. Carter, C.S. Joglekar, E.A. Stach, R. Agrawal, Prog. Photovoltaics Res. Appl. **23**, 654 (2015)
5. K. Mokurala, S. Mallick, P. Bhargava, Energy Procedia **57**, 73 (2014)

6. W. Wang, M.T. Winkler, O. Gunawan, T. Gokmen, T.K. Todorov, Y. Zhu, D.B. Mitzi, Adv. Energy Mater. **4**, 7 (2014)
7. Q. Guo, H.W. Hillhouse, R. Agrawal, J. Am. Chem. Soc. **131**, 11672 (2009)
8. Y. Liu, D. Yao, L. Shen, H. Zhang, X. Zhang, B. Yang, J. Am. Chem. Soc. **134**(17), 7207 (2012)
9. M. Li, W.-H. Zhou, J. Guo, Y.-L. Zhou, Z.-L. Hou, J. Jiao, Z.-J. Zhou, Z.-L. Du, S.-X. Wu, J. Phys. Chem. C **116**, 26507 (2012)
10. A.D. Collord, H. Xin, H.W. Hillhouse. IEEE J. Photovolt. **1** (2014)
11. Andrew D. Collord, Hugh W. Hillhouse, Chem. Mater. **27**(5), 1855 (2015)
12. T.K. Todorov, J. Tang, S. Bag, O. Gunawan, T. Gokmen, Y. Zhu, D.B. Mitzi, Adv. Energy Mater. **3**, 34 (2013)
13. B. Shin, Y. Zhu, N. A. Bojarczuk, S. Jay Chey, S. Guha. Appl. Phys. Lett. **101**, 053903 (2012)
14. W. Wang, M.T. Winkler, O. Gunawan, T. Gokmen, T.K. Todorov, Y. Zhu, D.B. Mitzi, Adv. Energy Mater. **4**, 1 (2013)
15. A. Fairbrother, X. Fontané, V. Izquierdo-Roca, M. Placidi, D. Sylla, M. Espindola-Rodriguez, S. López-Mariño, F. A. Pulgarín, O. Vigil-Galán, A. Pérez-Rodríguez, and E. Saucedo, Prog. Photovolt. Res. Appl. **22**, 479 (2014)
16. A. Fairbrother, M. Neuschitzer, E. Saucedo, A. Pérez-Rodríguez, Phys. Status Solidi A **212** (1), 109 (2015)
17. P. Chawla, S. Singh, S.N. Sharma, Beilstein J. Nanotechnol. **5**, 1235 (2014)
18. Y. Yuan, T.R. Lee., in *Surface Science Techniques* (Springer, Berlin, 2013), p. 3
19. M. Xie, D. Zhuang, M. Zhao, Z. Zhuang, L. Ouyang, X. Li, J. Song. Int. J. Photoenergy. **2013** (2013)
20. S. Lee, D. Song, D. Kim, J. Lee, S. Kim, I.Y. Park, Y.D. Choi, Mat. Lett. **58**, 342 (2004)
21. K. Jayanthi, S. Chawla, H. Chander, D. Haranath, Cryst. Res. Technol. **42**(10), 976 (2007)

Optical Optimization of Solar Cells Having Extremely Thin SnS Layer on ZnO Nanowires

Shilpi Shital, Firoz Alam and Viresh Dutta

Abstract Use of non-toxic earth abundant materials is necessary for popularization of photovoltaic power generation. Here we have tried to optimize the dimensions of ZnO nanowires for maximum light absorption using Mie scattering. The light extinction was found maximum for ZnO nanowires of 140 nm. Approximations used for optimization and their validity have also been discussed. Here in this paper, formation of a semiconductor junction by depositing a thin layer of p type-SnS on n-type ZnO nanowires have also been reported.

1 Introduction

Low toxicity, abundance of elements on earth, low cost and easy tunability of electronic properties and high conductivity make SnS and ZnO suitable candidates for solar cells. Researchers have successfully fabricated SnS/ZnO solar cells by different methods. Hirano et al. fabricated p-SnS/n-ZnO solar cells by sulpherization [1]. Ghosh et al. fabricated ZnO/SnS photovoltaic device by growing thin films of SnS onto the ZnO layer by thermally evaporating high-purity SnS powder [2]. There had been efforts to fabricate SnS and ZnO nanowire solar cells having the advantage of better light absorption with lesser material being used in the device and less effect of bulk impurities. SnS has been used for fabrication of homojunction nanowire solar cells with an efficiency of 1.95 % by Yue et al. [3]. Alam et al. reported junction formation upon deposition of SnS on ZnO nanowires (NWs) by continuous spray pyrolysis (CoSP) technique [4]. CoSP technique has the benefit of being a low cost single step process in which fabrication of SnS nanoparticles (NPs) and their deposition on ZnO NWs happen in single step,

S. Shital · F. Alam · V. Dutta (✉)
Photovoltaic Laboratory, Centre for Energy Studies,
Indian Institute of Technology Delhi, Hauz Khas, New Delhi 110016, Delhi, India
e-mail: vdutta@ces.iitd.ac.in

V.K. Jain et al. (eds.), *Recent Trends in Materials and Devices*,
Springer Proceedings in Physics 178, DOI 10.1007/978-3-319-29096-6_46

enormously simplifying the whole process. By careful design absorption of light in the nanowire solar cells may further be increased. Mie scattering have been used to optimize light absorption in photovoltaic and photocatalytic devices effectively by many researchers [5, 6].

This paper talks about effect of nanowire diameter on extinction efficiency of a SnS coated ZnO nanowire, estimates the optimum diameter of NWs for maximum photogeneration in the junction with some approximation and present study of effect of scattering from ZnO/SnS NWs on the electromagnetic field inside the SnS coating layer. It also reports formation of junction upon deposition of SnS on ZnO NWs by CoSP.

2 Theory

Calculation of Mie scattering from cylinders involves expansion of electric and magnetic field in terms of the vector cylindrical harmonics. Incident, transmitted and scattered fields are expressed in such a way. The total field inside the cylinder is sum of incident and transmitted field and total field outside the cylinder is sum of incident and scattered field [7]. The coefficients for expansion are then calculated by applying appropriate boundary conditions. In this paper, boundary conditions for electric and magnetic field at the boundaries of different materials in stratified cylinder were applied as described by Kerker [8]. The coefficients for electric field expansion was then solved subjected to these boundary conditions. The extinction efficiency (Q_{ext}), scattering efficiency (Q_{sca}), absorption efficiency (Q_{abs}) are given by expressions below.

$$Q_{ext} = \frac{2}{x^2}\sum_{n-1}^{\infty}(2n+1)\mathrm{Re}[a_n + b_n] \tag{1}$$

$$Q_{sca} = \frac{2}{x^2}\sum_{n-1}^{\infty}(2n+1)\left[a_n^2 + b_n^2\right] \tag{2}$$

$$Q_{abs} = Q_{ext} - Q_{sca} \tag{3}$$

Here size parameter x is taken as $x = 2\pi r/\lambda$, m is the refractive index of the cylinder and λ is wavelength of light.

For calculation of scattering from multiple cylinders, for evaluation of electric field, solution to the scalar wave equations was obtained by using the boundary value method. The total wave potentials near a cylinder were evaluated by summing the potentials due to primary incident wave and that due to scattered waves from all the cylinders. Expressions for the coefficients of the scattered wave potentials were

obtained in terms of, those for independent scattering. The unknown coefficients in the wave potentials were found by imposing the usual boundary conditions, i.e., continuity of the tangential components of the electric and magnetic field vectors across the surface of each cylinder. The far field solution was obtained by finding limiting value of the near field formulas at infinity [9, 10].

Rather than simulating scattering from NWs in exact working condition in a solar cell, some approximations were made while optimization for ZnO NW diameter. Perpendicular and parallel polarised light was assumed to be incident perpendicular to the NWs, in spite of the fact that in an actual solar cell, the light is incident at angles other than perpendicular. This approach had been found to predict the optimum diameter of TiO_2 NWs for dye degradation quiet correctly by Chen et al. [5], hence it was expected that it will hold true for this application. Scattering efficiencies for unpolarised light was assumed to be the mean of these parameters for parallel and perpendicular polarization. Optical constants for scattering simulations were taken from reported literature [11, 12].

The light interacting with SnS coated ZnO NWs can either be absorbed by the SnS coating and or may get scattered. Not only the absorption, but the scattering of light also contribute to light absorption enhancement as it increases the path length of light which in turn increases light absorption. Hence in this paper extinction efficiency rather than absorption efficiency was used as parameter to optimize the diameter of the ZnO NWs.

3 Fabrication of SnS/ZnO Nanowires

First ZnO NWs were electrodeposited on cleaned ITO-coated glass. The substrate was kept at an electrical potential of −1.0 V versus saturated calomel electrode (SCE) from an electrolyte in DI water containing 1 mM $Zn(NO_3)_2{\cdot}6H_2O$ and 10 mM KCl. A standard three-electrode electrochemical cell having platinum (Pt) wire is used as a counter electrode and a SCE as a reference electrode was used for electrodeposition. The electrolyte was saturated using intense molecular oxygen bubbling for 30 min before electrodepositing ZnO. Temperature was kept at 70 °C and charge density was fixed at 10 C cm^{-2} during deposition.

Upon these ZnO NWs, SnS NPs were deposited by CoSP technique with the spray solution containing tin chloride (0.05 M) and thiourea (0.05 M) as precursor materials dissolved in DI water. The temperature in the CoSP reactor was non-uniform with a profile as: Zone I 350 °C, Zone II 700 °C and Zone III 300 °C. The SnS NPs were formed in the second zone and ZnO NWs coated ITO substrates were exposed to these SnS NPs stream in the third zone for 5 min.

4 Results and Discussion

Figure 1 shows the scanning electron microscope (SEM) image of SnS NPs deposited on the ZnO NWs using the CoSP technique. Length of the ZnO NWs, was in range of 1–2 μm and their diameters are in the range of 120–140 nm. It is clear from Fig. 1 that most of the SnS NPs are deposited on the tips of ZnO NWs, which indicates that the site-selective growth of SnS NPs on the tips of ZnO NWs can be achieved by CoSP technique. On deposition of SnS NPs, the surface morphology of ZnO NWs does not change much (Fig. 1). This type of interaction between SnS NPs and ZnO NWs can hinder the effective separation and directional transfer of photo-excited electron-hole pairs, thus adversely affecting the photo-conversion properties.

The thickness of SnS coating for simulation was taken as 50 nm, as observed [4]. Figure 2 clearly indicates that with an exception of x-component, scattered electric field inside the nanowire and coating is greater than the surrounding. Figure 3 shows scattering and absorption efficiency for different diameter of ZnO having a 50 nm coating. The absorption coefficient of SnS decreases rather rapidly at longer wavelength range, which give arise to need of increasing path length in that region. Figure 3 shows absorbance of ZnO NWs with and without SnS coating. It is clear form Fig. 3 that SnS coating considerably increases the light absorption. As it is clear from the Fig. 4 extinction efficiency peaks for ZnO diameter 160 nm in the above mentioned wavelength region. However albedo defined as the ratio of scattering cross-section to extinction cross-section is quiet high when diameter is increased beyond 140 nm which will adversely affect absorption. So it suggest that a diameter 140 nm will be optimum. In addition to efficient light absorbtion, sepration of photgenrated carriers are essential for photovoltaic action. Figure 5 shows that a rectifying junction can be formed upon CoSP deposition of SnS on ZnO NWs to assist charge sepration. This with good absorption of light in the SnS coated ZnO NWs suggest a possibility of photovoltaic action.

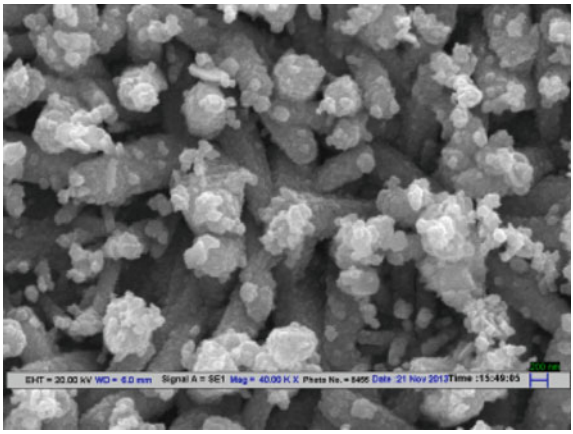

Fig. 1 SEM image of ZnO/SnS heterostructure

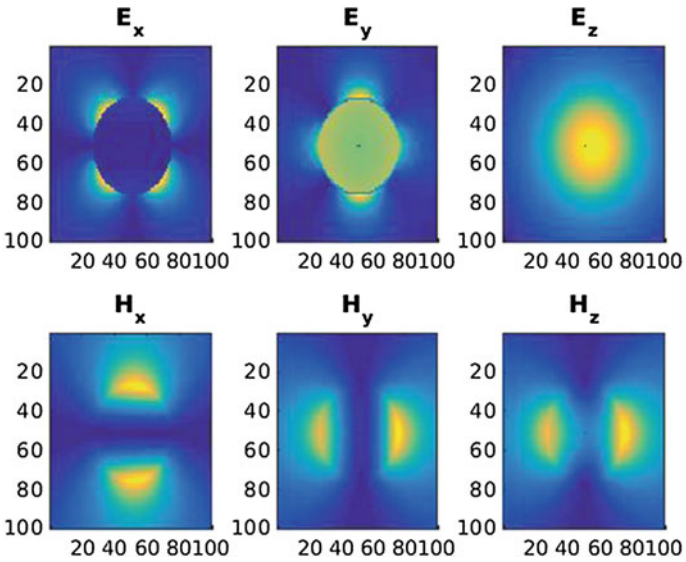

Fig. 2 Scattered electric field *inside* and *outside* coated nanorods

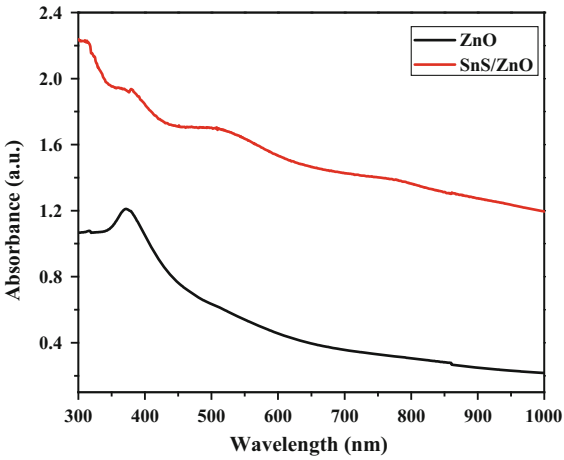

Fig. 3 Absorbance of ZnO NWs (*black*), and ZnO/SnS nanostructure (*red*)

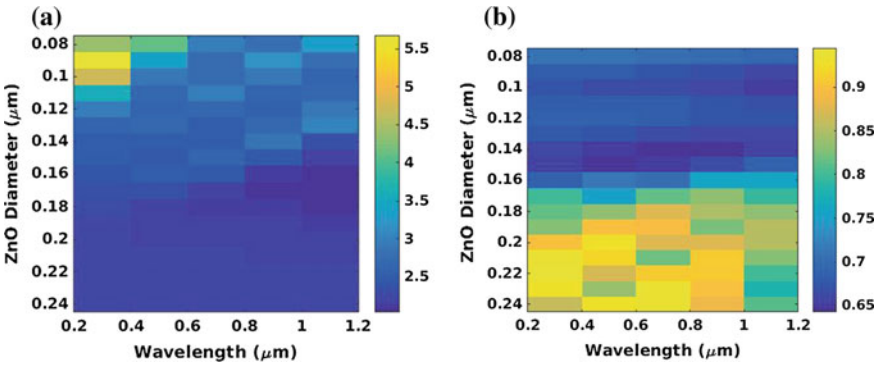

Fig. 4 **a** Extinction efficiency **b** Albedo as function of wavelength and ZnO diameter

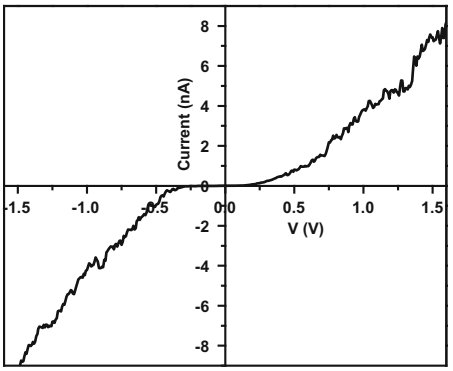

Fig. 5 Dark IV characteristic of SnS/ZnO junction

5 Conclusions

Rectifying junction was formed by CoSP deposition of SnS NPs over ZnO NWs. Scattering parameters of single stratified SnS/ZnO cylinder suggest that for a 50 nm SnS coating 140 nm ZnO NWs seemed to be optimum. Absorbance was greatly enhanced upon deposition of SnS over ZnO NWs. The dimensions of NWs also affect its charge transport properties, and recombination at junction hence full optoelectronic simulation will be needed to optimize dimensions of SnS/ZnO nanowire for maximum performance of solar cells. Still 140 nm diameters will be a good starting point for optoelectronics simulation.

References

1. T. Hirano, T. Shimizu, K. Yoshida, M. Sugiyama, in *Conf. Rec. IEEE Photovolt. Spec. Conf.* (IEEE, 2011), pp. 001280–001282
2. B. Ghosh, M. Das, P. Banerjee, S. Das, Semicond. Sci. Technol. **24**, 025024 (2009)
3. G. Yue, Y. Lin, X. Wen, L. Wang, D. Peng, J. Mater. Chem. **22**, 16437 (2012)
4. F. Alam, A. Misra, D. K. Pandya, V. Dutta, MRS Proc. **1738**, mrsf14 (2015)
5. Y.-L. Chen, Y.-H. Chang, J.-L. Huang, I. Chen, C. Kuo, J. Phys. Chem. C **116**, 3857 (2012)
6. H. Xu, X. Chen, S. Ouyang, T. Kako, J. Ye, J. Phys. Chem. C **116**, 3833 (2012)
7. C.F. Bohren, D.R. Huffman, in *Absorption and Scattering of Light by Small Particles* (Wiley, New York, 1982)
8. M. Kerker, in *The Scattering of Light and Other Electromagnetic Radiation* (Elsevier Science, Netherlands, 1969)
9. S.C. Lee, J. Appl. Phys. **68**, 4952 (1990)
10. J. Schäfer, S.C. Lee, A. Kienle, J. Quant. Spectrosc. Radiat. Transf. **113**, 2113 (2012)
11. M. Patel, A. Ray, RSC Adv. **4**, 39343 (2014)
12. W.L. Bond, J. Appl. Phys. **36**, 1674 (1965)

Development of Novel Cathode Materials Based on MWCNT for Energy Storage/Conversion Devices

Shruti Agnihotri, Sangeeta Rattan and A.L. Sharma

Abstract In Chap. 1, already available technology for energy storage solutions like capacitors, lead acid batteries, compressed air energy storage, flywheels has been discussed in order to compare their energy and power densities. Emphasis has been laid on Rechargeable Lithium ion Battery (Li-ion). Various materials which are already explored and used as cathode of battery has also been discussed with their merits and demerits. Further introduction of prepared orthosilicate material with used conductive additive Multiwalled carbon nano tube (MWCNT) has also given. In Chap. 2, methodology used to prepare respective $Li_2MnFeSiO_4$ material and its composite with MWCNT has been discussed in detail. Further, in order to validate its electrochemical application, different steps of cell assembly of Lithium half cell fabrication has also been discussed. Chapter 3 comprises of results obtained using standard Field emission scanning electron microscope (FESEM). Effect of used MWCNT on its morphology has been discussed in this chapter. A.C Impedance spectroscopy has been used to study variation in conductivity with respect to bared material. Possible reasons for increased conductivity with morphology has also been discussed in discussion. Chapter 4 includes conclusions drawn from mentioned results. This chapter summarizes measured conductivity values with different concentrations of MWCNT. Improved conductivity with respect to bared orthosilicate material has been pointed in this chapter.

S. Agnihotri · S. Rattan · A.L. Sharma (✉)
Centre for Physical Sciences, Central University of Punjab, Bathinda 151001, India
e-mail: alsharmaiitkgk@gmail.com

S. Agnihotri
e-mail: cecm.appsc.sa@gmail.com

S. Rattan
e-mail: sangeetarattan@gmail.com

V.K. Jain et al. (eds.), *Recent Trends in Materials and Devices*,
Springer Proceedings in Physics 178, DOI 10.1007/978-3-319-29096-6_47

1 Introduction

Energy demand and supply has always been one of the crucial factors for the evolution of civilization. Besides (green) energy production, storage of energy in any form is a serious issue. The possibility to collect the excess energy and having it available when energy shortage occurs are important tasks. Some technologies are already present in the market since many years. Examples of energy storage solutions are: **capacitors**, which store and release electrical energy; **lead-acid batteries**, which store chemical energy and convert it into electrical energy, e.g., to start car engines; **compressed air energy storage (CAES)**, in which air is compressed and stored in caves underground and, when required, its mechanical energy is used in turbines, to produce electricity; **superconducting magnetic energy storage systems (SMES),** which store energy in a form of a current owing inside a superconducting coil; **Flywheels**, which store energy as momentum in a rotating wheel. Different storage devices, visualized according to their power and the time required to deliver the energy [1]. A Ragone plot for different electrochemical devices can compare energy and power densities. Each device occupies a certain area, giving information not only on the performances, but also on the time in which the energy and power are delivered. The region between fuel cells and capacitors in Fig. 1 is occupied by rechargeable batteries. In this respect, rechargeable batteries are one of the most promising devices suitable for medium-sized applications, i.e., delivering a high amount of energy in a few hours. In this context, electrochemical energy storage devices such as batteries play an important role in the efficient use of renewable energy. Battery is a collective arrangement of electrical cells that stores and produces electricity by chemical reaction Li ion batteries have gained the considerable interest in recent years interms of high specific capacity, energy density, power density, cell voltage [2].

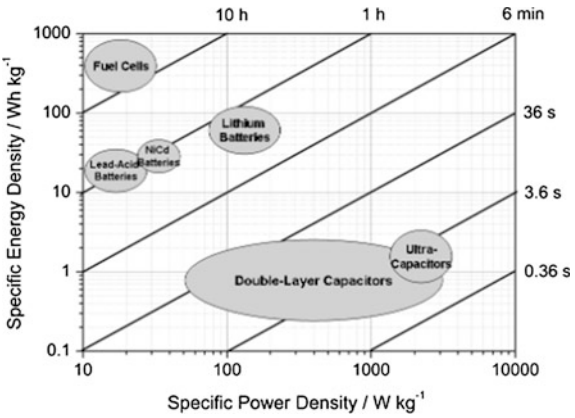

Fig. 1 Ragone plot for different energy storage devices

1.1 Basics of Lithium Ion Batteries

Li-ion batteries almost full the requirements for (hybrid) electric vehicles and, therefore, many industries and research groups are interested in these devices. Their great performances are based on the use of Li-ions, which are shuttled between the positive and the negative electrodes through the electrolyte. The use of Li-ions is appealing because lithium is the lightest metal on earth (m.w. = 6.941 g mol, density = 0.534 gcm^{-3} and as also the highest absolute electrochemical potential [3]. These properties are then responsible for high gravimetric energy density for li ion batteries. A Li ion battery consists of three main components, positive and negative electrode separated by a separator dipped in electrolyte. Negative electrode is normally an electron donor group which is electropositive in nature like lithium metal [4]. Positive electrode is normally an electron acceptor which is strongly electronegative. During discharge process, the negative electrode electrochemically oxidized and releases electron. This electron moves through outer circuit to the positive electrode which accepts electron.

In batteries the electrode itself takes part in chemical reaction. Consequently, the chemistry associated with electrode-electrolyte interface determine the battery performance. Thus performance of lithium ion battery crucially depends on the nature of electrode material used. Consequently, the research is focused on finding materials able to exchange a large amount of Li ions. Double-layer charge storage in a super capacitor is a surface process and hence surface characteristics of the electrodes greatly influence the capacitance of a super capacitor. Similarly, the open circuit voltage, energy density, power density, cyclability and self life of a lithium polymer cell also depend on electrode material properties. In general, electrode should have the following properties; (i) high electronic conductivity (ii) high surface area (iii) high temperature stability (iv) controlled pore structure (v) low equivalent series resistance (ESR) and (vi) relatively low cost (cost effective) (vii) High electronic conductivity [5]. Out of the aforementioned properties, foremost properties for improving the performance of Li ion battery are the development of suitable low cost, safety and high energy density cathode materials Recently, a new group of polyanion material Li_2MSiO_4 has been demonstrated as a promising candidate of Li ion insertion cathode material. Especially Li_2MnSiO_4 shows high theoretical capacity of 334 $mAhg^{-1}$. This is key feature of ortho silicate where two electron redox processes has been occurring. In Li_2MSiO_4 more than one Li ion per formula extraction is possible which significantly increases its experimental specific capacity and electrochemical performance.

1.2 Carbon Nano Tubes

CNTs have excellent mechanical, electrical, and chemical properties due to their light weight and perfect connection in their hexagon structure. In recent years, with

the progress in the research on CNTs and nano materials, the prospect of wide application of CNTs is emerging, because of its excellent electrochemical properties [10^{-6} Sm^{-1} at 300 K for singlewalled CNTs (SWCNTs) and $>10^{-5}$ Sm^{-1} for multiwalled nanotubes (MWCNTs)], low density, high rigidity, and high tensile strength. As our selected cathode material $Li_2Mn_{0.5}Fe_{0.5}SiO_4$ suffers from Low electronic conductivity. Use of CNTs is beneficial interms to improve this intrinsic property. It has been claimed in literature that the enhanced electrochemical activity can be achieved by few factors like (1) providing proper channels for electron and ions to react inside the material (by nanostructuring process) and (2) conductive coating on electrode material, which would benefit the electron transfer to the adjacent particles, thereby making electronic bridge between them and hence reducing grain boundary impedance for mass and electron transfer [6].

In the present report, $Li_2Mn_xFe_{1-x}SiO_4$ is prepared using standard Sol Gel technique and substitution of manganese place of iron (Fe) takes place. As polyanion materials $Li_2MnFeSiO_4$ suffers from poor electronic conductivity. To improve the conductivity of oxide materials, further modification by making its composite with Carbon nano tube. Field Emission scanning electron microscopy (FESEM) reveals the homogeneous topology of the materials sample. Impedance spectroscopy has been characterized for the estimation of electrical conductivity.

2 Experimental

2.1 Synthesis of $Li_2MnFeSiO_4$

Standard Sol Gel Method is used for the preparation of $Li_2MnFeSiO_4$. Stoichiometric amounts of Lithium carbonate (Li_2CO_3), Iron oxide (Fe_2O_3), Manganese Oxide (MnO_2), Silicon dioxide(SiO_2), Citric acid are used as precursors. Above mentioned precursors get hydrolyzed to form a solution. Formed solution was magnetically stirred continuously for 12 h. Further evaporation of solvent was done continues stirring at 80 °C. With continues heating and stirring, a dry gel is formed. This dry Gel is further ground to powder. Finally cathode material was sintered by first heating at 350 °C for 2 h and second heating at 900 °C for 12 h. Prepared cathode material is labeled as LMFS.

2.2 Synthesis of $Li_2MnFeSiO_4$/MWCNT

Further to improve the particle–particle connectivity, composite of $Li_2MnFeSiO_4$/Multi walled carbon nano tube (MWCNT) was prepared via solution method. Stoichiometric amount of MWCNT was well dispersed in solution containing 10 ml distilled water and 10 ml acetonitrile through sonication. Then the active

material ($Li_2MnFeSiO_4$) was added in sequence and finally 0.5 ml of hydrazine was added. As obtained solution was refluxed at 80 °C for 2 h with stirring to obtain $Li_2MnFeSiO_4$/MWCNT composite. This mentioned procedure was further followed to prepare samples with 6 and 9 wt% of MWCNT. These prepared samples are labeled as LMFS-C6 and LMFS-C9 respectively.

2.3 Lithium Half-Cell Fabrication

Electrochemical characterizations were performed using two- electrode coin cells. The positive electrodes were prepared by dispersing 80 wt% active material powder, 10 wt% carbon black and 10 wt% polyvinylidenefluoride (PVDF) in *N*-methyl pyrroli- dinone (NMP) to form a slurry mixture. Then the slurry was deposited on the current collectors of aluminum foils by a blade and cut into circular discs as the cathode. The electrode was dried under vacuum at 105 °C for 20 h and then assembled into cells [7]. The specific capacity of the cathode material is calculated with the mass of $Li_2MnFeSiO_4$/MWCNT, not including the carbon content. Copper foil was used as the negative electrode. The electrolyte was $LiPF_6$ in ethylene carbonate (EC)/diethyl carbonate (DEC) solvents and micro porous polypropylene film as the separator. Electrochemical impedance spectroscopy EIS) was performed to measure electronic conductivity.

2.4 Material Characterization

FESEM The field emission scanning electron microscopy (FESEM) analysis was performed using Card Ziess Merlin Compact to investigate the morphology of prepared samples. In FESEM Electrons are liberated from a field emission source and accelerated in a high electrical field gradient. Within the high vacuum column these so-called primary electrons are focussed and deflected by electronic lenses to produce a narrow scan beam that bombards the object. As a result secondary electrons are emitted from each spot on the object. The angle and velocity of these secondary electrons relates to the surface structure of the object. A detector catches the secondary electrons and produces an electronic signal. This signal is amplified and transformed to a video scan-image that can be seen on a monitor or to a digital image that can be saved and processed further.

A.C. Impedance Spectroscopy Electrochemical Impedance Spectroscopy or EIS is a powerful technique for the characterization of electrochemical systems. The promise of EIS is that, with a single experimental procedure encompassing a sufficiently broad range of frequencies, the influence of the governing physical and chemical phenomena may be isolated and distinguished at a given applied potential. Electrical conductivity of prepared samples is measured by electrochemical analyzer (model: CH-760).

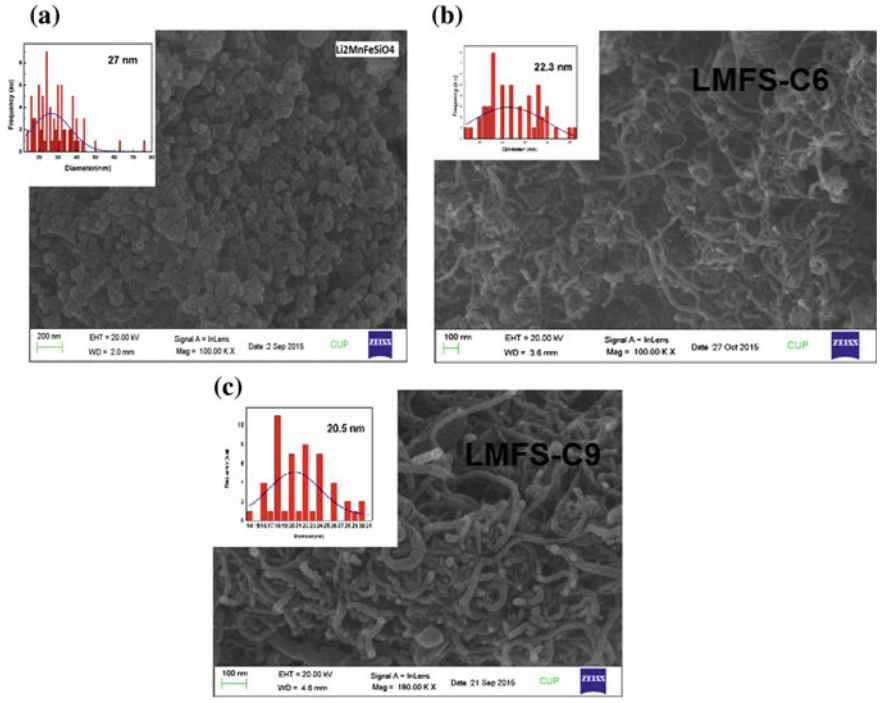

Fig. 2 FESEM images of prepared samples **a** LMFS **b** LMFS-C6 **c** LMFS-C9

3 Results and Discussion

A major aspect of our research was synthesizing the cathode, consisting of $Li_2Fe_{0.5}Mn_{0.5}SiO_4$ and Multiwalled carbon nano tube. It was important to characterize the cathode materials using FESEM in order to determine the average particle size and the distribution of particle size.

3.1 FESEM Analysis

FESEM is very powerful tool in order to get the surface morphology/topology in a very fine way. The high magnifications attainable combined with a large depth of field makes FESEM an outstanding diagnostic system for micro fabrication. Figure 2 shows the Field emission electron microscopy (FESEM) image of the prepared cathode materials. The obtained image of the FESEM clearly depicts the homogeneous distribution of the materials sample all over the sample. A small particle size could reduce the internal stress, because the binding force between particles may increase with the relative area of the grain boundaries. The particle

size was measured from the software 'ImageJ' and the particle size was found to be of the order of ~27 nm (Fig. 2) for LMFS. This particle size is improved size as compared with Li_2FeSiO_4 and Li_2MnSiO_4. It is reported in literature that material with lesser particle size reveals better electrochemical properties due to reduction of path length of Li^+ ions.

Further particle size also decreases on addition of MWCNT. From Fig. 2b, c it is revealed that all the CNTs are evenly adhered to the surface of the $Li_2MnFeSiO_4$/MWCNTs micro- spheres which is highly beneficial for network formation for smooth ion transference. All the samples show a narrow particle size distribution, but the CNT-free $Li_2MnFeSiO_4$ sample exhibits larger geometric mean diameter, one possible reason is that the small precursor particles aggregate during the sintering process without added MWCNT. It is reported that samples with a smaller particle diameter reveal better electro-chemical performance, which reduces the path length of Li+ions. The $Li_2MnFeSiO_4$/MWCNT composites exhibit small particle diameter and porous structure, which facilitates to improve the electrochemical property in the electrode. Key point for expectation of improved electronic conductivity is that coating layer of MWCNT prevents the surface area of the $Li_2MnFeSiO_4$ in direct contact with the electrolyte, which is able to inhibit side

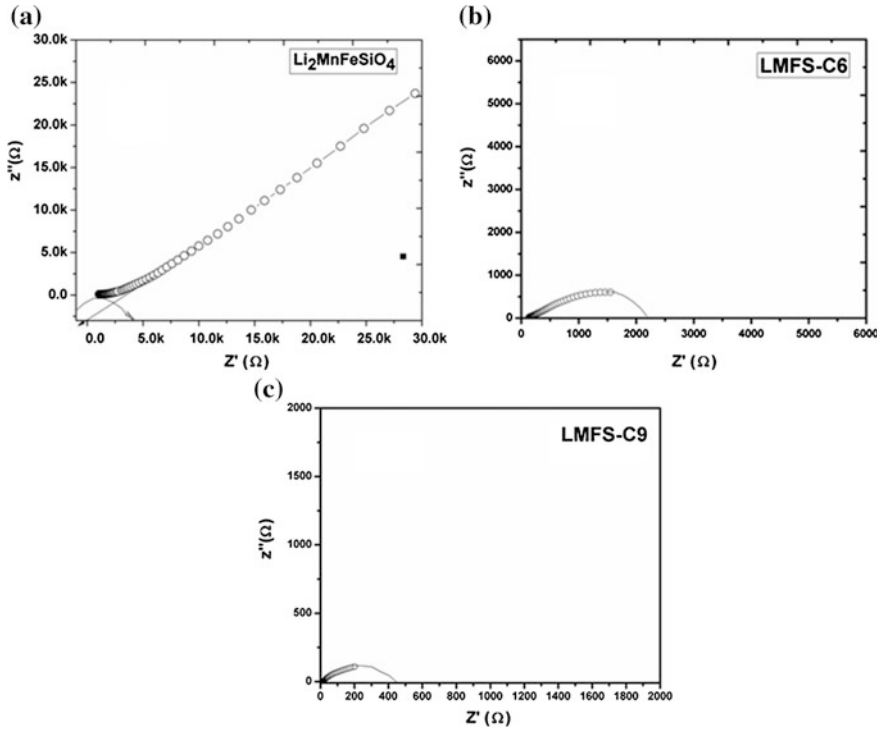

Fig. 3 Nyquist plots **a** LMFS, **b** LMFS-C6, **c** LMFS-C9

Table 1 Representing increase in electronic conductivity with MWCNT

Sample	Thickness (cm)	Contact area (cm^2)	Bulk resistance (Ω)	Electric conductivity (Scm^{-1})
LMFS	0.2	1.47	2787	4.881×10^{-5}
LMFS-C6	0.2	1.47	2160	6.29×10^{-5}
LMFS-C9	0.2	1.47	497	2.73×10^{-4}

reactions between the active material and electrolyte so as to extend the service life of the batteries [8].

3.2 A.C Impedance Spectroscopy

The A.C impedance measurement of the cathode material was carried out in the frequency range from 10 to 1 MHz at a input A.C signal level of 10 mV. The impedance spectrum is comprised of a small semicircle at high frequency is followed by sharp spike at lower frequency (Fig. 3). The small semicircle contribution is due the bulk response of the cathode materials whereas the lower frequency spike is due to the electrode electrolyte interface. The bulk resistance of the cathode materials is estimated by extrapolating the semicircle and cut on real axis, which comes out of order of ∼2787 Ω, ∼2160 Ω and ∼497 Ω for LMFS, LMFS-C6 and LMFS-C9 respectively.

The lower frequency spike clearly shows the capacitive behavior of the cathode materials. The electrical conductivity of the cathode material is estimated by the formula: $\sigma_{dc} = \frac{1}{R_b}\frac{\ell}{A}$ where, symbols have their usual meanings. The electrical conductivity has been calculated for LMFS, LMFS-C6 and LMFS-C9 comes out to be of order of $\sim 4.881 \times 10^{-5}$ and 6.29×10^{-6} and 2.73×10^{-4}S cm^{-1} respectively (Table 1).

4 Conclusion and Future Scope

In summary, sphere $Li_2MnFeSiO_4$/MWCNT composite with improved electronic conductivity was successfully synthesized via standard sol-gel method followed by solution method. Improved electronic conductivity of modified cathode material is caused by the unique composite structure. The nanosized $Li_2MnFeSiO_4$ provides short path- ways for the Li^+ diffusion and the CNTs network facilitates electron transport and avoids agglomeration of $Li_2MnFeSiO_4$ particles. Prepared composite cathode material overcome the drawback of $Li_2MnFeSiO_4$ cathode material by improving its electronic conductivity. We have observed the enhanced electronic conductivity of $Li_2MnFeSiO_4$/MWCNTs material due to better fueling of electrons

at particle-particle interface. In the present case, nano dimension along with MWCNT additive helps in improving the desire kinetic behavior as lithium-ion battery cathode. More over particle size can also be optimized by utilizing a more effective mechanical processing method to crush the cathode, such as use of a ball-milling machine rather than use of a mortar and pestle. We believe that continued research on lithium silicates is both necessary and viable for the future of electronics.

References

1. W. Xiaozhen, Xinjhang, H. Qisheng, Z. Youxiang, Electrochem. Acta **80**, 50–55 (2012)
2. M. Armand, M. Tarascon, Nature **451**, 652–657 (2008)
3. BinShao, Y.L. Taniguchi, Powder Technol. **235**, 1–8 (2013)
4. Z. Zhang, Xingquan, L. Wang, Electrochim. Acta **168**, 8–15 (2015)
5. A. Rai, A.L. Sharma, A.K. Thakur, Solid State Ionics **262**, 230–233 (2014)
6. K. Ding, L. Wang, J. Li, H. Jia, X. He, Int. J. Electrochem. Sci **6**, 6165–6176 (2011)
7. M.S. Whittingham, MRS Bull. **33**(04), 411–419 (2008)
8. S. Singh, S. Mitra, Electrochim. Acta **123**, 378–386 (2014)

Part IV
Sensors

Sensitivity Enhancement of Lossy Mode Resonance Sensor with Addition of Dielectric Layer

Davinder Kaur, Divya Madaan, V.K. Sharma and A. Kapoor

Abstract A lossy mode resonance (LMR) sensor with additional layer of dielectric integrates the enhancement in the sensitivity of the sensor. The enhanced sensitivity will future enhances the monitoring of biomolecular interactions that occur into the analyte. Finally the higher sensitivity of the proposed configurations makes it be a much better option to be employed for biosensing applications.

1 Introduction

The refractive index sensitivity of the conventional Kretschmann SPR sensors is the highest theoretically and is best for thin silver (Ag) films. Ag films are not suitable for Kretschmaan configuration as they are highly susceptible to oxidation. So Ag films need to be coated with either a dielectric layer or a lesser reactive metal like gold (Au). But this leads to reduce refractive index sensitivity. The sensors should be sensitive for refractive indices around 1.33 for biosensing applications. The sensitivity reduces of the SPR sensors which require a high index over layer to shift the operating point towards aqueous environment [1]. If we use sensors employing thin conducting oxides such as indium tin oxide (ITO) these limitations can be overcome. There are two types of modes supported by ITO thin films and these are the SP modes and the lossy modes. In ITO films the surface plasmon resonance has been studied extensively and their application as chemical sensors has been proposed [2, 3]. In the visible and near IR region the ITO films have large real part of index and smaller imaginary part due to this the ITO films support the lossy modes at these wavelengths [4]. Similar to SPR, these lossy modes can also cause

D. Kaur (✉) · D. Madaan · A. Kapoor
Photovoltaics and Opto Electronics Lab, Department of Electronic Science, University of Delhi, South Campus, Benito Juarez Road, New Delhi 110021, India
e-mail: davinderkaur19@gmail.com

V.K. Sharma
Keshav Mahavidyalaya, University of Delhi, New Delhi 110034, India

V.K. Jain et al. (eds.), *Recent Trends in Materials and Devices*,
Springer Proceedings in Physics 178, DOI 10.1007/978-3-319-29096-6_48

resonance called lossy mode resonance (LMR). In this paper,we will investigate theortically our proposed sensor based on the lossy mode resonance (LMR).

2 Lossy Modes Supported by ITO Film

The light is absorb by ITO layers and are characterized by a complex value of relative permittivity. The oscillatory model can be used to represent the dielectric constant of ITO films and is expressed as [4]:

$$\varepsilon(\omega) = \varepsilon_{\infty} - \frac{\omega_p^2}{\omega^2 + i(\omega/\tau)} + \frac{s_o \omega_o^2}{\omega_o^2 - \omega^2 - i\gamma\omega} \tag{1}$$

where ε_{∞} is the high frequency dielectric constant = 3.57, Γ is the electronic scattering time = 6.34×10^{-15} s/rad, ω_p is the plasma frequency = 1.89×10^{15} rad/s, s_o is the oscillator strength = 0.49, ω_o is the oscillator resonance frequency = 5.61×10^{15} rad/s and γ is the oscillator damping constant = 9.72×10^{13}. The ITO film is assumed to be coated on a prism and its real part of refractive index ($n = \sqrt{\varepsilon} = n + jk$) is always higher than that of prisms used and hence support guided modes. Because of the imaginary part of refractive index of the ITO films these guided modes are lossy.

3 Structure and Analysis Method

Our proposed structure includes a low index dielectric layer between the prism and ITO layer and also an additional layer of titanium dioxide (TiO_2) between the ITO layer and analyte. Using Fresnel reflection coefficients we calculated the reflectance for the structure. Reflectivity analysis is done for spectral interrogation of all the considered optimized structures.

4 Results and Discussion

The proposed structure consists of a low index matching layer between the prism and the ITO film as shown in Fig. 1. This matching layer produces perfect phase matching between the evanescent prism mode and the guided lossy mode supported by ITO film. High sensitivity of 4652 nm/RIU for TM polarized has been achieved for properly optimized multilayer structure [5]. An additional dielectric layer of TiO_2 is introduced to this structure between the ITO film and analyte. As TiO_2 refractive index is 2.5 which is higher than that of ITO, this will shifts the mode

energy of waveguide towards analyte. This future enhances the sensitivity of the sensor as higher energy towards analyte results into higher sensitivity. For properly optimized layer thickness (shown in Fig. 1), the sensitivity for TM polarized sensor is 6107 nm/RIU which is large as compared to that obtained without TiO_2 layer. The reflectivity versus wavelength curves is shown in Fig. 2 for TM mode.

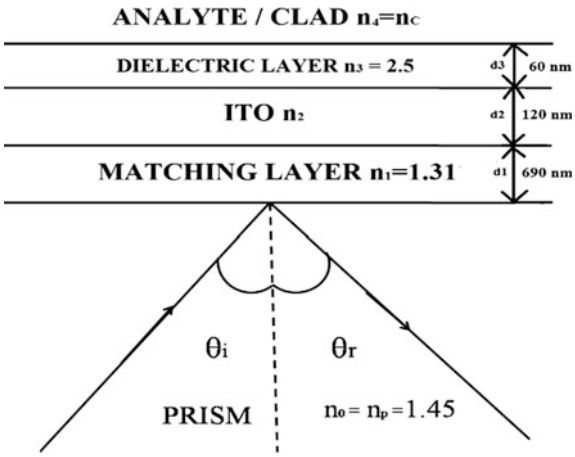

Fig. 1 Lossy mode resonance sensor structure

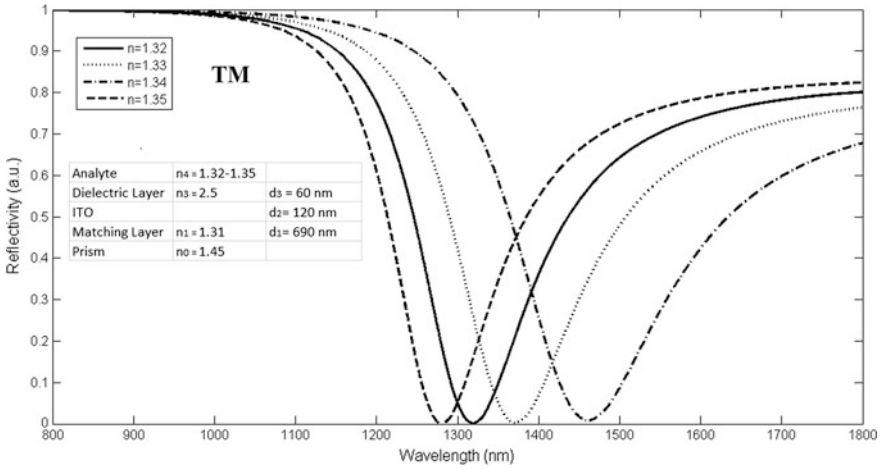

Fig. 2 Reflectivity as a function of wavelength for LMR sensor (TM polarization)

5 Conclusions

In conclusion, we proposed a sensor based on spectral interrogation of lossy mode resonance for measurement of variation in the refractive index of the bulk media. It is shown that a dielectric layer of TiO_2 introduced between the ITO and analyte enhances the sensitivity. Sensitivity as high as 6107 nm/RIU can be achieved for spectral monitoring. Using Fresnel reflection coefficients the reflectivity is calculated. Also since ITO is chemically stable and higher sensitivity of the sensor make it be a much better option to be employed in biosensing applications.

References

1. J. Dostalek, J. Ctajroky, J. Homola, E. Brynda, M. Skalsky, P. Nekvindove, J. Spirkove, J. Skvor, J. Schrofel, Sens. Actuators B **76**, 8–12 (2001)
2. C. Rhodes, S. Franzen, J.P. Maria, M. Losego, D.N. Leonard, B. Laughlin, G. Duscher, S. Weibel, J. Appl. Phys. **100**, 054905 (2006)
3. M.D. Losego, A.Y. Efremenko, C.L. Rhodes, M.G. Cerruti, S. Franzen, J.P. Maria, J. Appl. Phys. **106**, 024903 (2009)
4. I.D. Villar, C.R. Zamarreno, M. Hernaez, F.J. Arregui, I.R. Matias, J. Lightwave Technol. **28**, 3351 (2010)
5. D. Kaur, V.K. Sharma, A. Kapoor, Sens. Actuators B **198**, 366 (2014)

Assessment of Dual Dielectric P-MOSFET as Cumulative Gamma Dose Sensor

Naresh Jingar, Manjeet Kulhar and Arun Pandya

Abstract In this paper we assess the capabilities of indigenously developed p-channel enhancement type Dual Dielectric MOSFETs for cumulative gamma dose measurement. Here we present the studies pertaining to electrical functionality, thermal behavior, radiation response and post irradiation response for three types of DDMOSFETs. The sensors respond linearly in the desired dose measurement range of 1 cGy to 10 Gy and have radiation sensitivity of 7, 2.9 and 2.7 mV/cGy for TEOS oxide, PECVD nitride and LPCVD nitride sensors respectively. The concept of Zero Temperature Coefficient Current (I_{ZTC}) has been utilized to make sensor response temperature compensated.

1 Introduction

Individual may encounter some radiological situations like nuclear explosions and missions in contaminated zones. In such a scenario the harmful radiation dose delivered to the individual is unavoidable. But the quantification of the dose during such operations can help the individual in two ways. First the individual can safely be taken apart from the operation without crossing the lethal dose range of 500 cGy. Secondly the exact determination of delivered dose can benefit the medical treatment planning and help categorizing the severity of patients. PMOS dosimeters are specially designed MOSFETs (Metal Oxide Semiconductor Field Effect Transistor) which allow radiation dose to be measured due to a radiation-induced change in the electrical characteristics of the sensor [1]. Initially, RADFETs were used for space applications where large doses (kGy) were

N. Jingar (✉) · M. Kulhar · A. Pandya
Defence Laboratory, Defence Research and Development Organisation (DRDO), Jodhpur, India
e-mail: naresh.dlj@gmail.com

V.K. Jain et al. (eds.), *Recent Trends in Materials and Devices*,
Springer Proceedings in Physics 178, DOI 10.1007/978-3-319-29096-6_49

monitored successfully. The continued improvements in the sensor sensitivity led the RADFETs in the medical and personnel monitoring applications. The aim of this study is to explore the use of dual dielectrics in the gate oxide region to improve the radiation sensitivity and stability of the PMOS sensors for cumulative gamma dose measurement. This involves the study of different set of sensors fabricated by CVD (Chemical Vapor Deposition) method for TEOS oxide and PECVD (Plasma Enhanced CVD) and LPCVD (Low Pressure CVD) method for nitride. The use of an extra dielectric layer is motivated by encouraging results presented by other authors [2–4].

2 Theory

When p-channel enhancement type MOSFET device is irradiated, electron-hole pairs are generated throughout the volume. Depending upon the electric field in the insulator layer (SiO_2), some generated electron-hole pairs recombines and remaining are separated. With the positive bias applied at the gate, electrons will rapidly drift toward the gate and holes will slowly drift toward the oxide/silicon interface, since the electrons whose mobility in SiO_2 at room temperature is about six orders of magnitude greater than the holes. As the holes approach the oxide/silicon interface, some fraction will be trapped, forming positive oxide-trap charges (Fig. 1a) and these trapped charges in long term sites causing a threshold

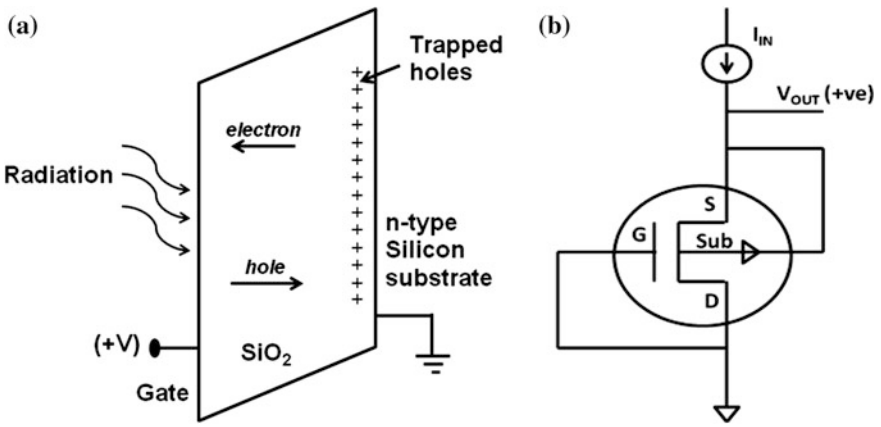

Fig. 1 **a** Basic ionizing radiation effects in SiO_2 under positive bias at Gate terminal and **b** Circuit configuration for threshold voltage measurement

voltage shift (ΔV_{TH}). The net result is the creation of permanent positive charges, which shifts the threshold voltage (V_{TH}) of the MOSFET by an amount of ΔV_{TH} as shown in Fig. 2. This shift depends on the absorbed dose, the gate bias during the irradiation and the insulator thickness. ΔV_{TH} is the measured dosimetric parameter and it is obtained by measuring the output voltage V_{OUT} before and after a fixed radiation exposure with a constant current source I_{IN} as shown in Fig. 1b.

In the case of Dual Dielectric MOSFET (DDMOSFET) (Fig. 3) the extra layer of Silicon-nitride/Silicon-di-oxide has different trapping sites than normal MOSFETs. As shown in Fig. 4a, the device is irradiated with negative bias at the gate terminal, the holes move towards to Nitride/oxide interface instead of oxide/silicon interface, other than the conventional MOSFET. This mechanism leads to improvement in the stability of the device and less fading due to tunneling of electrons from the silicon substrate. Also, in another type of device where TEOS oxide is used over thermal oxide, when this device is irradiated with positive bias at the gate terminal, the holes moves towards oxide/silicon interface which leads to improvements in the radiation sensitivity (shown in Fig. 4b).

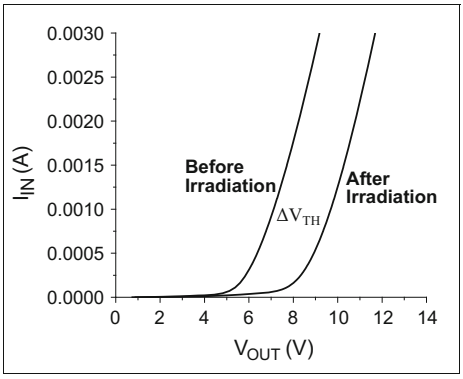

Fig. 2 Typical I–V characteristic of p-MOSFET sensor before and after irradiation

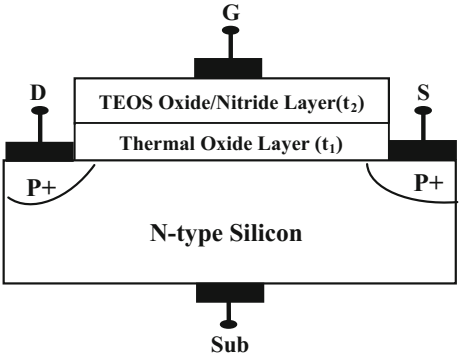

Fig. 3 Basic DDMOSFET sensor structure

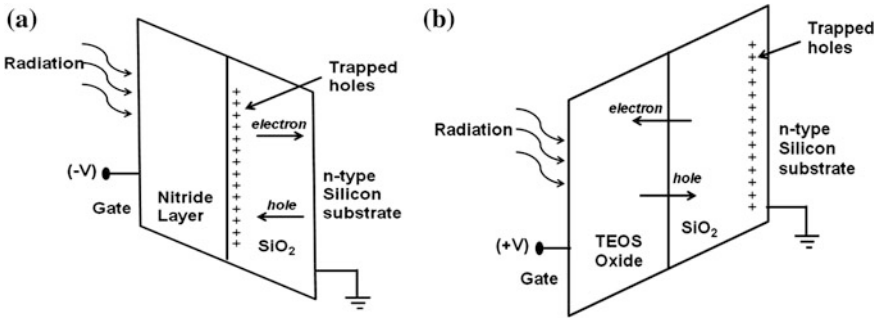

Fig. 4 Radiation effects in **a** Nitride/SiO_2 interface with negative bias and **b** TEOS oxide/SiO_2 interface with positive bias during irradiation at Gate terminal respectively

3 Experimental Details

The three distinct types of DDMOSFET sensors examined in this paper are: (a) Thermal oxide + LPCVD deposited TEOS oxide (sensor type S1), (b) Thermal oxide + PECVD deposited nitride (sensor type S2) and (c) Thermal oxide + LPCVD deposited nitride (sensor type S3). The specifications of these sensors are shown in Table 1.

The DDMOSFET sensors were fabricated on n-type silicon wafer of 4–7 Ω cm resistivity and <100> orientation. The gate contact is fabricated by aluminum metal. The sensors are of rectangular geometry and packaged in 16 pin SOIC package. These sensors were designed by DL, Jodhpur and fabricated at SITAR, Bangalore. For the threshold voltage measurement the gate and drain terminals were tied to the common terminal and the source-substrate terminals were tied to the Zero Temperature Coefficient Current (I_{ZTC}) as shown in Fig. 1b [5]. The voltage developed at source terminal was then measured. The sensors were biased at I_{ZTC} to make the output voltage temperature compensated. The plot of sensor current and sensor voltage is shown in Fig. 5. Irradiations were carried out using Cobalt-60 gamma source at DL, Jodhpur. Sensors were irradiated in the cumulative gamma dose range of 1 cGy–10 Gy (in step of 1 Gy) with a gate bias of either 0 or ±3 V and at dose rate of 4 Gy/h. The post irradiation fading/build-up of the threshold voltage after the final irradiation was monitored for two months.

Table 1 Specifications of DDMOSFET sensors

Specifications	S1	S2	S3
1st dielectric layer (t_1)	Thermal oxide 0.4 μm	Thermal oxide 0.7 μm	Thermal oxide 0.7 μm
2nd dielectric layer (t_2)	TEOS oxide 0.6 μm	PECVD nitride 0.3 μm	LPCVD nitride 0.3 μm
Threshold (V_{TH})	−13 to −14 V	−4 to −6 V	−4 to −6 V

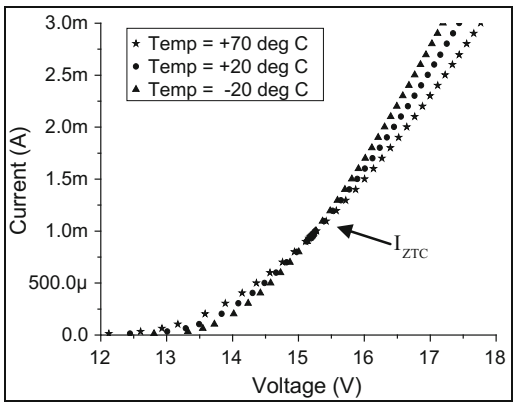

Fig. 5 Determination of I_{ZTC} current for S1 sensor

4 Results and Discussion

Extensive electrical, thermal and radiation studies have been performed on fabricated sensors. Some significant results are presented here. The I_{ZTC} values for S1, S2 and S3 sensors are found to be 955, 510 and 719 µA respectively. The sensor readout during gamma irradiation studies have been made at these I_{ZTC} values. To get a higher linear sensitivity and low buildup/fading the sensors were irradiated at gate biases of +3, −3 and −3 V for S1, S2 and S3 sensors, respectively. The radiation sensitivity, for all types of sensors, as a function of cumulative gamma dose is shown in Fig. 6. The sensitivity of S1, S2 and S3 are found to be 7 mV/cGy, 2.9 and 2.7 mV/cGy respectively.

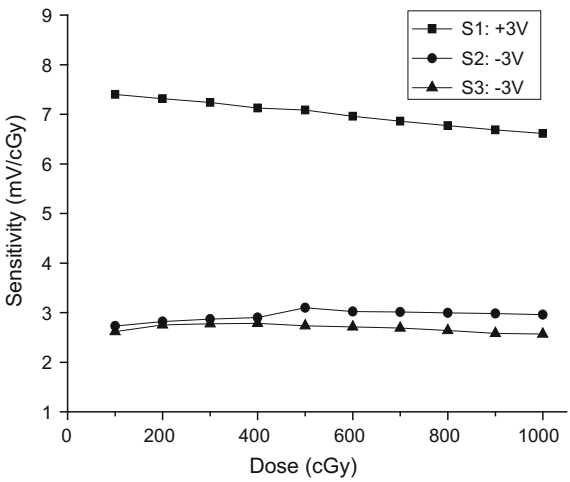

Fig. 6 Comparison of radiation sensitivities

It may be noted that the sensitivity of S2 and S3 type of sensors are comparable and less than that of type S1. This is because of the S1 has an overall oxide thickness of 1 μm whereas S2 and S3 have only 0.7 μm. The additional nitride layer in S2 and S3 does not contribute in radiation sensitivity because it traps both the electron and holes causing no net charge buildup in nitride layer. In contrast oxide traps only holes and hence net positive charge builds with irradiation. Another reason for higher sensitivity of S1 type sensors is the polarity of applied field during irradiation. It is because in S1 type sensors the direction of field is such that the holes are trapped near the $Si–SiO_2$ interface causing more change in threshold voltage. In contrast the holes are trapped near the $SiO_2–Si_3N_4$ interface in S2 and S3 type of sensors. Figure 7 shows the relative effect of irradiation bias on the sensitivity of the S1 type of sensors.

It may be noted that applying the positive gate bias during irradiation improves the radiation sensitivity for the sensors in comparison to unbiased gate. This increase in sensitivity is because of reduced recombination of radiation generated electron hole pairs and decreased electron trapping in the oxide.

The long term annealing or fading of the sensors were investigated by monitoring the post irradiation threshold voltage of each sensor over the period of two months [6]. During this period the sensors were kept under the gate bias of +3, −3 and −3 V for S1, S2 and S3 sensors respectively. The threshold voltages were recorded at various time intervals and the results are shown in Fig. 8. The S1 and S3 sensors show an overall fading of 6 and 8 % respectively. The best post irradiation stability has been observed in S2 type of sensors and is within 3 %.

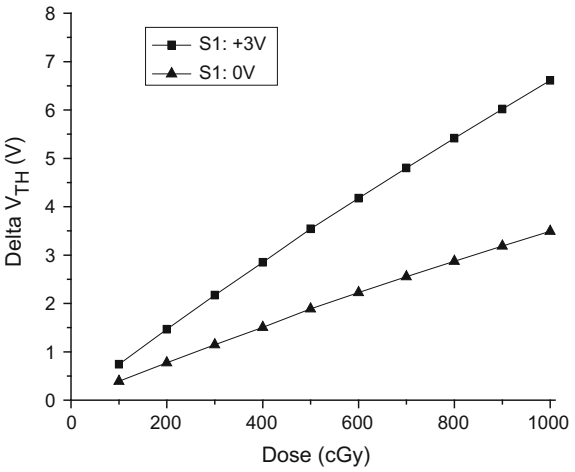

Fig. 7 Change in V_{TH} with Dose as a function of gate bias during irradiation

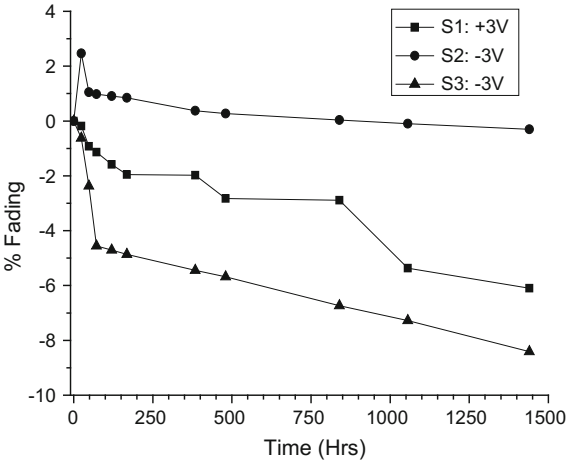

Fig. 8 Comparison of % fading with time of irradiated sensors

5 Conclusions

The electrical, thermal, radiation and post irradiation responses have been studied for three different types of indigenously developed DDMOSFETs. The sensors having the LPCVD deposited TEOS oxide as a second dielectric layer show the best radiation sensitivity of 7 mV/cGy, whereas the sensors having PECVD deposited nitride show the best post irradiation stability. The indigenously developed DDMOSFET sensors can be effectively utilized to measure a cumulative gamma dose in the range of 1 cGy–10 Gy.

Acknowledgments Our sincere thanks are due to Dr. S.R. Vadera, OS & Director, Defence Laboratory, Jodhpur and Sh. G.L. Baheti, HOD, NRMA for providing all the support and encouragement.

References

1. A.G. Holmes-Siedle, Nucl. Instrum. Methods **121**, 169 (1974)
2. B. O'Connell, A. Enright, C. Conneely, W. Lane, L. Adams, in *Proceedings of the 4*th *European Conference on Radiation Effects on Components and Systems (RADECS'97)*, Cannes, France, 1997, pp. 282–287
3. G. Ristic, S. Golubovic, M. Pejovic, Sens. Actuators A **A51**, 153–158 (1996)
4. R.C. Hughes, W.R. Dawes, W.J. Meyer, S.W. Yoon, J. Appl. Phys. **65**(3), 1972 (1989)
5. F. Vettese, C. Donichak, P. Bourgeault, G. Sarrabayrouse, IEEE Trans. Nucl. Sci. **43**(3), 991–996 (1996)
6. N.G. Blamires, D.H.J. Totterdell, A.G. Holmes-Siedle, L. Adams, IEEE Trans. Nucl. Sci. **NS-33**(6), 1310–1315 (1986)

Part V
Polymeric Materials

Structural and Electrical Properties of Polymer Nanocomposite Films

Chandni Bhatt, Ram Swaroop and A.L. Sharma

Abstract A free standing transparent film of solid state polymer electrolyte based on PEMA/PVC+$NaPF_6$ with different compositions of nano sized TiO_2 in weight percent (x = 0, 1, 2, 7, 10, 15, 20) is synthesized by using standard solution cast technique. The homogeneous surface of above polymer composition is examined by FESEM. The microscopic interaction among polymer, salt and nano-ceramic filler has been analyzed by Fourier Transformed Infra-Red (FTIR) spectroscopy. The reduction of ion pair formation in polymeric separator is clearly observed on addition of nano-filler in the polymer salt complex film. Electrical conductivity has been recorded of the prepared polymeric separator which is of the order of $\sim 1.5 \times 10^{-5} Scm^{-1}$ after addition of nano-filler (15 % wt/wt) which support the FTIR results. Electrochemical potential window has been observed of the order of ~ 6 V by the cyclic voltammetry results. The observed data of the prepared separator are at par with the desirable value for device application.

1 Historical Background

In 1833 Michael Faraday performed an experiment on ionic conductivity of inorganic solids. He observed enhancement in the value of electrical conductivity of Ag_2S with increasing temperature. At that time it was difficult to analyze because it was on strong contradiction to the behavior of metallic phases. Faraday reported similar observations on several other inorganic solids, in 1838. In 1851, Hittorf

C. Bhatt · R. Swaroop · A.L. Sharma (✉)
Centre for Physical Sciences, Central University of Punjab, Mansa Road, Bathinda 151001, Punjab, India
e-mail: alsharmaiitkgp@gmail.com

C. Bhatt
e-mail: bhattchandni84@gmail.com

R. Swaroop
e-mail: ramcuhp11pas18@yahoo.com

V.K. Jain et al. (eds.), *Recent Trends in Materials and Devices*,
Springer Proceedings in Physics 178, DOI 10.1007/978-3-319-29096-6_50

investigated that electrolytic conduction mechanism had exist in material Ag_2S and Cu_2S from decomposition during current flow.

In 1884, Warburg verify Faraday's law during electrolysis between sodium amalgam electrodes by using soda lime glass or crystalline SiO_2, founded that sodium ions migrate through solids. The first major invention by Nernst of an electric lighting device by using solid electrolytes. Nernst lamp was replaced by tungsten filament lamp in 1905—this gave a path in the development of solid state Ionics.

Haber was the first to give patent on electrical energy production from coal and gaseous fuels using solid electrolyte cell. In 1908, Katayama reported various cells based on solid electrolytes. In 1920, Tubandt and Eggert confirmed the validity of Faraday's laws of electrolysis for the case of solid-ionic conductors. In 1935, Schottky file a patent on fuel cell using solid electrolytes, halides, sulfates, carbonates, and phosphates, but no oxides. In 1950, Wagner studied thermodynamic and kinetic properties of materials by using solid electrolyte cells. Also Wagner improved direct current polarization technique with blocking electrodes for the determination of partial ionic and electronic conductivities of mixed conductor, which was based on Hebb idea, now it is known as Hebb-Wagner polarization technique.

In 1960, solid electrolytes of light weight and high power density batteries with the fulfillment of sufficient ionic conductivity was developed, for e.g. $RbAg_4I_5$. In 1967, Yoo and Kumer developed sodium-sulfur battery by performing an experiment in which molten sodium and sulfur separated by a Na^+-ion conductive membrane of β-Al_2O_3. This research gave an impulse to the growth of solid state ionics because it was working as alternative for liquid electrolyte system.

In 1973, further enhancement in ionic conduction was done by Liang with the dispersion of small particles of Al_2O_3 in the matrix of moderate ionic conductor LiI. Founded material was heterogeneous, having conductivity 50 times higher ionic conductivity than homogeneous LiI. This doping effect was further confirmed by Wagner and Maier for numerous other ionic conductor and interpreted as space charge layer model, in 1984. This enhancement is expected due to the properties of nanostructured material, which is a very active topic of research in the field of solid state ionics [1].

2 Introduction

There are two types of conduction in materials that is electronic and ionic conduction, electronic conduction are those in which electrons/holes are charge carriers whereas in ionic conduction the charge carriers are ions. Firstly, the ionic conductivity on inorganic solids has been studied by Michael Faraday in 1833. There was large enhancement in electrical conductivity of Ag_2S with increasing temperature. But it was became difficult to observe behavior of metallic phases at that time. But in the year 1978, Professor M.B. Armand highlighted the significance of

polymer electrolyte as a medium of ion transport which is capable of dissolving salts in a meeting held at University of St Andrews. Polymer electrolytes is now topic of interest for researcher in the development of battery technology. Solid state polymer electrolyte with high ionic conductivity have been desired for all solid state battery due to the reason that solid electrode/solid electrolyte contact. Flexible material like organic polymers can produce excellent solid/solid interface between solid electrode and solid electrolyte.

As portable electronics is becoming more and more common in our society, and many aspects of our lives are now dependent on the performance of our portable electronics, demand for safe, reliable and efficient mean to store electrical energy for portable devices has increased. Also, recent advances in processing power, screen size and urge for thinner and lighter devices, have increased the demand for lighter batteries with higher energy density. Li ion batteries have high voltage and energy density so they have great demand in electronics market. The outstanding energy capacity, high volumetric density and long life cycle of Li ion batteries have made them preferred choice for application in portable electronics and electric vehicles. Widespread use of Li ion batteries growing demand for Li commodity chemically. These demand raised question whether the Li natural reserves will continue to meet industrial needs in a commercially viable manner [2].

But there are several drawbacks that mostly found in Li ion batteries like flammability, leakage of the toxic electrolyte, rapid degradation of cathode material and cost of procuring and using Li metal [3].

Sodium is light alkali metal with single electron in outermost shell. This metal exhibit unexpected complexity properties [4]. Sodium are more environmentally friendly than Li, less expensive, more abundant, easily distributed and easier to extract than lithium [5]. Although sodium has molecular weight 23 g mol^{-1}, which is three times heavy than Li. But because of sodium is fourth most abundant element in earth crust and easy to recycle, it is used for sodium ion batteries. Sodium batteries provide low cost energy storage device, they operate at ambient temperature [6].

Polymer electrolyte act as a electrolyte cum separator material in batteries, because by using polymer electrolyte one can obtain flexible, compact, solid state structure that is free from leaks, free standing consistency, high ionic conductivity. Their main purpose is to separate anode and cathode material in batteries and act as ions transport medium for the conduction of ions during the electrochemical process that is charging and discharging, the ions in the electrolyte adsorb and desorb on the porous electrode. Which cause rapid charging and discharging of the polymer so that the capacitor like performance is obtained [7]. In most system conductivity much lower than the desirable values for the device application under surrounding conditions. The factor responsible for that are—low ambient ionic conduction, concentration polarization, poor stability (thermal, mechanical and electrochemical) [8]. These factor are due to the fact that slow ion movement in host polymer because of poor chain mobility in polymer, also ion—ion interaction [9].

PEO based polymer electrolyte are mostly used but PEO has high degree of crystalline behavior, the ionic conductivity of PEO-based electrolytes is low and

varies from 10^{-8} to 10^{-4} Scm^{-1} at temperature between 40 and 100 °C. The use of poly (ethyl methacrylate) (PEMA) as a host polymer was first reported by Han et al. and Fhamy et al. PEMA shows excellent chemical and high surface resistance and offers high optical transparency. Poly (vinyl chloride) (PVC) can act as a mechanical stiffener in the electrolyte due to its immiscibility with the plasticizer.

Various approaches are carried out by scientist to improve the conductivity of polymer electrolyte. As the ion motion is faster within the amorphous region than crystalline, so therefore various method employed to increase the amorphous nature of polymer, reduce crystalline phase and hence increasing ionic conductivity. The addition of nano-sized inorganic ceramic fillers particles such as Al_2O_3, SiO_2, TiO_2, ZrO_2 etc. in host polymer and other the addition of low molecular weight plasticizers such as ethylene carbonate (EC), propylene carbonate (PC), dimethyl carbonate (DMC), polyethyleneglycol (PEG) [10].

In this work, investigation of solid state polymer electrolyte cum separator is fabricated by taking various composition of TiO_2 nano-filler added in PEMA/PVC polymer blend complexed with anatomic ratio of (O/Na = 20) $NaPF_6$ salt. Addition of nano-filler with different composition increases interaction between polymer and nano-filler.

2.1 Advantage of Solid Electrolyte

Initially liquid electrolyte was used for battery application, but these batteries suffer from several problems. So these batteries are replaced by solid electrolyte which contain following qualities.

- Absence of liquid containment.
- No leakage problems.
- Moldability and miniaturization shape.
- Ability to operate with more highly reactive electrodes over a wider range of temperature.
- Possess High ionic conductivity and negligible electronic conductivity.
- Suitable mechanical properties.
- Stability with respect to adjacent phases and to thermal and electrochemical decomposition.
- Easy to fabricate.
- Reasonable cost.

3 Experimental Work

3.1 Material and Material Method

Following polymer, salt and nano-filler is to be used for the synthesis of free standingpolymer electrolyte film are Poly (ethyl meth acrylate) (PEMA), and Poly (vinyl chloride) (PVC) purchased from Sigma Aldrich as shown in Table 1.

Preparation of solid state polymer electrolytes
The solution cast technique was used for preparation of free standing thin film of polymer electrolyte. In solution cast method appropriate amount of polymer is dissolved in solvent. The solvent should be water free and boiling point not exceed from 65 °C. At the same time appropriate amount of complexing salt is also dissolved in same solvent. Solvent should be a common for both salt and polymer [11].

Procedure In experiment the pure polymer blend of composition (PEMA/PVC) films complexed with $NaPF_6$ salt prepared by solution cast technique. The weight percent ratio such as 50 weight percent of PEMA, PVC, and salt of Ö/Na ratio is 20 mixed by a solution casting technique using THF (Tetrahydrofuran) as solvent. The solution of above composition mixed for several hours by means of stirrer, until the solution mixed properly, and then casted onto polypropylene dishes and left for evaporation at room temperature, dried under vacuum at 10^{-3} m bar pressure for 2–3 days. Whereas in another samples the same polymer blend nanocomposites doped with different composition of nano-filler (TiO_2) was prepared in different proportion such as 1, 2, 5, 7, 10, 15, and 20 weight percent. The above composition of TiO_2 is added as a dopant, and stirred for about 10 h. These solutions were cast and left for evaporation with a similar manner. Finally the free standing film of pure and doped polymer electrolyte is obtained. Fig. 1 shows the schematic flowchart of solution cast technique.

Table 1 Shows material selection for polymer nanocomposite films based on $(PEMA/PVC)_8NaPF_6$ + x wt% TiO_2 nano-filler

Sr. no.	Name of material	Glass transition temperature (°C)	Melting point (°C)	Density (g/cm^3)
1	PEMA	66	120	1.119
2	PVC	80	240	1.385

Salt $NaPF_6$ (sodium hexafluorophosphate), m.pt. 200 °C, molar mass 167.95 g/mol, and density 2.369 g/cm^3
Nano-filler/Plasticizer TiO_2 nanoparticle

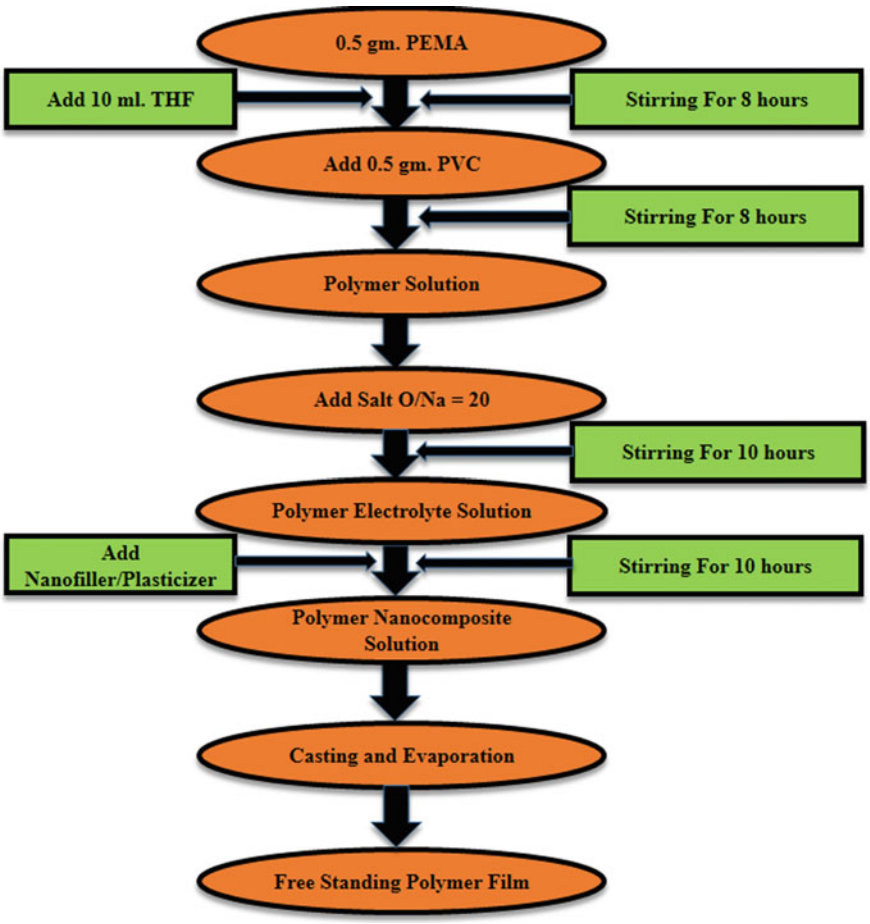

Fig. 1 Flow chart of solution cast technique

4 Experimental Techniques

FESEM To understand the properties of any material it is very necessary to understand the structural morphology of ions in the solid polymer electrolyte film, as the properties of material are closely related to its structure. Microstructural characterization of solid was done by field emission scanning electron microscopy [FESEM (Card Ziess Merlin Compact)] to investigate the influence of salt on polymer surface and morphology.

Impedance Spectroscopy Impedance spectroscopy was carried out for conductivity measurement with CHI electrochemical workstation over the frequency range

1 Hz to 1 MHz, the sample sandwiched between stainless steel electrodes and an a.c signal is applied.

FTIR Fourier Transform Infrared (FTIR) spectroscopy was done by Bruker Tensor-27, and spectrum was observed in the range of 600–4000 cm^{-1} to detect the presence of various functional groups. In infrared spectroscopy, IR radiation is passed through a sample. Some of the infrared radiation is absorbed by the sample and some of it is passed through (transmitted). The resulting spectrum represents the molecular absorption and transmission, creating a molecular fingerprint of the sample.

Electrochemical Analysis For electrochemical devices such as batteries, capacitors and electrochromic devices the electrochemical stability window curve is very necessary, observed by cyclic Voltammetry (CV) technique in the voltage range between −3 V and +3 V at scan rate of 0.1 V/s.

5 Result and Discussion

5.1 SEM Analysis

The properties associated with polymer nanocomposites are a function of the filler size, shape, dispersion, and of the polymer matrix - filler interaction. The morphological and structural analysis of nanocomposites is often done with scanning electron microscopy (SEM). Phase separation in polymer electrolyte due to rapid evaporation of solvent are shown by various pores in micrograph image Fig. 2a. The difference in pores is due to the difference in driving force for phase separation. The polymer with the nano-filler (TiO_2) lessen the difference in driving force for phase separation and produce homogeneous film of better quality.

Agglomerations in Fig. 2 (b) results due to weaker polymer/nano-filler interfacial interactions and higher stress concentration regions. As the dispersed particle size becomes smaller and the particle dispersion is more uniform then homogeneous film was produced which have better electrical as well as mechanical properties [12].

5.2 Electrical Conductivity

The electrical conductivity of polymer blend nanocomposite has been evaluated by using complex impedance spectroscopy technique. The representative complex impedance spectrum pattern of polymer nanocomposite film at x wt% (0, 7, 15, and 20) concentration of TiO_2 at room temperature is shown in Fig. 3. As shown in Fig. 3 the semicircular arc in the lower frequency region followed by rising spike in

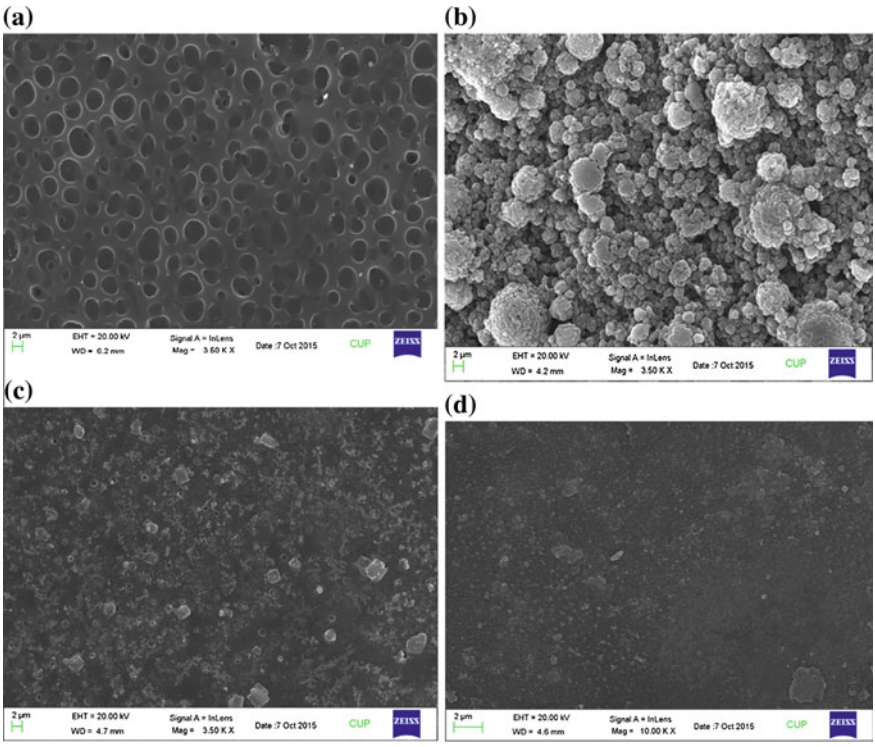

Fig. 2 FESEM micrograph of polymer electrolyte for **a** PEMA/PVC + $NaPF_6$ **b** PEMA/PVC + $NaPF_6$ + 7 wt% TiO_2 **c** PEMA/PVC + $NaPF_6$ + 15 wt% TiO_2 **d** PEMA/PVC + $NaPF_6$ + 20 wt% TiO_2

the higher frequency region on the real axis shows estimated values for bulk resistance (R_b). Conductivity will be measured with the help of following formula.

$$\sigma = t/R_bA$$

where't' is thickness of the polymer electrolyte in cm, which can be measured with the help of Barmier calliper, 'A' is the area of blocking electrode in cm^2, and R_b is the bulk resistance. The bulk resistance will be measured from the frequency intercept on the real axes [13]. With the addition of nano-filler and plasticizer, there is enhancement in conductivity was absorbed as shown in Table 1. Initial conductivity without addition of nano-filler, it is in the range of 10^{-9} S/cm, but with the addition of nano-filler it becomes 1.5×10^{-5} S/cm because addition of nano-filler improves the host polymer amorphous region by slowing the recrystallization rate.

A nonlinear least square fitting of impedance response of all samples agrees well with electrical equivalent circuit model comprising a series combination of constant phase element (CPE) with another constant phase element (CPE) and resistance

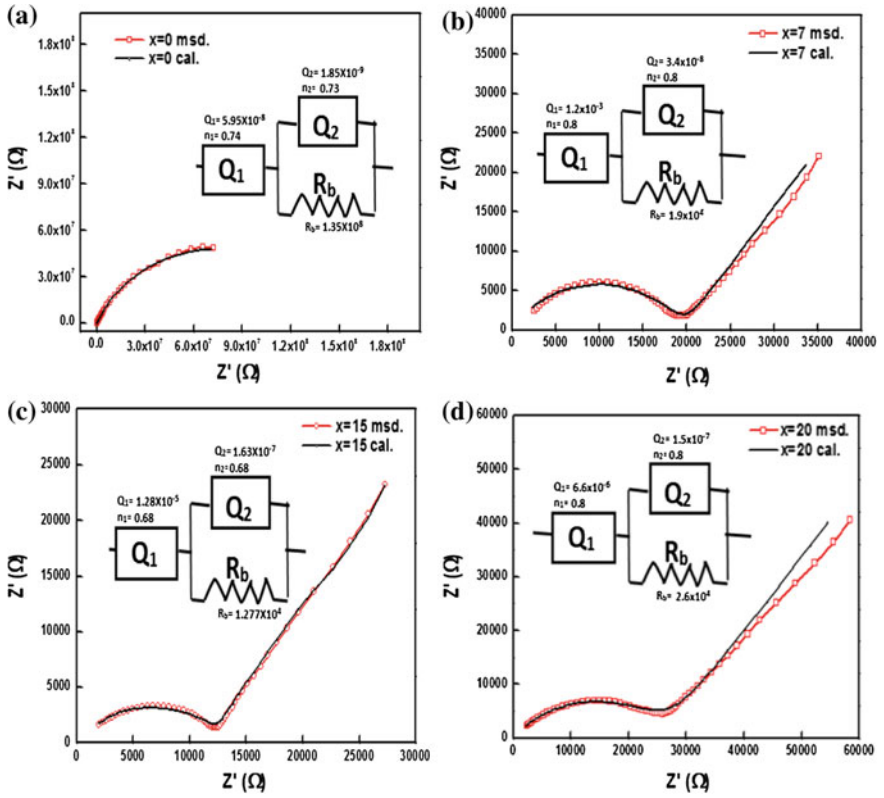

Fig. 3 Electrical impedance spectroscopic measurement of polymer nanocomposite (PEMA/PVC + $NaPF_6$)$_8$ + x wt% TiO_2 (x = 0, 7, 15, 20)

(R_b) also shown in Fig. 3. CPE describe both crystalline and amorphous phase of polymer nanocomposite film [14]. The conductivities values obtained for x = 0, 15 wt% concentration TiO_2 are 1.5×10^{-9}, 1.5×10^{-5} Scm^{-1}. The impedance of CPE is normally represented as.

$$Z_{CPE} = \frac{1}{Q_0(i\omega)^n}$$

where i = $(-1)^{1/2}$, "Q_0" and "n" are fitting parameter, it may behave as an electrical analogue of resistance, Warburg impedance capacitance and inductance for different values of 'n' [8].

In Table 2 there is continous increase in conductivity with the addtion of nano—filler up to x = 15 wt% concentration of TiO_2. But there is further decrease in the value of ionic conductivity for further addition of nano-filler. This is may be due to gradual formation of neutral aggregates of nano-filler, which creates blockages in the conducting path, reduces free volume, and increase crystallinity of the polymer

Table 2 Shows ionic conductivity of polymer nanocomposite films based on $(PEMA/PVC)_8NaPF_6$ + x wt% TiO_2 nano-filler

Polymer electrolyte	Nano-filler TiO_2 (in wt%)	Bulk resistance (R_b) In (Ω)	Conductivity (S/cm)
(PEMA/PVC + $NaPF_6$)	0	1.3×10^8	1.5×10^{-9}
(PEMA/PVC + $NaPF_6$)	7	1.9×10^4	1.0×10^{-5}
(PEMA/PVC + $NaPF_6$)	15	1.2×10^4	1.5×10^{-5}
(PEMA/PVC + $NaPF_6$)	20	2.6×10^4	7.8×10^{-6}

blend film. These factor may be responsible to resist the movement of mobile ions and polymer segments through the polymer matrix. Moreover, the formation of neutral aggregates also lower the number of mobile ions participating in conduction process. All these factors reduce the ion and segmental mobility through the polymer blend and hence, lead to the drop in conductivity [15]. We observe this type behavior of prepared polymer nanocomposite film at x = 20 wt% concentration of doped TiO_2.

5.3 FTIR

Fourier Transfer infrared (FTIR) microscopy analysis of the sample was done to detect the presence of various functional groups. FTIR spectrum was observed in the range of 600–4000 cm^{-1} as shown in Fig. 4. Also shift in peak position with addition of salt was clearly seen in Fig. 4. Because Na^+ ion from $NaPF_6$ was attracted toward the negative charge lone pair on oxygen atoms of carbonyl (C=O) and (C–O–C_2H_5) groups in PEMA. Carbonyl stretching [ν (C=O)] and asymmetrical O–C_2H_5 [ν (O–C_2H_5)] bending of PEMA was upshifted toward higher wavenumber. Which confirms the coordination of Na^+ ions of $NaPF_6$ on the oxygen atom of carbonyl group of PEMA. The peak in the wavenumber range 800–900 cm^{-1} corresponds to salt which causes due to the vibrational mode of PF_6^- anion. The characteristic absorption peak observed in the spectral pattern at the wavenumbers ~749, ~1149-52-53-54, ~1163-75-76-75-62, ~1388-89 and 2988 cm^{-1} are attributed to rock(CH_2), ν_a(C–O–C), υ(CO), τ(CH_2) and ν(C–H) mode of PEMA respectively [16]. The FTIR peaks at ~967-68-65, ~1064-65, ~1247-48-50-51 cm^{-1} are related to rock(C–H_2), stretching of C–C, def(C–H) of CHCl in PVC. The vibrational peak at 2988 $cm^{-1}$are assigned to asymmetric stretching of CH_2 [17]. One additional peak at ~1633-34-35-36 cm^{-1} due to the H–O–H group from TiO_2.

Characteristic absorption peak observed in the spectral pattern in the wavenumber 600–4000 cm^{-1} was shown with the help of band assignment in Table 3. Peak due to the vibrational modes of PF^{6-} anion has been observed at 847 cm^{-1}. Asymmetric stretching observed on peak keeps on changing with change in the nanofiller concentration in the composite phase [18].

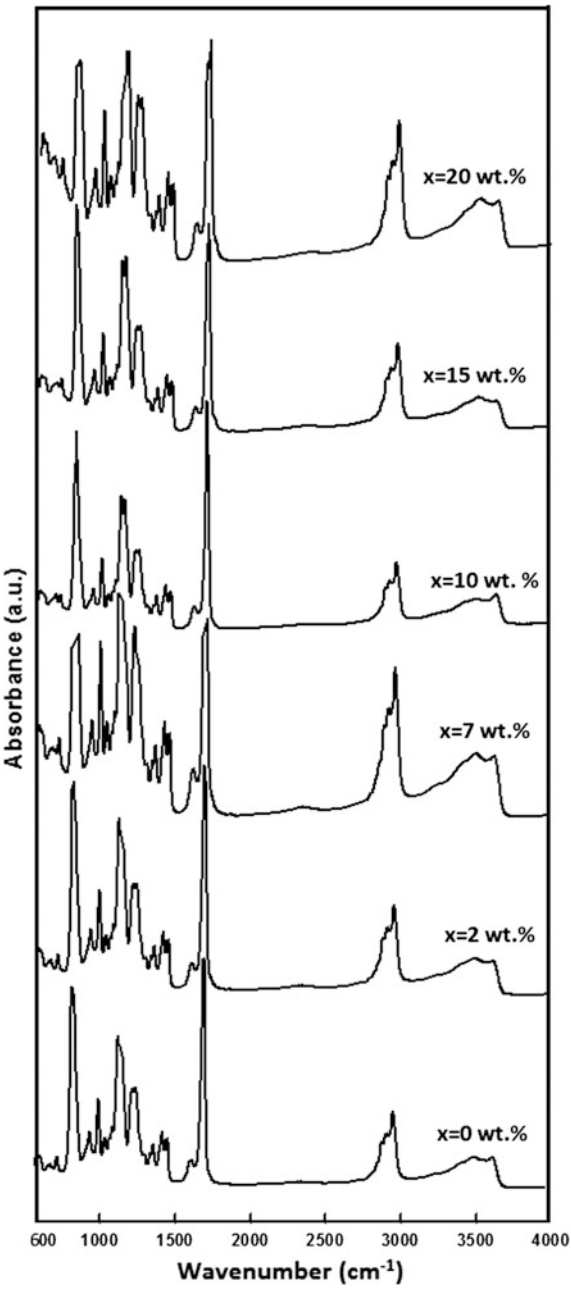

Fig. 4 FTIR spectra for polymer nanocomposite (PEMA/PVC + $NaPF_6)_8$ + x wt% TiO_2 (x = 0, 1, 7, 10, 15, 20) in in wavenumber 600–4000 cm^{-1}

Table 3 FTIR band assignment of polymer nanocomposite films based on $(PEMA/PVC)_8NaPF_6$ + x wt% TiO_2 nano-filler

$(PEMA/PVC)_8NaPF_6$ x = 0	$(PEMA/PVC)_8NaPF_6$ + x wt % TiO_2					Assignment mode	Source
	x = 2	x = 7	x = 10	x = 15	x = 20		
749	750	749	749	749	749	rock ($C–H_2$)	PEMA
845	847	853	853	846	849	ν (F_2P)	Salt
967	967	968	965	968	968	rock ($C–H_2$)	PVC
1064	1064	1065	1064	1065	1065	ν (C–C)	PVC
1154	1153	1149	1152	1152	1152	ν_a (C–O–C)	PEMA
1173	1173	1178	1176	1175	1162	ν (CO)	PEMA
1251	1250	1248	1247	1249	1249	def (C–H)	PVC
1389	1388	1388	1387	1388	1388	τ ($C–H_2$)	PEMA
1445	1446	1448	1448	1449	1447	ν ($O–C_2H_5$)	PEMA
1479	1479	1479	1480	1480	1481	δ ($C–H_2$)	PEMA
1633	1634	1634	1635	1635	1636	ν (H–O–H)	TiO_2
1720	1722	1729	1720	1725	1730	ν (C=O)	PEMA
2988	2981	2983	2982	2982	2981	ν (C–H)	PEMA

This asymmetry in the anion stretching vibrational mode is an outcome of the degeneracy arising out of more than one contribution possibly due to the presence of free anion and ion pairs.

In order to be sure the band pattern in the wavenumber 800–900 cm^{-1} has been deconvoluted using Voigt profile with a commercial software peak fit analyser. Two distinct contribution observed at 850 and 872 cm^{-1} in the deconvoluted pattern as shown in Fig. 5. The peak appearing at 850 cm^{-1} has been attributed to free anions and peak appearing at 872 cm^{-1} has been attributed to presence of ion pairs in the solid polymer electrolyte film [8].

Free anion area increases whereas ion pair area decreases with the addition of nano-filler up to certain limit of nano-filler that is x = 15 wt% TiO_2 here, further addition of nano-filler at x = 20 wt% TiO_2 nano-filler it decreases. Also Table 4 shows Peak position of deconvoluted free anion peak of polymer nanocomposite films based on $(PEMA/PVC)_8NaPF_6$ + x wt% TiO_2 nano-filler. The presence of two distinct degenerate FTIR band in the deconvoluted pattern for experimental spectrum provides an evidences of strong ion–ion interaction in the prepared polymer nanocomposite films.

5.4 Electrochemical Stability

For electrochemical devices such as batteries, capacitors and electrochromic devices, electrochemical stability window curve is very necessary. This stability window curve (Charging and discharging) for polymer blend electrolyte based on sodium ion batteries were observed by cyclic Voltammeter (CV) analysis. This

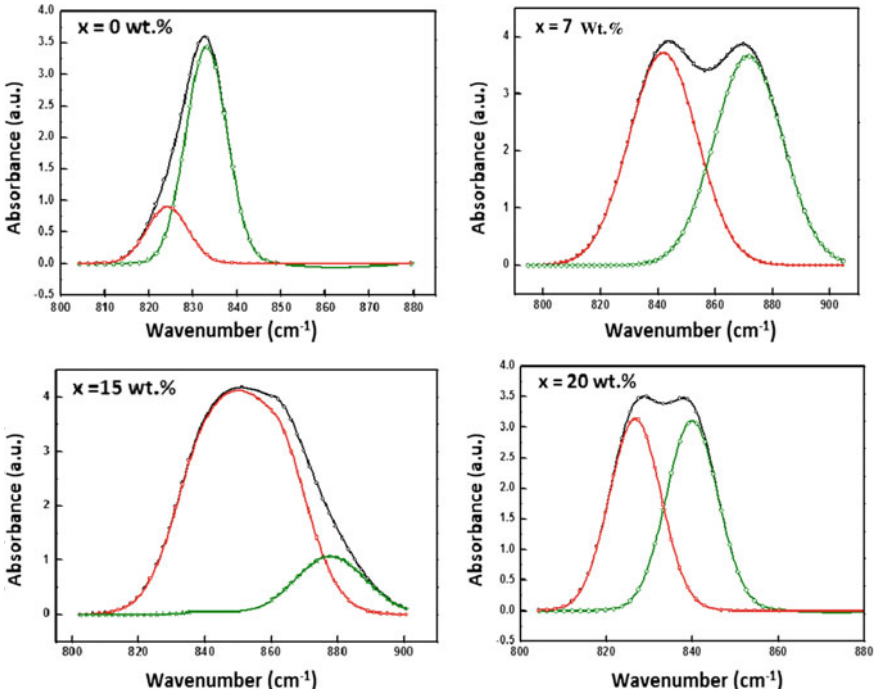

Fig. 5 Deconvolution pattern of ν (PF_6^-) in $(PEMA/PVC)_8NaPF_6$ + x wt% TiO_2 nano-filler

Table 4 Peak position of deconvoluted free anion peak of polymer nanocomposite films based on $(PEMA/PVC)_8NaPF_6$ + x wt% TiO_2 nano-filler

Nano-filler TiO_2 (in wt. %)	Deconvoluted anion peak data				Correlation coefficient (r^2)
	Free anion peak		Ion pair peak		
	Position (cm^{-1})	Area (%)	Position (cm^{-1})	Area (%)	
0	836	20.8187	850	79.1812	0.998
7	841	50.3925	871	49.6074	0.983
15	850	78.1155	872	21.8844	0.995
20	840	50.2524	862	49.7475	0.995

process was observed in the potential range of −3 to 3 V for x = 20 wt% as shown in Fig. 6. through blocking electrode of stainless steel. Electrochemical stability window curve is obtained in the range from about −3 to 3 V, which is an acceptable voltage range for device application [19, 20].

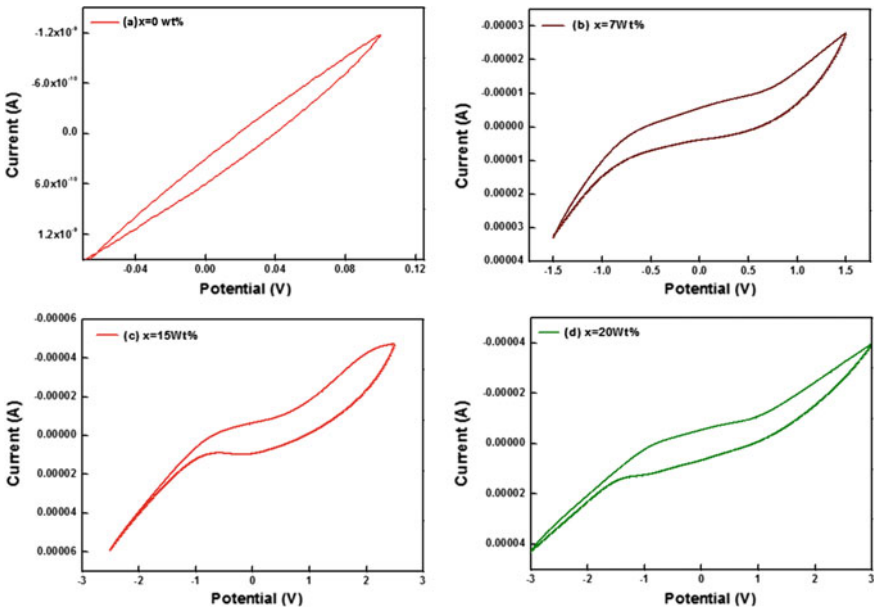

Fig. 6 Cyclic Voltammetry images of $(PEMA/PVC)_8NaPF_6$ + x wt% TiO_2 nano-filler

6 Conclusions

At $x = 0$ wt% of TiO_2 in polymer nanocomposite film was observed. The polymer with the nano-filler (TiO_2) lessen the difference in driving force for phase separation and produce homogeneous film at $x = 15$ wt% of nano-filler, and produce polymer film of better quality which can enhance the electrical as well as mechanical properties of prepared polymer films.

There is enhancement in conductivity. Without addition of nano-filler conductivity is in the range of 10^{-9} S/cm, but with the addition of micro range inorganic nano-filler it becomes 1.5×10^{-5}. Addition of nano-filler improves the host polymer amorphous region by slowing the recrystallization rate. A nonlinear least square fitting of impedance response of all samples agrees well.

FTIR confirms ion-polymer, polymer-polymer interaction and the presence of various functional groups present in prepared polymer electrolyte film by observing the spectra in the wavenumber 600–4000 cm^{-1}. The presence of two distinct degenerate FTIR band in the experimental spectrum provides an evidences of strong ion–ion interaction in the prepared polymer nanocomposite films.

Electrochemical stability window curve is obtained in the range from about −3 to 3 V for $x = 15$ and 20 wt%, which is an acceptable voltage range for device application.

Acknowledgments One of authors is thankful to Central University of Punjab for providing fellowship during M. Phil. Course and partial support received from the UGC Start-up-Grant (GP-41).

References

1. P. Knauth, H.L. Tuller, J. Am. Ceram. Soc. **85**(7), 1654 (2002)
2. F. Yuan, H.-Z. Cheng, H.-Y. Yang, H.-Y. Li, M. Wang, Mater. Chem. Phys. **89**, 390 (2005)
3. M. Mortazavi, J. Deng, B. Shenoy Vivek, V. Medhekar Nikhil, J. Power Sources **225**, 207 (2012)
4. K. Kiran Kumar, M. Ravi, Y. Pavani, S. Bhavani, A.K. Sharma, V.V.R. Narasimha Rao, J. Membr. Sci. **454**, 200 (2014)
5. Ho KhacHieu, Vacuum **120**, 13 (2015)
6. J. Serra Moreno, M. Armand, M.B. Berman, S.G. Greenbaum, B. Scrosati, S. Panero, J. Power Sources **248**, 695 (2014)
7. M.L. Verma, M. Minakshi, N.K. Singh, I & EC Res. **53**, 14993–15001 (2014)
8. A.L. Sharma, K. Awalendra Thakur, J. Mater. Sci. **46**, 1916 (2011)
9. H.P.S. Missan, B.S. Lalia, K. Karan, A. Maxwell, Mater. Sci. Eng. B **175**, 143 (2010)
10. H.M.J.C. Pitawala, M.A.K.L. Dissanayake, V.A. Seneviratne, Soild State Ionics **178**, 885 (2007)
11. A. Arya, A.L. Sharma, Appl. Sci. Lett. **2**(2), 72–75 (2016)
12. S. Rajendran, M. Ramesh Prabhu, M. Usha Rani, Int. J. Electrochem. Sci. **3**, 282 (2008)
13. Y.L. Ni'mah, M.-Y. Cheng, J.H. Cheng, J. Rick, B.-J. Hwang, J. Power Sources **278**, 375 (2014)
14. A.L. Sharma, A.K. Thakur, Ionics **19**(5), 795–809 (2013)
15. P. Joge, D.K. Kanchan, P. Sharma, N. Gondaliya, IOSR J. Appl. Phys. **1**, 55 (2014)
16. S. Rajendran, M.R. Prabhu, M.U. Rani, Int. J. Electrochem. Sci. **3**, 282 (2008)
17. N.F. Zain, N. Zainal, N.S. Mohamed, Phys. Scripta **90**, 015702 (2015)
18. P. Pradeepa, S. Edwinraj, M.R. Prabhu, Chin. Chem. Lett. **26**, 1191 (2015)
19. C. Cao, H. Wang, W. liu, X. Liao, L. Li, Int. J. Hydrogen Energy **39**, 16110 (2014)
20. A. Arya, S. Sharma, A.L. Sharma, M. Sadiq, J. Integr. Sci. Technol. **4**(1), 17–20 (2016)

Dielectric Study of Polymer Nanocomposite Films for Energy Storage Applications

M. Sadiq, Anil Arya and A.L. Sharma

Abstract In the present study we have a novel report on the types of dielectric studies of the two blend polymer consisting of polyacrylonitrile (PAN) as the host polymer-polyethylene oxide (PEO) as a copolymer, $LiPF_6$ as lithium salts and clay containing different weight percent of DMMT as modified montmorillonite. The polymer nanocomposite (PNC) films were prepared by using solution cast technique. However the pure PAN-PEO+$LiPF_6$ film was prepared as a reference. Keeping in view of characterization of PNCs films were study by impedance spectroscopy technique. The high frequency range of dielectric measurement is 1 Hz–1 MHz. This technique is shown to be a viable and straight forward means of obtaining dielectric data on polymer electrolytes. Permittivity ($\in'$), dielectric loss ($\in''$) and a.c. conductivity variation with frequency was studied to estimate the relaxation times for PAN-PEO polymer electrolyte.

1 Introduction

Energy storage has become more important in the 21st century due to increasing demand of renewable energy for everyone. Solid Polymer Electrolyte batteries having Li as mobile cation are playing an important role as energy storage/conversion devices in particular, consumer electronics, electric or hybrid cars, fuel cell, super capacitors, solar cells and electro chromic display devices. However, safety issues of batteries must be addressed before their use at commercial level, since aprotic organic solvents are prone to under the abuse

M. Sadiq
Department of Physics, I.I.T. (BHU), Varanasi 221005, India
e-mail: sadiqjk.89@gmail.com

M. Sadiq · A. Arya · A.L. Sharma (✉)
Centre for Physical Sciences, Central University of Punjab, Bathinda 151001, India
e-mail: alsharmaiitkgp@gmail.com

A. Arya
e-mail: aniljaglan0581@yahoo.com

V.K. Jain et al. (eds.), *Recent Trends in Materials and Devices*,
Springer Proceedings in Physics 178, DOI 10.1007/978-3-319-29096-6_51

condition [1]. As electrolyte is a crucial part of the battery system, therefore, the research on electrolyte become important for the research community. Polymer electrolytes (PEs) are a suitable candidate in this context. SPEs that exhibit high ionic transport, high energy density, long cycle life, flexible characteristics, and safety are important for the application. Solid polymer electrolytes (SPEs) are gaining more interest worldwide since the first report was given by Peter V. Wright and a major focus on technological potential observed by Michel Armand in 1978. The SPEs are solid solutions of monovalent ($LiClO_4$, $NaClO_4$, $LiCF_3SO_3$, $LiBF_4$, etc.) or divalent ($Ca(ClO_4)_2$, $MgCl_2$, Mg $(CF_3SO_3)_2$) metal salts in host polymer. From all host matrices so far the best polymer which is used as host is having –CH_2–CH_2–O– repeat unit (PEO), also it have lower glass transition temperature which provides film flexibility and faster ionic transport [2]. Especially, free standing thin polymeric membrane would be suitable to be used as electrolyte due to advantage of good contact with electrodes. Polymer plays a dual role as a separator and electrolyte. Currently growing interest for lithium-ion storage devices based on nano filler such as SiO_2, Al_2O_3, TiO_2, ZrO_2, and $BaTiO_3$ because of their high surface area, porosity, etc. The addition of nano filler leads to improved ionic conductivity as well as enhanced mechanical strength and stability of the prepared free standing polymeric films. These SPNCs, generally formed by integrating the ion for mobile ionic species into a solid polymer matrix. However, ionic conductivity is one of the key parameters that need to be optimized for the better performance of the devices [3]. Also the dielectric properties and dielectric relaxation in these PNC films are studied. When the dielectric material is exposed to an alternating electric field that is generated by applying a sinusoidal voltage the displacement polarization leads to electric oscillations in the materials. The response of the orientation polarization to a change of the electric field is therefore always opposite in direction of the field. This process is known as dielectric relaxation. The characteristic time constant of such a relaxation process is the time for reaching a new equilibrium after changing the excitation is called the relaxation time ($\omega\tau = 1$) and is obtained from the graph of tangent loss vs. frequency [4, 5]. The response of dielectric has been shown to be a function of the salt complex. Few examples of polymer electrolytes have been performed for improving the dielectric properties of polymer electrolytes using various combinations,

PEO/$LiClO_4$ [6], PAN/LiTFSI [7], PEO/NH_4I [8], PEO/PMMA/$LiClO_4$ [9], PEO-PMMA-$AgNO_3$/Al_2O_3 [10], PAN-$LiCF_3SO_3$+DMMT [11], PVA-PEOAg NO_3, PEG/Al_2O_3 [12], (PVP coVAc) and (PMMA)/Tetrapropyl ammonium iodide (TPAI) and Potassium iodide (KI) [13], PEO-$LiClO_4$+MMT [14], PEO/PVP+MMT [15], PEO/NaI+DMMT [16], PEO/$LiPF_6$+CNT [17], PEO-PDMS-$LiPF_6$ [18] has been found report in the literature.

The Present report is done to study the effect of different clay concentration on the dielectric properties in terms of dielectric permittivity, ac conductivity and relaxation time in prepared polymer salt complex films comprised of $(PAN\text{-}PEO)_6$–$LiPF_6$+ wt% DMMT clay. The variation of dielectric parameters Permittivity ($\in'$), dielectric loss ($\in'$) and ac conductivity with the frequency and concentration at room temperature are presented and studied.

2 Experimental Section

Free standing polymer electrolyte-cum separator films have been prepared by solution cast technique reported elsewhere [19]. This is one of the traditional procedures for casting films of Solid Polymer Electrolyte (SPE) as well as Composite Polymer Electrolyte (CPE). In this technique, appropriate amount of polyacrylonitrile [PAN; M/S Aldrich, average molecular weight 1.5×10^5, (USA); 0.7 gm] and polyethylene oxide [PEO; M/S Aldrich, average molecular weight 6×10^5, (USA); 0.3 gm], *N,N*-dimethylformamide (10 ml), (E-Merck Germany) was used as organic solvent, lithium hexaflourophosphate ($LiPF_6$; Sigma Aldrich) as the salt and modified montmorillonite (SWy-2 variety) procured from Clay Minerals Society (USA). The modification process of montmorillonite clay is reported elsewhere [20]. Although the addition of an appropriate amount salt by stoichiometric ratio has been calculated considering nitrogen of PAN. The formula for the stoichiometry ratio ae shown below:

For Poly(acrylonitrile) (PAN);

$$\frac{\ddot{N}}{Li^+} = \frac{\text{No. of monomer unit in half gram of PAN}}{\text{No. of } LiPF_6 \text{ molecular inhalf gram of salt}} \times \frac{\text{wt.of PAN taken}}{\text{wt.of salt taken}}$$

The detail of stoichiometric calculation has been reported by [17]. On the basis of the above stoichiometric ratio in the blend polymer host (PAN-PEO) matrix be maintained at an optimized proportion of ($\ddot{N}/Li = 6$) is obtained. Preparation sample was approved in the three stages via solution casting technique using the subsequent stage as shown in the Fig. 1.

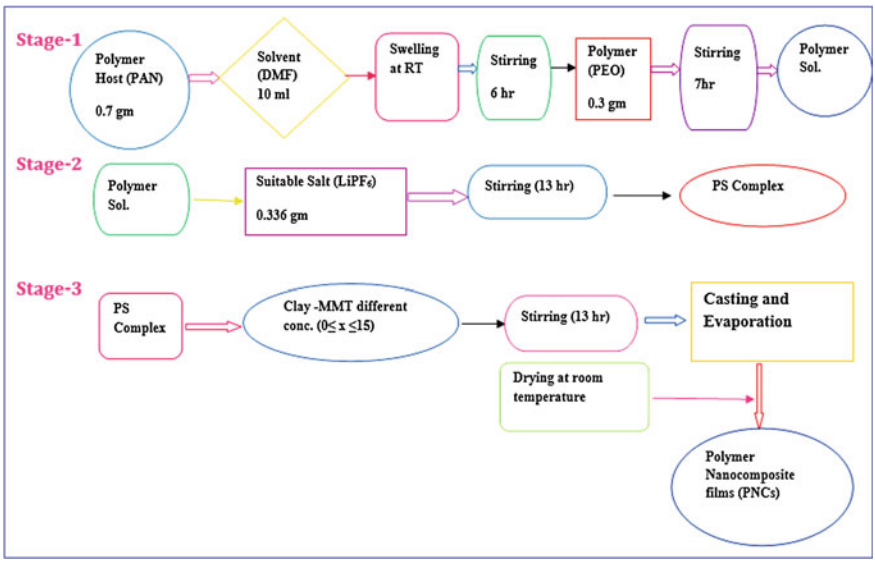

Fig. 1 Flow chart of solution cast technique method

2.1 Material Characterization

Dielectric properties of PNCs films were measured using computer interfaced CHI 760—impedance analyzer over the frequency range 1 Hz–1 MHz at room temperature. The sampled are placed in cell configuration SS/PNC/SS with an ac input signal of 10 mV.

3 Results and Discussion

3.1 Study of Electrical Property

The dielectric constant of material is represented by $\varepsilon^* = \varepsilon' - j\varepsilon''$, ε' is related to the stored energy within the medium and ε' is related to the dielectric energy loss of energy within the medium. The frequency dependent real part of dielectric constant (ε') can be calculated by using the relation $\varepsilon' = \frac{-Z''}{\omega c_o(Z'^2 + Z''^2)}$, $\varepsilon'' = \frac{Z'}{\omega c_o(Z'^2 + Z''^2)}$ where ω is angular frequency, where $C_o = \frac{\varepsilon_o A}{d}$ is vacuum capacitance of sample, A is the contact area of the electrode and d is the thickness of the composite films. It is observed from the Fig. 2 that decreases with increase in frequency and attains an independent value at a higher frequency. The initial value of permittivity is high, and decreases with increase in the frequency, which could be due to the polarization

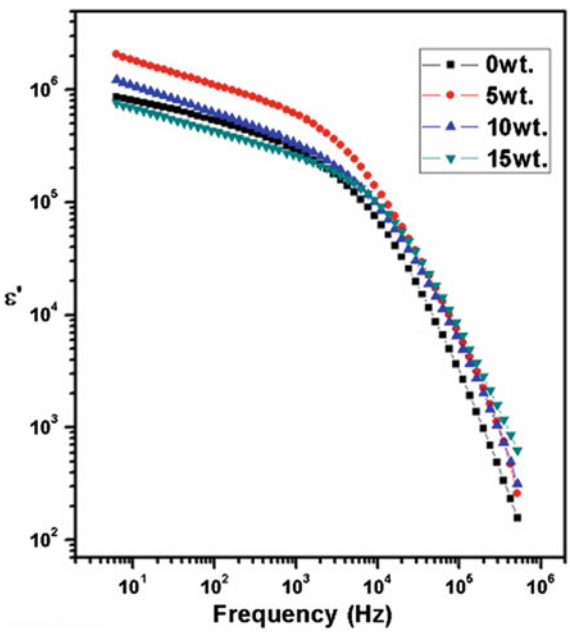

Fig. 2 The variation of real part of permittivity versus frequency at room temperature of the sample $(PAN\text{-}PEO)_6 - LiPF_6$ + wt% DMMT

effects led to the disability of dipole to follow the field at higher frequencies. The low frequency region appears due to the contribution of charge accumulation at the electrode-electrolyte interface or space polarization effect. At higher frequencies, the periodic reversal of the electric field leads to a reduction of charge carriers in the system so that there is no diffusion of ions in the direction of the field and is related to hoping process in host polymer matrix PAN-PEO [21].

It has been observed that same trend is observed of dielectric permittivity with frequency in all the samples. With the increase in clay concentration from 0 to 10 % there is higher dielectric constant at lower frequencies which clearly shows the faster ion dynamics. The polarization reduction takes place with an increase in frequency which leads to a corresponding decrease in the value of ε' at high frequency. The high frequency region attributed to hopping process (forward backward motion) of charge carriers from one available site to another in the host polymer matrix PAN. These moving charge carriers behave as dipoles depending on the frequency applied [22].

The dielectric constant increases initially with increasing clay concentration up to 5 %. This increase in dielectric constant represents the increase in a number of free ions provided by interaction of clay with polymer host which enhances more conductivity. At high frequency, charge accumulation is eliminated and the periodic flipping reversal of the electric field due to alternating current, which results in back and forth motion of the charge carriers and limits the ion diffusion along the direction of alternating electric field.

The low frequency dispersion for ε' and absence of loss peak for ε' are characteristics of purely ionic transport systems. Initially ε' increases sharply at low frequency and is independent of frequency at a higher frequency as shown in Fig. 3. The higher the value of dielectric loss at lower frequency shows presence of electrode polarization and confirming the non-Debye dependence [23]. At higher frequency the periodic reversible of the field prevents charges from the orientation in the direction of electric field, results in the decrease in ε' and hence reduction in the ε' [24]. The higher value of ε' in the PNC films is due to the presence of more number of charge carriers.

The conductivity spectrum for the sample with low salt concentration consists of two frequency regions: (i) a frequency-independent zone at high frequency and (ii) an increase in conductivity at higher frequencies as shown in Fig. 4. The ac conductivity of the PNC films is obtained from dielectric loss using the relation

$$\sigma_{ac}=\varepsilon_o\omega\varepsilon''=\varepsilon_o\omega\varepsilon'\tan\delta.$$

Where ϵ_0 is the dielectric permittivity of free space and ω. angular frequency. The similar results of frequency-dependent conductivity are obtained for ionically conducting ceramic glasses and polymers. At lower frequencies, ions transport is faster and easily jumps from one available site ($C \equiv \ddot{N}$) to another in the host polymer PAN matrix. A hoping is said to be successful hopping if ion goes to neighboring site easily having long relaxation time and contributes to electronic conductivity [25]. This observation evidences the complex ion transport process

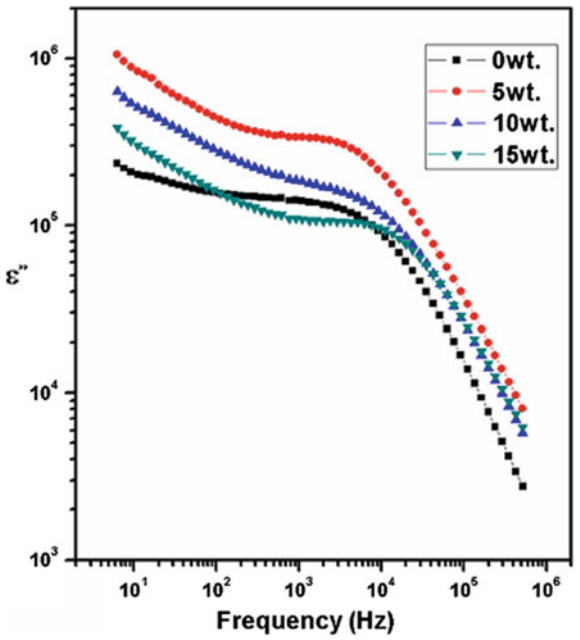

Fig. 3 The variation of imaginary part of permittivity with frequency at 30 °C of the sample (PAN-PEO) $_6$ −$LiPF_6$ + wt% DMMT

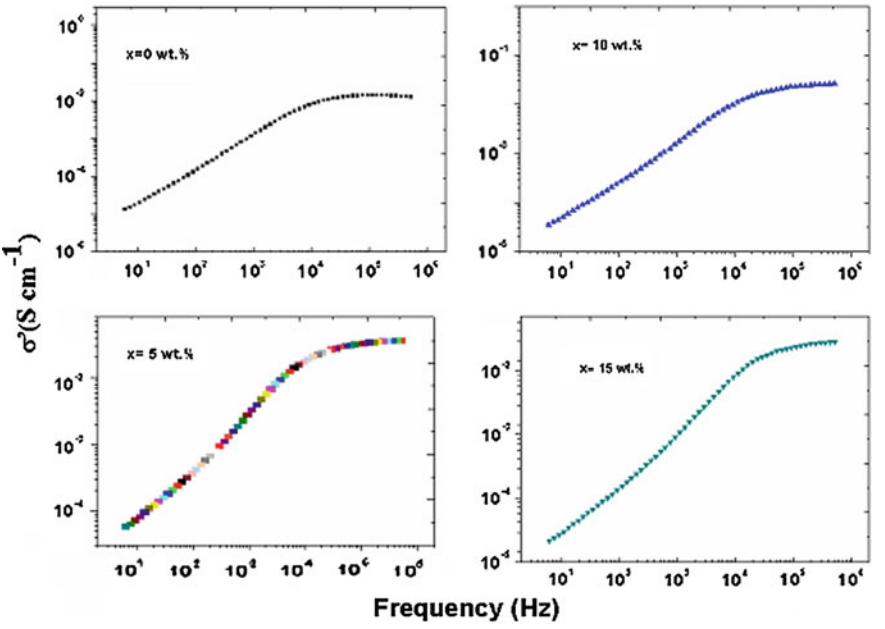

Fig. 4 Variation of ac conductivity versus frequency at RT of the sample (PAN-PEO) $_6$ + $LiPF_6$ + wt% DMMT

due to both electrode polarizations at low frequency followed by long range ion migration at higher frequencies. At low frequency ionic charges drift for a long range on the application of the field. In the high frequency region, both ε' and ε'' increase with increasing frequency and may be attributed to the dielectric contribution [26]. At higher frequency there is frequency independent region where electrode polarization is steady and a new mechanism of ion migration is supported by ions.

From this Fig. 4 it is observed that the conductivity of x = 0 wt% of pure PAN-PEO+$LiPF_6$ at 30 °C. But when we addition the varying amount of clay then it is obtained that the conductivity is increased. But at higher concentration x = 15 wt% the conductivity is a decrease of the order of magnitude. As the concentration of clay increases there is a decrease in mobile cation concentration due to clustering of free ions ac conductivity decreases as shown in the Fig. 4. There are two mechanisms that ac conductivity follows one is long range conduction and other is hopping of ions through the electron lone pair site. The first effect is due to transport of free anions or cation in polymeric films and later one is due to a reduction in mean charge carrier displacement which makes conductivity dependent on frequency [27, 28]. In polymer Nanocomposites films active role is played by clay and is clearly visible in results. The clustering of filler leads to slow ion dynamics, commonly expressed as rates of hopping/mobility [4, 25].

3.2 Summary and Conclusion

Intercalated PNC films based on $(PAN\text{-}PEO)_6$ +$LiPF_6$+x wt% DMMT has been prepared using solution cast technique. Variation of ac conductivity versus frequency shows three regions low-frequency region, intermediate saturation, followed by high-frequency dispersion region. Ion transport in PNC films is contributed by the effect of clay concentration in increasing free carriers and hopping process in amorphous phase and concentration of DMMT plays a crucial role in the transport of ions. In future we may expect that the hopeful ways to improve the electrochemical performance and surface morphology of polymer electrolytes are by fabricating a nanocomposite electrolyte and addition of modified montmorillonite clays to such an electrolyte, retaining an ionic conductivity of 10^{-3} S cm^{-1} and negligible electronic conductivity is 10^{-7} S cm^{-1}. These polymer nanocomposite electrolytes are associated with considerably better capacity and high cycle efficiency in lithium polymer secondary batteries while inhibiting the formation of dendrite growth in films between the electrolyte and the electrodes.

Acknowledgments Authors would like to appreciate the support of research facility of Central University of Punjab and partial financial support from UGC Start up Grant (GP 41).

References

1. H. Aydın, A. Bozkurt, J. Mater. Res. **29**(05), 625–632 (2014)
2. F.M. Gray (1997), Polym. Electrolytes. Ayman Salim Ayes Polym. J. **41**(8), 616–621 (2009)
3. A. Ahmad, S. Saqa'an, Y. Ramadin, A. Zihlif, J. Thermoplast. Compos. Mater **19**, 531 (2006)
4. N. Shukla, A.K. Thakur, S. Archana, Marx T. David, Int. J. Electrochem. Sci. **9**, 644–7659 (2014)
5. F.M. Gray, C.A. Vincent, M. Kent, State Ionics **28**, 936–940 (1988)
6. P.A.R.D. Jayathilaka, M.A.K.L. Dissanayake, I. Albinsson, B.E. Mellander, Solid State Ionics **156**(1), 179–195 (2003)
7. A.S. Ayesh, Polym. J. **41**(8), 616–621 (2009)
8. S. Farheen, R.D. Mathad, Int. J. Innovative Res. Sci. Eng. Technol. (An ISO 3297: 2007 Certified Organization) **3**(11), (2014)
9. S. Poonam, K. Dinesh Kumar, G. Nirali, Open J. Org. Polym. Mater. (2012)
10. A.L. Sharma, A.K. Thakur, Ionics **17**(2), 135–143 (2011)
11. P. Joge, D.K. Kanchan, P. Sharma, N. Gondaliya, A comparative study
12. M.K. Jawad, S.R. Majid, E.A. Al-Ajaj, M.H. Suhail, Adv. Phys. Theor. Appl. **29**, 14–22 (2014)
13. R.J. Sengwa, S. Choudhary, S. Sankhla, Compos. Sci. Technol. **70**(11), 1621–1627 (2010)
14. S. Choudhary, R. Sengwa, Indian J. Phys. **86**, 335–340 (2012)
15. D.K. Pradhan, R.N.P. Choudhary, B.K. Samantaray, Express Polym. Lett. **2**(9), 630–638 (2008)
16. S. Ibrahim, S.M.M. Yasin, N.M. Nee, R. Ahmad, M.R. Johan, Solid State Commun. **152**(5), 426–434 (2012)
17. A. Das, A.K. Thakur, K. Kumar, Solid State Ionics **262**, 815–820 (2014)
18. S.K. Tripathi, A. Gupta, M. Kumari, Bull. Mater. Sci. **35**(6), 969–975 (2012)
19. A. Arya, A.L. Sharma, Appl. Sci. Lett. **2**(2), 72–75 (2016)
20. X. Qian, N. Gu, Z. Cheng, X. Yang, E. Wang, S. Dong, Electrochim. Acta **46**(12), 1829–1836 (2001)
21. S. Ramesh, A.H. Yahaya, A.K. Arof, Solid State Ionics **152**, 291–294 (2002)
22. A.S. Nowick, A.V. Vaysleyb, I. Kuskovsky, Phys. Rev. B **58**(13), 8398 (1998)
23. N. Shukla, A.K. Thakur, A. Shukla, D.T. Marx, An applicability of almond-west formalism. Int. J. Electrochem. Sci. **9**, 7644–7659 (2014)
24. T. Furukawa, M. Imura, H. Yuruzume, Jpn. J. Appl. Phys. **36**(3R), 1119 (1997)
25. A.L. Sharma, A.K. Thakur, Ionics **21**(6), 1561–1575 (2014)
26. A.L. Sharma, N. Shukla, A.K. Thakur, J. Polym. Sci. Part B Polym. Phys. **46**(23), 2577–2592 (2008)
27. N. Shukla, A.K. Thakur, A. Shukla, R. Chatterjee, J. Mater. Sci. Mater. Electron. **25**(6), 2759–2770 (2014)
28. C. Bhatt, R. Swaroop, A. Arya, A.L. Sharma, J. Mater. Sci. Eng. **5**(11–12), 418–434 (2015)

Correlation of Microscopic Interaction with Electrical Conductivity in Polymer Separator of Energy Storage Devices

Parul Kumar Sharma, Anshul Kumar Sharma, M. Sadiq and A.L. Sharma

Abstract In the present report solid polymer nanocomposite (PNCs) comprising of $(PEO)_{14}$ + $NaClO_4$ + wt% $BaTiO_3$ has been prepared by solution casting method. Important characterization like: FTIR (Fourier Transform Infrared Spectroscopy), and conductivity have been performed for the applicability of the prepared materials in device application. The highest conductivity of the prepared polymer nanocomposite materials has been estimated 1×10^{-4} Scm^{-1} for 15 wt% of $BaTiO_3$. A very fine correlation has been built among polymer-ion, ion-ion and polymer ion interaction with obtained conductivity results.

1 Historical Background and Introduction

Solid State Ionics, a big research of in the branch of Materials Science and it manages the solid materials which have quick particle transport. The ionic conductivity of these solids is high when contrasted with that of liquid electrolytes. Subsequently, they can be conceivably utilized as incredible interchanges of liquid/aqueous electrolytes to create solid state electrochemical gadgets viz. batteries [1]. The exploration in the field of Solid State Ionics envelops examinations of physical and concoction conduct of the solids with quick particle development inside of the mass and additionally their mechanical perspectives. These materials typically called as 'Solid Electrolytes' and have degree to build up all-solid-state electrochemical gadgets for e.g., Batteries, power modules, super capacitors, electro chromic shows, sensors photograph electrochemical sunlight based cells (PESCs) [2]. Ionic ally directing solid polymeric movies have been used in numerous

P.K. Sharma · A.L. Sharma (✉)
Centre for Physical Sciences, Central University of Punjab, Bathinda 151001, India
e-mail: alsharmaiitkgp@gmail.com

A.K. Sharma
Department of Physics, Guru Nanak Dev University, Amritsar, Punjab, India

M. Sadiq
Department of Physics, IIT BHU, Varanasi, India

V.K. Jain et al. (eds.), *Recent Trends in Materials and Devices*,
Springer Proceedings in Physics 178, DOI 10.1007/978-3-319-29096-6_52

enerplogy related divisions like high vitality thickness solid polymer batteries, PEM energy components, and super capacitors, and so forth. Such applications require an alluring conductivity esteem 10^{-3} Scm^{-1} at room temperature. With a specific end goal to accomplish this conductivity esteem, an extensive assortment of particle directing material frameworks, for example, solid polymer electrolytes (SPEs), gel polymer electrolytes (GPEs), and composite polymer electrolytes (CPEs), and so forth have been arranged and assessed. On the other hand, the vast majority of the frameworks have shown conductivity much lower than the alluring worth for gadget application under encompassing conditions. In any case, various confinements came to be recognized later, when assessed for their suitability in gadget application. The essential variable forcing extreme restriction on their relevance are (i) low encompassing ionic conduction, (ii) focus polarization, and (iii) poor strength (warm, mechanical, synthetic and electrochemical, and so forth properties). Another purpose behind lower ionic conduction is concentration polarization whose origin lies in ion association effect because of the presence of both cations and anions in the host polymer matrix [3]. The advancement of polymeric framework with high ionic conductivity is one of the principal focuses in polymer research. This is a result of their potential applications in solid state batteries. Polymer batteries have inclinations, for instance, high ionic conductivity, high energy densities, dissolvable free conduction, leak proof, wide electrochemical dependability windows, ease in technique limit and light weight. Generally, ionic conduction in polymer electrolytes is told by the unclear elastomeric stage. Polymers having the dipole moment aligned parallel to the chain shape show a dielectric relaxation because of the end's variance to-end vector of the chains. The investigation of dielectric relaxation in solid polymer electrolytes is an intense methodology for acquiring data with respect to the qualities of ionic and atomic collaborations. The dielectric parameters connected with relaxation procedures are of specific centrality in particle leading polymers where the dielectric steady assumes a principal part, which demonstrates the capacity of a polymer material to dissolve into salts [4]. The frequency-dependent conductivity and dielectric relaxation are both sensitive to the motion of charged species and dipoles of the polymer electrolytes. Winters gill and Fontanilla, studied low-frequency dielectric parameters of polyethylene oxide (PEO) and polypropylene oxide based polymer electrolytes. The high molecular weight poly (ethylene oxide) (PEO)-based composite polymer electrolytes are emerging as the best candidates to be used as polymer matrix because of their solvation power, complexion ability and ion transport mechanism directly connected with the alkaline salt (Li^+). $LiPF_6$ is the most common lithium salt employed in lithium-ion batteries because it offers good electrolyte conductivities and film forming. However, the ionic conductivity of PEO–lithium salts (LiX) electrolytes at ambient temperature (10^{-7}–10^{-6} Scm^{-1}) is not high enough for most practical

applications. In order to over- come this problem, consistent research efforts have been devoted to improve the ionic conductivity in PEO–LiX (X = ClO_4–, CF_3, SO_3−, BF_4−, PF_6− etc.) composite polymer electrolytes [5]. A common approach is to add low molecular weight plasticizers to the polymer electrolyte system. The plasticizers impart salt-solvating power and high ion mobility to the polymer electrolytes. However, plasticizers tend to decrease the mechanical strength of the electrolytes, particularly at a high degree of plasticization. Alternatively, inorganic fillers are used to improve the electrochemical and mechanical properties. The fillers affect the PEO dipole orientation by their ability to align dipole moments, while the thermal history determines the flexibility of the polymer chains for ion migration [6]. They generally improve the transport properties, the resistance to crystallization and the stability of the electrode/electrolyte interface. The conductivity enhancement depends on the filler type and size. In 1999, the addition of carbon to improve the conductivity and stability of polymer electrolytes was proposed by Appetecchi and Passerini. However, the room temperature conductivities for various weight percent of carbon are within the range of 10^{-6} Scm^{-1}. Formation of intercalated polymer nanocomposite (PNC) is considered an effective approach where ion pair formation [7]. Solid state polymer nanocomposite films deals under the area of solid state ionic devices. Solid state ionic devices are a multidisciplinary branch of science. Firstly polymer were considered to be insulator, after the discovery of ionic conductivity phenomenon in solid state has started first by Peter Wright and Michel Armand who had introduced the first newly branch of solid ionic conductors in the 1970s. These studies showed that liquid electrolyte has higher ionic conductivity compared to other electrolyte systems. This ionic liquid has several disadvantages such as leakage problem; gas formation during operation can be difficulty in handling for portable applications, which has great resulted in increasing studies conducted on solid polymer electrolyte and its potential for applications in solid batteries, electro chromic windows, sensors, fuel cell, and others. Presently, science and technology is very advanced and provide the comfort for human being [8]. With the advancement in science and technology, the demand for fuel and energy is increasing, but on the other hand power sources like fossil fuel and other power sources are very limited. Therefore we have to be mindful about new power sources like energy storable devices i.e., battery. It is a replacement of the fossil fuel. Technology has made our life luxurious and gazettes like mobiles, calculator, tabs, and paper screen are in full use. But all of them required a power source like battery, fuel cell, and capacitors. So power sources having high capacity are desirable. Many researchers are working in this direction to enhance the properties (storage capacity, life cycles) of power sources like battery, fuel cell and super capacitor. There can be no hesitation if we can say that the demand of electricity will increase in future and humans completely depend on it. In present day's batteries offer a high energy which makes life easier and handier, so use of batteries will likewise increase. Enormous use of fossil fuels leads to the greenhouse effect and environment degradation and one need to aware about these harmful

effects. We have to follow technological development that uses limited energy resources more efficiently and reduces the burden on the environment. Fossil fuels are the lifeline for vehicles including surface transport and other utilities [9]. To increase the conductivity of the materials, we coat it with the thin film of carbon. It increases the cycling and safety of the battery and helps to prevent internal corrosion of the electrodes and electrolyte. The thin film provides more surface area for the intercalation of ions or electrons and increases the charging and discharging rate of battery.

2 Experimental Work

2.1 Materials

Poly (ethyl oxide) (PEO) as purchased from sigma Aldrich with average molecular weight of 600,000 and was used without further purification. Dissolved in acetonitrile, (<130 nm) were also purchased from sigma Aldrich, and salt $NaClo_4$.

2.2 Preparation of Polymer Electrolyte

Free standing polymer clay nanocomposite (PNCE) films were prepared using high purity (AR grade) poly (ethylene oxide) (PEO) from Aldrich (USA), salt ($NaClo_4$) from (M/s Across Organics) and $BaTiO_3$ supplied by the Clay Minerals Society (USA). T. PCNE films were prepared by a solution-casting technique with different weight ratios of modified $BaTiO_3$ clay. The host polymer (PEO) and salt ($NaClO_4$) were dissolved in acetonitrile at a constant ratio of ether oxygen to lithium ion (O/Na) $\sim$14:1 [10]. The polymer–salt solution was stirred for 8 h followed by the addition of $BaTiO_3$ clay. Subsequently, this viscous composite fluid was cast into a polypropylene dish and the solvent was allowed to evaporate slowly. The resulting free-standing clay based polymer nanocomposite (PNCE) films have the general formula PEO+$NaClO_4$ +wt% $BaTio_3$) where x varies from 0 (pure polymer–salt complex, (PS) to 20 wt% with respect to the host polymer (w/w) [11].

3 Experimental Technique

3.1 FTIR Spectroscopy

Fourier transform infrared spectroscopy (FTIR) Bruker Tensor-27 was used in the range from 4000 to 500 cm^{-1} in transmission mode. FTIR relies on the fact that the

most molecules absorb light in the infra-red region of the electromagnetic spectrum. This absorption corresponds specifically to the bonds present in the molecule [12]. The frequency range are measured as wave numbers typically over the range 4000–400 cm^{-1}. In FTIR the background emission spectrum of the IR source is first recorded, followed by the emission spectrum of the IR source with the sample in place. The ratio of the sample spectrum to the background spectrum is directly related to the sample's absorption spectrum. The resultant absorption spectrum from the bond natural vibration frequencies indicates the presence of various chemical bonds and functional groups present in the sample. FTIR is particularly useful for identification of organic molecular groups and compounds due to the range of functional groups, side chains and cross-links involved, all of which will have characteristic vibrational frequencies in the infra-red range was used to study the interactions between constituents of polymer and filler interactions [13]. Such interactions should be manifested through FTIR spectra as frequency shift, band intensity changes, splitting of bands and alterations of band shapes. The work was carried out using FTIR Bruker Tensor-27 in the range from 4000 to 400 cm^{-1} in transmission mode. Impedance spectroscopy is carried out by ch instrument 760. For this sample is placed between two electrodes.

3.2 Impedance/Dielectric Analysis

Complex impedance spectroscopy(CIS) is a most important tool used mostly used in characterize the microstructure and electrical property. It can be analysis of the a. c response of a system to sinusoidal perturbation and calculation of impedance resistance for an ac circuit as a function of frequency. This spectroscopy is also very effective to study properties of intragranular and interfacial regions and their interrelations, their temperature and frequency dependent phenomena in order to separate the individual contributions from the total impedance and their interfaces with electronically conducting electrode [14, 15]. Also, it enables us to calculate the relaxation frequency, which is an intrinsic property of the sample, independent of its geometrical factors. Apart from these it also helps us to find

(i) a.c and d.c conductivity
(ii) Dielectric constant
(iii) Dielectric loss (tan δ) the frequency dependence of various impedance parameters of a material can be described via the complex permittivity (ε^*), complex impedance (Z*), complex admittance (Y*), complex electric modulus (M*) and dielectric loss or dissipation factor (tan δ). They are in turn related to each other as follows:

$$\textit{Complex Impedance}:\ \mathrm{Z}(\omega) = \mathrm{Z}' - \imath\,\mathrm{Z}'' = \mathrm{Rs} - \mathrm{j}/\omega\, C_s$$
$$\textit{Complex Admittance}:\ Y(\omega) = Y' + jY'' = \tfrac{1}{Rp} + j\omega Cp = G(\omega) + jB(\omega)$$
$$\textit{Complex Modulus}:\ M(\omega) = \tfrac{1}{\varepsilon(\omega)} = M' + jM'' = j\omega C_o Z(\omega)$$
$$\textit{Dielectric Constant}:\ \varepsilon(\omega) = \varepsilon' - j\varepsilon''$$
$$\textit{Loss Tangent}:\ \tan\delta = \tfrac{\varepsilon''}{\varepsilon'} = \tfrac{M''}{M'} = -\tfrac{Z'}{Z''} = \tfrac{Y'}{Y''}$$
$$\textit{Complex Resistivity}:\ \rho(\omega) = \rho' - j\rho'' = Z \times \left(\tfrac{C_o}{\varepsilon_o}\right)$$
$$\textit{Complex Conductivity}:\ \sigma(\omega) = \sigma' - j\sigma'' = Y \times \left(\tfrac{\varepsilon_o}{C_o}\right)$$

where square root of C_o Is vacuum capacitance of the cell, G is conductance and B is susceptance, now the subscripts s and p for series parallel combination of the circuits elements, respectively. Out of these parameters, the impedance and admittance plane representation provide useful information when various within the cell have different relaxation time as in the case of the solid electrolytes cells.

4 Result and Discussion

In this chapter effect of adding $BaTio_3$ with varying weight percent from nano filler on polymer have been discussed in this chapter (nanocomposite where x = 0, 1, 2, 5, 7, 10, 15, 20 and have been done from various characterizing techniques. Results obtained from FTIR, impedance spectrometer, in this chapter.

4.1 Fourier Transform Infrared (FTIR) Analysis

Fourier transform infrared (FTIR) spectroscopy has been used to probe the possibility of interaction among the composite components at the microscopic level. The FTIR spectrum of PNC films based on PEO + $NaClO_4$ + wt% $BaTio_3$ with different oregano clay concentrations (0, 1, 2, 5, 7, 10, 15 and 20) in the wavenumber region (400–4000 cm^{-1}). The characteristic absorption peak observed in the spectral pattern at the wavenumber 630, 957, 1107, 1294, 1340, 1481, 1645, 1982, and 2640 cm^{-1} are attributed to ClO_4, $\gamma(CH_2)_a$, $\gamma(CH_2)_a$, $\gamma(COC)_S$, $(CH_2)_s$, $w(CH_2)$, $\delta(CH_2)_s$, C=O and assemtric C–H stretching respectively. The detailed assignment of the experimentally observed FTIR bands and effect of clay on changes in their. It appears that even at a very low filler concentration, the fraction of free anion and hence free cation available in the PNC matrix appears to be more when the data is compared with that of pure polymer salt (PS) complex provides a clear picture of enhancement in the available free charge carrier (Na^+ ions) on immediate addition of

filler (5 wt%) into the polymer salt complex matrix. The fraction of free anion and hence fraction of free cations for various filler concentration. A comparison indicates relatively higher fraction of free charge carriers at 15 wt% filler concentration. Beyond this, the free anion these results clearly suggest convincing evidence for filler assisted ion dissociation effect in the polymer nanocomposite films [16–17]. This feasibility due to stronger filler ion interaction seems logical in view of the dipolar characteristics of $BaTiO_3$ filler. The variation in free anion fraction with filler concentration is expected to have a direct impact on electrical transport. Such fraction gets reduced however, the available free charge carrier is still more in the composite film in comparison to that of the pure polymer salt (Fig. 1 and 2, Table 1).

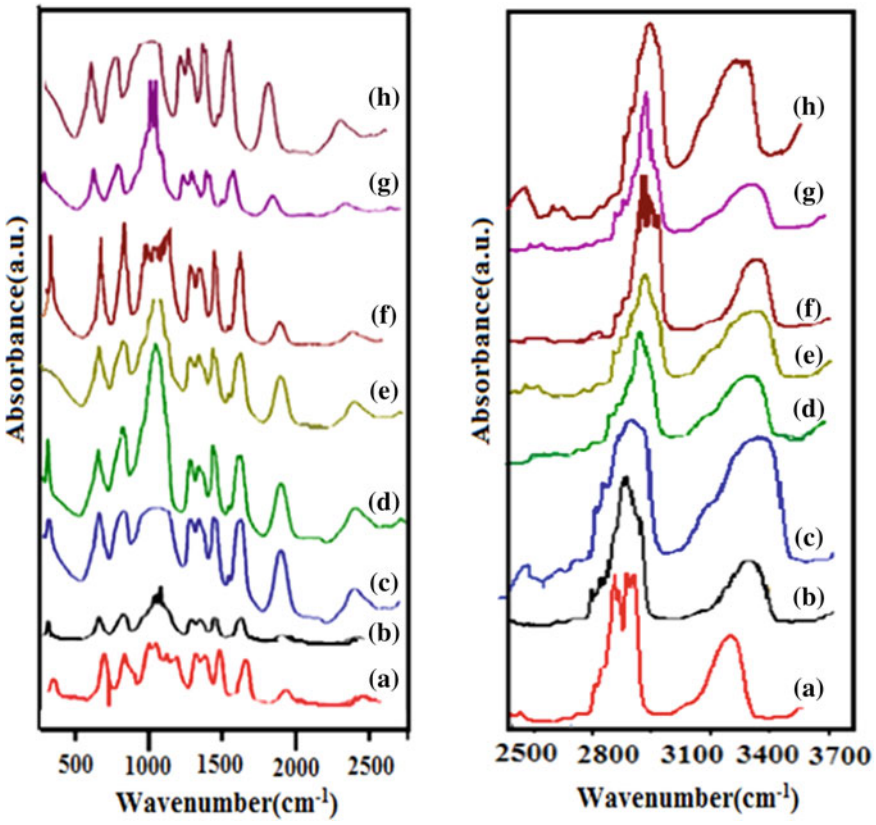

Fig. 1 FTIR spectrum for polymer electrolyte films *(PEO)$_{14}$NaClO$_4$ + x wt% BaTiO$_3$* (x = 0, 1, 2, 5, 7, 10, 15, 20)

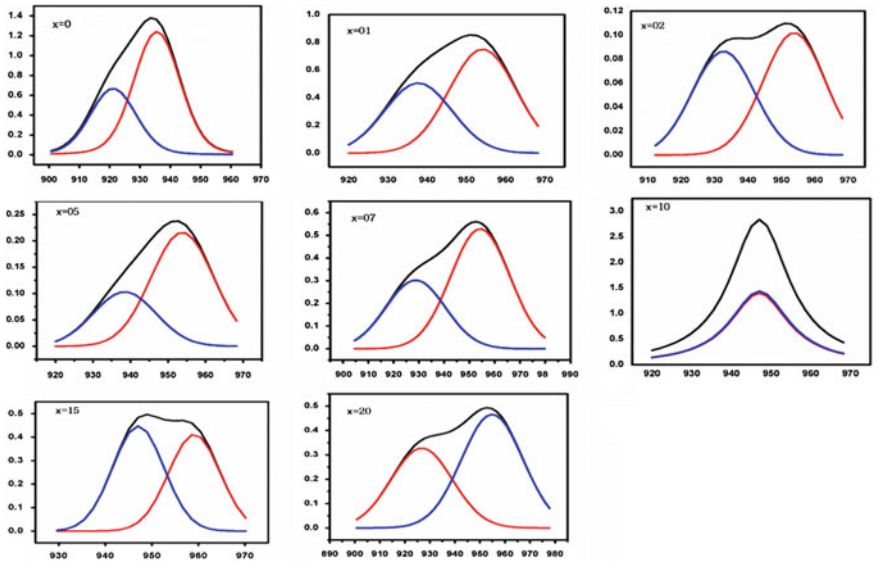

Fig. 2 deconvolution pattern of ClO_4^- in *(PEO)$_{14}$NaClO$_4$ + x wt% BaTiO$_3$* (x = 0, 1, 2, 5, 7, 10, 15, 20)

Table 1 Band Assignment of free standing PNC films comprising of $(PEO)_{14}NaClO_4$ + x wt% $BaTiO_3$

wt% of $BaTio_3$	Free ion position	% Area	Ion pair position	% Area	Correlation coefficient
00	921	30	953	69	0.99692588
01	938	40	953	59	0.98261451
02	932	45	954	54	0.92931351
05	928	32	951	67	0.95760567
07	929	36	953	63	0.97196511
10	931	22	946	77	0.92962323
15	931	31	954	68	0.98141858
20	935	41	958	58	0.95905313

5 Conductivity

PEO-based polymer electrolyte systems with various weight percent's of $NaClo_4$ have been synthesized using solution casting technique. The system with 15 wt% $Batio_3$ exhibits a maximum conductivity of 10^{-4} Scm^{-1} at room temperature. The temperature dependence of ionic conductivity of the electrolytes obeys the VTF relationship [18]. At the molecular level, FTIR studies provide strong evidence that

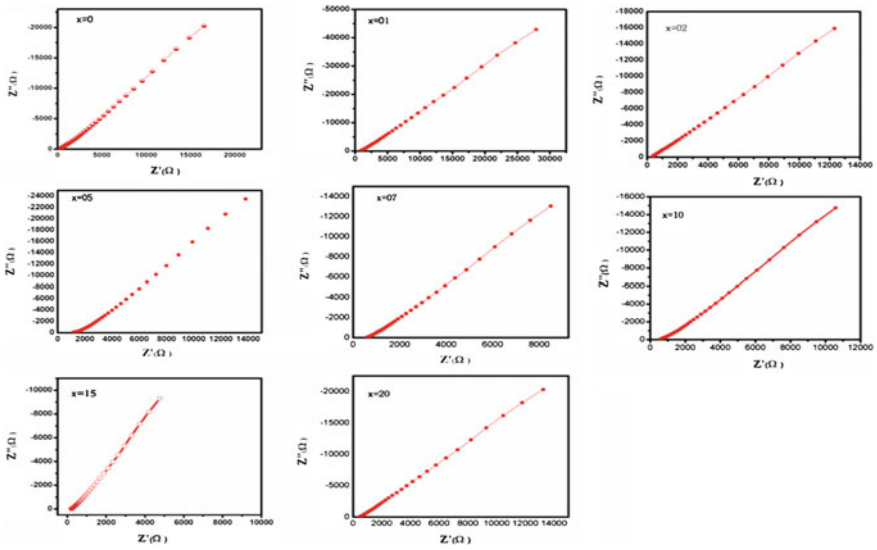

Fig. 3 Impedance plot at room temperature of $(PEO)_{14}NaClO_4$ + *wt% BaTiO*$_3$ (x = 0, 1, 2, 5, 7, 10, 15, 20)

Table 2 Conductivity values of SPEs based on PEO-$NaClO_4$ + $BaTiO_3$

Polymer electrolyte	Nano filler (x wt% of $BaTio_3$)	Conductivity (s/cm^{-1})
PEO + $NaClO_4$	0	5.7×10^{-6}
PEO + $NaClO_4$	1	7.2×10^{-6}
PEO + $NaClO_4$	2	1.2×10^{-5}
PEO + $NaClO_4$	5	6.5×10^{-6}
PEO + $NaClO_4$	7	1.2×10^{-5}
PEO + $NaClO_4$	10	1.2×10^{-5}
PEO + $NaClO_4$	15	1×10^{-4}
PEO + $NaClO_4$	20	3×10^{-5}

there is a specific interaction between PEO, $NaClo_4$ and $BaTio_3$. The change in peak intensity, shape and position confirms the complexation process of PEO+ $NaClo_4$ + $BaTiO_3$ systems [19–21] (Fig. 3 and Table 2).

6 Conclusions

PEO-based polymer electrolyte systems with various weight percent's of $NaClO_4$ have been synthesized using solution casting technique. The system with 15 wt% $Batio_3$ exhibits a maximum conductivity of 10^{-4} Scm^{-1}at room temperature. The temperature dependence of ionic conductivity of the electrolytes obeys the VTF

relationship. At the molecular level, FTIR studies provide strong evidence that there is a specific interaction between PEO, $NaClO_4$ and $BaTio_3$. The change in peak intensity, shape and position confirms the complexion process of PEO–$NaClO_4$–$BaTiO_3$ systems.

Acknowledgments Author (P.K. Sharma) is thankful to UGC, New Delhi for providing fellowship during M.Phil. One of the authors (A.L. Sharma) is grateful UGC, New Delhi for providing the Start-up-Grant (GP-41).

References

1. A.L. Sharma, A.K. Thakur, P **19**(5), 795–809 (2013)
2. S. Ramesh, K. Ramesh, A.K. Arof, Int. J. Electrochem. Sci. **8**, 8348–8355 (2013)
3. A.K. Mikitaev, M.K. Ligidov, G.E. Zaikov (eds.), *Polymers, Polymer Blends, Polymer Composites and Filled Polymers: Synthesis* (Nova Publishers, Properties and Applications, 2006)
4. A.L. Sharma, A.K. Thakur Ionics, **21**(6), 1561–1575 (2015)
5. A. Manuel Stephan, Eur. Polym. J. **42**(1), 21–42 (2006)
6. R.R. Parajuli, Developing conducting polymer nanocomposite with carbon nanomaterials for molecular detection and fuel cell applications (Doctoral dissertation, Rutgers University-Graduate School-Newark), 2011
7. D.E. Fenton, J.M. Parker, P.V. Wright, Polymer **14**(11), 589 (1973)
8. J.R.M. Giles, F.M. Gray, J.R. MacCallum, C.A. Vincent, Polymer **28**(11), 1977–1981 (1987)
9. B. Scrosati, F. Croce, S. Panero, J. Power Sources **100**(1), 93–100 (2001)
10. G. Girish Kumar, N. Munichandraiah, Electrochem. Acta **47**(7), 1013–1022 (2002)
11. A.L. Sharma, A.K. Thakur, J. Appl. Polym. Sci. **118**(5), 2743–2753 (2010)
12. R. Prucek, J. Tucek, M. Kilianova, A. Panacek, L. Kvitek, J. Filip, M. Kolar, K. Tomankova, R. Zboril, Biomaterials **32**(21), 4704–4713 (2011)
13. J. Zhang, H. Han, S. Wu, S. Xu, Y. Yang, C. Zhou, X. Zhao, Solid State Ionics **178**(29), 1595–1601 (2007)
14. Z.H. Li, H.P. Zhang, P. Zhang, Y.P. Wu, X.D. Zhou, J. Power Sources **184**(2), 562–565 (2008)
15. A.L. Sharma, A.K. Thakur, Ionics **17**(2), 135–143 (2011)
16. A. Abdullah, S.Z. Abdullah, A.M. Ali, T. Winie, M.Z. Yahya, R.H. Subban, Mater. Res. Innov. **13**(3), 255–258 (2009)
17. S. Ramesh, L.C. Wen, Ionics **16**(3), 255–262 (2010)
18. C. Tang, K. Hackenberg, Q. Fu, P.M. Ajayan, H. Ardebili, High ion conducting polymer nanocomposite electrolytes using hybrid nano fillers. Nano Lett. **12**(3), 1152–1156 (2012)
19. C. Bhatt, R. Swaroop, A. Arya, A.L. Sharma, J. Mater. Sci. Eng. B **5**(11–12), 418–434 (2015)
20. A. Arya, A.L. Sharma, Appl. Sci. Lett. **2**(2), 72–75 (2016)
21. A.L. Sharma, A.K. Thakur , J. Appl. Polym. Sci. **118**(5), 2743–2753 (2010)

Improved Electrical and Thermal Properties of TETA Functionalized NGPs/Epoxy Nanocomposites

Payal Mazumdar and Sunita Rattan

Abstract The present work reports the synthesis of nanocomposites (NCs) prepared by amine functionalization of nanographite platlets (NGPs) coupled with diglycidyl ether of bisphenol A (DGEBA) epoxy resin. NGPs were treated with 3:1 mixture of concentrated H_2SO_4/HNO_3, and then grafted with triethylene-tetramine (TETA) that contributes uniform dispersion of NGPs within the epoxy matrix. In particular, the amine functionalization of NGPs with triethylene-tetramine (TETA) purposed to attain better dispersion and strong interfacial interaction between the filler and the matrix. The TETA functionalized NGPs/epoxy nanocomposites (DGEBA/TETA-NGPs) were produced by molding curing method. The synthesized nanocomposites were characterized by FTIR and SEM techniques. The electrical and thermal properties of the nanocomposites at various TETA-NGP loadings were investigated and found to attain an increase in the conductivity and thermal stability compared with that of neat epoxy resin.

1 Introduction

Carbon fillers have gained high importance for their exceptional electrical, mechanical and thermal properties. Polymer nanocomposites reinforced with carbon fillers have been investigated for numerous potential applications [1]. In particular, the epoxy composites are extensively used for aerospace application, electronic materials and many other industrial applications [2]. Moreover, the synergistic effect between the epoxy matrix and the carbon filler can generates a superior nanocomposite material which hold the promise of providing high mechanical strength, lightweight, flexibility and multifunctional properties. However, the challenges faced while incorporating the carbon filler into the epoxy matrix are phase separation, aggregation, lack of interfacial bonding, poor

P. Mazumdar · S. Rattan (✉)
Amity Institute of Applied Sciences, Amity University Uttar Pradesh,
Sec-125, Noida, India
e-mail: srattan@amity.edu

V.K. Jain et al. (eds.), *Recent Trends in Materials and Devices*,
Springer Proceedings in Physics 178, DOI 10.1007/978-3-319-29096-6_53

dispersion and adhesion within the matrix. These problems can be overcome by functionalization of the reinforced carbon filler, which provides multiple bonding sites without affecting the desired properties to make them simply dispersible in the polymer matrix [3]. So far, various physical and chemical methods of carbon filler functionalization have been reported. Among them, the chemical modification by reactive functional group mainly the amine-functionalization of the carbon filler are much researched because of the high reactivity of the amine group to enhance the interfacial adhesion and homogeneous dispersion of the filler into the matrix [4, 5]. The chemical functionalization was proposed to provide the stable covalent bond between the filler and the matrix as compared to the weak Vander wall interaction acquired by non-functionalized filler. Moreover, after amine functionalization the hydrophobic carbon filler become more hydrophilic in nature due to presence the amine functional groups and can easily react with the functional groups present in the epoxy matrix [6].

In the present study efforts have been made to synthesize epoxy nanocomposite using nanographite platlets (NGPs) as filler and Bisphenol A diglycidyl ether (DGEBA) epoxy as matrix. The NGPs after the acid treatment were functionalized by the amine groups using triethlyenetetramine (TETA). Epoxy based nanocomposites were prepared by molding curing method. The main objective of the paper is to study the influence of the TETA functionalized NGPs on the covalent interaction and their effect on the electrical and thermal properties of the composite (DGEBA/TETA-NGPs) at various TETA-NGPs loadings. The morphology of the composites was analyzed. The development of such material has significant potential for various engineering application.

2 Experimental Details

2.1 Materials and Characterization

The natural graphite was purchased from (Asbury Carbon Inc) to prepare NGPs. Bisphenol A diglycidyl ether (DGEBA, Sigma-Aldrich), triethyltetramine (TETA, Sigma-Aldrich, 99 %), thionyl chloride ($SOCl_2$, Sigma-Aldrich, 97 %), sulphuric acid (H_2SO_4, Merck), Nitric acid (HNO_3, Merck) were used as received.

FTIR spectra were recorded using KBr pellet on a Nicolet 5700 FTIR spectrophotometer from 400 to 4000 cm^{-1} wave number at room temperature. The spectra were collected with a resolution of 4 cm^{-1} performing 32 scans. The morphology of the NGPs and epoxy nanocomposite samples were determined by scanning electron microscopy (SEM) [SEM, Zeiss (MA EVO-18 Special Edition)]. The sample preparation was executed by dispersion of the material in ethanol using ultra-sonication. The samples were gold coated after placing the small drop of suspended material on the silicon wafers. The thermal stability of the samples were measured by thermogravimetric analyzer (Mettler Toledo TGA/SDTA 851e) at

temperature range of 25–700 °C under an inert atmosphere (flowing N_2 gas). The standard two-probe technique (Keithley programmable current source-model 6517 B) was used to measure the conductivity of the films at room temperature. The rectangular films of (2 cm × 2 cm) were prepared for electrical measurement and the ohmic contacts were made on the films by using the silver paste.

2.2 Acid Treatment of NGPs

NGPs were prepared by the modified Hummer's method as reported earlier by our group [7]. In a round bottom flask the pristine NGPs flakes were first treated with nitric acid (20 ml, 50 wt%). After 40 h reflux, the mixture was cooled at room temperature. Enormous amount of de-ionized water was diluted in the resulting mixture and then filtered using vacuum pump. The mixture was washed numerous times using de-ionized water until the pH reached 7, and then dried at 110 °C for 2 days under vacuum. The acid modified NGPs were obtained by 5 h ultrasonication of unmodified NGPs (U-NGPs) with H_2SO_4/HNO_3 with (3:1) volume ratio at room temperature. The resulting solution was filtered and washed several times with deionized water till the solution pH reached neutral. Then the mixture was dried at 60 °C in vacuum and the A-NGPs were obtained.

2.3 TETA Modification of NGPs

The acid treated NGPS (A-NGPs) were functionalized with thionyl chloride for acylation. The reaction was performed with the treatment of thionyl chloride along with the DMF (N, N dimethyl formamide) solvent, and the mixture was allowed to stir at 70 °C and refluxed for 24 h. After the acyl functionalization, the solution was washed and extracted with anhydrous THF. The material was then dried and the solvent was evaporated in vacuum at 60 °C. The resulting acyl-chlorinated NGPs (AC-NGPs) were obtained. The surface acylated NGPs (AC-NGPs) were further treated with TETA at 100 °C for 96 h for amine functionalization. The mixture attained was washed by anhydrous ethanol to remove excessive TETA within the amine functionalized NGPs, and then filtered and dried in vacuum for 24 h. The TETA functionalized NGPs were then obtained.

2.4 Preparation of TETA-NGPs/DGEBA Composites

The composite of functionalized NGPs and epoxy matrix was prepared by molding curing method. In a typical experiment a 100 ml flask charged with proper amount of TETA-NGPs was dispersed in acetone. After 40 min sonication at room

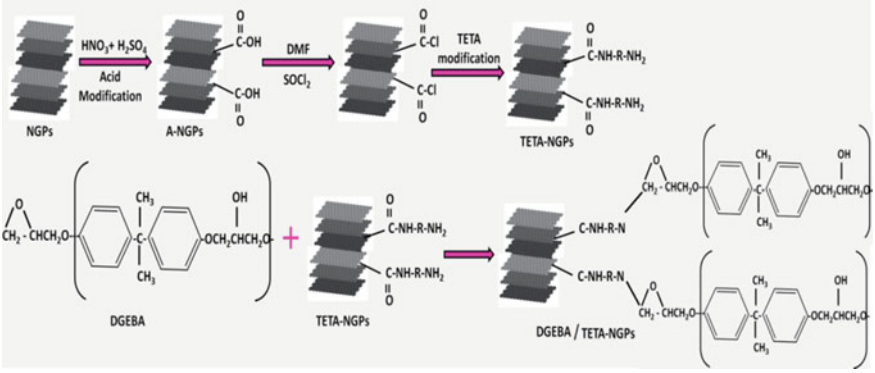

Scheme 1 Schematic illustration of the synthesis of DGEBA/TETA-NGP

temperature, epoxy resin (DGEBA) was added to the black suspension. The reaction mixture was ultrasonicated at 50 °C until the acetone was removed completely. After stirring for 1 h, 10 % TETA curing agent was added and further stirring was performed in a magnetic stirrer for 6 h. The reaction mixture was degassed for 0.5 h to remove bubbles in a vacuum oven. After degasification, the reaction mixture was quickly poured into the stainless steel molds which were coated with the mold releasing agent. The curing time of 2 h at 50 °C and 2 h at 100 °C was obtained by the mixture in an oven. The epoxy nanocomposite was prepared at various compositions by varying the TETA-NGPs loadings (1, 2, 3, 4 and 5 %) in the epoxy matrix (DGEBA). Thus the modified TETA-NGPs/DGEBA were obtained at various TETA-NGPs loadings. The process of synthesis for preparing TETA-NGPs/DGEBA was depicted in Scheme 1.

3 Results and Discussion

3.1 Fourier Transform Infra-red Spectroscopy (FTIR)

In Fig. 1 the NGP shows characteristic absorption bands at 3430, 1635 and 1500 cm^{-1} which is attributed to hydroxyl group, C=C and deformed C–C bond, receptively. The TETA modified NGPs shows the band at 1610 cm^{-1} corresponds to the absorption of –NH bending and stretching. Whereas the –C=O stretching was obtained at 1650 cm^{-1} [8]. In addition, a strong peak at 1130 cm^{-1} is attributed to the existence of—CN stretching in TETA functionalization. Moreover, a distinct peak at 3100 cm^{-1} reveals the stretching of amide groups ($–NH_2$) [9]. However, in the case of DGEBA/TETA-NGPs, there are characteristic peaks of DGEBA at 2935, 2846, 1432 and 1385 cm^{-1} which is due to the symmetric and asymmetric vibration of methylene and the absorption of benzene ring of DGEBA molecule. A prominent peak at 1715 cm^{-1} confirms the existence of C=O bond of ester,

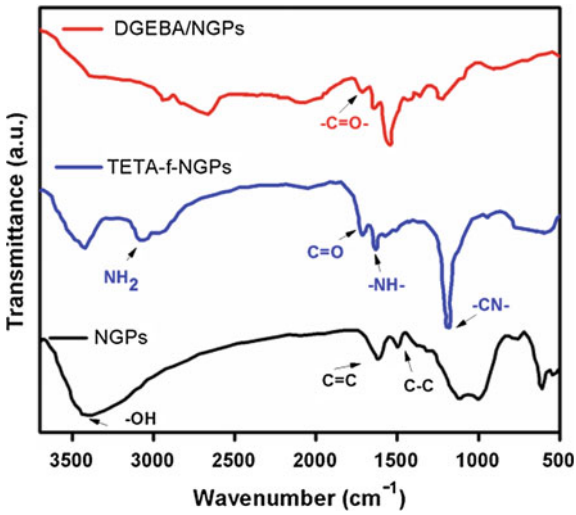

Fig. 1 FTIR spectra of **a** Pristine NGPs **b** TETA-f-NGPs **c** DGEBA/TETA-NGPs

indicating the presence of covalent ester bond after grafting with functionalized TETA-NGPs. The results of FTIR indicate the successful synthesis of DGEBA/TETA-NGPs through strong covalent interaction between the amine functionalized NGP and DGEBA molecules.

3.2 Scanning Electron Microscopy (SEM)

The morphology of the NGPs and the TETA-NGPs/DGEBA within the epoxy matrix were observed by using SEM analysis. Figure 2a shows the SEM micrograph of the pristine NGPs depicting bare flat and flaky structure of the layered graphene sheets. A strong interconnected structure due to the dispersion of TETA functionalized NGPs within the DGEBA matrix was observed for TETA-NGPs/DGEBA in Fig. 2b.

3.3 Electrical Conductivity

The conductivity of the TETA-NGPs/DGEBA films at various TETA-NGPs loadings was measured at room temperature with a potential window from −10 to 10 V. The variation of the electrical conductivity of the epoxy nanocomposites as a function of NGP wt% at room temperature is shown in Fig. 3. The conductivity of DGEBA/TETA-NGPs increased from 5.2×10^{-15} S/cm for neat epoxy to 1.4×10^{-3} S/cm for 5 wt% TETA-NGPs loadings. The conductivities of the DGEBA/TETA-NGPs nanocomposites increases with the increase in the

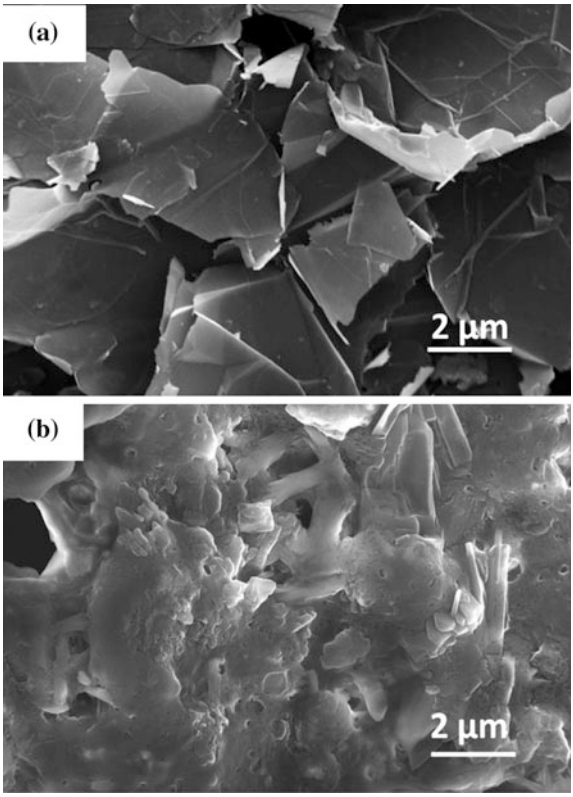

Fig. 2 SEM image of **a** Pristine NGPs and **b** TETA-NGPs/DGEBA

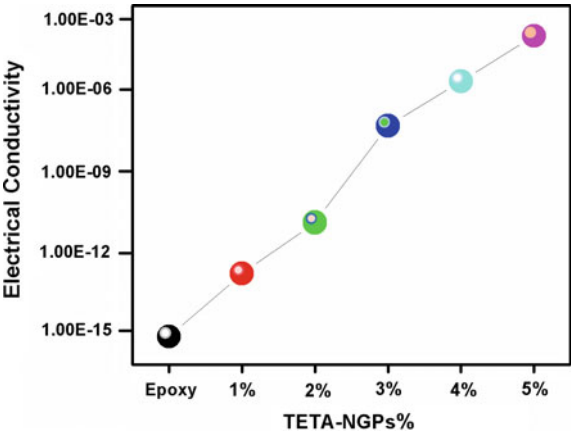

Fig. 3 Variation of electrical conductivity at various TETA-NGPs loadings

TETA-NGPs content in wt% and then levels off at 5 wt% of NGPs loadings. Consequently adding more nanofiller did significantly alter the resistance. This shows that the amine functionalization of NGPs facilitates the homogeneous dispersion within the DGEBA matrix which resulting into the formation of conductive networks and hence increase in the electrical conductivity of the composite [10]. Moreover on increasing the filler concentration, more charge carriers may be able to "hop" by tunneling, resulting in increase in electrical conductivity. The critical nanofiller content above which sharp increase in electrical conductivity occurs is known as "percolation threshold". According to the percolation theory, the percolation threshold is the certain critical concentration of nanofiller at which a conductive path is formed within the composite which exhibits the transition of the material from non-ohmic to ohmic conduction. TETA-NGPs/DGEBA exhibits electrical percolation around 3 wt% of TETA-NGPs loadings after which electrical conductivity increases sharply.

3.4 Thermogravimetric Analysis (TGA)

Thermogravimetric analysis (TGA) under N_2 atmosphere was used to investigate the thermal stability of the TETA-NGPs/DGEBA composite. Figure 4 shows the TGA spectra of NGPs, pure DGEBA and TETA-NGPs/DGEBA. NGP shows initial decomposition at 100 °C and becomes rapid at 150 °C then the major mass loss occurs at 460 °C where it decomposes completely which is presumably due to the pyrolysis of labile oxygen-containing groups such as –OH, COOH etc. Pure DGEBA epoxy decomposes at 280 °C and begins degradation at 460 °C, which is ascribed to the main-chain pyrolysis. The TETA-NGP/DGEBA begin to

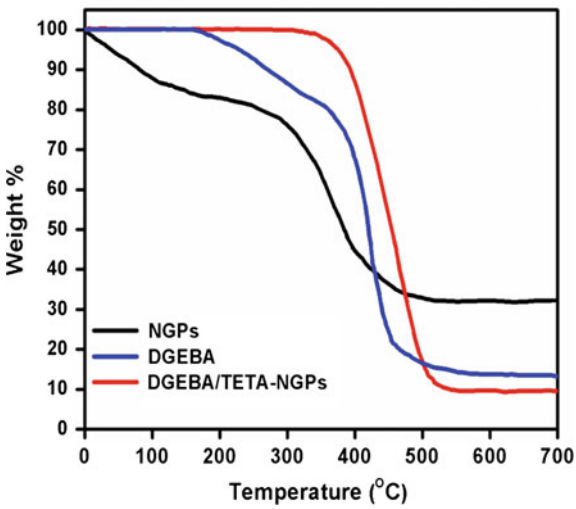

Fig. 4 TGA spectra of NGPs, pure DGEBA and TETA-NGPs/DGEBA

decompose at higher temperature (360 °C) as compared to that of pure DGEBA at (280 °C). This remarkable improvement in the thermal stability of the TETA-NGPs/DGEBA composite is due to the strong covalent interaction between the TETA functionalized NGPs and DGEBA. The amine functionalized NGPs in the composite act as a physical barrier which delays the degradation. Moreover, the ultrahigh aspect ratio of the filler could create a tortuous path for the volatile degradation products. The slow degradation of the epoxy chains that absorbed at the matrix filler interface may also contribute to the enhanced thermal stability of the TETA-NGP/DGEBA nanocomposites [11].

4 Conclusions

In the work, TETA functionalized NGPs was successfully attached to the epoxy DGEBA with molding curing method. The uniform dispersion of the functionalized NGPs in the DGEBA matrix was demonstrated by SEM morphology. The homogeneous dispersion and the strong interfacial bonding of TETA modified NGPs and DGEBA at different loadings are supportive to improve the electrical properties by forming conducting pathway within the matrix. A remarkable thermal property of TETA-NGPs/DGEBA nanocomposite was obtained with 5 wt% of TETA-NGPs loadings due to the strong covalent interaction of TETA-NGPs and DGEBA matrix which act as a physical barrier to delay the degradation. The proposed reinforcement of TETA functionalized NGP filler into the DGEBA matrix significantly improve the electrical and thermal properties of the composite.

References

1. T. Ramanathan, A.A. Abdala, S. Stankovich, D.A. Dikin, M. Herrera-Alonso, R.D. Piner, D. H. Adamson, H.C. Schniepp, X. Chen, R.S. Ruoff, S.T. Nguyen, I.A. Aksay, R.K. Prud'Homme, L.C. Brinson, Nat. Nanotechnol. **3**, 327–331 (2008)
2. J. Jia, X. Sun, X. Lin, X. Shen, Y. Mai, J. Kim, ACS Nano **8**, 5774–5783 (2014)
3. S.H. Park, P.R. Bandaru, Polymer **51**, 5071–5077 (2010)
4. H. Ribeiro, W.M. Silva, M.F. Rodrigues, J.C. Neves, R. Paniago, C. Fantini, H.D.R. Calado, L.M. Seara, G. Goulart Silva, J. Mater. Chem. **48**, 7883–7892 (2013)
5. Q. Zehua, W. Guojian, J. Appl. Poly. Sci. **124**, 403–411 (2012)
6. J. Langea, B. Nicolasa, J. Galy, J.-F. Gerar, Polymer **43**, 5985–5994 (2002)
7. P. Mazumdar, S. Rattan, M. Mukherjee, RSC Adv. **5**, 69573–69582 (2015)
8. J.F. Shen, W.S. Huang, L.P. Wu, Mater. Sci. Eng. A **464**, 151–156 (2007)
9. J.Z. Kovacs, B.S. Velagala, K. Schulte, W. Bauhofer, Compos. Sci. Technol. **67**, 922–928 (2007)
10. J. Karippal, H.N. Narasimha Murthy, K.S. Rai, M. Krishna, M. Sre jith, Polym. Bull. **65**, 849–861 (2010)
11. F. Jin, C. Ma, S. Park, Mater. Sci. Eng. A **528**, 8517–8522 (2011)

Polypropylene/Glass Fiber Composites for Low Cost Orthotic Aid

Prachi Singhal, Sonu Raghavan, Sunita Rattan and R.K. Diwan

Abstract Orthotic aid is an externally applied device used to modify the structural and functional characteristics of the neuromuscular and skeletal system. The orthotic devices are fabricated using polymer resins such as HDPE, polypropylene, acrylics etc. of which polypropylene (PP) is the most widely accepted material for this application. However, the limitations associated with polypropylene devices are decreased durability because of material tears or splits. In the present work, silanized glass fibers (GF) of varied length were used to reinforce and improve the performance of PP for fabricating polypropylene-glass fiber (PP-GF) composites through melt blending process, which provides high performance orthotic aid material with dramatic improvement in properties such as strength, stiffness, dimensional stability etc. Maleic anhydride grafted PP (PP-g-MAH) was used as compatibilizer to improve the compatibility between PP and silanized GFs in the composite. The PP-GF composites were characterized with Scanning electron microscopy (SEM) and Fourier Transform Infra Red spectroscopy (FTIR). Mechanical properties of PP-GF composites was investigated as per ASTM standards. Mechanical studies claimed that the hardness, tensile properties, of PP-GF composites increases over PP-resin, while elongation at break and impact strength decreases. Compatibilized PP-GF composites reinforced with 10 wt% GFs with elongation at break $\sim$50 % at room temperature, showed improved mechanical performance over PP resin, which makes them suitable material for developing orthotic aid. Thus, PP-GF composites will offer lighter, stronger orthotic devices at lower cost.

P. Singhal (✉) · S. Raghavan · R.K. Diwan
Directorate of Innovation and Technology, Amity University Uttar Pradesh, Sec-125, Noida, India
e-mail: psinghal2@amity.edu

S. Rattan
Amity Institute of Applied Sciences, Amity University Uttar Pradesh, Sec-125, Noida, India

V.K. Jain et al. (eds.), *Recent Trends in Materials and Devices*,
Springer Proceedings in Physics 178, DOI 10.1007/978-3-319-29096-6_54

1 Introduction

An Orthosis is an orthopedic appliance used to support, align, prevent, or correct deformities of a body part or to improve the function of moveable parts of the body. Thermoplastic resins offered relatively strong, light weight, easy to shape, mold, corrosion resistant orthotics [1]. Among various thermoplastic resins, Polypropylene (PP) in orthotics have been the target of extensive research, which possesses outstanding properties such as low density, crystalline, relatively high melting point, strength, easy thermoforming and impact resistant. Thus, a PP grade has been selected with good thermoforming and impact property. But, PP has limitations with respect to durability, poor melt strength and tendency to sag during thermoforming. The deterioration of PP orthotics over time causes the patient to face a rather expensive and time-consuming replacement process.

Fiber reinforced thermoplastics (FRTP) are the newer class of orthotic materials offering a versatile and economically viable solution to improve the performance of engineered plastics [2].

Various natural and synthetic reinforcement fibers are used such as flax, hemp, silk, jute, sisal, kenaf, glass, carbon etc. [3–6]. Among various natural and synthetic fibers, glass fibers are widely used due to their low-cost, easy availability and better physico-mechanical properties [7]. The mechanical properties of the polymer-GF composites are affected by interfacial adhesion between the GFs and polymer matrix, the length of the GF and their concentration in the composites. In the present work, short glass fibers of 3 and 6 mm have been used for reinforcement for random distribution of fibers within the matrix so that the composite can be used in any dimension.

The fiber dispersion in the polymer matrix is an important consideration in the processing of FRTPs. The surface adhesion between the polymer matrix and fibers plays an important role in the transmission of stress from matrix to the fibers and thus determine the mechanical properties of FRTPs [8]. A compatibilization strategy is used to make the two components of the composite compatible. The glass fibers have poor wettability with respect to the organic polymer matrices, thus APTMS (amino propyl tri-methoxy silane) silanzed glass fibers are used to achieve better adhesion between the fibers and the polymer matrix. Apolar polymers such as polypropylene has limited interaction with the surface treated glass fibers, thus polypropylene grafted maleic anhydride (PP-g-MA) has been used as an interfacial coupler between the polypropylene matrix and silanized glass fibers. Thus, the present work aims to develop low cost Polyproplene/glass fiber (PP-GF) composites with improved physico-mechanical properties for orthotic application.

2 Experimental Details

2.1 Materials

Polypropylene (PP) with grade Repol CO15EG from Reliance polymers with melt flow index of 1.8 g/10 min at 230 °C/2.16 kg is used as matrix resin. Silanized glass fibers of length 3 and 6 mm supplied by Vaani Fiber Glass, Delhi, are used as reinforcing fibers. The Polypropylene-grafted-Maleic anhydride (PP-g-MA) from Pluss Advanced Technologies Pvt. Ltd., Gurgaon is applied as compatibilizer.

2.2 Polypropylene-Glass Fiber (PP-GF) Composite Preparation

The Composites were prepared by blending glass fiber and polypropylene in pellets form using co-rotating twin-screw extruder (Thermo Haake poly Drive R600/610). The temperature used was 170 °C and rotor speed 50 rpm. The extruded specimen were injection moulded into dumbell-shaped specimens for mechanical tests. PP was first mixed with compatibilizer at 4 phr. The loading level of glass fibers is taken as 10 %. The samples were labelled according to the length of glass fiber used, GF loading level and use of compatibilizer and are tabulated in Table 1.

2.3 Materials Characterization

The morphology of blends was examined on the fractured surfaces of composites with Quanta 200 FEG scanning electron microscope to investigate the interfacial interaction between fibers and the matrix. The samples were sputter-coated with a fine layer of gold and analyzed. Prior to examination, specimens were sputter-coated with a fine layer of gold to render conductive the sample surface.

Table 1 Formulation of the prepared Polypropylene/glass fibre composites

	Polypropylene (phr)	Glass fiber-3 mm (phr)	Glass Fiber-6 mm (phr)	Compatibilizer (phr)
PP	100	–	–	–
PP-GF(3)	100	10	–	–
PP-GF(3)-comp	100	10	–	2
PP-GF(6)	100	–	10	–
PP-GF(6)-comp	100	–	10	2

FT-IR spectra of films of composites were recorded by means of a Perkin-Elmer spectrophotometer in the 4000–400 cm^{-1} frequency range to analyze the structural composition.

2.4 Mechanical Properties

Tensile tests of the composites were conducted by using an Instron 4411 Universal Testing machine. Tensile strength, modulus, impact and elongation at break were measured according to ASTM D 638-10 [ref ASTM]. The Izod impact measurements were performed according to ASTM D256. Average results from five dumbbell shaped samples were reported.

3 Results and Discussion

3.1 Scanning Electron Microscopy (SEM)

Figure 1a, b represented SEM images of fractured surfaces of PP-GF(3) and PP-GF (6) composites hich revealed poor adhesion between matrix and fibers. The addition of reactive compatibilizers to PP-GF composites determined a marked change in the morphology with improved interfacial adhesion and quite a diffused polymer-fiber interface as shown by SEM micrographs in Fig. 1c, d. The improved adhesion between the matrix and fibers is ascribed to the occurrence of chemical interactions between maleic anhydride (MA) group and the amino groups on the silanized fiber surface as depicted in Scheme 1.

The SEM analysis of PP-GF composites clearly indicated an improved compatibility of the fibers to the matrix as a consequence of the effective interactions at the interface in the presence of PP-g-MA compatibilizer.

3.2 Fourier Transform Infra-red Spectroscopy (FTIR)

Figure 2 represents and compares the FTIR spectra of PP-GF(3), PP-GF(3)-comp, PP-GF(6) and PP-GF(6)-comp composites. The presence of characteristic peaks at 2950 (asymmetric CH3 stretching vibration), 2918 (asymmetric CH2 stretching vibration), 2867 (symmetric CH3 stretching vibration), 2840 (symmetric CH2 stretching vibration), 1455 (is due to the overlapping of the asymmetric bending mode of the methyl (CH3) and the methylene (CH2) scissoring mode), 1375

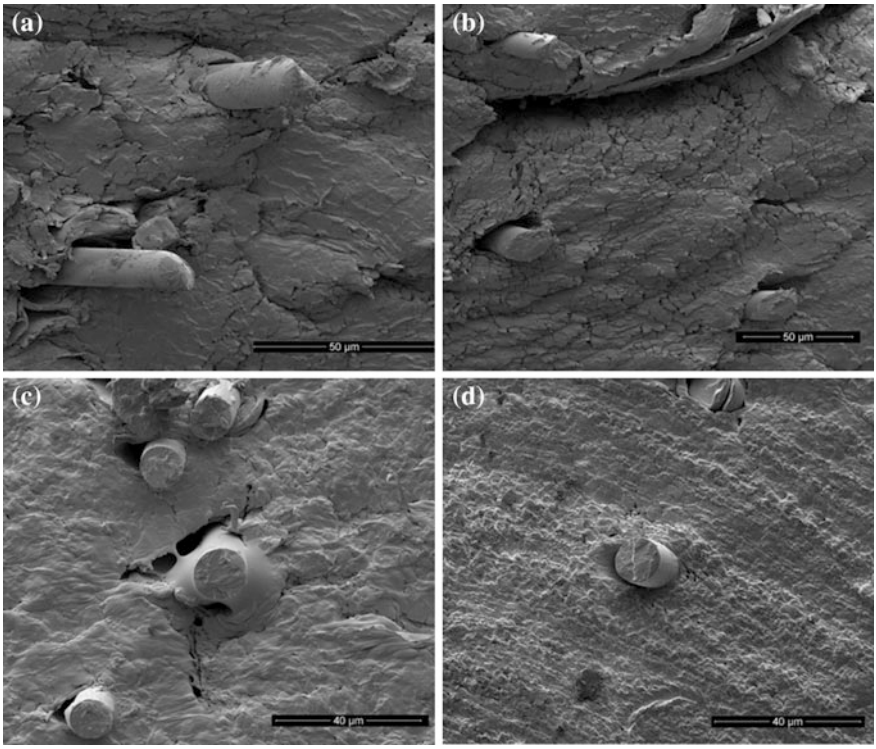

Fig. 1 SEM images of **a** PP-GF(3) **b** PP-GF(6) **c** PP-GF(3)-comp **d** PP-GF(6)-comp composites

(symmetric CH3 deformation), and 716 cm^{-1} (rocking vibrations of methylene groups 32) are attributed to polypropylene [9, 10]. The peaks around 800–900 cm^{-1} could be assigned to a Si–O–Si bond of silanized glass fiber [11]. The band at 1735 cm^{-1} corresponds to stretching of C=O in esters/carbonyl. The small peak around 1060 cm^{-1} are assigned to stretching of C–O and Si–O. In compatibilized PP-GF composites, no peak around around1100 cm^{-1} for C–O group, indicating good interaction between anhydride group of PP-g-MA and amino group of silanized glass fibers. The broad band between 3200 and 3600 cm^{-1} in uncompatibilized PP-GF composites is assigned to the stretching vibration of OH and/or NH present on the silanized glass fibers [12]. A decrease in the intensity of this band in compatibilized PP-GF composites was observed, indicating that the hydroxyl and amino group contents in glass fiber were reduced in composites with compatibilizer (PP-g-MA). Absorption peak at around 1720 cm^{-1} which is characteristic absorption of C=O (stretching) of amide group formed as a result of interaction between amino group at silanized glass surface and anhydride group of PP-g-MA.

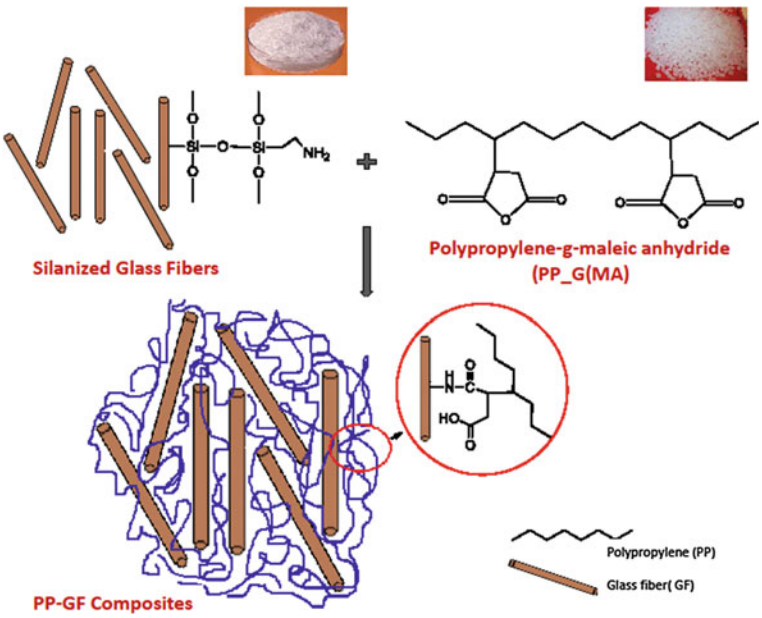

Scheme 1 Schematic representation of reaction between silanized glass fibers and maleic anhydride grafted PP on the polymer-fiber interactions at the surface of PP-GF composites

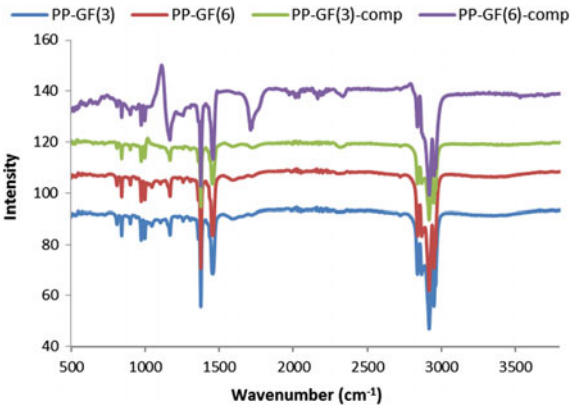

Fig. 2 FTIR of PP-GF composites with 3 and 6 mm glass fibers with and without compatibilizer

3.3 Mechanical Properties

The tensile strength, tensile modulus, impact strength and elongation at break of PP-GF composites with 3 and 6 mm glass fibers, with and without using compatibilizers are discussed.

3.3.1 Tensile Strength

The values of tensile strength for PP-GF(3), PP-GF(6), PP-GF(3)-comp and PP-GF (6)-comp composites are compared in Fig. 3. The figure shows that tensile strength is increased by 18 and 22 % in PP-GF(3) and PP-GF(6) composites respectively over pure PP resin. The silanized glass fiber incorporation in the thermoplastic PP matrix has induced better tensile strength in PP-GF composites over pristine PP because of the stiffness of the reinforced glass fibers. Although there is an interface between both components, observed by SEM, what indicates a low compatibility between them. To improve the interaction tween the two components of the composite, PP-g-MA was added as coupling agent. It is evident that the tensile strength was increased further in PP-GF composites compatibilized by PP-g-MA. There is increase in tensile strength by 27 and 33 % in PP-GF(3)-comp and PP-GF (6)-comp composites respectively over virgin PP. The significant increase in tensile strength of compatibilized composites is due to better adhesion of the glass fiber to the PP resin in presence of compatibilizer as depicted in SEM images, which makes it possible for stress transfer from the weaker plastic matrix to the stronger glass fiber during loading, thereby improving the strength of the composites [12]. This demonstrates the strong interactions between the aminopropyl groups of the silanized GF and the maleic anhydride groups of PP-g-MA and therefore better adhesion between the reinforcing agent and polymer matrix due to the formation of strong hydrogen bonds. The positive effect of the simultaneous use of PP-g-MA and silanized-GF is proved by comparing the tensile strength of PP-GF(3)-comp and PP-GF(6)-comp composites with the PP-GF(3) and PP-GF(6) composites.

3.3.2 Tensile Modulus

The values of tensile modulus for PP-GF(3), PP-GF(6), PP-GF(3)-comp and PP-GF (6)-comp composites are compared in Fig. 4. Tensile strength of PP-GF(3) composite is increased by 18 and 31 % in PP-GF(6) composites over pure PP. Further, there is an increase of 148 % in compatibilized PP-GF(3)-comp composite and

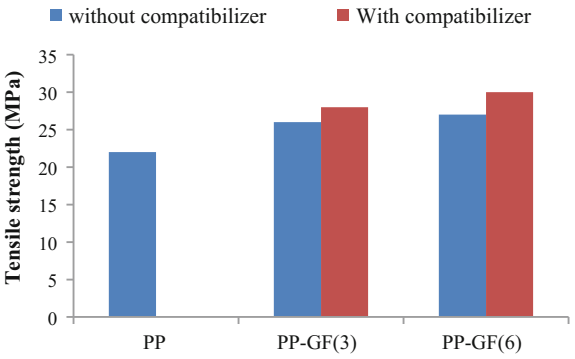

Fig. 3 Tensile strength of neat PP, PP-GF composites with and without compatibilizer

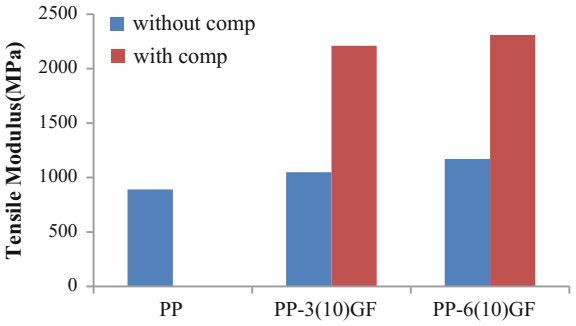

Fig. 4 Tensile Modulus of neat PP, PP-GF composites with and without compatibilizer

159 % in compatibilized PP-GF(6)-comp composites. A significant increase in tensile modulus of compatibilzed PP-GF composites over uncompatilized PP-GF composites was observed which can be attributed to the better adhesion of the glass fiber to the PP resin in presence of compatibilizer which further supports the observations by SEM and FTIR.

3.3.3 Impact Strength

The values of impact strength of PP-GF(3), PP-GF(6), PP-GF(3)-comp and PP-GF (6)-comp composites are compared in Fig. 4. The impact strength decreases on glass fiber incorporation in PP matrix form 200 to 139 J/m and from 200 to 165 J/m in PP-GF(3) and PP-GF(6) composites respectively. The glass fibers are stiff with high strength and high modulus, which cannot generate deformation when impact is exerted on them, so they cannot absorb impact energy which increases the brittleness of the composites and decrease impact strength. The use of compatibilizer further has negative effect on the impact strength of PP-GF(3)-comp and PP-GF(6)-comp composites which may be due to inhibited polymer mobility in the compatibilized PP-GF composites thereby lowering the ability of the system to absorb impact energy (13, 14). However, still composites with this impact strength value is able to resist the fracture (Fig. 5).

3.3.4 Elongation at Break:Thermoformability

Elongation at break (Eb%) of the composites, i.e. the elongation that a polymer could withstand without breaking, determines the thermoformability characteristic of FRTPs, which is significant as the thermoforming process is one of the most common techniques used for fabrication of orthotic device. Thermoforming entails heating of the composite sheet until it reaches its ‘plastic’ state and then forced over the prescribed shape under pressure until it is cooled.

Fiber incorporation in the PP matrix associated with a significant decrease in elongation at break from 600 to 157 % in PP-GF(3) composites and further from

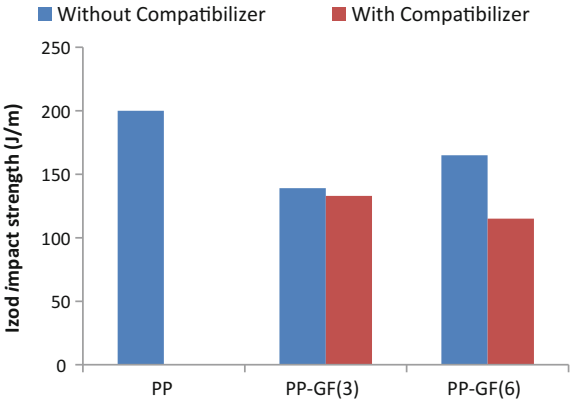

Fig. 5 Impact Strength of neat PP, PP-GF composites with and without compatibilizer

600 to 75 % in PP-GF(6) composites. Percentage elongation at break (Eb%) results revealed that the addition of glass fibers decrease the elongation at break of the PP-GF composites because the glass fibers are brittle in comparision to PP and thus PP-GF composites have lower elasticity than pure PP. The addition of compatibilizer further decreases the Eb% from 157 to 50 % in PP-GF(3)-comp and 75–20 % in PP-GF(6)-comp. The use of compatibilizer improves the adhesion between PP and GF which results in enhancement in the rigidity and reduction of mobility of the polymer chains in the composites, and thus lowers the Eb% of compatibilized PP-GF composites.

Still the PP-GF(3), PP-GF(6) and PP-GF(3)-comp composites with their respective values of Eb% are able to thermoform for fabrication of the orthotic devices. However, PP-GF(6)-comp composite with Eb% = 20, is not suitable for the thermoforming process.

4 Conclusions

Glass fiber reinforced PP-based composites (10 wt%) were successfully fabricated using twin screw extrusion and their mechanical properties were evaluated. The effect of functionalization of reinforcing agent alone and simultaneous effect of functionalisation of reinforcing agent as well as matrix, on the morphology and mechanical properties of PP-GF composites was analyzed.

Based on the SEM images, the best adhesion occurs in PP-GF(3)-comp and PP-GF(6)-comp composites with simultaneous effect of APTMS functionalized GFs and PP-g-MA as compatibilizer because the functionalization of both matrix and reinforcing agent results in introduction of reactive groups on the surface of GF and PP, between which very strong hydrogen bonds can develop, which is also demonstrated by the FTIR results.

Both PP-GF(3)-comp and PP-GF(6)-comp composites showed better tensile properties over PP resin, which improves its durability and makes them suitable material for developing orthotic aid. However, the improved adhesion in compatibilized composites results in improved tensile properties with simultaneous drastic decrease in elongation at break. The PP-GF(6)-comp composites with 20 % Eb is not suitable for fabrication of orthotic aid as the composite will not be able to thermoform. Thus, the study demonstrates the feasibility of the PP-GF(3)-comp composites reinforced with 10 wt% of 3 mm GFs, with elongation at break $\sim$50 % at room temperature, for orthotic aid fabrication with improved strength at low cost.

References

1. A.G.A. Coombes, C.D. Greenwood, J.J. Shorter, *Plastic Materials for External Prostheses and Orthoses, Ch. Human Biomaterials Applications* (Humana Press, Springer), pp. 215–255
2. F. Sarasini, J. Tirillò, D. Puglia, J.M. Kenny, F. Dominici, C. Santulli, M. Tofanid, R. De Santis, RSC Adv. **5**, 23798–23809 (2015)
3. M. Etcheverry, S.E. Barbosa, Materials **5**, 1084–1111 (2012)
4. I. Angelov, S. Wiedmer, M. Evstatiev, K. Friedrich, G. Mennig, Compos Part A **38**(5), 1431–1438 (2007)
5. S. Li, S. Sun, H. Liang, Environ. Technol. **35**(21), 2743–2751 (2014)
6. H. Mohamed, H. Gabr, W. Okumura, H. Ueda, W. Kuriyama, K. Uzawa, I. Kimpara, Compos. B **69**, 94–100 (2015)
7. K.A. Ruhul, A.K. Mubarak, U.Z. Haydar, P. Shamim, K. Nuruzzaman, S. Sabrina, J. Reinforc. Plast. Compos. **29**(7), 1078–1088 (2012)
8. L.A. Pothan, S. Compos, Sci. Technol. **63**, 1231–1240 (2012)
9. A.K. Gupta, M. Biswal, S. Mohanty, K. Nayak, Polymer **15**, 994 (2014)
10. M. Sonmez, M. Georgescu, M. Valsan, M. Radulescu, D. Ficai, G. Voicu, A. Ficai, L. Alexandres, J. Appl. Polym. Sci. **132**, 42163 (2015)
11. P.J. Herrera-Franco, A. Valadez-Gonzalez, Compos. Part B **36**, 597 (2005)
12. M. Bengtsson, K. Oksman, Compos. Part A **37**, 752 (2006)
13. G.E. Myers, I.S. Chahaydi, C.A. Coberly, D.S. Erner, Int. J. Polym. Mater. **15**, 21 (1991)
14. R. Sharma, S.N. Maiti, Polym. Bull. **72**, 627–643 (2015)

Part VI
Semiconductor Materials and Devices

Photothermoelectric and Photoconducting Properties of Layer-by-Layer Deposited Nanocrystalline PbS Films

Dhaval Vankhade and Tapas K. Chaudhuri

Abstract Photothermoelectric and photoconducting properties of layer-by-layer deposited nanocrystalline PbS films have been investigated at 300 K. The thicknesses of the films are in the range 250–500 nm and are p-type. The carrier concentration of films decreases with thickness due to interaction with atmospheric oxygen. However, the mobility of holes in films increases with thickness because of surface scattering effect. The photoconductivity of nanocrystalline PbS films is predominantly due to increase in mobility rather than carrier concentration.

1 Introduction

Thermoelectric power (TEP) and Photothermoelectric power (PTEP) properties of semiconductor films are powerful tools for studying the transport properties of semiconductor. Investigations on PTEP effect has been very few, mostly in the early 70s [1–5]. Studies on PTEP effect has been limited to CdS crystals [3], n-type and p-type monocrystalline Si and CdS films [4, 5]. However, even though the TEP properties of vacuum evaporated PbS films has been reported [6, 7], there has been no systematic analysis of PTEP effect of PbS films. This paper reports the photothermoelectric and thermoelectric properties of layer-by-layer (LBL) solution deposited nanocrystalline PbS films. For this study, a photothermoelectric power measurement system was developed in laboratory.

D. Vankhade (✉) · T.K. Chaudhuri
Dr. K. C. Patel Research and Development Centre,
Charotar University of Science and Technology, Changa, Anand District 388421,
Gujarat, India
e-mail: vankhadedhaval@yahoo.com

V.K. Jain et al. (eds.), *Recent Trends in Materials and Devices*,
Springer Proceedings in Physics 178, DOI 10.1007/978-3-319-29096-6_55

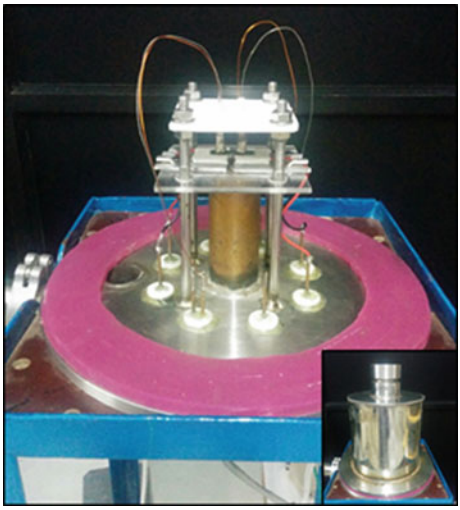

Fig. 1 Photothermoelectric power and photoconductivity measurement setup

2 Experimental

Nanocrystalline PbS thin films are deposited [8] from the methanolic solution of lead acetate and thiourea by dip-coating method on ultrasonically cleaned glass substrate 75 × 25 mm. The single coating has a thickness of ∼50 nm. Higher thicknesses of films are obtained by layer-by-layer (LBL) deposition. These films are cut into 5 × 25 mm for the photo thermoelectric power and photoconductivity measurements. The ohmic contact is made by conducting colloidal graphite paint (Ted Pella).

The experimental setup for the measurement of the PTEP is shown in Fig. 1. The Peltier elements used for heating one side of film, copper-constantan thermocouple used for measure the temperature. The measurement is carried out in the 1 mTorr by rotary vacuum pump. The top side of the chamber have circular quartz window for the illumination of light as shown in insight Fig. 1. These temperature and thermoelectric emf are measured by Kiethley 2700 multimeter and the conductivity of films measured by 2611 source meter at 20 V dc biasing voltage. The photo-thermoelectric power and photoconductivity is measured by illuminating the samples with 100 mW/cm^2 light from a halogen lamp.

3 Results and Discussion

The PbS thin films deposited in the present investigation are basically nanocrystalline with crystalline size of 10 nm. Each coating had a thickness of about 50 nm. To obtain higher thicknesses, films were deposited on top of each other

layer-by-layer. The TEP of films with 50–200 nm thicknesses could not be measured due to very high impedance of the samples and unreliability of data. Hence, PbS films of thicknesses 250–500 nm have been used as samples for determination of TEP and conductivity. The films were p-type. TEP in dark and under light was determined by measuring the voltage (ΔV) generated by applying a temperature difference (ΔT) of 5 K across the planer electrodes. The TEP (α_{th}) was calculated by the relation:

$$\alpha_{th} = \frac{\Delta V}{\Delta T} \tag{1}$$

The carrier (hole) concentration was estimated from:

$$p = N_v \exp\left(A - \frac{e\alpha_{th}}{k}\right) \tag{2}$$

The mobility (μ) of holes was calculated from:

$$\sigma = pe\mu \tag{3}$$

In the above equations (2) and (3), p is carrier concentration of hole, A is scattering factor, N_v is effective density of state, α_{th} is thermoelectric power, k is Boltzmann constant, μ is mobility, σ is conductivity and e is electronic charge.

The variation of TEP and PTEP of PbS films as a function of thickness are shown in Fig. 2. In general, both TEP and PTEP increases linearly with thickness. TEP of the films decreases on illumination indicating increase in hole concentration because of photo-generated carriers. The electrical conductivity of PbS films as a function of thickness in dark and light is presented in Fig. 3. The dark conductivity of PbS films increases slowly with thickness from 0.006 to 0.014 S/cm. However the conductivity in light of these films increases exponentially from 0.015 to 0.039 S/cm as thickness increases from 250 to 500 nm.

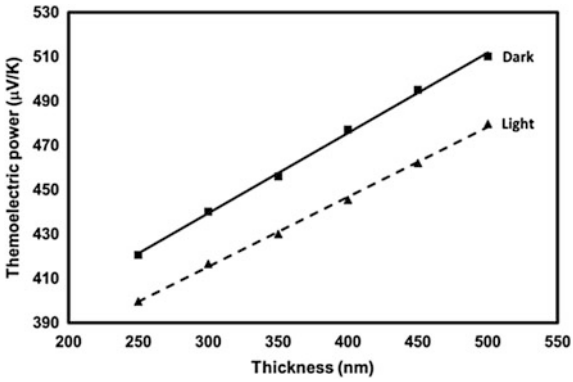

Fig. 2 Variation of thermoelectric and photo thermoelectric power of PbS films with thickness

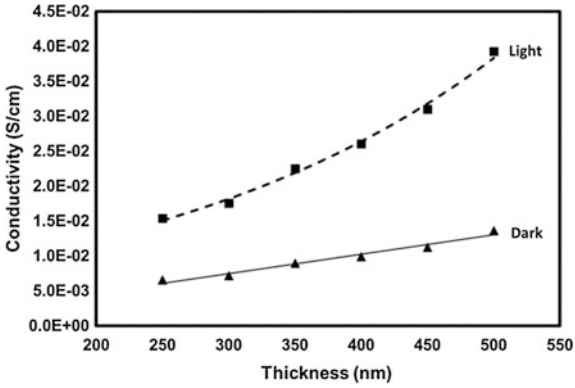

Fig. 3 Variation of conductivity and photoconductivity of PbS films with thickness

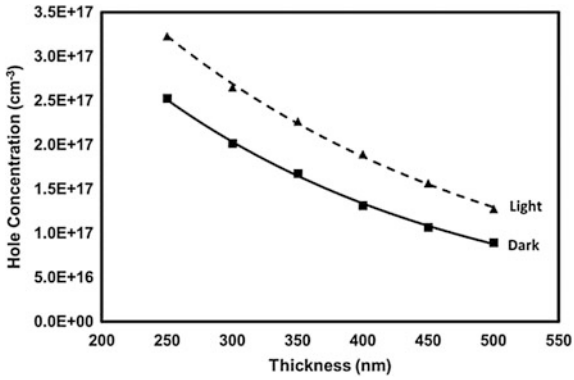

Fig. 4 Variation of hole concentration in dark and in light of PbS films with thickness

The carrier concentration (p) and mobility (μ) of holes in the PbS films were derived from (2) and (3). Figure 4 shows the thickness variation of p of films in dark and light. In general, p decreases as thickness increases. In dark p varies from 2.5×10^{17} cm^{-3} (for 250 nm) to 0.8×10^{17} cm^{-3} (for 500 nm). On illumination p of films increases by $\sim 0.7 \times 10^{17}$ cm^{-3} (Δp) over dark values.

The decrease in p with can be explained as follows. The deposition of each layer of PbS involves heating at 100 °C in air for about 10–15 min. During this step atmospheric oxygen reacts with PbS which reduces the hole concentration [9]. This is repeated for each time a layer is deposited on top of another. Hence, the hole concentration reduces with number of depositions, that is, increase in thickness.

Figure 5 shows that both dark mobility and light mobility increases as the thickness increases. The mobility in dark increases from 0.1 (for 250 nm) to 0.9 cm^2 V^{-1} s^{-1} (for 500 nm). On the other hand mobility in light increases more rapidly from 0.2 (for 250 nm) to 1.9 cm^2 V^{-1} s^{-1} (for 500 nm). The mobility of films increases on illumination. The increment of mobility ($\Delta\mu$) increases as the thickness of film increases. The PbS films in the present study are basically nanocrystalline and has no grain boundaries to affect the mobility, but mobility is

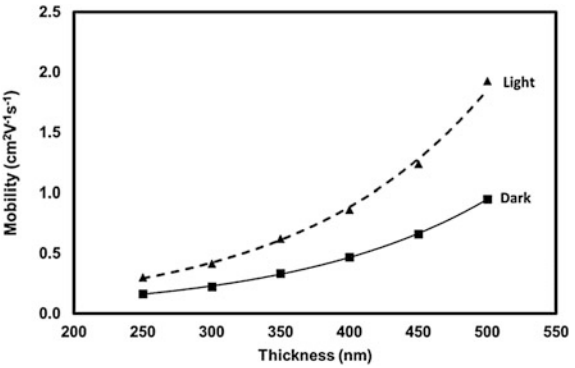

Fig. 5 Variation mobility of PbS films in dark and light with thickness

restricted by scattering from the surfaces of the film as observed in case of CdS films [10]. The mobility of these films can be written as:

$$\mu_f = \mu_b - \mu_s \tag{4}$$

where the subscripts *f*, *b* and *s* indicates film, bulk and surface, respectively. As the thickness of the films increases the μ_s decreases which in turn increases the ultimate mobility μ_f.

The photoconductivity ($\Delta\sigma_{PH}$) of the films is given by:

$$\Delta\sigma_{PH} = \sigma_L - \sigma_D \tag{5}$$

where, σ_L is conductivity in light σ_D is conductivity in dark are presented in Fig. 3. After evaluating, $\Delta\sigma_{PH}$ is plotted as a function of thickness of PbS films in Fig. 6. $\Delta\sigma_{PH}$ monotonically increases with increase in thickness of films. Again, photoconductivity of films can be expressed in terms of carrier concentration and mobility as follows:

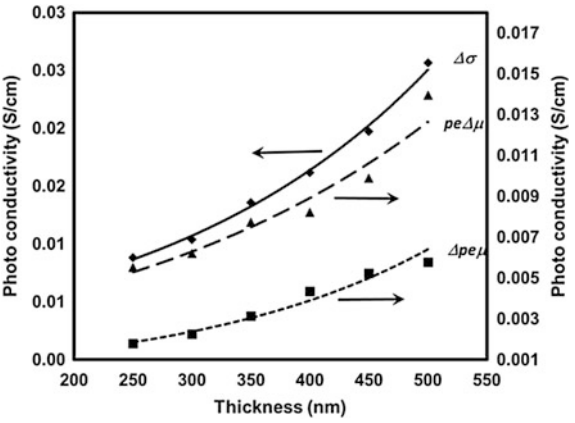

Fig. 6 Thickness dependence of photoconductivity of PbS films and contribution of carrier concentration, mobility due to light

$$\Delta\sigma_{PH} = \Delta pe\mu + pe\Delta\mu \tag{6}$$

Equation (6) shows that the change in photoconductivity due to change in carrier concentration and/or change in mobility. Using the data of Figs. 4 and 5, $\Delta pe\mu$ and $pe\Delta\mu$ was calculated and plotted in Fig. 6. It can be seen that $pe\Delta\mu$ is much greater than $\Delta pe\mu$, so that $pe\Delta\mu$ is a major component of $\Delta\sigma_{PH}$ while $\Delta pe\mu$ is minor. This implies that ultimate photoconductivity of the PbS films is mainly because of increase in mobility under illumination.

4 Conclusion

Photothermoelectric and photoconducting properties of nanocrystalline PbS thin films have been studied at room temperature (300 K). These films are p-type and have been deposited layer-by-layer with thicknesses ranging from 250 to 500 nm. The hole concentration of films decreases with thickness while mobility increases with thickness. Photoconductivity of these films is mainly due to increase in mobility on illumination.

Acknowledgments The authors are Thankful to President and Provost of CHARUSAT for supporting this work. D.V. is grateful to Department of Science and Technology (GoI) for providing Inspire Fellowship.

References

1. J. Tauc, Cechoslov. Fiz. Z. **5**, 528 (1955)
2. R. Lawrance, R.H. Bube, J. Appl. Phys. **39**, 1807 (1968)
3. H.B. Kwok, R.H. Bube, J. Appl. Phys. **44**, 138 (1973)
4. J.G. Harper, H.E. Matthews, R.H. Bube, J. Appl. Phys. **41**, 765 (1970)
5. C. Wu, R.S. Feigelson, R.H. Bube, J. Appl. Phys. **43**, 756 (1972)
6. E.I. Rogacheva, I.M. Krivulkin, O.N. Nashchekina, A.Y. Sipatov, V.V. Volobuev, M.S. Dresselhaus, Appl. Phys. Lett. **78**, 1661 (2001)
7. E.I. Rogacheva, O.N. Nashchekina, Y.O. Vekhov, M.S. Dresselhaus, S.B. Cronin, Thin Solid Films **423**, 115 (2003)
8. D. Vankhade, A. Kothari, T.K. Chaudhuri, J. Electron. Mater. **45**, 2789 (2016)
9. R.H. Harada, H.T. Minden, Phys. Rev. **102**, 1258 (1956)
10. L.L. Kazmerski, Thin Solid Films **21**, 273 (1974)

Synthesis and Properties of Inorganic Organic Chloride Based Perovskite

Nidhi Gupta, Omita Nanda, Pramod Kumar, Rakhi Grover and Kanchan Saxena

Abstract Here we report single step synthesis of lead chloride based organic inorganic hybrid perovskite. Thin films of the material show nanostructured morphology dependent on the fabrication method. Thin films deposited by drop casting method exhibit cubical structures. This morphology changes itself to randomly oriented platelets on spin coating. This evolution of morphology is verified by using scanning electron microscopy (SEM). However as revealed by optical microscopy both the films exhibit identical fluorescence spectra with PL peaks at around 500 nm. Such type of materials may be highly useful in photonic applications requiring varying morphological properties.

1 Introduction

During last decade hybrid inorganic-organic halide based perovskites appeared as very attractive material for various applications like solar cell, organic light emitting diodes and sensors etc. These material also became much popular due to their easy

N. Gupta (✉) · O. Nanda · P. Kumar · R. Grover · K. Saxena
Amity Institute of Advance Research and Studies (Material & Devices),
Amity University, Noida, Uttar Pradesh, India
e-mail: nidhi.dbc@gmail.com

O. Nanda
e-mail: omitananda@gmail.com

P. Kumar
e-mail: pramodkumar355@gmail.com

R. Grover
e-mail: grover.rakhi@gmail.com

K. Saxena
e-mail: ksaxena@amity.edu

N. Gupta · O. Nanda · P. Kumar · R. Grover · K. Saxena
Amity Institute of Renewable and Alternative Energy, Amity University, Noida,
Uttar Pradesh, India

V.K. Jain et al. (eds.), *Recent Trends in Materials and Devices*,
Springer Proceedings in Physics 178, DOI 10.1007/978-3-319-29096-6_56

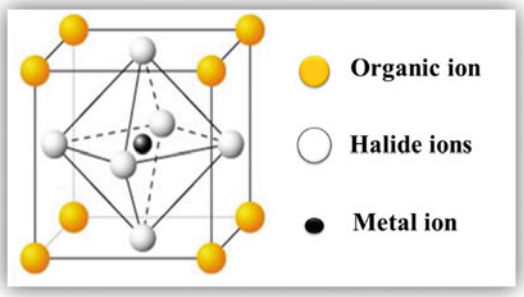

Fig. 1 Crystal structure of hybrid halide perovskites

synthesis and magnetic, electrical and optical properties like high absorption coefficient, good charge transfer and photoluminescence properties. General formula of hybrid perovskites is ABX_3, where A is organic species like CH_3NH^{3+}, B is metal ions (e.g. Pb, Sn etc.) and X is halide (Cl^-, Br^-, I^-). In crystal structure A is present at corner position, B at centre of the crystal lattice and halide ions occupy the face centres (Fig. 1) [2].

Synthesis of hybrid perovskites was described by different investigators [1, 2]. Synthesis process plays vital role in deciding the structure of hybrid perovskites. Different structures can be obtained by altering their chemical composition as well as physical and environmental conditions during synthesis process. Effect of different metal ion, numerous organic ions and type of halide ions on the structure and properties of hybrid perovskites is already reported. Keith et al. reported the effect of halide ion over the optical properties of perovskites [3]. Concentration effect of precursor solution was also studied by Jeong et al. [4].

In the present work, we report the single step synthesis of lead chloride based organic inorganic hybrid perovskite. Different morphologies obtained by drop casting and spin coating were studied.

2 Experimental Methodology

Chemical used:
Lead halide ($PbCl_2$) having MW: 278.1 g/mol.
Ethylenediamine dichloride ($C_2H_8N_2Cl_2$) having MW: 151.99 g/mol.
Dimethyl sulfoxide (DMSO) used as solvent.

All chemicals were used without any further purification. Lead halide ($PbCl_2$) was purchased from Sigma Aldrich.

Lead halide ($PbCl_2$) and ethylenediamine dichloride were used as precursor material. Both inorganic and organic precursors were mixed in molar ratio of 2:1 in DMSO. This precursor mixture was then heated at 80 °C for 2 h. This material was characterized by FT-IR spectroscopy. After heating perovskites solutions were drop casted and spin coated separately on pre-cleaned glass substrates and dried in

vacuum. SEM analysis were done using Ziess scanning electron microscope (EVO-18). Photoluminescence was measured using spectrofluorometer (shimadu).

3 Results and Discussion

FT-IR Analysis: Synthesized material was characterized by FT-IR spectroscopy shown in Fig. 2. Peak at 2924 cm^{-1} is attributed to N-H stretching. Peaks at 2850, 1460 and 1380 cm^{-1} is assigned to C-N stretching. Peaks at 1630 and 1024 cm^{-1} shows N-H bending and C-H bending respectively. Similar peaks were reported by Jeon and group [5].

SEM Analysis: Morphology of thin films fabricated by drop casting and spin coating method were studied using scanning electron microscopy shown in Fig. 3a and b, respectively. Thin films deposited by drop casting method exhibit cubical structures whereas randomly oriented platelets were seen on spin coating. In drop casting perovskites get enough time to get its cubic crystal structure but in case of spin coating film formation is fast as compare to drop casting method hence randomly arranged structure was found.

UV-Vis and Photoluminescence Analysis: UV-Vis and Photoluminescence spectra for drop casted and spin coated films are shown in Fig. 4a and b, respectively. Absorption for the films is same in visible region. Photoluminescence for both the films exhibit identical fluorescence peak at 500 nm. This shows optical properties for both the films are similar and does not depend upon the film fabrication technique.

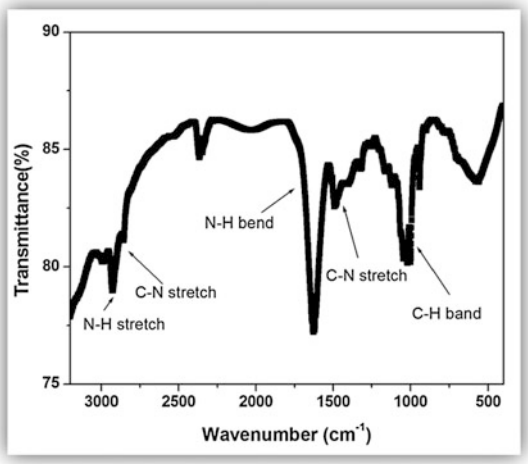

Fig. 2 FT-IR of synthesized hybrid perovskite

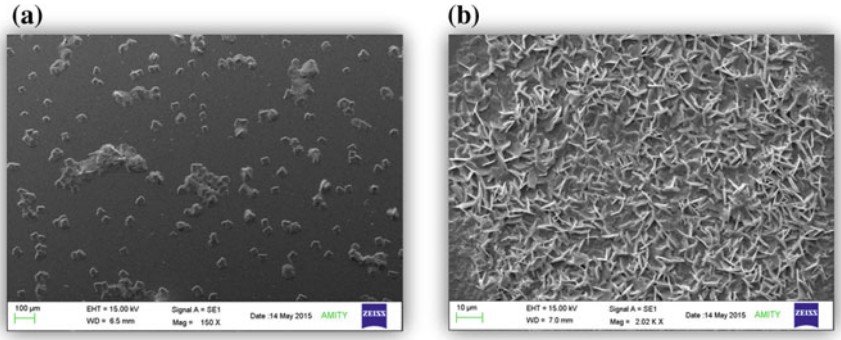

Fig. 3 SEM images of thin film fabricated by **a** drop casting **b** spin coating

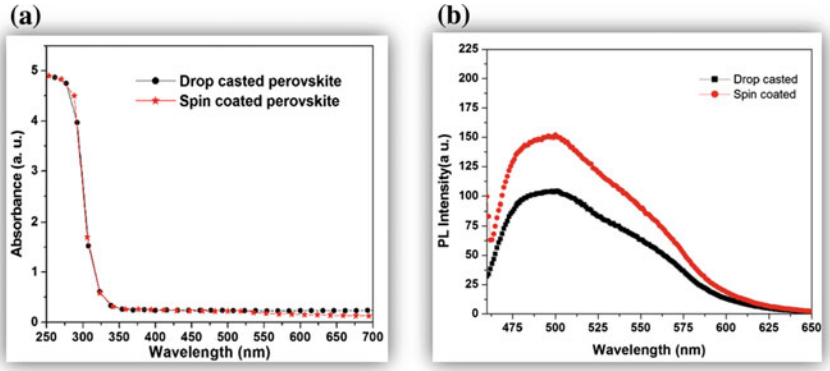

Fig. 4 **a** UV-Vis **b** Photoluminescence spectra of thin film fabricated by drop casting and spin coating

4 Conclusion and Future Scope

Synthesis of hybrid lead halide perovskite was done using single step method and confirmed by FT-IR. Two different morphologies of perovskites were successfully fabricated using different techniques of film fabrication. Cubical structures were found on drop casting whereas randomly oriented platelets were obtained by spin coating method. Both morphological properties shows similar identical properties with a PL peak at around 500 nm. Such type of materials may be highly useful in photonic applications requiring varying morphological properties.

Acknowledgments The authors are grateful to Dr. Ashok K Chauhan, Founder President, Amity University and Dr. V K Jain, Distinguished Scientist and Professor, Amity University, Noida, India for their continuous encouragements in carrying out this work. One of the authors is grateful to the Department of Science and Technology for the financial assistance through (Grant No. DST/TSG/PT/2011/192).

References

1. T. Baikie, Y. Fang, J.M. Kadro, M. Schreyer, F.W. Subodh, G. Mhaisalkar, M. Graetzeld, T. J. White, J. Mat. Chem. A **1**, 5628–5641 (2013)
2. P. Gao, M. Grätzel, M.K. Nazeeruddin, Energy Environ. Sci **7**(7), 2448–2463 (2014)
3. K.T. Butler, J.M. Frost, A. Walsh, Mater. Horiz. **2** (2015)
4. J.H. Im, J. Luo, M. Franckevicius, N. Pellet, P. Gao, T. Moehl, S.M. Zakeeruddin, M.K. Nazeeruddin, M. Gratzel, N. G. Park, Nano. Lett. 46 (2015)
5. N.J. Jeon, J.H. Noh, Y.C. Kim, W.S. Yang, S. Ryu, S. Seok, Nat. Mat. **13** (2014)

Design, Simulation and Analysis of 4 × 1 Mux at 90 nm CMOS Technology

Prateek Singh, Rohan Jain, Anmol Sharma, Ayesha Manocha and Rajiv Sharma

Abstract Power and delay are regarded as the most fundamental design constraints that form the basis of comparative analysis of logic style implementation of any arbitrary circuit. Previously published research works and investigations have proposed various low power logic style implementations of 2:1 multiplexer circuits. This paper focuses on the design, simulation and analysis of 4:1 multiplexer circuit using CMOS, CVSL, PTL and dynamic logic styles at 90 nm technology followed by a comparison of the circuit performance w.r.t. power, delay and power-delay product. Further, based on this evaluation of circuit families; it has been shown that transmission gate (CMOS+) is the logic style of choice which is most optimized and efficient both in terms of power and speed within 1.6–2.4 V supply voltage range. The circuits have been designed and simulated using BSIM 3V3 90 nm technologies on Tanner EDA tool.

1 Introduction

Multiplexer is a universal logic element that is most commonly used in communication systems including TDM and optical communication systems. Hence, it needs to be optimized in terms of both power and speed in order to obtain high

P. Singh · R. Jain (✉) · A. Sharma · A. Manocha · R. Sharma
Electronics and Communication Engineering Department, Northern India Engineering College, New Delhi, India
e-mail: rohanjain.06.01@gmail.com

P. Singh
e-mail: prateek10singh@gmail.com

A. Sharma
e-mail: adwatsharma@gmail.com

A. Manocha
e-mail: ayesha_manocha11@yahoo.co.in

R. Sharma
e-mail: rsap70@rediffmail.com

V.K. Jain et al. (eds.), *Recent Trends in Materials and Devices*,
Springer Proceedings in Physics 178, DOI 10.1007/978-3-319-29096-6_57

performance digital systems. The increasing demand for low-power VLSI can be addressed at different design levels, such as the architectural, circuit, layout and the process technology level. At the circuit and layout level, the power dissipation can be minimized by effectively reducing the sub-threshold conduction as well as reverse biased leakage currents. Short circuit currents, although assumed to be negligible, have been found to constitute 10–30 % of overall power consumption [1]. Minimizing delay is also an important design objective that needs to be addressed. The delay of a logic gate usually depends upon the width of transistors in the logic gate, its output current, output load capacitance and the output voltage swing [1, 2]. Faster circuit families, therefore attempt to reduce one of these parameters. Sections 2 and 3 includes a brief theoretical description of some of the basic concepts related to power, delay and power-delay product as well as the various static and dynamic logic styles. Simulation waveforms and results in the form of graphical and tabular representations have been shown in Sect. 4. Finally, some conclusions have been drawn in Sect. 5.

2 Parameters Analyzed

2.1 Power Analysis

Power is considered to be one the most important factors in designing today's VLSI circuits. Total power losses constitute both static and dynamic losses.

$$P_{(total)} = P_{(static)} + P_{(dynamic)} \tag{1}$$

Unlike a few years back, when the dynamic power losses dominated any other type of power losses [3]; with the recent shift towards UDSM level designing, nowadays static power losses too have become a key concern. Subthreshold conduction, gate oxide tunneling current, leakage through reverse biased diodes, and contention current in ratioed circuits are the main reasons for static losses [4]. These losses occur primarily because of ultra-thin channel length and carrier power overcoming barrier voltages. High doping levels of about 1×10^{18} cm^{-3} leads to decreased barrier potential and more carrier concentration; thus helping more charge movement even at very low voltages. Frequent charging-discharging of the load capacitances and short circuit currents make the major portion of dynamic power losses.

$$P_{dyn} = V_{DD}^2 \cdot f_{clk} \cdot \sum_n \alpha_n \cdot c_n + V_{DD} \cdot \sum_n I_{scn} \tag{2}$$

With the modern day technology, though decreased supply voltages should lead to low losses, however the need of fast switching activity, high clock frequency

(f_{clk}), high short circuit currents (i_{sc}) and highly complex circuits leads to more transitions and thus more dynamic power losses [3].

2.2 Delay Analysis

Delay present in any circuit increases with the increase in the number of inversion levels in series. Inter-wire capacitance, intra-wire capacitance, junction capacitance, interconnect capacitance all account for the increased delays.

$$t_{pd} = (C/I)\Delta V \tag{3}$$

Logical effort(C/I) accounts for all these factors quantitatively. Dynamic circuits were developed with the idea to use the internal capacitances to hold some valuable information which in case of static circuits is cause of only delays [5]. These circuits prove to be beneficial when fast operation speeds are required. pMOS transistors have higher internal and node capacitances and also the hole carrier speed is less as compared to the electrons; it is for these reasons nMOS are chosen over pMOS to implement circuits [6, 3].

2.3 Power Delay Product Analysis

The power delay product is a fundamental parameter which is used for measuring the quality and performance of a CMOS process and gate design. As a physical quantity, the power delay product can be interpreted as the average energy required for a gate to switch its output voltage from low to high and vice versa.

To reduce power delay product,

- Reduce load capacitance
- Reduce supply voltage
- PDP does not capture the fact that reducing supply voltage lowers power con-sumption but increases delay.

3 Logic Styles

3.1 Cmos/Cmos+

CMOS has been the logic style of choice of many VLSI circuit designers for any arbitrary circuit because of the lucrative features of CMOS like full swing, theoretically no steady state losses and robustness against transistor downsizing

(ratioless) and voltage scaling. However it must be noted that optimum logic style for any circuit is technology independent. However a new class of CMOS circuits i.e. CMOS+ also called Transmission Gate has proved to be better than CMOS in terms of effective circuit orientation and providing near constant resistance throughout its operative lifecycle. It is a non-restoring circuit providing very less isolation between input and output. It can pass both 1s and 0s in an acceptable fashion.

3.2 Cascode Voltage Switch Logic

CVSL is dual rail logic. It uses almost the same number of transistors as CMOS does to implement the logic function but also generates non-inverted output. The two additional pMOS act as load driver circuits which have gates connected to the complementary output. CVSL has no steady state losses but is ratioed circuit. *Modified CVSL* or *MCVSL* is similar to CVSL implementation of function with the only modification that is to improve the driving capabilities of pMOS load by adding nMOS in parallel to it or in other words we can say we have a transmission gate as the load driver circuit. This improves the swing restoration at the output as well.

3.3 Cascode Voltage Switch Logic

PTL logic family has inputs connected not only to the gate of MOSFET but to either drain or source as well. This reduces the transistor count significantly w.r.t. CMOS or CVSL and size of transistor can be kept minimal as well. These features seem to fascinate IC designers; but higher delays in chaining and multi-threshold voltage drop when cascaded pose a serious problem to circuit efficiency. These problems including sneak path problem need to be taken care of by adding extra circuitry in the form of buffers and pull up transistors. All these factors annihilate the advantage of less MOSFET count, small area and small input load. Short circuit currents are also large due to competing signals in swing restoration circuitry.

3.3.1 *Complementary PTL* has both inverting buffers to restore the output levels and weak pull up PMOS to restore the inputs of those inverting buffers. These have low input loads and higher output driving capabilities.

3.3.2 *Swing restored PTL* forms a latch like structure by cross coupling the output buffers. Weak PMOS pull up networks are removed and the pMOS of the output inverting buffers acts as the level restoration transistor for the input of complementary output inverter. These circuits have slow switching, poor output driving capabilities and unreliable operation.

3.3.3 *Energy economized PTL* has the sources of pMOS transistor of CPL gate connected to complementary output signal instead of Vdd. It has low power losses, full swing and shorter delays. This circuit has the capabilities to make efficient circuits.

3.3.4 *Push Pull PTL* is a CPL without output buffers. Besides low transistor count, its output driving capabilities are worse than SRPL.

3.4 Dynamic Circuits

Dynamic circuits provide the advantages of CMOS (no steady state losses, full swing, low dynamic losses) and Pseudo nMOS (faster operation and less transistor count). In addition to this, the node capacitances which accounts for only delays in static circuits can be used to store some useful information in dynamic circuits. *Domino-circuits* are fast, synchronize the output and are ratioless circuits. They have an nMOS network in series with a pMOS transistor supplied with a clock signal. During the high clock, the output node precharges and evaluates only when clock is low. Output can only make a single high to low transition giving it monotonicity. Thus multiple stages are cascaded by having invertors at the output of each stage. Additionally nMOS footer transistor can be placed to guard against output discharging during precharge phase. Dynamic losses can be reduced by reducing the duty cycle of the clock to less than 50 %.

4 Simulation and Analysis

4.1 Simulation Environment

All the circuits have been simulated using BSIM 3V3 90 nm technologies on Tanner EDA tool. All the circuits have been simulated on exactly same input patterns to make sure of impartial testing environment. Every simulation has been performed on range of voltage varying from 1.6 to 2.4 V W/L ratio for NMOS transistors were kept 1.8/1.2 and [(W/L) p/(W/L) n] = 2.

4.2 Schematics

We present schematics of 4:1 multiplexer circuit that were designed in S-Edit using different logic styles which have been discussed in Sect. 3 (Figs. 1, 2, 3, 4, 5, 6, 7, 8 and 9).

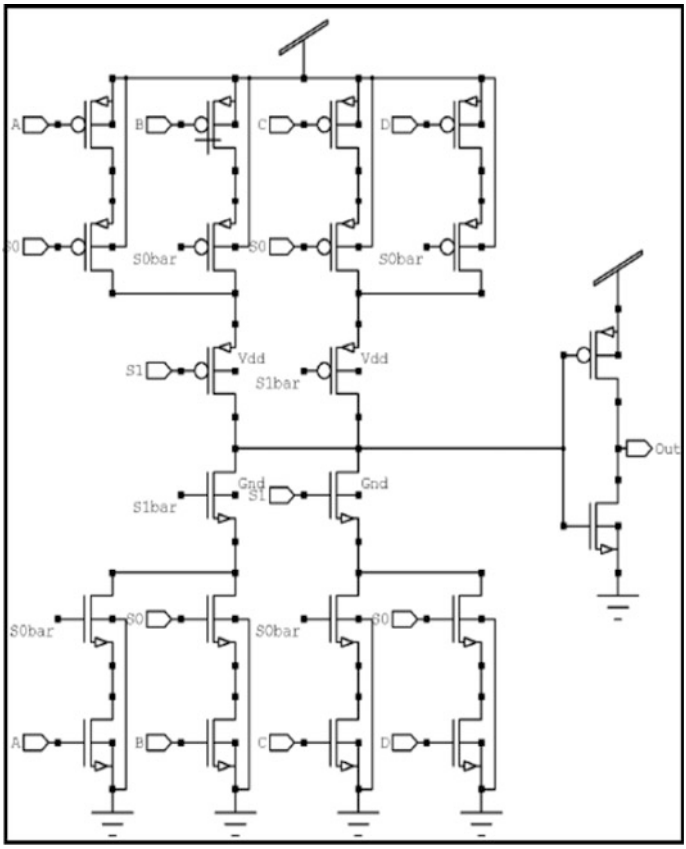

Fig. 1 Schematic of CMOS

4.3 Performance Analysis

This work includes power analysis, delay analysis and PDP analysis of the logic styles discussed above. In addition to them the same analysis was done for Pseudo-nMOS, LEAP and Dual Rail domino logic. Figure 10 depicts the power consumption versus Vdd for leap, pseudo nMOS, srpl, ppl, eepl, cpl, cmos, cmos +, cvsl, mcvsl, domino, dual-rail domino based 4:1 multiplexer circuit. CMOS + (transmission gate) circuit implementation of 4:1 multiplexer shows the least power consumption. Figure 11 shows maximum power consumption versus Vdd and Fig. 12 shows minimum power consumption versus Vdd for all 12 logic styles implemented for 4:1 multiplexer circuit. It shows that transmission gate absorbs least power in both the maximum power consumption state at Vhigh and also in the minimum power consumption state at Vlow. Here EEPL circuit shows least delay among all other design techniques (Figs. 13 and 14).

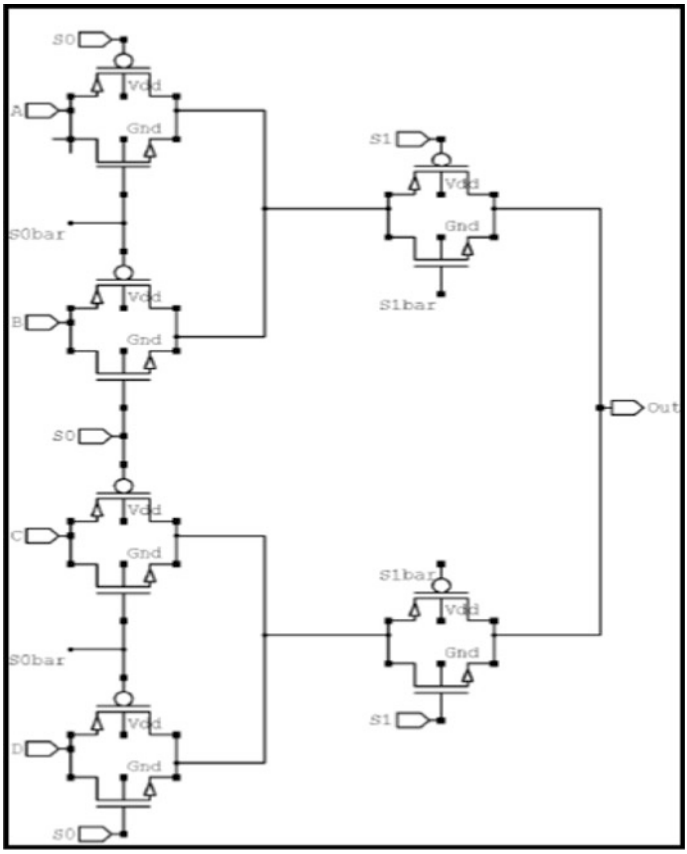

Fig. 2 Schematic of CMOS+

4.4 Results and Discussion

Waveform analysis of the different logic styles during realizing 4:1 multiplexer circuit using W-edit has been done. While performing waveform analysis of the designed circuits, we applied all the possible input values individually using bit pattern interface and also provided random values using pulse interface as voltage source. Finally using the given two figures below we show two categories of signal used in circuits. Figure 15 shows simulation of 4:1 multiplexer circuit using static circuits and Fig. 16 shows simulation of 4:1 multiplexer circuit using dynamic circuits.

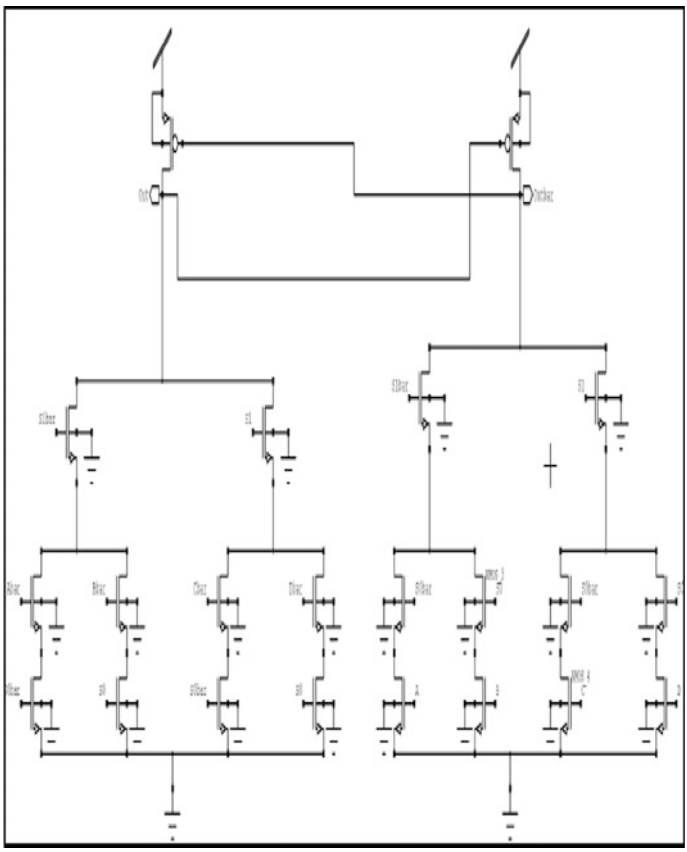

Fig. 3 Schematic of CVSL

Table 1 depicts the power delay product over a range of power supply voltages and it is shown in the table that transmission gate (CMOS+) circuit for 4:1 multiplexer shows minimum power delay product for a range of voltage values taken in consideration for low power circuits.

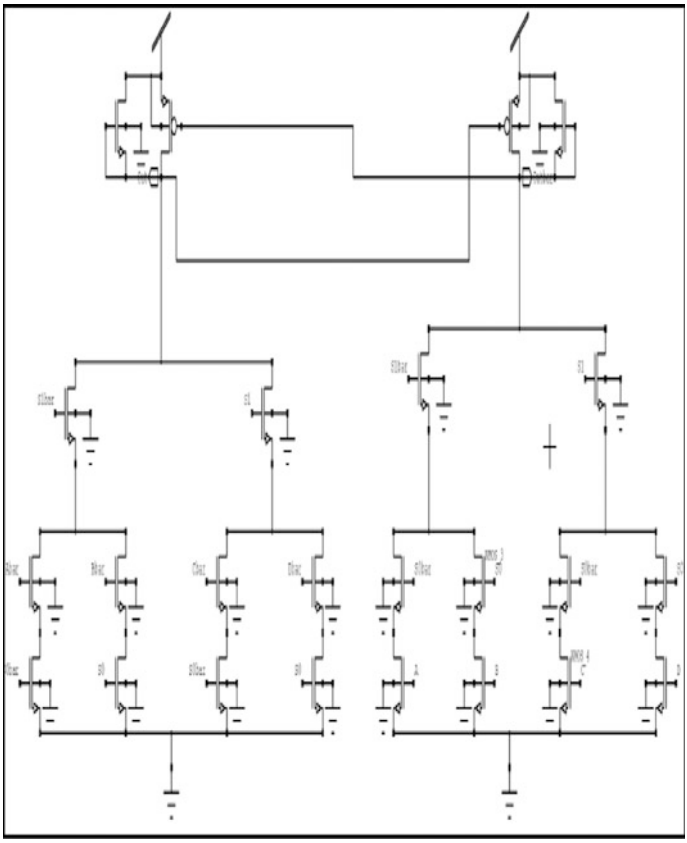

Fig. 4 Schematic of MCVSL

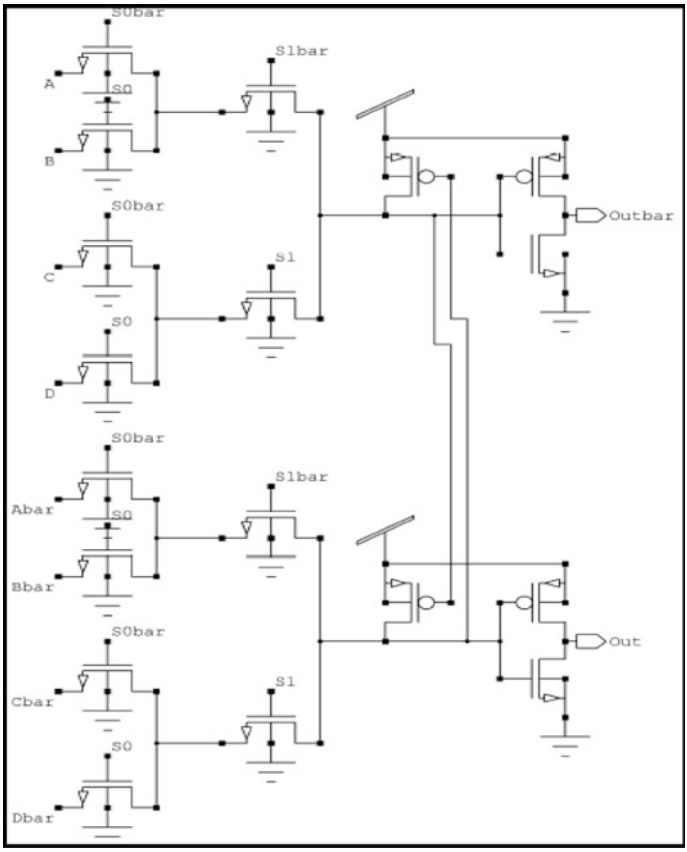

Fig. 5 Schematic of CPL

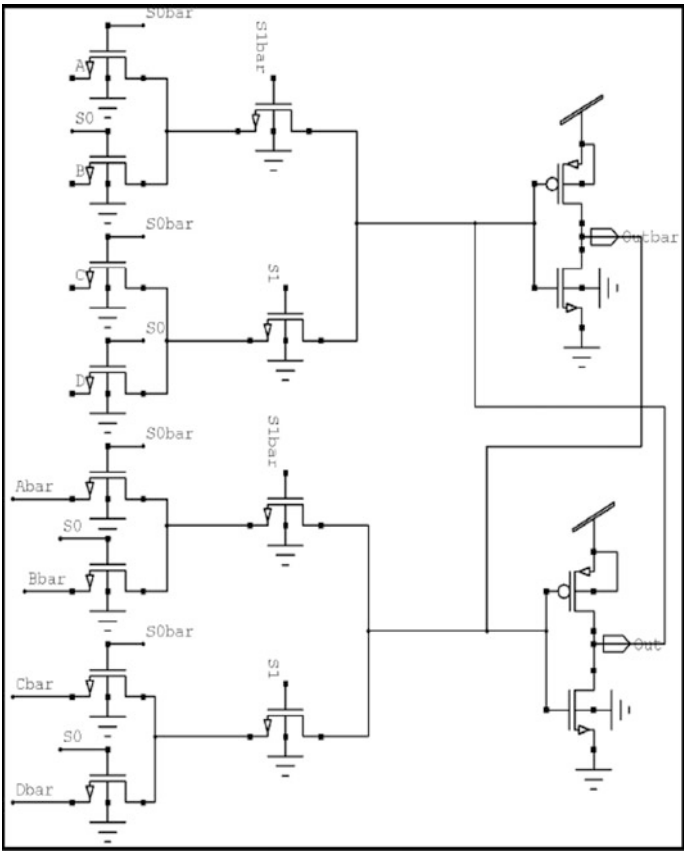

Fig. 6 Schematic of SRPL

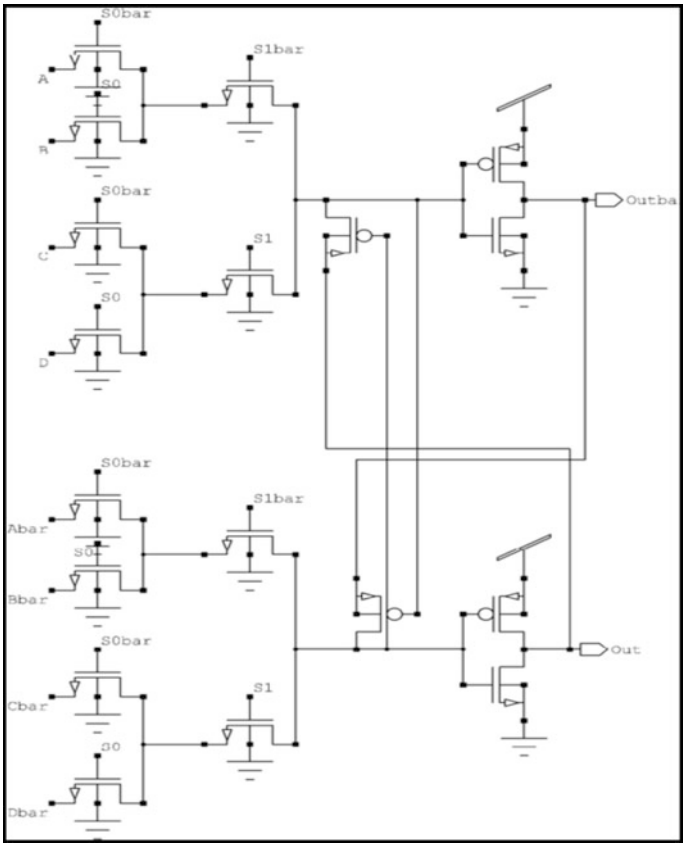

Fig. 7 Schematic of EEPL

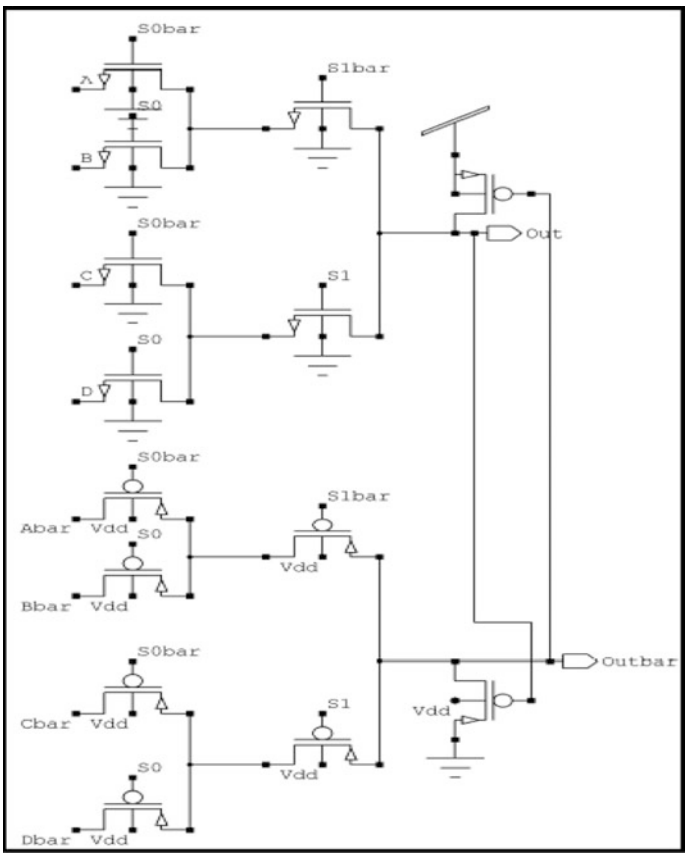

Fig. 8 Schematic of PPL

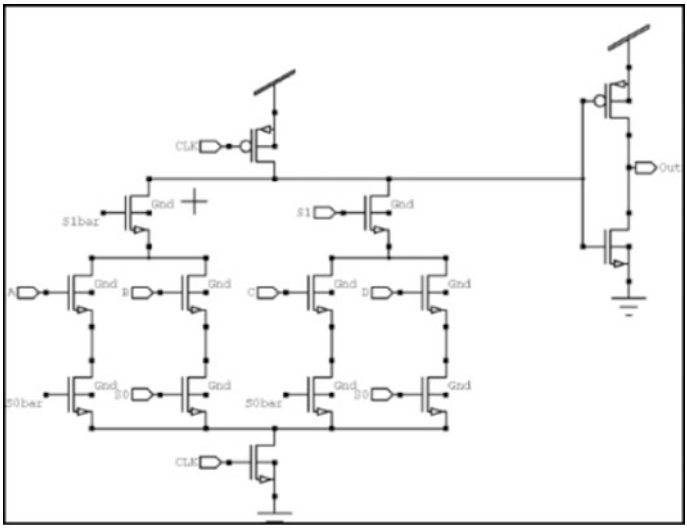

Fig. 9 Schematic of Domino

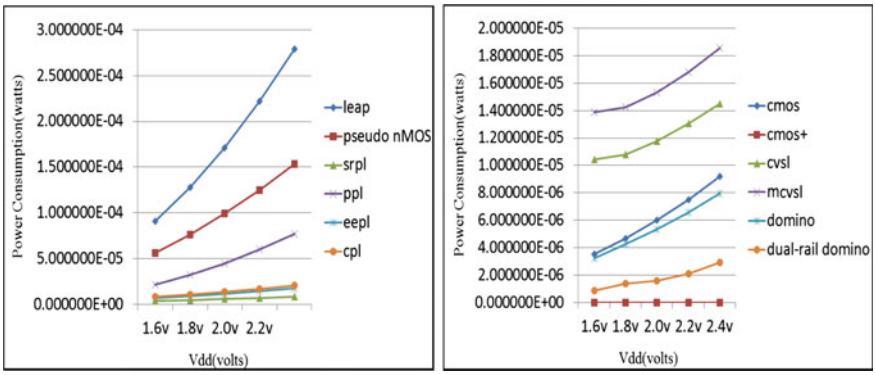

Fig. 10 Power consumption versus Vdd for leap, pseudo NMOS, srpl, ppl, eepl, cpl, cmos, cmos+, cvsl, mcvsl, domino, dual-rail domino based multiplexer circuits

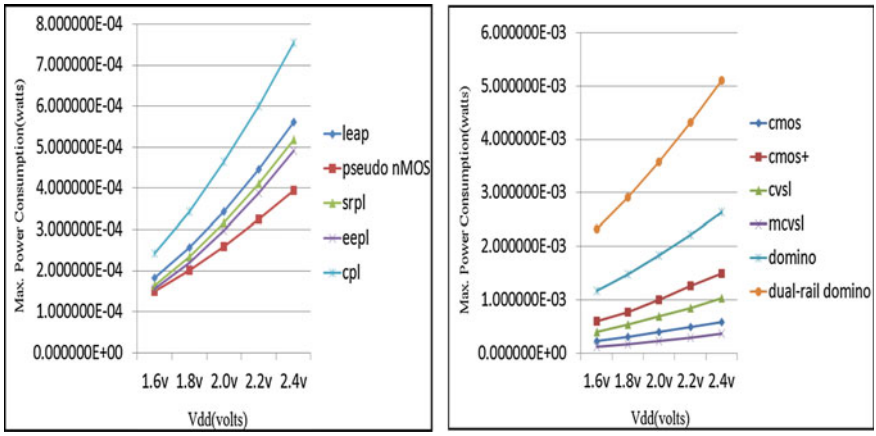

Fig. 11 Maximum power consumption versus Vdd for leap, pseudo NMOS, srpl, eepl, cpl, cmos, cmos+, cvsl, mcvsl, domino, dual-rail domino based multiplexer circuits

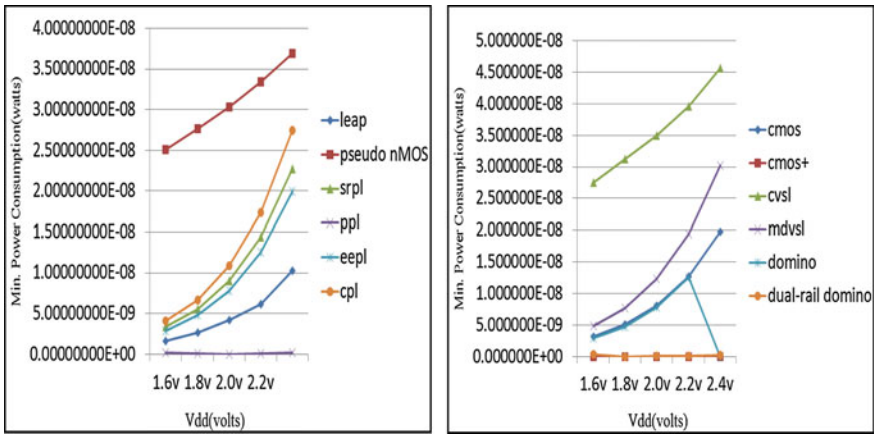

Fig. 12 Minimum power consumption versus Vdd for leap, pseudo NMOS, srpl, ppl, eepl, cpl, cmos, cmos+, cvsl, mcvsl, domino, dual-rail domino based multiplexer circuits

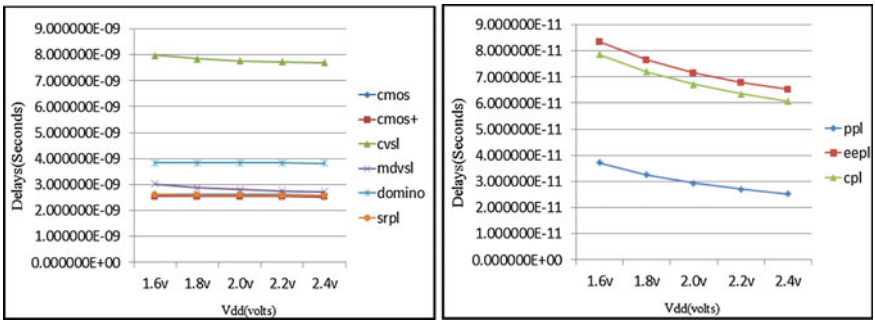

Fig. 13 Delay versus Vdd for cmos, cmos+, cvsl, mcvsl, domino, srpl, ppl, eepl, cpl based multiplexer circuits

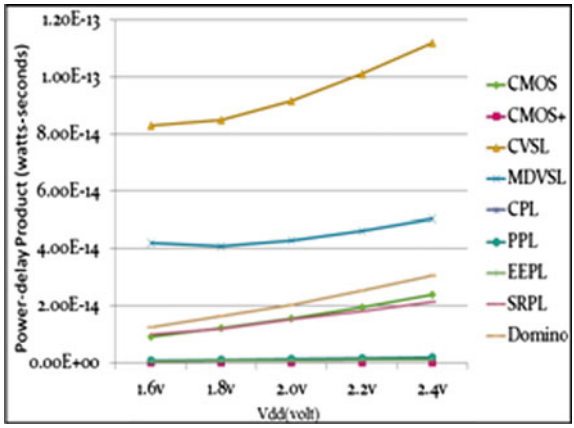

Fig. 14 Power-delay product versus Vdd for cmos, cmos+, cvsl, mcvsl, cpl, ppl, eepl, srpl, domino based multiplexer circuits

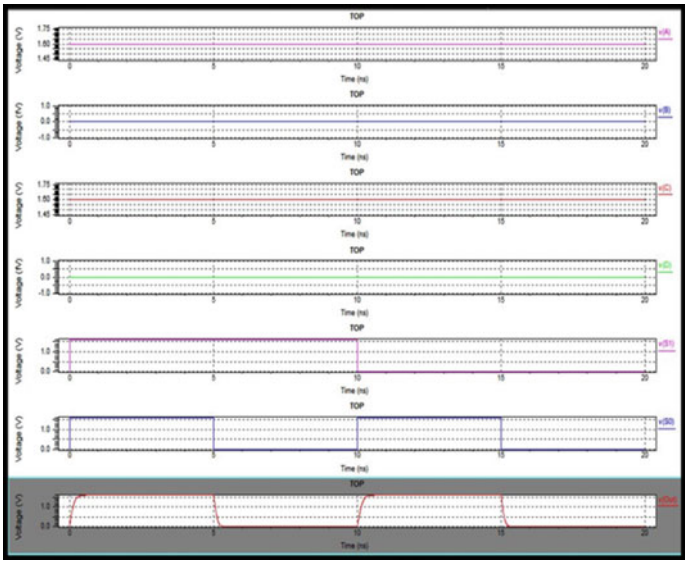

Fig. 15 Simulation result for input signal v(A), v(B), v(C), v(D), v(S1), v(S0) and output signal v(Out) for 4:1 multiplexer based circuits using static signals

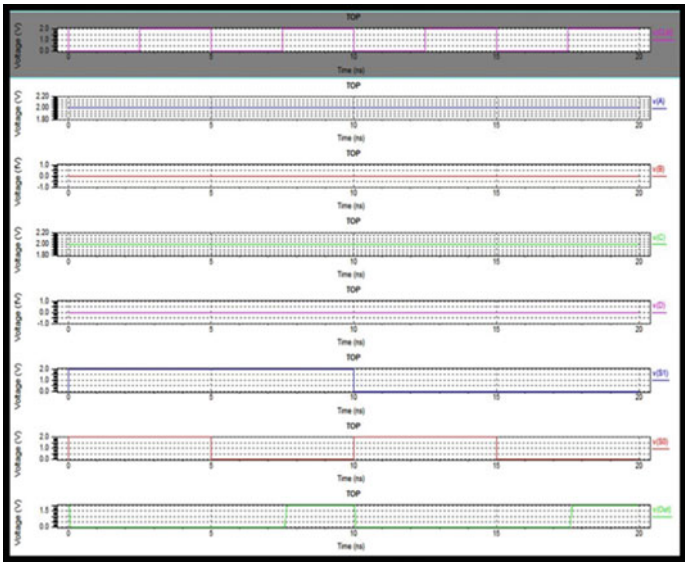

Fig. 16 Simulation result for input signal v(CLK), v(A), v(B), v(C), v(D), v(S1), v(S0) and output signal v(Out) for 4:1 multiplexer based circuits using dynamic signals

Table 1 Power delay product (Watt-Sec) comparison of different 4:1 multiplexer circuits

Voltage applied (V)	Power delay product (W-s)								
	CMOS	CMOS+	CVSL	MCVSL	CPL	PPL	EEPL	SRPL	Domino
1.6	9.25062E−15	6.95442E−18	8.30278E−14	4.18711E−14	6.41908E−16	7.88522E−16	5.88807E−16	9.93263E−15	1.24159E−14
1.8	1.22167E−14	7.55963E−18	8.47726E−14	4.10079E−14	7.70903E−16	1.04411E−15	7.04684E−16	1.2516E−14	1.64033E−14
2.0	1.56345E−14	6.62833E−18	9.1537E−14	4.29699E−14	9.15227E−16	1.32424E−15	8.36842E−16	1.52801E−14	2.0443E−14
2.2	1.95271E−14	7.14547E−18	1.00817E−13	4.62746E−14	1.07565E−15	1.62442E−15	9.85979E−16	1.82457E−14	2.51653E−14
2.4	2.39206E−14	1.0393E−17	1.11641E−13	5.04432E−14	1.25332E−15	1.94936E−15	1.15208E−15	2.14337E−14	3.05314E−14

5 Conclusion

In this paper, design, simulation and analysis of 4:1 multiplexer circuit using CMOS, CVSL, PTL and dynamic logic styles has been done on BSIM 3V3 90 nm PTM technology on Tanner EDA tool. On the basis of comparison of the circuit performance w.r.t. power, delay and power-delay product, Transmission gate (CMOS+) implementation of 4:1 multiplexer was found to be the most efficient logic style at 90 nm CMOS technology within the supply voltage range of 1.6–2.4 V. Pass transistor logic styles, particularly CPL, PPL and EEPL give better performance as compared to CMOS as far as the speed of operation is concerned. Other logic styles such as SRPL and Domino logic perform nearly as good as CMOS in terms of power, delay and power-delay product. But, due to weak output driving capability and less isolation, both SRPL and PPL are less suited while designing circuits with cascaded stages. Modified CVSL shows a slight improvement over existing CVSL w.r.t. delay. However, in case of CMOS, correct gate functionality is independent of transistor sizing and voltage scaling (ratioless logic). Its robustness and ease of use makes it a suitable candidate for the implementation of any arbitrary circuit.

References

1. R. Zimmermann, W. Fichtner, Low-power logic styles: Cmos versus pass-transistor logic. IEEE J. Solid-State Circ. **32**(7), 1079–1090 (1997)
2. S.-M. Kang, Y. Leblebici, in *CMOS Digital Integrated Circuits, Analysis and Design*
3. H.E. Weste Neil, D.M. Harris, *CMOS VLSI Design, A circuits and Systems perspective*, 4th edn.
4. Prof. A. Pal, in *Dynamic Power Dissipation* (2012), https://www.youtube.com/watch?v=I99B5bMWVr0&index=20&list=PLB3F0FC99B5D89571. Accessed 23 Nov 2015
5. A. Chaudhry, *Fundamentals of Nanoscaled Field Effect Transistors* (Springer Science, Business Media, New York, 2013). doi:10.1007/978-1-4614-6822-6_2
6. Prof. A. Pal, in *Dynamic Power Dissipation* (2012), https://www.youtube.com/watch?v=Eu9MLCekmwU&list=PLB3F0FC99B5D89571&index=12. Accessed 23 Nov 2015

Part VII
Smart Materials

Clean Energy Harvester Using Rare Earth Magnet and Ferro-Fluid

Vivek Kumar, Kshitij Chopra, Amit Kumar, Abhishek Verma and Vinod Kumar Jain

Abstract Herein we report a clean energy electrical generator based on rare earth magnet and kerosene oil based Ferro-fluid. The rare earth magnet move relative to a conducting coil by a support structure in the presence of kerosene oil based Ferro-fluid providing an ultralow friction interface between the magnet and support structure. In present work, an open circuit voltage of 5.0 V and a short circuit current of 2.08 mA have been generated in the tested assembly. Upon connecting two conducting coils in series the short circuit current remains 2.02 mA, but the open circuit voltage increased to 9.1 V and, upon connecting in parallel the current increased to 3.8 mA and voltage remains 4.8 V. The assembly can be attached with human leg/arms and an electrical signal has been generated in the conducting coil by the moving magnetic field with the moment of leg/arms while moving or running. The generated energy has been used to charge a small gadget's battery of around 3.7 V–50 mA h.

1 Introduction

Ambient sources dependent miniature energy harvesters gained significant research interest in recent years. Possible applications of energy harvesters include self-powering of autonomous devices such as wireless sensor nodes and implantable biomedical devices. Renewable power can be generated from environmental

V. Kumar · A. Kumar · A. Verma (✉) · V.K. Jain
Amity Institute for Advanced Research and Studies (Materials and Devices), Amity University, Noida 201303, Uttar Pradesh, India
e-mail: averma5@amity.edu

K. Chopra
Amity School of Engineering and Technology, Amity University, Noida 201303, Uttar Pradesh, India

A. Kumar · A. Verma · V.K. Jain
Amity Institute of Renewable and Alternative Energy, Amity University, Noida 201303, Uttar Pradesh, India

V.K. Jain et al. (eds.), *Recent Trends in Materials and Devices*, Springer Proceedings in Physics 178, DOI 10.1007/978-3-319-29096-6_58

energy sources such as light, wind, heat, acoustic signals and vibration. Electromagnetic induction based power generators have been widely used and researched in macro and miniature scale applications up to the present [1]. Utilization of cylindrical magnet in the presence of Ferro-fluids can be used as energy harvested in clean manner [2]. Chae et al. [3] have also demonstrated that the linear motion of cylindrical magnet under the presence of Ferro-fluid passing through the coils can generate voltage and current and a clean energy harvested can be fabricated.

2 Experimental Details

The kerosene oil based magnetic fluids used in this study is purchased from Charuset and used as supplied. The specifications of used Ferro-fluid are listed in Table 1. Here, we have designed and fabricated a testing assembly for the generation of clean energy using Ferro-fluid, in which rare earth magnet (REM) moves to and fro in the presence of tested Ferro-fluid with the help of fields generated by fixed magnets at the end as shown in Fig. 1. In order to increase the current and generated voltage, the coils are connected in series and parallel combinations as shown in Fig. 2.

Table 1 The specifications of used ferro-fluid

Physical Properties	HMB-1 magnetic fluid
<DM> (nm)	9.18 ± 0.5
σ in ln <D>	0.45
Carrier	Kerosene oil
Saturation magnetization, Ms (Gauss)	222 ± 10
Fluid density @ 27 °C (g/cc)	1.044
Viscosity η @ 30 °C, $\gamma > 100\ s^{-1}$ (cP)	2.9 ± 0.5
Boiling point (of the carrier) (°C)	85
Flash point (of the carrier) (°C)	80
Magnetic volume fraction	0.0498

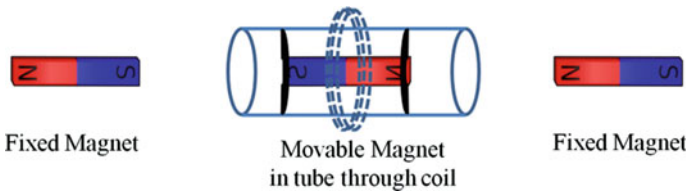

Fig. 1 Testing assembly, to record the generated energy

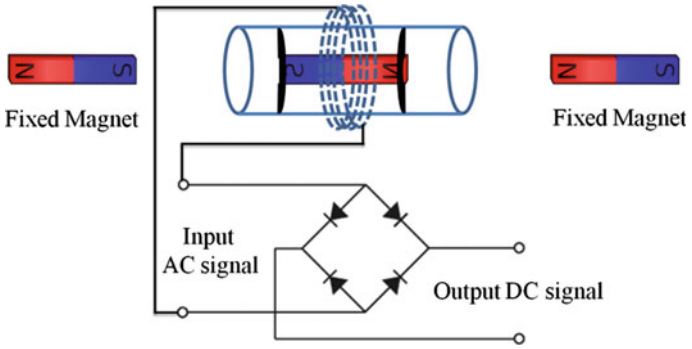

Fig. 2 The coils are connected in series and parallel combinations

3 Results and Discussion

Figure 1 demonstrates the testing assembly includes, fixed magnets, moving magnet in the presence of magnetic field in a sealed tube having kerosene oil based Ferro-fluid. The tube having copper coiling and as a result of the motion of the magnet through the coils, due to electromagnetic induction current and voltage is generated. An open circuit voltage of 5.0 V and a current of 2.08 mA are generated in the coil having 3200 turns. In order to increase the generated voltage, two coils are connected in series as shown in Fig. 2a and a open circuit voltage of 9.0 V is generated but the current remains almost same of 2.02 mA. The same coils when connected in parallel as shown in Fig. 2b shows the increase in current up to 3.8 mA with almost constant voltage of 4.8 V.

The current and voltage can be increased by adding more coils in series and parallel combination and desired amount of clean energy can be harvested from this device for small scale application. We have connected an LED directly with the coil and enlightened with generated energy with electromagnetic induction in the coil by the motion of magnet through the coil in the presence of kerosene oil based Ferro-fluid. When the LED was connected to single coil the V_{LED+R} becomes 1.65 V from V_{open} of 5.0 V and also the I_{LED} become 0.70 from 2.08 mA (I_{short}).

When coil 1 and 2 are in series and the LED was connected, the V_{LED+R} become 2.02 V from V_{open} of 9.0 V and also the I_{LED} become 0.83 from 2.02 mA (I_{short}).

Similarly for the coils connected in parallel, V_{LED+R} become 2.35 V from V_{open} of 4.8 V and also the I_{LED} become 0.72 mA from 3.8 mA (I_{short}) upon connecting with LED. The whole assembly was attached with human leg and the generated clean energy in the conducting coil by the moving magnetic field with the moment of leg while moving or running used to charge the battery of 3.7 V and 50 mA h.

4 Conclusions

In conclusion, the room temperature clean energy generator is demonstrated utilizing kerosene oil based Ferro-fluid and rare earth magnet. The generated voltage can be increased by combining more coils in combination and the current by combining more coils in parallel combination. In present work, a maximum voltage of 9.0 V and a maximum current of 3.8 mA have been harvested from this generator by combining only two coils in series and parallel combinations, respectively. Further, more current and voltage can be generated by combining more coils in various combinations or by further upgrading the generator and a desired amount of clean energy can be generated for small electronic equipments.

References

1. F. Herrault et al., Ultraminiaturized high-speed permanent-magnet generators for milliwattlevelpower generation. J. Microelectromech. Syst. **17**, 1376–1387 (2008)
2. P. Pillatsch et al., A scalable piezoelectric impulse-excited energy harvester for human body excitation. Smart Mater Struct. **21**, 115018A (2012)
3. S.H. Chae, S. Ju, Y. Choi, S. Jun, S.M. Park, S. Lee, H.W. Lee, C.-H. Ji, J. Phys: Conf. Ser. **476**, 012013 (2013)

Temperature Attuned Charge and Strain Co-mediated Giant Magnetoelectric (M-E) Coupling for Non-volatile Memory Device Applications

Kirandeep Singh and Davinder Kaur

Abstract The current study explored the investigation of direct strain and charge co-mediated Magnetoelectric (ME) coupling in magnetron sputtered ultra thin PZT/Ni-Mn-In (80 nm/30 nm) multiferroic heterostructure. The evidence of interfacial charges responsible for interaction between FE and FM layers at low thickness regime was manifested from abnormalities of C-V curves from typical butterfly behavior of ferroelectrics, resistance versus voltage plots as well as from magnetodielectric measurements. The signature of strain mediated coupling was evident from the profound variation in maximum polarization (P_{max}) with temperature.

1 Introduction

Artificial multiferroic composites comprising of ferroelectric (FE) and ferromagnetic (FM) layers which offers the possibility of strong magnetodielectric coupling at room temperature has attracted continually increasing research interests in past few years due to its promising application potentials in power efficient, fast dynamic response, low loss and compact devices [1]. In artificial multiferroic heterostructures robust room temperature ME coupling can be achieved through (i) strain induced ME effect across the interface, (ii) an interface charges driven ME effect, and (iii) magnetic exchange bias [2]. However, strain mediated ME coupling play a dominant role in heterostructures composed of highly strained strong piezoelectric and magnetostrictive layers. The strain mediated converse ME (CME) effect has been well studied and established. However strain mediated ME was significantly reduced in thin film heterostructures due to substrate clamping effect. At atomic level other coupling mechanism which is not limited by substrate clamping effect like charge mediated CME coupling plays a dominant role.

K. Singh · D. Kaur (✉)
Functional Nanomaterials Research Lab, Department of Physics
and Centre of Nanotechnology, Indian Institute of Technology Roorkee,
Roorkee 247667, Uttarakhand, India
e-mail: dkaurfph@iitr.ac.in

V.K. Jain et al. (eds.), *Recent Trends in Materials and Devices*,
Springer Proceedings in Physics 178, DOI 10.1007/978-3-319-29096-6_59

However, till date very few reports are available in literature on direct magneto-electric, due to low piezo-magnetic response of existing FM materials. However ferromagnetic shape memory alloys are potential multifunctional materials having giant magnetostriction. In current report we have shown the co-existence of direct strain and charge mediated coupling in FSMA based PZT/Ni-Mn-In heterostructure.

2 Experimental

The PZT/Ni-Mn-In heterostructure was fabricated by magnetron sputtering on P-type Si (100) substrate using 50 mm × 3 mm (diameter × thickness) $PbZr_{0.52}Ti_{0.48}O_3$ and $Ni_{50}Mn_{35}In15$ targets of 4 N purity. The complete heterostructure was fabricated ex situ at a constant temperature of 550 °C. The complete procedure for the growth of Ni-Mn-In heterostructure, thickness measurement, and phase identification was already reported in our previous studies [3]. To measure the ferroelectric properties, complete bilayer system was transformed into thin film capacitor structure. To measure the temperature and magnetic field dependent ferroelectric and resistivity properties of the heterostructure, Precision Premier II ferroelectric tester of Radiant technologies, Agilent 4294A Precision Impendence analyzer and 4200 SCS semiconductor characterization systems were coupled to vibrating sample magnetometer (VSM) using resistivity probe.

3 Results and Discussion

Figure 1 represents the polarization hysteresis loops of PZT/Ni-Mn-In (80/30 nm) heterostructure registered at different temperatures in ±400 kV/cm electric field range. The well saturated P-E loops indicate that PZT retains its ferroelectric character in the heterostructure. The huge variation in maximum polarization (P_{max}) with temperature was ascribed to temperature driven shape memory behavior of Ni-Mn-In. With variation in temperature Ni-Mn-In undergoes structural change from high temperature austenitic cubic phase to low temperature austenitic phase. This structural change was accompanied by huge volume change and large strain generation inside Ni-Mn-In. This strain on subsequently transferred to top PZT layer causes changes in its ferroelectric characteristic. A maximum polarization was observed around transformation region of Ni-Mn-In (250 K), where both austenitic and martensitic phases co-exists and resulted in maximum strain generation in Ni-Mn-In.

To confirm the presence of interfacial charges dc electric field dependent capacitance curves was recorded at room temperature in ±400 kV/cm electric field range (Fig. 2). The capacitance of the heterostructure was recorded in absence and in presence of magnetic field at an oscillator level of 10 mV and 1 MHz frequency. The significant deviation C(E) profile from typical butterfly shaped loops was

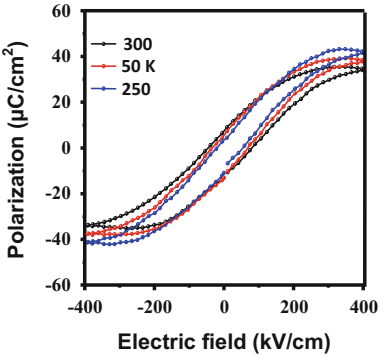

Fig. 1 P-E loops of PZT/Ni-Mn-In bilayer

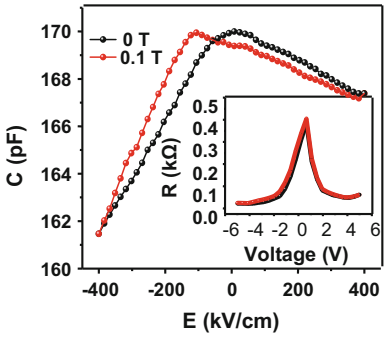

Fig. 2 C(E) loops, *Inset* R(V) plots of bilayer

ascribed to presence of interfacial charges at the interfaces. The negative electric field points the electric polarization of the PZT away from the interface resulting in negative bound charges at the interface of the heterostructure. These negative bound charges at the bilayer interface repel the free of Ni-Mn-In away from the PZT surface and resulting in formation of depletion layer at the interface. Thus the large negative electric field resulted in reduced effective capacitance by the increase of associated series depletion capacitance at the interface. Positive biasing directs the ferroelectric polarization of PZT towards the interface and resulting in positive bound charges close to Ni-Mn-In. The presence of positive charges at the interface during positive biasing results in accumulation of electrons which is reflected from the almost flat surface of C-E curves at positive biasing. The shifting of C(E) profiles with applied magnetic field indicates the coupling of grain boundary interfacial charges with magnetic field [4]. The confirmation of coupling of interfacial charges with magnetic field was also indicated from the significant change in R(V) profiles with magnetic field.

Figure 3 represents the frequency dependence of dielectric constant (ε)/dielectric loss (tan (δ)) plots of bilayer. The dielectric relaxation peak at lower frequency can arise from film electrode interface or grain boundaries at the interface, while high frequency peak can be attributed to grain capacitance [4]. The effect of magnetic field on dielectric relaxation was shown in Fig. 4. The sharp decrease in $\Delta\varepsilon/\Delta\tan\delta$

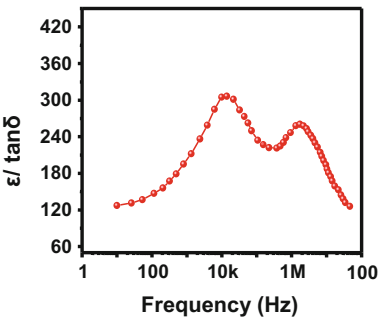

Fig. 3 ε/tanδ versus frequency plots of bilayer

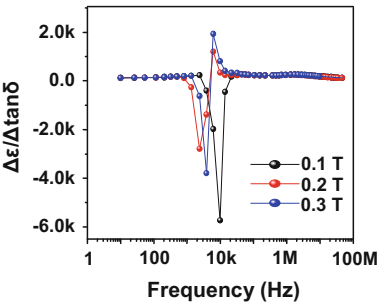

Fig. 4 Magnetodielectric measurements of bilayer

at ~10 kHz was due to increase in tanδ with magnetic field at 10 kHz. High magnetic field dependence of Δε/Δtanδ at lower frequency compared to higher frequency indicates that magnetic field mainly affects grain boundary charge relaxation not the charges at grains.

4 Conclusions

In conclusion strain and charge co-mediated DME coupling was demonstrated in PZT/Ni-Mn-In heterostructure through temperature dependent P-E loops and magneto-dielectric measurements.

References

1. J. Hu, Z. Li, L.-Q. Chen, C.-W. Nan, Nat. Commun. **2**, 1–8 (2011)
2. P. Borisov, A. Hochstrat, X. Chen, W. Kleemann, C. Binek, Phys. Rev. Lett. **94**, 117203 (2005)
3. K. Singh, D. Kaur. J. Phys. D. Appl. Phys. (In Press)
4. R. Gupta, S. Chaudhary, R.K. Kotanal. ACS Appl. Mater. Interfaces. **7**, 8472–8479 (2015)

Fly Ash Based Zeolite as an Anti-corrosive Pigment in Paints

Ruchi Shaw, Richa Sharma and Sangeeta Tiwari

Abstract In the present study, waste fly ash, a by-product from coal power stations was converted into zeolite NaY for its successful utilization as an anticorrosive pigment in paints. The synthesized zeolite NaY was modified by exchanging its nominal cation Na^{+1} with Mo^{+1} ion. The Mo^{+1} exchanged zeolite was used as an anticorrosive pigment in coatings. The synthesized zeolite was characterized using X-ray diffraction and Scanning electron microscopy techniques. Coatings were formulated using various percentages of the synthesized pigment in epoxy resin. The coatings in epoxy resin were applied on mild steel substrate and tested using Electrochemical Impedance Spectroscopy (EIS). The results indicate effective anti-corrosive properties of the fly ash based zeolitic pigments containing Mo^{+1}.

1 Introduction

Corrosion is a natural chemical process [1] and over decades it has emerged as a serious problem affecting mankind directly or indirectly. Corrosion is very disastrous in terms of safety and health. Sudden failures due to corrosion cause construction collapses [2], depletion of natural resources, accelerated ageing of goods [3], release of toxic chemicals into environment etc. It affects high end industries such as railways [4, 5], petroleum [6, 7], chemical processing plants [8, 9], pipeline industries [10, 11], etc.

Effective anti-corrosive measures need to be undertaken which should be user friendly, cheap and environment friendly in nature. Various methods such as galvanizing, copper plating, enameling, coatings etc. are already being opted. The present work is focused on anti-corrosive coatings which is based on the isolation of the concerned material from the corrosive media. Coatings can be of various types, such as metallic coatings, organic coatings, inorganic coatings etc. In the present

R. Shaw · R. Sharma · S. Tiwari (✉)
Amity Institute of Applied Sciences, Amity University, Noida 201301
Uttar Pradesh, India
e-mail: stiwari2@amity.edu

V.K. Jain et al. (eds.), *Recent Trends in Materials and Devices*,
Springer Proceedings in Physics 178, DOI 10.1007/978-3-319-29096-6_60

study, we have used fly ash which is a waste by product from thermal power stations and is generated every year in enormous quantities [12]. At present only a small amount of fly ash which is generated is put to gainful uses. In terms of composition, fly ash is a very rich material containing useful minerals such as silica and alumina [13] which can be converted/modified into value added materials such as such as zeolites, cenospheres, carbon, domestic cleaning powder etc. thereby paving a way for their successful utilization.

Herein we report the synthesis of fly ash based NaY zeolite and preparation of anti-corrosive coatings by modifying the synthesized zeolite with Mo^{+1} ion. The Mo^{+1} based anti-corrosive coatings is non-toxic and less active oxidant as compared to the existing chromium and lead based coatings and thus is a successful alternative to the existing harmful forms of coatings.

2 Experimental Details

Materials Used

Coal fly ash (Badarpur thermal power station), Sodium hydroxide (HPLC), Molybdic acid (CDH), Xylene (Avantor), Epoxy Resin and hardener. All the chemicals used were of analytical grade or of the highest purity available.

Cleaning of raw fly ash

Raw fly ash contains a large amount of un-burnt carbon which was removed by magnetic separation method. It also contains iron oxides which was removed using acid leaching method.

Synthesis of zeolite NaY from fly ash

Zeolite NaY was synthesized using conventional method. The cleaned fly ash was mixed with NaOH and fused at 592 °C for 3 h. 1 M sodium aluminate was then mixed with the fused mixture and treated hydrothermally at 110 °C for 4 h. The obtained product was filtered and dried at 70 °C for 2 h.

Modification of the fly ash based zeolite

The fly ash based NaY zeolite was modified by exchanging with Mo^{+1} ions. The Mo^{+1} ion exchanged zeolite was designated as FPMo and pure zeolite was designated as FAZ. Molybdic acid ($MoO_3 \cdot H_2O$) solution was used for loading the Mo^{+1} ion using conventional ion exchange process.

Formulation of the coatings

The fly ash based zeolitic pigments were taken in a very small amount (2 % and 5 %) and mixed with epoxy resin for the formulation of the coatings. Xylene was used as the medium of dispersion. Table 1 shows the formulation of the coatings.

Table 1 Formulation of the coatings

S.no	Code	Detail of coding
1.	FAZ5	5 % FAZ coating in epoxy resin
2.	FPMo2	2 % FPMo coating in epoxy resin
3.	FPMo5	5 % FPMo coating in epoxy resin

3 Results and Discussion

The SEM image of the raw fly ash confirms that the fly ash particles are spherical in nature. They have cenospheric morphology (Fig. 1a) while the SEM images of the fly ash based zeolite confirms the conversion of fly ash into zeolite having cubic morphology of well-defined crystals (Fig. 1b–d). Cubic crystals having sharp edges can be seen.

The XRD image of the fly ash based zeolite NaY shows the characteristic peaks of silica and alumina (Fig. 2a). The XRD spectra of the Mo^{+1} ion exchanged zeolite (Fig. 2b) is similar to that of the pure unexchanged zeolite thereby confirming that the Mo^{+1} ion exchanged zeolite are as stable as the pure zeolite NaY.

The particle size analysis confirmed that the average particle size of the fly ash based zeolite NaY was 664.3 nm. The density of pure zeolite was 1.530 g/cc whereas the density of Mo^{+1} exchanged zeolite was 1.660 g/cc. Greater density of the Mo^{+1} exchanged zeolite is attributed to the greater density of the Mo metal as

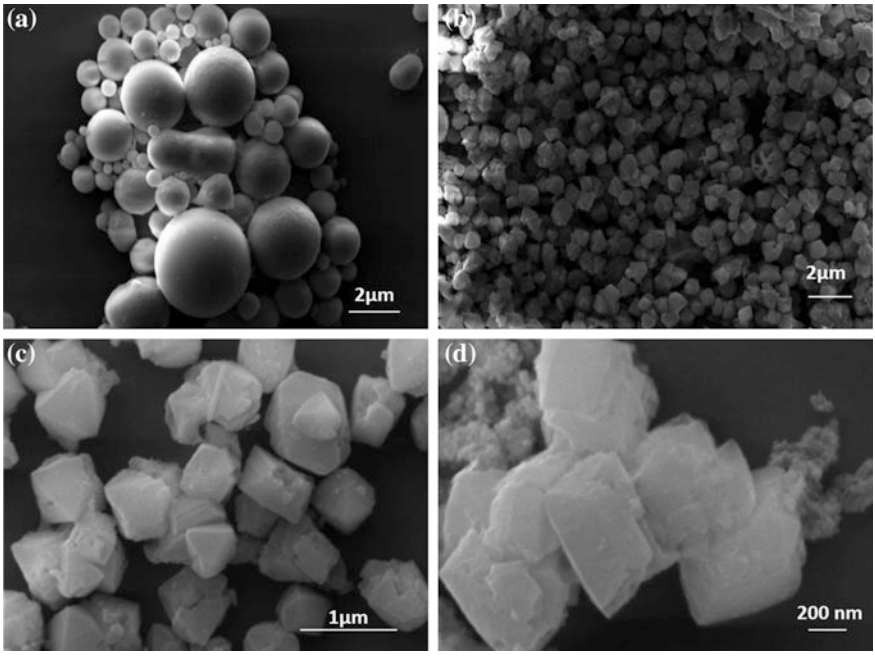

Fig. 1 **a** SEM of fly ash particles **b–d** SEM images of fly ash based zeolite NaY

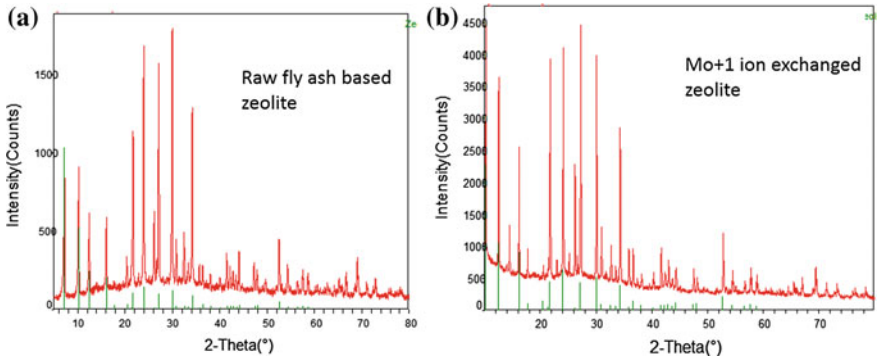

Fig. 2 XRD spectra of **a** Raw fly ash based zeolite NaY (unexchanged) **b** Mo^{+1} ion exchanged zeolite NaY

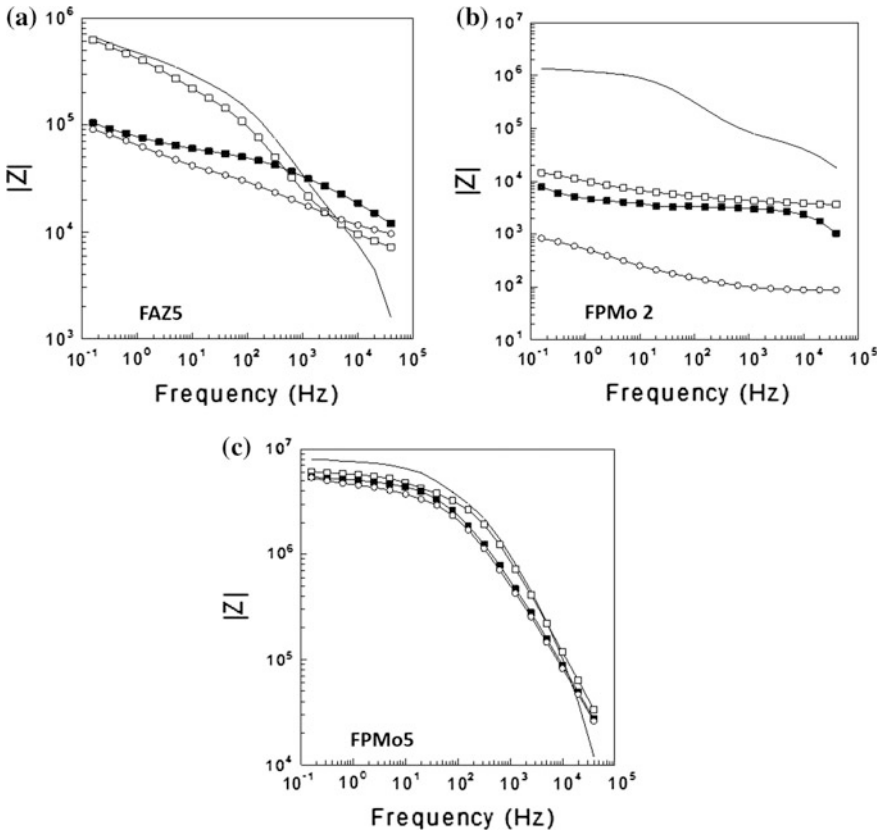

Fig. 3 Bode plots **a** FAZ2 **b** FPMo2 **c** FPMo5

Table 2 Electrochemical Impedance Spectroscopy data

Sample	RCT (Ω)	CDL (F)	Thickness (μm)
FAZ5 initial	1.0365×10^{6}	5.0091×10^{-7}	50 ± 5
1st day	1.1498×10^{6}	3.7353×10^{-7}	50 ± 5
3rd day	1.2412×10^{5}	7.4109×10^{-10}	50 ± 5
5th day	1.5091×10^{5}	3.5614×10^{-8}	50 ± 5
FPMo2 initial	1.3186×10^{6}	6.6185×10^{-9}	50 ± 5
1st day	4.1843×10^{4}	2.9867×10^{-6}	50 ± 5
3rd day	3.875×10^{3}	2.4797×10^{-9}	50 ± 5
5th day	1.988×10^{3}	4.202×10^{-5}	50 ± 5
FPMo5 initial	8.0895×10^{6}	3.1062×10^{-10}	50 ± 5
1st day	6.2038×10^{6}	2.6431×10^{-10}	50 ± 5
3rd day	5.2571×10^{6}	4.9695×10^{-10}	50 ± 5
5th day	4.8336×10^{6}	5.2619×10^{-10}	50 ± 5

compared to that of Na metal. Due to high density, pigment FPMo has a better barrier property. The anti-corrosive pigments of the coatings were accessed using 3 % NaCl solution for 5 days. Their Bode plots and EIS measurement data were obtained.

Figure 3a describes the Bode plot of unexchanged zeolite FAZ5 containing 5 % of the pigment in epoxy resin. Figure 3b, c contains Mo^{+1} ion exchanged zeolitic pigment (2 and 5 %) in epoxy resin. The resistance of FAZ5 coating was around 10^{6} Ω on the initial day while it decreased to 10^{5} Ω on the 3rd day and this value remained constant till the 5th day. The resistance value of FPMo2 decreased considerably till the 5th day. The coating did not retain a constant resistance thereby showing its non-effectiveness for corrosion protection. Contrary, FPMo5 showed a very good resistance of the order of the 10^{7} Ω. It is clear from the graph that it has nearly retained the resistance values till the 5th day of analysis. This signifies that the coating was very effective in anti-corrosion protection. It is also henceforth proved that only 5 % of Mo^{+1} exchanged zeolite is enough for a good anti-corrosion protection against mild steel panels. Table 2 provides detailed data of anti-corrosive pigments and the thickness films formed on the steel panels coated by all the three coatings.

4 Conclusion

In the present study, raw fly ash was converted into zeolite NaY using conventional methods and exchanged with high density Mo^{+1} ion to increase its barrier properties and introduce anti-corrosive properties to it. The coatings were formulated in epoxy resin and the concentration of the zeolitic pigment used was 2 % and 5 %. The Mo^{+1} exchanged zeolitic pigment FPMo was compared with that of the pure

unexchanged zeolitic pigment FAZ. The study reveals that 5 % concentration of Mo^{+1} exchanged zeolitic pigment in epoxy resin is enough to maintain a resistance of 10^7 Ω cm^{-2} which can be regarded as an appropriate value for smart anti-corrosive pigments according to Mayne's concept. The developed zeolitic pigments are cost friendly as they are processed from an abundant waste material; coal fly ash. Also, the developed material is nontoxic as it does not contain any harmful toxic metal ions. Thus the Mo^{+1} exchanged zeolitic pigments are an eco-friendly alternative to the existing Pb and Cr based pigments.

References

1. T.E. Graedel, J. Electrochem. Soc. **136**(4), 204C–212C (1989)
2. M.V. Biezma, F. Schanack. J. Perform. Constr. Facil. **21**(5), 398–405 (2007)
3. G. Wang, J. Spencer, H. Sun, J. Offshore Mech. Arct. Eng. **127**(2), 167–174 (2005)
4. S. Beretta, M. Carboni, G. Fiore, A. Lo, Conte. Int. J. Fatigue **32**(6), 952–961 (2010)
5. B. Panda, R. Balasubramaniam, G. Dwivedi. Corr. Sci. **50**(6), 1684–1692 (2008)
6. R.J. DeGray, L.N Killian Ruiz. Indus. Eng. Chem. **52**(12), 74A–76A (1960)
7. M.A. Migahed, A.M. Al-Sabagh, Chem. Eng. Commun. **196**(9), 1054–1075 (2009)
8. H.P. Herbert, Fang, Li Chong Xu and Kwong Yu Chan, Water Res. **36**(19), 4709–4716(2002)
9. G. Bereket, E. Hür, C. Öğretir, J. Mol. Struct :THEOCHEM, **578**(1–3), 79–88 (2002)
10. A. Cosham, P. Hopkins and K.A Macdonald. Eng. Fail. Anal. **14**(7), 1245–1265 (2007)
11. T. Mori, T. Nonaka, K. Tazaki, M. Koga, Y. Hikosaka, S. Noda, Water Res. **26**(1), 29–37 (1992)
12. P. Janoš, H. Buchtová, M. Rýznarová, Water Res. **37**(20), 4938–4944 (2003)
13. M. Inada, Y. Eguchi, N. Enomoto, J. Hojo, Fuel **84**(2–3), 299–304 (2005)

Effect of Temperature and Ferro-Fluid on Rotation of Rare Earth Magnet Used for Clean Energy Generation

Vivek Kumar, Kshitij Chopra, Bidyut Barman, Amit Kumar, Abhishek Verma and Vinod Kumar Jain

Abstract Herein, we have tested kerosene and transformer oil based Ferro-fluids and optimized the rpm of the rare earth magnet (REM) for the best possible efficiency. Rotation per minute of the REM decreases with increase in temperature in case of kerosene oil based Ferro-fluids, whereas it increases with increase in temperature in case of kerosene oil based Ferro-fluids. In the tested system, REM exhibit similar rpm around 50 °C for both the Ferro-fluids. At room temperature clean energy can be generated in this circular model by using kerosene oil based Ferro-fluid. The maximum voltage and current of 0.2 V and 0.2 mA can be generated in this model with kerosene oil based Ferro-fluid at room temperature.

1 Introduction

Ferro-fluids are in the commercial arena for over few decades but generation of electricity using Ferro-fluids attract great attention since last few years [1–4]. Moving magnetized Ferro-fluid or magnetic nanoparticle fluid through a specially-shaped sealed conduit coiled with insulated conducting wires creates a change in magnetic flux through the coils, results in the generation of convection current in the fluid due to induction [5]. The rate of change of the flux through the coils depends upon the speed of the magnet in the presence of Ferro-fluid. Rare earth magnets are possess various advantageous properties over ferrite magnets

V. Kumar · A. Kumar · A. Verma (✉) · V.K. Jain
Amity Institute for Advanced Research and Studies (Materials and Devices), Amity University, Noida 201303, Uttar Pradesh, India
e-mail: averma5@amity.edu

K. Chopra
Amity School of Engineering and Technology, Amity University, Noida 201303, Uttar Pradesh, India

B. Barman · A. Kumar · A. Verma · V.K. Jain
Amity Institute of Renewable and Alternative Energy, Amity University, Noida 201303, Uttar Pradesh, India

V.K. Jain et al. (eds.), *Recent Trends in Materials and Devices*, Springer Proceedings in Physics 178, DOI 10.1007/978-3-319-29096-6_61

such as, very high adhesive force, light weight, miniaturized shape, etc. and hence can give better results. In the testing assembly, rotation of the magnet per minute depends upon various parameters such as viscosity, fraction, temperature etc. Hence the testing of various types of Ferro-fluids with different specifications is important to develop a good quality clean energy generator operable in a broad range of temperature.

2 Experimental Details

The magnetic fluids (HMB-1 & HMB-4) used in this study are purchased from Charuset and used as supplied. The carrier in these fluids is kerosene oil and transformer oil. The specifications of used Ferro-fluids are listed in Table 1. Here, we have designed and fabricated a testing assembly for the generation of clean energy using Ferro-fluid, in which rare earth magnets (REM) rotates in the presence of tested Ferro-fluid with the help of hot air thrust given from outside. In order to investigate the effect of temperature on the rotation per minute of the REM, the temperature of the tested assembly was varied from 30 to 80 °C using 245 V, 250 W IR lamp and the temperature was controlled by controlling the distance between them and measured continuously with thermometer.

3 Results and Discussion

Figure 1 demonstrates the testing assembly includes, vacuum pump for compressed air inlet, rare earth magnets, sealed acrylic tube in which the REM can rotate. The arrows show the direction of air inlet, outlet and direction of rotation of the magnet. At constant pressure of the inserted air, rpm of the REM mainly depends on type of carrier oil present in the Ferro-fluids and the operational temperature. We found that in case of kerosene oil based Ferro-fluid the rpm of the REM decrease with

Table 1 The specifications of used ferro-fluids

Physical properties	HMB-1 magnetic fluid	HMB-4 magnetic fluid
<DM> (nm)	9.18 ± 0.5	8.45 ± 0.05
σ in ln <D>	0.45	0.4
Carrier	Kerosene oil	Transformer oil
Saturation magnetization, Ms (Gauss)	222 ± 10	205 ± 10
Fluid density @ 27 °C (g/cc)	1.044	1.042
Viscosity η @ 30 °C, $\gamma > 100\ s^{-1}$ (cP)	2.9 ± 0.5	67 ± 5
Boiling point (of the carrier) (°C)	85	150
Flash point (of the carrier) (°C)	80	140
Magnetic volume fraction	0.0498	0.0442

increased temperature. Whereas, the rpm of the REM increased in case of transformer oil based Ferro-fluid with elevated temperature.

The rpm of the REM was found to be of 270 and 100 with kerosene oil and transformer oil based Ferro-fluids, respectively. The rpm of the REM decrease continuously and become zero at 80 °C in case of kerosene oil based Ferro-fluids. This decrease in rpm is may be because of the low viscosity of the carrier at room temperature and become zero at around 80 °C, is also because that the carrier oil evaporate at this temperature.

Figure 2, illustrate as in: Curve A: rpm of magnet with different temperature in kerosene oil based Ferro-fluid; Curve B: rpm of magnet with different temperature in transformer oil based Ferro-fluid. The rpm of the REM increased with increase in temperature having transformer oil based Ferro-fluid.

Generation of clean energy: According to Faraday's Law of electromagnetic induction, any change in the magnetic environment of a coil of wire will cause a voltage (emf) to be "induced" in the coil. Hence coiling was done on the frame

Fig. 1 Testing assembly, to record the rotation of REM in the presence of Ferro-fluid

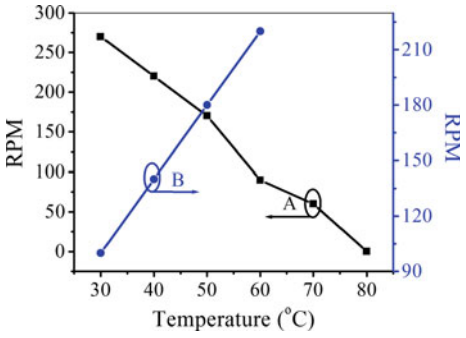

Fig. 2 Temperature dependent rpm of REM

(shown in Fig. 1) in which REM was moving in the presence of kerosene oil based Ferro-fluid and a maximum voltage and current of 0.2 V and 0.2 mA can be generated in this system, respectively.

4 Conclusions

In conclusion, the Ferro-fluid based clean energy generator requires a specific type of carrier oil based Ferro-fluids for various temperature applications. The rpm of REM decreases with increase in temperature in devices having low viscosity carrier oil based Ferro-fluid, where as it increases with high viscosity carrier oil based Ferro-fluid. Hence, for low temperature (around room temperature) application, low viscosity carrier oil based Ferro-fluid become the better options, where as for high temperature applications, high viscosity carrier oil based Ferro-fluid become the superior choice. The generated current and voltage can be increased by further optimizing the rpm, temperature and the shape of the testing assembly.

References

1. K. Raj, R. Moskowitz, J. Magn. Magn. Mater. **85**, 233 (1990)
2. J. Roger, J.N. Pons, R. Massart, A. Halbreich, J.C. Bacri, Eur. Phys. J. Appl. Phys. **5**, 321 (1999)
3. A.S. Lübbe, C. Alexiou, C. Bergemann, J. Surg. Res. **95**, 200 (2001)
4. A. Bibo, R. Masana, A. King, G. Li, M.F. Daqaq, Phys. Lett. A **376**, 2163 (2012)
5. R.A. Bayliss, C.B. Forest, M.D. Nornberg, E.J. Spence, P.W. Terry, Phys. Rev. E **75**, 026303 (2007)

Microstructures, Mechanical Properties and Strengthening Mechanisms of cast Cu–Al Alloys Processed by Cryorolling

S.M. Dasharath and Suhrit Mula

Abstract In the present work, the cast structures of Cu-4.5wt% Al alloy was homogenized by annealing at 800 °C for 4 h. The samples were kept under LN_2 before and during the rolling process in each pass to maintain a constant LN_2 temperature. Mechanical properties were evaluated by the tensile test. Microstructural analysis was carried by optical microscopy and TEM analysis. The maximum yield strength (YS) of the 75 % cryorolled samples of Cu-4.5wt% Al alloy was found to be 786 MPa with a ductility of 4.8 %. This is due to the formation of ultrafine grains and nano-twins possibly play the pivotal role for the improved YS and ductility.

1 Introduction

The strength of the materials can be improved through a grain size refinement as per the Hall-Petch relationship between the strength and grain size. In order to fabricate these nano/ultrafine grained material, several severe plastic deformation (SPD) processes such as equi-channel angular pressing (ECAP), high pressure torsion (HPT) accumulative roll bonding (ARB), Ball milling (BM) Friction stir processing and cryorolling have been used in the present days [1]. Cryorolling has been identified as one of the potential route for producing ultrafine grained microstructures in different metals and alloys because the end product of this process is generally sheet metal which has a major application in the several industries. Rolling at cryogenic temperature results in a suppression of dynamic recovery, large amount of dislocation can be accumulated and promote the twin activity [2].

Several reports are available on the investigation of Cu alloys to develop ultrafine grained materials [3]. But, the role of SFE on the deformation mechanisms

S.M. Dasharath (✉) · S. Mula
Department of Metallurgical and Materials Engineering, Indian Institute of Technology, Roorkee, Roorkee 247667, Uttarakhand, India
e-mail: dashmech@gmail.com

V.K. Jain et al. (eds.), *Recent Trends in Materials and Devices*,
Springer Proceedings in Physics 178, DOI 10.1007/978-3-319-29096-6_62

at cryogenic temperature and on the mechanical properties has not been addressed systematically for the Cu–Al alloy. Therefore, an attempt has been made to investigate the mechanical behaviour and microstructural features of the cryorolled low (Stacking fault energy) SFE Cu–Al alloy.

2 Experimental Details

Copper with 4.5 % Al (wt%) were produced by metal mould casting technique from electrolyte grade copper and aluminium (purity level >99.99 %). After that the material was machined to remove the rough casting surface and homogenized at 800 °C for 4 h in a high purity argon atmosphere. The rolling set up was modified to keep the working zone of the rollers in the liquid nitrogen to effectively suppress dynamic recovery and recrystallisation during the deformation process. Each sample was subjected to multiple rolling passes to attain maximum limit of deformation and approximately 2 % reduction in area (RA) is given per pass. Tensile specimens were prepared as per ASTM: E8 sub size with 12.5 mm gauge length. The samples were machined along the plane parallel to the rolling direction. Uniaxial tensile tests were conducted with a constant strain rate of 2×10^{-4} s^{-1} using a Tinius Olsen machine of 25 kN capacity. Microstructural analysis was carried out by optical microscopy and TEM analysis. Optical microstructure was examined using a LEICA DMI 5000 M optical microscope. TEM investigation was carried out using FEI Technai 20 G2S-Twin transmission electron microscope operated at 200 kV.

3 Results and Discussion

Figure 1 shows the optical micrograph of the as homogenised and cryorolled Cu–Al alloy. Homogenised Cu-4.5 % Al alloy samples contains equiaxed grains with a small number of twins can be observed from the micrograph (Fig. 1a). The line intercept method was used to estimate the average grain size was from such 300 grains using, and the size is 180 ± 5 μm. In the 50 % RA cryorolled samples, it can be noticed that severely deformed elongated grains (Fig. 1b) in the rolling direction along with the parallel intersecting slip/deformation bands were formed. Figure 1c and d show the bright field TEM micrograph and SAD pattern of cryorolled 4.5 % Al alloys deformed to 75 % RA. Formation of dislocation cells and subgrain could be observed from the bright field TEM image. Generally in the maximum RA, increases the dislocation cells/substructures accompanied by formation of a significantly larger number but finer subgrains. The associated continuos ring—like SAD pattern of the 4.5 % Al shows that the grain boundaries are mainly high angle with different orientations.

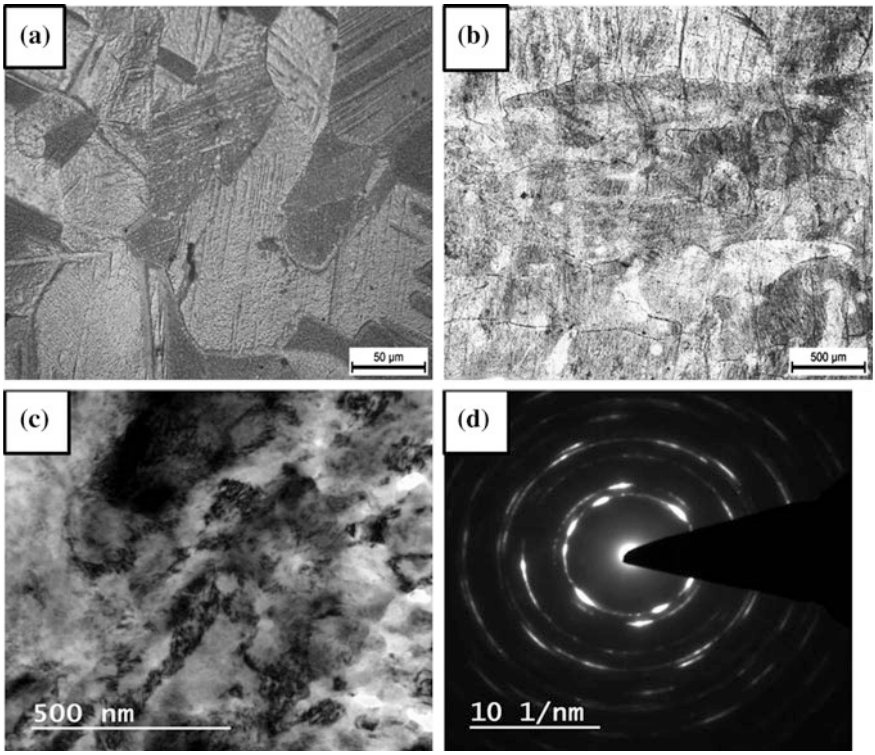

Fig. 1 Optical micrographs of **a** as homogenised, **b** 50 % cryorolled and **c** 75 % cryorolled specimens **d** SAD pattern of 75 % cryorolled specimens

Figure 2 shows the tensile mechanical behaviour of the homogenized and cryorolled Cu-4.5 % Al alloy. The yield strength (YS) and ultimate tensile strength (UTS) of homogenized Cu-4.5 % Al alloy found to be 75.9 and 280.4 MPa. The YS of 50 and 75 % RA cryorolled Cu-4.5 % Al samples found to be 567 and 786 MPa, respectively. The YS and UTS of the annealed samples followed by casting increased due to the solid solution strengthening. Plastic deformation at the liquid nitrogen temperature results in suppression of dynamic recovery and recrystallisation [3]. Simultaneously, there is an increase in the dislocation density, which produces the dislocation cells. Finally the formation of these ultrafine grained materials occurs due to rearrangement of the dislocation cells subjected to aging/short annealing. As per the Hall-Petch equation, YS increases due to the reduction in grain.

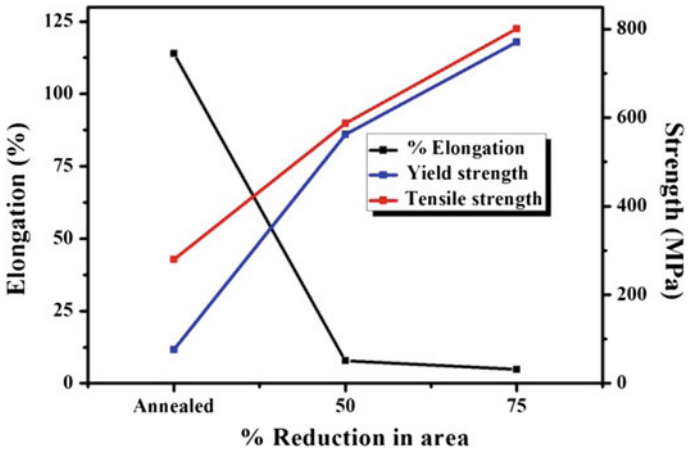

Fig. 2 UTS, YS and % elongation of the homogenised and cryorolled samples

4 Conclusions

Cryorolled samples of 4.5 % Al alloy with 75 % RA showed the highest value of mechanical properties (YS-786 MPa and ductility-4.8 %) as compared to that of homogenised samples. This is due to the saturation of dislocations density and refinement of grain size because of low SFE.

References

1. I. Sabirov, M.Y. Murashkin, R.Z. Valiev, Mater. Sci. Eng., A **560**, 1–24 (2013)
2. H. Bahmanpour, A. Kauffmannb, M.S. Khoshkhooc, K.M. Youssef, S. Mulaa, J. Freudenberger, J. Eckert, R.O. Scattergooda, C.C. Koch, Mater. Sci. and Eng. A **529**, 230–236 (2011)
3. S.M. Dasharath, C.C. Koch, S. Mula, Mater. Charact. **110**, 14–24 (2015)

Investigation of Capping-Ligand Effect on Colloidal CIGSe Nanocrystals Prepared via Colloidal Route for Thin Film Solar Cell Applications

M. Ahamed, Parul Chawla and Shailesh Narain Sharma

Abstract Chalcopyrite Cu (In_xGa_{1-x}) Se_2 is a low-cost and potential alternative to present thin film silicon based photo-voltaic (PV) technology. Studies on nanocrystals of CIGSe prepared via colloidal route method with different capping agents, viz., oleylamine (OLA) and oleic acid (OA) have been done systematically. An exploration for binding abilities and plausible mechanism for the interaction between nanocrystals and capping agents employed has been envisaged.

1 Introduction

Sun is the primary source of energy. Unlike other forms of energy, sunlight is the most abundant, available throughout the year and most importantly a green energy source. Present PV are silicon based and relatively costly. II-generation photo-voltaic materials such as CIGSe and related materials are proving to be excellent alternatives to Si-based solar cells. In recent years, the efficiency of CIGSe solar cell have recorded to be 21.7 % [1] and research for making further progress in efficiency is in pace globally.

CIGSe is tetrahedral bonded structure with a variable band gap of 1.0 and 1.7 eV [2, 3]. The band gap can be tuned by varying the Indium/Gallium ratios, parametric variations [4] and fine tuning of particle size of the nanocrystals. Therefore the binding effect of ligand plays an important role on CIGSe's structural,

M. Ahamed · P. Chawla · S.N. Sharma (✉)
CSIR Network of Institutes for Solar Energy (NISE), CSIR-National Physical Laboratory, New Delhi, India
e-mail: shailesh@nplindia.org

M. Ahamed
e-mail: mansoorahamed@hotmail.com

P. Chawla
e-mail: prl.parull@gmail.com

M. Ahamed
Amity Institute of Nanotechnology, Amity University, Noida, India

V.K. Jain et al. (eds.), *Recent Trends in Materials and Devices*,
Springer Proceedings in Physics 178, DOI 10.1007/978-3-319-29096-6_63

morphological and electrical properties. Copper-poor p-type CIGSe acts as an absorber layer in PV modules. A thickness of 1.5 μm of CIGSe (absorber) is enough to capture most of the light owing to an advantage of multilayered structure that offers it to cover most part of the solar spectrum [5]. Moreover non-vacuum colloidal synthesis makes the preparation of CIGSe easier, cost effective and less time consuming.

2 Experiment Detail

Colloidal route was followed for the synthesis of CIGSe nanocrystals using hot injection technique in a two neck round bottom flask. Firstly, CIGSe was prepared using oleylamine and dodecanethiol; wherein hot-injection of selenium-oleylamine in dodecanethiol into metal chloride solution of Copper (Cu), Indium (In), Gallium (Ga) in oleylamine was done at an elevated temperature of 300–320 °C in an inert atmosphere. The product obtained was washed with methanol and toluene to remove excess ligand. Similar experiment was done using oleic acid instead of oleylamine as capping ligand.

3 Results and Discussion

The samples were characterized using XRD to study the key signature of CIGSe structure. The peaks of CIGSe originated from (112), (220), and (312/116) have been indexed using the JCPDS (File No- 40-1487). The presence of these peaks clearly indicates the perfect chalcopyrite structure in the product. Table 1 shows the calculated values of FWHM to determine the crystallite structure. Using Scherrer's formula, crystallite size has been calculated (given in Table 1). However, correlation between FWHM, crystallite size and band-gap values (as calculated from Tauc's plot) has been done systematically to extract the structural nature of nanocrystals.

The SEM micrograph reveals morphology of nanocrystals synthesized by two different capping ligands as shown (Fig. 1a). Further investigation on the particle size from SEM reveals that OA as capping agent shows lesser agglomeration than OLA capped CIGSe (Fig. 1). CIGSe-capped with oleylamine exhibits larger particle size in comparison to oleic-acid capped CIGSe. This could be attributed to the possibility of three binding modes in the long chain fatty acid (Oleic Acid). The

Table 1 Significant parameters obtained from X-ray diffraction and Tauc's plot

CIGSe-capping	Band gap Eg (eV)	XRD-FWHM	XRD-crystallite size (nm)
Oleylamine (OLA)	1.3	2.16	38
Oleic acid (OA)	1.5	2.58	32

carboxylic group present can passivate the nanocrystal surface well with its three modes of attachment (monodentate, bridged and chelating) [6] as shown in Fig. 1.

Although steric hindrance is also one of the contradictory factor that comes into play in case of oleic-acid binding, but the ligand is strong enough to dominate the binding ability of amines where only one binding site can effectively bind the nanocrystals' surface resulting in agglomeration. While in case of oleic acid-capping, nanocrystals are well-passivated and thus sparsely distributed. The corresponding SAED pattern shown as insets of OLA-capped CIGSe and OA-capped CIGSe also in Fig. (2a, b) respectively even support the highly crystalline nature of OLA-capped as compared to OA-capped CIGSe due to the presence of sharp rings in SAED; in contrast to OA-capped CIGSe where presence of diffused rings can be observed. However, for photovoltaic applications, it is beneficial to synthesize particles of larger size in order to limit grain boundaries that lead to more defects and therefore reduced performance of the device. Smaller nanocrystals have more surface to volume ratio and thus high defect density that create more trap states for the charge carriers.

Electrical studies of as-prepared CIGSe nanocrystals with two different capping were done and corresponding series resistance (R_s), shunt resistance (R_{sh}) and resistivity values (ρ) have been calculated. Figure 2 shows the I-V characteristics of CIGSe capped with (a) OLA, and (b) OA respectively. The values of R_s, R_{sh} and ρ are given in Table 2. However, OLA-capped CIGSe shows smaller values of series resistance (121 Ω) and resistivity (3.2×10^3 Ωm) in comparison to OA-capped CIGSe where series resistance and resistivity are 260 Ω and 6.93×10^3 respectively. The values of series resistance and resistivity reveal that more current can flow through OLA-capped CIGSe nanocrystals at lower voltage as compared to OA-capped CIGSe. This could be due to easier removal of capping ligand owing to loose binding to the nanocrystals as compared to OA-capped CIGSe where stripping off excessive ligand from the nanocrystals' surface is an arduous task.

Further confirmation has been done by carrying stability studies via annealing thin-films of CIGSe capped with two different ligands. Annealing studies were done at different ranges of temperature and a corresponding graph is shown in Fig. 3. It has been observed that the percentage of weight loss in OLA-capped CIGSe is

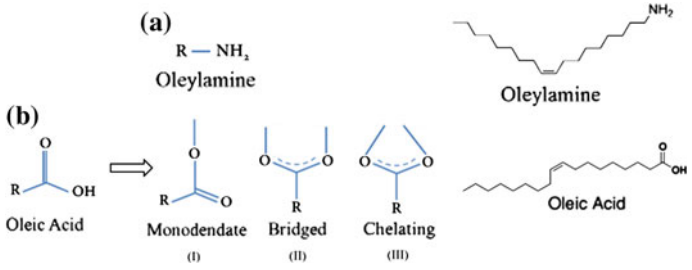

Fig. 1 Structures of capping ligand (a) Oleylamine; (b) Oleic acid with three different binding sites

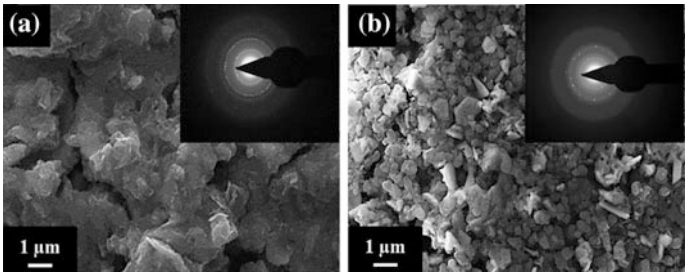

Fig. 2 SEM micrographs of **a** OLA-capped CIGSe and, **b** OA- capped CIGSe; corresponding SAED are shown as *insets* respectively

Table 2 Table depicting R_s, R_{sh} and ρ values of CIGSe (a) OLA-capped, (b) OA-capping

CIGSe capping	R_s (in Ω)	R_{sh} (in Ω)	ρ (in Ω-m)
Oleylamine (OLA)	121	–	3.2×10^3
Oleic acid (OA)	260	366	6.93×10^3

∼28 % while in case of OA-capped CIGSe is ∼80 %. These results indicate that since oleylamine was not that strongly bound to the nanocrystals' surface as oleic acid, annealing at even highest temperature resulted in minimal weight loss as sequential removal of all impurities has taken place.

But, such a strong binding of oleic acid could have resulted in destruction of nanocrystals' structure due to the inability of capping ligand to leave the nanocrystal surface with much ease thus resulting in a high value of weight loss percentage. Confirmation of these studies with other characterizations are underway.

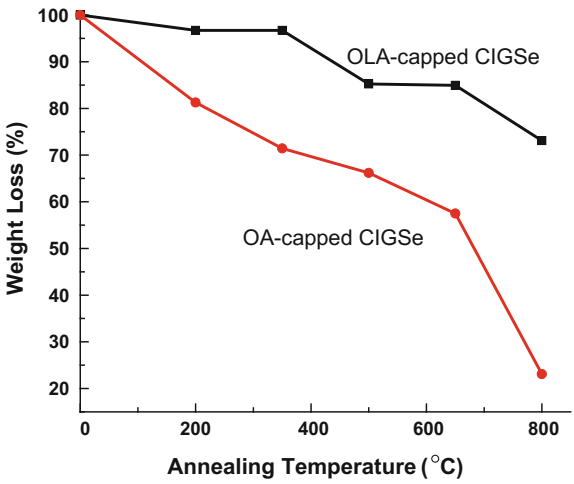

Fig. 3 Annealing studies of CIGSe capped with OLA and OA

4 Conclusions

CIGSe capped with oleylamine (OLA) shows better properties as an absorber layer since it shows better properties in comparison to OA-capped CIGSe. Since OA has three different binding modes due to the presence of three active sites as shown in Fig. 2b, there is greater probability of strong binding to the nanocrystals' surface thus limiting nanocrystals' to grow to a larger size while existence of only one binding mode couldn't control the particle size to much extent and agglomeration effects have been observed. Removal of capping ligand in OLA-capped CIGSe is much easier than in OA-capped CIGSe which has therefore resulted in lower values of resistivity as compared to OA-capped CIGSe. Further studies for investigating the percentage of weight loss also support the same fact and thus OLA-capped nanocrystals' are found to be much more applicable for photovoltaic applications in contrast to well-passivated OA-capped nanocrystals.

References

1. ZSW, ZSW Brings World Record Back to Stuttgart, 2014. http://www.zsw-bw.de/uploads/media/pr12-2014-ZSW-WorldrecordCIGS.pdf, 18 Dec 2014
2. M. Bär, L. Weinhardt, C. Heske, S. Nishiwaki, W.N. Shafarman, O. Fuchs, M. Blum, W. Yang, J.D. Denlinger, IEEE, 1–4 May 2008
3. M. Gloeckler, J.R. Sites, J. Phys. Chem. Solids, 1891–1894, (2005)
4. Y.H.A. Wang, X. Zhang, N. Bao, B. Lin, A. Gupta, J. Am. Chem. Soc. **133**, 11072–11075 (2011)
5. P. Chelvanathan, M.I. Hossain, N. Amin, Curr. Appl. Phys. **10**, 387–391 (2010)
6. H. Liang, W. Liu, S. Lee, J. van Duren, T. Franklin, M. Patten, S. Nijhawan, in *38th IEEE on Photovoltaic Specialists Conference (PVSC) 2012*, (2012), pp. 3–8
7. M.A. Watzky, R.G. Finke, J. Am. Chem. Soc. **119**, 10382–10400 (1997)
8. X. Peng, J. Wickham, A.P. Alivisatos, J. Am. Chem. Soc. **120**, 5343–5344 (1998)
9. J. G. M. van Berkum, PhD thesis, p. 136, Delft University of Technology, (1994)
10. J. Tauc, *Optical Properties of Solids* (Academic Press Inc, New York, 1966)
11. H. Liang, W. Liu , S. Lee , J. van Duren, T. Franklin, M. Patten, S. Nijhawan, S. Photovoltaic Specialists Conference (PVSC), 38th IEEE, 3–8 (2012).

Comparative Studies on Chalcopyrite CIGSe Nanocrystals Prepared via Two Different Ligand Systems

Parul Chawla, Mansoor Ahamed, N. Vijayan and Shailesh Narain Sharma

Abstract A comparative study on CIGSe nanocrystals prepared by two different ligands has been envisaged. This piece of study aims at comparing the properties obtained when toxic as well as non-toxic ligands are used for CIGSe, which is a potential photovoltaic material with performance at par with Si-based photovoltaics.

1 Introduction

An environmental benign approach for the development of active absorber layer of CIGSe by colloidal route bestows a captivating vision for the researchers around the globe. This is due to their potential in being exhibiting innumerable properties which are at par with already entrenched technology; which however, is, vacuum-based processing of CIGSe thin-film for photovoltaics [1, 2]. In recent years, high efficiency devices of CIGSe, the value close to $\sim$20.8 % have been fabricated but the technology used is very expensive and complicated. An important research area that has been focused nowadays is adoption of printing technology to utilize solution-processed CIGSe [3–8].

Thin film solar cells fabricated by utilization of colloidal semiconductor nanocrystals represent a promising low-cost approach to cut-down the expensive ways of fabricating solar cells [9–11]. The size, shape, crystal phase, and composition of the nanocrystals play an important role in determining the performance of solar conversion devices [12–14]. Non-vacuum based processing of solar cell absorber materials is one of the most inexpensive ways which offers lot of scope in tuning the material according to the desirable solar cell applications [15]. But the preparation methods for this layer has varied complexities as it is an ordered-defect compound and control of stoichiometry is a strenuous task to overcome. Moreover,

P. Chawla · M. Ahamed · N. Vijayan · S.N. Sharma (✉)
CSIR Network of Institutes for Solar Energy (NISE),
CSIR-National Physical Laboratory, Dr. K.S. Krishnan Marg,
New Delhi 110012, India
e-mail: shailesh@nplindia.org

V.K. Jain et al. (eds.), *Recent Trends in Materials and Devices*,
Springer Proceedings in Physics 178, DOI 10.1007/978-3-319-29096-6_64

employing toxic-ligands, such as hydrazine to obtain high-efficiency devices has been a widely accepted approach [16]. But, these type of ligands propound serious issues for the entire ecosystem. So, an efficacious way for overcoming this problem is to search for more environment-friendly precursors that can lead to highly-efficient devices and causing least harm to our environment.

2 Experimental Details

Our synthesis approach is based on utilization of two different ligand systems i.e. n-trioctylphosphine oxide (TOPO/TOP) and combination of oleic acid (OA) and oleylamine (OLA). Dodecanethiol has been also used in combination-capped synthesis to ensure formation of Se-OLA complex. For this, hot-injection method wherein, one of the precursor is to be added into the other at elevated temperature, has been followed. The highest range of temperature is maintained at 290–300 °C. Preparation of both of these differently-capped nanocrystals involves initialization by preparing a soluble Se-precursor that is utilized for injecting at high temperature range. Both of these capping agents are made to react with other precursors, i.e. chlorides of Cu, In, Ga followed by injection of Se-TOP and Se-OLA in TOPO-capped and combination-capped CIGSe respectively. Different characterization techniques that have been used include X-ray Diffraction done by Bruker D-8 Advance XRD, Jeol-made TEM for TEM, HRTEM and SAED analysis.

3 Results and Discussions

Synthesized nanocrystals of CIGSe using toxic TOPO and green chemical route were structurally investigated using X-ray Diffraction technique. Figure 1 depicts X-ray diffraction studies of both the nanocrystals. Phase identification by indexing different planes characteristic to chalcopyrite structure were suitably done using JCDPS data. However, both the nanocrystals prepared exhibit planes (112), (220/200) and (312/116), but difference lies in crystallinity, full-width at half-maximum (FWHM), crystallite size values. As can be seen in Fig. 1, CIGSe-synthesized by TOPO exhibits highest crystallinity in comparison to combination-capped CIGSe.

Table 1 depicts the tabulated values for CIGSe crystallite size and FWHM of both the nanocrystals prepared by varying capping agents. However, deviation of capping agent from highly toxic to greener route reveals reduction in crystallite size (40.87–3 nm) and increment in FWHM values (0.216–2.83). The variation could be attributed to the ability of combination of ligands to confine nanocrystals in quantum regime as compared to the TOPO that offers weak binding ability, which in turn lead to enhancement in crystallite size. This parameter also attributes to the adhesion capabilities of these nanocrystals to the desired substrate. CIGSe prepared using TOPO offers poor adhesion, thereby creating voids in the film that hinders

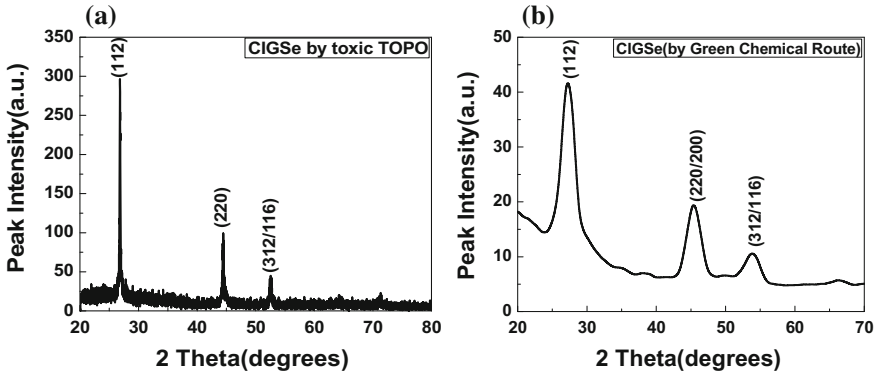

Fig. 1 X-ray diffraction patterns of CIGSe nanocrystals prepared by TOPO method (**a**), Green chemical route (**b**)

charge transport in these nanocrystals by making films more susceptible to shorting (as in fabricated device). In contrast, CIGSe by OLA-OA combination has very good adhesion that can even sustain mechanical stress still remaining intact to the substrate, crack-free, highly beneficial for device applications.

Table 2 depicts the values for percentage of carbon and oxygen present in CIGSe nanocrystals prepared by two different capping agents. Carbon and oxygen are usually considered as impurities that are highly responsible for reducing the performance of fabricated devices [17]. Thus, their content should be as low as possible so that there is minimal hindrance in device performance. The tabulated values in Table 2 have been extracted using Energy Dispersive X-ray analysis that gives an idea about the atomic percentage of C– and O– impurities in both the films and distribution of other elements as a whole. As given in the table, TOPO-caped nanocrystals has high content of carbon and oxygen, viz. 12 and 10 % respectively, making up to a total of 22 % being occupied by high content of impurities despite the employment of several washing steps to get rid of these undesirable moieties. On the other hand, combination-capped CIGSe has relatively very less amount of impurities that are occupying nanocrystals' surface. Dominance of main elements, viz, Cu, In, Ga, Se can be observed from the table that reveals difference in presence of these elements in differently-capped CIGSe nanocrystals.

Figure 2a, shows the TEM micrograph of TOPO_capped CIGSe. As can be observed from the TEM image, the particles are large in size (∼120 nm) and agglomeration tendency of nanocrystals can be figured. HRTEM image shown in

Table 1 Crystallite sizes and FWHM values for TOPO-capped and combination-capped CIGSe

CIGSe thin-film	Crystallite size (nm)	FWHM (112)
TOPO-capped	40.87	0.216
OLA + OA capped	3	2.83

Table 2 Atomic % of carbon and oxygen content (taken from EDAX data) in CIGSe prepared by two different routes

CIGSe thin-film	Carbon (%)	Oxygen (%)	Rest (Cu, In, Ga, Se) (%)
TOPO-capped	12	10	78
OLA + OA capped	5	7	88

Fig. 2b demonstrates the High resolution TEM image of combination-capped CIGSe depicting planes. However, due to agglomeration, appearance of interloping planes being resulted by crystals overlaying over one another is observed. This fact can also be related to weak binding ability of TOPO which is a bulky ligand that results in high steric hindrance, thereby leading to weak binding of ligands with nanocrystals' surface. SAED rings as an inset in Fig. 2b reveals the presence of sharp rings with clearly visible spots that also point towards the large particle size of CIGSe synthesized by using toxic TOPO.

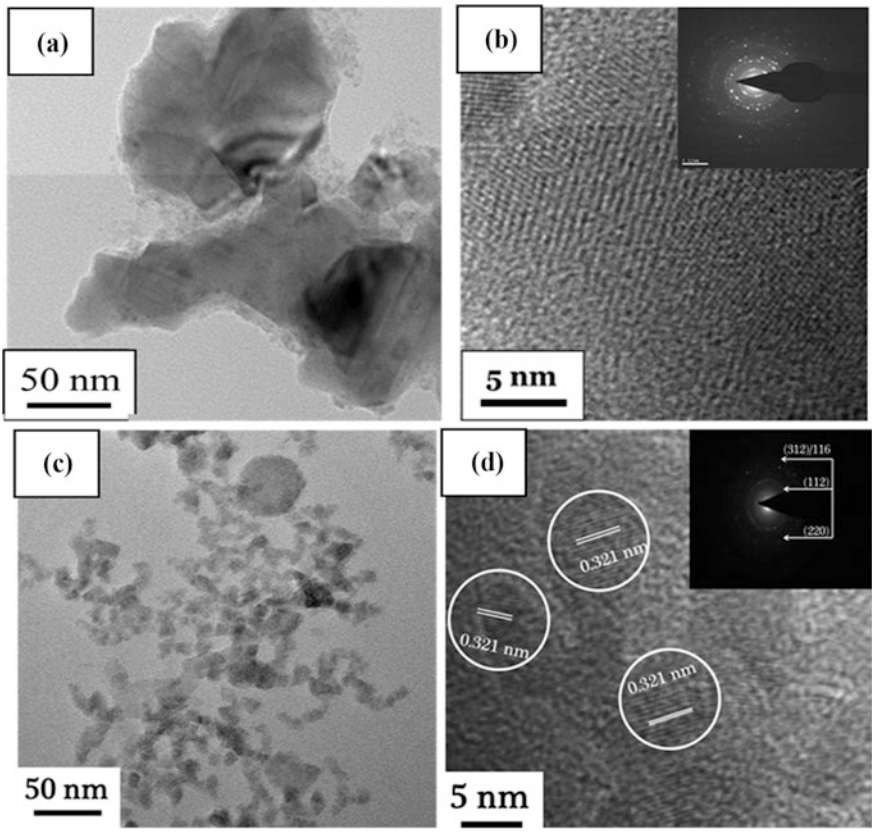

Fig. 2 TEM, HRTEM of CIGSe nanocrystals prepared by (**a**, **b**) TOPO method, (**c**, **d**) Green chemical route respectively. Corresponding SAED pattern have been shown as *insets*

In contrast, combination-capped CIGSe which, however, is relatively environment-friendly route shows nanocrystals of smaller dimensions (Fig. 2c) with particle size (∼7–8 nm). Figure 2d depicts HRTEM image for combination-capped CIGSe showing presence of fringes owing to smaller size of nanocrystals and their even distribution also rules out the agglomeration effects that slow down the transport of charge carriers. Well separated particles aid in better separation of charge carrier resulting in better device performance. SAED pattern showed as an inset in Fig. 2d reveals the formation of diffused rings that clearly explain the formation of smaller sized nanocrystals. Thus, TOPO-capped CIGSe, although larger in size, but high agglomeration tendency and weak binding of capping agent to nanocrystals shows weak adhesion, reduced device performance due to high porosity while such issues have been resolved in OLA + OA-capped CIGSe.

Figure 3 shows the summarized pictorial demonstration of two different nanocrystals prepared for a comparative study of toxic as well as non-toxic capping agents for better device performance. CIGSe nanocrystals synthesized using TOPO demonstrates larger particle size and high carbon content resulting in black coloured colloidal solution of nanocrystals. While, combination of OLA + OA leads to quantum confinement due to stronger ability of these capping agents to bind to the nanocrystals' surface. Also, lesser carbon content and smaller crystallite size results in brown colour of colloidal nanocrystals' solution.

Larger-sized nanocrystals of CIGSe synthesized by TOPO exhibit shorter shelf-life and inks prepared by colloidal route using highly toxic TOPO begin to destabilize in a very short span of time. This instability makes the deposition of thin-film of CIGSe a difficult task to accomplish. The various ways that are generally used for thin-film fabrication by colloidal nanocrystals involve spin-coating, dip-coating, spray-coating etc. and the most superior above all is inkjet-printing [18–20]. Ink-jet printing is one of the most advanced method that surpasses all the conventional methods of fabrication of CIGSe thin-films by solution-route.

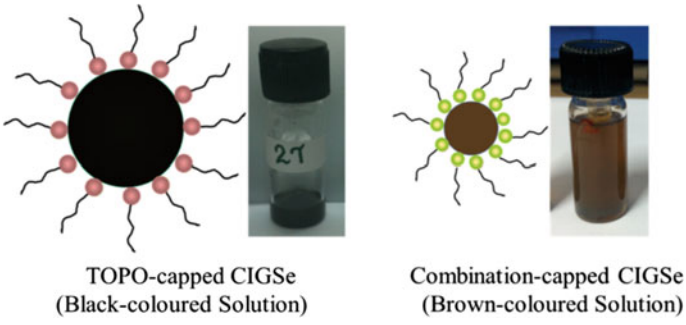

Fig. 3 Pictorial representation of differently-capped CIGSe

However, shortcomings in depositing CIGSe thin-film by TOPO that have been observed experimentally includes non-uniformity in the entire film due to poor dispersion of larger size nanocrystals in solution, creation of voids that make coating of subsequent layers, viz. CdS, ZnO etc. more difficult and then frequent shorting of fabricated device. Ink-jet printing of such a solution is even more problematic as larger particles can clog the nozzle making the process even more complicated. Settling of these nanocrystals takes place very rapidly while coating with dip-coating method and other techniques leads to the formation of non-uniform layers.

On the other hand, combination capped CIGSe nanocrystals have an enhanced shelf-life to a greater extent that makes the nanocrystals to sustain in solution for a longer period of time and this sustainment is attributed to proper dispersion of nanocrystals in solution owing to smaller size. Film fabricated from such a solution has high degree of uniformity without the presence of voids, and coating of other layers over this layer doesn't cause inter-diffusion of other elements into the absorber layer and prominent role of absorber layer is realized without device shorting.

4 Conclusions

We have tried to realize the essence of green route by deviating from existing toxic route of preparing CIGSe, particularly to adopt greener colloidal route synthesis method.

Comparison of toxic TOPO-capping on CIGSe with combination of green ligands oleylamine + oleic acid has been done by different studies. Stability, particle size, crystallinity etc. are the key factors that are essentially required for implementing the applicability of synthesized nanocrystals for device applications.

The tried combination of oleylamine & oleic acid along-with dodecanthiol is a novel combination which has improved the existing CIGSe properties in terms of band-gap, adhesion to the substrate, order of current obtained, hydrophobicity etc. Reduction of impurities that deteriorate the performance of fabricated device using nanocrystals of CIGSe has been achieved. The main undesirable impurities, viz. carbon and oxygen have been reduced in combination-capped CIGSe in contrast to TOPO-capped CIGSe where the atomic percentage of both these elements is higher and subsequent washing steps have been unsuccessful leading to higher percentage and consequently reduced performance of the device. The comparison done between CIGSe (TOPO) and CIGSe (oleylamine + oleic acid) can enable one to decide the quintessence of switching over from one route to another.

References

1. D.B. Mitzi, M. Yuan, W. Liu, A.J. Kellock, S.J. Chey, L. Gignac, A.G. Schrott, Thin Solid Films **517**, 2158–2162 (2009)
2. T. Todorov, O. Gunawan, S.J. Chey, T.G. de Monsabert, A. Prabhakar, D.B. Mitzi, Thin Solid Films **519**, 7378–7381 (2011)
3. K.C. Huang, C.L. Liu, P.K. Hung, M.P. Houng, Appl. Surf. Sci. **273**, 723 (2013)
4. J. Olejnícek, L.E. Flannery, S.A. Darveau, C.L. Exstrom, S. Kment, N.J. Ianno, R.J. Soukup, J. Alloys Compd **509**, 10020 (2011)
5. O. Zaberca, A. Gillorin, B. Durand, J.Y. Chane-Ching, J. Mater. Chem. **21**, 6483 (2011)
6. C. Ye, M.D. Regulacio, S.H. Lim, Q.H. Xu, M.Y. Han, Chem. Eur. J. **18**, 11258 (2012)
7. K. Srinivas, J.N. Kumar, G.H. Chandra, S. Uthanna, J. Mater. Sci.: Mater. Electron. **17**, 1035 (2006)
8. J. López-García, C. Guillén, Thin Solid Films. **517**, 2240–2243 (2009)
9. Y. Vahidshad, R. Ghasemzadeh, A. Irajizad, S.M. Mirkazemi, J. Nanostruct. **3**, 145 (2013)
10. S.E. Habas, H.A.S. Platt, M.F.A.M. van Hest, D.S. Ginley, Chem. Rev. **110**, 6571–6594 (2010)
11. A.H. Ip et al., Nat. Nanotech. **7**, 577–582 (2012)
12. G.I. Koleilat et al., Sci. Rep. **3**, 2166 (2013)
13. M.A. El-Sayed, Acc. Chem. Res. **37**, 326–333 (2004)
14. Y. Xia, Y. Xiong, B. Lim, S.E. Skrabalak, Angew. Chem. Int. Ed. **48**, 60 (2009)
15. A. Kongkanand, K. Tvrdy, K. Takechi, M. Kuno, P.V. Kamat, J. Am. Chem. Soc. **130**, 4007–4015 (2008)
16. L. Li, A. Pandey, D.J. Werder, B.P. Khanal, J.M. Pietryga, V.I. Klimov, J. Am. Chem. Soc. **133**, 1176–1179 (2011)
17. M.G. Panthani, V. Akhavan, B. Goodfellow, J.P. Schmidtke, L. Dunn, A. Dodabalapur, P.F. Barbara, B.A. Korgel, J. Am. Chem. Soc. **130**, 16770–16777 (2008)
18. G.M. Ilari, C.M. Fella, C. Zeigler, A.R. Uhl, Y.E. Romanyuk, A.N. Tiwari, Sol. Energy Mat. Solar Cells **104**, 125 (2012)
19. Q. Tian, X. Xu, L. Han, M. Tang, R. Zou, Z. Chen, M. Yu, J. Yang, J. Hu, Cryst. Eng. Comm. **14**, 3847 (2012)
20. A. Carrete, M. Placidi, A. Shavel, A. Perez Rodriguez, A. Cabot, Phys. Status Solidi A, (2014)

Optical and Thermo-Dynamical Properties of Twist Grain Boundary Phases in Liquid Crystals

Manisha Chaudhry and S.S. Bawa

Abstract The studies of binary mixture of cholesteric liquid crystal, Cholesteric Nonanoate and nematic liquid crystal, N-(4-Ethoxy benzylidine)-4-butyle aniline (EBBA), exhibiting the Twist Grain Boundary phases in different structural group. The thermodynamic phase transition of binary mixture was recorded by the Differential Scanning Calorimeter (DSC) at different scanning rate. Optical investigations of Twist grain boundary (TGB) phases showing different types of domain textures. The TGB existence region increases as the weight percentage of EBBA is increased till virtual tricritical point (TCP). This is very excited fact that the temperature range of one type of TGB (TGBA*) phase in the CN—EBBA mixture at lower concentration of EBBA is lower than those at higher concentration of EBBA.

1 Introduction

Twist Grain Boundary is a unique phase in liquid crystal field. Over the last four decades, the Twist Grain Boundary (TGB) phases have been noticed in binary mixtures of nematic and cholesteric liquid crystals. The characteristics of these an isomorphism are frustrated and they have very few in nature in which there is an equilibrium distribution of topological defects. The presence of TGB phases was theoretically predicted likewise the analogy between the nematic (N) to smectic A (SmA) transition in liquid crystals and the normal to superconductor transition in metals was first beautifully recognized by de Genes in 1972 [1]. Theoretically, Renn and Lubensky in 1988 [2] and by Renn in 1992 [3], explained the structures of TGBA and the TGBC mesophase, respectively. First time in 1989 by [4] and [5] observed experimentally the TGB phases. There are many interesting TGB phases

M. Chaudhry (✉)
Department of Physics, JSS Academy of Technical Education, Noida, India
e-mail: dr.manishachaudhry@gmail.com

S.S. Bawa
Polymeric and Soft Material Section, CSIR (NPL), New Delhi, India

V.K. Jain et al. (eds.), *Recent Trends in Materials and Devices*,
Springer Proceedings in Physics 178, DOI 10.1007/978-3-319-29096-6_65

found in the binary mixtures of pure cholesteric and nematic liquid which is based on the molecular interaction.

For the formation of TGB phases, molecules must be habitual with strong chirality and weak layer ordering tendency. These two properties incorporated by the binary mixtures of cholesteric and nematic liquid crystal. To show the TGB phases in the liquid crystals it is necessary that the binary mixtures have like the one component of cholesteryl ester and the other component having the tendency with weak layer ordering. Within the frame work of the chiral Chen–Lubensky model, a mean-field phase diagram for chiral systems has derived by [3], which predicts in the vicinity of the A–N*–C* tri-critical point the occurrence of various types of TGB phases. The predicted phase diagram by Renn suggests the N*–NL*–TGBC–SmC* for the $C_{\perp} < 0$ and N*–NL*–TGBA–SmA phase sequence for $C_{\perp} > 0$.

In a few chiral series of pure materials the phase diagram by [3] has been experimentally predicts [5, 6]. In the mixtures having one component as cholesteryl ester so many types of TGB phases (TGBA, TGBC, TGBC*) [7–11] have been experimentally observed. Several binary and ternary mixtures having the one component is ester of cholesterol have been investigated [9–12] for the phase diagram predicted by Renn [3]. These mixtures have shown TGBA phase in a narrow temperature range, and that too was away from the A–N*–C* tri-critical point. Re-occurrence phenomenon of TGB phases has also been thermodynamically reported in the binary mixtures [13]. All the textures depend on typical molecular short-range order that, in turn, depends on molecular structure. This texture is the LC analog to 'morphology' in solid crystals where as different short-range orders correspond to thermodynamically different phases, one and the same phase can exist in many different textures depending on geometrical, mechanical, magnetic, electrical and other boundary conditions. Certain textures called type textures are characteristic of a given microstructure. There are other textures that do not correspond to a specific microstructure.

The characterization of the mesogenic compounds showing simultaneously different types of textures were reported by in 1994, Rebeiro et al. [14]. Simultaneous first time, Kleman [15] compile the planar helical and developable domains textures in binary mixture.

Many types of TGB structures have been experimentally observed like TGBC, TGBC*, TGBQ, etc. In the TGBC structure [16], showing direction of the molecules in the smectic slabs are twisted with respect to the smectic layer normal. Basically the smectic slabs filled SmC* structure that is why in TGBC* the two helices mutually perpendicular to each other [17, 18]. Binary mixture of nematic and cholesteric liquid crystals shows the TGB phases. Similar type of binary mixture shows, Developable domain textures found in TGB phases which is exhibited by columnar phases [19]. The TGB phases showing the CC-cylindrical and cone like domain texture [20] in binary mixture by the Optical investigation.

2 Experimental

Cholesteric Nonanoate (CN), a high-purity chiral liquid crystal was purchased from New Jersey, USA, and nematic liquid crystal N-(4-Ethoxy benzylidine)-4-butyl aniline (EBBA) was purchased from Aldrich chemical company. First we weigh out pure samples of Cholesteric Nonanoate and N-(4-Ethoxy benzylidine)-4-butyl aniline in different ratios by using electrobalance with highly accuracy and mixed. The mixtures were heated in vacuum oven up to isotropic state, shaken well and kept in vacuum oven for 2 h at 100 °C temperature. After two hours these mixture are again shaken, kept at room temp.

(1) CN10 − − − 90 % CN and 10 % EBBA
(2) CN20 − − − 80 % CN and 20 % EBBA
(3) CN30 − − − 70 % CN and 30 % EBBA
(4) CN70 − − − 30 % CN and 70 % EBBA

Different mesophase transition temperatures were determined by using a Differential Scanning Calorimeter (DSC) of Mettler Toledo (Model DSC822^e with STAR^e software) at different scanning rates, 1.0, 5.0 and 10.0 °C/min. DSC thermograms were located with an accuracy of ±0.2 °C whereas the temperature reproducibility of the measurements was better than ±0.1 °C. Optical textures of different TGB phases of binary mixture of liquid crystals have been seen on a polarizing microscope of Olympus model BX 51P and photographs have been taken by an digital camera of model DP 70 fitted with microscope and computer controlled with Lynsis software. The magnification of the polarizing microscope is 100X.

3 Results and Discussion

The binary mixtures show the different types of frustrated structures by the differential scanning calorimeter thermograms and optical microscopy observations. The thickness of liquid crystal cell was 6 mm. The optical textures of pure CN and different binary mixtures have been recorded by polarizing microscope which was having the different TGB phases and other liquid crystalline phase.

3.1 Features of CN Thermograms

The DSC thermograms of CN at 1 °C/min, scanning rate in heating cycle are shown in Fig. 1a.

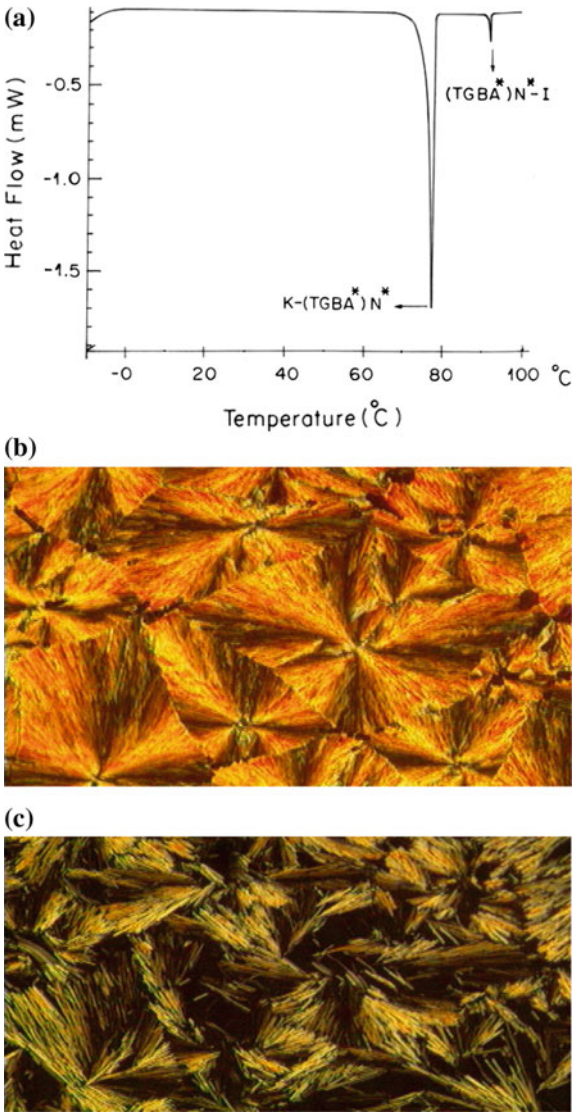

Fig. 1 **a** DSC thermogram of CN at 1 °C/min scanning rate. **b** K–(TGBA*) N* transition at 75.7 °C. **c** (TGBA*) N* → I transition at 90.3 °C

The DSC thermogram of CN at 1 °C/min scanning rate (Fig. 1a) in heating cycle has two peaks at 76.9 and 91.4 °C respectively. The peak at 76.9 °C is broadened towards the low temperature side. TGBA* is not separately observed. The one peak corresponds for a mixed K − (TGBA*) N* transition at 76.9 °C and other one peak corresponds to (TGBA*) N* → I transition occurs at 91.4 °C. The enthalpies of K–(TGBA*) N* and (TGBA*) N* → I transitions are 46.1 and 1.0 J/gm respectively. The mass of the sample was 3.4 mg.

The optical textures were obtained in heating cycle at I °C/min of pure CN liquid crystal. Figure 1b and c shown the transition corresponds for a mixed K–(TGBA*) N* transition. (TGBA*) N*–I. Transition temperatures through the polarizing microscope were slightly different as compared to differential scanning calorimeter. Basically the samples for the optical investigations is not properly isolated from the surroundings as compared to the DSC investigations that why the transition temperature of mesophases are different.

The K–(TGBA*) N* transition shown the planar textures of mixed crystal phase at 75.5 °C and (TGBA*) N* → I transition shown the filamentary texture for TGBA* at 90.3 °C.

3.2 *Features of EBBA Thermograms*

The DSC thermograms of EBBA at 1 °C/min scanning rates in heating cycle are shown in Fig. 2. At 1 °C/min scanning rate the DSC thermogram of EBBA (Fig. 2) shows two peak at 36.7 and 74.7 °C. First and second peaks correspond to the K → N transition and N → I transition respectively. The enthalpies of these transitions are 91.2 and 3.1 J/gm respectively. The mass of the sample was 4.2 mg for these studies. The optical investigation of pure EBBA were not shown the TGB phase. EBBA has thread like textures. Such types of phases are leading the orientational directions instead of translational directions.

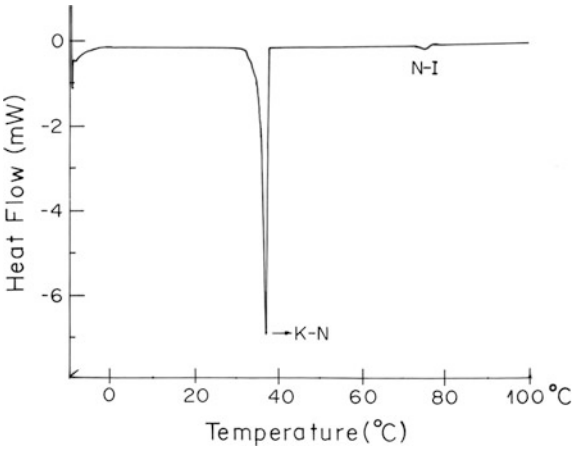

Fig. 2 DSC thermogram of EBBA at 1 °C/min scanning rate

3.3 *Features of CN 10 Thermograms*

The DSC thermogram of the binary mixture CN 10 [90 % CN and 10 % EBBA] at 1 °C/min scanning rates in heating cycle have shown in Fig. 3a. The transition temperatures of TGBC*–TGBA* phase was 64.4 °C and enthalpy was (2.42 J/gm). For the TGBA*–N* phase recorded transition temperature was 67.7 °C and enthalpy was (33.1 mJ/gm) at 1 °C/min scanning rate. We find that the transition

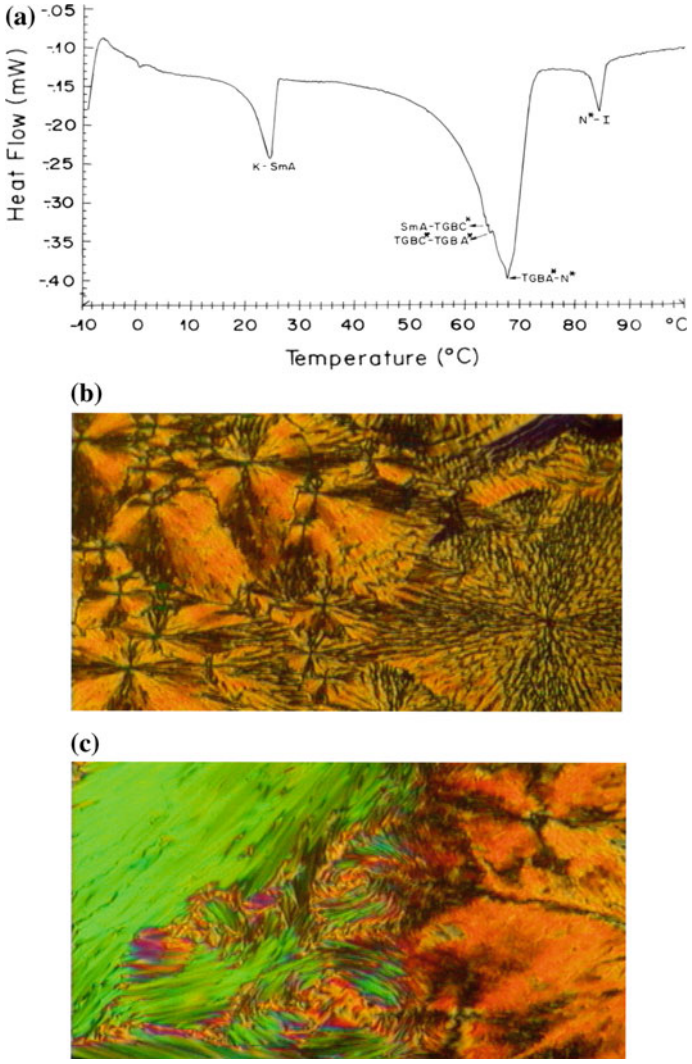

Fig. 3 **a** DSC thermogram of CN10 at 1 °C/min scanning rate. **b** Black brushes in cylindrical domain type texture in TGBC*–TGBA* phase of CN 10. **c** Perfect TGBA* phase of CN 10

temperatures have a tendency to increase linearly with increase in heating rate. Figure 3b shown black brushes in cylindrical domain type texture in TGBC*–TGBA* phase of CN 10. Figure 3c exhibits the perfect TGBA* phase of CN 10.

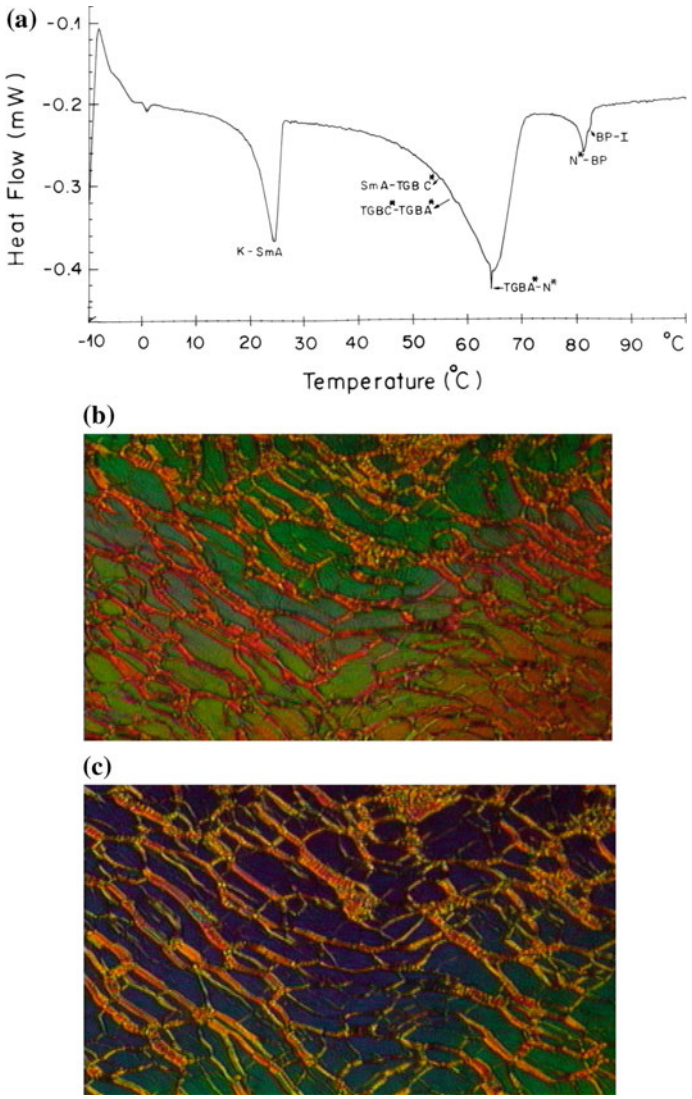

Fig. 4 **a** DSC thermogram of CN 20 at 1 °C/min scanning rate. **b** Grandjean texture of TGBA* phase of CN 20. **c** Oily streaks TGBA*–N* phase of CN 20

3.4 Features of CN 20 Thermograms

The transition temperature of TGBC*–TGBA* phase and TGBA*–N* phase were shown in DSC thermogram of CN 20 [80 % CN and 20 %] (Fig. 3a) at 1 °C/min scanning rate in heating cycle. The transition temperature of TGBC*–TGBA* phase and TGBA*–N* phase were 57.8 and 64.2 °C respectively. The enthalpy of both transition phases were 87.1 and 4.3 J/gm. Figure 4b shown the Grandjean texture of TGBA* phase. Figure 4c Oily streaks of TGBA*–N* phase.

3.5 Features of CN 30 Thermograms

The DSC thermogram of CN 30 [70 % CN and 30 % EBBA], in heating cycle at 1 °C/min scanning rate have shown in Fig. 5a. The transition temperature and enthalpy of TGBA*–TGBH is 35.2 °C and 0.65 J/gm respectively. Figure 5b exhibits the cholesteric texture of TGBA*–TGBH phase.

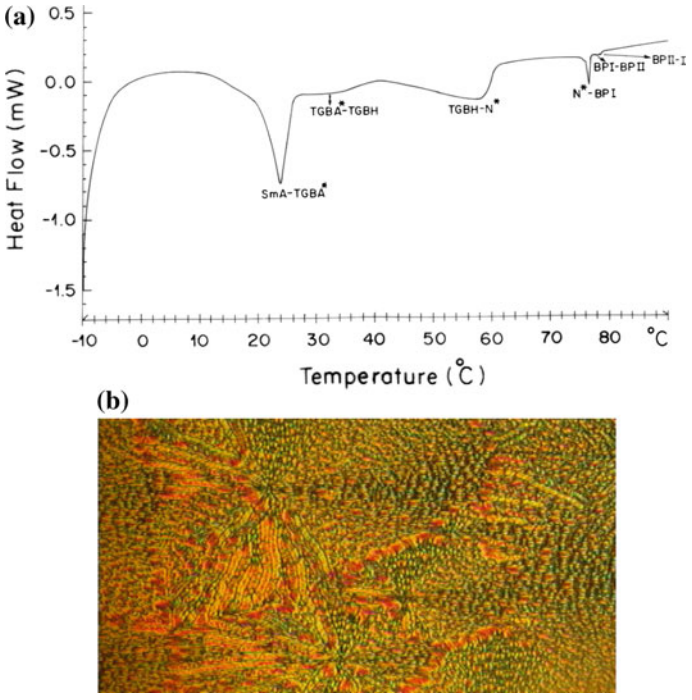

Fig. 5 **a** DSC thermogram of CN 30 at 1 °C/min scanning rate. **b** Cholesteric texture of TGBA*–TGBH phase

3.6 *Features of CN 70 Thermograms*

Figure 6a displayed the DSC thermogram of CN 70 [30 % CN and 70 % EBBA]. CN 70 mixture (Fig. 6a) shows TGB phases in a very wide range and could serve as a future candidate for studying TGB properties. The transition temperatures of solid

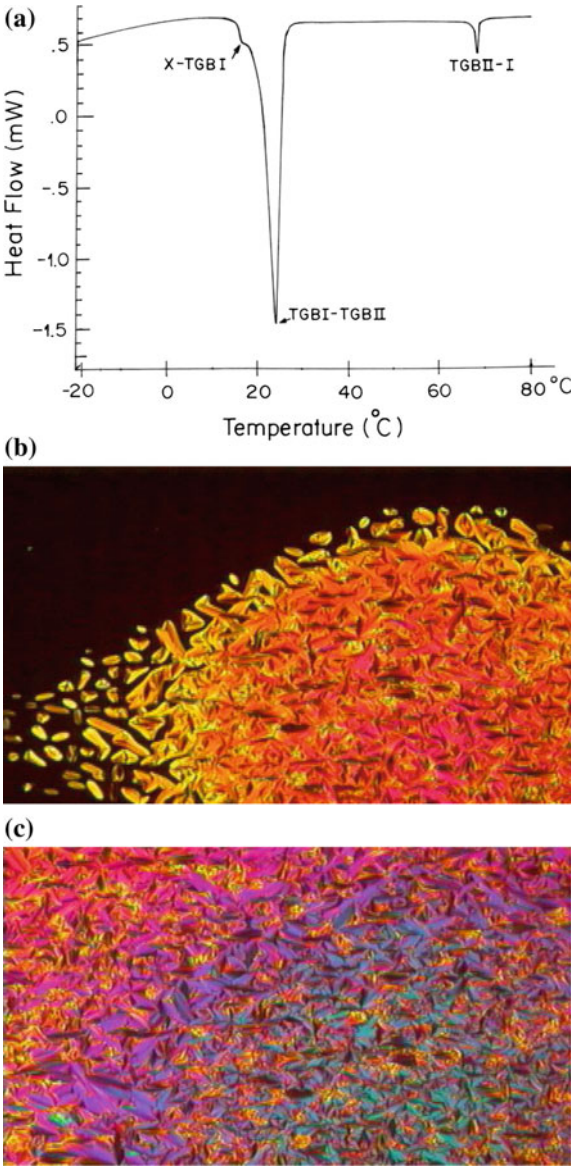

Fig. 6 **a** DSC thermogram of CN 70 at 1 °C/min scanning rate. **b** Transformation K–TGB phase for CN 70. **c** Perfect TGB phase of CN 70

to TGB phase and TGB and isotropic phase were 24 and 67.9 °C respectively. The enthalpies of these two phases were (54.6 J/gm) and (1.4 J/gm).

The phase sequences observed in CN–EBBA system is found to be similar to the mean-field phase diagram derived by [3] within the framework of the chiral Chen–Lubensky model. The predicted phase diagram by Renn suggests N*–NL*–TGBA–SmA for $C_{F05E} > 0$. We have observed this phase sequence for mixtures having EBBA percent less than 30. For $C_{F05E} < 0$, the predicted phase diagram suggests N*–NL*–(TGBA)–TGBC–TGBC*–SmC* phase sequence. In the present case similar phase sequence is observed for the mixture CN 30. In this mixture we are getting a new phase between N*–TGBA*. This is thought to be the twist grain boundary phase of hexatics (TGBH) [19].

TGB phases have been recorded in mixtures CN 10, CN 20, CN 30, and CN 70, We have recorded TGBA phase in pure CN for the very first time in thin unaligned film [20]. In two geometries—suspended droplets with tangential anchoring conditions and free standing films Nastishin et al. [21] have shown earlier the presence of TGBA phase in CN by observing defect transformations at the N*–SmA transition.

4 Conclusion

The observation of CC textures of CN 10 (90 % CN and 10 % EBBA). Grandjean texture of TGBA* observed in CN 20 (80 % CN and 20 % EBBA). Such types of mixtures preferably form the planar cholesteric texture. Basically the double twisting of molecules exhibits the elastic energies of the between the molecules. They provide the maximum possibilities for the adoption. The shows the various parameters like shape, orientation and size of the domain in the CC type configuration of textures. We have observed by the microscope that twisting of the molecules does not depend on the cell thickness. It can be in few μm or can be compared to their size several hundred μm. In the present work thermodynamical and optical observations are very prominent evidence of different TGB phases in binary mixtures.

Acknowledgments I sincerely wish to express my thankfulness to reverend Dr. K.K. Raina, V. C., Material Science, Dehradun Institute of Engineering and Technology, Patiala, for allowing me to use Polarizing Microscope and providing other facilities. My heartfelt thanks are due to for his valuable discussion and kind co-operations. We acknowledge financial support from the University Grants Commission (UGC) New Delhi for our work on the above topic.

References

1. P.G. de Gennes, Solid St. Commun. **10**, 753 (1972)
2. S.R. Renn, T.C. Lubensky, Phys. Rev. A **38**, 2132 (1988)

3. S.R. Renn, Phys. Rev. A **45**, 953 (1992)
4. J.W. Goodby, M.A. Waugh, S.M. Stein, E. Chin, R. Pindak, J.S. Patel, Nature **337**, 449 (1989)
5. L. Navailles, C.W. Garland, H.T. Nguyen, J. Phys. II (France) **6**, 1243 (1996)
6. C.W. Garland, Liq. Cryst. **26**, 669 (1999)
7. O.D. Lavrentovich, Y.A. Nastishin, V.I. Kulishov, Y.S. Narkevich, A.S. Tolochko, S.V. Shiyanovskii, Euro. Phys. Lett. **13**, 313 (1990)
8. W. Kuczynski, H. Stegemeyer, Mol. Cryst. Liq. Cryst. **260**, 377 (1995)
9. S.L. Srivastava, R. Dhar, A. Mukherjee, Mol. Cryst. Liq. Cryst. **287**, 739 (1996)
10. S.L. Srivastava, R. Dhar, Indian Mol. Cryst. Liq. Cryst. **317**, 23 (1998)
11. R. Dhar, M.B. Pandey, V.K. Agarwal, Mol. Cryst. Liq. Cryst. **396**, 31 (2003)
12. S.L. Srivastava, R. Dhar, Mol. Cryst. Liq. Cryst. **366**, 79 (2001)
13. V. Vill, H.W. Tunger, D. Peters, Liq. Cryst. **20**, 547 (1996)
14. A.C. Ribiero, A. Dreyer, L. Oswald, J.F. Nicoud, A. Soldera, D. Guillon, Y. Galerne, J. Phys. II France **4**, 407 (1994)
15. M. Kleman, J. Physique **41**, 737 (1980)
16. S.R. Renn, T.C. Lubensky, Mol. Cryst. Liq. Cryst. **209**, 349 (1991)
17. P.A. Pramod, Y. Hatwalne, N.V. Madhusudana, Liq. Cryst. **28**, 525 (2001)
18. M. Brunet, L. Navailles, N.A. Clark, Euro. Phys. J. **7**, 5 (2002)
19. M. Chaudhry et al., **489**, 298–309 (2008)
20. M. Chaudhry et al., **511**, 59–74 (2009)
21. YuA Nastishin, M. Kleman, J. Malthete, H.T. Nguyen, Eur. Phys. J. E **5**, 353 (2001)

Solvent Effect on Electronic Transitions, Homo Lumo Analysis of 2,6-Dichloro-3-Nitro Pyridine Under Hartee-Fock and Density Functional Theory

Sarvendra Kumar, Surbhi, M.K. Yadav and Jayant Teotia

Abstract In the present work, the ultraviolet absorption spectrum of 2,6-dichloro-3-nitro pyridine (2,6,3 DCNP) has been carried out experimentally (in water, n-hexane, ethanol, methanol and Mgo) and theoretically (in water, ethanol and methanol) in the range 3500–2300 cm^{-1} in the solution phase. Predicted electronic absorption spectra from time dependent density functional theory density functional theory (TD-DFT) calculation have been analyzed and compared with the experimental UV–Vis spectrum. The effects of chloro and nitro group substituent in pyridine ring have been analyzed. The electronic properties such as excitation energy, wavelength corresponding to absorption maxima (λ_{max}), oscillator strength (*f*), HOMO and LUMO energies are calculated by Time-Dependent Density Functional Theory (TD-DFT) using HF/6-311++G(d, p) and B3LYP/6-311++G(d, p) as basis sets. In addition Mulliken atomic charges of the atoms are also calculated.

1 Introduction

Pyridine has been extensively studied from the spectroscopic point of view, due in parts to its presence in many chemical structures of high interest in a variety of biomedical and industrial fields [1]. Nitrogen-containing cyclic organic molecules (N-heterocyclic) play important roles in terrestrial biology, for example as the nucleobases in genetic material. The study becomes more important in view of their biological and pharmaceutical importance as it acts as herbicides [2], insecticides [3], for prevention of diabetic neuropathy [4] and plant growth regulators [5] etc.

S. Kumar (✉) · Surbhi
Amity Institute of Applied Sciences, Amity University, Noida, Uttar Pradesh, India
e-mail: sarvendraricky@rediffmail.com; smalik1@amity.edu

M.K. Yadav · J. Teotia
Department of Physics, D.N.College, Meerut 250002, Uttar Pradesh, India

V.K. Jain et al. (eds.), *Recent Trends in Materials and Devices*,
Springer Proceedings in Physics 178, DOI 10.1007/978-3-319-29096-6_66

The electronic spectra of pyridine has been motivated for its use to understand the specific biological process and relatively complex systems [6]. Due to different substitution pyridine compounds normally shows bathochromic and hyposochromic shifts in their electronic transitions [7]. The present paper deals the solvent effect on the electronic transition of the said compound in various polar and non-polar solvents as increasing the order of polarity both experimentally and theoretically. The homo and lumo energies also plays an important role to describe the chemical stability [8] of the molecular structure of the compound.

2 Experimental Details

Spectroscopic pure sample of 2,6-dichloro-3-nitro pyridine was purchased from M/S Sigma Aldrich chemicals, U.S.A. The compound was used in their original form, the purity of the said compound was confirmed by elemental analysis and melting point determination. The ultraviolet spectra of this compound was recorded on Beckman Spectrophotometer model M-35 in the region 400–200 nm using different polar and non-polar solvents(viz. N-hexane, Ethanol, methanol, water). All the solvents used were of spectroscopic grade. The concentration of all the solution in all the cases was kept to be constant (8×10^{-3} g/l). The theoretical UV spectra has analysed with the help of Gaussian03 using TD-6311++G(d,p) basis set.

3 Computational Details

The computational work was done to determine the optimized geometry of the title compound. The HF (Hartree Fock) and DFT (hybrid B3LYP: the Becke's three-parameter hybrid method with the Lee, Yang and Parr correlation functional) method was chosen for compound **2,6,3 DCNP**. The entire calculations were performed by using the Gaussian 09 program package on a personal computer. The electronic absorption spectra for optimized molecule calculated with the time dependent density functional theory density functional theory (TD-DFT) at HF/6-311++G(d, p) and B3LYP/6-311++G(d, p) levels. The time-dependent HF and DFT (TD-HF and TD-DFT) proved to be a powerful and effective computational tool for the study of ground and excited state properties by comparison to the available experimental data. Hence, we used TD-B3LYP to obtain excitation energy, wavelengths (λ_{max}), oscillator strengths and compare with the experimental results of **2,6,3 DCNP**. The HOMO and LUMO energies are calculated by using HF and DFT methods with the same basis sets. Mulliken atomic charges of the atoms are calculated by using HF and DFT methods with the same basis sets.

4 Results and Discussion

The structural formula of the compound 2, 6-dichloro-3-nitro pyridine is shown in Fig. 1. The homo lumo homo lumointermolecular structure is shown in Fig. 2 and some important parameters are shown in Table 4. The electronic transition of the said compounds recorded in the different solvents both experimentally and theoretically (a) ethanol (b) methanol (c) water are shown in Figs. 3, 4 and 5 and corresponding wavelength are shown in Tables 1, 2 and 3 using HF and DFT methods. The mulliken charges mulliken chargescorrespond to different atoms are shown in Table 5.

4.1 Electronic Spectra

West [9] has suggested that changing of the solvent, effect the position of the band in the electronic spectra, which may be used to identify the band as n-π^*, π-π^* and n-σ^*. Then n-π^* transition of substituted pyridine occur at distinct bands in the region 340–300 nm [10]. In electronic absorption spectra n-π^* transition corresponds to out-of-plane transitions while π-π^* and n-σ^* in-plane transitions [11]. The electronic structure of the π system in pyridine is very similar to that of benzene, as the perturbation caused by introducing nitrogen atom into the benzene ring being small [12]. Theoretical calculations and experimental data show that the first excited states of the π electrons are close in energy in benzene and pyridine.

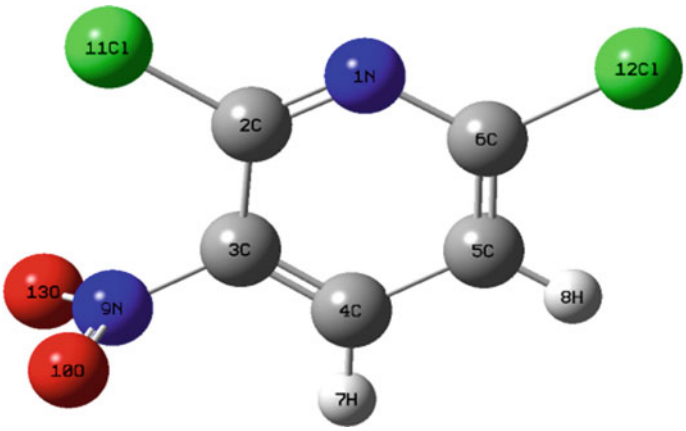

Fig. 1 The optimized geometric structure with atoms numbering of 2,6,3 DCNP

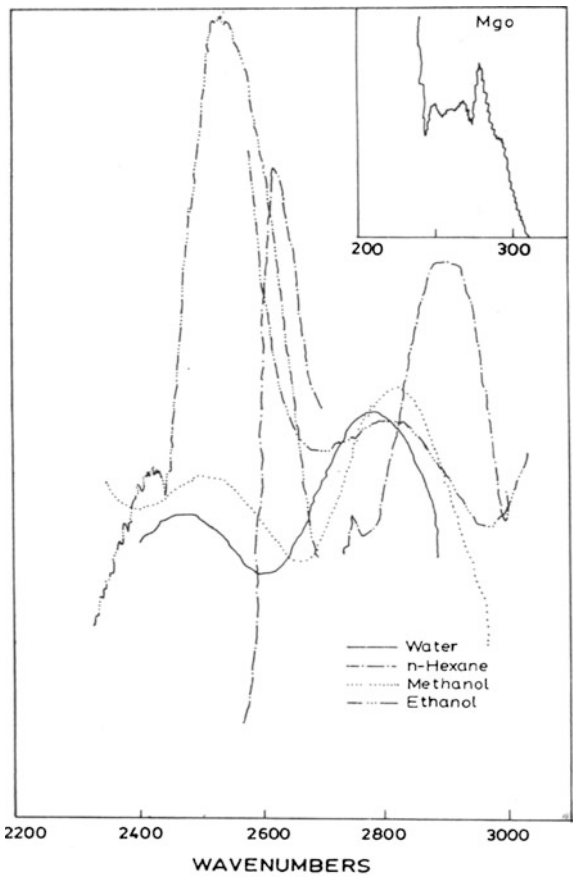

Fig. 2 Electronic absorption spectra of 2,6,3 DCNP in different solvents

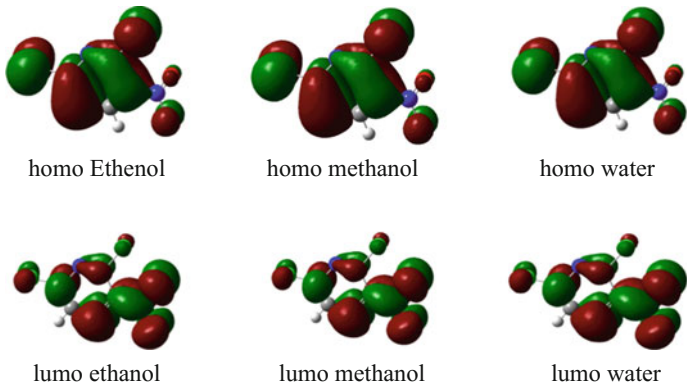

Fig. 3 Contours of the occupied and unoccupied molecular orbitals in different solvents using DFT/B3LYP6-311++G(d, p)

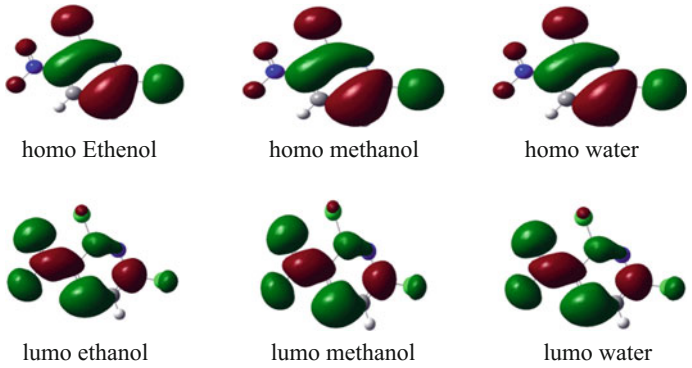

Fig. 4 HOMO and LUMO frontier molecular structure using HF/6-311++G(d, p)

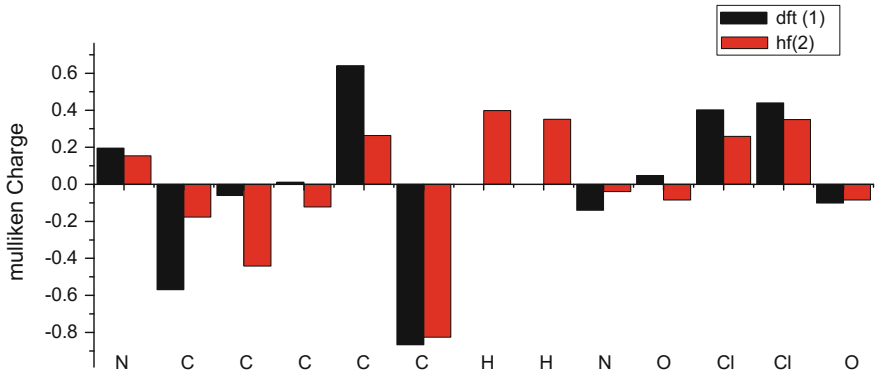

Fig. 5 Mulliken charges mulliken chargesof 2,6,3 DCNP computed by HF/6-311++G(d, p) and B3LYP/6-31+G(d, p) basis sets in ethanol, methanol and water [N-nitrogen, C-carbon, H-hydrogen]

Table 1 Experimental ultraviolet analysis of 2,6-dichloro-3-nitro pyridine

Solvents	Refractive index	Dielectric Constant	Wavelength	Assignment
Ethanol	1.3713	25.0	352	π-π^*
			396	n-π^*
Methanol	1.3362	32.0	353	π-π^*
			398	n-π^*
Water	1.3380	80.5	404	n-π
			347	π-π

Table 2 Theoretical absorption spectra of 2,6-dichloro-3-nitro pyridine using TD-SCF/HF/6-311 ++G(d,p) method in solvents ethanol, methanol, water as

Solvents	Refractive index	Dielectric constant	Wavelength	Oscillation strength	Excitation energy (ev)	Assignment
Ethanol	1.3713	25.0	340	0.0001	3.6413	n-π^*
			329	0.0650	3.7573	π-π^*
Methanol	1.3362	32.0	356	0.0842	3.4761	π-π^*
			385	0.0001	3.2126	n-π^*
Water	1.3380	80.5	329	0.0616	3.7626	π-π^*
			340	0.0001	3.6428	n-π^*

Table 3 Theoretical absorption spectra of 2,6-dichloro-3-nitro pyridine using TD/SCF/DFT-6311 ++B3LYP-G(d,p)

Solvents	Refractive index	Dielectric constant	Wavelength	Oscillation strength	Excitation energy	Assignments
Ethanol	1.3773	25.0	348	0.0051	3.5612	n-π^*
Methanol	1.3362	32.0	348	0.0051	3.5577	π-π^*
Water	1.3380	80.5	359	0.0049	3.4490	n-π^*

Where λ max wavelength, *R.I* refractive index of solvent, *DC* dielectric constant, *E(ev)* excitation energies in ev, *f* oscillation strength

Table 4 HOMO and LUMO analysis using DFT and HF methods

Parameters	DFT/6-311++B3LYP	HF/6-311++
HOMO	−0.00232	−0.38089
LUMO	0.01945	−0.01767
Ionisation Potential	0.00232	0.38089
Energy Gap	0.02177	0.36322
Hardness	0.010885	0.18161
Softness	91.869	5.5063

E_{HOMO} = −0.00232a.u, E_{LUMO} = 0.01945 a.u, Energy Gap = 0.02177 a.u

4.2 Solvent Effect

Due the solvent effect on electronic absorption spectra, the bands are shifted towards lower wavelength called blue shift or hypsochromic shift and higher wavelength called red shift or bathochromic shift. The band which are blue shifted on a change from non-polar to polar solvents are attributed to n-π^* transition and the red shifted bands are considered to be π-π^* transistion (Becker et al.) [11]. The amount of blue shift has been used as a measure of the strength [12] of the H-bonding in ethanol, methanol, water, acelonitrile, dimethylsulphoxide and increase in transistion energy. This energy required to weaken or break the

Table 5 Mulliken charges

Atoms	DFT	HF
1N	0.195567	0.153743
2C	−0.569409	−0.176563
3C	−0.060960	−0.442266
4C	0.011640	−0.122162
5C	0.641313	0.264193
6C	−0.867002	−0.826657
7H	0.000000	0.398088
8H	0.000000	0.351352
9N	−0.139509	−0.039339
10O	0.047521	−0.084669
11Cl	0.402122	0.258900
12Cl	0.439622	0.349989
13O	−0.100906	−0.084610

hydrogen bond. In the present investigation, the n-π^* transition is blue shift in the compound with increasing the polarity of the solvents [13].

In the title compound π-π^* and n-π^* transition are found due to the presence of nitro group. Nitro group basically electronically complementary group [14] gives bathochromic shift due to this extension of the chromophore from the electron donating group to the electron withdrawing group through the benzene ring [14]. This chromophore consist both π and n (non-bonding) electrons. Becker et al. suggested that chlorine has an ionisation energy of 13.0 eV, so due to the presence of chlorine group band will shifted to longer wavelength side [15].

The attraction between the solute and solvents molecule will be more if the polarity of the molecule will be more, which results the system more stable [16]. This with increasing the dielectric constant of the solvent, the ionizing polarity of the solute molecule will be increase [17]. Hence, greater the polarity of the solvents, greater will be the degree of the solution.

4.3 Homo-Lumo Analysis

Some important parameters of molecule for quantum chemistry like chemical reactivity, kinetic stability are found with the help of homo and lumo analysis and frontier orbital gap. According to frontier molecular orbital theory homo acts as electron donor and lumo acts as electron donor. In view of energetic behaviour of title compound, homo and lumo analysis is very important. The energy gap of homo-lumo explains the eventual charge transfer interaction within the molecule [18], which influences the biological activity [19] of the molecule. Global hardness and global softness of molecules have been calculated.

The contours of the occupied and unoccupied molecular orbitals in different solvents using B3LYP/6-311++G(d, p) basis set is shown in Fig. 3 and using HF/6-311++G(d, p) basis set is shown in Fig. 4.

4.4 Mulliken Charges

According to the results, the Mulliken charges mulliken chargescovers a very broad range of values from at the low side to at the high side at the Hartee-Fock level and at the low side to at the high side at the B3LYP method. The reactive atomic charges play an important role in the application of quantum chemical calculation [20] to molecular system. Mulliken atomic charges are calculated by B3LYP/6-311 ++G(d, p) and HF/6-311++G(d, p). The maximum atomic positive charge is obtained by chlorine atom both in HF and DFT methods. The large negative charge is obtained by N9 and C atom shows the formation of intramolecular interaction in solid forms.

5 Conclusion

In the present work, an attempt has been made on the experimental and theoretical UV-vis spectral studies, HOMO-LUMO energies, Mulliken charges and properties of industrially important 2,6,3 DCNP. Equilibrium geometries, electronic parameters and thermodynamic parameters of 2,6,3 DCNP have been analyzed at HF and DFT/B3LYP using 6-311++G(d, p) basis set. The TD-DFT calculations on the molecule provided deep insight into their electronic structures and properties. In addition, the calculated UV–Vis results functions are all in good agreement with the experimental data. The lowering of HOMO–LUMO band gap supports bioactive property of the molecule.

References

1. V. Krishnakumar, R. John Xavier, Spectrochim. Acta Part A **63**, 454–463 (2006)
2. J.G. Contreras, V. Seguel, Spectrochim. Acta A **48**, 525 (1992)
3. A. Pullman, Adv. Hetrocycl. Chem. **13**, 77 (1971)
4. H. Camp, J. Perk, Handb. Am. Chem. Soc., p. 31 (2000)
5. B.S. Yadav, M.K. Yadav, V. Kumar, V. Singh, Asian J. Chem. **9**(3), 372 (1997)
6. B. Machura, A. Switlicka, M. Wolff, D. Tabak, R. Musio, J. Polanski, R. Kruszynski, J. Organomet. Chem. **696**, 731–738 (2011)
7. K. Chaitanya, C. Santhamma, K.V. Prasad, V. Veeriaiah, J. At. Mol. Sci. **3**(1), 1–22 (2012)
8. H. Moghanian, A. Mobionikhaledi, R. Monjezi, J. Mol. Struct. **1052**, 135–145 (2013)

9. W. West, *Chemical Application of Spectroscopy* (Inter Science Publishing Co., New York, 1965), p. I
10. M. Baron, A. Chamayou, Solvent free mechanochemical route for green synthesis of pharmaceutically attractive phenol-hydrazones. RSC Adv. **4**, 56736–56742 (2014)
11. R.S. Becker, A.B.F. Duncan, F.A. Matsen, D.R. Scott, W. West, *Chemical Application of Spectroscopy* (John Wiley and Sons, New York, 1968)
12. T. Gnanasambandan, S. Gunasekaran, Int. J. Recent Sci. Res. **3**, 590–597 (2012)
13. V. Krishnakumar, R. John Xavier, Spectrochim. Acta Part A **63**, 454–463 (2006)
14. P.S. Kalsi, *Spectroscopy of Organic Compounds, Ch 2* (New Age International, New Delhi, 2001), p. 7
15. S.P. Gupta, (Km.) A Gupta. Indian J. Phys. **61B**, 418–426 (1987)
16. R.T. Baily, D. Steele, Spectrochim. Acta **23A**, 2997 (1967)
17. L.J. Bellamy, *The Infrared Spectra of Complex Molecule* (Chapman and Hall, London, 1975)
18. M.V.S.Prasad, N.Udaya Sri, A.Veeraiah. J.At. Mol. Sci. **4**(1), 1–17 (2013)
19. B.D. Joshi, P. Tondon. BIBICHANA **9**(2013), 38–49
20. E. Gladis Anitha, S. Joseph Vedhagiri, K. Parimala. Spectrochim. Acta Part A: Mol. Biomol. Spectrosc. (2015)

Part VIII
Emerging Technologies

A Novel Design of Fractal Antenna: Effect of Different Dielectric Substrate Materials

Ishita Aggarwal, Malay Ranjan Tripathy and Sujata Pandey

Abstract In this paper we propose a novel microstrip fractal multiband antenna for RF applications. The antenna is designed on different substrate materials and performance analyzed for return loss, radiation pattern and gain. The substrate material used for antenna design are FR4 and RT-Duriod. Required properties of antenna such as high gain, low return loss, compact and high efficiency can be obtained by selecting the right substrate for the antenna and choosing proper parameters for dielectric constant, values of permeability, permittivity and loss tangent that effect the performance of the antenna.

1 Introduction

In the world of wireless communication, there is a need of selecting right antenna [1–7] for the right application. This can be done by analyzing the performance of antenna by finding the return loss, gain and radiation pattern of antenna at desired frequency range.

The choice of substrate [4–7] plays an important role in antenna performance but is affected by production issues like price and reproducibility. FR4 [1, 2] is cheaper as compared to RT-Duroid and also has a smooth surface. Normally depending on application, for microwave a Teflon substrate is used and Ceramic is used for GPS patch antennas. The important parameter concerning substrate materials are dielectric constant, dissipation factor, coefficient of thermal expansion, thermal coefficient of dielectric material, thermal conductivity of the substrate material and capacity for transferring heat away from a source on a circuit.

In this paper, we have proposed Fractal antenna by using different substrates like RT-Duriod, FR-4 epoxy, RT-Duriod with metamaterial, FR-4 with metamaterial. The height of the substrates is constant for all the antennas which is 1.6 mm.

I. Aggarwal · M.R. Tripathy · S. Pandey (✉)
Department of Electronics and Communication Engineering,
Amity University, Noida, Uttar Pradesh, India
e-mail: spandey@amity.edu

V.K. Jain et al. (eds.), *Recent Trends in Materials and Devices*,
Springer Proceedings in Physics 178, DOI 10.1007/978-3-319-29096-6_67

Parameters of antenna such as VSWR, Return Loss, Antenna Gain and Bandwidth is analyzed. The length of the patch is taken as 29.5 mm and width of the patch is taken as 38 mm. Finite element modelling based HFSS software has been used for all the analyses.

These antennas can be used for application like wireless communication, IOT band application, Radar, Wi-fi communication.

2 Antenna Design and Structure

The fractal antenna design consists of a metallic patch with a substrate and a ground. The substrates such a RT-Duriod and FR4 have been used for comparing the performance of antennas. To get an improved bandwidth, slots are cut in the patch of the antenna. To see the effect of metamaterial on these antenna the CSRR is loaded on the ground of the microstrip patch antenna.

Figure 1 shows the fractal antenna design. Two different substrates are used to compare the performance on the same design (Fig. 2).

2.1 Properties of the Materials

FR-4 is a composite material composed of woven fiberglass cloth with an epoxy resin binder that is flame resistant. The FR-4 substrate considered in this paper can

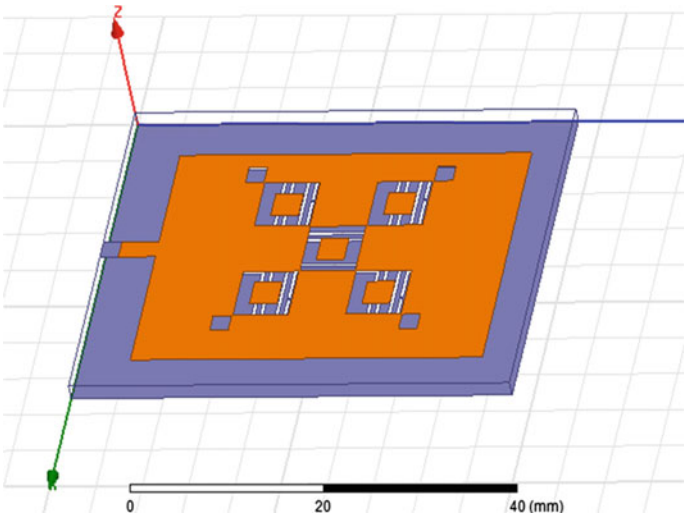

Fig. 1 Fractal antenna design

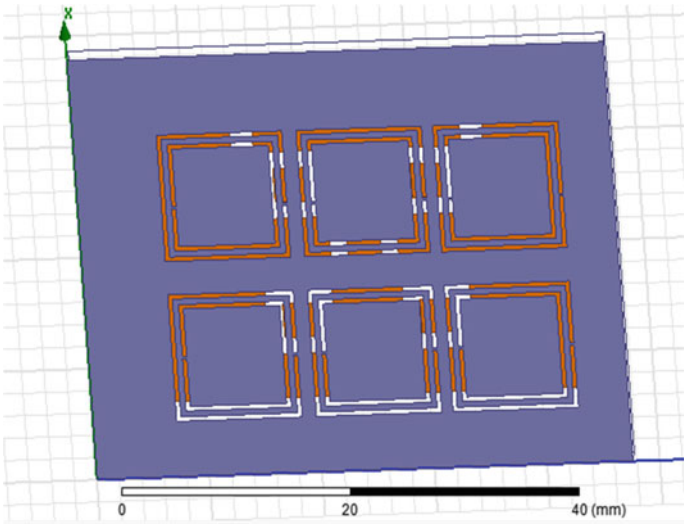

Fig. 2 Substrate with metamaterial (CSRR)

be used for multiple lamination cycle. Table 1 shows the dielectric constant of substrates used.

Metamaterial antennas are the antennas which use the metamaterial to enhance the performance of antenna systems. The main aim of metamaterial antenna is to launch energy in space. The dielectric constant effect the performance of the antenna. The substrate having low dielectric constant will give better performance than having higher dielectric constant.

3 Results and Discussion

FEM software HFSS is used to do the simulations. The following parameters have been analysed in details:

(i) Return Loss and VSWR

Figures 3 and 4 shows the comparison of all the return loss and VSWR obtained from the four different deigns of antenna at 2 GHz frequency range.

FR4 Glass epoxy, with dielectric constant 4.36, is simulated at 2.4 GHz frequency gives a return loss of −16 dB at 2 GHz. The FR4 epoxy gives a return loss

Table 1 Substrates with dielectric constants

S. No.	Substrate	Dielectric constant
1	FR4	4.4
2	RT-Duriod	2.2

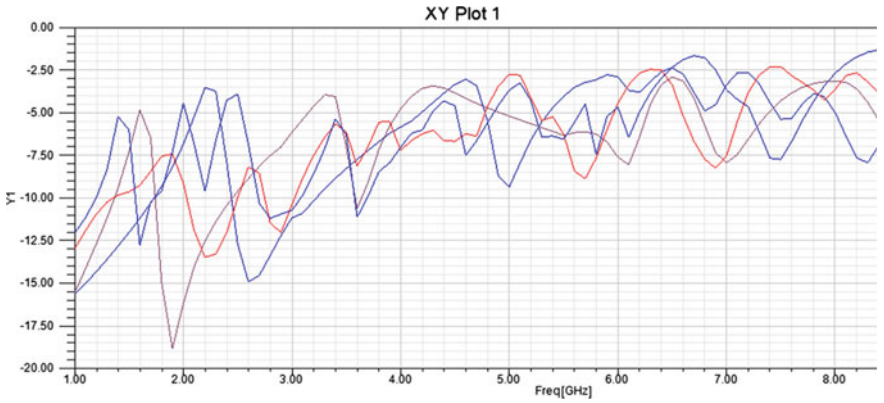

Fig. 3 Return loss characteristics

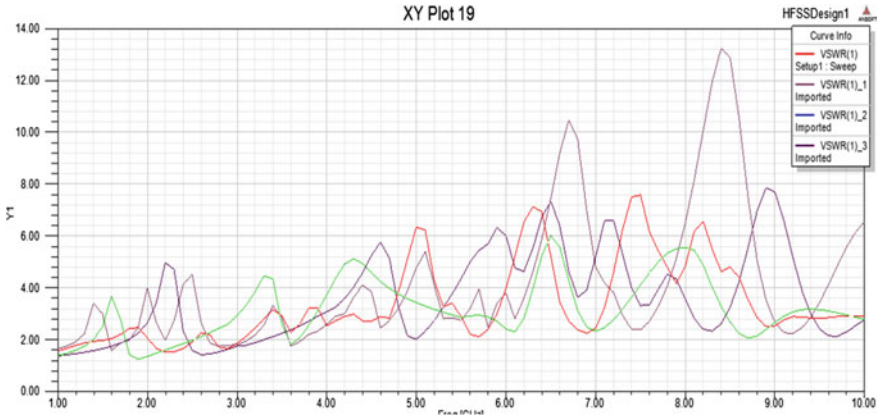

Fig. 4 VSWR comparison

of −13.8 dB at 2.2 GHz i.e. band is shifting towards the resonance frequency. RT-Duriod with metamaterial at 2.2 GHz is giving a return loss of 9.8 dB whereas at 2 GHz RT-Duriod has return loss −15.

(ii) Radiation Pattern

Figure 5a, b show the radiation pattern of the antenna. The results show that at 2.4 GHz resonance frequency range the return loss of FR4 epoxy substrate antenna is less than the RT-Duriod substrate antenna.

The radiation pattern obtained for E and H plane shows that the gain value is higher for FR4 substrate antenna than the RT-Duriod antenna. Figure 6a, b show the same substrate with metamaterial.

Table 2 shows the variation in antenna characteristics when substrate is changed.

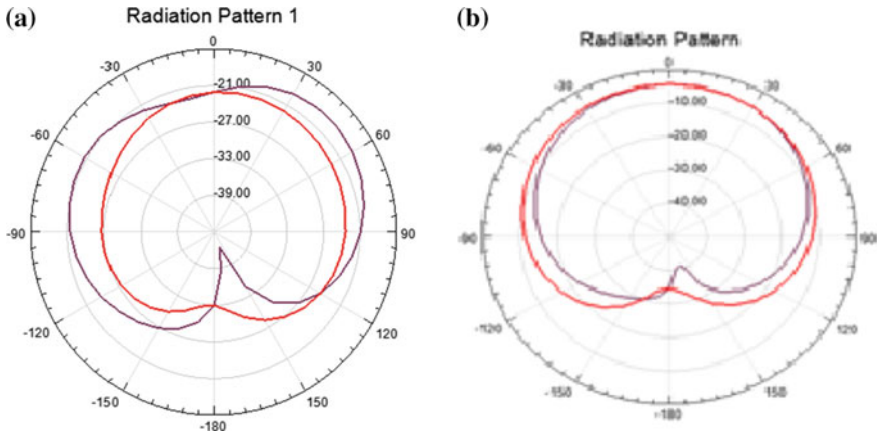

Fig. 5 **a** Radiation pattern for FR4 at 2.4 GHz in E-plane. **b** Radiation pattern for RT-Duroid at 2.4 GHz in E-plane

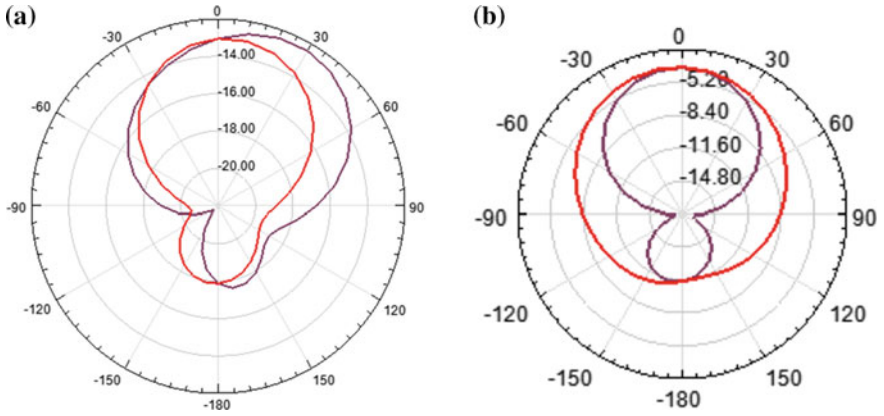

Fig. 6 **a** The radiation pattern for FR4 with metamaterial. **b** The radiation pattern for RT-Duriod with metamaterial

Table 2 Results obtained after simulation at 2.4 GHz resonating frequency

Antenna	Return loss (dB)	VSWR
FR4	−16	1.29
RT-Duriod	−15	1.2
FR4 with metamaterial	−13.8	1.2
RT-Duriod with metamaterial	−9.8	2

4 Conclusions

Two different substrates FR4 and RT-Duriod have been used for microstrip patch antenna. The design selected for antenna is fractal. It can be concluded that the performance of RT-Duriod is better than FR4 as the dielectric constant of RT-Duriod is less than FR4. We have analysed these antennas by introducing CSRR at the base of the antenna which have further improved the performance of the antennas. This metamaterial antenna provides a high gain, loss return loss, low VSWR and miniaturized size. The proposed antenna can be used for different applications.

References

1. R. Pandeeswari, S. Raghavan, Microstrip antenna with split ring complementary split ring resonator loaded ground plane for gain enhancement. Microw. Opt. Technol. Lett. **57**(2), (2015)
2. M.M. Islam, M.T. Islam, M. Samsuzzaman, M.R.I. Faruque, Compact metamaterial antenna for UWB applications. Electron. Lett. **51**(16), 1222–1224 (2015)
3. A. De, N.S. Raghava, S. Malhotra, P. Arora, R. Bazaz, Effect of different substrates on compact stacked square microstrip antenna. J. Telecommun. **1**(1), 63–65 (2010)
4. M.R. Ahsan, M.T. Islam, M. Habib Ullah, H. Arshad, M.F. Mansor, Low-cost dielectric substrate for designing low profile multiband monopole microstrip antenna. Sci. World J. **2014**, Article ID 183741, 10 pages (2014)
5. K.R. Jha, G. Singh, Analysis and design of rectangular microstrip antenna on two-layer substrate materials at terahertz frequency. J. Comput. Electron. **9**(2), 68–78 (2010)
6. H.A. Rahim, M.F.A. Malek, I. Adam, N.A.M. Affendi, N. Saudin, L. Mohamed, A.B. Ali, L.Y. Seng, P. Hall, Effect of different substrate materials on a wearable textile monopole antenna, in *2012 IEEE Symposium on Wireless Technology and Applications (ISWTA)*, 23–26 Sept 2012, Bandung, Indonesia
7. T.-C. Tang, C.-H. Tsai, K.-H. Lin, Y.-T. Huang, C.-Y. Chen, Fractal GPS antenna design on piezoelectric substrate, in *Proceedings of Asia-Pacific Microwave Conference 2010*, pp. 991–995

Dielectric Behaviour of Pure and Dye Doped Nematic Liquid Crystal E-24

Satyendra Pratap Singh, Vishal Singh Chandel and Rajiv Manohar

Abstract Dielectric behaviour of a nematic liquid crystal nematic liquid crystal mixture E-24 and its dye doped sample has been investigated in the temperature range 30–58 °C. The dielectric constant (ε′) and the dielectric loss dielectric loss (ε″) of the mixtures (pure and dye doped) have been measured in a frequency range of 100 Hz–10 MHz on a Hewlett-Packard impedance/gain phase analyzer (HP 4194-A). The dielectric study has exhibited relaxation behaviour giving rise to different relaxation frequencies for given temperatures. These frequencies have been used to calculate the relaxation time and activation energies in nematic phase of the pure and dye doped samples.

1 Introduction

Liquid crystals liquid crystals are a fascinating state of matter as they possess properties of liquids as well as of crystals. The peculiar state of liquid crystals makes them useful for many applications. The applications of liquid crystals include medical, electro optic devices, toys, etc. Major applications of liquid crystals liquid crystals are in display devices. For display applications they should have high positive anisotropy and low threshold voltage. Many liquid crystals in pure form cannot be used for device applications. So the researchers have alternative options as binary mixtures of different liquid crystals, liquid crystal doped with dyes, polymers, nano particles, carbon nano tubes, and their many combinations [1–16].

S.P. Singh (✉)
Physics Department, AIAS, Amity University, Noida 201301, India
e-mail: spsingh9@amity.edu

V.S. Chandel
Department of Physics, Integral University, Lucknow 226026, India

R. Manohar
Department of Physics, Lucknow University, Lucknow 226007, India

V.K. Jain et al. (eds.), *Recent Trends in Materials and Devices*,
Springer Proceedings in Physics 178, DOI 10.1007/978-3-319-29096-6_68

It is well known that the presence of a guest dye in a nematic liquid crystal nematic liquid crystal (NLC) affects the range of the nematic phase, the nematic-isotropic transition temperature [17].

The electro-optical parameters of the display devices depend considerably on the value of the dielectric constants and the anisotropy ($\Delta\varepsilon$), the knowledge of the dielectric properties of the dye doped liquid crystal mixtures have technical significance in display devices based on guest-host liquid crystal composites. Bauman and Haase have already shown that dielectric permittivity permittivity and the relaxation frequency of the guest-host mixture may increase or decrease depending upon the structure and the functional group associated with the dye. Our group has also published the dielectric and optical properties of pure and doped liquid crystals [18–25].

The present paper reports the study of the influence of the dye on the dielectric properties of the NLC E-24 in order to obtain more information about specific intermolecular interactions between liquid crystal liquid crystals and guest molecules.

2 Experimental Details

The sample and dye used for the dielectric measurements are nematic liquid crystal nematic liquid crystal E-24 and anthraquinone dye. The transition scheme of the sample is

Crystal $\overset{-5^0C}{\leftrightarrow}$ Nematic $\overset{54^0C}{\leftrightarrow}$ Isotropic. The sample was supplied by BDH England (BDH catalogue, 1970, BDH chemicals, pp. 19–28) and was used without further purification. The IUPAC name and chemical composition and structure of dye has already been published in our earlier paper [17].

For the measurement of dielectric constant (ε') and dielectric loss (ε'') the impedance/gain phase analyser (model No. HP 4194 A) was used.

The method for preparation of guest-host mixture and formula for calculation of dielectric parameters have also been published in our earlier paper [17]. The sample holder for planer alignment has been used and was purchased from Linkham Scientific Corporation, U.K.

A microprocessor based temperature controller Julabo (model No. F25HD) has been used for sustaining the constant temperature of the samples. The temperature controller circulates synthetic oils through its tubes and its details has also been published in our earlier paper [17].

3 Result and Discussion

Figure 1 shows the variation of real part (ε') of dielectric permittivity permittivity with natural log of frequency at two representative temperatures for the nematic mixture E-24 along with its guest-host mixture. In the lower frequency region the

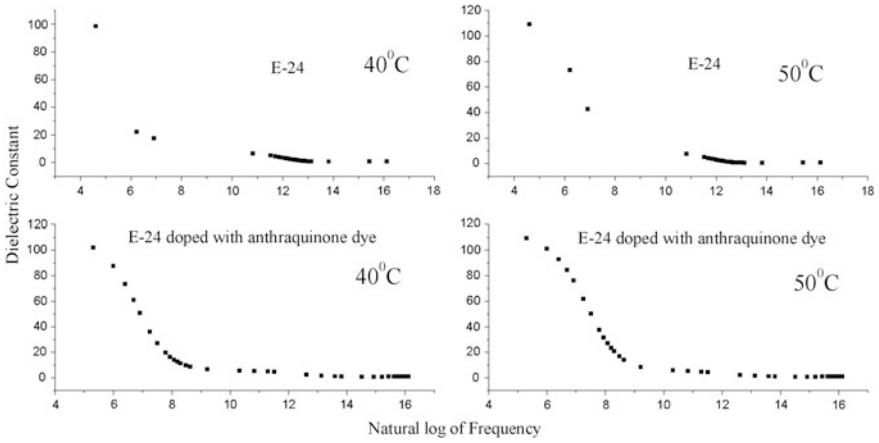

Fig. 1 Variation of dielectric constant with natural log of frequency for nematic mixture along with anthraquinone dye

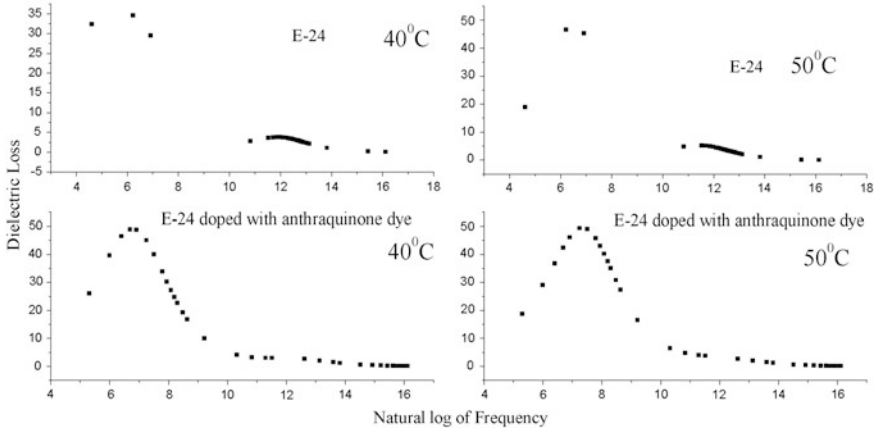

Fig. 2 Variation of dielectric loss with natural log of frequency for nematic mixture along with anthraquinone dye

value of dielectric constant ε′ is quite high for all the samples but the values of ε′ for guest-host mixture are higher than that for nematic mixture E-24 [17]. With increase in frequency the dielectric constant decreases, and in higher frequency region the dielectric constant remains almost constant for the nematic mixture E-24 as well as for guest-host mixture [17].

Figure 2 shows the variation of dielectric loss dielectric loss (ε″) with natural log of frequency at two different temperatures for the nematic mixture E-24 along with its guest-host mixture. In the lower frequency region the dielectric loss increases sharply with increase in frequency for all the samples, and attains a maximum value

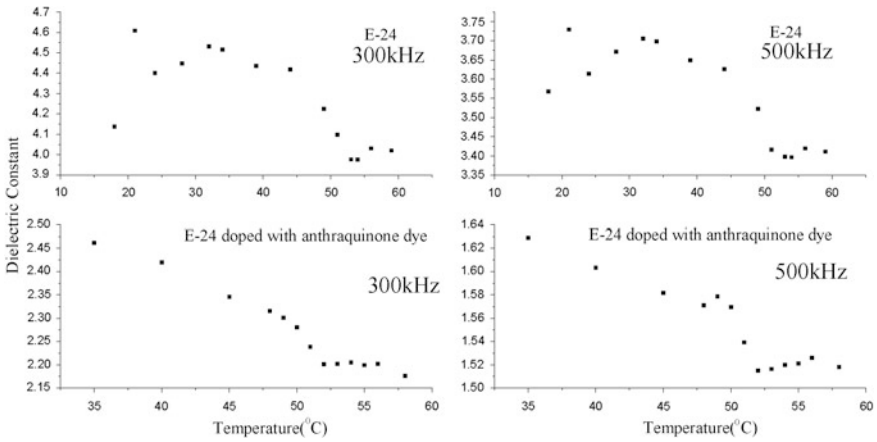

Fig. 3 Variation of dielectric constant with temperature for nematic mixture along with dye anthraquinone at two representative frequencies (300, 500 kHz)

which indicates some sort of molecular relaxation. From Fig. 2 the relaxation frequencies are found to be 538.69 Hz and 1.067 kHz for the sample E-24, E-24 doped with anthraquinone dye at temperature 54 °C respectively. The relaxation frequencies for the nematic mixture E-24 as well as for the guest-host mixtures are found to increase with increase in temperature [17]. In the higher frequency region the dielectric loss for all the samples is almost constant.

Figure 3 shows the variations of dielectric constant of the nematic mixture E-24 along with its guest-host mixture at two different representative frequencies with temperature. For all the samples the nature of the variation of dielectric constant with temperature is almost similar. For the guest-host mixture the values of dielectric constants are quite high for both the frequencies with respect to the nematic mixture E-24. The value of dielectric constant shows an abrupt change at (54 °C) for the nematic mixture E-24, while for the guest-host mixture of the same sample the change in dielectric constant value is not sharp. From the Fig. 3 it may be seen that the values of dielectric constant decreases with increase in frequency [17].

Figure 4 shows the variations of dielectric loss dielectric loss of the nematic mixture E-24 along with guest-host mixture at two different representative frequencies with temperature. The nature of variation of dielectric loss curve with temperature is almost similar for all the samples. The dielectric loss decreases with increases in temperature for all the samples [17]. The transition temperatures of the samples are not very sharp because the nematic sample E-24 is a mixture and the different components present in the sample may act as impurity for each other, while in case of dye doped sample the dye molecules probably act like impurity.

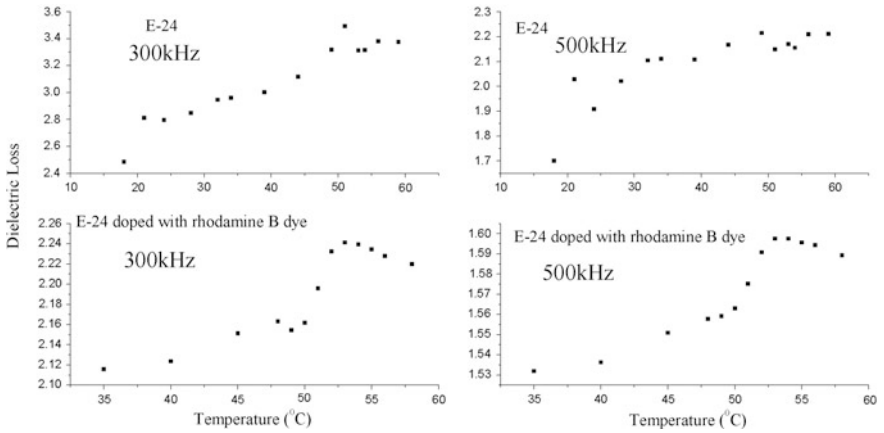

Fig. 4 Variation of dielectric loss dielectric loss with temperature for nematic mixture along with dye anthraquinone at two representative frequencies (300, 500 kHz)

The relaxation times of the nematic mixture E-24 along with guest-host mixture are also obtained from the Cole-Cole plots using the Cole-Cole modification of the Debye equation

$$\varepsilon^* = \varepsilon_\infty + \frac{\varepsilon_0 - \varepsilon_\infty}{1 + (\omega\tau)^{1-\alpha}} \tag{1}$$

where the symbols have their usual meanings. It may be easily seen that the relaxation times relaxation time obtained from direct measurement of the loss peak and from Cole-Cole plots are in good agreement. The relaxation times of the dye doped sample is different from that of the nematic mixture E-24. This type of behaviour has also been reported by other workers [17]. The change in relaxation time depends upon the concentration of the dye molecule and the compatibility of the dye molecules with the host molecules.

For the measurement of activation energy of the above mentioned samples, the Arrhenius equation is used which is given as [17]

$$f_R = h \exp\left(-\frac{E_a}{K_B T}\right) \tag{2}$$

The symbols of the (2) have their usual meanings. The cause of increase in activation energy of the guest-host mixture with anthraquinone dye may be because of the functional group associated with the dye affecting the alignment of the mixture. This type of behaviour has been also reported by [26] (Tables 1, 2 and 3).

Table 1 Activation energies of nematic sample E-24 along with its two guest-host mixtures

Sample	Activation energy (eV)
Nematic sample E-24	0.267
Nematic sample E-24 doped with anthraquinone dye	0.489

Table 2 Comparison of relaxation times relaxation time of nematic sample E-24 by two different techniques

Temperature (°C)	From cole-cole plot	From direct measurement of loss peak
40	0.00053	0.000429
45	0.000348	0.000296
47	0.000288	0.000263
49	0.000243	0.00024
50	0.000226	0.000231
52	0.001856	0.000203
55	0.000143	0.000201

Table 3 Comparison of relaxation times of nematic sample E-24 doped with anthraquinone dye by two different techniques

Temperature (°C)	From cole-cole plot	From direct measurement of loss peak
30	0.000126	0.000118
40	8.81×10^{-5}	8.3×10^{-5}
45	7.42×10^{-5}	7.08×10^{-5}
48	6.82×10^{-5}	6.56×10^{-5}
49	7.27×10^{-5}	6.3×10^{-5}
50	6.6×10^{-5}	6.29×10^{-5}
51	6.65×10^{-5}	6.2×10^{-5}
52	6.74×10^{-5}	6.15×10^{-5}
53	6.57×10^{-5}	6.09×10^{-5}
54	6.29×10^{-5}	5.98×10^{-5}
56	6.34×10^{-5}	5.9×10^{-5}
58	6.03×10^{-5}	5.94×10^{-5}

4 Conclusion

It may be concluded that the phase transitions obtained by dielectric measurement technique are in good agreement with that from the optical measurement techniques discussed in our earlier paper. The dielectric constant (ε') values for the guest-host mixture are greater than that of undoped nematic sample E-24. The dielectric loss (ε'') values are quite high at the relaxation frequencies for the guest-host mixture with respect to the nematic mixture E-24. The relaxation times obtained from different techniques are in good agreement. The relaxation times relaxation time of

the dye doped nematic sample is high enough with that of undoped sample. The activation energy is high and the possible reasons have been discussed.

References

1. M. Zennyoyi, J. Yokoyama, Y. Takanishi, K. Ishikawa, H. Takezone, K. Itoh, Jpn. J. Appl. Phys. **37**(11), 6071 (1998)
2. L.M. Blinov, V.G. Chigrinov, *Electrooptic Effects in Liquid Crystal Materials* (Springer, New York, 1996)
3. I.C. Khoo, M. Shih, M.V. Wood, B.D. Guenther, P.H. Chen, F. Simoni, S.S. Slussarenko, O. Francescangeli, L. Lucchetti, Proc. IEEE **87**, 1897 (1999)
4. S. Bartkiewicz, A. Januszko, A. Miniewicz, J. Parka, Pure Appl. Opt. **5**, 799 (1996)
5. S.E. San, O. Koysal, F.N. Ecevit, Opt. Commun. **212**, 405 (2002)
6. S.T. Wu, Phys. Rev. A **33**, 1270 (1986)
7. S. Ghosh, G.O. Carlisle, J. Mat. Sci. Mat. Elect. **16**, 753 (2005)
8. Y.S. Suleiman, S. Ghosh, M.E. Abbasov, G.O. Carlisle, J. Mat. Sci. Mat. Elect. **19**, 662 (2008)
9. I. Dierking, G. Scalia, P. Morales, J. Appl. Phys. **97**(4), 044309 (2005)
10. W. Lee, C.Y. Wang, Y.C. Shih, Appl. Phys. Lett. **85**, 513 (2004)
11. S.E. San, O. Koysal, F.N. Ecevit, S. Ozder, D. Dvornikov, Sythn. Met. **142**, 283 (2004)
12. O. Koysal, S.E. San, Sythn. Met. **158**, 527 (2008)
13. M.E. Abbaso, G.O. Carlisle, J. Nanophoton. **2**, 023510 (2008)
14. R. Manohar, S.P. Yadav, A.K. Srivastava, A.K. Misra, K.K. Pandey, P.K. Sharma, A.C. Pandey, Jpn. J. of Appl. Phys. **48**, 101501 (2009)
15. S.P. Yadav, K.K. Pandey, A.K. Misra, R. Manohar, Acta Phys. Pol., A **119**(6), 824 (2011)
16. D. Pal, P. Mishra, A.K. Mishra, R. Manohar, J.P. Shukla, Res. J. Phys. **1**(1), 10 (2007)
17. R. Manohar, S. Manohar, V.S. Chandel, Mater. Sci. Appl. **2**, 839 (2011)
18. S. Manohar, S.N. Shukla, V.S. Chandel, J.P. Shukla, R. Manohar, Trans. Elect. Electron. Mater. **14**(3), 111 (2013)
19. V.S. Chandel, S. Manohar, S.P. Singh, A.K. Singh, R. Manohar, Akademeia (Phys. Sci.). **3**(1) (2013)
20. S. Manohar, S.N. Shukla, V.S. Chandel, J.P. Shukla, R. Manohar, J. Sci. A. **20**(3), 317 (2012)
21. V.S. Chandel, A.K. Singh, S. Manohar, J.P. Shukla, R. Manohar, J. Adv. Res. Phys. **3**(2), 021203, (pages 1–6) (2012)
22. V.S. Chandel, S. Manohar, J.P. Shukla, R. Manohar, Trans. Elect. Electron. Mater. **13**(5), 221 (2012)
23. V.S. Chandel, S. Manohar, J.P. Shukla, R. Manohar, A.K. Prajapati, Mater. Sci. Poland **30**(3), 290 (2012)
24. A.K. Singh, S. Manohar, J.P. Shukla, R. Manohar, V.S. Chandel, J. Phys. Sci. **23**(2), 33 (2012)
25. R. Manohar, D.P. Shashwati, V.S. Chandel, Z.U. Mazumdar, M.K. Paul, N.V.S. Rao, Mol. Cryst. Liq. Cryst. **552**, 71 (2012)
26. D. Bauman, W. Haase, Mol. Cryst. Liq. Cryst. **168**, 155 (1989)

Study of Varying Tubes in Carbon Nanotube FET Based Inverter

Shalaka V. Bhole, Ulhas S. Sonawane, Chetan K. Kasar, Jaspal P. Bange and D.S. Patil

Abstract In today's era, Carbon Nanotubes (CNT) are becoming more popular than CMOS due to its electrical and mechanical properties. The devices using Carbon Nanotube FET's (CNTFET) provide fast switching, high electron mobility, high current density as well as high transconductance. In this paper a Stanford Leland junior universities standard mode of CNTFET is used for implementing HSPICE. This work involves study of varying number of nanotubes in CNTFET based inverter. Initially the optimization for gate oxide thickness with number of nanotubes has been done. The optimized result shows that maximum average output power of 2.0503 μW is observed with gate oxide thickness of 4 nm and 40 nanotubes. These optimized parameters were used to study effect on varying number of CNT on gain of CNT based inverter. The study reveals that increasing number of CNT's does not affect on the gain.

1 Introduction

Moor's law states that the number of transistors of an integrated circuit increases exponentially by almost doubling every two years. In today's era of nanotechnology, in electronic industry the approach of scaling MOSFET technology is being carried out. Carbon Nanotubes (CNT) are becoming more popular than Silicon based Complementary Metal Oxide Semiconductor (CMOS) due to its electrical and mechanical properties. As in CMOS technologies evolves well into short channel length, the supply voltage decreases and device characteristics deteriorate. These conditions pose severe challenges in Op-Amp designs. The transistor intrinsic gain becomes low due to inferior device output impedance. Now in order

S.V. Bhole
Department of Electronics Engineering and Technology,
North Maharashtra University, Jalgaon, India

U.S. Sonawane · C.K. Kasar · J.P. Bange · D.S. Patil (✉)
Department of Electronics, North Maharashtra University, Jalgaon, India
e-mail: patildsp@rediffmail.com

V.K. Jain et al. (eds.), *Recent Trends in Materials and Devices*,
Springer Proceedings in Physics 178, DOI 10.1007/978-3-319-29096-6_69

to ensure further improvement in FET performance with sustaining Moore's Law, it is necessary to look for alternative like Carbon Nanotube Field Effect Transistors (CNFETs) [1] that promise to deliver much better performance than existing MOSFETs. Carbon nanotube based Field effect transistor(CNFETs) is viable due to its fast switching, high electron mobility, high current density, high trans conductance than bulk silicon based CMOS and thus has become an extensive area of interest for research [2, 3]. In this paper a Stanford Leland junior universities standard mode of CNTFET is used for implementing HSPICE. This work involves study of varying number of nanotubes in CNFETs based inverter. Initially the optimization for gate oxide thickness with number of nanotubes has been done.

2 Carbon Nanotube Field Effect Transistors

Iijima observed multiwalled carbon nanotube (MWCNTs) structures in 1991 [4]. After two year's single-walled carbon nanotubes (SWNTs) have been discovered. At the time semiconducting industry was facing some problems regarding power and performance optimization, device fabrication and control of process variations at nanoscale. CNTs have been expected for Nano scale electronic devices. Metallic CNTs can be good candidate as an interconnecting wire in integrated circuits due to their ability to carry current with density up to 1×10^9 A/cm^2 [5, 6]. Perfect combination of small size, extremely high carrier mobility and long mean-free-path length, large current density, small intrinsic gate delay and high intrinsic cut-off frequency of semiconducting CNTs proves its potential in high performance nano-electronics. One of the advantage of CNTFET is it can be easily combine with the bulk CMOS technology on a single chip with utilization of the same infrastructure [7, 8].

Basically CNTs are sheets of graphene rolled into tube depending on their chirality. A SWCNT has only one cylinder. A SWCNT can act as conductor or semiconductor depending on the angle of the atom arrangement alongside the tube. This is summarized to the chirality vector and is corresponding to the integer pair (n, m). A simple technique to determine if a carbon nanotube is metallic or semiconducting is regard to its indices (n, m). The nanotube is metallic if n = m or n − m = 3i, i is an integer. Otherwise, the tube is semiconducting. Chirality and Diameter can be calculated by (1) and (2) respectively where 'a' is the grapheme lattice constant.

$$Ch = a\sqrt{n^2 + m^2 + nm} \tag{1}$$

$$D_{CNT} = \frac{Ch}{\pi} \tag{2}$$

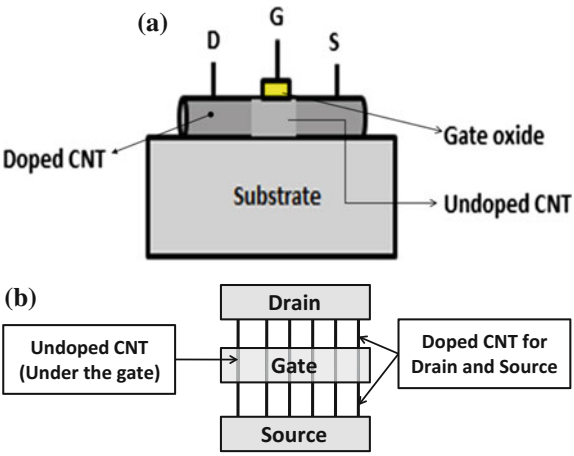

Fig. 1 Basic structure of CNTFETs

Silicon transistor restrictions avoided by CNFETs which have ballistic or near ballistic transport in their channel. Thus CNTs are appropriate to be used as the channel of field effect transistors. Electrical conductance of CNT controlled by applied biasing voltage to the gate. Threshold voltage can be achieved by appropriate diameter of CNT. Threshold voltage can be determined by following (3).

$$Vth = \frac{\sqrt{3}aV_{\pi}}{3eD_{CNT}} \tag{3}$$

where a is the carbon to carbon atom distance, V_{π} is the carbon π–π bond energy in the tight bonding model, e is the unit electron charge, and D_{CNT} is the CNT diameter.

Figure 1 shows the basic structure of carbon nanotubes field effect transistors (CNTFET). As in the silicon device CNTFET has been fabricated. Apart from that the channel has been replaced by undoped CNT. Undoped CNTs are placed under the gate and doped CNTs are placed between gate and source/drain terminals. Figure 2 represents the symbol of CNTFETs.

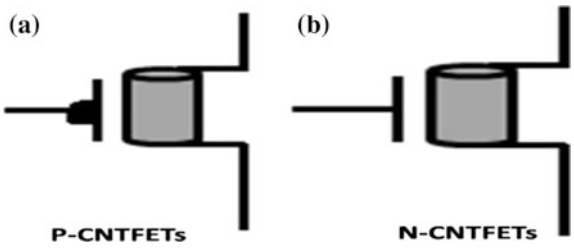

Fig. 2 Symbol of CNTFETs **a** P-CNTFET **b** N-CNTFET

3 Carbon Nanotube Field Effect Transistors Based Inverters

CMOS technology with complementary and symmetrical pairs of p-type (hole) and n-type (electron) MOS field-effect transistors is used for digital circuitry, although perfect symmetric CMOS has been never realized. As typically effective electron mass is less than that of holes the performance of n-FET is much better than that of p-FET. Besides that it has found that by the use of SWCNT as the conduction channel material, the almost symmetric nature [9]. Figure 3 shows the structures of CNFETs based inverters. As in Si-CMOS, inverter has been realized by combination of P-CNTFET and N-CNTFET. Following input output waveforms of CMOS and CNTFET based inverter confirms that both the inverters have same working.

Figure 4b clearly indicates that our model of CNTFET inverter works accurately, moreover careful observation of output waveform reveals that output has lower rise time and fall time. Here, HSPICE simulating software is used for studying the effects due to change in number of tubes on average power and gain. For the simulation a Stanford Leland junior universities standard mode of CNTFET has been used. Initially, the effect due to change in number of tubes of CNT varying from 1 to 40 on average power is studied and then by keeping tubes constant on 5

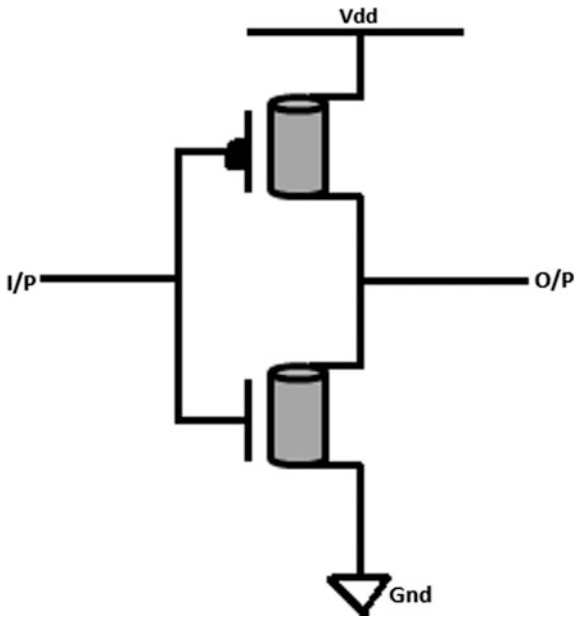

Fig. 3 Schematic diagram of CNTFETs based inverter

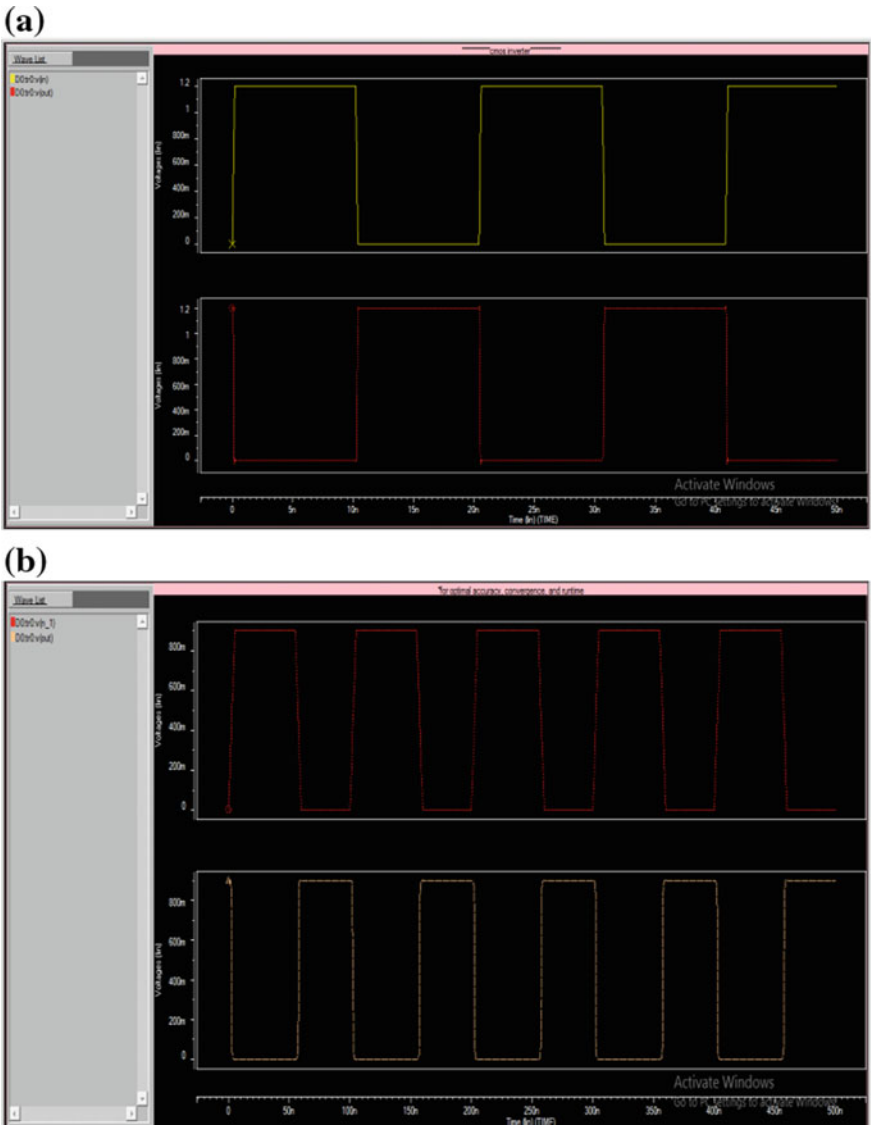

Fig. 4 Input output waveform of **a** CMOS based inverter **b** CNTFET based inverter

Table 1 Technological parameters used for simulation

Parameter	Value
Oxide thickness (Tox)	4–80 nm
Physical channel length (Lch)	32 nm
Power supply	0.9 V
Dielelctric constant (Kox)	16
Chiral index	m = 19, n = 0

and 40 the average power is studied with varying in gate oxide thickness. Following Table 1 gives the details of parameters used for simulation.

4 Results and Discussion

The effect of number of CNT on the average power of the inverter is plotted in Fig. 5. It is depicted from the figure that increasing the number of CNT in the channel gradually increases the average power of the inverter. The increase in the number of CNT increases the channel width of the CNTFETs hence the average power of the inverter increases with increase in numbers of CNT. At this point it becomes importance to optimize the channel width of the CNTFETs hence the optimization of number of CNT is carried out. It has been seen in case of gate oxide thickness that increasing gate oxide thickness decreases the average power. It was observed that for gate oxide thickness of 4 nm and 40 CNT tubes the average power obtained was maximum 2.0503 μW which is shown in Fig. 6, where T is number of tubes. These parameters are used for the study of gain of CNT based inverter.

As the process parameters like gate oxide thickness and number CNTs can be controlled it is needed to study its effect on performance of the device along with average power. The performance of CNTFET based inverter has been studied for number of CNTs and gate oxide thickness with the help of gain results.

Figure 7 demonstrates gain for varying CNT tubes in Inverter while Fig. 8 tells about gain with gate oxide variation and number of CNTs. Although both results indicate the changes in gain with process parameters it can be noted that variation is minimum. For varying number of tubes gain value changes from 15.498 to 15.586 db as in Fig. 6. In case of gate oxide thickness gain value alters from 15.414 db for one CNT and gate oxide thickness of 70 nm to 15.739 db for number of CNTs equal to 40 and gate oxide thickness of 40 nm as in Fig. 8 where T is number of tubes.

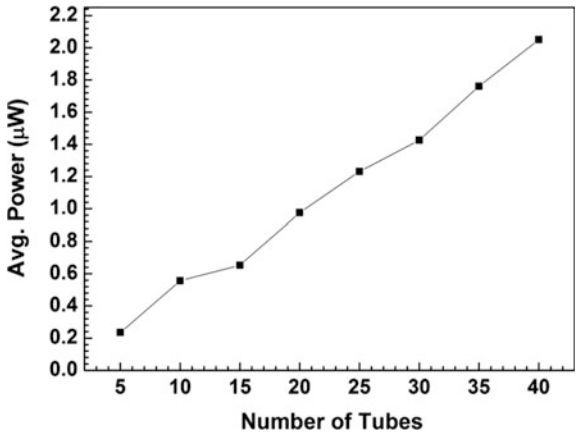

Fig. 5 Average power versus number of CNT tubes

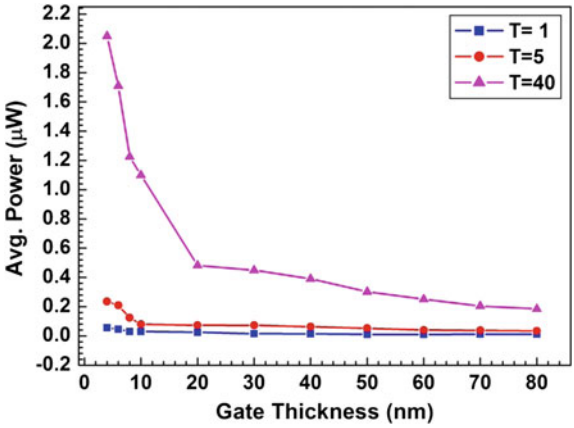

Fig. 6 Avg. power versus gate oxide thickness with varying no. of tubes

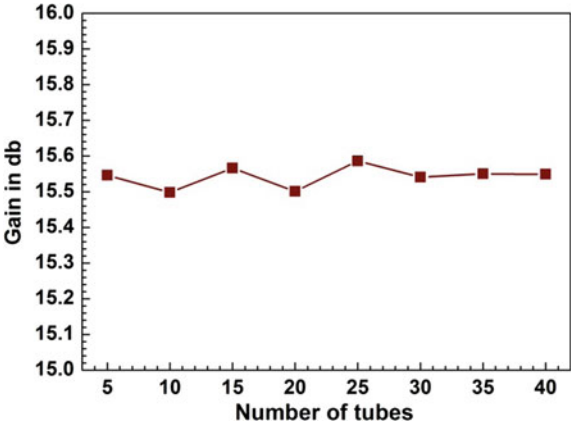

Fig. 7 Gain versus number of CNT tubes

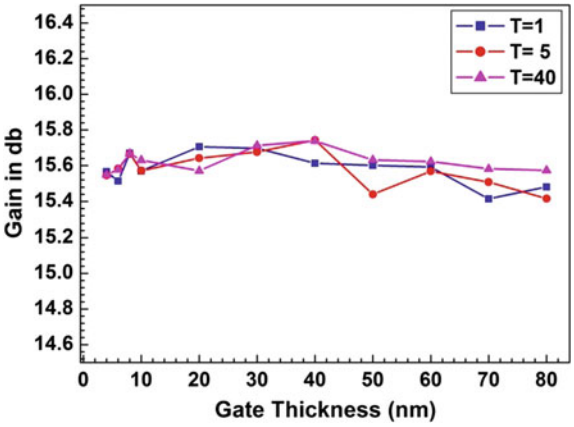

Fig. 8 Gain versus number of gate oxide thickness

5 Conclusions

We have carried out the study of CNTFET based inverter. HSPICE simulation clearly shows that CNTFET based inverter works as that of Si-CMOS inverter. The maximum average power of 2.0503 μW was obtained for inverter having gate oxide thickness of 4 nm, channel length 32 nm and 40 CNT. The study of gain reveals that change in number of tubes and gate oxide thickness has negligible effect on overall gain of the CNTFET based inverter.

Acknowledgments Authors Ulhas S. Sonawane and Chetan K. Kasar would like to thank University Grant commission, New Delhi, India for providing financial assistance to carry out this work through UGC-BSR Research fellowship scheme.

References

1. W. Wang et al., Semicond. Sci. Technol. **30**, 055018 (2015)
2. X. Liu, C. Lee, C. Zhou. Appl. Phys. Lett. 79–20 (2001)
3. M.H. Moaiyeri, R.F. Mirzaee, K. Navi, O. Hashemipour. Nano-Micro Lett. **3**(1), 43–50 (2011)
4. S. Iijima. Nature **354**, 56–58 (1991)
5. S. Frank, P. Poncharal, Z.L. Wamg, W.A. DeHeer, Science **280**(5370), 1744–1746 (1998)
6. R. Martel, V. Derycke, J. Appenzeller, S. Wind, P. Avouris. Design Autom. Conf. **39**, 94–98 (2002)
7. B. Krishan, S.K. Agarwal, S. Kumar. Int. J. Emerg. Technol. **6**(1), 24–29 (2015)
8. T. Panahi, S. Naderi, T. Heidari, E.Z. nejad, P. Keshavarzian. Int. J. Soft Comput. Eng. **2**(6), 214–19 (2013)
9. Z. Zhang, S. Wang, Z. Wang, L. Ding, T. Pei, Z. Hu, X. Liang, Q. Chen, Y. Li, L.-M. Peng. ACS Nano. **3**(11), 3781–3787 (2009)

Index

V.K. Jain et al. (eds.), *Recent Trends in Materials and Devices*,
Springer Proceedings in Physics 178, DOI 10.1007/978-3-319-29096-6